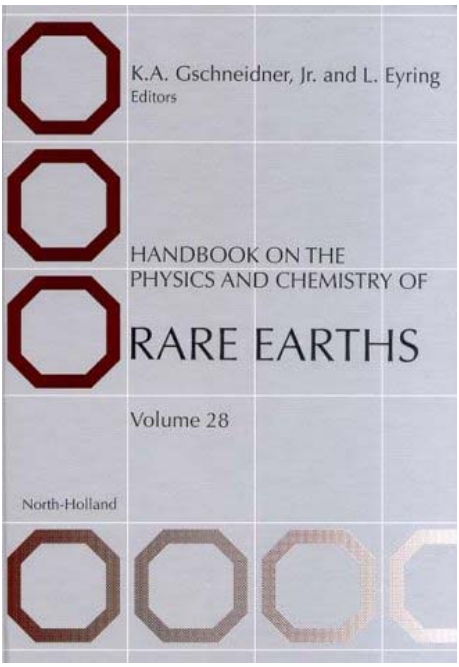

Handbook on the Physics and Chemistry of Rare Earths, volume 28

Elsevier, 2000

Edited by: Karl A. Gschneidner, Jr. and LeRoy Eyring
ISBN: 978-0-444-50346-6

Handbook on the Physics and Chemistry of Rare Earths
Vol. 28
edited by K.A. Gschneidner, Jr. and L. Eyring

PREFACE

Karl A. GSCHNEIDNER, Jr., and LeRoy EYRING

These elements perplex us in our rearches [sic], *baffle us in our speculations, and haunt us in our very dreams. They stretch like an unknown sea before us – mocking, mystifying, and murmuring strange revelations and possibilities.*

Sir William Crookes (February 16, 1887)

Even at the beginning of this new millennium the mocking mystery of the rare earths still "haunt us in our very dreams". In the filling of the 4f electronic orbitals the lanthanides defy the elementary aufbau principle that underlies the periodic sequence of the elements. J.P. Connerade and R.C. Karnatak introduce some of us to the basic physics of the "orbital collapse" leading to that failure, and explain it in terms of double-well potentials. Furthermore, this phenomenon is illustrated using the valence transitions observed in some of the rare-earth atoms, including Sm-group metals and the higher oxides of cerium, praseodymium and terbium.

G. Meyer and M.S. Wickleder have described the synthesis and structures of the many types of rare-earth halides. They have classified them as simple, complex, binary, ternary, quaternary, multinuclear complex, and other categories needed to deal with this most studied of the rare-earth compounds. The structure types are skillfully illustrated to show the elementary architecture of each type.

Once considered rare among solids, fast ionic conduction has been found characteristic of hundreds of compounds. R.V. Kumar and H. Iwahara discuss the science and application of these rare-earth superionic conductors as solid electrolytes. Conduction by oxygen and fluorine anions as well as hydrogen and other cations associated with these electrolytes are emphasized. They deal with extrinsic and intrinsic types together with their associated structures and structural types including structural defects. They conclude by outlining the many applications of these solid electrolytes.

After introducing the reader to the principles that underlie thermoluminescence and its application to dosimetry, A. Halperin provides detailed information on the R-activated phosphors that support dosimetry. This is a selective review of a copious literature based on that fraction deemed to have most advanced the field.

The analytical separation of the individual rare-earth elements utilizing chromatographic techniques is one of the heroic accomplishments of 20th century chemistry. This

achievement made available adequate supplies of pure rare-earth compounds for research and application that had not been available before. The 28 volumes in this series have begun the task of publishing the data gained by these studies and their interpretation.

K.L. Nash and M.P. Jensen have elected to build upon the broad reviews of the separation procedures available for analysis of various types of sources by describing the fundamental chemistry that underpins contemporary analytical separation techniques for lanthanide separation and analysis. This is achieved after a description of the rich assortment of separation methods in use.

CONTENTS

CONTENTS OF VOLUMES 1–27

VOLUME 4: Non-metallic compounds – II

1979, 1st repr. 1984; ISBN 0-444-85216-6

VOLUME 5

1982, 1st repr. 1984; ISBN 0-444-86375-3

VOLUME 6

1984; ISBN 0-444-86592-6

VOLUME 7

1984; ISBN 0-444-86851-8

VOLUME 8

1986; ISBN 0-444-86971-9

VOLUME 9

1987; ISBN 0-444-87045-8

VOLUME 10: High energy spectroscopy

1988; ISBN 0-444-87063-6

VOLUME 11: Two-hundred-year impact of rare earths on science

1988; ISBN 0-444-87080-6

VOLUME 12

1989; ISBN 0-444-87105-5

VOLUME 13

1990; ISBN 0-444-88547-1

VOLUME 14

1991; ISBN 0-444-88743-1

VOLUME 15

1991; ISBN 0-444-88966-3

MASTER INDEX, Vols. 1–15
1993; ISBN 0-444-89965-0

VOLUME 16
1993; ISBN 0-444-89782-8

VOLUME 17: Lanthanides/Actinides: Physics – I
1993; ISBN 0-444-81502-3

VOLUME 18: Lanthanides/Actinides: Chemistry
1994; ISBN 0-444-81724-7

VOLUME 19: Lanthanides/Actinides: Physics – II

1994; ISBN 0-444-82015-9

VOLUME 20

1995; ISBN 0-444-82014-0

VOLUME 21

1995; ISBN 0-444-82178-3

VOLUME 22

1996; ISBN 0-444-82288-7

VOLUME 23

1996; ISBN 0-444-82507-X

VOLUME 24

1997; ISBN 0-444-82607-6

VOLUME 25

1998; ISBN 0-444-82871-0

VOLUME 26

1999; ISBN 0-444-50815-1

VOLUME 27

1999; ISBN 0-444-50342-0

Handbook on the Physics and Chemistry of Rare Earths
Vol. 28
edited by K.A. Gschneidner, Jr. and L. Eyring

Chapter 176

ELECTRONIC EXCITATION IN ATOMIC SPECIES

J.-P. CONNERADE[1] and R.C. KARNATAK[2]
[1] *The Blackett Laboratory, Imperial College, London SW7 2BZ, UK*
[2] *Laboratoire de Spectroscopie Atomique et Ionique, Bât. 350, Université Paris-Sud, 91405 Orsay, France*

Contents

1. Introduction

The elements with partially filled *n*d and *n*f subshells constitute a separate group within the Periodic Table, because their properties are quite distinct. Their fundamental characteristic is that they do not follow the simple rule of the *aufbau* or building-up principle. For this reason, they are often left out of elementary discussions in courses on Quantum Mechanics, or merely referred to as complicated exceptions, whereas in fact they are a wonderful example of another class of elementary principles, namely the properties of short-range asymmetric wells. We shall refer to these elements as Q-elements, to distinguish them from the related class of rare earths (R-elements) as defined elsewhere in this Handbook.

We can arrange the Q-elements into a single separate table, which is not strictly periodic and is therefore referred to as a *quasiperiodic* table. It is interesting that this table (which will be presented and discussed in sect. 2.3) was put together not by atomic

physicists, but by scientists interested in the magnetic and conductive properties of alloys and compounds containing these elements. Note that all the elements in this table share common properties. As we will show, the underlying physics of their behaviour has a common origin.

From the standpoint of Atomic Physics, the study of the Q-elements has historically been concentrated on the complexity of their spectral structure, arising from the presence of incomplete d and f shells. This aspect was extremely important for the development of group-theoretical techniques, perfected by Racah (1942, 1943) and others, and usually referred to as 'Racah algebra'. Since these mathematical techniques find wide application in science, this aspect of the physics of these elements is well documented. Readers interested in this subject can consult the excellent text by Wybourne (1965) entitled *Spectroscopic Properties of Rare Earths.*

The present chapter does not cover complexities of atomic structure, or indeed any of the aspects discussed by Wybourne, which depend on the angular properties of wavefunctions. Rather, we concentrate on a more recent aspect of the physics of the radial Schrödinger equation, underpinning all the properties of Q- and R-elements, namely why the *aufbau* principle suddenly ceases to operate properly at certain points in the Periodic Table, i.e. the reason why it becomes necessary to consider the Q-elements as a separate group. It turns out that the physics involved is not only important in achieving their characterization as elements, but also in explaining why their behaviour is unique in terms of spectral, dynamical and chemical properties.

The origin of the physical effect (known as orbital collapse) which determines their occurrence turns out to lie, not in the angular part of the quantum-mechanical wavefunctions, but in the radial part. We therefore spend some time explaining the origin of this idea, and how it has gradually been developed into a quantitative theory.

2. Atomic properties of the Q-elements

2.1. *A brief history of 'orbital collapse'*

The peculiarities of filling of the d and f shells are a well-known complication in Atomic Physics. This is not merely a question of energy, but also of radius. When the 4f subshell is filled, this occurs deep inside the atom, i.e. well below its surface defined by the valence electrons. This is unusual, because one normally thinks of electrons being added on the periphery of the atom in the picture in which atoms are progressively 'built-up' to form the different elements in the Periodic Table. If one consults the classic textbooks on the subject (Herzberg 1937) some rather qualitative explanations are provided in terms of the screening of nuclear charge by the other electrons in the system. It was Fermi (1928) who first noticed that there was an inconsistency in this idea: it requires screening forces to act on some electrons rather than on others, and it is not clear why this should happen. Fermi also pointed out the crucial fact, which is that the electrons involved have fairly high angular momentum ($\ell = 2$ for the d sequence, and $\ell = 3$ for the f sequence). By

looking at the radial Schrödinger equation, he concluded that the centrifugal force, which adds a term $\ell(\ell+1)\hbar^2/2mr^2$ to the radial potential, might provide the explanation.

This idea was taken up by Göppert-Mayer (1941), who seems to have done the earliest *ab initio* quantitative work on the problem. She used the Thomas–Fermi model, and computed the effective radial potential (i.e. the potential including both the electrostatic term and the centrifugal term) acting on f electrons. She was able to show that this potential has a double-well structure, which becomes rather pronounced around atomic number $Z = 56$, and that the eigenfunction corresponding to the lowest state in this double-well can suddenly transfer from the outer to the inner well over a rather small range of Z. In principle, therefore, Göppert-Mayer had solved the problem of what is termed the *lanthanide contraction*. However, she was unable to explain the behaviour of the d transition elements on the same basis, and consequently her theory was not fully satisfactory. Because of this failure, qualitative arguments on screening, despite their inconsistencies, remained in vogue.

Some pioneering work was done, however, using double-well potentials, even before Göppert-Mayer: Wu (1933), in connection with the rare-earth and actinide sequence, developed a WKB model for the eigenfunctions of a potential consisting of a short-range inner well and a long-range (Coulombic) outer well. By using this model, he was able to show that the sudden change in the orbital affects not only the ground state, but also all the excited states of the system, which move together in order to preserve the Rydberg periodicity characteristic of the outer well.

A fully *ab initio* numerical treatment of this problem was first presented by Griffin et al. (1969, 1971), in two papers which established for the first time that the explanation originally advanced by Fermi and Göppert-Mayer accounts, not only for the f transition sequences, but also for the d elements, and therefore that the underlying physics is the same for all the sequences in the quasiperiodic table.

There remained the question of understanding in simple terms the meaning of the numerical solutions, and the physical origin of the transfer between the two wells. Connerade (1978a,b, 1984) presented an interpretation of the physical origin of the double minimum, together with an analytic model which explains the sudden transfer into the inner well. There was also a change in the vocabulary used to describe this effect. Initially, Griffin et al. (1969, 1971) had suggested the term 'wavefunction collapse' because of the suddenness of the transfer from the outer to the inner well as a function of atomic number. However, it was noticed that this name is unsatisfactory, because it is also used in the quantum theory of measurement with a totally different meaning. It was therefore suggested by Karaziya (1981) to call it 'orbital collapse' and this is now the accepted term.

In concluding this brief history, it is worth noting that the atomic double-well model has ramifications in the discussion of orbital localization in solids, and is therefore germane to the problems associated with valence determinations in solids and compounds containing rare earths.

2.2. *The double-well potential and its physical origin*

The concept of an effective potential involving two ranges, namely a short-range inner well and a long-range outer well, underpins the whole understanding of the properties of the Q- and R-elements. We therefore present the idea first, and refer back to it in later sections.

The physical origin of the double well is readily understood. In hydrogen, if the centrifugal repulsive term is included within an effective potential then, since it grows as $\ell(\ell+1)\hbar^2/2mr^2$, there is a repulsive potential at small radius ($r < r_0$, say) which can only expel wavefunctions of high angular momentum into the outer Coulombic reaches. At all radii, the potential is the net result of a centrifugal repulsive term, which varies as $1/r^2$ and therefore dominates at small r, and an attractive Coulombic term which varies as $1/r$ and therefore dominates at large r. In the heavier atoms, a core develops within a radius r_0. Coming in from very large radii, the potential starts off as in hydrogen. Thus, on the outside, it is a shallow Coulombic well with a repulsive shoulder around r_0. However, within r_0 the potential becomes strongly attractive, because the electron penetrates the core and sees an incompletely screened nuclear charge, leading (for heavy atoms) to a deep inner well with a fast-rising repulsive wall near the centre, where the repulsive term (which varies as $1/r^2$) must eventually win. The inner valley is a short-range well and (like all short-range potentials in physics) can support only a finite number of bound states. If the well is 'squeezed' these states rise into the continuum and become virtual states or short-lived resonances. In this respect, its behaviour is quite different from that of the long-range outer or Coulombic well, which supports an infinite number of bound states, because these can never cross above the threshold and rise into the adjoining continuum.

Since the centrifugal term is present in the radial Schrödinger equation for *all* atoms, we must appreciate why centrifugal effects only dominate the inner valence spectra of fairly heavy atoms. Centrifugal barrier effects are of course present even in hydrogen, but result in very different properties from those of the transition elements or lanthanides.

One reason is very straightforward: the ground state of H has $\ell = 0$, and therefore only p states are accessible directly by a dipole transition from the ground state. For $\ell = 1$, the centrifugal barrier term is small at the mean radius of the np electrons, so centrifugal effects do not intrude in the spectra. The other, more profound reason, is the emergence of the electronic core in heavy atoms, which leads to a noncoulombic potential, and its interplay with the repulsive centrifugal barrier.

2.3. *The quasiperiodic table*

In solids, one emphasizes the distinction between *localized* and *itinerant* states. In a localized state, the electron remains attached to an individual atomic centre, whereas, in an itinerant state, it may move throughout the lattice. Under circumstances governed by the nature and excitation state of the atom or ion a given orbital can be poised at the critical point where it will live in either the inner or the outer reaches for small changes in the environment. In solid-state physics, this gives rise to a first-order Mott transition.

Table 1
The quasiperiodic table of Smith and Kmetko

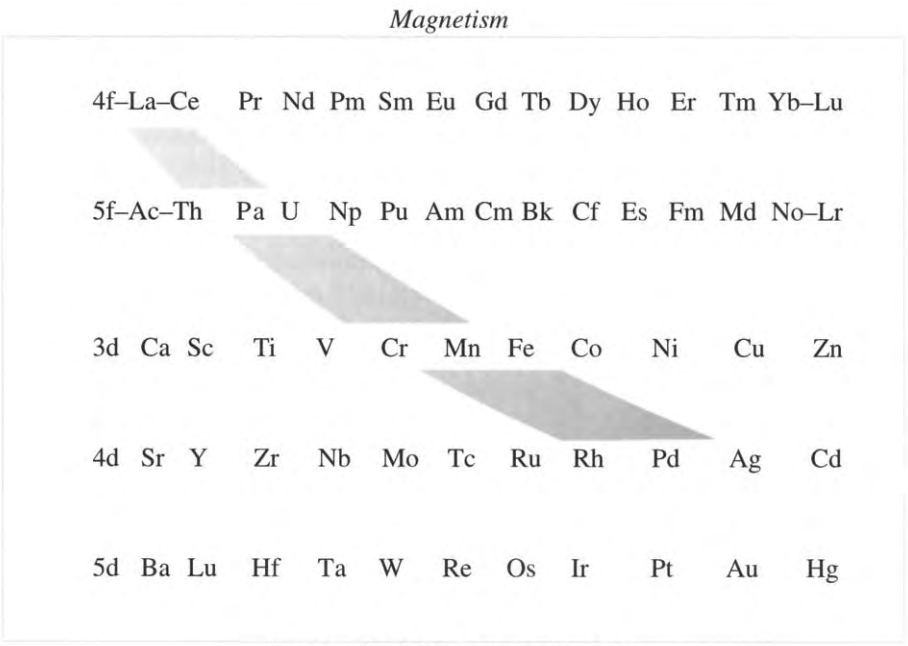

This table was derived from empirical data on conductivity and magnetism in solids. A broad sweep across the table from La and Ce through Pa and U, Mn and Fe to Pd and Ag maps the transition between localised and itinerant behaviour in the solid, and the elements which lie on it tend to have sensitive (e.g. pressure-dependent) properties. However, they are also remarkable in atomic physics for their giant resonances, are noted catalysts, or provide good materials for H storage, and then exhibit photon-stimulated desorption peaks which replicate the giant resonance profiles. Many of these properties seem to depend on the critical localisation of f and d electrons.

This situation is clearly a manifestation of orbital collapse, and it is therefore no surprise that it occurs for the Q and R: the inner well is essentially atomic, and conditions of near-critical binding for the inner well tend to persist from the atom to the solid. If a solid is built up from free atoms with a double-well potential and orbitals in the outer well, the latter hybridize easily, the external part of the orbital going into itinerant states. If one forms a solid from atoms with collapsed orbitals, then these will remain localized.

An example of this kind of transition is shown in table 1, taken from the work of Smith and Kmetko (see Boring and Smith 1987). It is a *quasiperiodic table* of all the transition elements and lanthanides arranged in order of mean localized radius in the vertical direction, and adjusted horizontally so that the lengths of d and f periods coincide. What Smith and Kmetko discovered is that a broad diagonal sweep across this table extending from Ce to Pd separates metals with localized electron properties (magnets) from those

with itinerant electron properties (conductors). This boundary (shown as a shaded area in the table) is the locus of the Mott transition between localized and delocalized states. Metals lying on this boundary are sensitive to pressure effects (Ce has an isomorphic phase transition from the α to the γ phase at about 1 kbar, becomes superconducting under pressure, etc). Many of them are noted as good catalysts or good H storage materials.

It is believed that these properties are connected. To the atomic physicist, the Smith and Kmetko table is also significant: the broad sweep across the table is related to the emergence of giant resonances, i.e. to the properties of the inner well of the double-well potential. More specifically we can interpret it as a frontier between two conditions: to the left, the electrons are delocalized, while to the right, they tend to be localized. This behaviour can also be inferred from the spectra. If we move down the table, then we notice that the order in which the sequences are arranged is not the normal ordering of the Periodic Table. In fact, it is the order of decreasing localization: the average radius of the 4f subshell is smallest, the 5f is larger, etc. Thus, the crucial property is seen to be the size of the subshell being filled, whereas, in the Periodic Table, the ordering of the rows is determined by the natural order of the quantum numbers, i.e. the table is treated as strictly periodic.

2.4. *Filling of the d subshells*

The filling of the d subshells is at first sight a more complicated affair than for f subshells, and this must also be explained. The explanation turns out to be quite simple: since $\ell = 2$ for d electrons, the $\ell(\ell + 1)\hbar^2/2mr^2$ term is smaller by a factor of two for a given radius than for f electrons. Consequently, the positive repulsive barrier has less effect. As a result, instead of two wells, clearly separated by a positive barrier, one has two wells of different range, with a 'knee' between them which does not rise to a positive value (fig. 1). In essence, the problem remains a double-well situation, but with less spatial segregation between the two classes of solutions. It follows that orbital collapse is less dramatic, and takes place over several adjacent elements, rather than suddenly and between two successive elements.

It is also a more subtle effect, which is why Göppert-Mayer (1941) had difficulty computing it by using the Thomas–Fermi model. Griffin et al. (1971) in their numerical study found that the mean radius of the 4s electron in the 3d sequence lies very close to the 'knee' between the two wells. Thus adding a 4s electron has a profound effect on the 3d effective potential, which accounts for the otherwise mysterious effect known as 'competition' between the filling of the d and s subshells.

2.5. *Potentials from ab initio theory*

Once it had come to light that the Mayer–Fermi theory is quite general, it was of interest to study radial potentials for both f and d electrons obtained from *ab initio* calculations.

In fig. 2, we show the double-well radial potential as computed by Griffin et al. (1969) for elements with $Z \approx 56$. Note that the radial scale used in plotting this figure is

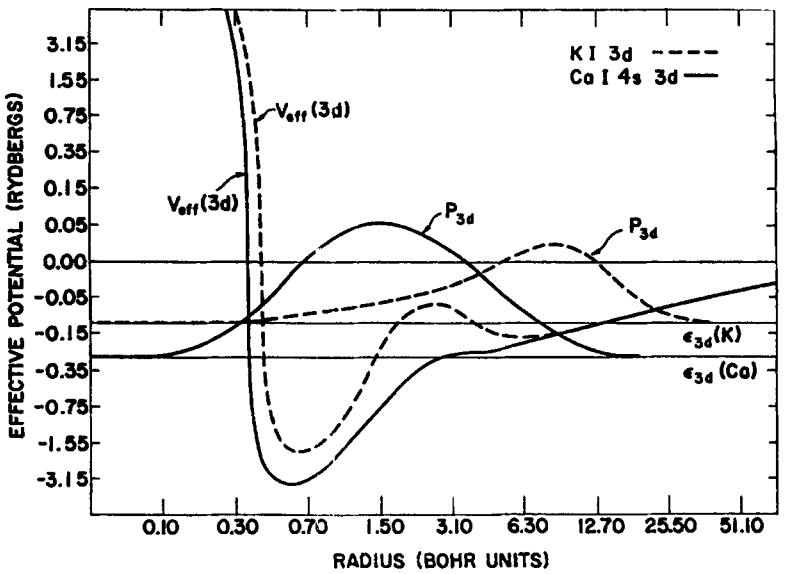

Fig. 1. The effective radial potential for 3d electrons, showing the knee at the edge of the inner well. After Griffin et al. (1971).

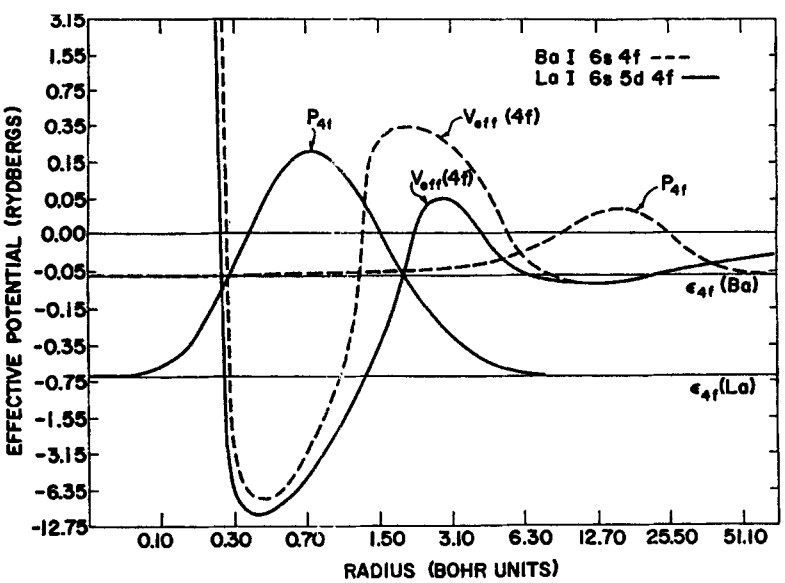

Fig. 2. The double-well radial potential for 4f elements close to the point at which orbital collapse occurs. Note the highly nonlinear scales on both axes, designed to show as much detail as possible for both wells. After Griffin et al. (1969).

highly nonlinear, so as to bring both wells within a small range, for clarity, and to show how small changes in the wells can precipitate a very large change in the radius of the 4f wavefunction: from a radius of about 13 atomic units in Ba I, it collapses to a radius of about 0.3 atomic units in La – a dramatic and very sudden contraction, since it occurs for a change in atomic number of just one unit.

2.6. *The d sequences*

We can draw up a table of filling in the d sequences as follows: As noted above, the exact point at which collapse occurs depends rather critically on the radial charge distribution. Since s–d competition depends on the radial equation and on the balance between the two wells, it does not necessarily repeat in the same way in each period, and indeed there are anomalies in the order of filling which derive from this fact. For instance, there is only one element in the whole Periodic Table (Pd) which has a closed outermost $4d^{10}$ subshell.

A good way to illustrate the breakdown of the *aufbau* principle is to draw up a table of configurations not only for the ground states of the atoms, but also for the corresponding ions. From table 2, one can see that, usually, it is easier to ionise the outermost s than the outermost d electron. The exceptions are:

(1) Pd: as just noted, the only element with a closed outer subshell which is neither s^2 nor p^6.

(2) Y, for which it is easier to ionise 4d than 5s: this is not unexpected from the order of filling, since 4d was also the 'last electron' in the building-up process.

(3) V, Co, Ni and La, *for which it is impossible to remove one electron from one occupied orbital and leave the ion in its ground configuration.*

Table 2
Ground state configurations of the d transition elements

3d period			4d period			5d period		
T	Atom	Ion	T	Atom	Ion	T	Atom	Ion
Ca	$\ldots 4s^2$	$\ldots 4s$	Sr	$\ldots 5s^2$	$\ldots 5s$	Ba	$\ldots 6s^2$	$\ldots 6s$
Sc	$3d4s^2$	$3d4s$	Y	$4d5s^2$	$\ldots 5s^2$	La	$5d6s^2$	$\ldots 5d^2$
Ti	$3d^24s^2$	$3d^24s$	Zr	$4d^25s^2$	$4d^25s$	Hf	$5d^26s^2$	$5d6s^2$
V	$3d^34s^2$	$3d^4\ldots$	Nb	$4d^45s$	$4d^4\ldots$	Ta	$5d^36s^2$	$5d^36s$
Cr	$3d^54s$	$3d^5\ldots$	Mo	$4d^55s$	$4d^5\ldots$	W	$5d^46s^2$	$5d^46s$
Mn	$3d^54s^2$	$3d^54s$	Tc	$4d^55s^2$	$4d^55s$	Re	$5d^55s^2$	$5d^56s$
Fe	$3d^64s^2$	$3d^64s$	Ru	$4d^75s$	$4d^7\ldots$	Os	$5d^66s^2$	$5d^66s$
Co	$3d^74s^2$	$3d^8\ldots$	Rh	$4d^85s$	$4d^8\ldots$	Ir	$5d^76s^2$	–
Ni	$3d^84s^2$	$3d^9\ldots$	Pd	$4d^{10}\ldots$	$4d^9\ldots$	Pt	$5d^96s$	$5d^9$
Cu	$3d^{10}4s$	$3d^{10}$	Ag	$4d^{10}5s$	$4d^{10}$	Au	$5d^{10}6s$	$5d^{10}$
Zn	$3d^{10}4s^2$	$3d^{10}4s$	Cd	$4d^{10}5s^2$	$4d^{10}5s$	Hg	$5d^{10}6s^2$	$5d^{10}6s$

2.7. *Breakdown of the independent particle model*

Case (3) is actually the most interesting, because it demonstrates most clearly the connection between breakdown of the *aufbau* principle and the appearance of many-body effects: excitation of one electron to an extended orbital in V, Co and Ni *must* be accompanied by a rearrangement of the parent ion core. In other words, for these three elements, one cannot specify which electron (3d or 4s) should be removed 'first'. Whichever is chosen, the result would be to leave the ion in an excited state.

The only possible explanation for this behaviour is that the 3d and 4s labels do not describe an individual electron correctly. Thus, *either* the configuration labels, *or* the notion that individual electrons can be excited, have broken down, which means that single-particle orbitals cannot really be defined in this region of the Periodic Table. In other words, it is no longer possible to identify individual particles with specific orbitals. Although this is an extreme example of this type of breakdown, there are many other situations where a confusion between the nature of two one-electron labels can arise, especially involving s and d electrons. Indeed, it is a general property of rare earths that many-body theory becomes necessary for a quantitative interpretation of their excitation spectra.

Without entering the full complexity of the theory, it is worth noting that there will be no such thing as a regular Rydberg series converging to the ground state of the ion in V, Co or Ni, and this is in line with the notion that a regular Rydberg series is associated with electrons behaving independently of each other.

2.8. *Homologous orbital collapse*

So far, we have discussed orbital collapse as an effect occurring *across* the Periodic Table. However, centrifugal barrier effects grow as one moves to heavier elements, and this suggests that one should also study orbital collapse *down columns* of the table. The difficulty in doing this is that we can assume small changes in the electrostatic potential occur in moving from one fairly heavy element in the Periodic Table to the next one, but we can no longer make such an assumption when moving from one row to the next. We therefore need some index or measure of the strength of the central field.

This problem has been addressed by Connerade (1991) who showed that the d sequence in particular possesses an internal marker through the binding energies of the ns and, to a lesser degree, the np states, which undergo no dramatic changes as a result of orbital contraction and, indeed, in the case of ns states, experience no centrifugal force whatsoever. One can therefore define a dimensionless number ξ which is simply the ratio of the binding energies of such states to the binding energies of the corresponding states in hydrogen. The value of ξ is not very dependent on which of these states is chosen but, in order to have just one value for each element and to be sure it is a comparable measure, one should define it the same way in all cases, for example, by using the binding energy for elements or ions with just one outermost ns electron in the ground state.

Once this has been done, a plot of bound state energies against ξ yields: (i) in the case of ns and even np states, a set of nearly straight lines, showing that these energies

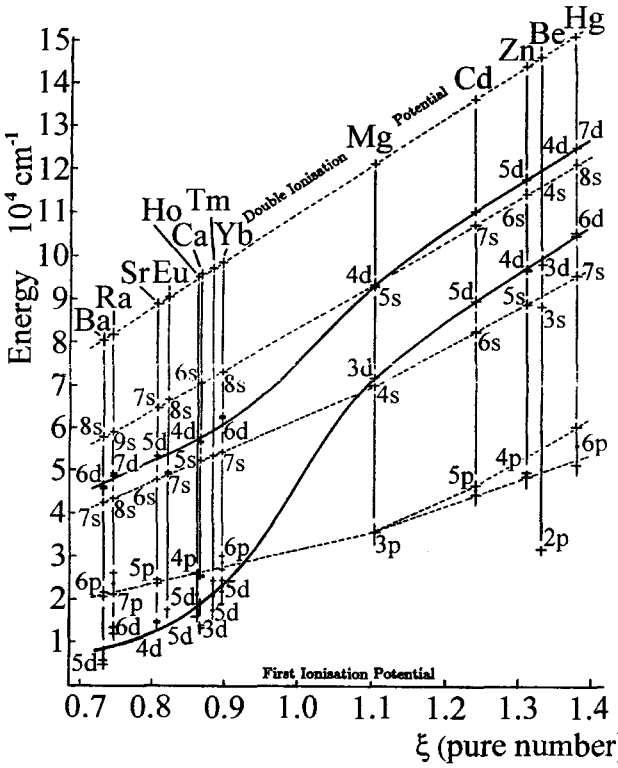

Fig. 3. Orbital collapse in an extended homologous sequence (see text for details). After Connerade (1991).

depend only on electrostatic screening; and (ii) in the case of *n*d states, curves which may suddenly cross over the grid of *n*s and *n*p lines whenever orbital contraction occurs. Such a graph is shown in fig. 3. The advantage of having a measure ξ of the electrostatic binding strength is that we are no longer confined to a single homologous sequence. Consider, for example, the sequences of singly charged ions of Zn, Cd and Hg. Quite clearly, we may consider them alongside the singly charged ions of Ca, Ba and Sr, since all of them involve an s electron in the ground state, and refer their binding energies to the singly charged ion of He. Such a plot is called an *extended homologous sequence* (Connerade 1991), and has the advantage that much more information may be included in a single graph, thereby allowing one to track orbital collapse systematically over a wide range of electrostatic binding strengths.

Such graphs provide a wealth of information. First, they explain the difference in character and chemistry of different sequences of elements which are otherwise apparently very similar if one merely looks at the angular wavefunctions or configuration labels. Second, they allow us to understand how orbital contraction is controlled from within the atom. Externally, all the atoms in the plot are similar: an electron in the outer reaches

of the atom always sees more or less the same effective nuclear charge. The differences between the atoms are due entirely to differences in the core as a function of atomic number.

2.9. *The f sequences*

A classification of lanthanide or rare-earth elements based on the number of 4f electrons in the atomic and condensed phases is presented in table 3.

We also present, in table 4, the changes Δn_f in the number of 4f electrons for these elements between the atom and the solid (Connerade and Karnatak 1990). It is interesting to note that, in table 4, seven out of fourteen rare-earth elements show valence changes in various environments of the solid. This in itself is a strong indication that valence instabilities are related to the quantum chemistry of this part of the Periodic Table. We can classify the elements presenting valence problems into two broad groups, based on

Table 3
Classification of the lanthanides according to the number of 4f electrons in the atom and the solid[a]

R	Z	Atom		Solid		R	Z	Atom		Solid	
		p	q	p	q			p	q	p	q
La	57	0	3	0	3	Gd	64	7	3	7	3
Ce	58	2	2	1	3	Tb	65	9	2	8	3
				0	4					7	4
Pr	59	3	2	2	3	Dy	66	10	2	9	3
				1	4	Ho	67	11	2	10	3
Nd	60	4	2	3	3	Er	68	12	2	11	3
Pm	61	5	2	4	3	Tm	69	13	2	13	2
Sm	62	6	2	6	2					12	3
				5	3	Yb	70	14	2	14	2
Eu	63	7	2	7	2					13	3
				6	3						

[a] Values of p and q in the electronic configuration $\overline{\text{Xe}}4f^p(5d6s)^q$ are given, where p is the number of 4f electrons and q is the number of valence electrons; R stands for a rare earth.

Table 4
Changes of valence Δn_f from the free atom to the solid

Δn_f	Rare earths
0	La,Gd
−1	Nd, Pm, Dy, Ho, Er
0 or −1	Sm, Eu, Tm, Yb
−1 or −2	Ce, Pr, Tb

the knowledge of their electronic configuration and known chemical valence, namely Sm, Eu, Tm and Yb (for which divalent and trivalent compounds exist) and Ce, Pr and Tb, which form a series of higher oxides.

2.9.1. *Divalent Sm, Eu, Tm and Yb*

The elements Sm, Eu, Tm and Yb, in which $|\Delta n_f|$ may be 1 or remain zero, exhibit characteristic spectroscopic features. Both divalent and trivalent compounds of Sm, Eu, Tm and Yb exist. The $3d \rightarrow 4f$ spectra of these compounds are found to be characteristic of the number of 4f subshell electrons present. The change from divalent to trivalent forms is accompanied by the delocalization of the 'last' electron, which enters into ionic bonding of the 3d–4f multiplet with one 4f electron removed from the 4f subshell.

These elements possess well-developed multiplet structure in the soft X-ray spectra of the condensed phase, which can be compared with the spectrum of the free atom: by performing *ab initio* Dirac–Fock calculations, the actual 4f occupancy in the solid can be deduced. An example is shown in figs. 4 and 5. The first point to note is that the multiplet structure of the atom survives in the solid, because of the strong localization of the 4f electrons, so that soft X-ray spectroscopy provides a useful probe of the 4f occupancy. To emphasize this point, we show, in fig. 4, a comparison between spectra of Sm vapour and Sm in the solid phase, which reveals the great similarity of structure between them. A multiconfigurational atomic structure calculation (fig. 5; Sarpal et al. 1991) demonstrates that, even in this complex situation, it is possible to deduce from *ab initio* atomic structure calculations what the 4f occupancy is.

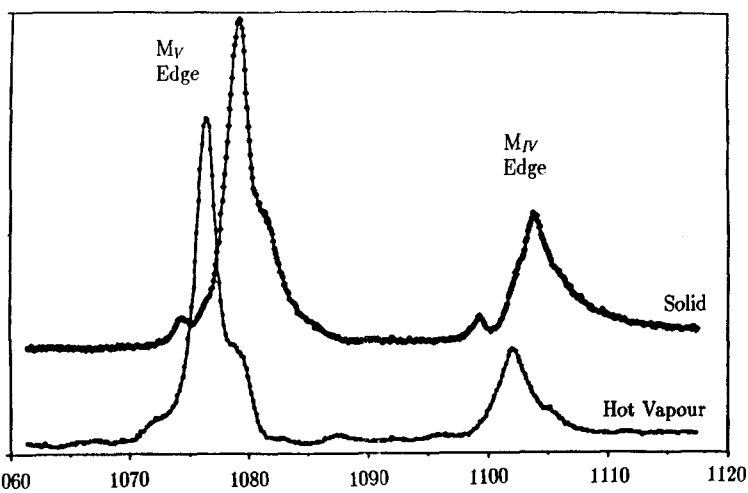

Fig. 4. The 3d spectra of Sm in the solid and hot vapour phases. Note the close correspondence of structure and the slight energy shift between them. Amongst other features, this comparison demonstrates the persistence of atomic multiplet structure in the spectrum of the solid. After Connerade and Karnatak (1990).

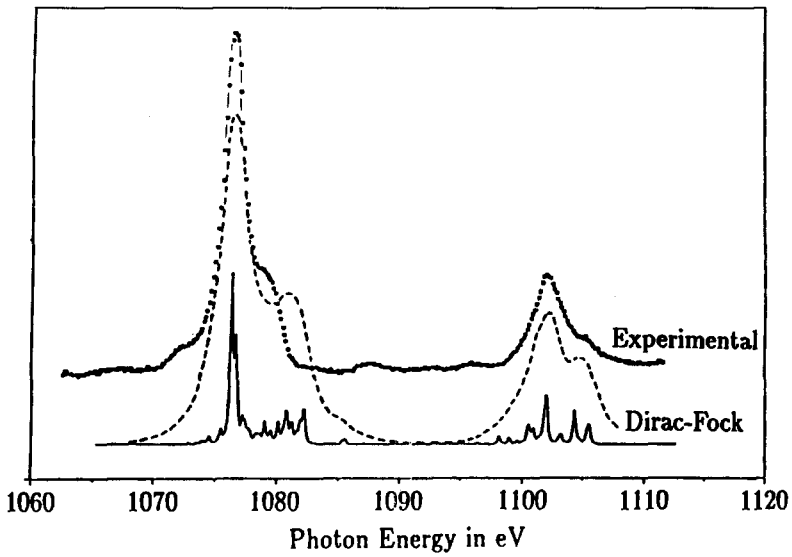

Fig. 5. The inner shell absorption spectrum of Sm vapour. Also included are results of multiconfigurational Dirac–Fock calculations for the free atom. After Connerade and Karnatak (1990).

The details of this approach, in which atomic properties are used to assist in the understanding of changes which occur in condensed matter, will be discussed more fully in sect. 3 below.

3. From the atom to the solid

In sect. 1, we considered how particular mechanisms affect the behaviour of d and f orbitals in free atoms. We now turn to the question of how these atomic properties are modified when dealing with the atom in the solid. A crucial aspect of rare earth physics is the persistence of quasi-atomic spectral multiplet structure in the solid. To explain this, we first note that a collapsed orbital, localized in the inner reaches of the atom, will tend to survive as a localized atomic orbital in the solid, whereas an orbital which lies in the outer reaches of the atom (or: in the outer well of the double-well potential described above) will be completely modified, and may hybridize with the conduction band.

We are thus faced with a complex situation. Orbital collapse survives in the solid, but the orbitals are only truly atomic in the fully collapsed condition. This provides us with a very useful experimental tool to probe the spectra of rare-earth elements, but is also a formidable challenge when one has to account for the complete situation. For the moment, the important point to note is that *orbitals recover their atomic character even in the solid once collapse has occurred.* It also follows that the depth and width of the inner well of the quasi-atomic double-well potential continue to play a crucial role in the solid.

Our approach to study the valence problem in rare earths is to search for its origin in the atomic phase and attempt to uncover a universal mechanism for the valence transition in these elements. As already noted in sect. 2.9, Connerade and Karnatak (1990) proposed a classification of the R based on the number of 4f electrons in the atomic and in the condensed phases (table 3) and on the change $|\Delta n|$ between the two (table 4). From table 4, seven out of fourteen R exhibit valence changes in certain environments of the solid. The elements presenting valence problems form two broad groups, based on the knowledge of their electronic configuration and known chemical valence. Thus, nature provides the strongest possible hint that valence instabilities are related to the underlying atomic physics in of this part of the Periodic Table.

3.1. *Multiplet structure*

Core-level spectroscopies are the appropriate tools to study the electronic distribution around free atoms and the changes induced in this distribution on condensation or on the formation of compounds involving other elements. These spectroscopies are also very useful to track the formation of clusters which finally coalesce to form well-defined solid phases. For the R, X-ray absorption spectroscopy is very useful because of the simplicity of the final multiplet structure, as the transitions obey dipole selection rules. Generally, two types of transitions are observed: one in which the 4f electron participates in the transition and another in which it remains as a spectator. In the former case, a transition of a d electron to the empty f shell is involved. This leads to the formation of the $nd^{10}4f^{n}$–$nd^{9}4f^{n+1}$ ($n = 3, 4$) multiplets which are in fact 'finger prints' of the R atom configurations. In the same way, the transitions from p levels scan the empty sd states of the conduction band.

In the above paragraph, we have purposely neglected the outer valence electron configuration in describing the *n*d–4f excitation transitions. The reason for this is simply that the 4f electrons generally behave as core electrons. For example, the metallic Eu and Gd which have two and three valence electrons respectively show similar atomic 3d–4f multiplets. So, the transitions involving $4f^7$ electrons can be considered as taking place in Eu^{2+} and Gd^{3+} ions. The 4d→4f absorption spectra of Eu vapour contained in a high-temperature furnace tube were first obtained by Mansfield and Connerade (1974) at the Synchrotron Facility in Bonn. The spectra of atomic Eu were found to be similar to those obtained by Zimkina et al. (1967) for Eu solid. This work was further extended to La and Tm (Radtke 1979a) and to the group of elements Pr, Nd, Sm, Tb, Dy, Ho and Er (Radtke 1979b) by using high-temperature, inductively heated furnaces. The vapour 4d–4f spectra of these elements were found to be similar in shape to those from the corresponding $(Z + 1)$ elements in the solid state. Due to the increase in nuclear charge, the spectra of $(Z + 1)$ elements in the solid state were shifted to higher energies with respect to those of Z elements in the atomic vapour. These observations correspond well with the data in the table on R configurations in atoms and solids obtained by magnetic and other spectroscopic studies. The R elements showing valence change yield different spectra. This is due to the change in the number of 4f shell electrons. Here again, the valence

states in different species forming an isoelectronic sequence yield similar spectra. For example, divalent Eu, trivalent Gd and tetravalent Tb give similar 3d–4f spectra. Similarly some of the spectral features of tetravalent Ce correspond well to those of trivalent La. For R elements near the beginning, middle and end of the R series, in certain chemical environments, some modifications in the spectral features due to the instability of the 4f shell are experienced. The temperature and pressure can be the origin of such instability in certain cases.

The ground-state properties of such solids, in relation to the instability of the 4f shell, define a subject area spanning a wide field of solid-state Physics and Chemistry.

On the theoretical side, the calculation of *n*d atomic multiplets attracted much interest in the past. Although the observation of multiplet structure in the 3d absorption spectra of rare-earth elements dates back to Lindberg (1931), it is only in the early 1970s that the penetration by the 4f wave function of the centrifugal potential barrier was invoked (Sugar 1972, 1974) to account for the rich photoabsorption structure in the vicinity of *n*d edges. Since then, several reports (Demekhin 1974, Bonnelle et al. 1974, 1977) on the observation and interpretation of *n*d–4f transitions in these elements appeared. Atomic calculations of the $nd^9 4f^{n+1}$ multiplets were performed by considering the initial state effectively as a triply-ionized free atom in the ground state. The energy matrices of $nd^9 4f^{n+1}$ are diagonalized with scaled Hartree–Fock (HF) values for the Slater–Condon parameters, and a value for the nd^9 spin–orbit parameter is estimated from X-ray data. The eigenvectors are used to calculate line strengths of the $nd^{10}4f^n$–$nd^9 4f^{n+1}$ transition array from LS to intermediate coupling, so as to predict the experimental line intensities. The energy eigenvalues are then fitted to the observed peaks by suitably scaled values of the HF G^1(df) and ζ_d Slater–Condon parameters.

It is interesting to note that the extensive overlap of the 4d and 4f orbits leads to a large exchange interaction, and results in a large splitting of the $4d^9 4f^{n+1}$ configuration. In the case of photoabsorption in the vicinity of the 3d edges, the 3d–4f overlap is much smaller than for 4d–4f, and the exchange integral is correspondingly much smaller. Due to dominant 3d spin–orbit interaction, the absorption lines cluster about the expected positions of the M_{IV} and M_V edges. In this situation, the lines are easier to identify than those arising from 4d–4f transitions. Consequently, in the present chapter, we will deal mainly with 3d–4f transitions.

It is worth mentioning here that the multiplet line structure is very simple at the beginning and the end of the R sequence. La, in the beginning of the R, shows only three 3d–4f transitions allowed by dipole selection rules. For trivalent compounds of Yb, only one transition is allowed. As we go to the middle of the R sequence, the number of transitions increases from 53 in Ce to 1077 in Gd. On the other side of Gd, it falls to 4 in the case of Tm. In earlier papers, because of the presence of a large number of spectral lines in the multiplet structure implying heavier computational effort, some simplifications were employed in the calculations. The intensities of lines under a certain small value were ignored. It was only in 1985, using Cowan's code, that complete 3d–4f atomic multiplet calculations were performed in intermediate coupling, including all the states of the configuration $4f^n$ for the ground state and $3d^9 4f^{n+1}$ for the excited

state (Thole et al. 1985) for all the rare-earth ions and for all ionization states known to be relevant to the solid state. The electrostatic and exchange parameters were all scaled down to 80% of their Hartree–Fock (HF) values. The spin–orbit parameter was adjusted by a factor to correct the energy splitting between $3d_{5/2}$ and $3d_{3/2}$ peaks. The resulting line intensities were broadened by a life-time broadening function for comparison with the observed 3d–4f spectra from metallic rare-earth samples. We omit here details of the experimental and theoretical procedures which can be found in the paper by Thole et al. (1985).

Excellent agreement between the experimental and calculated spectra was found for all the rare-earth metals excepting metallic Sm for which some discrepancy was observed (Thole et al. 1985). However, the M_{V-IV} spectrum from a Sm metal surface freshly scraped under UHV resembled closely the one reported (Kaindl et al. 1984) for Sm_2O_3. The small separation (~100 meV) between the ground-state Sm $4f^5\ ^6H_{5/2}$ configuration and the first excited state Sm $^6H_{7/2}$ and possible overlap or even mixing between them was invoked as a possible explanation for this discrepancy. In a spherical configuration these are not allowed to mix but this might no longer be true in the lower symmetry of the solid. The calculated Sm^{2+} absorption spectrum from the $Sm^{2+}\ ^7F_0$ ground state was found to be in good agreement with the experimental M_{V-IV} spectrum of SmS(100) at room temperature.

In order to understand the above mentioned discrepancy between observed and calculated 3d–4f spectra of Sm when empirically adjusted parameters were used, Sarpal et al. (1991) performed an experimental and theoretical study of Sm and Tm vapour spectra at the 2.5 GeV electron synchrotron in Bonn and the ACO storage ring at LURE (Orsay). As opposed to empirically adjusted HF parameters, Sarpal et al. (1991) used unscaled *ab initio* multi-configurational Dirac–Fock calculations to interpret the M_{IV-V} spectra of Sm and Tm. The results of these calculations are presented in fig. 5. Similar results were obtained for the 3d–4f spectra of Tm in the vapour and solid phases together by the same method (fig. 6). These calculations show that an unambiguous interpretation of the spectra of the free atom is possible without using *any* adjustable parameters, and consequently that the multiplet structure can be interpreted unambiguously. These unscaled *ab initio* calculations yield positions of levels in the ^7F manifold in agreement with the observed optical data (Dupont 1967). The results give M_{IV} and M_V multiplet lines whose total intensities plotted in fig. 6 are comparable to those observed for divalent Sm atoms. By including the transitions from the $J = 1$ level (populated according to Boltzmann's distribution) one finds a spectrum (Blancard et al. 1990b) which resembles that of the vapour. In these calculations, a weaker structure corresponding to that observed at 1071 eV, is present within 1 eV from the main line for both $J = 0$ and $J = 1$. This feature is much weaker for transitions from $J = 0$. Also, the predicted intensity of the $J = 1$ spectrum is about three times larger than that obtained for $J = 0$ (due to the higher multiplicity of the $J = 1$ level). The calculation becomes cumbersome for transitions from the $J = 2$ level due to the increased number of allowed transitions. A simplified calculation of the transitions from the $J = 2$ level shows that the total intensity of these transitions is lower than the total intensity from the $J = 0$ level. Its inclusion, however, was found

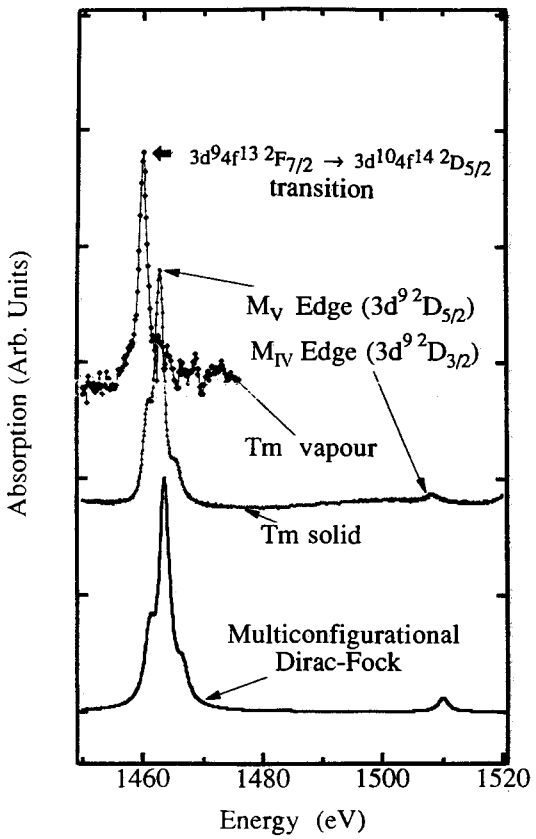

Fig. 6. Comparison between the spectrum of atomic Tm and the spectrum of the metal. Note the difference in structure between the two. A simulated spectrum based on Dirac–Fock calculations for the ion is shown alongside the spectrum of the condensed phase. After Sarpal et al. (1991).

to further improve agreement with the observations. The results of the calculations by Sarpal et al. (1991) will be used below to account for the complexity of the Sm $4f^6(^7F_0)$ ground state and the observed 3d–4f multiplet structure for Sm atoms and small clusters embedded in rare gas matrices at low temperatures.

3.1. *Widths and profiles of absorption lines*

The widths and profiles of M_{IV-V} absorption lines provide important information on the 4f potential barrier which shields 4f electrons from the external electrons in a R solid. This effect is more or less visible in the widths and profiles of absorption lines. The lines in the M_V spin–orbit group are almost symmetric and are well represented by a Lorentzian shape. The M_{IV} lines are asymmetric and exhibit a Fano-like profile. Final states with either $3d_{3/2}$ or $3d_{5/2}$ core holes decay primarily by Auger transitions. The fluorescence decay is small (Connerade and Karnatak 1981). States built on the $3d_{3/2}$ hole state have an additional decay channel, leading to autoionization if they interact with

the continuum associated with the $3d_{5/2}$ core hole. This interaction yields an asymmetric (Fano) line shape. The widths and profile of these transitions also provide information on the 4f level width. This width is crucial in understanding the mechanism of the valence transition or of changes of configuration in the 4f shell during the transition from the atom to the condensed phase. Usually the M_{IV-V} absorption spectra of R compounds exhibit a quasi-atomic character. They are almost independent (with certain exceptions, particularly for higher valence compounds of Ce, Pr and Tb) of chemical combination. It is worth mentioning here that the 3d–4f linewidths observed under similar resolution for R fluorides are generally narrower (Karnatak et al. 1981) than those for metals and other normal oxides (Kaindl et al. 1984, Thole et al. 1985) under similar experimental conditions.

The localized nature of 3d–4f transitions in some normal R was also demonstrated in the past by comparing the $3d^94f^{n+1}$ multiplets obtained by atomic calculations with the observed spectra. The multiplet calculations yield data on positions and strengths of the lines corresponding to the $3d^{10}4f^n$–$3d^94f^{n+1}$ dipole-allowed transitions. In order to compare them with experimental spectra one needs to broaden the line strengths by taking into account the lifetime width of the upper state and the instrumental broadening function. Useful data on the total integrated intensities of the $3d_{3/2}$ and $3d_{5/2}$ peaks and the absorption length (Thole et al. 1985) were obtained from theoretical spectra by using the estimated values of lifetime widths. Under these circumstances, it becomes crucial to know the instrumental resolution precisely. If the instrumental resolution and other broadening functions are known, one can, by trial and error, optimize the agreement between the theoretical prediction and experiment by choosing different values for the lifetime widths.

Published data (Sugar et al. 1985, Thole et al. 1985) on the corrected 3d–4f linewidths of R were obtained by the photoyield method. It is interesting to note that the observed spectra reported by Sugar et al. (1985) and Thole et al. (1985) were obtained with similar spectrometers and are quite comparable to those obtained earlier (Karnatak et al. 1981) at the same resolution by transmission through thin films. Karnatak et al. (1981) estimated the instrumental broadening to be small in comparison to the observed linewidths, and therefore neglected it in the determination of the natural width of the 3d–4f lines. The corrected linewidths determined by Sugar et al. (1985) were obtained by taking into account the width of the rocking curve of the double crystal spectrometer as the instrumental broadening function and the width showed better agreement with the theoretical estimate of the 3d lifetime width by McGuire (1972). Thole et al. (1985) invoked line saturation effects due to comparable photon penetration depth (absorption length) and electron sampling depths as the cause of the broadening of the 3d–4f lines. The estimated width for the $3d_{5/2}$–4f line of La was found to be as low as 0.2 eV.

Natural line widths are of fundamental importance in studies of fluorescence yield and lineshapes by various core-level spectroscopies. In the context of the 3d core-level lifetimes in R, Crecelius et al. (1978) determined the 3d level widths from the X-ray photoelectron spectra (XPS) of La–Pr metals and compared them with the theoretical lifetime widths obtained by McGuire (1972). In the case of La, the appreciable

difference observed between the $3d_{5/2}$ XPS linewidth (1.8 eV) and the theoretical 3d level width (0.7 eV) was attributed to neglect, in the theory, of decay paths in which an empty short-lived 4f level is filled. For La, a similar mechanism, which involves decay paths connected with the capture of two electrons in the short-lived 4f states was suggested (Karnatak et al. 1981) as an explanation for the residual difference between the $3d_{5/2}$ XAS linewidth (1.1 eV) of La and the theoretical 3d level width. These experiments underlined the importance of including *all* the available decay paths due to the presence of the short-lived 4f states in R. In fact, the width of a line due to a transition between two atomic levels (in this case 3d and 4f levels) is the sum of the lifetime widths of all the individual levels involved in the transition. Thus the theoretical estimate of the level width (McGuire 1972) and the experimental linewidth (Karnatak et al. 1981) both yield $0.4 \pm 0.1eV$ for the width of the 4f level. This is, in fact, of the order of the 4f level widths used in other theoretical models [see for example Koskenmaki and Gschneidner (1978) for a short review of theoretical models using different 4f level widths] to describe the core-level and outer-level spectra of intermediate valence R materials.

We see that the values of 3d–4f linewidths of normal R metals and oxides obtained either (i) by neglecting the instrumental broadening effects or (ii) by overestimating these and (iii) invoking line saturation effects differ considerably. Also, some doubt persists as to whether 3d–4f linewidths of R are really influenced by the existence, in solids, of further decay paths for the 3d hole in the presence of an excited 4f electron. From the experimental standpoint, this situation is further complicated if we consider an observation under the same resolution of the narrower 3d–4f lines in R fluorides (Karnatak et al. 1981) and unusually broad lines or multiplets in R dioxides (Karnatak et al. 1987a,b). Thus, it became crucial to know whether, in certain chemical environments, the change observed in the 3d–4f line or multiplet widths is a real one. For this reason a quantitative estimate of instrumental and other broadening effects became necessary.

Esteva and Karnatak (1987) proposed a semi-quantitative estimate of line saturation effects usually encountered in absorption measurements by transmission and photoyield methods. The estimate of line saturation was obtained by comparing the 3d linewidth of La obtained by photo yield and by resonant photon scattering. Some quantitative information on the line saturation effect was obtained from resonant photon scattering experiments. As opposed to the electron yield method, in the latter experiments, the scattered photon is detected as a function of incident photon energy. Spectra are scanned around the $3d_{5/2}$ and $3d_{3/2}$ resonance absorption lines. The process involved in the scattering is complementary to photoexcitation, in which remission of a photon due to de-excitation of a 4f electron occurs.

In this case, the energy of the emitted photon is equal to that of the incident photon. This is demonstrated by the coincidence between spectral peaks obtained by scattering and by yield spectroscopy. At the resonance peak energy, the photon penetration length is almost equal to the photon escape depth. This is equivalent to saying that $\mu L = 1$ (where μ is the absorption coefficient and L, the sampling depth, cannot be greater than the absorption path length). Esteva and Karnatak (1987) studied the M_V line of La by resonant scattering compared to electron yield for 45° and 60° angles of incidence in both cases.

A least square fit of a Lorentzian shape to the electron yield spectrum gave a FWHM of 1 eV. A similar fitting procedure for the photon-scattering spectrum yielded 1.7 eV as the linewidth. By considering the width of the scattering line as the maximum, saturated value, then the ratio of these widths measured by scattering and yield methods after simulating the broadening of a 1 eV wide Lorentzian line for different values of $\mu L/\cos q$ (where q is the angle of incidence) indicated that, for values of $\mu L \ll 0.01$, the width of the photo yield peak converges to that for the electron yield peak. This behaviour clearly demonstrates that saturation effects for the La M_V line are negligible. This experiment confirms that the line saturation effects in R are small and are in agreement with earlier measurements of sampling depths in La and Gd (Esteva et al. 1983b) which are associated with a much smaller photon penetration length.

Esteva and Karnatak (1987) also found that the broadening introduced by the instrumental function is less than 0.1 eV in the case of the 3d–4f lines and could therefore be neglected. This argument is further supported by the recent observation of extremely fine lines in the double-excitation range of the K absorption spectrum of atomic Na with a similar resolution to that used in earlier studies. In the K absorption spectrum, the width of the Na 1s–3p4s double-excitation line was measured to be 0.38 eV (Teodorescu et al. 1997) as compared to 0.55 eV for the Na 1s–3p line (Tuilier et al. 1982) and 0.50 eV for Ne 1s–3p lines (Gauthé et al. 1983). We emphasize here that this is the narrowest width (0.38 eV) so far observed for a line in the keV region scanned by a double beryl-crystal spectrometer. We believe that this value is very close to the resolution limit. The 3d–4f linewidths in the R sequence exhibit smooth and slowly increasing values as reported in our earlier work (Karnatak et al. 1981). This suggests that, in the 3d–4f excitation process, the excited 4f electron in some way influences the Auger decay rate of the 3d hole. Autoionization and filling of the available short-lived 4f states may be additional mechanisms to account for the difference between the theoretical estimates (McGuire 1972) and the experimental widths. The observation of narrower 3d–4f lines in R fluorides suggests an influence of the surrounding fluorine cage on excited 4f states. The fluorine atoms surrounding the R atom form a cage which repels the excited 4f electron and further reinforces the centrifugal potential barrier. This diminishes the probability of the excited electron leaking into the continuum, thereby reducing the 3d–4f linewidth in the fluorides.

In the following paragraphs we discuss photoabsorption features of atoms, clusters and solids of some of the Sm group elements, whose 3d–4f linewidths exhibit normal behaviour in their different valence phases. This will lead us to invoke a new mechanism involving 4f-covalence to account for the unusually broad 3d–4f lines observed for Ce group dioxides.

3.2. *3d–4f absorption spectra of Tm and Sm clusters*

It is interesting to note that Sm, Eu, Tm and Yb occupy the places just at the middle and before the middle and end of the R sequence. Because of the relatively low melting and boiling points of Sm, Eu, Tm and Yb, the R valence transition in these metals can easily

be tracked by usual spectroscopic methods. The M_{IV-V} spectra of Sm group elements and their compounds possess multiplet lines characteristic of the valence of rare-earth ions. As clearly seen in table 3, these elements contain two 6s valence electrons in the vapour phase. In the solid phase, Eu and Yb metals are divalent and retain their $6s^2$ valence configuration. Sm metal, which is normally trivalent, is divalent on its surface whereas divalence in Tm metal occurs only on very rough surfaces. In fact the electronic configuration of atomic Tm is $[Xe]4f^{13}6s^2$ and it may remain the same or become $[Xe]4f^{12}(5d6s)^3$ in the solid. The corresponding 3d–4f XAS dipole transitions in Tm which are the signature of the ground configurations are relatively simpler than for Sm and Eu. The study of the intermediate valence Tm compounds has attracted much scientific interest, as they provide the unique example in which both configurations involved in the valence change are magnetic. This contrasts with other rare-earth elements exhibiting intermediate valence for which one of the ground states involved in the valence instability is non-magnetic.

3.3. *Coordination-dependent valence in small Sm and Tm clusters*

Wertheim and Crecelius (1978) were able to resolve and identify for the first time the photoemission spectrum of surface atoms of metallic samarium. They were able to prove that divalent samarium is clearly present in the initial state and is not a final-state satellite. The origin of the unusual valence instability of samarium is uncovered in the calculations of Herbst et al. (1972, 1976) which show that the energy required to promote a d electron from the Fermi level to an empty 4f state is only 0.2 eV in metallic Sm. Thus, any perturbation which can raise the Fermi level by this amount will allow the flow of electrons in the 4f level. The valence transition can then be attributed to the narrowing of the 5d band by virtue of reduced coordination at the surface. The same calculations predicted the energy required to promote an electron from the valence band to the 4f level in Tm as ~ 1 eV, making it less likely to have a valence transition at the surface. Indeed, Tm metal was subsequently observed to remain ordinarily trivalent at the surface (Johansson et al. 1981, Lang et al. 1981). It was only in 1986 that experimental evidence of coordination-dependent valence from low-coordinated Tm at surfaces was obtained by Domke et al. (1986). Their photoemission measurements of Tm-metal films grown on a Cu substrate at low temperature revealed a partial surface valence transition to divalent Tm. The size-dependent valence change in small matrix-isolated Sm clusters was also studied by L_{III} absorption spectroscopy (Lübcke et al. 1986, Niemann et al. 1987). From the relative intensities of the dominant L_{III} white lines corresponding to divalent and trivalent atoms in the clusters, an average valence for the rare-earth atom in the cluster was deduced. The occurrence of coordination-dependent divalence in Tm was further substantiated quantitatively by the study of the 3d–4f absorption spectra of small clusters of metallic Sm and Tm (Blancard et al. 1989, 1990a). The study of clusters allows one to track the configurational changes which occur during the passage from vapour to solid phases.

Matrix-isolated Tm and Sm atoms and clusters were obtained by co-deposition of the evaporated metal sample and the carrier gas (Ar) onto a sample holder cooled by a

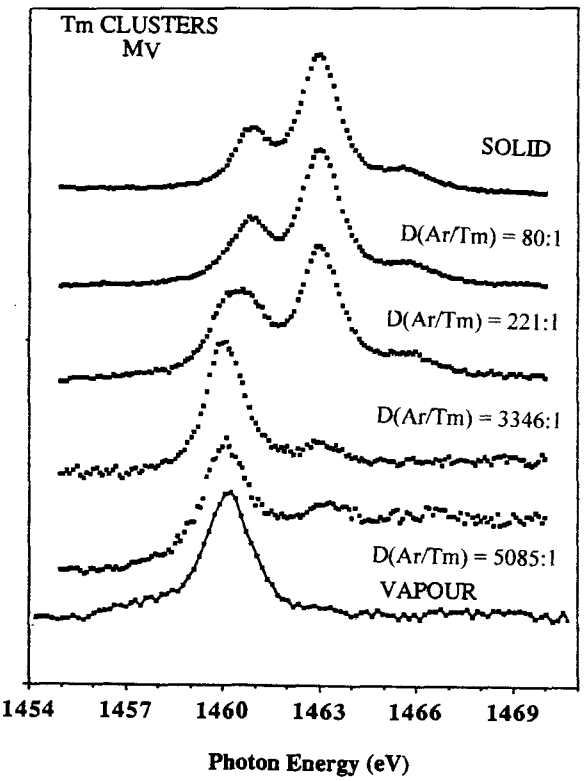

Fig. 7. The 3d (M_{IV-V}) spectrum of Tm, showing the evolution from the spectrum of the vapour to that of the solid via intermediate concentrations of trapped clusters of Tm in an Ar matrix. After Blancard et al. (1989).

liquid He cryostat. Details of sample preparation and the absorption measurements using synchrotron radiation are given by Blancard (1989) and Blancard et al. (1989). From the measured quantities of Tm and Ar deposited on the cooled sample holder the dilution D(Ar/Tm) can be determined. In fig. 7, the 3d–4f spectra of Tm atoms and clusters at different dilutions D are shown with, in addition, one from a solid sample and one from Tm vapour. A glance at fig. 7 shows that a remarkable evolution occurs in the spectra as one moves from the vapour, through matrix isolated atoms, to clusters and to the solid. The single line in the atomic vapour spectrum finally turns into a four-line spectrum in the trivalent metal (a weak line observed on the M_{IV} spectrum for Tm solid is not shown in fig. 7). In fact, the latter correspond to four dipole transitions from the ground state $3d^{10}4f^{12}$ ($^3H_6$) to $3d^9\,4f^{13}$ ($^3G_5$, $^3H_5$, $^1H_5$ and $^3H_6$) and are better described in j–j coupling (Belrhmi-Belhassan et al. 1981). The new single-line spectrum of the vapour, as well as those from atoms and very small clusters embedded in matrix with large D(Ar/Tm) is due to the only dipole-allowed transition from $3d^{10}4f^{13}$ ($^2F_{7/2}$) to the $3d^9$ ($^2D_{5/2}$)$4f^{14}$ level. In fact the appearance of this single line is the fingerprint indicating Tm divalence in the solid state. Blancard (1989) deconvoluted the cluster spectrum, which contains the contribution from divalent and trivalent Tm into a single line spectrum by subtracting

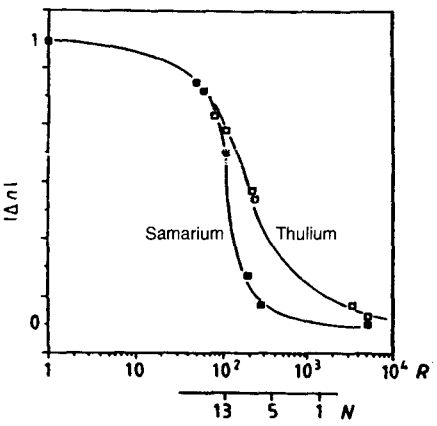

Fig. 8. The evolution of valence with cluster concentration for Sm(n) and Tm(o). Both the relative concentration of host to trapped atoms and the cluster size, estimated by EXAFS (Lübcke et al. 1986, Niemann et al. 1987) are plotted. Note that cluster size used in this context is not, in fact, the true cluster size, but the average number of atoms in the first coordination cell. After Blancard et al. (1989).

a suitably weighted spectrum of Tm solid. He compared the single line spectrum thus obtained to the one Sarpal et al. (1991) obtained for Tm vapour. He measured their widths to be 1.55±0.1 and 1.66±0.1 eV respectively for Tm in cluster and vapour phases respectively, and found that their position remained unchanged. This procedure provides a clear identification of the spectral features and indicates the presence of both divalent ($4f^{13}$) and trivalent ($4f^{12}$) atoms in the clusters. These observations for Tm show that, from the vapour to the solid, the change in the 4f population Δn is either 0 or 1. In fact, the fractional value of Δn in the condensed phase represents the number of trivalent atoms relative to the total number of divalent and trivalent atoms in a given average size of cluster. In the case of Sm and Tm, for a given dilution R, Δn is proportional to the ratio of the area under the $4f^{n+1}$ spectral component to the total area under the $4f^{n+1}$ and $4f^{n}$ spectral features, also taking into account the effective cross section for the transitions. In fig. 8, we plot the Δn values for Sm and Tm thus obtained from several spectra of Ar matrix-isolated clusters for different dilutions R (Ar/R).

The curves of Δn against D for Sm and Tm each show an abrupt discontinuity, indicating distinct valence transitions for different R. Using published EXAFS data for Sm cluster sizes (Lübcke et al. 1986, Niemann et al. 1987) as a function of D, the relevant coordination for the atoms in an average size cluster of Sm and Tm is estimated. Different values of coordination for the valence transitions in clusters of Sm and Tm are observed. The ordinate of fig. 8 indicates the value of $|\Delta n|$ which range from 0 to 1. In order to obtain the valence of Sm (Tm) one must add 2 to the $|\Delta n|$ values. For Sm clusters, divalence is found to stabilize for a coordination of 8–10, whereas it is only 6–7 for Tm. These are exactly the coordination numbers one observes at smooth or rough metallic surfaces (Domke et al. 1986). The experimental observations thus provide a quantitative and straightforward explanation for coordination-dependent surface valence in metallic Sm and Tm. They account for the observation of divalence only on very rough surfaces, where the coordination is further reduced. A qualitative description of the surface valence in Sm and Tm can be obtained by invoking a model in which the

metal cluster atoms are simulated (Blancard 1989, Karnatak and Connerade 1996) by the close non-crystallographic packing of identical hard spheres. In this type of packing, one can put 12 spheres around a single sphere, forming a shell. In this configuration (icosahedral), each sphere of the shell touches five other spheres of the same shell as well as the central sphere. We can insert more spheres to complete a second shell, and so on, to constitute further shells. The number (N) of spheres in a shell (Mackay 1962) is given by $N = 10n^2 - 2$, where n is the number of the shell. Thus, each new shell gives the number of surface atoms. The number of bulk atoms can readily be obtained by adding all atoms in different shells which are inside a given shell. In order to compare the results of the icosahedral model with the experimental valence versus D curves, we first plot the fraction of the bulk atoms [(Bulk atoms/(Bulk+surface atoms)] against the fraction of the total bulk and surface atoms in the icosahedral configuration. We see immediately that the curve thus obtained is similar in shape to that observed for the valence transition in Sm (Tm) clusters. We then add 2 to the Y values to allow for the fact that, for Sm metal, all surface atoms are divalent, and then multiply the X values of this curve by an appropriate constant which describes the dilution D in the Ar matrix. We take the value of this constant as the D-value at the inflection point of the experimental valence transition curve for Sm. On such a normalized curve for the icosahedral model, one inserts the experimental points for Sm and Tm. Such a plot reveals that the experimental points lie on a curve with a more abrupt valence transition than is obtained from the non-crystallographic icosahedral model. These results also reveal that, in Sm and Tm clusters, the well-defined crystallographic configuration of the clusters due to bonding and valence band formation undergoes rather abrupt changes.

According to this comparison, in matrix isolation experiments, the collision probability between the R atoms and the carrier gas atoms can be taken as proportional to the gas pressure. The affinity of R atoms to clusters is ignored for simplicity. Moreover, in this model, the 15% difference between the trivalent metallic (Beaudry and Gschneidner 1978) and the hypothetical divalent metallic radius (interpolated) of Sm for a coordination 12 is also ignored. A related situation occurs for divalent to trivalent valence transitions in free Sm, Eu, Tm and Yb oxide clusters (Bréchignac et al. 1993): as a function of oxidation the transition is much more abrupt than is observed for matrix-isolated Sm and Tm metallic clusters (Blancard et al. 1989). The $|\Delta n|$ versus D(Ar/R) curves in fig. 8 show an abrupt change in slope, indicating the change in the ground configuration for Tm and Sm. For values of D(Ar/R) up to 100:1, both curves overlap. Beyond this value, they separate and $|\Delta n|$ tends to zero at $D = 290{:}1$ in the case of Sm, whereas it is about 0.03 for a dilution D as high as 5000:1 in Tm. This means that the change from $4f^{12}$ to $4f^{13}$ is taking place for much higher dilution as compared to Sm where the atoms are already $4f^6$ (divalent) for $D = 290{:}1$. This implies that atom-to-solid phase transition and the configuration changes in the condensed phase for Sm and Tm depend upon the number (N) of atoms in a cluster (or the cluster size). Therefore, we need to know whether there exists a relationship between the dilution D and the mean size N of the clusters.

The processes of metal cluster formation in a carrier gas jet and their modification on condensation at the cold surface are rather complex. In the experimental setup the

inert gas is introduced through a narrow tube placed in front of the cold sample holder in such a way that the inlet gas stream and the metal atoms from the evaporation source overlap. The metal atoms collide with the gas atoms and the clusters, and have a high probability of colliding with other metal atoms coming from the evaporation source, to form small seeding clusters which are carried away by the gas stream to condense on the cold sample holder. Here again, depending on the dilution of metal atoms and clusters already condensed on the sample surface, there is some probability they can be 'subjoined' by incoming metal atoms and small clusters and thus, still bigger clusters isolated in inert solid rare gas matrix are formed. As the gas pressure is increased (1) the probability of the collision with the incoming metal atoms becomes greater and bigger clusters form and (2) these clusters become more and more isolated owing to the increased number of rare gas atoms arriving at the surface. Thus, a compromise between the metal deposition rate and the inlet rare gas pressure, or the condensation rate of the rare gas is needed to obtain a desired mean cluster size. An estimate of the distribution of cluster sizes in a carrier rare gas stream can be obtained by mass spectrometry of the constituent atoms and clusters present in the gas stream. In an actual situation, the EXAFS analysis of clusters embedded in the rare gas matrix is the most appropriate tool to estimate cluster sizes. It is also worth noting that M_{IV-V} EXAFS of R atoms have not been observed. This is due to the fact that their 3d ionization cross section is extremely small as compared to the 3d–4f excitation cross section. So one must rely on L_{III} EXAFS results for the estimation of R coordination and, consequently, the determination of cluster size. For Sm, such information on the size of matrix isolated clusters has successfully been obtained from L_{III} EXAFS measurements (Lübcke et al. 1986, Niemann et al. 1987) for different concentration D(Ar/Sm). In fig. 8, we have included the average size N estimated for Sm clusters and different values of R. In the absence of any L_{III} EXAFS data for Tm, we use published values of the Sm average cluster size (N) for different D(Ar/Sm), as these authors have also done for Nd and Pr. In fact, the N values should depend on the masses of the colliding particles (atoms and clusters in the metal and carrier gas beams). Since the ratio of the atomic weights of Sm, Pr, Nd and Tm does not vary by more than 10%, one can consider the collisional process leading to an average cluster size to be almost the same for Pr, Nd, Sm and Tm in a common matrix rare gas material at a given inlet pressure. Thus, the cluster size N estimated from EXAFS analysis for different values of D(Ar/Sm) can also be used for Tm and are included in fig. 8 for this purpose.

The most important fact emerging from the data in fig. 8 is the marked difference in N for the divalent to trivalent transition in Sm and Tm. In the case of Sm, for $N < 10$, all clusters become divalent whereas trivalence persists up to $N = 6$ for Tm. This quantitative observation relates directly with the coordination dependence of surface valence in Sm and Tm. In fact, a bulk metal may be considered to be formed by an assembly of an infinite number of clusters closely packed together (with all surface effects neglected). Within this assembly, in the particular case of Sm and Tm, any given atom is surrounded by 12 other atoms (coordination number). Probing such atoms yields a spectrum characteristic of the bulk. On the other hand, a surface

can be visualized as a packing of clusters smaller than those in the bulk. A further reduction in the size of the constituent clusters is expected from smooth to rough surfaces (with edges and corners). We thus find a very simple explanation for the differences in valence which can occur between the bulk, the smooth and the rough surfaces, as described above.

In an assembly of matrix-isolated clusters, the cluster size N may vary from a single atom to several atoms. The X-ray spectrum, in such cases, yields information on the coordination of a particular atom which might be either inside or trapped at the surface of a given cluster.

Surface core-level shifts in the XPS of rare earths are due to the reduction in coordination at the surface as compared to the bulk. In Sm, the reduction of coordination from 12 in the bulk (a close packed structure) to 9 at the surface is found to stabilize divalence at the surface readily. Further reduction of the coordination of atoms at the surface in the case of Tm was invoked by Domke et al. (1986) to explain the observation of divalence for only rough or heavily bombarded surfaces. This interpretation stems from the well-known phenomenon of surface core-level shifts observed for divalent Yb metal (Schneider et al. 1983). From these results, it was argued that a coordination as low as 7 will be able to stabilize divalence at rough surfaces, with edges and corners.

Lübcke et al. (1986) substantiated the findings of Domke et al. (1986) by determining the stable valence for a free cluster of size N. For atoms, the estimate of the difference in total energy between the divalent and trivalent forms was obtained from known optical absorption data (Martin et al. 1978) yielding the energy difference between the $4f^n\,6s^2$ ground state and the $4f^{n-1}\,5d6s^2$ excited state. In bulk metals, a similar energy difference occurs: it is the energy required to change the state of an atom in the bulk metal from divalent to trivalent forms, obtained by bremsstrahlung isochromat spectroscopy (BIS – Lang et al. 1981). Rare-earth clusters represent a situation intermediate between the vapour and the bulk metal, for which the coordination numbers are 0 and 12 respectively. By using optical absorption and BIS data, the estimated coordination numbers for valence changes of Pr, Nd, Sm, Yb, Dy, Ho, Er and Tm clusters have been determined. For Pr, Nd and Sm clusters, good agreement between the critical cluster size determined from EXAFS analysis and theoretical values was obtained.

The pair bonding model of Rosengren and Johansson (1982) also supports the above interpretation. In this model, the total configurational energy of a cluster is approximated by a sum of interaction energies (cohesive energy) E_{ab} between nearest neighbour pairs. Trivalent clusters become stable for a critical coordination number which can be evaluated by using values of the cohesive energies obtained by interpolation.

This study tracks the configurational changes in Tm (Sm) from the vapour phase to clusters isolated in the rare gas matrix and solid. The most important information we obtain is a quantitative picture of coordination-dependent valence changes in matrix-isolated Tm (Sm) clusters and a straightforward explanation for the occurrence of surface divalence in metallic Tm only on rough surfaces where the atoms experience a reduced coordination. This is demonstrated by the observation of divalence in clusters still smaller than those of Sm.

3.4. *The ground state of Sm*

The electronic configurations of Sm in the vapour and in the solid phases are $4f^6$ and $4f^5$ respectively. In the solid, however, both configurations exist. For corresponding ions the Hund's rule ground states are $4f^6$ ($^7F_0$) (non-magnetic) and $4f^5$ ($^6H_{5/2}$ (magnetic), respectively. The population of low-lying states close to $4f^6$ ($^7F_0$) and $4f^5$ ($^6H_{5/2}$) ground states also plays an important role in determining the magnetic properties of divalent and trivalent Sm compounds. The states in the ^7F manifold of Sm divalent compounds have been widely investigated as a function of temperature by various methods such as inelastic neutron scattering (Shapiro et al. 1975, McWhan et al. 1978), Raman scattering (Güntherodt et al. 1981) and electron paramagnetic resonance (EPR) (Mehran et al. 1971), etc.

Thole et al. (1985) suggested the possibility of improving the agreement between observed and calculated Sm^{3+} $3d^94f^6$ multiplet structure by including in the calculations transitions from the first $^6H_{7/2}$ excited level situated about ~ 100 meV above the $4f^5(^6H_{5/2})$ ground state. As opposed to this, the multiplet calculation for Sm^{2+} performed by considering only the $^7F_0$ ground level yielded a spectrum similar to that observed for divalent SmS by Kaindl et al. (1985). In this case, the first excited $^7F_1$ level lies 30 meV above the $4f^6(^7F_0)$ ground state, and its inclusion in the calculation merits special attention for the interpretation of spectra obtained at room and higher temperatures. To clarify this puzzling situation, Sarpal et al. (1991) studied the 3d–4f spectra of Sm metal vapour at 1300 K, and of Sm atoms and small clusters (Blancard et al. 1989) embedded in a solid Ar matrix at 10 K, in order to obtain some insight into the role of states lying close to the $^7F_0$ ground level of Sm^{2+}. In fig. 9, we present the metal vapour spectrum obtained at 1300 K, together with those of the two selected examples of small Sm clusters embedded in an Ar matrix at 10 K at medium and high dilutions D(Ar/Sm) = 190:1 and 2300:1 respectively. The 3d–4f spectrum of SmS obtained by Kaindl et al. (1985) at room temperature is also included in this figure for comparison. The Sm vapour spectrum and the divalent SmS spectrum in fig. 9 are similar. The medium-size clusters (D(Ar/Sm)=190:1) yield a spectrum consisting of contributions from both trivalent and divalent Sm. On subtracting the trivalent contribution from this spectrum, a spectrum is obtained (also shown in fig. 9) which at first sight, also resembles the vapour or divalent SmS spectrum. Thus, we see that the high-temperature Sm vapour, SmS and the divalent component of the medium-size Sm cluster spectra are similar, and fit HF predictions (Thole et al. 1985) for transitions from the $^7F_0$ ground state only. This would actually be physically incorrect, since other ^7F levels are also populated in the hot vapour (Tracy 1976) and this points to a inconsistency in the interpretation given by Thole et al. (1985).

On the other hand, the spectrum for very small clusters and atoms (D=2300:1) embedded in Ar matrix is markedly different. Due to the great dilution, the lines in the spectrum (fig. 9) are weak. A weak structure on the high-energy side of M_V is parasitic and originates from the monochromator crystals. In this spectrum, the contribution of the Sm^{3+} lines is barely observable. At the same time we do observe the absorption lines corresponding to Sm^{2+}, both on M_{IV} and M_V, in contradiction with the lowest term

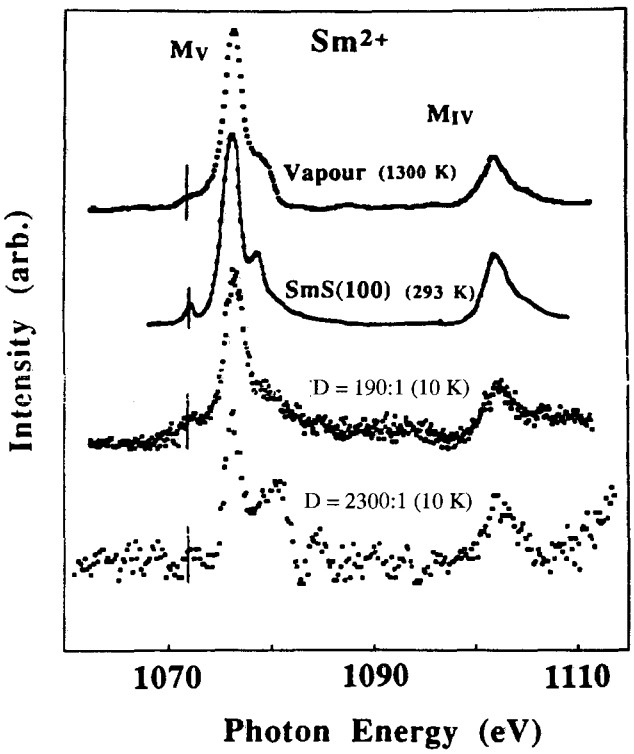

Fig. 9. M_{IV-V} spectra of Sm vapour, SmS and Sm clusters at two dilutions, showing the Sm^{2+} contributions. After Blancard (1989) and Blancard et al. (1990b).

approximation, in which a single dipole-allowed transition is expected on M_V. Blancard et al. (1989) also measured the M_V/M_{IV} line intensities and the widths of the M_{IV} and M_V lines (see fig. 10). We note that, if correct, the HF calculations of Thole et al. (1985) should correspond to the spectra of atoms deposited at large dilution in an Ar matrix at low temperature, but, in fact, they do not.

The observed 3d–4f multiplet structures for Sm atoms and small clusters at low temperature were compared to multiconfigurational Dirac–Fock (DF) calculations (Sarpal et al. 1991). As mentioned above, these unscaled ab initio calculations also yield positions of levels in the ^7F manifold in agreement with observed optical data (Dupont 1967). The results of our *ab initio* calculations (fig. 5) for transitions from the $^7F_0$ ground state give M_V and M_{IV} multiplet lines whose total intensities (fig. 10) are comparable to those observed for Sm atoms and clusters at low temperature. These calculations, by including the transitions from the $J = 1$ level (populated according to Boltzmann's distribution) now do yield a spectrum resembling that of the vapour. In these calculations, a weaker structure corresponding to that observed at 1071 eV is present within 1 eV from the main line both for $J = 0$ and for $J = 1$. This feature is much weaker for transitions from $J = 0$.

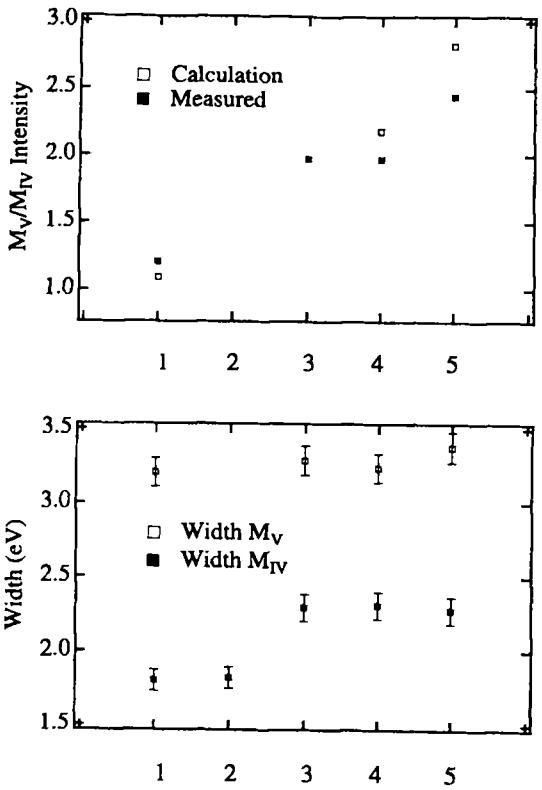

Fig. 10. The M_V/M_{IV} intensity ratios and the widths of Sm^{2+} lines for samples: (1) $D = 2300:1$; (2) $D = 512:1$; (3) $D = 190:1$; all at 10 K; (4) SmS at 293 K and (5) Sm vapour at 1300 K. After Blancard (1989) and Blancard et al. (1989).

Also, these calculations predict that the intensity of the $J = 1$ spectrum is about three times larger than for $J = 0$ (due to the higher multiplicity of the $J = 1$ level). This explains why, for Sm, it is rather difficult to observe a spectrum below a dilution $D = 2300:1$, which implies the presence of more Sm atoms and small clusters with mainly a $J = 0$ ground state. In the corresponding situation for Tm, there is no thermally populated low-lying level, and spectra were obtained for dilutions as large as $D = 5600:1$. The calculations for Sm did not include the full manifold of transitions from the $J = 2$ level because of the large complexity involved. A simplified calculation of transitions from the $J = 2$ level shows that their total intensity is lower that the total intensity from the $J = 0$ level. The inclusion of these states does, however, improve the agreement with observation.

Another intriguing question is: why should the spectrum of the medium-sized cluster ($D = 190 : 1$) resemble closely that of SmS and, to a lesser, extent that of the vapour (the structure is similar, but the widths and the intensities of M_{IV} and M_V lines differ in fig. 10)? The similarity between the cluster spectrum and that of SmS suggests that a parallel mechanism, independent of temperature in these bulk materials, could be responsible for the population of the low-lying states of the ^7F manifold. If the natural width of the 4f level is smaller than the $^7F_0$–$^7F_1$ separation, this mechanism may also

broaden the 4f level in the solid, leading to overlap with, and population of low-lying ^7F levels. This mechanism would produce an effect analogous to the thermal population of low-lying states in Sm vapour. This idea is consistent with the fact that the divalence of Sm is only stabilized either on an Sm-metal surface with reduced coordination, or in medium-sized clusters (D = 190 : 1) where the appearance of metallic character is evidenced by the emergence of the conduction band.

These studies have demonstrated the important role of low-lying states of the ^7F manifold in the spectroscopy of 3d–4f transitions in Sm at different temperatures and in different environments. The finite width (< 100 meV) of the ground 4f level and its overlap with the $^7F_{1,2}$ excited levels provide a means of populating the low-lying levels of Sm.

As the size of the Sm clusters increases, the Sm^{2+} lines in the spectrum weaken and, at a dilution D(Ar/Sm) = 19, the Sm^{3+} spectrum gains prominence. This means that the overlap of 4f with the vacant conduction band should occur at a specific cluster size and, beyond it, Sm^{2+} switches over to trivalent Sm^{3+} by complete delocalization of the 4f electron. In the next paragraph, we discuss this type of valence transition in Tm and Sm.

Mechanisms for pure valence and mixed valence transitions in the Sm group elements become of even greater interest in clusters. For Tm and Sm, as described above, the clusters are formed from atoms produced inside a heating source. Depending on the pressure of the carrier rare gas, aggregates can experience slow multiple collisions with gas atoms and thus coalesce to form clusters of sizes ranging from atoms, dimers, trimers, through to small and larger cluster sizes. In large clusters (N > 3), some surface atoms are divalent and well coordinated while the remaining atoms are trivalent. The fundamental question is: how do atoms which are initially divalent in the vapour phase become trivalent when brought in contact with other rare-earth atoms? Niemann et al. (1987) studied the valence transition of Sm clusters embedded in Ne, Ar and Kr matrices by L_{III} EXAFS and measured the Sm–Sm bond lengths. They found that the Sm–Sm distance varies from 3.59 Å, in evaporated films to 3.68 Å, in different rare gas matrices and at various R/Sm concentrations. They attributed the valence transition to an internal pressure exerted on the clusters by the rare gas lattice. The results of M_{IV-V} (Blancard et al. 1989) and L_{III} (Niemann et al. 1987) spectroscopies for Sm clusters clearly demonstrate that the number of trivalent atoms increases with cluster size. In the beginning, the Sm atoms retain a divalent $4f^6$ configuration. As cluster size increases, the number of well-coordinated atoms grows and, due to the internal pressure exerted by surrounding atoms and, to a lesser extent, by the solid rare gas lattice on the clusters, trivalent $4f^5$ Sm atoms are observed. This implies that, somewhere between the condensed atoms and the size range of small to larger clusters, a $4f^6$–$4f^5$ valence transition takes place. The spectral multiplets which are precursors of configurational or valence change testify to the occurrence of this transition in both Tm and Sm clusters.

Theoretical understanding of mixed valence or even of the pure valence transition in the Sm-group compounds is much poorer than for compounds of the Ce group. Mixed valence in the latter group is well-understood in the framework of the Anderson impurity

model. Core-level spectra and solid-state properties such as magnetic susceptibility are reconciled (Gunnarsson and Schönhammer 1983, 1985) by using the same type of empirical parameters.

Among the Sm group of compounds, SmS was the first mixed-valence system to be widely studied. It exhibits a first-order transition from an integral-valent semiconducting phase to a metallic mixed-valent phase at 6 kbar. The pressure-dependent change in the valence can be simulated by alloying SmS by using Y, a trivalent atom. Doping by Y atoms exerts an internal pressure on the lattice, thus reducing the Sm–S distance at suitable concentrations of Y. Ramakrishnan (1987) mentioned the possibility of a magnetic polaron invoking a phase transition from a Mott-type (Mott 1974) semiconductor to collapsed metallic-like phase. Kasuya (1993) reviewed studies of Eu chalcogenides compounds, concentrating on the exchange mechanism in its various aspects. It is only recently that Wachter (1995) demonstrated experimentally the existence of excitonic insulators. The intermediate-valent compounds $TmSe_{0.45}Te_{0.55}$ and $TmSe_{0.32}Te_{0.68}$ under pressure and low temperature have been studied (Neuenschwander and Wachter 1990, Bucher et al. 1991). Additionally, compounds such as $Sm_{0.75}La_{0.25}S$, YbO and YbS were shown to fall into the category of excitonic insulators.

If we look carefully at the valence transition in Tm(Sm) clusters, we find that atoms are located in such a way that some are well-coordinated while others are poorly so. The well-coordinated atoms experience a higher internal pressure than those on the surface. If a large number of clusters coalesce to form an extended solid, one finds in this extreme case that surface atoms are poorly coordinated as compared to atoms just below them in the bulk. In these clusters ($N > 3$) one can imagine that one or more of the surface atoms may also be coordinated by other atoms. Take the case of Tm ($4f^{13}$) or Sm ($4f^6$) atoms brought together to form a nascent insulator in which $4f^{13}$ (or $4f^6$) and $(5d6s)^2$ are the outer electrons, separated by a gap from the unoccupied ds conduction band. As the atoms are brought still closer together, the valence transition, which implies the transfer of a 4f electron to the vacant conduction band, also occurs closer to the atoms. Eventually, as the Tm (Sm) atoms are packed even more tightly, the gap to $4f^{13}$ ($4f^6$) narrows down, and excitonic levels appear. With a slight increase in internal pressure, crossing of 4f and excitonic levels may occur and the 4f electron, via an excitonic ladder, may finally decay into the vacant conduction band. This leads to a valence transition $4f^{13}(4f^6)6s^2 \rightarrow 4f^{12}(4f^5)5d6s^2$. As a result, the metallic radius of Tm (Sm) is reduced, and a smaller number of other Tm (Sm) atoms is required to produce a given well-coordinated Tm (Sm) atom. This is in agreement with observations of the onset of the valence transition in Tm (Sm) clusters at sizes below 10 rather than 13 (Rademann et al. (1987).

As the Tm (Sm) concentration in the matrix is increased, the atoms in the matrix are brought closer together than those in the dilute matrix. This can be envisioned as a passage from isolated atoms to clusters growing in size, with decreasing distances between the R atoms. In other words, at the onset, the smaller clusters up to a critical R–R separation may be considered as insulators. For larger clusters (> 8–13) the onset of the valence transition to trivalent atoms leading to a metallic phase occurs as expected.

In contrast with Sm (Tm) clusters, divalent metals such as Ba (Rayane et al. 1989) and Hg (Bréchignac et al. 1985, 1988) form clusters for which, in the beginning, the atoms are held together by van der Waals forces. These switch over to metallic bonding above a critical cluster size by a delocalization of the $6s^2$ closed shell electrons with formation of p bands. Extensive data on the size-selected free clusters of Hg are now available. Bréchignac et al. (1985, 1988) studied the 5d–6p photoionization efficiency of Hg_n clusters. In fact, transitions of 5d–6p type probe the localized or delocalized character of the electron. These can be recognized in spectra showing the size dependence of the line shapes. The critical size for the van der Waals to metallic transition is estimated to be at $n_{cr} \approx 13$–20. The ionization potential (In) as a function of the cluster radius R for Hg_n was studied by Rademann et al. (1987). They observed a qualitative change in the size dependence of In for $n \sim 13$. Pastor and Bennemann (1994) developed a theory for the electronic properties of divalent-metal clusters by using the tight-binding approximation. They obtained a Mott criterion for the metal–insulator transition. For further details of the model, we refer the reader to Pastor and Bennemann (1994). In experiments on Sm (Tm), the clusters grow to their full size mainly before becoming embedded in rare gas matrices. Thus, Sm (Tm) atoms in clusters are probably bound by van der Waals forces, and retain their atomic configurations $4f^n\,6s^2$ below a certain critical cluster size (10 and 6 respectively for Sm and Tm). Above this size, the transition from van der Waals to the metallic state can occur by a mechanism similar to the Mott type transition. It seems that this transition in Sm (Tm) and in other rare earths which, when condensed, retain the electronic configuration of the vapour state, is precocious, and more abrupt than the s^2Z–sp delocalization transition in non-rare-earth divalent metal clusters.

The most important and characteristic feature of 3d–4f transitions in Sm-group elements and compounds is the absence of any observable change in the widths of the absorption lines when the valence change occurs. Quantitative estimates of the fractional valence in mixed-valence compounds (Kaindl et al. 1985) for this group of elements can be performed by using the weighted contributions from corresponding pure valent, divalent or trivalent compounds.

3.5. *Unusually broad features in the 3d resonances of Ce, Pr and Tb dioxides*

We next discuss the case of Ce, Pr and Tb oxides in which abnormally large 3d–4f multiplet linewidths are observed. These elements belong to the second group of sect. 2.9.

Among the R elements, Ce, Pr and Tb form a series of higher oxides RO_x (with R = Ce, Pr, Tb and $1.5 < x < 2$) which are classic examples of non-stochiometric systems characterized by the existence of several compounds with well-defined x. These compounds are difficult to obtain in large amounts and some of their physico-chemical properties are not yet well known (Eyring 1979, Zhang et al. 1993a,b). The basic structure for these compounds is of the fluorite type (CaF_2). The RO_2 ($x = 2$; R = Ce, Pr, Tb) are cubic, and the rare-earth valence in these oxides is considered to be +4. On the other side of the system, for $x = 1.5$, the R_2O_3 structure is bixbyite type. This corresponds to a fluorite structure for which 1/4 of the anionic sites are vacant. Most of the compounds

in the sequence are structurally not well identified. The order of the oxygen vacancies is probably a factor which governs the occurrence of different phases.

Among the RO_2, the insulating and nonmagnetic material CeO_2 has attracted much interest in relation with fascinating studies of the intermediate-valence (IV) compounds. The description of the ground state of CeO_2 from its spectral response to relatively high-energy probes such as X-ray photoelectron spectroscopy (XPS), Bremsstrahlung isochromat spectroscopy (BIS), electron energy loss spectroscopy (EELS) and X-ray absorption spectroscopy (XAS) remains an interesting subject of research. The optical and magnetic measurements (Wachter 1982, Marabelli and Wachter 1987), the earlier L_{III} edge (Bauchspiess et al. 1981) and XPS and BIS (Wuilloud et al. 1984, Schneider et al. 1985) data on CeO_2 led to some controversial opinions concerning its valence and the description of its ground state (Kaindl et al. 1984, 1985, Karnatak et al. 1985). In fact, the valence behaviour, the ground-state properties and various spectral features of CeO_2 were reconciled within the framework of existing Anderson impurity models in both the zero- (Fujimori 1983) and finite- (Kotani et al. 1985, Jo and Kotani 1988) bandwidth limits. Moreover, the calculations (Kotani et al. 1985, Jo and Kotani 1988) based on this model, by taking into account 4f–2p oxygen hybridization, distinguish between f^0, f^1 and f^2 character or their admixtures in the ground and final states involved in the core-level spectra of CeO_2. Later on, complex quasi-atomic multiplet effects (Kotani and Ogasawara 1992) were inserted into the model. Wuilloud et al. (1984) applied Gunnarsson-Schönhammer (GS) many-body states calculations (see for example Baer and Schneider 1987) to reproduce outer level and 3d excitation spectra. These calculations yield 4f spectral weights for a choice of parameters corresponding to 0.5 f-band electrons in the ground state. The two low binding energy peaks of appreciable intensity observed below the isolated f^0 peak in the 3d XPS of CeO_2 were found to be due to close and strongly mixed f^1 and f^2 final configurations and band excitations. The observation of a large intensity due to states of this type was considered as a consequence of an initial population in $4f^1$ extended states whose properties were thus indirectly demonstrated. Other impurity calculations (Kotani et al. 1985, Kotani 1996) leading to a similar description of the 3d XPS of CeO_2 treat the f^0 and f^1 admixture in the ground state as a precursor of mixed valence. The 4f occupancy (n_f) thus obtained was also found to be in agreement with band calculations for CeO_2 (Koelling et al. 1983), which show considerable mixing of 4f Ce states into the oxygen 2p band, corresponding to about 0.5 electrons. Recently, Douillard et al. (1994) studied the local electronic structure of Ce-doped Y_2O_3 by 3d XPS and L_{III} absorption edge spectroscopy of Ce, and K-edge spectroscopy of oxygen. They found that K-edge spectra of Ce-doped samples exhibit a low-energy feature which grows with increasing doping with CeO_2. They interpret the new feature as due to transitions to vacant Ce 4f states mixed with oxygen 2p-band states in the conduction band. One aim of the present short review is to highlight persistent differences in opinion over the valence state of CeO_2 between the impurity model approach and other experimental or theoretical methods. The differences are concerned with whether the population of f electrons in this compound is in localized or in extended states.

In the present context, 3d XAS offers some advantage over other core-level spectroscopies. In contrast to XPS, XAS transitions are governed by dipole selection rules, and the reduction in the number of accessible final states (Esteva et al. 1983a,b) facilitates the identification of spectral features. Thus, the study of valence transitions in R materials by 3d XAS is advantageous. The signature of the quasi-atomic multiplet structure associated with the $3d^9 4f^{n+1}$ final configuration provides an unambiguous identification of the localized state. The identification of the additional weaker structures in the 3d XAS of these materials may lead to a clearer understanding of the nature of the 4f electron at R sites.

In order to gain such insight into the CeO_2 valence problem in relation with the study of localized and extended 4f states, M_{IV-V} XAS measurements have been performed (Karnatak et al. 1985, 1987a,b) on Pr and Tb homologues with related fluorite structure.

The M_{IV-V} yield spectra of CeO_2, PrO_2 and TbO_2 are shown in fig. 11a, b and c, respectively. The two 3d spin–orbit groups of lines and structures are found to be separated by 17.7, 19.5 and 31.5 eV respectively for CeO_2, PrO_2 and TbO_2. In these spectra, additional weaker features (labelled Y in fig. 11) at about 3–5 eV on the higher energy side of the main line in each spin–orbit group are systematically observed. The CeO_2, PrO_2 and TbO_2 spectra are found to be shifted as a whole towards higher energies by 1.7, 1.7 and 1.2 eV respectively as compared to those for the corresponding trivalent oxides or compounds. In the 3d XAS of fluctuating valence Sm, Eu and Tm compounds, the separation between two types of final multiplets is observed (Kaindl et al. 1984, 1985) to be 2.5–3 eV. These spectral shifts correspond well to the magnitude of the energy difference between the $4f^n$ and $4f^{n+1}$ final spectroscopic states relevant to a valence change and are also in good agreement with those obtained from the results of quasiatomic self-consistent field calculations (Thole et al. 1985) for the $3d^9 4f^{n+1}$ multiplets. One expects a diminution of the local f count at a given R atom in a tri-to-tetra valence change for a R oxide. Thus the 3d XAS transitions in RO_2 can be compared with the corresponding transition in $Z-1$ elements (where Z is the atomic number of R). In order to identify the main line features of these oxides, we compare them with the M_{IV-V} spectra of the trivalent compounds of the corresponding $Z-1$ elements. The M_{IV}/M_V intensity ratios observed in the present cases are similar to those for corresponding spectra of $Z-1$ elements. As expected, we observe an increase in the 3d spin–orbit separation between the two main features of these spectra with respect to those obtained for $Z-1$ elements. In fig. 11a–c, we present on a separate energy scale (bottom axes) the M_V and M_{IV} spectra of La_2O_3, Ce oxalate and Gd_2O_3 for comparison with those of the dioxides referred to top axes. The correspondence between the lines and the multiplet structures of RO_2 and the trivalent $Z-1$ compounds is apparent in these spectra. The CeO_2 main lines in fig. 11a are similar to the three $3d^9 4f^1$ lines (the weak $^3P_1$ line and the intense $^3D_1$ and $^1P_1$ lines) observed for La_2O_3. The PrO_2 broad main-line features in fig. 11b closely resemble the $3d^9 4f^2$ (trivalent Ce-like) multiplet. Finally we find, for TbO_2, the $3d^9 4f^8$ (Gd-like) multiplets (fig. 11c), which are broad and whose structures can easily be identified by comparison with the Gd_2O_3 spectra. We therefore identify the main lines of CeO_2, PrO_2 and TbO_2 respectively as transitions from the atomic-like f^0,

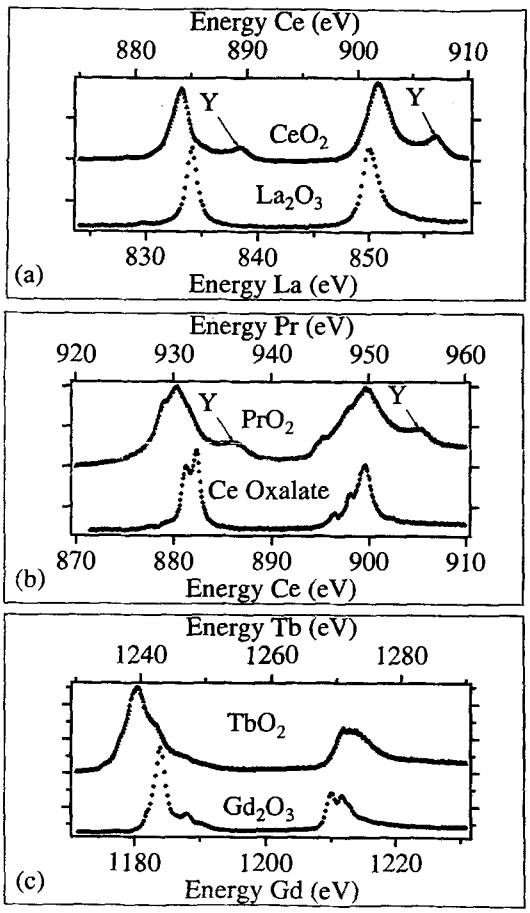

Fig. 11. M_{IV-V} yield spectra of CeO_2, PrO_2 and TbO_2 oxides compared to those of trivalent (a) La_2O_3; (b) Ce oxalate and (c) Gd_2O_3, respectively. Note that the top axes in panels (a), (b) and (c) represent the energies for the dioxides, and the bottom axes represent the energies for the corresponding trivalent compounds. After Karnatak et al. (1987a,b).

f^1 and f^7 ground-state configurations. These nearly localized configurations are in fact, the precursors of tetravalence, indicating that the 4f electron has left the inner reach of the R atom in each case.

The most interesting fact in these oxide spectra is the observation of unusual broadening of the constituent main multiplet lines. The broad RO_2 and the corresponding trivalent compounds spectra (fig. 11a–c) were obtained at similar resolution. A comparison between the individual structures within the multiplets of RO_2 and those observed in the corresponding $Z-1$ elements reveals: (1) an increase in the widths of the $^3D_1$ and $^1P_1$-like lines in CeO_2, (2) an increase in the separation between the structures within the multiplets of RO_2 and (3) a correspondence between the relative intensities of RO_2 structures and those for $Z-1$ elements. In fig. 11a–c, the energy intervals of each scan for the dioxides (top axis) and the corresponding trivalent compound (bottom axis) are similar. This type of presentation greatly facilitates the comparison of spin–orbit separations and

widths of the multiplet lines. The measured full width at half maximum (FWHM) of the 3d–4f lines or multiplets for RO_2 and those for the corresponding $Z-1$ elements in trivalent compounds have been reported earlier (Karnatak et al. 1987a,b). The 40–50% increase in the line or multiplet width in these oxides with respect to that observed in the corresponding $Z-1$ element is found to be too high to be explained by invoking an increase in the spin–orbit separation. These broadened multiplets approximately retain the usual forms observed for the normal R elements. A careful examination of the $^3D_1$ and $^1P_1$-like lines of CeO_2 show small deviations from the usual Lorentzian or Fano lineshapes.

The structure labelled Y (figs. 11a, b) appearing about 5 eV above the main lines of CeO_2 and PrO_2 have similar forms, and the M_{IV} Y structures are somewhat higher in intensity than for M_V. They are asymmetric and appear to extend up to the bottom of the main lines. In TbO_2, these structures are found to lie within the wide Gd-like multiplets. In the M_V spectrum of TbO_2, we observe a weak shoulder about 1.5 eV below the main line (fig.11c). Its position corresponds approximately to the expected energy of the main M_V peak of the trivalent oxide. A corresponding low-energy shoulder on the M_{IV} line corresponding to the trivalent component is not observed. Due to increased splitting of such multiplet lines in TbO_2, at the spectral resolution available in these experiments some modification in the line shape and the appearance of a weaker shoulder are also expected.

The signatures of the $3d^9 4f^{n+1}$ multiplets and their positions in R_2O_3 as compared to those in the corresponding RO_2 indicate that, in the valence transition, a diminution of the f count in the ground state local occupancy occurs. Our identification of the main lines in CeO_2 as transitions from a mainly f^0 ground state implies that the Y structures in CeO_2 *cannot* be due to another localized configuration. In PrO_2 and TbO_2, such a possibility can easily be excluded as it would lead to an improbably high valence state for Pr and Tb.

Thus, we see that the Y structures in CeO_2 and PrO_2 do not correspond to *any* known multiplet features of nearby R elements. The systematic increase in separation (3–5 eV) between the Y structures and the RO_2 main atomic lines as compared to RO_2–R_2O_3 multiplet separation, and the similar form of the Y structures both indicate that their origin lies in the degree of core hole screening by the excited f electron. Such considerations suggest that the Y structures in RO_2 originate from transitions to a 4f admixture in the conduction states. The interaction an excited 4f electron with a finite f continuum admixture may lead to further broadening of the 3d–4f lines in these oxides.

In what follows below, we understand by a localized f electron an electron which attaches to the inner reaches of the R atom, and by a delocalized electron, one which overlaps with the valence band.

The picture of the ground state of the rare-earth atom in RO_2 emerging from our discussion is that in each case, owing to R–oxygen covalent bonding, only a *fraction c* of the delocalized 4f electron remains on the R site. Its presence is detected in XAS by transitions to the 4f-admixture within the conduction continuum. The remaining fraction $(1-c)$ is used up in a partial ionic type of bonding and, as a result, appears as a

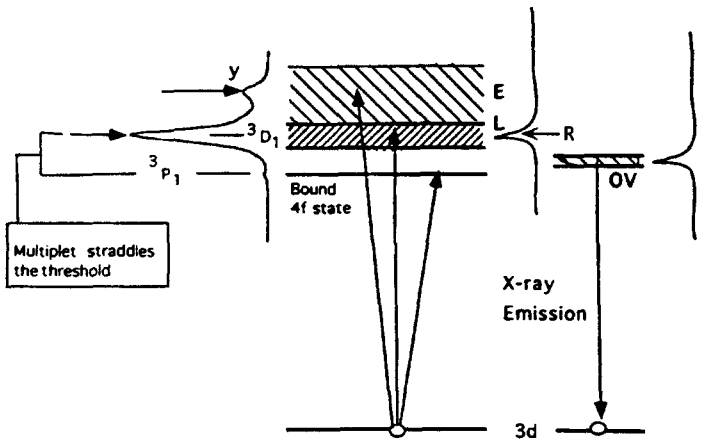

Fig. 12. A schematic diagram of $3d$–$4f$ transitions involved in (left) X-ray absorption spectra and (right) emission processes (right) in CeO_2. E and L are, respectively, the continuum and continuum-localised states. OV are the occupied valence (extended) states below the threshold. After Karnatak and Connerade (1996).

vacant localized f state. The present description of this specific valence state in the dioxides is different from that of the Ce intermetallics obtained by 3d XAS (Fuggle et al. 1983a, Gunnarsson et al. 1983) and other high-energy spectroscopies (Wuilloud et al. 1984, Schneider et al. 1985, Fuggle et al. 1983b). In these materials, nearly one electron occupies the localized f orbital and only a small fraction of this electron is delocalized into the valence band. In contrast to the La-like lines observed in CeO_2, the observation of the f^2-type atomic multiplet lines in Ce-based intermetallics (Fuggle et al. 1983a) confirms the presence of a localized f electron (with 4f occupation higher than 0.8 counts) in the ground state. The Y type structures similar to those observed in RO_2 with varying relative intensity according to f level hybridization are also observed about 5 eV above the main f^2 lines in the Ce intermetallics. In fact, this separation corresponds well to the 4–6 eV difference observed in XPS between a well-screened f^2 peak and an f^1 peak screened by a valence electron. The descriptions of the final states giving rise to f^1 and f^2 peaks in XPS and the f^2 multiplet and the Y structures in 3d XAS are now essentially the same.

The existence of both localized and extended 4f states is further supported by the findings of recent X-ray fluorescence measurements (Butorin et al. 1995) in CeO_2. In these experiments, a monochromatic X-ray beam is tuned successively to different energy positions in the M_{IV-V} spectrum of CeO_2, and fluorescence spectra are recorded. When the incident beam, as indicated by a horizontal arrow in fig. 12, is tuned to the 884 eV main $^3D_1$ line of the M_V spectrum, the fluorescence spectrum exhibits a resonant X-ray emission line at the same energy. If the photon energy is tuned to the Y structure at 889 eV, the resonance line disappears, and the normal fluorescence emission line appears much below the energy of the corresponding Y structure. These observations demonstrate that the excited 4f electron does not fall back to fill the 3d hole, and thus does not form any

3d–4f multiplet. Instead, an electron from the valence band drops in, and gives rise to an emission line in fluorescence. Thus, the spectra provide direct and unambiguous evidence of the existence of extended 4f states in CeO_2.

The argument that, in CeO_2, the 3 eV-wide oxygen 2p band (Koelling et al. 1983) contains a substantial amount of extended 4f character is further supported by recent XAS and XPS experiments on Y_2O_3 doped with CeO_2 (Douillard et al. 1994). They measured the L_{III} edge and 3d XPS of Ce in samples containing 5% and 13% of Ce atoms. They found that the local arrangement in the solid solution is well-represented by an eightfold coordination around Ce atoms, with a Ce–O distance shorter than that in CeO_2. The oxygen K-edge spectra of the doped samples demonstrated the existence of extended unoccupied f-character states, characteristic of tetravalent Ce.

The impurity Anderson model calculations (Kotani and Ogasawara 1992) on the Ce and Pr dioxides provide a reasonable description of the positions of the various 3d XAS structures, and 4f occupancies which are in agreement with those obtained by band structure calculations (Koelling et al. 1983). However, the distinction between the 4f occupancies pertaining to an f electron in a localized state and that of an extended state is not so clear in this model – hence the controversy over CeO_2 as to whether it is a covalent or mixed valent insulator. One does observe the presence of local f^0, f^1 and f^7 components in the 3d XAS of CeO_2, PrO_2 and TbO_2 respectively. Surprisingly, the high-energy feature shows no recognizable trace of $3d^9f^2$, $3d^9f^3$ or $3d^9f^8$ final multiplets in these cases. Instead, one observes structures due to transitions to extended states. Thus, we see that 3d XAS distinguishes a quasi-atomic final state from extended states by a careful analysis of multiplet identification, and that the persistence of multiplets in XAS spectra is the best evidence for quasi-atomic localization.

In the context of mixed valence and covalence it is worth mentioning here the recent work of Hu et al. 1995 on 4f covalence of Cs_2RbTbF_7. These authors studied Tb-L_{I-III}, Tb-$M_{IV,V}$ and F-K XAS as well as 3d core-level photoemission (3d-PES) of this compound. The spectral features revealed the weakest 4f-ligand hybridization known, and their F-K spectrum provided new insight into 4f-ligand–p mixing. Here again, a simplified Anderson impurity model calculation (Imer and Wuilloud 1987) provides a simple interpretation. Calculations for Tb-$3d_{5/2}$ PE and Tb-M_V XAS yield the 4f occupation $n_f = 7 + 0.2$. The width of the Tb-M_V multiplet in XAS was observed to be 2.8 which is similar to that given for Gd_2O_3.

These results demonstrate that, in Cs_2RbTbF_7, seven 4f localized electrons are used to form the 3d–4f multiplets, and that the remaining 0.2 electron is delocalized into F-2p bands. These delocalized or extended electrons in the valence band are, in fact, responsible for the line broadening observed in M_{IV-V} spectra. The situation is similar to molecular spectral lines originating on a specific atom, leading to much wider spectral lines than those of the corresponding free atom. In a solid, the 4f-valence band mixing in the initial state can be described as a $4f^0 + 4f^1\upsilon$ mixture, where υ is a hole in the valence band; f^0 and f^1 are localized quasiatomic states, and result of this ground state mixing is the formation of bonding and antibonding states. Clearly, the bonding states in the valence band cannot be localized, and must extend over the valence band.

The concept of an extended 4f state is better understood by invoking a quasi-atomic model based on the principles described in sect. 2 of this chapter. The general idea is that a barrier is formed, owing to the combined effects of the Coulomb interaction in a many-electron atom and the centrifugal repulsion for a 4f electron. This gives rise to a double-well potential in which the outer well is shallow and extended. We discuss this idea in more detail below, in connection with the XAS of higher oxides of Ce, Pr and Tb.

3.6. *Rare-earth valence in RO_x ($R = Ce, Pr, Tb$; $1.5 < x < 2$)*

The fluorite structure-related and oxygen-deficient binary higher oxides of Ce, Pr and Tb are interesting compounds in which to study R valence. Eyring (1979) reviewed the phase diagrams and structural aspects of these oxides, and some further work on their structure is reported by Zhang et al. (1993a,b). Among the two higher oxide phases, one is the homologous sequence having the generic formula R_nO_{2n-2}. There are other fluorite-related structures with compositions unrelated to this homologous sequence. The determination of the structural architecture of the members of this sequence took several decades (see e.g. Zhang et al. 1993a,b). The parent structure R_7O_{12} consists of parallel strings of oxygen vacancies along $\langle 111 \rangle$. The beads of the string consist of two vacant oxygen sites separated by $\frac{1}{2}\langle 111 \rangle$ formed as a cluster of composition R_7O_{12} from the coordination cube of a metal atom string. The unit cell of the parent R_7O_{12} contains one bead. All known members of the series have the $\frac{1}{2}\langle 211 \rangle$ axis in common. This defect cluster provides an element of structure which, when appropriately combined with units of RO_2 for the more oxidized members, could account for the compositions for the entire series. Later, neutron diffraction data showed that some of the structures suggested by this model are not correct. With better knowledge of three members of Pr_nO_{2n-2} and two members of the Tb_nO_{2n-2} sequence, Zhang et al. (1993a,b) developed a new hypothesis for the structural principles involved. Here, we will not go into the details of the structural model described by Zhang et al. (1993a,b). We merely mention that the defect cluster whose composition is $R_7/2O_6\upsilon_O$ (υ_O is a vacant oxygen site) is considered as the basic structural element. In order to represent all intermediate phases they also introduced another structural element, namely tetrahedrally coordinated oxygen, represented as $R_{1/2}O$. When combined in the right proportions, all known or proposed structures can be represented in this way.

From the standpoint of valence, the intermediate oxides are very interesting. The presence of oxygen vacancies as lattice defects leads to a variation in the R–O separations which may result in changes as high as 19% lowest and highest R–O separations in Tb_7O_{12} listed by Zhang et al. (1993a,b). We will see in the following paragraphs how the valence transition was tracked in these oxides by using XAS measurements and crystallographic data on R–O distances.

The X-ray absorption measurements were performed on a large number of Pr and Tb intermediate oxides. Samples were prepared (see Gasgnier et al. 1989) in the Department of Chemistry, Arizona State University, Tempe, USA and the Laboratoire de Terres Rares at Bellevue, France. In the CeO_x sequence, only CeO_2 is stable. Intermediate oxides of

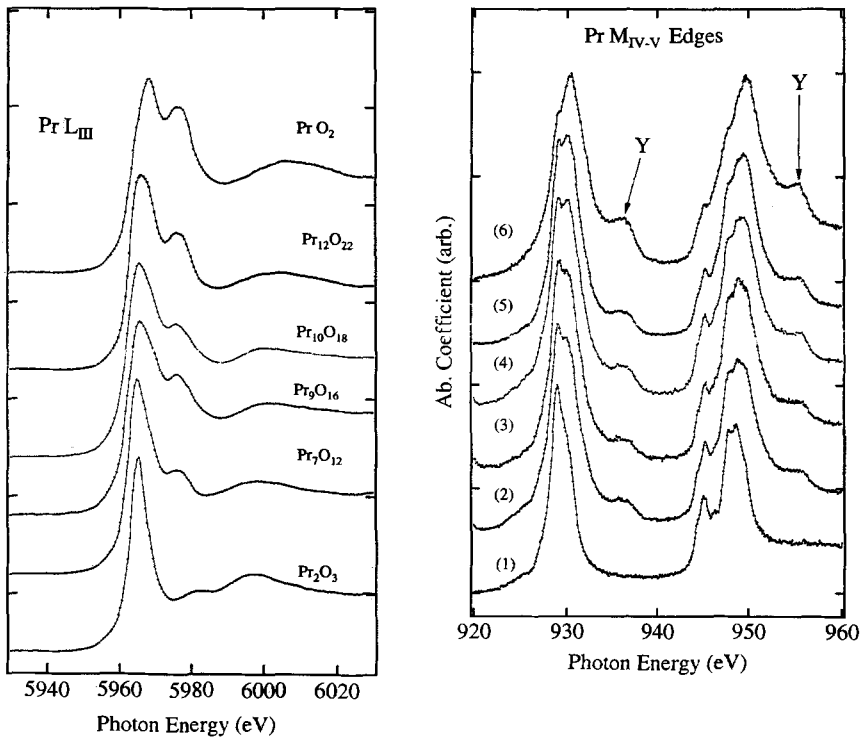

Fig. 13. spectra of binary higher oxides of Pr. (a) L_{III} and (b) M_{IV-V} spectra of Pr oxides. For brevity, in panel (b) the spectra are numbered and correspond to the same oxides as in panel (a). After Gasgnier et al. (1987, 1989).

Ce get oxidized slowly to higher phases when left under ordinary atmospheric conditions. The XAS measurements were only performed for stable compounds in the PrO_x and TbO_x systems. The results of L_{III} and M_{IV-V} XAS measurements were previously known. In the new series of experiments, the spectra of the sesquioxides and dioxides were used as references. Examples of selected absorption measurements on the L_{III} edge of Pr in Pr_2O_3, Pr_7O_{12}, Pr_9O_{16} (Gasgnier et al. 1987), $Pr_{10}O_{18}$, $Pr_{12}O_{22}$ (Gasgnier et al. 1989) and PrO_2 are given in fig. 13a and those of Tb in Tb_2O_3, Tb_7O_{12}, $Tb_{11}O_{20}$ (Esteva et al. 1986) and TbO_2 in fig. 14a. The corresponding M_{IV-V} spectra of these compounds are given in figs. 13b and 14b, respectively.

The L_{III} absorption spectra (normalized to the absorption jump) for trivalent Pr and Tb oxides (figs. 13a and 14a) exhibit a single absorption line and are similar in form. At the other end of the RO_x system, the L_{III} edges of CeO_2, PrO_2 and TbO_2 exhibit complex structure (Dexpert et al. 1987). In the case of CeO_2 and PrO_2, the main structure consists of two well-resolved features of comparable intensity, whereas, in TbO_2 (fig. 14a), the low-energy feature appears as a shoulder. The intermediate oxide spectra in general show a clear evolution of the spectral features as compared to those from the corresponding

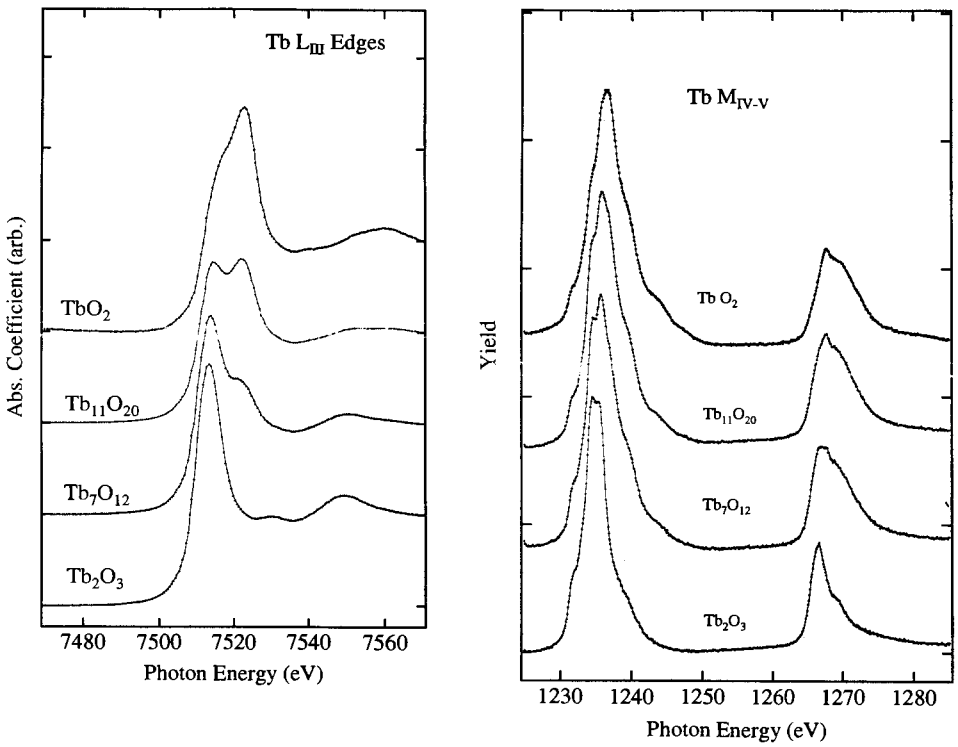

Fig. 14. spectra of binary higher oxides of Tb. (a) L_{III} and (b) M_{IV-V} spectra of Tb oxides. After Esteva et al. (1986).

trivalent oxides. These oxides exhibit a doublet structure, in which the low-energy line for smaller values of x is almost coincident with that of the trivalent oxides. From R_2O_3 to RO_2 (R = Pr and Tb) in RO_x, it is apparent that (i) the first peak shifts 3 eV towards higher energies; (ii) a second peak of gradually increasing intensity but constant energy appears, approximately 8 eV above the first one in both systems; and finally (iii) in PrO_2, the intensities of both peaks are comparable, whereas, in TbO_2, the first peak appears only as a shoulder.

The M_{IV-V} spectra from trivalent Pr and Tb oxides (figs. 13b, and 14b) are characteristic of $3d^94f^{n+1}$ multiplet structures separated into two spin–orbit groups. The observed RO_2 spectra are rather complex (wide multiplets, Karnatak et al. 1987b) and exhibit additional features such as Y shown in fig. 13b due to involvement of the 4f electron in R–oxygen. It is worth emphasizing yet again that the M_{IV-V} spectra of the R in general are characteristic of the $3d^94f^{n+1}$ final configuration involved in the transition. Thus, the spectral weights of the different 3d–4f multiplets observed in a given intermediate oxide give a direct and quantitative measure of the R^{3+} and R^{4+} ions present in the oxide phase. As an example, we show in fig. 15 a M_V spectrum of Tb_7O_{12} (Gasgnier et al. 1989) deconvoluted into

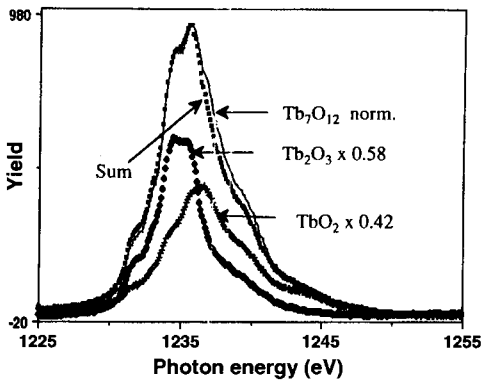

Fig. 15. Deconvolution of the M_V peak of Tb_7O_{12}. After Gasgnier et al. (1989).

the Tb_2O_3 (Tb^{3+}) and TbO_2 (Tb^{4+}) spectra in appropriate proportions, as given by the chemical formula. Considering the purities of the three independently prepared oxides involved in the deconvolution procedure the agreement between the spectrum obtained by summing the respective contributions from Tb^{3+} and Tb^{4+} ions and that of Tb_7O_{12} is satisfactory. Similar results are obtained for all other intermediate oxides studied. This fact is important, as it indicates that the 4f distribution around a given ion in the lattice is not modified by the presence of different ions. Similar deconvolutions performed in the case of the L_{III} edges of the intermediate oxides have so far remained unsuccessful. For example, an attempted deconvolution for $Tb_{11}O_{20}$ yielded the following result: about 25% discrepancy was found in the peak height of $Tb_{11}O_{20}$ between experiment and the spectrum synthesized by summing suitably weighted Tb_2O_3 and TbO_2 spectra. This discrepancy was found to be 12% in the case of Tb_7O_{12}. This implies that, in an intermediate oxide at a given ion site, the electronic structure cannot be described by a simple linear combination of the contributions of randomly distributed R^{+3} and R^{+4} ions. At this stage, it is useful to reconsider the relationship between the RO_2 dioxide on one hand and different forms of the sesquioxides on the other. We shall not go into the details of the crystal chemistry of these oxides and simply refer to the article by Eyring and Holmberg (1963). In the dioxide, the metal atoms are eight-coordinated, and in the (C, B, A-type) sesquioxides the metal atom may be 6- and/or 7-coordinated. Whereas the C-type is fluorite related, B-type is monoclinic and related to the A-type which is hexagonal. The L_{III} measurements (Karnatak et al. 1985) on C-Pr_2O_3 and A-Pr_2O_3 show a similar single absorption line, and the peak in the former is slightly higher than in the latter. One might seek to attribute this modification of the line to the change in density of the sd conduction states of A-Pr_2O_3 as compared to C-Pr_2O_3, but this is too small to account for the discrepancy between the observed intermediate oxide spectrum and that obtained by summing the R_2O_3 and RO_2 spectra.

Thus the picture emerging from the observations on intermediate oxides RO_x is:

(1) the M_{IV-V} spectra which probe the 4f distributions of individual ions show only two distinct type of ions. As the oxygen content x is increased in a higher oxide, the relative number of R^{4+} ions increases. We emphasize that the intermediate oxide

(RO_x) spectra are *faithfully reproduced* by summing suitable spectral weights of the individual precursors trivalent sesquioxide and tetravalent dioxide spectra. Moreover, the present results are *not* in agreement with the presence of $R^{3.5+}$–average valence ions inferred from electrical conductivity measurements (Inabe and Naito 1983a,b).

(2) The L_{III} edges of intermediate oxides exhibit structures which are the residue of the individual valence band structure of the trivalent and tetravalent R atoms. Since the valence band electrons of the metal atoms are delocalized over the crystal lattice, deviation of the density of states at a given site from that obtained by suitably weighted individual density of states of trivalent and tetravalent atoms is always expected for a given intermediate oxide.

In order to understand the L_{III} and M_{IV-V} spectral behaviour in intermediate oxides, we must examine carefully recent precise crystallographic data for these oxides. In this context, we examine the relevant data on R–O distances in Tb_7O_{12} (Zhang et al. 1993a,b) determined by Rietveld analysis of high resolution neutron diffraction data. We also consider similar information on Pr_7O_{12} (von Dreele et al. 1975). The reason for selecting data on the R–O separation is that XAS selectively probes the electronic distribution around only the R atoms in these oxides.

Neutron and X-ray diffraction studies of RO_x (von Dreele et al. 1975, Zhang et al. 1993a,b) show that a given R ion may be coordinated by 6, 7 or 8 oxygen atoms and may be tri- or tetravalent. The R–O distances vary appreciably around a given ion. A crucial question about RO_x is: how are the R^{3+} and R^{4+} ions distributed in the fluorite lattice? In a previous X-ray absorption study of RO_x, we emphasized that R ions are randomly distributed in the fluorite lattice and that the $R^{3.5+}$ type of mixed valence ions do not exist.

In isostructural Pr_7O_{12} (von Dreele et al. 1975) and Tb_7O_{12} (Zhang et al. 1993a,b), the rhombohedral cell contains one Pr(1) or Tb(1) atom coordinated by six O atoms. There are six Pr(2) or Tb(2) atoms each coordinated by seven O atoms. This gives a total of $6+6x7=48$, the number of R–O bonds in the cell. The Pr(1) or Tb(1) atoms are each surrounded by six equidistant O atoms whereas the Pr(2) or Tb(2) atoms are each surrounded by seven O atoms with variable R–O distances. In these oxides, the O atom, being more electronegative than the central R atom induces an attractive interaction on an f electron of the R atom. This interaction is proportional to $(1/a)^2$, where a is the R–O separation. As a decreases, at a critical value a_0, the interaction becomes sufficient to pull out a 4f electron and to drive a trivalent to tetravalent transition. This process implies an increase in the population of the valence electron by transfer of a 4f electron to the oxygen band.

In order to understand the behaviour of the valence transition and its $(1/a)^2$ dependence, we arrange the different $1/a^2$ values in ascending order and then index(n) them. The final plot in fig. 16 is, in fact, a $1/a^2$–bond index plot. For brevity the six equal $1/a^2$ values for R(1) are represented by a single lozenge. We also give in this plot the $1/a^2$ values (shaded squares) for the ionic radii of Pr(III) and Pr(IV) in the octahedral coordination (Shannon and Pretwitt 1969). We immediately see that at least four points of the graph lie on a plateau. We draw a mean horizontal line passing through them. The points falling

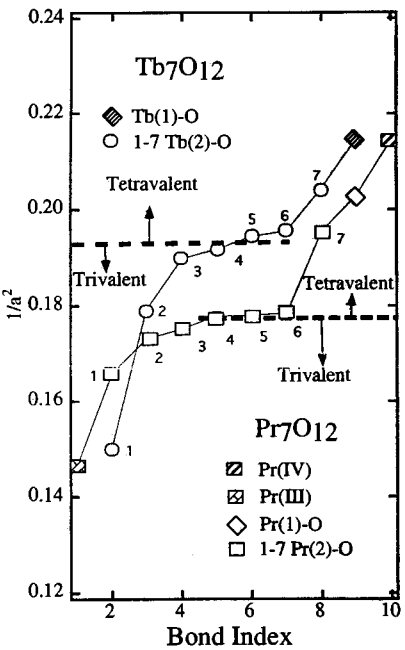

Fig. 16. Valence transition in Pr and Tb intermediate oxides. The six oxygen-coordinated Tb(1) and Pr(1) are obviously tetravalent. Note that the trivalent to tetravalent transition takes place in seven oxygen-coordinated Pr(2) and Tb(2) atoms. The critical *R*–O lengths below which the localised 4f electron leaks into the valence band to form a tetravalent bond are estimated to be 2.267 and 2.370 Å, respectively, for Tb and Pr atoms. After Karnatak and Connerade (1996).

above this line can be assigned as arising from tetravalent bonds and those below, from trivalent R–O bonds. For six 7-coordinated R(2) atoms, unit cells of R_7O_{12}, the R–O– bond lengths vary appreciably. Four of the $1/a^2$ points corresponding to Bond indices 1, 2, 3 and 4 are below the horizontal line showing trivalence, whereas the other four points including R(1)–O bonds are above the horizontal line in the tetravalent region. A similar plot obtained from recent neutron diffraction data (Zhang et al. 1993a,b) on Tb_7O_{12} is also included in fig.16 for comparison. The present graph concerns only the similar unit cells of Pr_7O_{12} and Tb_7O_{12}. The six R–O bonds around the R(1) atom together with 42 bonds from six 7-coordinated R(2) atoms form a total of 48 R–O bonds belonging to a unit cell. To maintain the stoichiometry of the oxide we should have at least about 21 R–O tetravalent bonds in the unit cell. This situation implies that the three R–O bonds with indices 5, 6 and 7 are clearly tetravalent above the respective horizontal lines for Pr_7O_{12} and Tb_7O_{12}. For R(2) atoms, this gives us a total of 18 bonds. The remaining three tetravalent bonds should belong to bond index 4 in six R(2) atoms. It is rather difficult to locate precisely which of the R–O bond with index 4 becomes tetravalent in one or two of the R(2) atoms. In our plots, we have only given the data for one R(2) atom by supposing that the other five atoms are equivalent. It is not surprising that the bond with index 4 of the R(2) atoms in both oxides adjusts its length to yield tetravalent bonds. It can be easily seen that, in fig. 16, the points representing the bonds having index 4 are quite close to the corresponding horizontal lines. The transition from the trivalent to the tetravalent ion is accompanied by transfer of a localized 4f electron into the valence band. This transfer

is governed by the typical value of a. For higher values of a, trivalence is stabilized by confining the 4f electron inside a potential barrier. This is clearly seen in the case of atoms at Pr(1) sites and atoms in $Pr(III)_2O_3$. In both cases, the $1/a^2$-values are different and are either above or below the horizontal line. The four $1/a^2$ points corresponding to the different Pr–O bond lengths of the Pr(2) site and that for Pr(IV)O2 lie above the horizontal line. For the shorter Pr–O bond lengths, the 4f electron overcomes the potential barrier and delocalizes as a valence electron to form a covalent bond. In this context, it is rather important to remember that the X-ray absorption method is a fast method which gives the instantaneous picture of the valence transition in the intermediate oxides RO_x.

It turns out that the M_{IV-V} XAS describes a situation in which a 4f electron belonging to the R(2) atom coordinated with seven oxygen atoms, has a finite probability of leaking to the corresponding oxygen atom and thus forming a covalent bond with it. In the other case, this electron remains attached to R if the surrounding oxygen atom is far away and is not able to pull it out. This situation leads to an ionic bond in which the 5d and 6s electrons from R and oxygen 2p electrons form the valence band. This picture is in agreement with the presence of ionic and covalent bonds around a given Sb atom in unconventional semiconducting chalcogenides (Olivier-Fourcade et al. 1991, 1993). Generally, ionic bonds are longer than covalent bonds, and this situation leads to deformed microstructures around R in RO_x similar to those observed in Sb–based chalcogenides.

This interpretation is supported both by our observation of M_{IV-V} XAS and by our analysis of the valence. It also provides an explanation for the failure of the L_{III} absorption analysis of valence in RO_x by using weighted absorption spectra of R_2O_3 and RO_2. From the crystallographic analysis (von Dreele et al. 1975, Zhang et al. 1993a,b) we see that, in general, RO_x contains nonequivalent atoms. They may have the same or different coordination numbers from those of the reference oxides. When coordination numbers are the same and the valence also remains the same as one of the reference oxides, we expect to see structure resembling the residue of the structure due to the reference oxide. In the particular case of R_7O_{12}, we do observe a structure due to R(1) atoms at the L_{III} edge which resembles the one for RO_2. The R(2) atom has a strongly deformed electronic distribution around it, due to bonds whose lengths and character are quite different. This explains the discrepancy at the L_{III} edge of RO_x.

We can now discuss the above observations in the light of the double-well potential model (Connerade 1978a,b, 1982, 1983) originally studied in the context of atomic 4f orbital collapse (Connerade 1978a,b – see also sect. 2 of the present chapter). The interpretation of the present experimental observations requires two type of 4f orbitals to coexist. This possibility was originally suggested by Gschneidner (1971) for rare earth metals on the basis of their melting points and sublimation energy data. Band and Fomichev (1980) and Band et al. (1988) made a similar suggestion for atoms of the 4f sequence. Schlüter and Varma (1983) approached the problem in a manner more adapted to the description of the condensed phase. Details of the double valley potential model and the role of centrifugal barrier effects on the valence changes in rare earths have previously been discussed by Connerade and Karnatak (1990). In the context of RO_x, this model was further discussed by Karnatak (1993), and coexistence of ionic and covalent

bonds in the fluorite lattice was invoked (Karnatak and Connerade 1996) to explain the valence in intermediate RO_x. We therefore concentrate on the main points.

As described in sect. 2, the potential of a free atom from the rare-earth sequence develops two wells. The outer well is the usual atomic well, with an asymptotically coulombic behaviour (long range potential), and contains an infinite number of states. The inner one is a short range well, which is close to the critical binding condition to support one state (4f). This model is backed up by central field self-consistent *ab initio* Hartree–Fock calculations for free atoms, and involves *no* adjustable parameters. It correctly describes (a) the order of filling of d and f subshells of the transition elements and R elements; (b) the fact that filling occurs deep inside the atom and (c) the behaviour of XAS of free atoms of the Q- and R-element sequences.

Concerning the present discussion (c) is particularly important. The reason is that the excited states responsible for giant resonances in free atoms are extremely sensitive to the degree of localization of the d and f orbitals *within the atom*. The double-well model explains why this occurs: since the inner well can (by the rules of elementary quantum mechanics) support only zero or one bound state, very small changes in the atomic radial potential deep inside the atom can precipitate large changes of localization. This effect is controlled by the binding strength of the inner well, and exists *even* when there is no positive barrier between the two wells (as usually occurs for d electrons). It is even possible to find situations where the 4f electron is evenly split between two wells and a hybrid or bimodal orbital occurs, with one maximum deep inside the atom, and one far outside.

It is evident that a solid made up of atoms of this kind would contain some of the 4f amplitude as localized states, while some, being external, would appear as extended 4f orbitals in the continuum or conduction band. It is also clear that a simplified model, in which all atomic states are regarded as possessing the fundamental property of being localized, and any form of delocalization is entirely attributed to a parametrised interaction representing the influence of the solid state fails to do justice to the complexity of the mechanism by which d and f shell filling actually occurs. The mere fact that *all* the elements which exhibit such behaviour come from the same part of the Periodic Table, and exhibit variations systematically related to atomic number, is clear evidence that the underlying mechanism cannot be reduced to a simple formulation in which changes of the internal atomic potential are not considered. Also, the persistence of atomic multiplet structure in the solid, normally used as a probe of the 4f count, shows that a form of quasi-atomic orbital collapse must underpin the localization-delocalization processes in Q–metals and compounds.

The challenge is to develop a description taking account of *both* atomic and solid state effects. Difficulties surrounding the theoretical description of extended 4f states within the prevailing Anderson localization models show that a fully consistent theory as yet does not yet exist.

Double-well potentials, on the other hand, provide an intuitive picture for trivalent and tetravalent R inside an intermediate oxide. Consider first trivalent R atoms. In the intermediate oxides, they yield M_{IV-V} spectra with recognizable sharp multiplets, interpreted as due to atomic $3d^9 4f^{n+1}$ final states. In this case, the 4f orbital is well

localized in the inner well. A potential barrier isolates these electrons from the outer valence electrons and, as a result, the absorption spectra become insensitive to the environment and the number of the outer valence electrons, and depend only on the number of electrons in the 4f subshell.

For tetravalent atoms, we observe that M_{IV-V} spectra show broader multiplets than those of trivalent atoms. The multiplet features appearing in the spectra of tetravalent atoms are easily identified with those appearing in the sesquioxides of the corresponding $Z-1$ elements. In other words, the M_{IV-V} multiplets in dioxides of Ce, Pr and Tb correspond well to those observed, respectively, in La, Ce and Gd sesquioxides, indicating that the outer 4f electron of the trivalent R has already left the inner reaches of the atom. If we think of an orbital delocalized from the inner well, it would now lie in the outer reaches of the atom, preserving its 4f character but giving rise to no observable multiplet structure *even for a free atom*. As we have noted above, the absorption transitions to the vacant extended 4f states in the conduction band give rise to broad Y type structures in dioxides. In the case of CeO_2 and PrO_2 these structures show no multiplet structure at all, confirming the extended character of the states responsible. It is thus very logical to consider them as extended states of 4f character.

The above results are significant in refining our understanding of the mechanisms involved. They are consistent with the double-well potential model. The transition from trivalent to tetravalent ion is associated with the transfer of a localized 4f electron into the valence band. This transfer is governed by typical values of a. For higher values of a, trivalence is stabilized by confining the 4f electron within a potential barrier. This is clearly seen for R(2) atoms and for atoms in $R(III)_2O_3$. The $(1/a)^2$ values for each oxide are then different, and fall either above or below a horizontal line. This observation is in line with the potential barrier model for rare earths. The four $(1/a)^2$ points corresponding to different Pr–O bond lengths of the Pr(2) atoms and that for Pr(IV)O2 lie above the same horizontal line. For shorter Pr–O bond lengths, the 4f electron overcomes the potential barrier and delocalizes as a valence electron to form a covalent bond. This situation is well described within the framework of a double-well potential model. In this context it is rather important to remember that the X-ray absorption method is a fast method which provides an instantaneous picture of the valence transition in the intermediate oxides RO_x.

4. Conclusion

The origin of the valence transition in 7 out of 14 rare-earth elements has been traced through from their atomic phase, to clusters and in solid oxides. Amongst Metallic elements of the Sm group, Sm and Tm both exhibit a coordination dependence of the valence. The study of small matrix-isolated clusters of these elements by X-ray absorption spectroscopy (XAS) yields a quantitative picture of the valence transition as a function of cluster size. This explains why one observes surface divalence only on a very rough surface of Tm-metal in comparison to Sm-metal, where it is easily observable. A comparison with an icosahedral model of the packing of the metal atoms is applied to estimate the number of surface and bulk atoms in small aggregates. Supposing that all

surface atoms in Sm are divalent and bulk atoms trivalent, the icosahedral model yields a curve which reveals a relative slow valence transition as compared to the one observed experimentally. This indicates that metallic bonding in the metallic clusters of Sm and Tm starts at much smaller sizes than predicted by the icosahedral model. The valence problem in Ce, Pr and Tb higher oxides is presented and discussed in detail. X-ray absorption data shows the presence of two type of spectral features in the intermediate oxides. These features in 3d–4f spectra are unambiguously identified as the stoichiometrically-weighted contributions of the trivalent and tetravalent sesqui- and dioxides. The dioxide spectra are observed to be complex, and are found to be characteristic of covalent M–O bonds. A potential barrier model is invoked to explain the valence transition in Sm group elements. For covalent features in Ce, Pr and Tb higher oxide spectra, a double-well potential barrier is applied to account for the delocalization of the 4f electron in the valence band.

In these oxides, the 6s and 5d and, to a lesser extent, the 4f electrons of the rare earth atom are mainly responsible for electrical transport and structural properties, whereas the localized 4f electrons govern the magnetic properties. X-ray absorption spectroscopy (XAS) offers the important advantage of simultaneously probing the 4f and the ds conduction states in these oxides. In XAS, the dipole selection rules are strictly obeyed and this facilitates the identification of the spectral features. Generally, the $3d \rightarrow 4f(M_{IV-V})$ or $4d \rightarrow 4f(N_{IV-V})$ absorption transitions are studied. In these absorption processes the excited 4f electron participates directly in the transition. The resulting multiplet structure is observed to provide a finger-print of the 4f population of the rare earth atom. The modification in the valence band electron distribution introduced by the delocalization of a 4f electron is probed by the transition of a 2p (L_{II-III}) electron in the vacant sd conduction states. In this case the 4f electron does not participate directly in the transition.

Two models exist which are in a sense complementary and allow valence transitions to be discussed. The Anderson localization model is mostly applied in a parametric scheme, and allows many phenomena to be considered together as resulting from hybridisation effects in the conduction band. However, atomic effects are not so well accounted for in this picture: essentially, they are added in by hand. Another approach is the quasi-atomic double-well model. This scheme is not parametric, since it is based on *ab initio* Hartree–Fock calculations. It accounts for atomic aspects, such as the general region of the Periodic Table where such phenomena are encountered. Also, it provides a mechanism for localization (orbital collapse). Finally, it allows one to understand and explain the properties of rather special states (the extended 4f states) which are delocalized, but retain certain atomic features. However, this model is unable to incorporate solid state effects in a simple way.

References

Baer, Y., and W.D. Schneider, 1987, in: High Energy Spectroscopy, Vol. 10 of Handbook on the Physics and Chemistry of Rare Earths, eds K.A. Gschneidner Jr, L. Eyring and S. Hüfner (North-Holland, Amsterdam) ch. 62, p. 1.

Band, I.M., and V.I. Fomichev, 1980, Phys. Lett. A **75**, 178.

Band, I.M., K.A. Kikoin, M.B. Trzhavskovskaya and D.I. Khomskii, 1988, Sov. Phys. JETP **67**, 1561.

Bauchspiess, K.R., W. Boksch, E. Holland-Moritz, H. Launois, R. Pott and D. Wohlleben, 1981, in: Valence Fluctuations in Solids, eds L.M. Falicov, W. Hanke and M.P. Maple, p. 417.

Beaudry, B.J., and K.A. Gschneidner Jr, 1978, in: Handbook on the Physics and Chemistry of Rare Earths, Vol. 1, eds K.A. Gschneidner Jr and L. Eyring (North-Holland, Amsterdam) ch. 2, pp. 173–232.

Belrhmi-Belhassan, A., R.C. Karnatak, N. Spector and C. Bonnelle, 1981, Phys. Lett. **82A**, 174.

Blancard, C., 1989, Docteur en Science Thesis (Université Paris-Sud, Orsay, France) unpublished.

Blancard, C., J.M. Esteva, R.C. Karnatak, J.-P. Connerade, U. Kuetgens and J. Hormes, 1989, J. Phys. B **22**, L575.

Blancard, C., J.M. Esteva, R.C. Karnatak, B.K. Sarpal, J.-P. Connerade, U. Kuetgens and J. Hormes, 1990a, in: 2nd European Conf. on Progress in X-ray Synchrotron Radiation Research, eds A. Balerna, E. Bernieri and S. Mobilio, Conf. Proc. Vol. 25 (SIF, Bologna) p. 117.

Blancard, C., J.M. Esteva, R.C. Karnatak, J.-P. Connerade, U. Kuetgens and J. Hormes, 1990b, in: 2nd European Conf. on Progress in X-ray Synchrotron Radiation Research, eds A. Balerna, E. Bernieri and S. Mobilio, Conf. Proc. Vol. 25 (SIF, Bologna) p. 113.

Bonnelle, C., R.C. Karnatak and J. Sugar, 1974, Phys. Rev. A **9**, 1920.

Bonnelle, C., R.C. Karnatak and N. Spector, 1977, J. Phys. B **10**, 795.

Boring, A.M., and J.L. Smith, 1987, in: Giant Resonances in Atoms, Molecules and Solids, eds J.-P. Connerade, J.-M. Esteva and R.C. Karnatak, NATO ASI Series B, Vol. 151 (Plenum Press, New York) p. 311.

Bréchignac, C., M. Broyer, Ph. Cahuzac, G. Delacretaz, P. Labastie and L. Wüste, 1985, Chem. Phys. Lett. **120**, 559.

Bréchignac, C., M. Broyer, Ph. Cahuzac, G. Delacretaz, P. Labastie and L. Wüste, 1988, Phys. Rev. Lett. **60**, 275.

Bréchignac, C., Ph. Cahuzac, F. Carlier and J.Ph. Roux, 1993, Z. Phys. D **28**, 67.

Bucher, B., P. Steiner and P. Wachter, 1991, Phys. Rev. Lett. **67**, 2717.

Butorin, S.M., D.C. Mancini, J.-H. Guo, N. Wassadhl and J. Nordgren, 1995, J. Alloys & Compounds **225**, 230.

Connerade, J.-P., 1978a, Contemp. Phys. **19**, 415.

Connerade, J.-P., 1978b, J. Phys. B **11**, L381.

Connerade, J.-P., 1982, J. Phys C **15**, L367.

Connerade, J.-P., 1983, J. Less-Common Met. **93**, 171.

Connerade, J.-P., 1984, in: The Physics of Non-Rydberg States, Les Houches School in Theoretical Physics, Session XXXVIII (Elsevier Science, Amsterdam).

Connerade, J.-P., 1991, J. Phys. B **24**, L109.

Connerade, J.-P., and R.C. Karnatak, 1981, J. Phys. F **11**, 1539.

Connerade, J.-P., and R.C. Karnatak, 1990, Comm. At. Mol. Phys. **XXIV**, 1.

Crecelius, G., G.K. Wertheim and D.N.E. Buchanan, 1978, Phys. Rev. B **18**, 6519.

Demekhin, V.F., 1974, Sov. Phys.-Solid State, **16**, 659.

Dexpert, H., R.C. Karnatak, J.-M. Esteva, J.-P. Connerade, M. Gasgnier, P.E. Caro and L. Albert, 1987, Phys. Rev. B **36**, 1750.

Domke, M., C. Laubschat, M. Prietsch, T. Mandel, G. Kaindl and W.D. Schneider, 1986, Phys. Rev. Lett. **56**, 1287.

Douillard, L., M. Gautier, N. Thromat, M. Henriot, M.J. Guittet, J.P. Durand and G. Tourillon, 1994, Phys. Rev. B **49**, 16171.

Dupont, A., 1967, J. Opt. Soc. Am. **57**, 867.

Esteva, J.M., and R.C. Karnatak, 1987, in: Giant Resonances in Atoms, Molecules and Solids, eds J.-P. Connerade, J.-M. Esteva and R.C. Karnatak, NATO ASI Series B, Vol. 151 (Plenum Press, New York) pp. 361–379.

Esteva, J.M., R.C. Karnatak, J.C. Fuggle and G.A. Sawatzky, 1983a, Phys. Rev. Lett. **50**, 910.

Esteva, J.M., R.C. Karnatak and J.-P. Connerade, 1983b, J. Electron. Spectrosc. Related Phenom. **31**, 1.

Esteva, J.M., R.C. Karnatak, H. Dexpert, M. Gasgnier, P.E. Caro and L. Albert, 1986, J. Phys. Paris **47**, C8-955.

Eyring, L., 1979, in: Handbook on the Physics and Chemistry of Rare Earths, Vol. 3, eds K.A. Gschneidner Jr and L. Eyring (North-Holland, Amsterdam) ch. 27, p. 337, and references therein.

Eyring, L., and B. Holmberg, 1963, Adv. Chem. Ser. **30**, 46.

Fermi, E., 1928, in: Quantentheorie und Chemie, ed. H. Falkenhagen (Hinzel-Verlag, Leipzig) p. 1.

Fuggle, J.C., F.U. Hillebrecht, J.M. Esteva, R.C. Karnatak, O. Gunnarsson and K. Schönhammer, 1983a, Phys. Rev. **27**, 4637.

Fuggle, J.C., F.U. Hillebrecht, Z. Zolnierek, R. Lässer, Ch. Freiburg, O. Gunnarsson and K. Schönhammer, 1983b, Phys. Rev. B **27**, 7330.

Fujimori, A., 1983, Phys. Rev. B **28**, 2281.

Gasgnier, M., L. Eyring, R.C. Karnatak, H. Dexpert, J.M. Esteva, P.E. Caro and L. Albert, 1987, J. Less-Common Met. **127**, 367.

Gasgnier, M., G. Schiffmacher, L. Albert, P.E. Caro, H. Dexpert, J.M. Esteva, C. Blancard and R.C. Karnatak, 1989, J. Less-Common Met. **156**, 59–73.

Gauthé, B., J.M. Esteva, P. Dhez and R.C. Karnatak, 1983, J. Phys. B **16**, L263.

Göppert-Mayer, M., 1941, Phys. Rev. **60**, 184.

Griffin, D.C., K.L. Andrew and R.D. Cowan, 1969, Phys. Rev. **177**, 62.

Griffin, D.C., R.D. Cowan and K.L. Andrew, 1971, Phys. Rev. A **3**, 1233.

Gschneidner Jr, K.A., 1971, J. Less-Common Met. **25**, 405.

Gunnarsson, O., and K. Schönhammer, 1983, Phys. Rev. B **28**, 4315.

Gunnarsson, O., and K. Schönhammer, 1985, Phys. Rev. B **31**, 4815.

Gunnarsson, O., K. Schönhammer, J.C. Fuggle, F.U. Hillebrecht, J.M. Esteva and R.C. Karnatak, 1983, Phys. Rev. **28**, 7330.

Güntherodt, G., A. Jayaraman, B. Baltogg and M. Croft, 1981, Phys. Rev. Lett. **46**, 855.

Herbst, J.F., D.N. Lowy and R.E. Watson, 1972, Phys. Rev. B **6**, 1913.

Herbst, J.F., R.E. Watson and J.W. Wilkins, 1976, Phys. Rev. B **13**, 1439.

Herzberg, G., 1937, Atomic Spectra and Atomic Structure (Dover Publications, New York).

Hu, Z., E.-J. Cho, G. Kaindl and B.G. Müller, 1995, Phys. Rev. **B 51**, 7514.

Imer, J.-M., and E. Wuilloud, 1987, Z. Phys. B **66**,153.

Inabe, H., and K. Naito, 1983a, J. Solid State Chem. **50**, 100.

Inabe, H., and K. Naito, 1983b, J. Solid State Chem. **50**, 111.

Jo, T., and A. Kotani, 1988, Phys. Rev. B **38**, 830; J. Phys. Soc. Japan **57**, 2288.

Johansson, L.I., J.W. Allen and I. Lindau, 1981, Phys. Lett. **86A**, 442.

Kaindl, G., G. Kalkowski, W.D. Brewer, B. Perscheid and F. Holtzberg, 1984, J. Appl. Phys. **55**, 1910.

Kaindl, G., G. Kalkowski, W.D. Brewer, E.V. Sampathkumaran, F. Holtzberg, A. Schach and V. Wittenau, 1985, J. Magn. Magn. Mater. **47&48**, 181.

Karaziya, R.I., 1981, Sov. Phys. Usp. **24**, 775.

Karnatak, R.C., 1993, J. Alloys & Compounds **192**, 64.

Karnatak, R.C., and J.-P. Connerade, 1996, in: Correlations in Clusters and Related Systems; New Perspectives on the Many-Body Problem, ed. J.-P. Connerade (World Scientific, Singapore) pp. 95–113.

Karnatak, R.C., J.-M. Esteva and J.-P. Connerade, 1981, J. Phys. B **14**, 4747.

Karnatak, R.C., M. Gasgnier, H. Dexpert, J.-M. Esteva, P.E. Caro and L. Albert, 1985, J. Less-Common Met. **110**, 377.

Karnatak, R.C., J.M. Esteva, H. Dexpert, M. Gasgnier, P.E. Caro and L. Albert, 1987a, J. Magn. Magn. Mater. **63&64**, 518.

Karnatak, R.C., M. Gasgnier, H. Dexpert, J.-M. Esteva, P.E. Caro and L. Albert, 1987b, Phys. Rev. B **36**, 1745.

Kasuya, T., 1993, J. Alloys & Compounds **192**, 217.

Koelling, D.D., A.M. Boring and J.H. Wood, 1983, Solid State Commun. **47**, 22W.

Koskenmaki, D.C., and K.A. Gschneidner Jr, 1978, in: Handbook on the Physics and Chemistry of Rare Earths, Vol. 1, eds K.A. Gschneidner Jr and L. Eyring (North-Holland, Amsterdam) ch. 4, pp. 337–377.

Kotani, A., 1996, in: Correlations in Clusters and Related Systems; New Perspectives on the Many-Body Problem, ed. J.-P. Connerade (World Scientific, Singapore) p. 115.

Kotani, A., and H. Ogasawara, 1992, J. Electron. Spectrosc. Related Phenom. **60**, 257, and references therein.

Kotani, A., H. Mitzuta, T. Jo and J.C. Parlebas, 1985, Solid State Commun. **53**, 805.

Lang, J.K., Y. Baer and B.A. Cox, 1981, J. Phys F **11**, 121.

Lindberg, E., 1931, Nova Acta Regiae Soc. Sci. Ups. **7**, 7.

Lübcke, M., B. Sonntag, W. Niemann and P. Rabe, 1986, Phys. Rev. **34**, 5184.

Mackay, A.L., 1962, Acta Crystallogr. **15**, 916.

Mansfield, M.W.D., and J.-P. Connerade, 1974, Proc. R. Soc. London A **352**, 125.

Marabelli, F., and P. Wachter, 1987, Phys. Rev. **B36**, 1238.

Martin, W.C., R. Zalubas and L. Hagan, 1978, Atomic Energy Levels – Rare Earth Elements, National Bureau of Standards Reference Data Series, Circ. No. 60 (US Government Printing Office, Washington, DC).

McGuire, E.J., 1972, Phys. Rev. A **5**, 1043.

McWhan, D.B., S.M. Shapiro, J. Eckert, H.A. Mook and R.J. Birgeneau, 1978, Phys. Rev. B **18**, 3623.

Mehran, F., K.W.H. Stevens, E. Anastassakis, E. Bucher and H. Bach, 1971, Phys. Rev. Lett. **27**, 1368.

Mott, N.F., 1974, Philos. Mag. **30**, 403.

Neuenschwander, J., and P. Wachter, 1990, Phys. Rev. B **41**, 12693.

Niemann, W., W. Malzfeldt, P. Rabe, R. Haensel and M. Lübcke, 1987, Phys. Rev. **35**, 1099.

Olivier-Fourcade, J., A. Ibanez, J.C. Jumas, H. Dexpert, C. Blancard, J.M. Esteva and R.C. Karnatak, 1991, Eur. J. Solid State Inorg. Chem. **28**,409.

Olivier-Fourcade, J., P.-E. Lippen, J.C. Jumas, M. Womes, I. Lefebvre, M. Lannoo, J.M. Esteva and R.C. Karnatak, 1993, Eur. J. Solid State Inorg. Chem. **30**, 139.

Pastor, G.M., and K.H. Bennemann, 1994, in: Clusters of Atoms and Molecules, ed. H. Haberland, Vol. 52 of Springer Series in Chemical Physics (Springer, Berlin) pp. 86–113.

Racah, G., 1942, Phys. Rev. **61**, 186; **62**, 438.

Racah, G., 1943, Phys. Rev. **63**, 367.

Rademann, K., B. Kaiser, U. Even and F. Hansel, 1987, Phys. Rev. Lett. **59**, 2319.

Radtke, E.R., 1979a, J. Phys. B **12**, L71.

Radtke, E.R., 1979b, J. Phys. B **12**, L77.

Ramakrishnan, T.V., 1987, J. Magn. Magn. Mater. **63&64**, 529.

Rayane, D., P. Melinon, B. Cabaud, A. Hoareau, B. Tribollet and M. Broyer, 1989, Phys. Rev. A **39**, 6056.

Rosengren, A., and B. Johansson, 1982, Phys. Rev. B **26**, 3068.

Sarpal, B.K., C. Blancard, J.-P. Connerade, J.-M. Esteva, J. Hormes, R.C. Karnatak and U. Kuetgens, 1991, J. Phys. B **24**, 1593.

Schlüter, M., and C.M. Varma, 1983, Helv. Phys. Acta **56**, 147.

Schneider, W.D., C. Laubschat and B. Reihl, 1983, Phys. Rev. B **27**, 6538.

Schneider, W.D., B. Delley, E. Wuilloud, J.-M. Imer and Y. Baer, 1985, Phys. Rev. B **32**, 6819.

Shannon, R.D., and C.T. Pretwitt, 1969, Acta Crystallogr. **B25**, 925.

Shapiro, S.M., R.J. Birgeneau and E. Bucher, 1975, Phys. Rev. Lett. **34**, 470.

Sugar, J., 1972, Phys. Rev. A **6**, 1764.

Sugar, J., 1974, Phys. Rev. B **5**, 1785.

Sugar, J., W.D. Brewer, G. Kalkowski, G. Kaindl and E. Paparazzo, 1985, Phys. Rev. A **32**, 2242.

Teodorescu, C.M., J.M. Esteva, R.C. Karnatak, A. Elafif and M. Womes, 1997, J. Phys B **30**, 4293.

Thole, B.T., G. van der Laan, J.C. Fuggle, G.A. Savatsky, R.C. Karnatak and J.-M. Esteva, 1985, Phys. Rev. **32**, 5107.

Tracy, D.H., 1976, Proc. R. Soc. London A **344**, 563.

Tuilier, M.H., D. Laporte and J.M. Esteva, 1982, Phys. Rev. A **26**, 372.

von Dreele, R.B., L. Eyring, A.L. Bowman and J.L. Yarnell, 1975, Acta Crystallogr. B **31**, 971.

Wachter, P., 1982, in: Valence Instabilities, eds P. Wachter and H. Boppart (North-Holland, Amsterdam) p. 145.

Wachter, P., 1995, J. Alloys & Compounds **225**, 133.

Wertheim, G.K., and G. Crecelius, 1978, Phys. Rev. Lett. **40**, 813.

Wu, T.Y., 1933, Phys. Rev. **44**, 727.

Wuilloud, E., B. Delly, W. Schneider and Y. Baer, 1984, Phys. Rev. Lett. **53**, 202.

Wybourne, B.G., 1965, Spectroscopic Properties of Rare Earths (Wiley, New York).

Zhang, J., R.B. von Dreele and L. Eyring, 1993a, J. Solid State Chem. **104**, 21.

Zhang, J., Z.C. Kang and L. Eyring, 1993b, J. Alloys & Compounds **192**, 57.

Zimkina, T.M., V.A. Fomichev, S.A. Gribovskii and I.I. Zhukova, 1967, Sov. Phys. Solid State **9**, 1128.

Handbook on the Physics and Chemistry of Rare Earths
Vol. 28
edited by K.A. Gschneidner, Jr. and L. Eyring

Chapter 177

SIMPLE AND COMPLEX HALIDES

Gerd MEYER and Mathias S. WICKLEDER
Institut für Anorganische Chemie, Universität zu Köln, Greinstrasse 6, D-50939 Köln, Germany

Contents

Symbols and abbreviations

°C	degrees Celsius
DTA	differential thermal analysis
IR	infrared part of the electromagnetic spectrum
K	Kelvin
VIS	visible part of the electromagnetic spectrum
XANES	X-ray absorption near-edge structure
μ_{eff}	effective magnetic moment
μ_B	Bohr's magneton
σ	electrical conductivity

1. Introduction

1.1. *Nomenclature and scope*

Halides belong to the most important classes of compounds of the rare-earth elements (R). Except for the "simple" binary halides, RX_z ($z = 2$–4), numerous complex halides, for example $A_wR_yX_z$ and $A_wB_xR_yX_z$, respectively, have been synthesized and were structurally characterized (Meyer 1982).

In the simplest possible way we may define *complex halides* as all halides that contain more than one kind of cation and/or more than one kind of anion, with cation and anion standing for the less or more electronegative partners in one compound. Therefore, $NdCl_2$ and $NdCl_3$, for example, are simple or *binary halides* and NdOCl and K_2NdCl_5 are *complex halides*. NdOCl is also called a *mixed-anion halide*. K_2NdCl_5 is normally referred to as a *ternary halide*, $Cs_2NaNdCl_6$ is then a *quaternary halide*, and so forth.

Eu_4OCl_6 (Schleid and Meyer 1987a) will be considered a ternary halide in this article. It may also be considered a *multinuclear complex halide* as it contains isolated tetrahedra of Eu^{2+} cations centered by an O^{2-} anion (in a certainly oversimplified ionic picture), hence $[Eu_4O]^{6+}$ "groups" that are surrounded by chloride ligands. In a *Wernerian* point-of-view one could consider these "groups" as complex cations with the O^{2-} anion as the central particle to which four Eu^{2+} cations are coordinated as ligands; the Cl^- anions would then be just counter-anions balancing the positive charge of the complex cation. Therefore, Eu_4OCl_6 could be considered simply as an *anti-complex* according to $Cl_6[OEu_4]$. Indeed, there are "normal" complex compounds with the same crystal structure, e.g., $K_6[HgS_4]$ (Sommer and Hoppe 1978).

Following this line, $Pr_5(C_2)Br_9$ (Uhrlandt and Meyer 1995a) could be formulated as $Br_9[(C_2)Pr_5]$ as it contains $(C_2)^{6-}$ dumbbells surrounded by a trigonal bipyramid of Pr^{3+} cations embedded in a matrix of bromide anions. However, as the $Pr_5(C_2)$ unit is usually considered a trigonal–bipyramidal *cluster* interstitially stabilized by an electron-donating C_2^{6-} ethanide anion, one could also consider $\{Pr_5(C_2)\}^{9+}$ as a large (*super*) central particle, and $\{Pr_5(C_2)\}Br_9$ would then be a *pseudo-binary* and $Rb[\{Pr_5(C_2)\}Cl_{10}]$ (Meyer and Uhrlandt 1993) a *pseudo-ternary* halide. Eu_4OCl_6 is then, of course, also a pseudo-binary chloride according to $\{Eu_4O\}Cl_6$.

In this article, we will begin with an overview of the structures of binary rare-earth halides, RX_z (with R^{z+} being a cation of a rare-earth element, scandium, yttrium, lanthanum and cerium through lutetium and X^- a halide ion). Because binary halides were the subject of several excellent reviews, also in this handbook (Haschke 1979, Eick 1994), they will be mentioned only briefly.

The discussion of the ternary halides will start with simple structural derivatives of the binary halides. For example, in $NaSm_2Cl_6$ sodium is *added* to UCl_3-type $SmCl_3$ thereby reducing half of Sm^{3+} to Sm^{2+} creating $Na_{0.5}[SmCl_3]$ with *mixed-valent* samarium (Lissner et al. 1994). On the other hand, $Na_{0.525}Ce_{0.825}Cl_3$ contains only Ce^{3+}. It is formed starting from $CeCl_3$ and Na by partly *substituting* Ce^{3+} for Na^+ and *adding* some Na^+ for electroneutrality according to $Na_{0.35}[Na_{0.175}Ce_{0.825}Cl_3]$ (Krämer and Meyer 1990).

After the derivatives of simple binary halides, we will discuss the formation and structures of ternary halides in the systems AX/RX_z (with $z=2$, 3 and with A an alkali metal, lithium through cesium, or an pseudo-alkali cation such as In^+, Tl^+, NH_4^+) and BX_2/RX_z (with B a divalent cation) and some mixed systems. Complex rare-earth halides have been reviewed eighteen years ago (Meyer 1982), so that we will focus on generalities and recent developments.

We will then move on to "super-central-particle" complexes with tri-, tetra-, penta- and hexanuclear monomeric clusters and a few oligomers. We will *not* discuss the so-called metal-rich halides with condensed clusters, mostly derived from $\{R_6(Z)\}$ clusters sharing common R edges. This has already been done in breadth in chapter 100 of this Handbook (Simon et al. 1991a).

1.2. *Oxidation states*

The rare-earth elements constitute together with the actinide elements group 3 of the Periodic Table of the elements, a total of 32 elements! The actinides excluded, there are 17 elements left with electron configurations of $4s^23d^1$ (Sc), $5s^24d^1$ (Y), and $6s^25d^14f^n$ (the lanthanides, La, Ce–Lu; $n=0$–14). Hence, they all have an "outer" valence electron configuration of s^2d^1 in common that qualifies them for all becoming trivalent in numerous compounds, in oxides, halides, as aqua complexes in aqueous solutions.

Few lanthanide elements may be oxidized to the tetravalent state and stabilized, almost exclusively, in fluorides and oxides. These are the elements cerium, terbium, praseodymium, dysprosium, neodymium, holmium, for example all in the ternary fluorides Cs_3RF_7 (Hoppe and Roedder 1961). There are also hints at pentavalent praseodymium, $CsPrF_6$ would be the example (Hoppe 1980).

On the other hand and especially with the triad chloride, bromide and iodide as anions, there is now a well-established chemistry of the divalent state of the lanthanides. With R^{2+} with the electronic configuration $s^0d^0f^n$, the halides RX_2 are "normal", insulating salts exhibiting a structural chemistry analogous to the heavy triad of the alkaline-earth elements, i.e., Ca, Sr, Ba. With the electronic configuration $s^0d^14f^{n-1}$, however, the dihalides may be semiconductors or even metallic conductors; NdI_2 is a prime example where the electronic *configuration crossover* $5d^04f^4 \rightarrow 5d^14f^3$ can be induced by pressure. The insulating salt $(Nd^{2+})(I^-)_2$ becomes a semiconducting salt, in the chemist's writing $(Nd^{3+})(e^-)(I^-)_2$ (Beck and Schuster 1992).

Clusters are also possible, as in Pr_2Br_5 (Schleid and Meyer 1987b) or PrI_2 (Warkentin and Bärnighausen 1979) but occur generally when the X to R ratio becomes less than 2 and with an "interstitial" whose electron(s) are needed to stabilize the multinuclear R_y arrangement. The use of the term "oxidation states" is rather obscure for these compounds.

For a more general view on how and when the mentioned types of compounds occur, two reviews might be helpful (Meyer 1988, Meyer and Meyer 1992).

2. Synthesis generalities

The synthesis of lanthanide and actinide compounds was the subject of a book (Meyer and Morss 1991). Detailed information is given on the synthesis of lanthanide fluorides (Müller 1991), binary lanthanide halides, RX_3 (X = Cl, Br, I) (Meyer 1991a), complex lanthanide(III) chlorides, bromides and iodides (Meyer 1991b), and on two alternative routes to reduced halides, the conproportionation route (Corbett 1991) and the action of alkali metals on lanthanide(III) halides (Meyer and Schleid 1991). Therefore, a brief outline of the main preparative routes and synthetic strategies might be sufficent.

2.1. *Rare-earth trihalides, RX_3, and derivatives*

Among the binary halides, the fluorides RF_3 are most easily obtained. Because of their stability against moisture and the constituents of air at ambient temperature, they may simply be precipitated from aqueous solutions of any soluble salt, chlorides, nitrates and so forth. In a subsequent step the crude material needs to be dried to remove any remaining water, preferably in an HF stream at 600°C. These steps must be carried out in inert containers, at ambient and slightly elevated temperatures in polyethylene or teflon containers and at higher temperatures in containers manufactured of nickel and its alloys, for example Monel, Cu32Ni68.

An alternative is the reaction of the respective sesquioxides with $(NH_4)HF_2$, in analogy to the ammonium chloride (bromide) route. In principle, this is a two-step procedure with the formation of a ternary fluoride first and, secondly, its thermal decomposition (see below). When elemental fluorine is available, the direct fluorination of the rare earths or any of their salts is also a possibility. Ternary fluorides are obtained by a solid state reaction of the respective binary components in sealed gold or platinum tubes.

More care has to be taken for the preparation of binary chlorides and bromides, RCl_3 and RBr_3. The anhydrous salts are moisture-sensitive and they are obtained as (hepta- or hexa-) hydrates upon crystallization from hydrochloric or hydrobromic acid solutions. Simple dehydration of the hydrates in an HCl or HBr gas flow, respectively, appears to be possible (Seifert et al. 1985) but the less skillful chemist produces halide products more or less contaminated with oxyhalide, ROX. Sublimation of the raw product in an all-tantalum apparatus at higher temperatures (650°C to 950°C) and low pressures (10^{-6} bar) produces pure trihalides (with the exception of the rare-earth elements europium and ytterbium where mixed-valent (+2/+3) or even dihalides are obtained under these conditions).

A common and most easily to follow way to prepare rare-earth halides, even in large quantities, is the so-called ammonium halide route (Reed et al. 1939, Meyer and Ax 1982, Meyer 1989). Two steps are involved in this procedure. In the first step, the respective rare earth (most commonly the sesquioxide, R_2O_3) is converted into a ternary ammonium halide, $(NH_4)_3RX_6$ or $(NH_4)_2RX_5$, which is, in the second step, decomposed to the respective rare-earth trihalide RX_3 recovering ammonium halide (box 1). The first step may be carried out by dissolving the oxide and ammonium halide in hydochloric

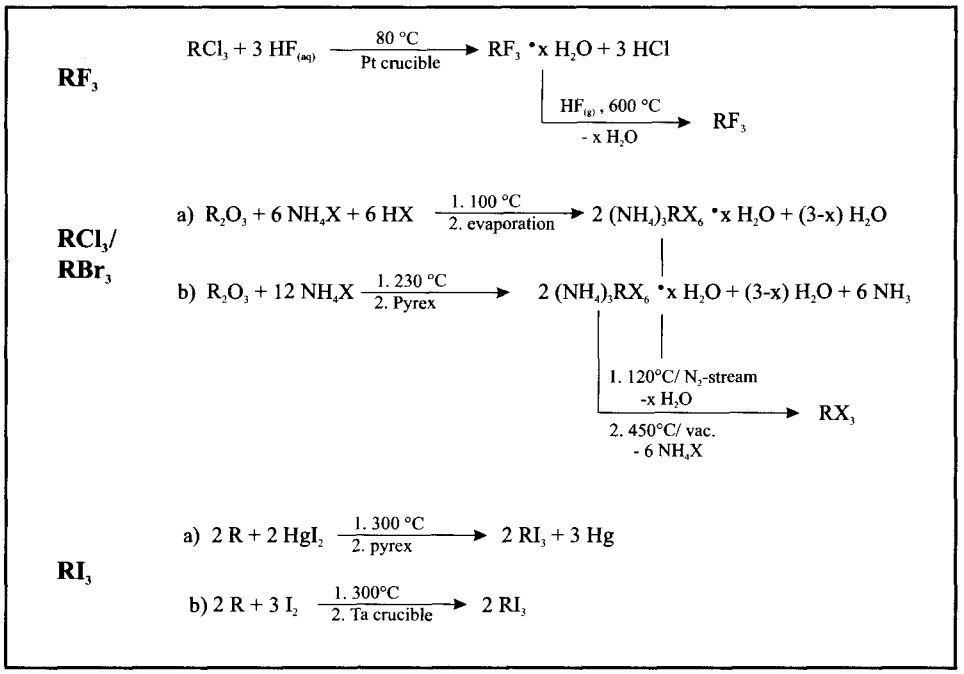

Box 1. Synthesis of binary rare-earth trihalides

or hydrobromic acid followed by evaporation to dryness ("wet" route); alternatively the solids NH_4X and R_2O_3 may be reacted directly ("dry" route).

This procedure might be extended to the production of ternary compounds. Then an alkali-metal halide is added to yield a quaternary halide, for example $(NH_4)_2LiGdCl_6$, that is subsequently decomposed to the ternary salt, $LiGdCl_4$ in the present example (Meyer 1984a) (see box 2 for another example).

For ternary and quaternary chlorides and bromides it is normally sufficient to dissolve the respective rare-earth and alkali halides or carbonates in hydrohalic acid solution, evaporate to dryness and heat this intermediate product in a stream of the respective hydrogen halide gas at temperatures between 300 and 500°C (Meyer 1983a,b).

The most obvious disadvantage of the latter two procedures is that they produce powder samples. Both, powder samples and single crystals, may be obtained from reactions of stoichiometric amounts of the respective binary halide components in sealed containers of silica, tantalum, or even glass (Pyrex). Knowledge of the respective phase diagrams of the AX/RX_3 systems is mandatory for the success of this route. Much progress has been made through the thorough investigations by the group Blachnik in the 1980s and that of Seifert quite recently.

Single crystals are also frequently obtained in the course of the investigation of special routes. For example, $LiGdCl_4$ and Na_3GdCl_6 came across by metallothermic reduction of $GdCl_3$ with lithium and sodium, respectively (Meyer 1984a,b).

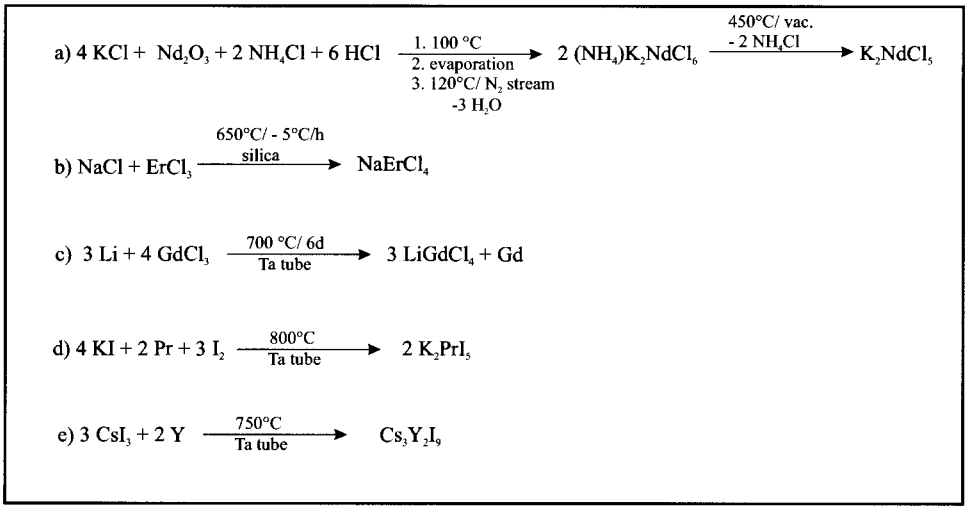

Box 2. Examples for reactions to ternary rare-earth(III) halides

Special efforts need to be taken for the preparation of rare-earth triiodides, RI_3. Apparently due to the special stability of the oxyiodides ROI, the above outlined procedures do not work well. It turned out that the best route to pure triiodides is the synthesis from the elements in sealed Pyrex containers. Small amounts of hydrogen (often present in rare-earth metals, especially powder samples) seem to catalyse the reaction. The reaction of rare-earth metals with HgI_2 also leads to pure triiodides (Corbett 1983). The formation of elemental mercury is the major drawback of this procedure and it is, therefore, not favorable especially for large batches.

Annealing of stoichiometric amounts of the binary iodides or, alternatively, a one-batch synthesis from AI, R, and I_2 yields satisfyingly pure ternary rare-earth iodides.

The procedures outlined so far, provide single crystals suitable for X-ray structure determination, if any. The measurement of physical properties, however, requires often large single crystals of a volume of up to 1 cm^3. The growth of such large crystals causes problems even when the phase diagram of the respective system is known in detail because solid/solid phase transitions and/or incongruent melting often occur for the ternary rare-earth halides under consideration. Nevertheless, quite a number of complex halides is now available as large single crystals. Some fluorides were grown under hydrothermal conditions. The growth technique mainly used is that named after Bridgman (Bridgman 1925). Large crystals of the incongruently melting compound Ba_2YCl_7 doped with various amounts of Er^{3+} have been grown recently applying the Czochralski technique (Riedener et al. 1997).

2.2. *Reduced halides*

Halides with the rare-earth element in an oxidation state of less than +3 may be obtained by reduction of the respective (tri-)halides with their rare-earth metals (conproportionation

route, see Corbett 1991) or other reducing agents such as hydrogen or alkali metals (metallothermic reduction, see Meyer and Schleid 1991), or by the electric current (cathodic reduction, see Masse and Simon 1981). Binary halides such as $YbCl_2$ (Beck and Bärnighausen 1971) $PrCl_{2,31}$ (Meyer et al. 1989) and LaI (Martin and Corbett 1995) are obtained and, with the proper design of the reaction, ternary halides such as $CsYbCl_3$ (Meyer 1978), $NaSm_2Cl_6$ (Lissner et al. 1994) and Eu_4Cl_9 (Lange 1992) as well. Small amounts of light elements like C, O, N and H drive the reactions in the direction of cluster formation, for example $Rb[\{Pr_5(C_2)\}Cl_{10}]$ (Meyer and Uhrlandt 1993) or to $Na_2[\{Pr_4O_2\}Cl_9]$ (Mattfeld and Meyer 1994). Reduction reactions following the conproportionation or metallothermic reduction routes are profitably carried out in He–arc welded tantalum or niobium capsules jacketed with a sealed silica tube.

Large single crystals of reduced halides, especially of those with non-salt-like structures are not available up to date, and, even worse, pure powder samples have in most cases not been obtained. This is certainly due to the thermodynamic instability of these compounds with respect to competing neighboring phases. Thermodynamic data are almost unknown, much work needs to be done!

3. Binary rare-earth halides

3.1. *Rare-earth trihalides, RX_3*

Binary trihalides RX_3 are well known for all rare-earth elements with the exception of EuI_3 which appears not to exist due to the relative stability of EuI_2. Their crystal structures change subject to the lanthanide contraction within the lanthanide series with high coordination numbers for the lighter lanthanides especially with small ligands (fluoride) and *vice versa*. Table 1 gives an overview of the crystal structures of the trihalides at ambient conditions.

The trifluorides of lanthanum and cerium through samarium adopt the tysonite type of structure with elevenfold coordination of the metal ion (Wells 1975). The $[RF_{11}]$ unit,

Table 1
Crystal structures of the trihalides RX_3 of the rare-earth elements

	La Ce Pr Nd Sm Eu Gd Tb Dy Ho Y Er Tm Yb Lu Sc
F	LaF_3 — YF_3 — ReO_3
Cl	$PuBr_3$ — $AlCl_3$
Br	UCl_3 — $FeCl_3$
I	$PuBr_3$

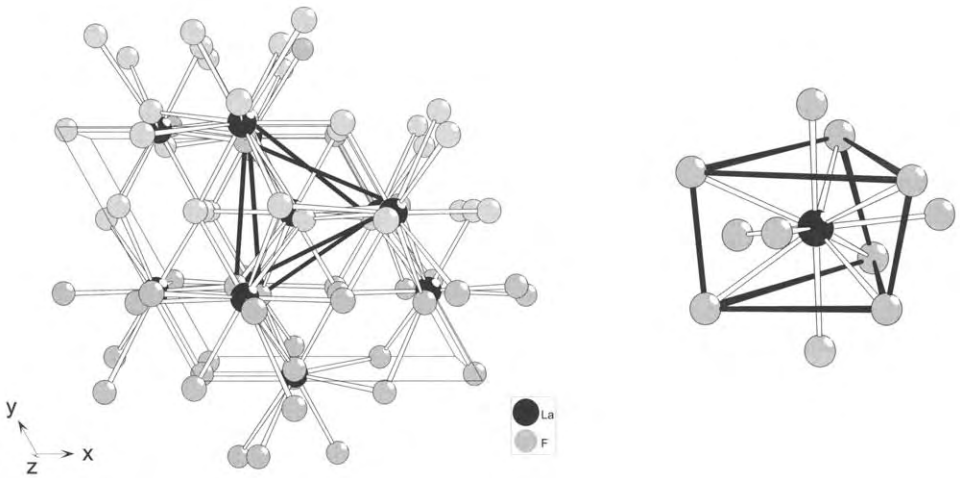

Fig. 1. Crystal structure of LaF_3 (tysonite).

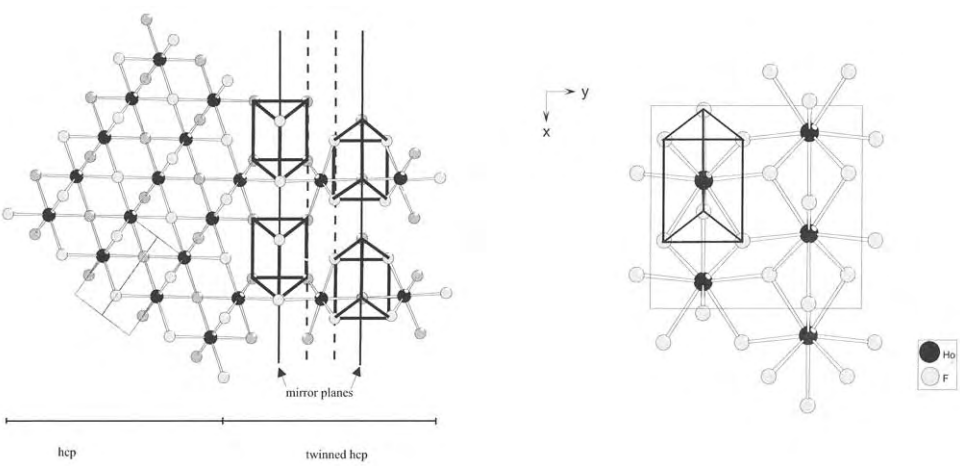

Fig. 2. Crystal structure of the YF_3-type derived from a hexagonal closest packing of anions by inserting twin planes at every third atom row.

the so-called *Edshammar* polyhedron (Hyde and Andersson 1989) may be described as a trigonal prism with all faces capped by additional ligands (fig. 1).

With the smaller lanthanide ions (europium through lutetium) the YF_3 type of structure occurs for the trifluorides which is the antitype structure of cementite, Fe_3C (Fasiska and Jeffrey 1965). The structure may be derived from a hexagonal closest packing of anions by a parallel reflection procedure at every third atom row of the packing (when projected on $(1\bar{1}.0)$) leading to trigonal prismatic voids in the twin plane (Hyde and Andersson 1989) (fig. 2). The still empty octahedral sites in the hcp arrays may be filled with additional cations as is the case for example in $CsDyI_3$ (see sect. 4.2.2). The R^{3+} ion in the

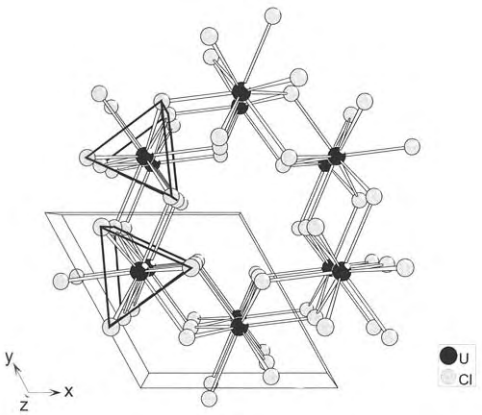

Fig. 3. Perspective view of the UCl_3 type of structure; trigonal prisms are emphasized.

YF_3 type of structure is then nine-coordinate (strictly speaking 8 + 1) and the coordination polyhedron is a distorted tricapped trigonal prism.

With the smallest of the rare-earth cations, Sc^{3+}, a third structure type is found for rare-earth trifluorides: ScF_3 crystallizes with the ReO_3 (AlF_3) type of structure (Lösch et al. 1982) with octahedral coordination of the cations and all octahedra [ScF_6] sharing common corners.

The chlorides, bromides and iodides of the trivalent rare-earth cations occur in four different structure types that are known from UCl_3, $PuBr_3$, $AlCl_3$ (YCl_3) and $FeCl_3$ (BiI_3) with coordination numbers of 9, 8, and 6 for the latter two, respectively.

The UCl_3 type of structure consists of [RCl_9] polyhedra, trigonal prisms capped on each rectangular face. These are connected via the triangular faces to form columns running along the *c*-axis. The columns are shifted against each other by $\frac{1}{2}c$ (fig. 3) so that ligands defining one prism serve as caps on adjacent prisms. The arrangement of the columns leads to channels in the [001] direction providing empty sites (octahedral and trigonal prismatic) for additional cations, an important feature in view of derivative structures as discussed below. Alternatively the structure may be described as a hexagonally closest packing of layers of the composition RCl_3. Due to the different sizes of the ions the packing is distorted reducing the coordination number of the R^{3+} ion from 12 (as it would be in a truly densest packing) to 9.

The $PuBr_3$ type of structure, the antitype of Re_3B (Aronsson et al. 1960), is closely related to that of UCl_3. The coordination number of the R^{3+} ion is, however, only eight. The coordination polyhedron is a bicapped trigonal prism. In analogy to the YF_3 type of structure it may be derived from a closest packing of anions although the stacking is cubic. There is also a variant with octahedral sites filled which is known as $CaIrO_3/FeUS_3/KTmI_3$ type of structure (fig. 4).

The $AlCl_3$ type of structure is best derived from the cubic closest packing of anions. Octahedral interstices between alternating layers are either empty or are filled to two thirds with cations (fig. 5). Again, octahedral holes that are empty in this structure may be filled with further cations (see below). In the closely related structure of RhF_3 octahedral holes

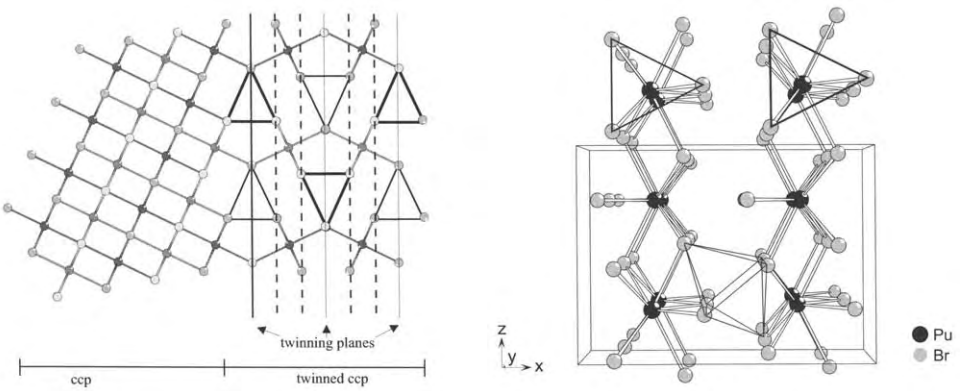

Fig. 4. The $PuBr_3$ type of structure derived from a ccp (NaCl) by twinning. When the marked octahedra are filled, the $CaIrO_3/FeUS_3/KTmI_3$ type of structure is obtained.

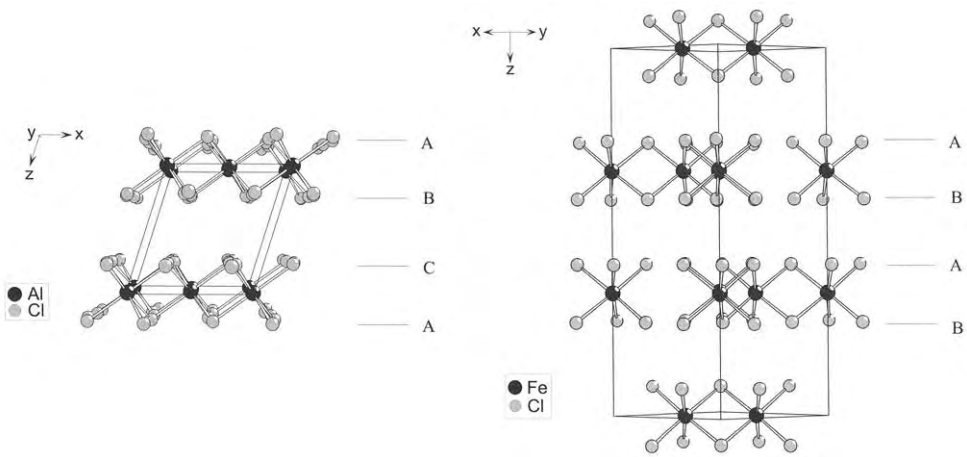

Fig. 5. Perspective views of the (left) $AlCl_3$ and (right) $FeCl_3$ types of structure.

between each layer are filled to one third. In fact, this variety was found as the high pressure modification for most of the $AlCl_3$-type trihalides (Beck and Gladrow 1983). The RhF_3 type may be seen as the parent structure of $LiSbF_6$ (Babel 1962), of which a stuffed variant is known for many ternary rare-earth halides (cf. sect. 4.1.5). Finally, the $FeCl_3$ type of structure is the hexagonally closest packed analogue to the $AlCl_3$ type of structure (fig. 5).

3.2. *Rare-earth dihalides, RX_2*

Depending upon the standard electrode potentials E^o of the R^{2+}/R^{3+} half cells (see Meyer 1988) two groups of dihalides, RX_2, of the rare-earth elements may be distinguished:

Table 2
Crystal structures of the dihalides of the rare-earth elements

Halide	La	Ce	Pr	Nd	Sm	Eu	Gd	Tb
F	–	–	–	–	CaF_2	CaF_2	–	–
Cl	–	–	–	$PbCl_2$	$PbCl_2$ CaF_2	$PbCl_2$ CaF_2	–	–
Br	$2H_2$-MoS_2	–	–	$PbCl_2$	$SrBr_2$	$SrBr_2$	–	–
I	$MoSi_2$	$MoSi_2$	$MoSi_2$ $2H_1$-MoS_2 3R-MoS_2 $CdCl_2$ PrI_2-V	$SrBr_2$ $MoSi_2$ [a] CaF_2 [a]	EuI_2	EuI_2 SrI_2	$MoSi_2$ 2H-MoS_2	–

Halide	Dy	Ho	Y*	Er	Tm	Yb	Lu	Sc
F	–	–	–	–	–	–	–	–
Cl	$SrBr_2$	–	–	–	SrI_2	SrI_2	–	–
Br	SrI_2	–	–	–	SrI_2	SrI_2 α-PbO_2 $CaCl_2$	–	–
I	$CdCl_2$	–	–	–	CdI_2	CdI_2	–	CdI_2

[a] High-pressure form.

(I) saltlike halides according to the formulation $(R^{2+})(X^-)_2$ with typically ionic crystal structures and

(II) metallic or semi-metallic halides with delocalized electrons according to the formulation $(R^{3+})(X^-)_2(e^-)$ which crystallize in more covalent/intermetallic structure types like those of MoS_2 or $MoSi_2$.

Compounds of type I are found with the elements Nd, Sm, Eu, Dy, Tm and Yb [$E^\circ(R^{2+}/R^{3+}) < -2.6$ V]. With Sm, Eu and Yb even the difluorides exist crystallizing with the CaF_2 type of structure. The remaining rare-earth elements form dihalides only with the "stronger reducing" halides I^- and (to a lesser extent) Br^-. With Ho, Er, Lu and Y dihalides seem not to exist. Table 2 summarizes the rare-earth dihalides known so far.

The salt-like dihalides crystallize with well known structures thereby establishing the close relationship between the rare-earth elements in their divalent states and the respective alkaline earth cations of similar ionic radii. Only EuI_2 and SmI_2 adopt an otherwise unknown structure type. It consists of monocapped trigonal prisms [EuI_7] that are connected in a rather complicated manner according to $^3_\infty[EuI^{e,c}_{4/4}I^{e,c}_{3/3}]$ to a three-dimensional network ($^3_\infty$) via corners (c) and edges (e) (fig. 6). A derivative of this structure is found for the ternary chloride $NaGdCl_4$ (see sect. 4.1.2). The same is true for the α-PbO_2 type of structure which is adopted by one modification of $YbCl_2$. It finds its ternary analogue in $NaErCl_4$.

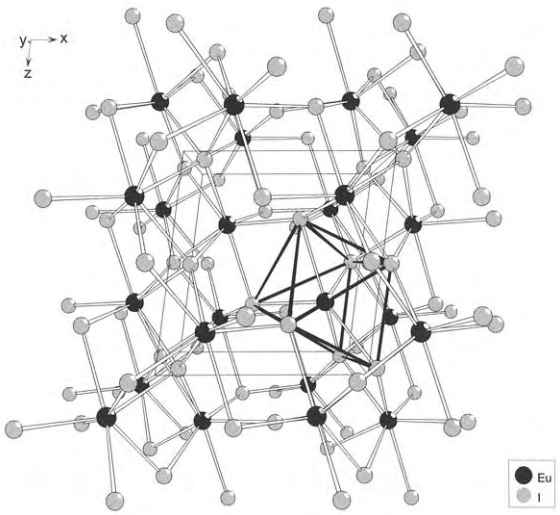

Fig. 6. Crystal structure of EuI_2.

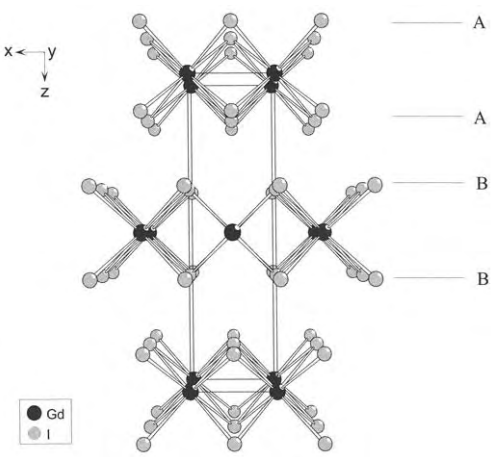

Fig. 7. The $MoSi_2$ type of structure for GdI_2.

The $(R^{3+})(e^-)(X^-)_2$-type dihalides often show interesting magnetic and electronic properties. Magnetic ordering occurs in GdI_2 below 313 K (Kasten et al. 1984). Within the layers of the $MoSi_2$ type of structure (fig. 7) the Gd^{3+} ions are coupled ferromagnetically, while the inter-layer coupling is antiferromagnetic. The latter is, of course, much weaker than the coupling within the layers so that the compound is approximately a two-dimensional Heisenberg system.

Resistivity and susceptibility measurements have been carried out for LaI_2 and the electronic band structure has been calculated (Burrow et al. 1987). Extended Hückel band structure calculations were also undertaken for the remarkable cubic modification of PrI_2 (PrI_2-V, fig. 8, Warkentin and Bärnighausen 1979). It resembles the spinel structure

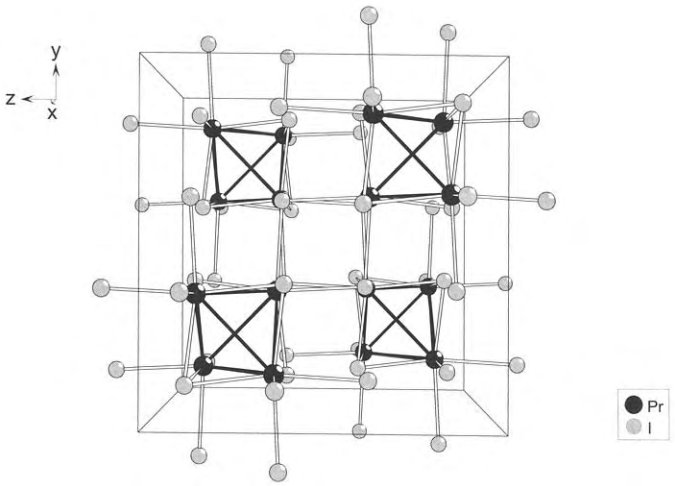

Fig. 8. Crystal structure of PrI_2-V.

($MgAl_2O_4$) with all of the Mg^{2+} sites empty. Considerable metal–metal interactions occur (see sect. 5.4).

As already mentioned, another most interesting compound among the dihalides is neodymium diiodide, NdI_2. To date, three modifications are known and their occurrence is dependent upon pressure (and temperature). Under ambient conditions, the ionic $SrBr_2$ type of structure appears. At higher pressures the metallic $MoSi_2$ type of structure is adopted and at even higher pressures the CaF_2 type occurs (Beck and Schuster 1992). The transformation from the $SrBr_2$ to the $MoSi_2$ type is accompanied with the electronic configuration crossover $5d^04f^4 \rightarrow 5d^14f^3$ or, for the chemist!, $Nd^{2+} \rightarrow Nd^{3+}e^-$.

It should be noted that some of the dihalides in the literature are truly halide hydrides to be formulated as RX_2H_{1-x} (Michaelis et al. 1992a–c). The source for this "impurity" is the hydrogen content of the rare-earth metal especially when metal powder is used in the conproportionation route.

4. Complex halides with mononuclear centers

4.1. *Ternary rare-earth(III) halides*

The crystal chemistry of the ternary rare-earth halides with monovalent cations A^+ of the general composition $A_wR_yX_{3y+w}$ has developed considerably in the past sesquidecade. Phase diagram determinations by Blachnik (Blachnik and Selle 1979, Blachnik and Jäger-Kasper 1980) have contributed much to get an overview of the existence of the more stable compound classes, especially with A = K, Rb, Cs. The respective crystal chemistry has been the subject of a previous review (Meyer 1982). Since then many systems have been reinvestigated or the phase diagram was even determined for the first time, especially by

Seifert applying a combination of DTA, X-ray and emf measurements (Seifert and Thiel 1982). Further preparative and X-ray work was done in the rare-earth halide systems with $A^+ = NH_4^+$ in order to understand the synthetic uniqueness of the ammonium ion (Meyer 1994), and in the systems with Li^+, Na^+, Cu^+, and Ag^+ aiming at new fast ionic conductors.

The relative stability of the ternary halides in the AX/RX_3 systems and the diversity of compound types increases with increasing A^+/R^{3+} ratio. For example, the system $CsCl/ErCl_3$ contains four compounds ($CsEr_2Cl_7$, $Cs_3Er_2Cl_9$, Cs_2ErCl_5 and Cs_3ErCl_6) (Blachnik and Selle 1979), the system $NaCl/ErCl_3$ only two ($NaErCl_4$ and Na_3ErCl_6) (Seifert and Sandrock 1997). No compound at all could be found in the system $CuCl/ErCl_3$ which may be attributed to the high contra-polarization of the Cu^+ ion because the $LiCl/ErCl_3$ system does at least contain the ternary chloride Li_3ErCl_6 (cf. sect. 4.1.5) (Cu^+ and Li^+ have practically identical ionic radii).

Even when the growth of single crystals for structural characterization was difficult for some of the compounds whose existence was indicated in the phase diagrams subject to incongruent melting, sometimes decomposition in the solid state and solid/solid phase transitions, it is believed that practically all crystal structure types are now known so that we can draw a comprehensive picture. Emphasized are recent developments.

4.1.1. *Derivatives of the UCl_3 type of structure*

As reported in sect. 3.1, the binary rare-earth chlorides RCl_3 with R = La–Gd and the binary bromides RBr_3 with R = La–Pr crystallize with the UCl_3 type of structure. Along the crystallographic *c*-axis this structure type provides empty sites (compressed octahedral and trigonal prismatic) that may accomodate additional cations (fig. 9). These are usually relatively small monovalent cations such as Na^+ (and K^+) but it is also possible to incorporate ions with higher charges. This is most prominently documented by the "line

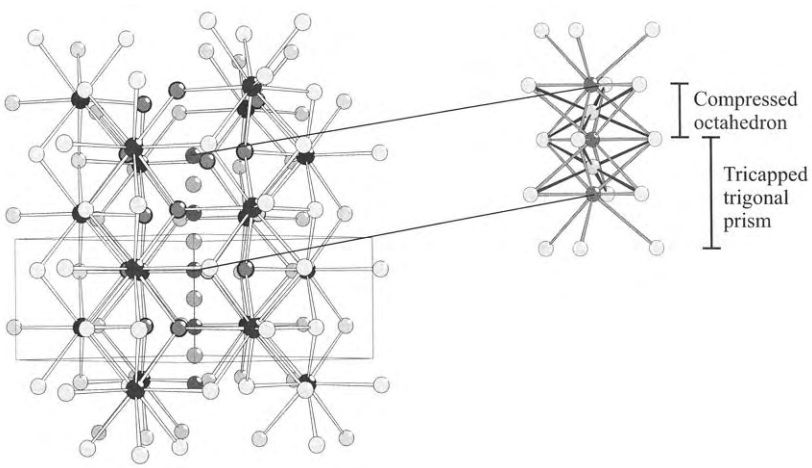

Fig. 9. Additional sites in the UCl_3 type of structure that might be partially occupied by monovalent cations.

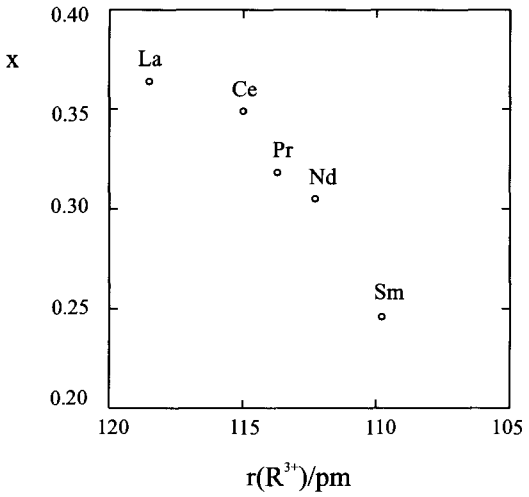

Fig. 10. Dependence of the sodium content x upon the ionic radius $r(R^{3+})$ in chlorides of the composition $Na_{2x}(Na_xR_{2-x})Cl_6$.

phase" $PrCl_{2.31}$ (Corbett 1973) which is in fact a UCl_3 derivative according to $Pr_{0.3}[PrCl_3]$ (Meyer et al. 1989). Due to the close proximity of the polyhedral centers complete occupation is not possible.

There are two possibilities to compensate for the charge of the cations added:
(1) Substitution of R^{3+} by A^+ leading to the general formula $A_{2x}(A_xR_{2-x})X_6$;
(2) Partial reduction of R^{3+} to R^{2+} leading to mixed-valent halides, $A_x(R^{2+})_x(R^{3+})_{2-x}X_6$.

Type 1 compounds are *substitution/addition* derivatives of the UCl_3 type of structure and are found for chlorides with A = Na, K and R = La–Sm (Lissner et al. 1994). They are sometimes referred to as "$A_3R_5X_{18}$"-type compounds but due to the more (La) or less (Sm) large phase widths this can only be an approximate formula. For the sodium compounds (which are the best characterized) there is indeed a strong relation between the maximum Na^+ content and the R^{3+} ionic radius (Lissner et al. 1994) (fig. 10). The larger the ionic radius of the R^{3+} cation is the more Na^+ can be incorporated.

It might be noteworthy that only the compressed octahedral site is occupied by sodium: the trigonal prismatic interstice remains empty.

With $x = 0.5$ we arrive, according to, e.g., $Na_1(Na_{0.5}Sm_{1.5})Cl_6 = NaSmCl_4$, at ARX_4-type compounds that are in fact known for a number of rare-earth fluorides and chlorides. For fluorides the UCl_3-type derivate is indeed found, the $NaNdF_4$ type of structure (cf. sect. 4.1.2) even when the binary fluoride does not crystallize with the UCl_3 type of structure. The chlorides $ARCl_4$, however, even though the chlorides with R = La–Gd are isotypic with UCl_3, adopt other structure types.

Type 2 compounds are pure *addition* derivatives of the UCl_3 type and occur with R = Pr–Eu and A = Na. They have normally the composition NaR_2Cl_6 ($= Na_{0.5}RCl_3$) except for $Na_{0.75}Eu_2Cl_6$. The crystals show blue ($NaEu_2Cl_6$), green ($Na_{0.75}Eu_2Cl_6$) and dark red ($NaSm_2Cl_6$) colours or are black ($NaPr_2Cl_6$, $NaNd_2Cl_6$). The valence of the lanthanide cations has been determined by means of X-ray absorption near edge

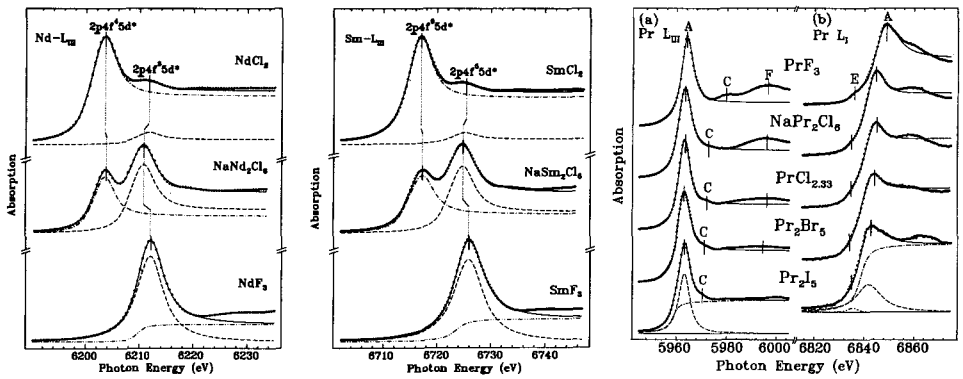

Fig. 11. X-ray absorption near edge spectra (XANES) for $NaNd_2Cl_6$ and $NaSm_2Cl_6$ as well as for $NaPr_2Cl_6$.

spectroscopy (XANES) for $NaNd_2Cl_6$ and $NaSm_2Cl_6$ (fig. 11) and was found to be 2.5, i.e., mixed-valent +2/+3 (Lissner et al. 1994).

For $NaPr_2Cl_6$, however, the XANES spectrum shows that there is only trivalent praseodymium present. Further evidence arises from the observation of the similarity of the lattice parameters of the (light green) $Na_{0.32}(Na_{0.16}Pr_{0.84})Cl_3$ addition-substitution compound and of black $Na_{0.5}(Pr)Cl_3$ indicating that the latter should be written as $Na_{0.5}(Pr^{3+})Cl_3(e^-)_{0.5}$.

In the *addition* compounds both sites, octahedral and trigonal prismatic, may be partly filled with sodium, except for $Na_{0.75}Eu_2Cl_6$ where the trigonal prismatic site is empty. The occupation of the trigonal prismatic site is strongly reflected by the increasing length of the *c*-axis.

In the mixed-valent $A(R^{2+})(R^{3+})Cl_6$-type compounds, the R^{2+} ion may be substituted by an alkaline-earth ion, B^{2+}, of preferably the same size. For example, $NaEu_2Cl_6$ and $NaSm_2Cl_6$ are paralleled by $NaSrEuCl_6$ and $NaSrSmCl_6$ (Wickleder 1994, Wickleder and Meyer 1998a) without structural changes. As these compounds are no longer mixed-valent and with the reducing Eu^{2+} and Sm^{2+} cations, Ag^+ can now be built in instead of Na^+, yielding $AgSrEuCl_6$ and $AgSrSmCl_6$. Even bromides like $NaBaLaBr_6$ are available although $NaLa_2Br_6$ is not known. Slight deviations from the exact stoichiometry seem to be tolerable as is indicated by elemental analysis.

Iodides of this class of compounds are not known. On the other hand, a fluoride with the idealized composition $NaCaYF_6$ and the same structure even occurs in nature as the mineral *gagarinite* (Hughes and Drexler 1994).

Conductivity measurements have been carried out on powder samples of $NaEu_2Cl_6$ by means of impedance spectroscopy (fig. 12). The activation energy for the conduction process was calculated to 0.23 eV. The value fits into the range one would expect for semiconductors; on the other hand, there should be contributions of the Na^+ ions to the overall conductivity. With the partial filling of the sodium sites and the channel along the *c*-axis the structure certainly fulfills the requirements for ionic conduction. Measurements on powder pellets of $NaSrEuCl_6$ and $AgSrEuCl_6$ indeed proved ionic motion but the

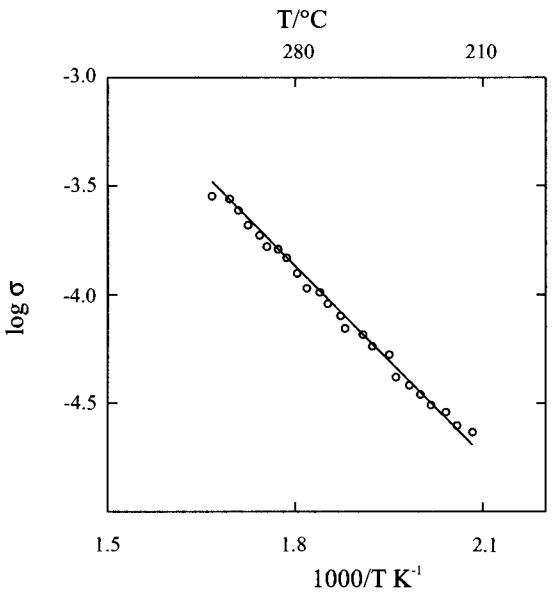

Fig. 12. Temperature dependence of the conductivity σ for $NaEu_2Cl_6$.

conductivity was significantly lower than that of $NaEu_2Cl_6$ so that in the latter electronic conduction must be predominant. The ionic conductivity of the UCl_3-type derivatives must be highly anisotropic (parallel [001]) so that conductivity measurements on single crystalline samples are most desirable.

4.1.2. *AR_2X_7-type halides*

AR_2X_7-type halides occur mainly in systems with large alkali cations (K^+–Cs^+) (Seifert et al. 1985–1988, Thiel and Seifert 1988, Blachnik and Selle 1979) and pseudo-alkali cations like In^+, Tl^+ and NH_4^+ (Blachnik and Enninga 1983, Meyer et al. 1984). They have not been observed with Li^+ and Ag^+. With Na^+ there is evidence from thermoanalytical investigations for NaR_2Cl_7-type compounds with R = Gd–Ho (Seifert et al. 1995, Seifert and Sandrock 1997). Table 3 gives a summary of the occurrence of AR_2X_7-type compounds.

Table 3
The occurrence of AR_2X_7-type compounds

A	X = F	X = Cl	X = Br
K	Gd–Lu, Y	Sm–Yb	La–Tb
Rb	Sm–Er, Y	La–Yb, Ce, Y	La–Ho
Cs	Nd–Ho, Y	La–Lu, Ce, Y	La–Ho

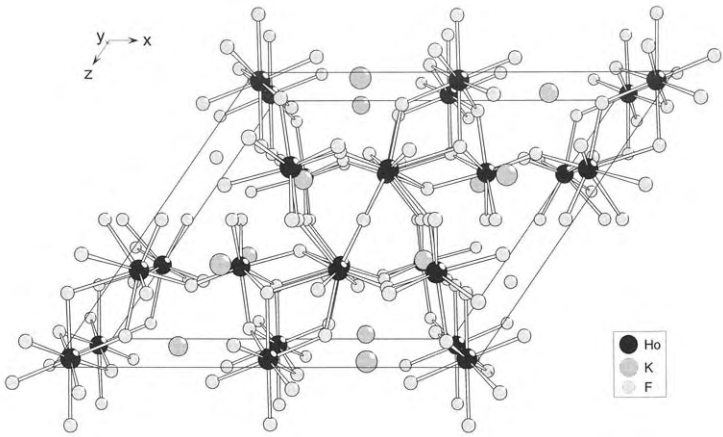

Fig. 13. Crystal structure of KHo_2F_7 viewed along [010].

For AR_2F_7-type fluorides four structure types may be distinguished which have first been determined for KHo_2F_7, KEr_2F_7, KYb_2F_7, and $RbEr_2F_7$.

The monoclinic structure of KHo_2F_7 was originally solved in space group Cm (Le Fur et al. 1982) but was recently corrected to C2/m (Marsh and Herbstein 1988). Three crystallographically different Ho^{3+} are present in the structure, all being in eightfold coordination with cube, square antiprism and dodecahedron as the coordination polyhedra (fig. 13). The same is true for KEr_2F_7 although the symmetry is orthorhombic (Aléonard et al. 1980, Marsh and Herbstein 1988). The coordination polyhedron of Yb^{3+} in KYb_2F_7 is a pentagonal bipyramid (Aléonard et al. 1980).

Single crystals of a size up to 10 mm of $CsGd_2F_7$ and CsY_2F_7 doped with Ce^{3+} have been grown under hydrothermal conditions. Scintillation properties have been measured (Schaart et al. 1995). However, the light yield after high energy irradiation (662 keV) is low.

AR_2X_7-type chlorides and bromides crystallize with at least three crystallographically distinguishable structures two of which have been determined first for KDy_2Cl_7 and $RbDy_2Cl_7$ (Meyer 1982); attempts to determine the structure of the third type from single crystals of $CsLa_2Cl_7$ and $RbLa_2Cl_7$ were never completely successful (Meyer 1981).

The principal features of the crystal structures of KDy_2Cl_7 and $RbDy_2Cl_7$ are the same. The main difference is that the symmetries are monoclinic (P1121/a, $\gamma = 89.3°$) and orthorhombic (supergroup Pnma), respectively. The structure consists of dimeric units built up from two monocapped trigonal prisms sharing a common triangular face (fig. 14). These are connected via four edges to form infinite layers stacked in the [100] direction and held together by A^+ cations (fig. 14). In accord with the face connection of the $[DyCl_7]$ polyhedra the Dy^{3+}–Dy^{3+} distance is quite short (385 pm), a situation that is also found in $Cs_3R_2X_9$-type compounds containing face-sharing octahedra (see below).

The close proximity of the R^{3+} ions in the face-sharing $[Dy_2Cl_{11}]$ groups appears to have great influence on the spectroscopic properties: Upconversion luminescence has been

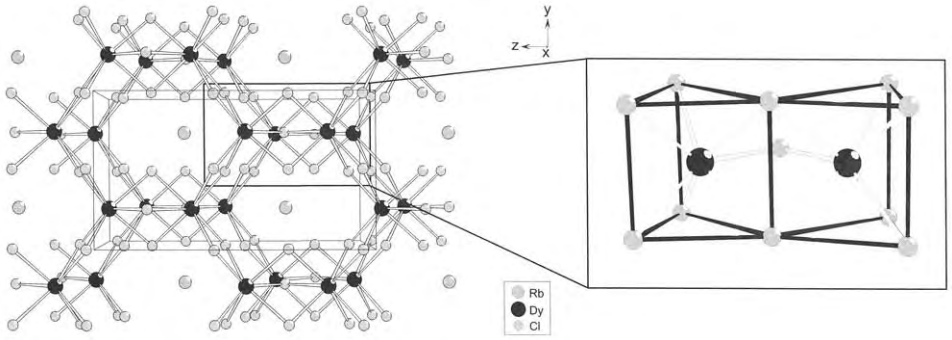

Fig. 14. Important features of the crystal structures of KDy_2Cl_7 and $RbDy_2Cl_7$.

investigated for orthorhombic $RbGd_2Cl_7$ and $RbGd_2Br_7$ single crystals doped with various amounts of Er^{3+} and grown via the Bridgman technique (Riedener et al. 1995). The interpretation of the spectra shows that energy transfer processes supported by the closely neighbored ions are involved. Scintillator properties of $RbGd_2Cl_7:Ce^{3+}$ are also under investigation (van 't Spijker et al. 1996) but its moisture sensitivity is a great hindrance in its becoming a scintillator material.

4.1.3. *ARX_4-type halides*

Ternary fluorides of the ARF_4 type with A = Li–Cs, Ag, In, Tl are long known and pretty well characterized (Greis and Haschke 1982) (table 4). $LiGdCl_4$ was the first ternary chloride of the ARX_4 type whose structure could be determined (anti-scheelite type, $Gd^{[8]}Li^{[4]}Cl_4 = Ca^{[8]}W^{[4]}O_4$). Single crystals were serendipituously obtained through metallothermic reduction of $GdCl_3$ with lithium (Meyer 1984a). Single crystals of $NaGdCl_4$ were obtained as a by-product of the oxidation of a reduced gadolinium compound with sulfur (Schleid and Meyer 1990). Subsequently, $NaRCl_4$ compounds were obtained with R = Eu–Lu, Y, Sc and their crystal structures determined (Wickleder and Meyer 1995b, Wickleder et al. 1996a, Bohnsack et al. 1996) Attempts to synthesize $NaRX_4$-type compounds with the heavier halides were not successful. There is, however, some evidence for the existence of $NaScI_4$ (Anderson 1976)

Table 4
The occurrence of ARX_4-type compounds

A	X = F	X = Cl	X = Br	X = I
Li	Eu–Lu, Y	Sm–Gd	–	–
Na	La–Lu, Ce, Y	Eu–Lu, Y, Sc	–	Sc
K	La–Lu, Ce, Y	–	–	–
Rb	La–Lu, Ce, Y	–	–	–
Cs	La–Lu, Ce, Y	–	–	–

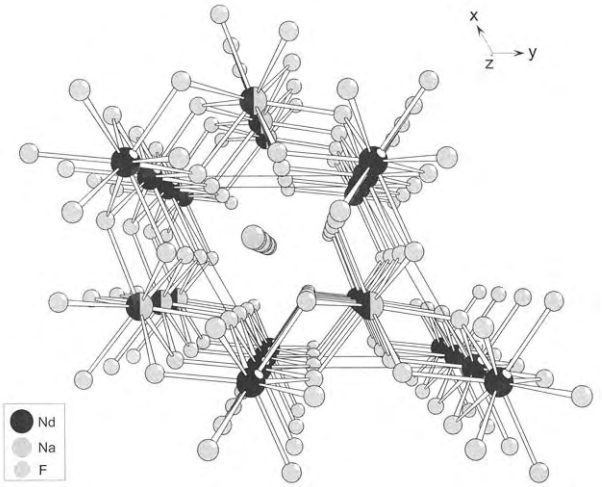

Fig. 15. Crystal structure of $NaNdF_4$: Every second row of face-sharing $[RCl_9]$ polyhedra contains Na^+ and Nd^{3+} (50% each).

which appears reasonable taking the existence of $NaRI_4$-type iodides with R = Al, In into account (Staffel and Meyer 1989, Burnus et al. 1994). With A^+ ions other than Li^+ and Na^+ no formation of ARX_4-type compounds with X = Cl, Br, I have been observed for ternary rare-earth chlorides, bromides and iodides.

Five structure types are known for ARF_4-type fluorides: the anti-scheelite type and the structure types that were first determined for $NaNdF_4$, $KErF_4$, $TlTmF_4$ and β-$KCeF_4$. In addition, the CaF_2 type occurs with high-temperature modifications for most of the ARF_4-type fluorides with statistical distribution of the cations A^+ and R^{3+} on the Ca^{2+} sites.

$NaNdF_4$ (hexagonal) crystallizes, as already mentioned in sect. 4.1.1., in an addition/substitution variant of the UCl_3 type of structure (Burns 1965). One fourth of the Nd^{3+} ions are replaced by Na^+ in a way that chains of pure $[NdCl_9]$ and mixed $[Na_{0.5}Nd_{0.5}Cl_9]$ polyhedra occur (fig. 15).

$KErF_4$- (trigonal) and $TlTmF_4$- (hexagonal) type compounds crystallize in CaF_2-type superstructures showing complex ordering schemes with 18 and 24 formula units in the unit cell, respectively (Aléonard et al. 1978, Lösch and Hebecker 1976).

The β-$KCeF_4$ type of structure (Brunton 1969) which occurs with the larger lanthanide and alkali metal ions might be understood as a "mixture" of the UCl_3 and $PbCl_2$ types of structure. Both ions are nine-coordinate in form of tricapped trigonal prisms. The $[CeF_9]$ polyhedra are linked just like the $[UCl_9]$ polyhedra in UCl_3 and the linkage of the $[KF_9]$ polyhedra represent a part of the $PbCl_2$ type of structure (fig. 16).

$ARCl_4$-type chlorides occur for A = Li with R = Sm, Eu, Gd only (Zajonc 1996). Systems with larger R^{3+} ions seem to be simply eutectic, systems with smaller R^{3+} ions are dominated by Li_3RCl_6-type chlorides (sect. 4.1.6).

X-ray single-crystal data of $LiGdCl_4$ show that the compound crystallizes with the anti-type of the scheelite structure ($CaWO_4$). The structure may be derived from the CaF_2 type of structure by substitution of the respective cations, causing the doubling of the *c*-axis

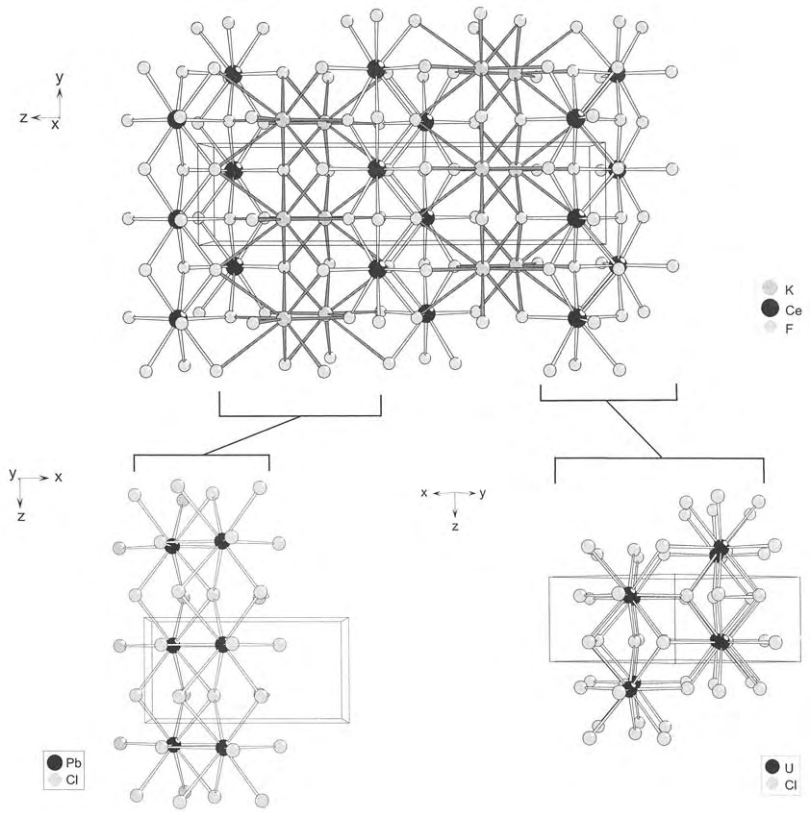

Fig. 16. Crystal structure of β-$KCeF_4$ and its relationship to the $PbCl_2$ and UCl_3 types of structure.

and shifting of the anions as indicated in fig. 17 leading to tetrahedral coordination of the smaller cations (W^{6+} and Li^+, respectively).

With A = Na three structure types are now known. For R = Gd–Tm the triclinic structure of $NaGdCl_4$ is found (Schleid and Meyer 1990). Two-dimensional layers are built up of $[GdCl_7]$ polyhedra (monocapped trigonal prisms) according to $^{3}_{\infty}[GdCl^{e}_{6/2}Cl^{t}_{1/1}]$ ($^{2}_{\infty}$: layer; e: edge-connecting; t: terminal; 6/2 and 1/1 are *Niggli* symbols meaning that there are 6 chloride ions connecting via common edges and thereby belonging to two Gd^{3+} centers). The layers are stacked in the [100] direction and are held together by Na^+ ions. These also show monocapped trigonal prismatic coordination and the same connection scheme as the $[GdCl_7]$ polyhedra. The complete structural network of the two sublattices is the same as in EuI_2 (as mentioned in sect. 3.2). Therefore, $NaGdCl_4$ is an ordered variant of EuI_2. Although the symmetry is only triclinic for $NaGdCl_4$ rather than monoclinic as for EuI_2, the relationship is strongly reflected by the lattice parameters bearing in mind the different sizes of iodide and chloride. Fig. 18 compares the two structures. Both structures

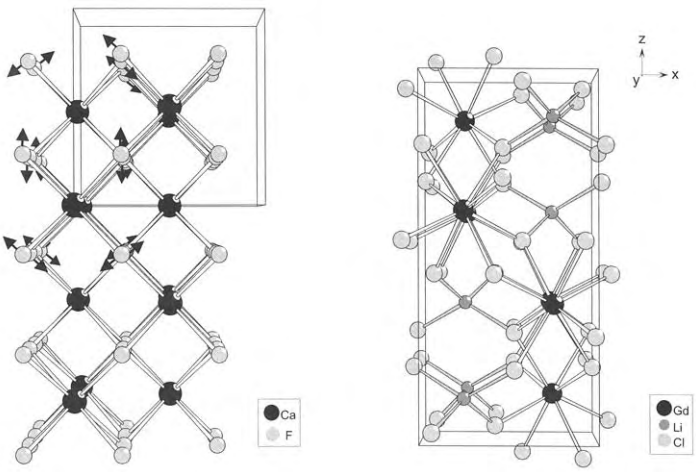

Fig. 17. Crystal structure of $LiGdCl_4$ (anti-scheelite type) and its relationship to the CaF_2 type of structure.

are related to the parent CaF_2 type of structure although the coordination number of the cations is seven now. The cationic positions are almost retained with respect to the fluorite type and mainly the anions are shifted.

The phase diagram of the system $NaCl/GdCl_3$ indicates a phase transition to occur for $NaGdCl_4$ at 285°C (Seifert et al. 1991). The structure of the high-temperature modification has been determined recently. It crystallizes with the $NaErCl_4$ type of structure (Wickleder and Meyer 1995b) which was first found for α-$NiWO_4$ (Keeling 1957). In a hexagonal closest packing of chloride ions, octahedral holes between alternating layers are filled with Na^+ and Er^{3+}, respectively, leading to the sequence ClNaClErCl. Both cations are arranged in a way that they form chains of "cisoid" edge connected $[RCl_6]$ octahedra according to $^1_\infty[RCl^e_{4/2}Cl^t_{2/1}]$ within the layers (fig. 19) and represent, taken by themselves, the structure of $ZrCl_4$. The same kind of filling of half of the octahedral sites in a hexagonal closest packing of anions can be found in α-PbO_2.

The close relationship of the structures of $NaGdCl_4$ and $NaErCl_4$ strikes the eye: they both form layer structures and there is only additional polyhedral linking in the former yielding the higher coordination number. Therefore, it is not astonishing that phase transitions between the two modifications occur quite readily even at lower temperatures (fig. 20).

The $NaErCl_4$ type of structure is also found under ambient conditions for $NaTmCl_4$ and $NaYbCl_4$. $NaLuCl_4$ and $NaScCl_4$ crystallize with a third type of structure first determined for $NaLuCl_4$ (Wickleder et al. 1996b, Bohnsack et al. 1996). The anionic arrangement is the same as in $NaErCl_4$ but the octahedral voids of the hexagonal closest packing of chloride ions are occupied in a different fashion: Na^+ and Lu^{3+} fill together the sites in an ordered manner to one fourth each. The connectivity of the $[LuCl_6]$ octahedra does not change when compared with that of Er^{3+} in $NaErCl_4$ but the $[NaCl_6]$ octahedra are no longer linked within the layers but isolated. They are connected, however, to

Fig. 18. Crystal structure of $NaGdCl_4$ and its relation to the EuI_2 type of structure.

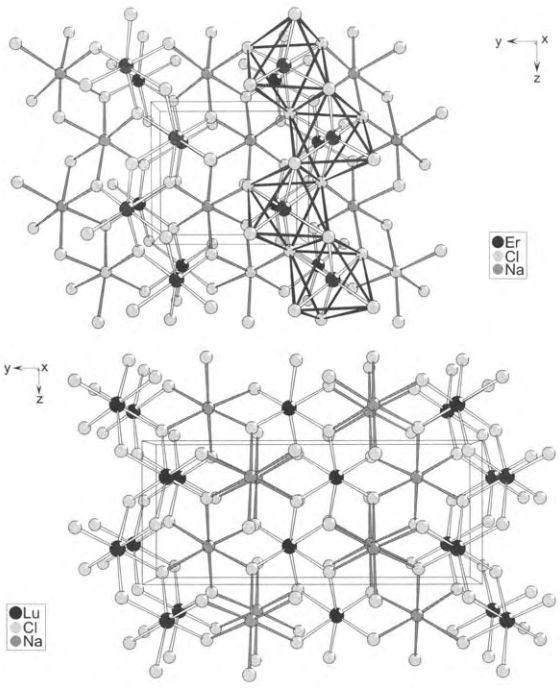

Fig. 19. Crystal structures of (top) $NaErCl_4$ and (bottom) $NaLuCl_4$. The chain of edge-connected $[RCl_6]$ octahedra according to $^{1}_{\infty}[RCl^{e}_{4/2}Cl^{t}_{2/1}]$ is emphasized.

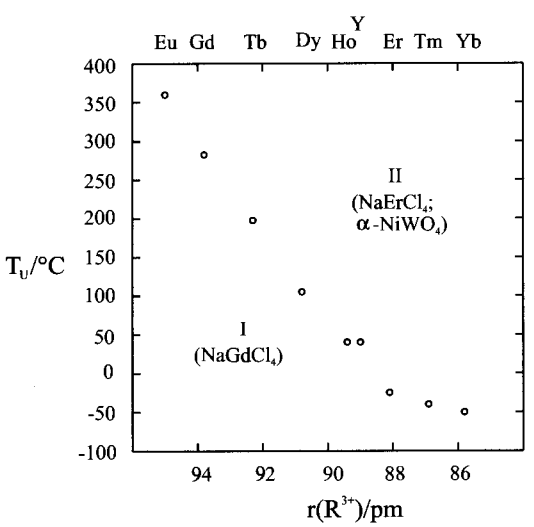

Fig. 20. Temperature dependence of the phase transition from the $NaGdCl_4$ to the $NaErCl_4$ type of structure in $NaRCl_4$-type chlorides (R = Eu–Yb, Y).

$[NaCl_6]$ octahedra of adjacent layers via vertices. No phase transition of the $NaLuCl_4$ type of structure to one of the other structure types has been observed, probably because the required cationic rearrangement needs too much activation energy.

Table 5
The occurrence of A_2RX_5-type halides

A	X=F	X=Cl	X=Br	X=I
Na	–	Sm–Gd	–	–
K	Sm–Yb	La, Ce–Dy	La, Ce–Gd	La, Ce–Nd
Rb	Ce–Er	La, Ce–Lu, Y	La, Ce–Gd	La, Ce–Nd
Cs	–	La, Dy–Lu, Y	–	–

4.1.4. *A_2RX_5-type halides*

Examples for ternary rare-earth halides of the A_2RX_5 type are known for all of the halides and most A^+ ions although there are only few examples with A=Na, Cs (table 5).

The sodium chlorides Na_2RCl_5 (R=Sm–Gd) melt incongruently (but crystals suitable for X-ray structure determination could be grown from off-stoichiometric mixtures of the binary educts (Thiel and Seifert 1988, Seifert and Sandrock 1990, Seifert et al. 1991). No compound formation could be detected in the $NaCl/RCl_3$ systems with the R^{3+} ion larger than Sm^{3+}; these systems are simply eutectic (Seifert et al. 1985, 1986, 1987, 1988). With R^{3+} ions smaller than Gd^{3+}, chlorides with other compositions such as Na_3RCl_6 and $NaRCl_4$ become more stable and no Na_2RCl_5 formation is observed. No Na_2RX_5 halides other than chlorides are known and the same is true for A=Cs.

All of the A_2RX_5-type halides crystallize with one of two structure types, the K_2PrCl_5 (Y_2HfS_5) (Meyer and Hüttl 1983) and the Cs_2DyCl_5 type of structure (Meyer 1980). The fluorides A_2RF_5 were said to crystallize in the K_2SmF_5 type of structure. Its structural arrangement is the same as in K_2PrCl_5. The space group is said to be $Pna2_1$ (Bochkova et al. 1973) which is the acentric variant of Pnma that is found for K_2PrCl_5.

The K_2PrCl_5 type of structure consists of monocapped trigonal prisms $[PrCl_7]$ which are connected via common edges to form infinite chains (fig. 21) according to $^1_\infty[MCl^e_{4/2}Cl^t_{3/1}]$ and running along the crystallographic *b*-axis. The chains are arranged as hexagonal packing of rods; these are held together by A^+ ions. The coordination number of the latter is between 8 and 9 and varies slightly depending upon the ionic size.

Ammonium chlorides and bromides $(NH_4)_2RX_5$ play an important role in the above-mentioned ammonium halide route for the synthesis of rare-earth trihalides. Only for $(NH_4)_2PrCl_5$, however, crystals suitable for an X-ray structure refinement were obtained serendipitously (Bohnsack and Meyer 1996a). Many other compounds, including reduced rare-earth halides (KSm_2Cl_5, see below) as well as intermetallic phases (Rh_5Ge_3; Geller 1955) and chalcogenides (Y_2HfS_5; Jeitschko and Donohue 1975), are structurally closely related to K_2PrCl_5. As can be seen from fig. 22, Rh_5Ge_3 is an intergrowth of the CsCl and the Ru_2Si types of structure (the latter may be derived by a glide twinning procedure from a primitive close packed array).

For A_2RX_5 halides with smaller R^{3+} ions or/and larger ligands the Cs_2DyCl_5 type of structure occurs. Chains of *cis*-vertex connected $[RCl_6]$ octahedra, $^1_\infty[MCl^e_{2/2}Cl^t_{4/1}]$, are the characteristic feature of this structure type, which is also found for several

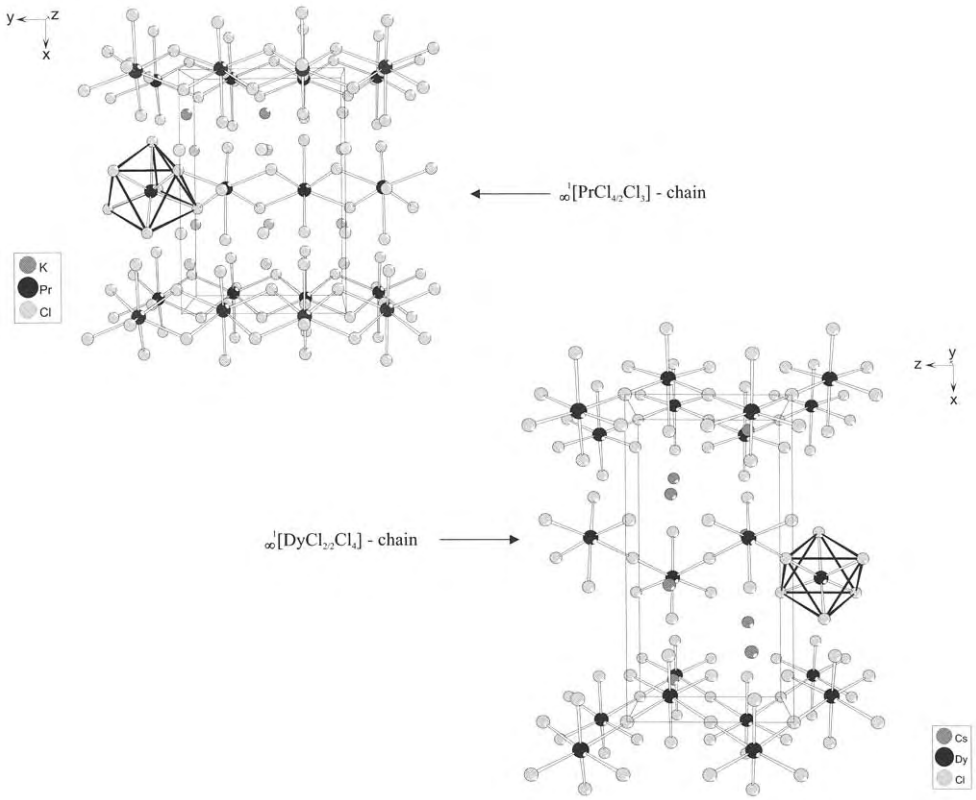

Fig. 21. Crystal structures of K_2PrCl_5 and Cs_2DyCl_5 emphasizing the chains of connected $[PrCl_7]$ and $[DyCl_6]$ polyhedra.

oxidehalides, e.g. $K_2VO_2F_3$ (Ryan et al. 1971). The chains are oriented parallel to [001] and in analogy to K_2PrCl_5 packed hexagonally like rods (fig. 21).

Single crystals of K_2LaCl_5 and K_2LaBr_5 doped with Er^{3+} were grown via the Bridgman technique and their IR to VIS upconversion properties have been investigated. Remarkable differences can be seen subject to the two host lattices in accord with the lower phonon energy of the bromide lattice (Krämer and Güdel 1995). Single crystals of K_2LaCl_5 doped with 10% of Ce^{3+} were found to have very interesting scintillation properties, comparable to the most frequently used scintillator NaCl:Tl (van 't Spijker et al. 1995).

4.1.5. *$A_3R_2X_9$-type halides*

One of the best known classes of ternary rare-earth halides is that of $A_3R_2X_9$-type compounds. As the A^+ cation takes part in closest packed layers of the composition AX_3 and, therefore, requires with respect to its coordination number of 12 large A^+ ions, namely Cs^+, Rb^+, and to a much lesser extent K^+. They also do not occur with X = F (table 6).

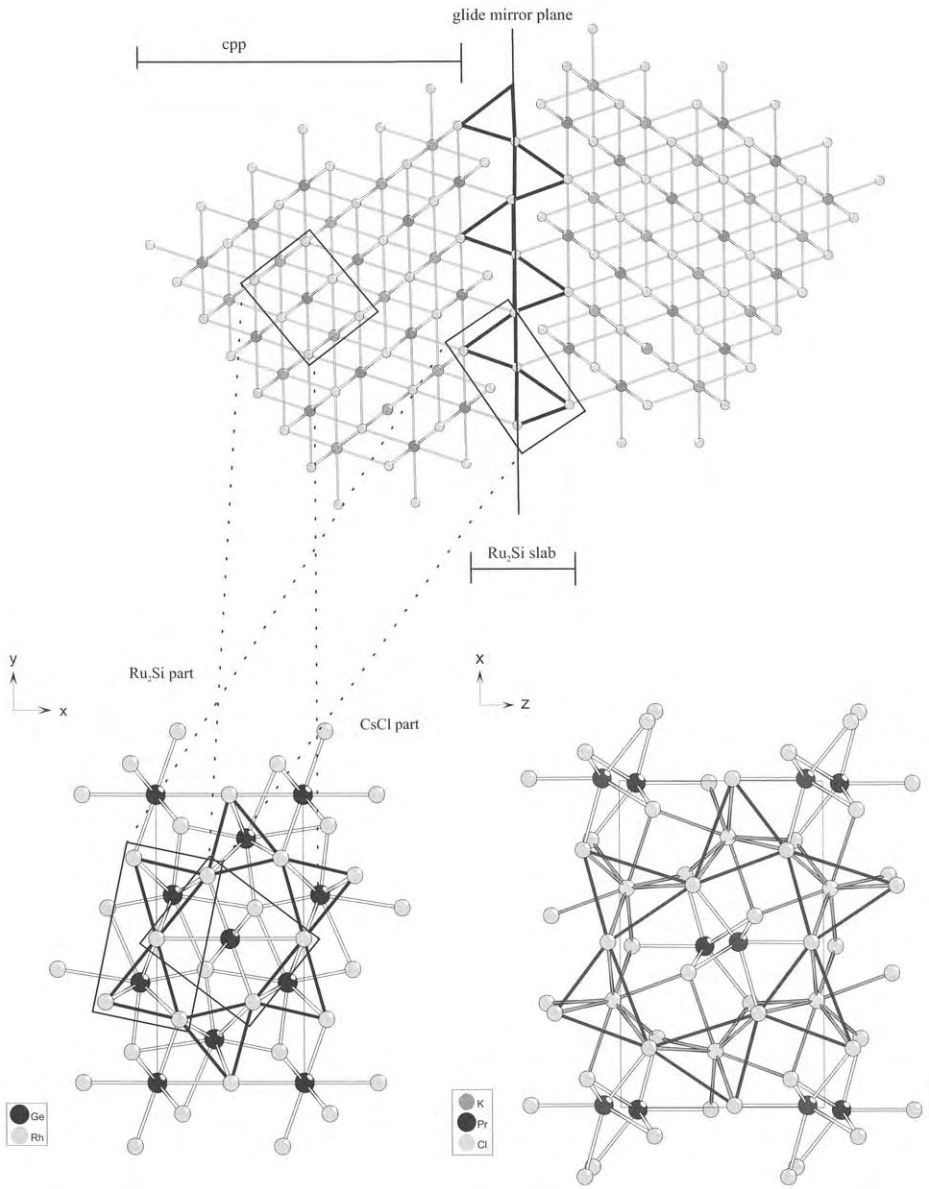

Fig. 22. Structural relationship between Rh_5Ge_3 and K_2PrCl_5. The Ru_2Si- and CsCl-type parts of the structure of Rh_5Ge_3 as derived from a primitive sphere packing.

Two structure types are observed for rare-earth-containing $A_3R_2X_9$-type compounds, the $Cs_3Cr_2Cl_9$ and the $Cs_3Tl_2Cl_9$ types of structure. Both may be derived from closest

Table 6
The occurrence of $A_3R_2X_9$-type halides

A	X = F	X = Cl	X = Br	X = I
K	–	Ce–Nd	–	–
Rb	–	Sc	Er–Lu, Sc	–
Cs	–	Ho–Lu, Y, Sc	Sm–Lu, Y, Sc	Tb–Lu, Y, Sc

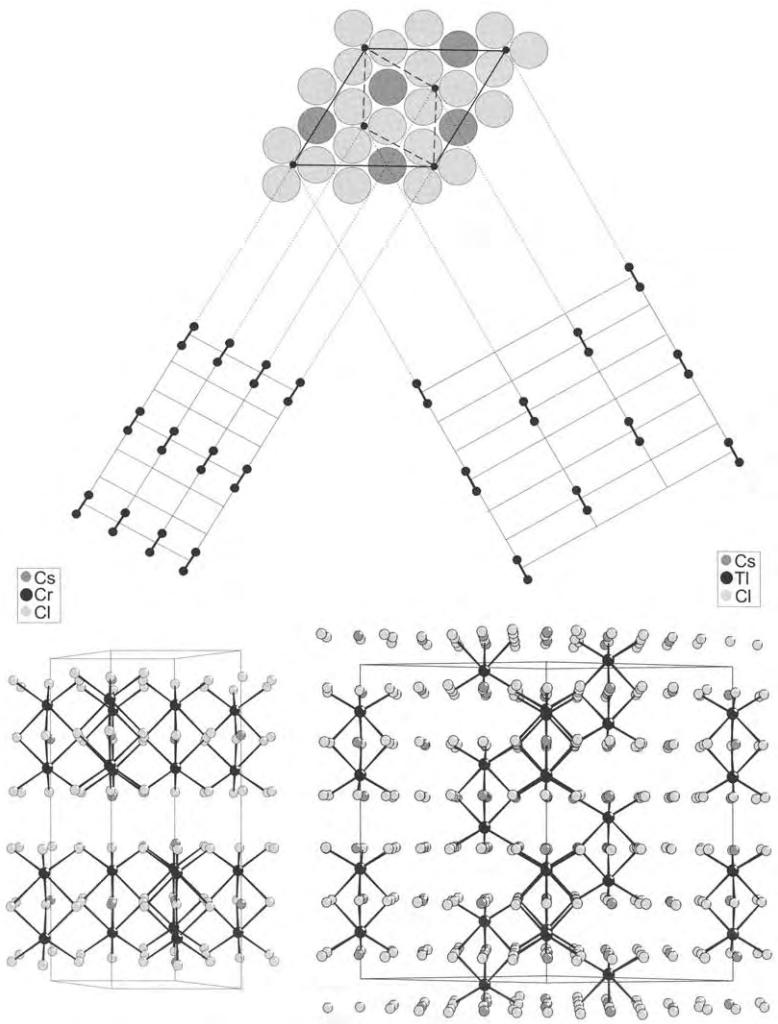

Fig. 23. Crystal structures of $Cs_3Cr_2Cl_9$ and $Cs_3Tl_2Cl_9$ as derived from hexagonally closest packed $[RCl_3]$ layers.

packed layers of the composition [$CsCl_3$] (fig. 23) (Wells 1975). In principle, such layers may be stacked in an infinite number of ways. The two structures represent ABACBC and ABABAB stacking, respectively, so that the two out of three octahedral holes filled with R^{3+} cations in $A_3R_2X_9$-type halides may share one common face leading to [R_2X_9] double octahedra.

If all possible sites are occupied one arrives at the composition ARX_3, known for example for $CsNiCl_3$ (and "$CsScCl_3$'", see sect. 4.2.2) in the case of the hexagonal closest packing and perovskite-type compounds for cubic closest packing, respectively. Removing half of the R ions leads to A_2RX_6-type compounds represented by K_2GeF_6 (hcp) and K_2PtCl_6 (ccp).

The common feature of the $Cs_3Cr_2Cl_9$ and the $Cs_3Tl_2Cl_9$ types of structure are bioctahedral [R_2X_9] dimers, resulting from the occupation of neighboring octahedra. This arrangement allows for the shortest distances between the cations R^{3+} in a closest packed array of anions. Therefore, exchange phenomena between neighboring centers have been studied extensively (Hehlen et al. 1996, Allenspach et al. 1997) including the IR to VIS upconversion properties of the respective erbium halides. In particular, $Cs_3Er_2Br_9$ seems to be interesting in view of laser applications (Pollnau et al. 1996).

Magnetic coupling between Er^{3+} centers has recently been investigated for $Cs_3Er_2I_9$ by means of neutron scattering (Krämer et al. 1997). At 27 mK, the compound undergoes a magnetic phase transition: The ferromagnetically coupled dimers are antiferromagnetically coupled three-dimensionally leading to a magnetic cell four times expanded in the hexagonal plane. However, due to a crystallographic phase transition at 158 K causing deviations from hexagonal symmetry, an exact magnetic description has not been given yet.

4.1.6. *A_3RX_6-type halides and derivatives*

A_3RX_6-type compounds occur quite frequently in the chemistry of rare-earth halides (table 7). At least seven structure types have been identified for A_3RF_6 type fluorides alone. Structures were determined first with β-Li_3VF_6 (Massa 1980), β-Rb_3ErF_6 (Aléonard et al. 1975), Rb_3TlF_6 (Reshetnikova et al. 1974), β-$(NH_4)_3ScF_6$ (Bode and Voss 1957), K_3TlF_6 (Bode and Voss 1957), Na_3AlF_6 (cryolite) (Hawthorne and Ferguson 1975) and for K_2NaAlF_6 (elpasolite) (Morss 1974).

Table 7
The occurrence of A_3RX_6-type halides

A	X = F	X = Cl	X = Br	X = I
Li	Sc	Tb–Lu, Y, Sc	Sm–Lu, Y, Sc	Dy–Lu
Na	Sc	Eu–Lu, Y, Sc	Sm–Lu, Y, Sc	Sm–Dy
K	Ce–Lu, Y, Sc	Ce–Lu, La, Y, Sc	Ce–Lu, La, Y, Sc	Pr–Er
Rb	Ce–Lu, Y, Sc	Ce–Lu, La, Y, Sc	Ce–Lu, La, Y, Sc	Ce–Er
Cs	Ce–Lu, Y, Sc	Ce–Lu, La, Y, Sc	Ce–Lu, La, Y, Sc	Ce–Er, La

These structures are all strongly related in a way that they can be derived from the elpasolite type of structure (see below) by tilting the $[RF_6]$ octahedra. This has been shown extensively years ago (Greis 1982) and will not be outlined here. For Rb_2KScF_6 temperature dependent neutron diffraction studies have been carried out resulting in the determination of the structures of three modifications: The low temperature form has the structure of cryolite (monoclinic), at ambient conditions the β-$(NH_4)_3ScF_6$ type (tetragonal) and at high temperatures the elpasolite type (cubic) occurs (Faget et al. 1996).

The cryolite and the elpasolite types of structure are also known for the higher halides together with a number of further structure types found for example for Cs_3BiCl_6 (Benachenhou et al. 1986), K_3MoCl_6 (Amilius et al. 1969), Na_3CrCl_6 (Friedrich et al. 1987), Na_3GdCl_6 (stuffed $LiSbF_6$) (Meyer 1984a), Na_3GdI_6 (Bohnsack and Meyer 1997), $Na_3GdBr_4I_2$ (Bohnsack and Meyer 1997), Li_3YCl_6 (Bohnsack et al. 1997a) and Li_3YbCl_6 (Bohnsack et al. 1997a).

The structures of these halides depend strongly on the size of the A^+ ion: If A^+ is large enough (e.g., Cs^+) closest packings of A^+ and X^- spheres are found (e.g., elpasolite). Small A^+ ions are, on the other hand, mostly located in octahedral sites of pure anion packings (e.g., Na_3CrCl_6). There is a common feature in all of these structures: The rare-earth ion R^{3+} is always octahedrally coordinated and the $[RX_6]$ octahedra are isolated from each other. This is the tribute to the high A^+ content of A_3RX_6-type halides which makes the connection of $[RX_6]$ octahedra rather unlikely.

Our survey of the A_3RX_6 structure types starts with the elpasolite type of structure (K_2NaAlF_6). Although this is not strictly a ternary compound, many of the ternary A_3RX_6 rare-earth halides adopt this structure at least at elevated temperatures. There is a plethora of A_2BRX_6 halides with the cubic elpasolite type structure, its tetragonally (or otherwise) distorted varieties or its hexagonal stacking variants, depending also upon temperature and pressure. Many of the features have been reviewed previously (Meyer 1982) and shall be left aside here.

The cubic face-centered elpasolite-type of structure (K_2NaAlF_6) is, in the crystal chemist's view, strongly related to the K_2PtCl_6 type of structure (Wells 1975). Both, with their general formulae A_2BRX_6 and A_2RX_6, consist of $[AX_3]$ layers stacked in the ABC (cubic closest packed) fashion in the [111] direction of the cubic face-centered Bravais lattice. Half of the available octahedral sites are occupied by Pt^{4+} cations in K_2PtCl_6 and all are occupied by Na^+ and Al^{3+} in K_2NaAlF_6 in an ordered way.

Note that, starting formally from A_2BRX_6-type compounds, with B = R and with B = A we will get to the classes of perovskite ($A_2R_2X_6 = ARX_3$) and A_3RX_6-type compounds with all their structural varieties.

On the other hand, the K_2PtCl_6 type is often referred to as the anti-fluorite type of structure (anti–CaF_2) according to $K_2[PtCl_6] = F_2[Ca]$ meaning that in a cubic closest packing of $[PtCl_6]$ octahedra all tetrahedral interstices are occupied with K^+ ions. Following this line, the crystal structure of $(NH_4)_3Cu_4Ho_2Br_{13}$ might also be derived from the CaF_2 parent type according to $2 \times (NH_4)_3Cu_4Ho_2Br_{13} = [HoBr_6]_4[(NH_4)_6(BrCu_4)_2] = Ca_4F_8$ with Cu^+ ions residing in tetrahedral holes created by one triangular face of one $[HoBr_6]$

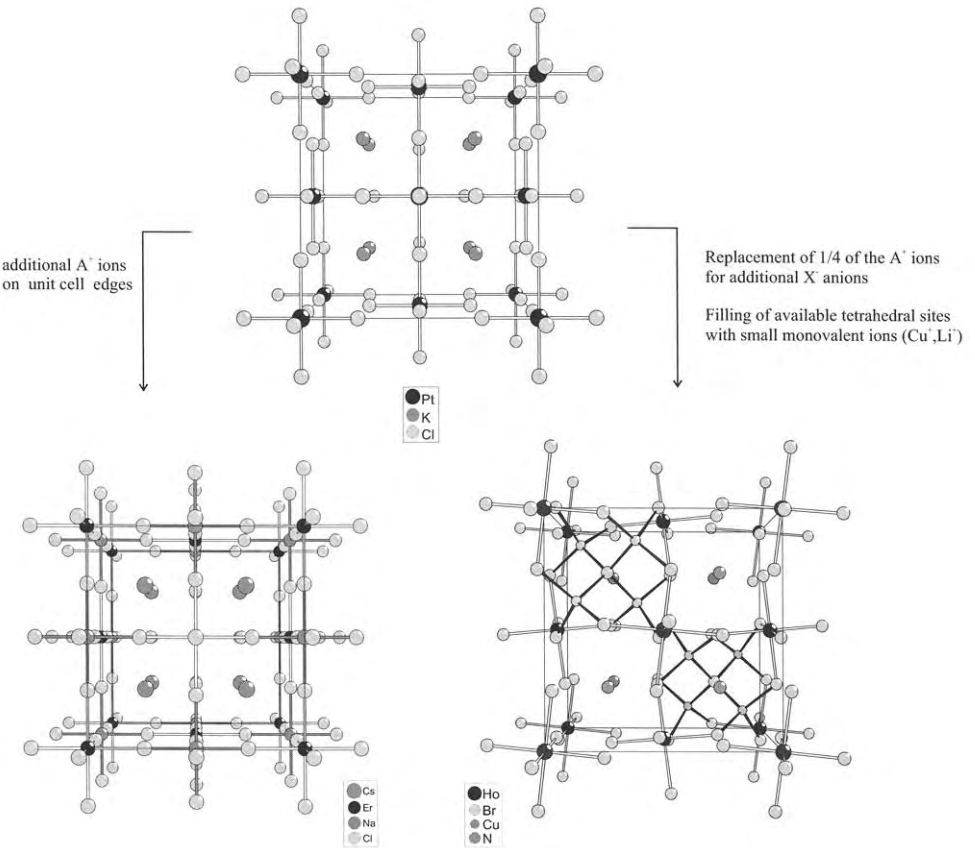

Fig. 24. The elpasolite type of structure (K_2NaAlF_6) and the crystal structure of $(NH_4)_3Cu_4Ho_2Br_{13}$ as derived from the K_2PtCl_6 type of structure.

octahedron and the thirteenth bromide ion of $(NH_4)_3Cu_4Ho_2Br_{13}$ (Wickleder et al. 1996b) (fig. 24). The Cu_4Br_{13} part of the structure is a section of the crystal structure of CuBr (zincblende).

It is obvious that the elpasolite type of structure is preferred with A^+ and B^+/R^{3+} cations of (very) different sizes because A^+ is part of the closest packing and B^+ and R^{3+} occupy the octahedral sites within the packing. Therefore, structural difficulties must arise when B^+ becomes chemically equal with A^+ as is the case in A_3RX_6 ($=A_2ARX_6$)-type halides. These difficulties are dealt with roughly in two ways:

(a) With large ions like Cs^+ and Rb^+ too big for octahedral coordination, structures are formed with these ions more or less incorporated in the layers that are then stacked. Examples are the structures of K_3MoCl_6 (Amilius et al. 1969) and Cs_3BiCl_6 (Benachenhou et al. 1986). Layers with the composition as put below in square brackets are stacked with Mo^{3+}/Bi^{3+} occupying octahedral interstices.

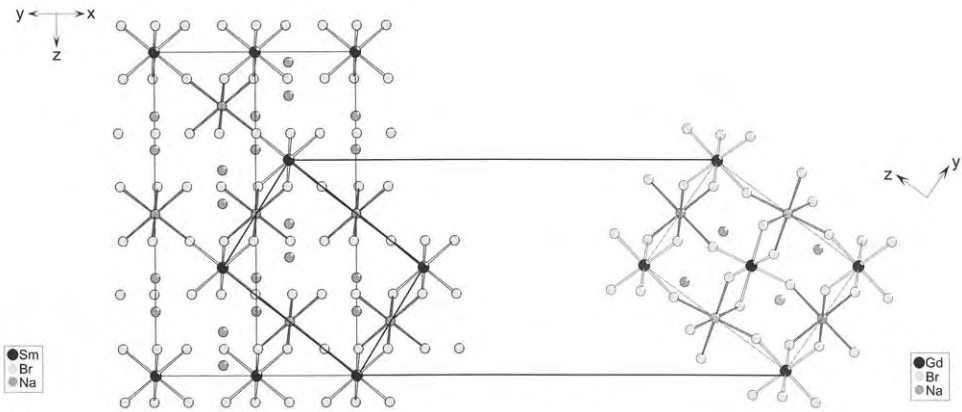

Fig. 25. Similarities between the cryolite (at right) and stuffed $LiSbF_6$ types of structure.

For K_3MoCl_6 one finds the sequence $\cdots[K_2Cl_2][MoCl_2][K_2Cl_2][KCl_3][Mo][KCl_3]\cdots$ and for Cs_3BiCl_6 $\cdots[Cs_2Cl_2][BiCl_2][Cs_2Cl_2]\cdots$ and there are others (Mattfeld and Meyer 1992). Note that the sequence $[KCl_3][Mo][KCl_3]$ is as observed in the elpasolite type of structure. As the packing is not ideal, rather low symmetries are normally observed, monoclinic for K_3MoCl_6 and Cs_3BiCl_6, although higher symmetries are possible as can be seen from the recently reported low-temperature modification of Cs_3RCl_6-type chlorides (Reuter et al. 1997).

(b) With all A^+ ions in A_3RX_6 structures equal and small, the elpasolite type of structure cannot be retained. The most prominent example is the cryolite type of structure, Na_3AlF_6, where according to $Na_2(NaAl)F_6$ the parent elpasolite is resembled in that the coordination number of the two Na^+ of formerly 12 is reduced to 8 through tilts of the $[RX_6]$ octahedra (fig. 25). Many of the Na_3RX_6-type chlorides and bromides also crystallize with the cryolite type of structure.

When the A^+ ions are small enough for octahedral coordination, they may all be incorporated in the octahedral holes of a closest packing of anions. The so-called stuffed $LiSbF_6$ type is a prominent example, first observed for Na_3GdCl_6 (Meyer 1984b) and subsequently for various Na_3RX_6 (Meyer et al. 1987, Wickleder and Meyer 1995a) and for all Ag_3RCl_6 compounds (Staffel and Meyer 1988). There is a strong structural similarity between the cryolite and the stuffed $LiSbF_6$ type (fig. 25). The latter may be derived from a hexagonal closest packing of anions (Cl^- in Na_3GdCl_6) with two of the six octahedral holes filled regularly with Gd^{3+} and $Na1^+$ and with the remaining two Na^+ ions distributed statistically over four empty interstices according to $Na_{4/2}(NaGd)Cl_6$.

Temperature dependent phase transitions between both structure types have been found for the respective chlorides and bromides as is indicated in fig. 26 (Wickleder and Meyer 1995a). Within the mixed cation series $Ag_{3-x}Na_xYCl_6$, the cryolite type occurs when the Na^+ content exceeds $x=2$ (Stenzel and Meyer 1993). With $x<2$ this structure is only stable at elevated temperatures, with $x=0$ (pure Ag_3YCl_6) the cryolite type of structure

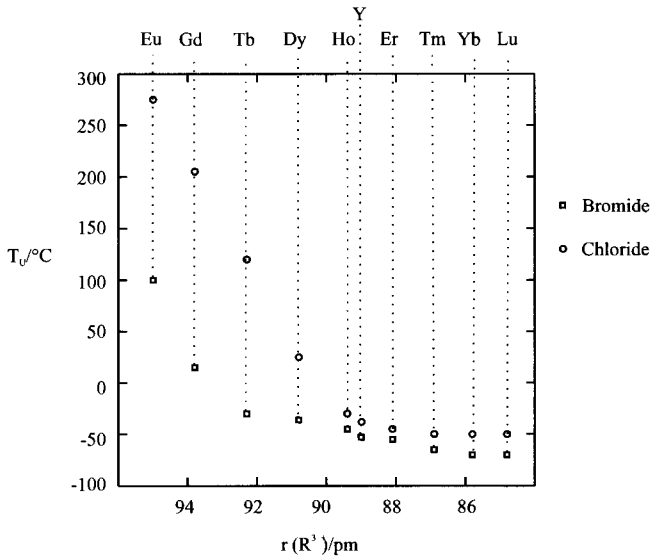

Fig. 26. The dependence of the phase transition temperature from the stuffed $LiSbF_6$ to the cryolite type of structure upon the size of the R^{3+} cation for ternary Na_3RX_6-type chlorides and bromides.

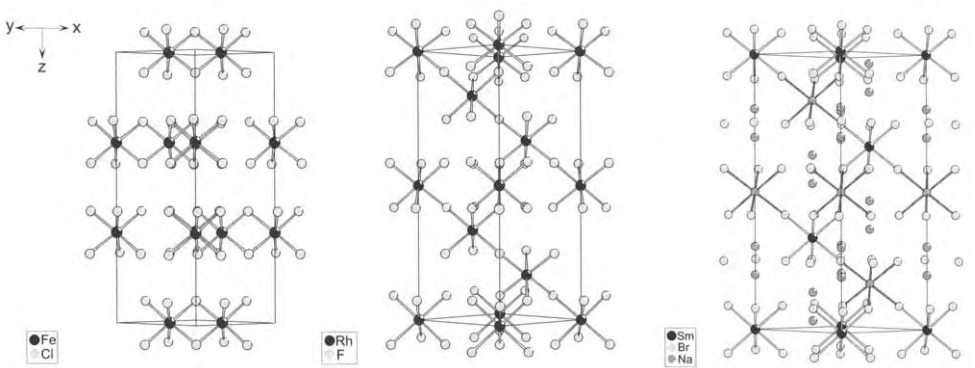

Fig. 27. A comparison of the crystal structures of $FeCl_3$, RhF_3 (HT-$TmCl_3$) and of the stuffed $LiSbF_6$ type of structure (Na_3SmBr_6).

does not appear, even at high temperatures, but two other hitherto unknown modifications have been reported (Lerch and Laqua 1990).

The stuffed $LiSbF_6$ type of structure might also be understood as a derivative of the RhF_3 type of structure which occurs as the high pressure form of various binary rare-earth halides of the $FeCl_3$ (BiI_3) type. According to $2 \times RX_3 = R_2X_6 \rightarrow (AR)X_6 \rightarrow A_2(AR)X_6$ the stuffed $LiSbF_6$ type is an addition/substitution variant of the RhF_3 type (fig. 27).

An analogous addition/substitution variant now derived from the cubic closest packing of halide anions is found for Na_3GdI_6, Li_3ErBr_6 and Li_3ScCl_6, to name only three (fig. 28)

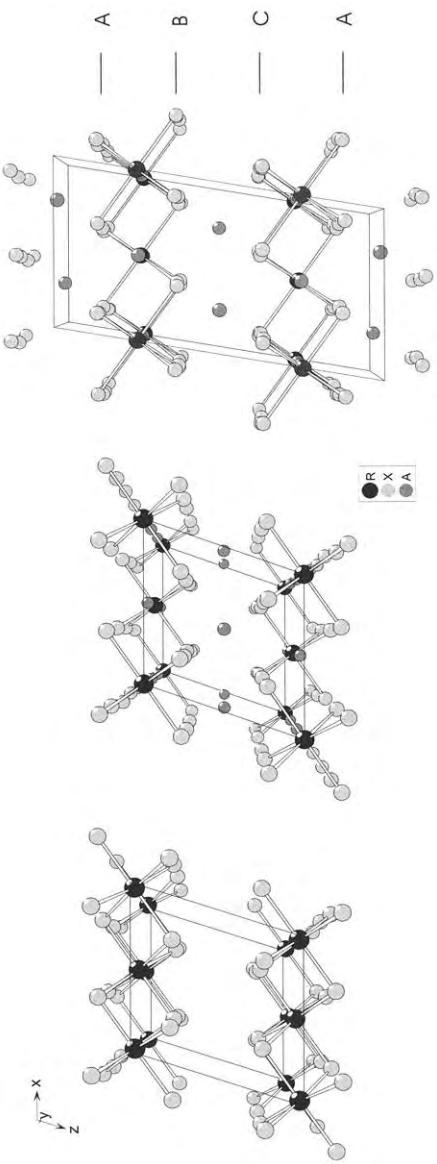

Fig. 28. Crystal structures of Na_3GdI_6 (Li_3ErBr_6, Li_3ScCl_6) and $Na_3GdBr_{1,2}I_{4,8}$ as derived from the $AlCl_3$ type of structure (at left).

(Bohnsack and Meyer 1997, Bohnsack et al. 1997a,b). The parent structure type is that of $AlCl_3$ which appears for numerous binary rare-earth halides at ambient conditions. Two thirds of the Na^+ ions with respect to Na_3GdI_6 are again statistically distributed over the four possible sites, but within the mixed anion series $Na_3GdBr_xI_{6-x}$ a more ordered variant is found for $Na_3GdBr_{1.2}I_{4.8}$ with a slightly higher symmetry (C2/c instead of C2/m) and a doubled *c*-axis (fig. 28) (Bohnsack and Meyer 1997).

The chlorides Li_3RCl_6 appear in three structure types of which Li_3ScCl_6 is isostructural with, for example, Li_3ErBr_6 and Na_3GdI_6 (see above). The other two structure types, first determined for Li_3YCl_6 and Li_3YbCl_6, are very similar and connected via a phase transition. They have the hexagonal closest packing of chloride ions in common in which the cations occupy octahedral sites. The kind of occupation, however, is somewhat curious in that there is one octahedral site in the structure of Li_3YCl_6 that is occupied by Y^{3+} to only a few percent. The investigation of several crystals shows that there is, depending on the synthesis, some variation possible (3 to 7%) but in no case the occupation can be neglected. If there is no occupation at all, the Li_3YbCl_6 type of structure occurs. Figure 29 points out the similarities between these two structures and the closely related structure of Na_3ScBr_6 (Na_3CrCl_6 type).

Temperature dependent X-ray investigations show that the Li_3YbCl_6 type is adopted at low temperatures and the Li_3YCl_6 type occurs as the high temperature modification. There is, however, a considerable hysteresis. From single crystals, the Li_3YCl_6 type was found at room temperature for Li_3ErCl_6. On heating to 210°C it transforms first to the Li_3YbCl_6 type of structure and then, at 310°C, the Li_3YCl_6 type occurs again. Hence, the Li_3YCl_6 type of structure is only kept metastable at ambient temperature (Bohnsack et al. 1997a).

The Na_3CrCl_6 type of structure which is found for Na_3ScBr_6 (Bohnsack and Meyer, 1996b) represents another variant of occupation of four out of the six octahedral sites in the hexagonal closest packing of anions. It is related to the two just mentioned structure types (fig. 29) and to the Na_3GdCl_6 type (stuffed $LiSbF_6$) as well.

The A_3RX_6 compounds with small A^+ cations fulfill several requirements with regard to ionic conductivity (Goodenough 1984):

- Small mobile ions with low charges (Li^+, Na^+, Ag^+);
- empty and (mostly) energetically equivalent sites available for the mobile ions;
- pathways for the mobile ions through the crystal with low energy barriers.

Measurements of the ionic conductivity have, therefore, been performed for sodium, silver, and lithium halides, mainly on powder samples. The results prove the expected trends. The best conductivity is found for structures with

- the hexagonal closest packing of anions as it leads to chains of anion octahedra sharing common triangular faces in the stacking direction thereby allowing an easy change of sites for the mobile ions;
- polarizing and/or very small cations (Li^+, Ag^+) and a polarizable anionic matrix (Br^-, I^-); this makes motion through the triangular face easier in that the activation energy for the conduction process decreases.

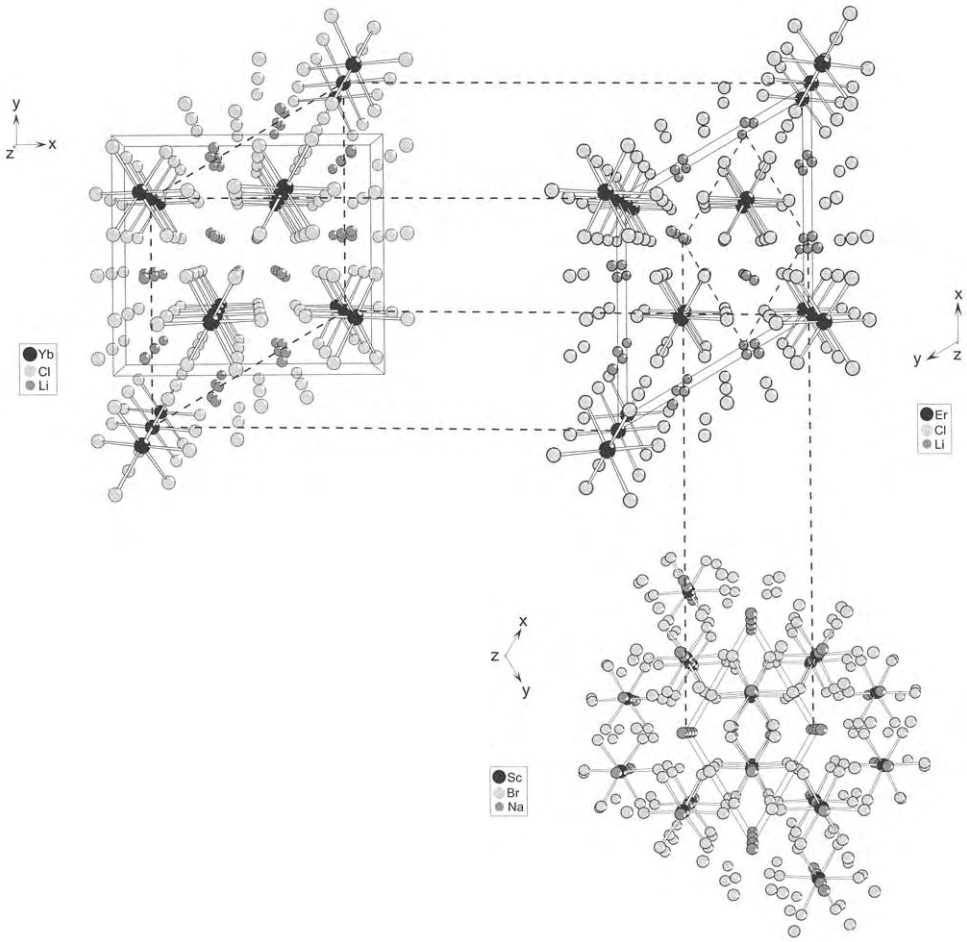

Fig. 29. Comparison of the crystal structures of Li_3ErCl_6 (Li_3YCl_6), Li_3YbCl_6, and Na_3ScBr_6.

The highest lithium ionic conductivity is observed for Li_3YCl_6. This can be understood as the sum of the above mentioned requirements: Li^+ is small and statistically distributed over octahedral sites which are connected along the stacking axis of the hexagonal closest packing of chloride ions. A more polarizable anionic matrix cannot be achieved because by substituting Cl^- for Br^- the structure changes to the less preferable cubic closest packing of anions in the structure of Li_3YBr_6. Very good ionic conduction is also found for Ag_3YCl_6 (stuffed $LiSbF_6$ type) (Lerch and Laqua 1990, Stenzel and Meyer 1993).

Because the conductivity was expected to be anisotropic for the compounds under investigation, measurements have been carried out on single crystalline samples of Li_3YBr_6, grown via the Bridgman technique. As can be seen from fig. 30, the conductivity changes

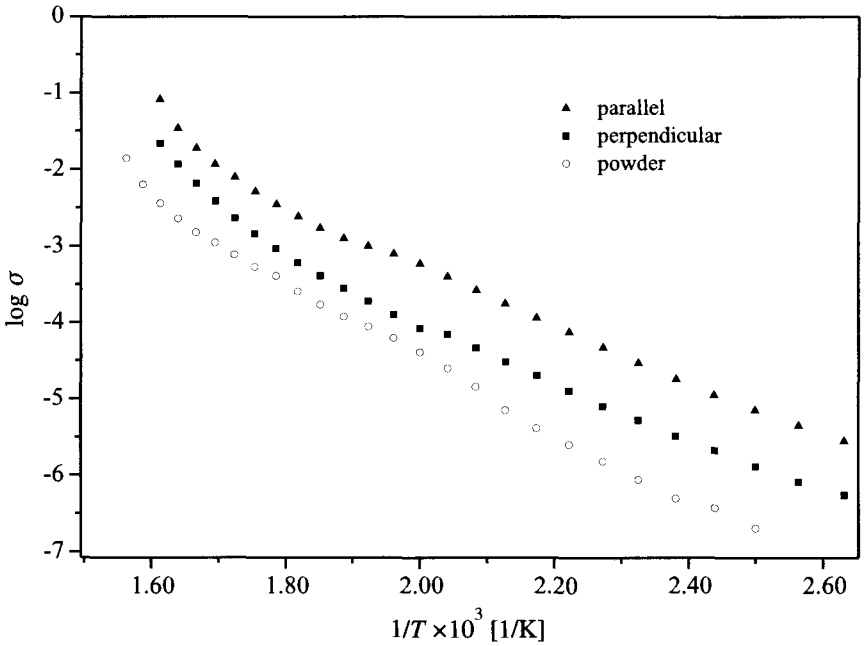

Fig. 30. Temperature dependence of the ionic conductivity of Li_3YBr_6. The measurements were performed on single crystals in the [100] and [001] directions (parallel and perpendicular to the closest-packed layers) and on powder samples.

not significantly when measured perpendicular or parallel to the stacking layers. The difference is expected to increase in hexagonally closest packed systems.

Figure 31 (overleaf) summarizes the structures of the investigated A_3RX_6-type halides with A = Li, Na, Ag in form of a structure field map.

4.1.7. *A_4RX_7-type halides*

A rather uncommon composition for ternary rare-earth halides is that of A_4RX_7-type compounds. Their structure and synthesis was reported only recently (Reuter et al. 1996) and, up to date, two examples are well established, Cs_4YbCl_7 and Cs_4YCl_7 (Seifert and Büchel 1998). The preparation is remarkable because it was carried out in aqueous solution.

The structure is strongly related to those discussed for A_3RX_6 compounds with A being a large ion like Rb^+ or Cs^+ (fig. 32). Cs^+ and Cl^- together form layers which are stacked in the direction of the *c*-axis and incorporate R^{3+} ions in octahedral interstices. The stacking sequence, however, is very special because besides the well-known $[CsCl_3]$ slabs

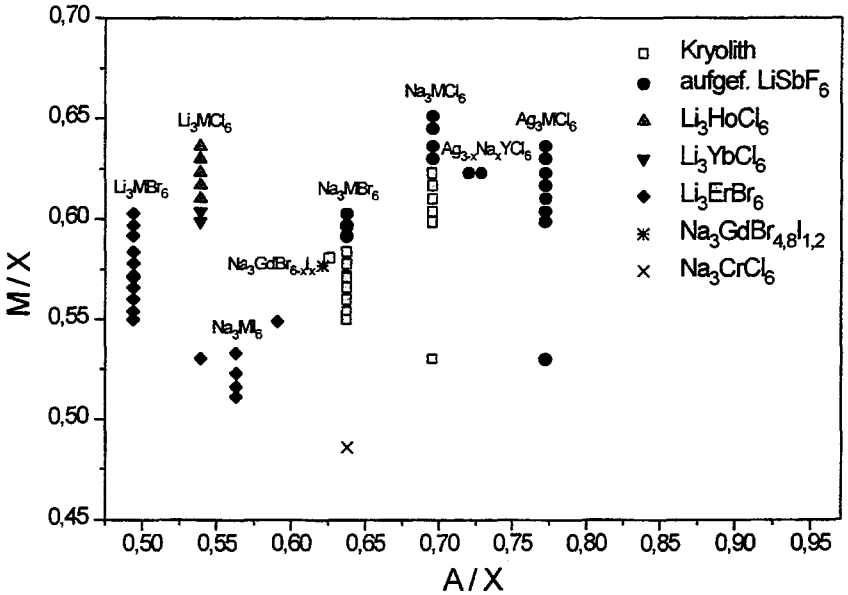

Fig. 31. Structure field map for A_3RX_6-type halides with A = Li, Na, Ag.

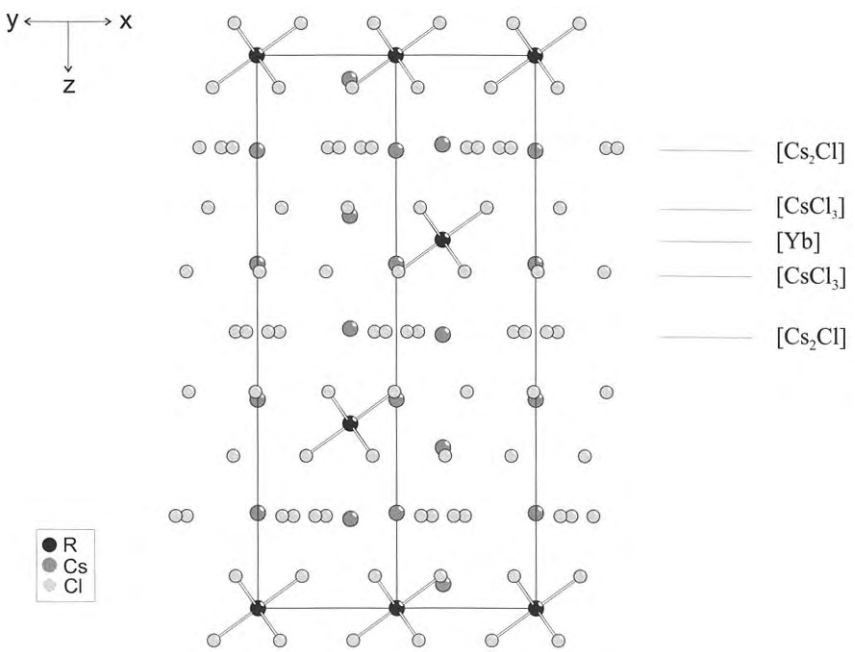

Fig. 32. Crystal structure of Cs_4RCl_7 (R = Y, Yb).

the unusual $[Cs_2Cl]$ slabs occur leading to the sequence $\cdots$ $[CsCl_3]$ $[Cs_2Cl]$ $[CsCl_3]$ [R] $[CsCl_3]$ $[Cs_2Cl]$ $[CsCl_3]$ $\cdots$. It should be mentioned that the formation of the $[Cs_2Cl]$ layers is achieved in a complicated manner with structural disorder in the Cl^- sublattice (Reuter et al. 1996).

4.1.8. *Complex halides in AX_2/RX_3 systems*

The systems AX_2/RX_3 with A now representing an alkaline-earth element have been investigated to a much lesser extent than the respective alkali metal halide systems. Phase diagrams indicate the formation of A_4RX_{11}, A_3RX_9, A_2RX_7, and ARX_5-type compounds and their occurrence is obviously related to the ionic radii of R^{3+} and A^{2+} (Blachnik and Alberts 1982, Blachnik et al. 1985). The existence of Ba_2RCl_7-type chlorides with R = Gd–Yb, Y has been proven very recently by means of X-ray single crystal studies on Ba_2ErCl_7 and Ba_2GdCl_7 (Wickleder et al. 1996c). They crystallize in a hitherto unknown structure type (fig. 33): In a three-dimensional network of egde-and face-connected $[BaCl_9]$ polyhedra, R^{3+} ions occupy seven-coordinate interstices. The $[RCl_7]$ polyhedra may be described as monocapped trigonal prisms and are isolated from each other.

Another variant of Ba_2RCl_7-type compounds is found for Ba_2ScCl_7 (Masselmann and Meyer 1998a). In its structure Sc^{3+} is octahedrally surrounded by six Cl^- ligands while the Ba^{2+} ions have coordination numbers of 9 and 10, respectively. The structure may also be described as being built up from $[BaCl_{3.5}]$ layers with Sc^{3+} in octahedral interstices (fig. 34).

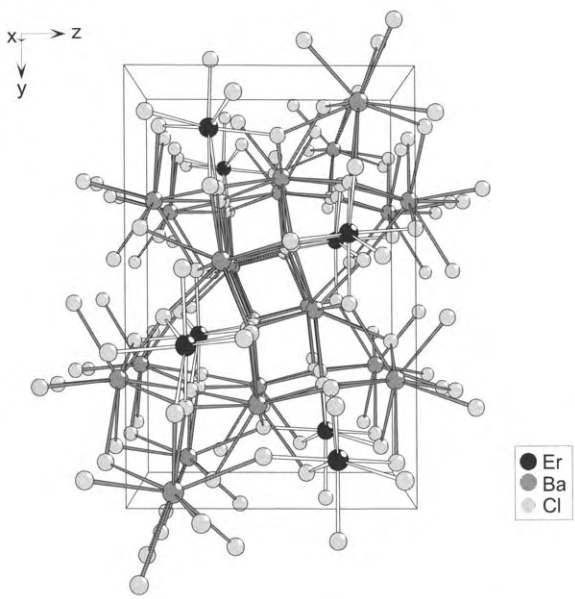

Fig. 33. Crystal structure of Ba_2ErCl_7.

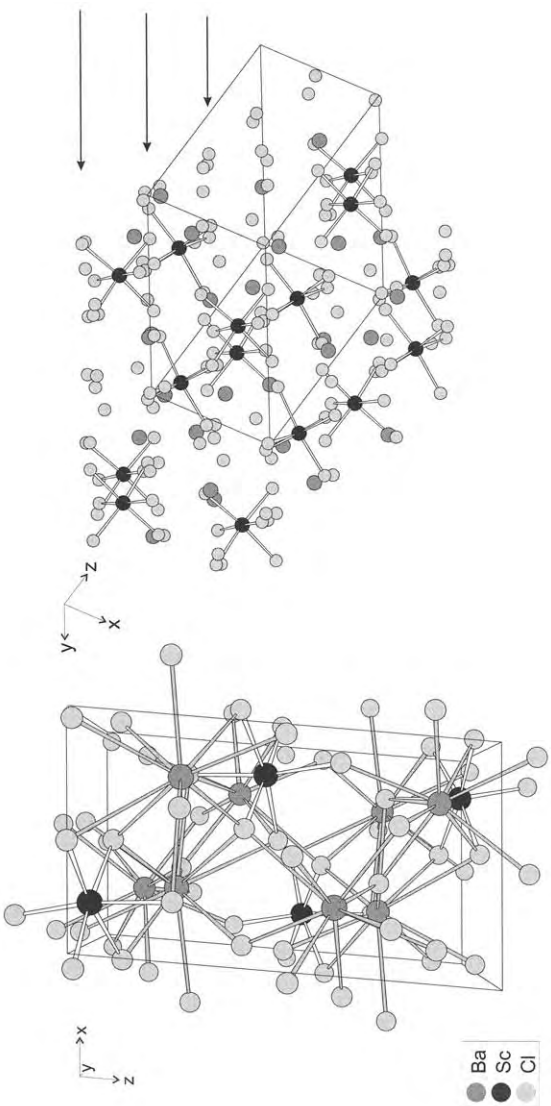

Fig. 34. Crystal structure of Ba_2ScCl_7; on the right the $[BaCl_{3,5}]$ layers are emphasized.

The approximate composition A_2RX_7 is also observed with R = La–Sm and A = Sr (Löchner and Blachnik 1988). These and the ARX_5-type compounds show a certain phase width which might be understood with respect to their crystal structures that represent superstructures of the CaF_2 type of structure: Tilting of cubes of the anionic sublattice (fig. 35) generates space for four additional anions leading to a $(A,R)_6X_{36}$ building unit. The cuboctahedral site in the center of this unit may be filled with an additional anion. This is quite well known and described for fluorides (Bevan et al. 1980a,b). Because the occupation of the void must not necessarily be complete, slight deviations from the exact stoichiometry may occur. Instead of additional halide anions, oxide ions may be incorporated.

The $(A,R)_6Cl_{36+x}$ polyhedral "clusters" may be linked in two different ways which leads to two different crystal structures, one with tetragonal (I4/m) and the other with trigonal rhombohedric ($R\bar{3}$) symmetry with the approximate compositions $(A,R)_{15}X_{34+x}$ ($\cong A_{10}R_5X_{35} = A_2RX_7$) and $(A,R)_{14}X_{32+x}$, respectively (fig. 36). Based on X-ray investigations alone it can often not be judged whether an additional anion occupies the cuboctahedron or not. Because A^{2+} and R^{3+} ions occupy, at least partly, equal crystallographic sites, electroneutrality can be achieved in any case. Very thorough research by Bärnighausen and co-workers on isotypic mixed-valent rare-earth halides (A = R) gave evidence for partial occupation of the cuboctahedron with oxide or chloride in some cases (see sect. 4.3). Recent research in the BaX_2/RX_3 and $SrCl_2/RCl_3$ systems led to compounds which may, for example, be formulated as $Sr_{10}Sm_4Cl_{32}$ and $Ba_{11}Pr_4Br_{34}$ or, if additional oxygen is concerned, as $Sr_8Sm_6Cl_{32}O$ ("$R_{14}X_{33}$") and $Ba_9Pr_6Br_{34}O$ ("$R_{15}X_{35}$"), respectively. The occupation of the cuboctahedral site, however, remains at least doubtful.

A second type of a CaF_2 superstructure occurs in the crystal chemistry of rare-earth/alkaline-earth halides, the so-called vernier phases (Hyde et al. 1974, Makovicky and Hyde 1981). These are one-dimensional derivatives of the fluorite type in a sense that part of the cubic closest packed 4^4 anion layers are transformed to the more dense 6^3 layers. Because these layers cannot be superimposed exactly, vernier-type structures are often incommensurate (Mann and Bevan 1972, Bevan and Mann 1975). The problem is solved for the ternary rare-earth chlorides of this kind by introducing so-called antiphase boundaries into the structure. This can be seen for the example for Ca_2GdCl_7 in fig. 37 (Wickleder and Meyer 1998b). According to the general formula A_nRX_{3+2n} of vernier-type phases, Ca_2GdCl_7 represents a member with $n = 2$. This is the lowest value known so far for vernier phases. The formally related chlorides Nd_3Cl_7 (Laptev et al. 1981) and Sm_3Cl_7 (Druding and Corbett 1961) as well as Sr_2SmCl_7 and Sr_2GdCl_7 (Blachnik et al. 1985) crystallize according to, for example, $Nd_3Cl_7 = Nd_{15}Cl_{35}$ with the three-dimensional tetragonal CaF_2 superstructure as described above (Lumpp 1988, Löchner and Blachnik 1988).

As mentioned above, ARX_5-type compounds crystallize with R = La, Ce–Sm with a three-dimensional CaF_2 superstructure. For $BaGdCl_5$, however, another structure has been found very recently (Masselmann and Meyer 1998b). The compound crystallizes monoclinic with cations strictly ordered. Both are in eightfold coordination, Ba^{2+} in form

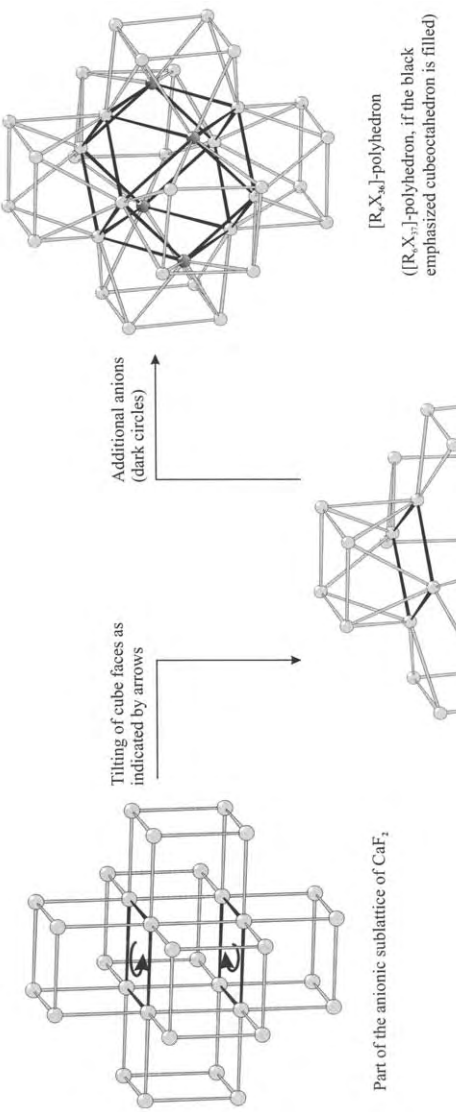

Fig. 35. Generation of the $(A,R)_6X_{36}$ polyhedral "cluster" from a section of the parent CaF_2 type of structure.

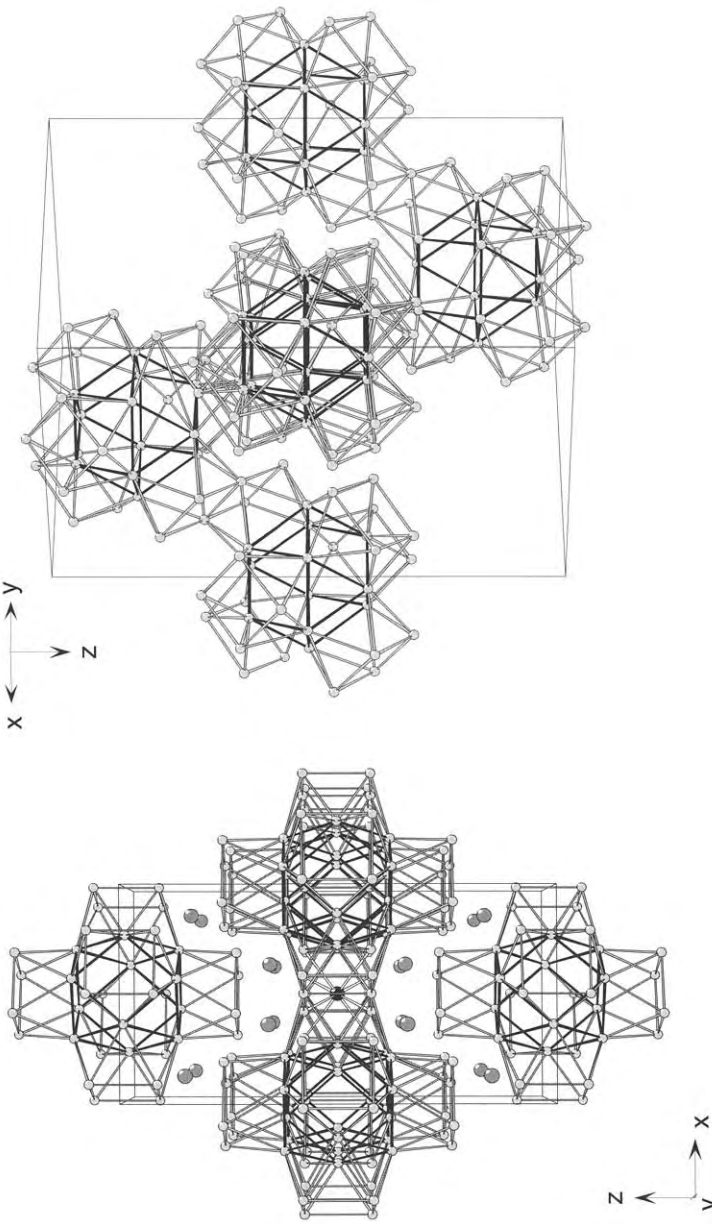

Fig. 36. The arrangement of $(A,R)_6X_{36}$ polyhedral "clusters" in the tetragonal "$R_{15}X_{55}$" and the trigonal–rhombohedral "$R_{14}X_{33}$" phases.

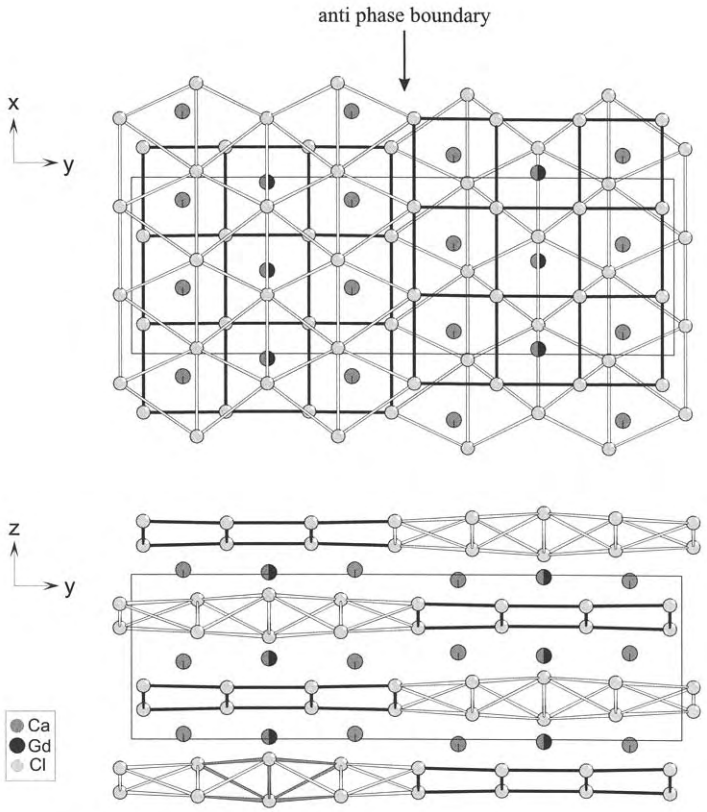

Fig. 37. Crystal structure of Ca_2GdCl_7.

of a slightly distorted dodecahedron, Gd^{3+} nearly as a square antiprism. The dodecahedra as well as the antiprisms are linked via common edges to form chains which are again connected to double chains sharing vertices. The double chains are running along the *a*-axis (fig. 38).

Again, this structure shows a certain similarity to that of CaF_2 and in fact both coordination polyhedra are at least deviations from the cubic polyhedron found in the fluorite structure. Contrary to the latter, however, linkage of the polyhedra is more complicated. Gd^{3+} is surrounded by three crystallographically different chloride ions which have coordination numbers of four, three and two, respectively, according to $GdCl_{4/3}Cl_{2/4}Cl_{2/2} = GdCl_{2.833}$. Ba^{2+} has only two different neighboring Cl^- ions which have according to $BaCl_{6/4}Cl_{2/3} = BaCl_{2.166}$ coordination numbers of four and three, respectively, so that the composition of $BaGdCl_5$ may be achieved.

It may be noteworthy that in both cases, Ba_2RCl_7 and $BaRCl_5$, a structural change from the rather complicated three-dimensional fluorite-type superstructures to well defined compounds occur.

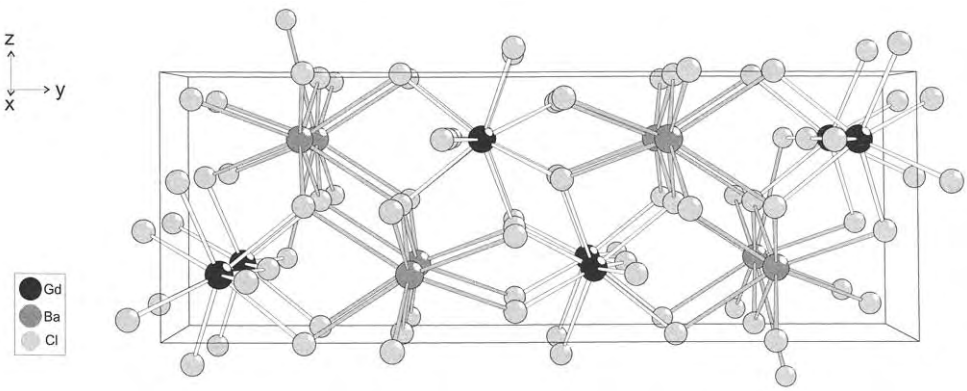

Fig. 38. Crystal structure of $BaGdCl_5$.

4.2. *Ternary rare-earth(II) halides*

4.2.1. *AR_2X_5-type halides*

Most of the AR_2X_5-type compounds crystallize with the $TlPb_2Cl_5$ type of structure (Keller 1976). Topologically this is the same structure as described above for A_2RX_5-type compounds, but the symmetry is monoclinic now. The monoclinic angle is, however, very close to 90°. Due to this similarity solid solutions of AR_2X_5 and A_2RX_5-type halides are formed, for example a 1:1 "mixture" of KSm_2Cl_5 and K_2SmCl_5 ("$K_3Sm_3Cl_{10}$") (Meyer 1983c). As one of the R^{2+} ions occupies according to $(AR)RX_5$ an A^+ position of A_2RX_5 and, hence, has a coordination number of $8+1$, the structure is mainly adopted with large rare-earth ions like Sm^{2+}. With the smaller ones, ARX_3 compounds are formed instead.

A second AR_2X_5-type structure is found for $LiDy_2Cl_5$, $LiTm_2Cl_5$ and $LiYb_2Cl_5$, respectively (fig. 39, overleaf) (Meyer and Schleid 1986). It is the same structural arrangement as in FeU_2S_5 (Noël et al. 1976) and may be grasped as a filled variant of the Pb_5B_2 type of structure (Stenberg 1961). The structure of the latter may be derived from a hexagonal closest packing of lead in much the same way as known for YF_3 with the difference that twinning occurs alternating every second and third atom row leading to the composition R_2X_5. In the non-distorted part of the hexagonal closest packing additional ions are incorporated being then in octahedral coordination.

4.2.2. *ARX_3-type halides*

Six structure types occur in the crystal chemistry of ARX_3-type rare-earth halides which may be addressed to the parents $CaTiO_3$ (perovskite), $NaNbO_3$–II, $GdFeO_3$, NH_4CdCl_3, $CaIrO_3$, and $CsNiCl_3$ (Schilling and Meyer 1996). They are all strongly related in a sense that they all contain the small cations in octahedral sites. $NaNbO_3$–II and $GdFeO_3$ belong to the perovskite type family and appear through octahedral tilting in two and three dimensions, respectively, with respect to the aristotype $CaTiO_3$. The $[RX_6]$ octahedra are connected via all six vertices in accord with the formulation $[RX_{6/2}]$. The large A^+ cations have the coordination number twelve and are, in turn, part of the cubic closest packing

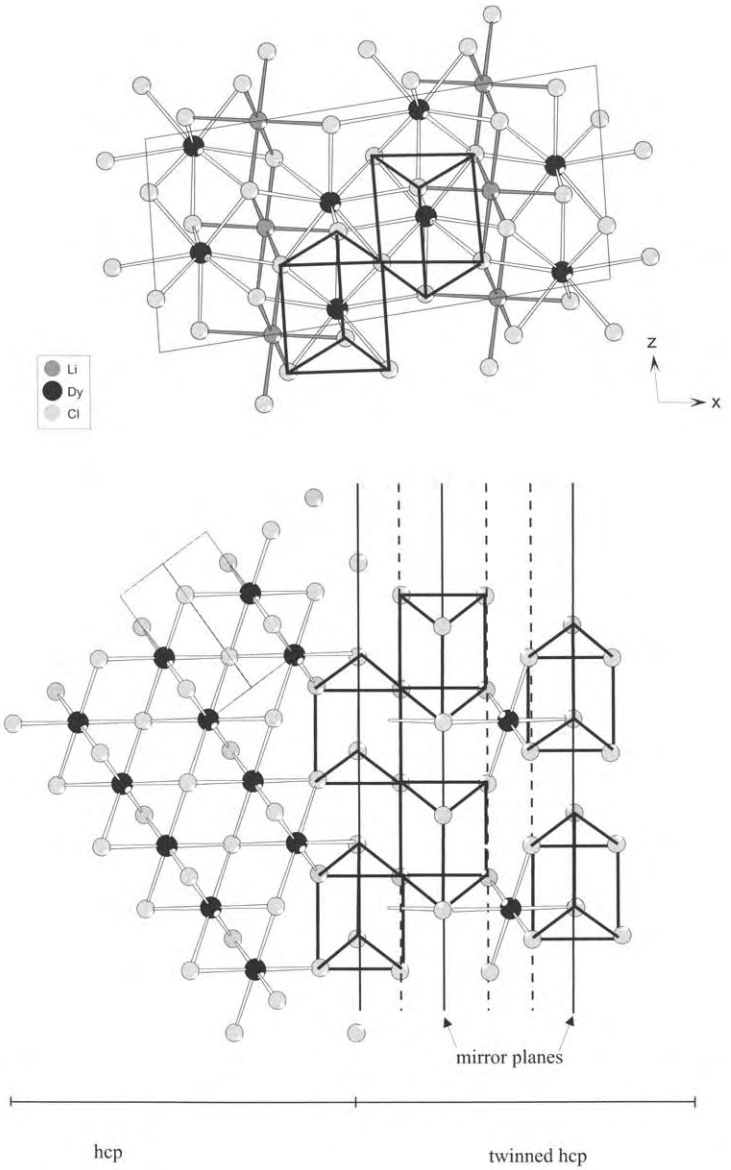

Fig. 39. Crystal structure of $LiDy_2Cl_5$ as derived from a hexagonal closest packing.

of $[AX_3]$ layers with all available octahedral interstices occupied. The hexagonal closest packed analogue is the $CsNiCl_3$ type of structure with all octahedra sharing common faces. This structure is only found for "divalent" compounds of scandium such as $CsScCl_3$ (Poeppelmeier et al. 1980).

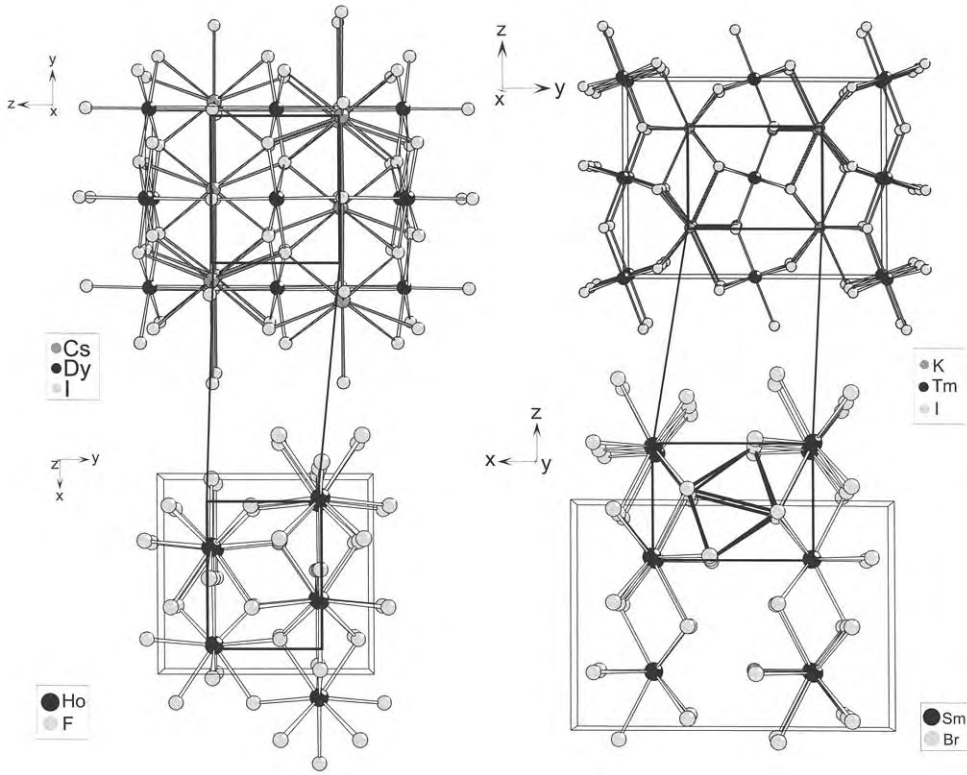

Fig. 40. Crystal structures of $CsDyI_3$ ($GdFeO_3$ type) and $KTmI_3$ ($CaIrO_3$ type) and their relation to the YF_3 (HoF_3) and $PuBr_3$ ($SmBr_3$) types of structure, respectively.

The $GdFeO_3$ type of structure may be derived from the YF_3 type of structure ($YF_3 = GdO_3$) through additional occupation of octahedral sites with cations (Fe). In the same way the $CaIrO_3$ ($FeUS_3$, $KTmI_3$) type is related to the $PuBr_3$ ($= CaO_3$) type of structure as mentioned already in sect. 3.1. (fig. 40).

In the NH_4CdCl_3 type of structure which is found for example for $RbTmI_3$, the A^+ ions have nine halide ligands. The $[AX_9]$ polyhedra may be described as tricapped trigonal prisms, which are connected via common triangular faces along the *b*-axis. Therefore, this part of the structure is very similar to that of $PbCl_2$. In fact the NH_4CdCl_3 structure may be understood as a (formal) intergrowth of the $PbCl_2$ and the NaCl types of structure. This may be seen from fig. 41.

Because the R^{2+} ions remain in sixfold octahedral coordination in all of the compounds described, the different structures may be associated with the radii of the A^+ ions. Figure 42 summarizes the structures as mentioned above, including the AR_2X_5-type compounds (see sect. 4.2.1), in form of a structure field map.

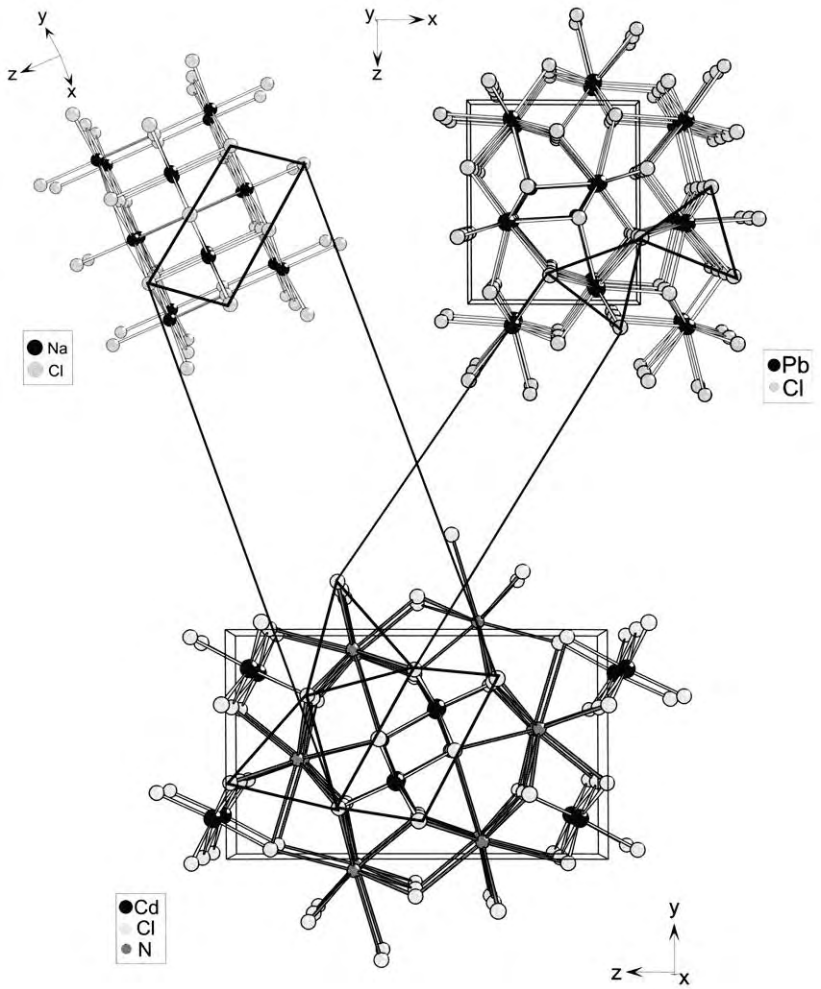

Fig. 41. Crystal structure of $RbTmI_3$ (NH_4CdCl_3) and its relation to the NaCl and $PbCl_2$ types of structure.

4.2.3. *A_2RX_4-type halides*

Few compounds are known with the composition A_2RX_4, namely K_2EuCl_4, Cs_2YbCl_4 and Cs_2TmCl_4. K_2EuCl_4 seems to be polymorphic, its high-temperature structure is said to be that of Th_3P_4 with statistical distribution of the cations over the Th sites (Fink and Seifert 1980). Cs_2YbCl_4 and Cs_2TmCl_4 (Gaebell and Meyer 1984, Schleid and Meyer 1994) crystallize with the well-known K_2NiF_4 type of structure (Balz and Plieth 1955). This structure consists of ReO_3-type slabs extended in the tetragonal (001) plane which are held together by A^+ ions. The relationship to the perovskite type of structure is obvious:

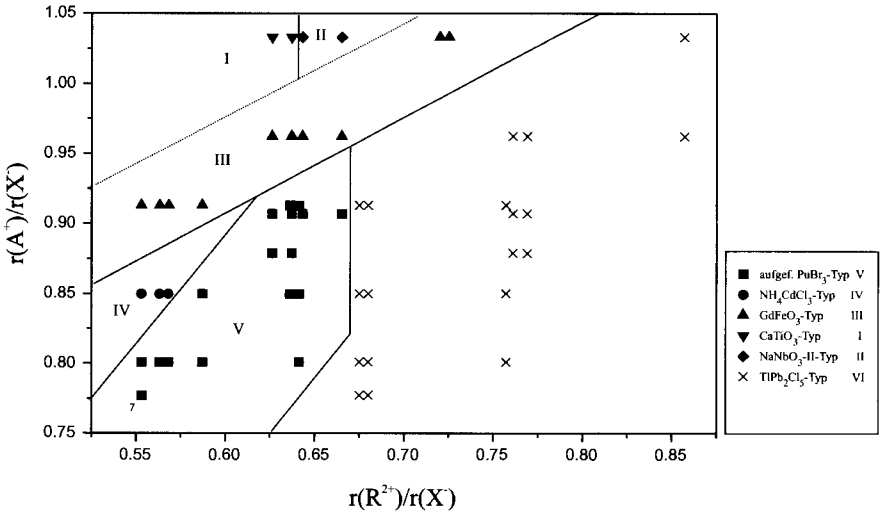

Fig. 42. Structure field map of ARX_3/AR_2X_5-type compounds.

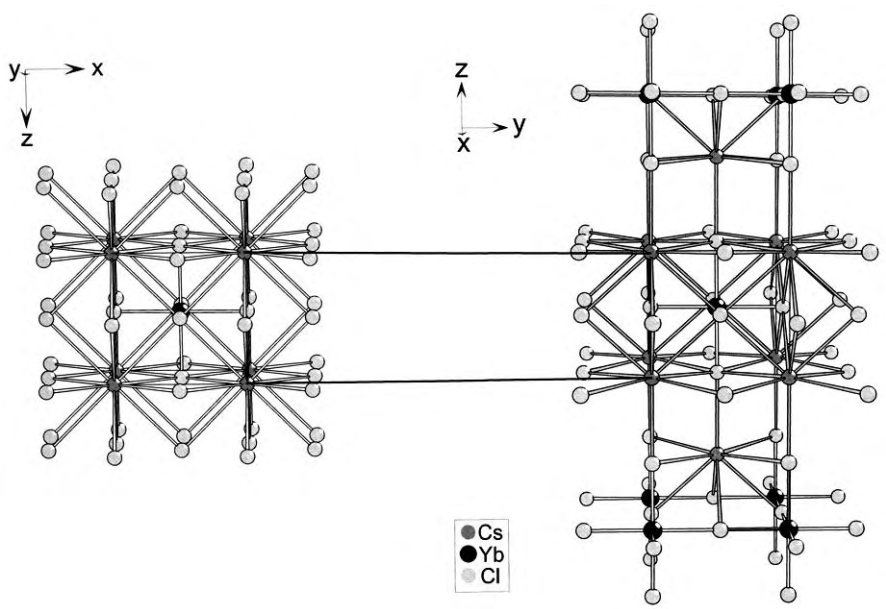

Fig. 43. Crystal structure of Cs_2YbCl_4 (K_2NiF_4 type) and its relation to the perovskite type.

Removing (formally) AX from the lattice and letting the remaining layers collapse by corner sharing gives this structure (fig. 43).

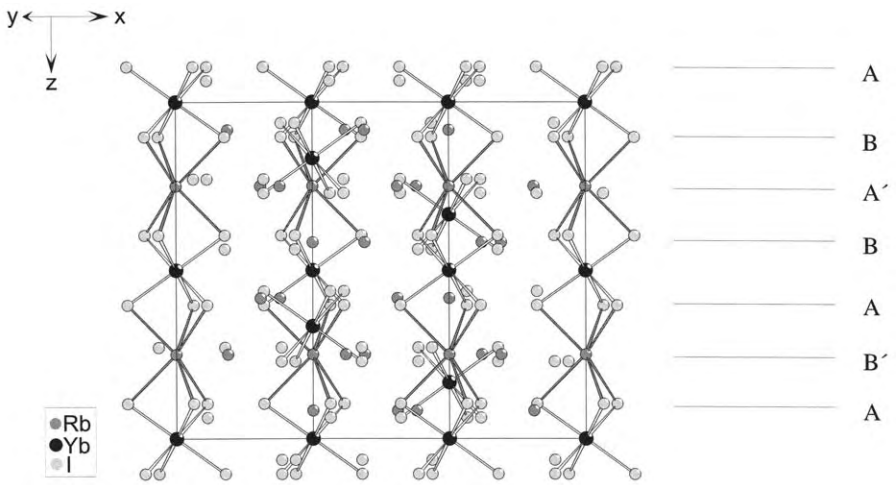

Fig. 44. Crystal structure of Rb_4YbI_6.

4.2.4. *A_4RX_6-type halides*

Compounds of the composition A_4RX_6 are very uncommon in the chemistry of divalent rare-earth halides. The only example known so far is Rb_4YbI_6 (Schilling et al. 1992). It crystallizes with the K_4CdCl_6 type of structure (Bergerhoff and Schmitz-Dumont 1956): Rods of face sharing trigonal prisms $[RbI_6]$ and $[YbI_6]$ octahedra are aligned along the *c*-axis of the trigonal-rhombohedric unit cell, held together by eight-coordinate Rb^+ ions (fig. 44).

The structure may be derived from a hexagonal closest packing of spheres. In alternating A and B layers, Rb^+ ions substitute for I^- ions in two different ways. Because Rb^+ is significantly smaller than I^- the hexagonal closest packing is distorted. The relationship with a regular hexagonal closest packing may also be seen from a group theoretical treatment (Beck and Milius 1986).

4.3. *Ternary rare-earth(II,III) halides*

Some complex rare-earth(II,III) halides have already been mentioned in previous chapters, for example NaR_2Cl_6-type halides, or will be discussed in the following chapters, like Pr_2Br_5. Mixed-valent rare-earth halides derived from the fluorite type of structure may be divided in two different groups. On one hand there are the so-called vernier-type compounds which may be grasped as onedimensional CaF_2 superstructures and on the other hand there are three-dimensional CaF_2 superstructures. Both structure types have been described extensively in sect. 4.1.8. because they are identical to those found in the systems AX_2/RX_3 with A being an alkaline-earth metal. This is not astonishing if one bears in mind that R^{2+} ions are of quite the same size as A^{2+} ions. Because of this analogy the structures will not be discussed here.

4.3.1. *$A_5R_3X_{12}$-type halides*

For the rare-earth elements dysprosium and thulium mixed valence compounds of the type $A_5R_3X_{12}$ have been observed with A = K, Rb (Hohnstedt and Meyer 1993, Böcker 1996), although $K_5Dy_3I_{12}$ has been described as $K_{5.13}Dy_3I_{12}$ at first. They are isotypic with some transition metal compounds of which $Na_5Ti_3Cl_{12}$ has been characterized quite recently (Hinz 1994). The structure consists of chains of different polyhedra running along the hexagonal *c*-axis: $[RX_6]$ octahedra and $[AX_7]$ monocapped trigonal prisms are connected via common edges and $[AX_6]$ trigonal prisms share common faces (fig. 45).

Chains of edge sharing octahedra and monocapped trigonal prisms are well known for the structure of Sr_2PbO_4 which is also adopted by several transition metal halides, for example Na_2MnCl_4 and Na_2TiCl_4 (Lutz et al. 1987). Bearing this in mind, the structure may be grasped as the Sr_2PbO_4 type with columns of $[AX_6]$ trigonal prisms inserted additionally. The arrangement of the latter is very similar to that found in the Fe_2P type of structure (Rundqvist and Jellinek 1959).

5. Complex halides with polynuclear centers

5.1. *Rare-earth clusters with interstitials*

Ever since the early days of cluster chemistry, we have been fascinated by these homopolyatomic (multinuclear) units $[M_x]$ built from like atoms of one element just like Plato was fascinated by polyhedra. They are observed most commonly with the first half of the 4d or 5d elements ("early" transition elements M) in low oxidation states when halide ligands are involved or, roughly, with the second half with carbonyl or comparable ligands.

From a *thermodynamic* point of view, it is the high enthalpy of sublimation of these elements that is highest for the 5d elements and there for tungsten which is secured partially when a cluster is formed with electrons in metal–metal bonding states. To achieve this kind of covalent bonding, a sufficient number of electrons is certainly needed.

As we know only little about the thermodynamic properties of cluster compounds, we have learnt to substitute this lack of experimentally accessible knowledge by theoretical calculations on different levels of sophistication, the simplest for a chemist being the use of *electron counting rules*.

With group 5 elements, $[M_6]X_{12}$ clusters and their derivatives are the most common. $K_4[Nb_6]Cl^i_{12}Cl^a_6$ (Simon et al. 1968) is a good example because there the octahedral $[Nb_6]$ cluster is surrounded by a maximum number of ligands, eighteen of which 12 are edge-capping (i = inner or μ_2 in this case) and 6 are terminal, above the corners of the octahedron (a = outer; "a" from German "äußere" (Schäfer and von Schnering 1964); or μ_1 (fig. 46). With the electropositive elements donating their valence electrons (K: 1; Nb: 5) and the electronegative elements accepting electrons (Cl: 1), there are $(4\times1)+(6\times5)-(18\times1)=16$ electrons left for cluster bonding. These are attributed

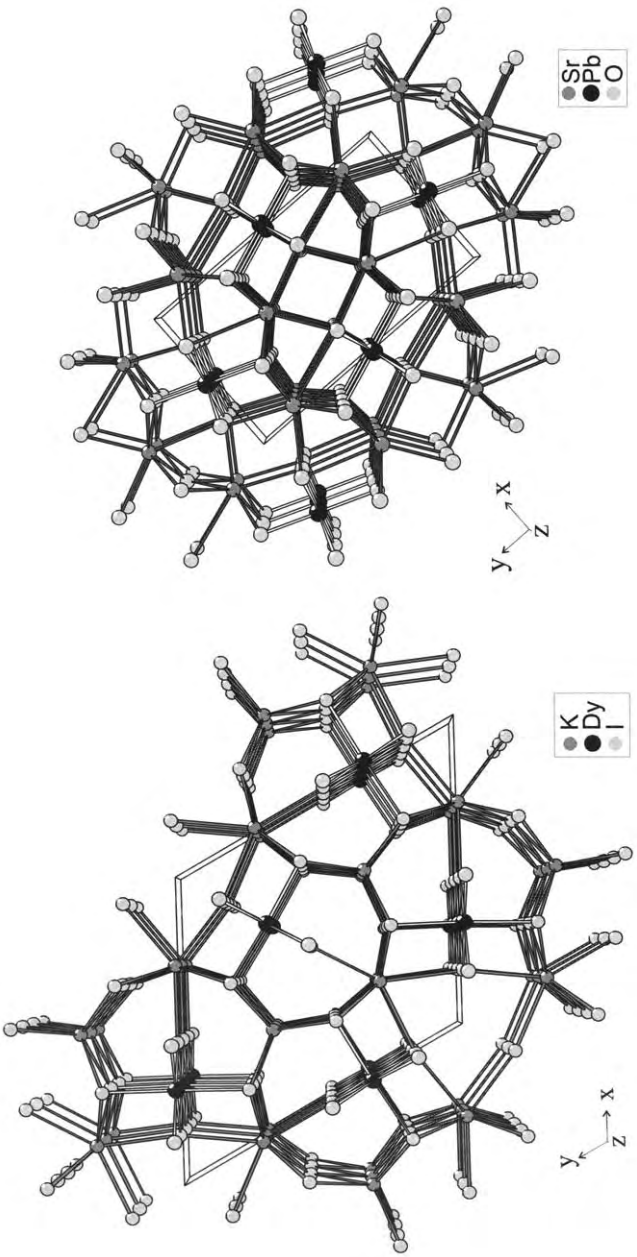

Fig. 45. Crystal structure of $A_5R_3X_{12}$-type compounds ($K_5Dy_3I_{12}$) and its relation to the Sr_2PbO_4 structure (Na_2TiCl_4).

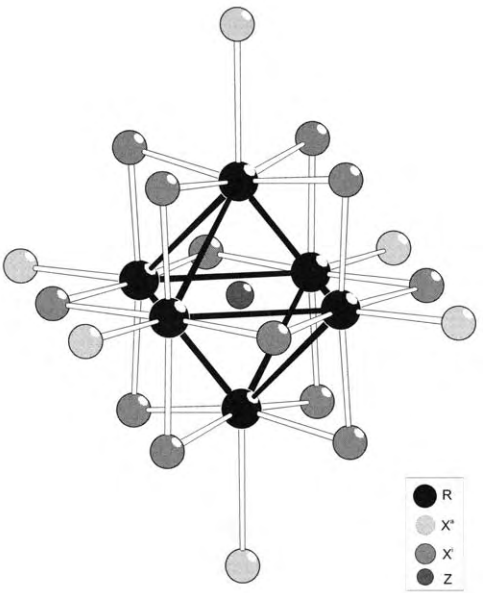

Fig. 46. $[M_6(Z)]X^i_{12}X^a_6$ unit in crystal structures with R being an element of group 3 to 5 (in group 5 without the interstitial Z).

to 8 two-electron–three-center bonds (2e–3c) associated with the eight faces of the octahedron which are not capped by ligands in this case.

They are, however, capped by ligands in the example $MoCl_2 \equiv [Mo_6]Cl^i_8Cl^a_2Cl^{a-a}_{4/2}$ (Schäfer et al. 1967, von Schnering et al. 1993) where i now stands for face-capping μ_3 ligands. While there are only inner μ_2 *or* μ_3 ligands in *octahedral* clusters, that means either 12 *or* 8 ligands, the number of outer ligands should always be six. There would only be four in $MoCl_2 \equiv [Mo_6]Cl^i_8Cl^a_4$, but the number of terminal ligands is raised by sharing them with neighbouring clusters. Only the two ligands apical to the $[Mo_6]$ octahedron are now terminal, the four basal ligands are shared by two octahedra, forming a–a bridges. The addition of two further chloride ligands, for example in hydrochloric acid solution with KCl leads to the formation of $K_2[Mo_6]Cl^i_8Cl^a_6$ (Potel et al. 1986).

Returning to the thermodynamic view for a moment, it is the high *lattice energy* that stabilizes the *salt* $K_2[Mo_6]Cl_{14}$ incorporating the covalently bonded *molecule* $[Mo_6]$. It is lattice energy, again, that favours $[Mo_6]Cl_{14}$ units connected via four a–a bridges forming a layer rather than $[Mo_6]Cl_{12}$ molecules that would have to form a van der Waals bonded molecular solid.

In $K_2[Mo_6]Cl_{14}$, for example, there are 24 electrons in cluster-based metal–metal bonding states to be attributed to twelve 2e–2c bonds, covalent σ bonds for the chemist. Deviations from the ideal 16 or 24 electron requirement (*electron precise clusters*) are possible and are known. Exceptions from $[M_6]X_{12}$ and $[M_6]X_8$ (or shortly 6–12 and 6–8) units for group 5 and 6 elements, respectively, are rare. $[Nb_6]I_{11} \equiv [Nb_6]I^i_8I^{a-a}_{6/2}$ is an example for a 6–8 cluster with a group 5 element (Simon 1967). The big size of the iodide ligand is apparently responsible for that only eight inner ligands fit to the cluster.

		Sc					**Ti**	V	Cr	Mn
		Y					**Zr**	**Nb**	**Mo**	**Tc**
		La	**Ce**	**Pr**	**Nd**	Pm				
Sm	Eu	**Gd**	**Tb**	**Dy**	**Ho**	**Er**				
Tm	Yb	**Lu**					**Hf**	**Ta**	**W**	**Re**

Box 3.

Electronically, it is an electron-deficient 19 electron cluster. The total electron count may be enhanced by adding Cs and/or H. $Cs[Nb_6H]I_{11}$ (Imoto and Corbett 1981), where the $[Nb_6]$ cluster incorporates a hydrogen atom as an interstitial, has now 21 electrons and there is Nb–Nb *and* Nb–H bonding present.

This concept, adding electrons via the incorporation of electropositive elements *outside* and *inside* the cluster, becomes more and more important when the number of valence electrons decreases. Zirconium, yttrium and the rare-earth elements associated therewith are well known to form octahedral clusters but virtually never without an interstitial. In box 3 elements that form halide clusters are printed in bold type, and the rare-earth elements (in the box) that seem to form clusters most easily are indicated by shading.

$K_2Zr[Zr_6C]Cl_{18}$ (Imoto et al. 1981) with $(2\times1+1\times4)+(6\times4+1\times4)-(18\times1)=16$ has the exact number of electrons for 2e–3c bonding, $[Zr_6C]Cl_{14}$ (Ziebarth and Corbett 1989) has not (only 14) and so does $[Ti_6C]Cl_{14}$ (Hinz and Meyer 1994). But these have essential carbon–metal (zirconium/titanium) bonding that stabilizes the clusters $[R_6Z]$ (Z stands for the interstitial atom) together with metal–metal bonding. $Cs_2Lu[Lu_6C]Cl_{18}$ (Artelt et al. 1992) appears to be at present the example with the lowest number of $[R_6C]$ cluster-based electrons, only 9!

One may, on the other hand, adopt in spite of the *covalent view* used so far, a more *ionic view*. The carbon atom, in accord with its location in the periodic table, may indeed act (formally) as a *zwitter*. In the covalent picture, carbon donates more or less its four valence electrons to the cluster $[R_6C]$ as a whole, in the ionic picture carbon (as the more electronegative atom) accepts four electrons, thus being (formally, of course) C^{4-} (carbide). In many octahedral rare-earth clusters, the dicarbon unit is also observed as the interstitial, for example in $Cs_2[Pr_6(C_2)]I_{12}$ (Artelt and Meyer 1993). With C–C distances usually around those known from hydrocarbons for a single bond (154 pm), this unit would be counted as $(C_2)^{6-}$ (ethanide). There must be some truth in this view as these compounds react with water emanating hydrocarbons, mostly methane and ethane in the mentioned cases. In this ionic view, there would be one excess electron for $Cs_2Lu[Lu_6C]Cl_{18}$ according to $(Cs^+)_2(Lu^{3+})[(Lu^{3+})_6(C^{4-})](Cl^-)_{18}(e^-)$ and two for $Cs_2[Pr_6(C_2)]I_{12}$.

5.2. *Monomeric and dimeric polyhedra*

In accord with and in addition to Plato's view of convex polyhedra, there is only a limited number of polyhedra, regular or irregular, mostly more or less distorted, that are observed as cluster polyhedra, mostly deltahedra.

The simplest deltahedron is the equilateral triangle. When considered as a *dihedron* (two triangular faces when viewed from above and below), it obeys Euler's law for convex polyhedra

corners + **f**aces = **e**dges + 2.

Box 4 gives an overview over some simple polyhedra with their number of corners, faces and edges that will be taken into account in the following. Except for the deltahedra [R_3], [R_4], [R_5], and [R_6] that are defined by equilateral triangles only, two *anti*-polyhedra with the number of corners and faces inter-changed are included. One of these has only square faces (cube), the other, the trigonal prism, like the also included square pyramid has mixed faces, i.e., triangles and squares.

Euler's law is also applicable to dimeric polyhedra sharing common corners, edges or faces. Box 5 gives a few examples.

Box 4
Characteristics of some simple polyhedra

c	+	**f**	=	**e**	+	**2**	(corner + faces = edges + **2**)	
3	+	**2**	=	**3**	+	**2**	**[R_3]**	**dihedron**
4	+	**4**	=	**6**	+	**2**	**[R_4]**	**tetrahedron**
5	+	**6**	=	**9**	+	**2**	**[R_5]**	**hexahedron (trigonal bipyramid)**
5	+	5	=	8	+	2	[R_5]	pentahedron (square pyramid)
6	+	5	=	9	+	2	**[R_6]**	*anti*-hexahedron (trigonal prism)
6	+	**8**	=	**12**	+	**2**	**[R_6]**	**octahedron**
8	+	6	=	12	+	2	[R_8]	*anti*-octahedron (cube)

Box 5
Examples of Euler's law for dimeric polyhedra

c	+	**f**	=	**e**	+	**s**	+	**2**	(corner + faces = edges + shared edges + **2**)	
4	+	4	=	5	+	1	+	2	[R_4]	butterfly
6	+	8	=	11	+	1	+	2	[R_6]	bitetrahedron
10	+	16	=	23	+	1	+	2	[R_{10}]	bioctahedron
14	+	24	=	33	+	3	+	2	[R_{14}]	2 octahedra + 2 tetrahedra sharing 3 common edges

5.3. *Triangles, [R_3], "Di(delta)hedra"*

Monomeric dihedra [R_3] are not known in rare-earth-element halide chemistry. The reason for this observation might be that the only interstitial that is known to enter triangular

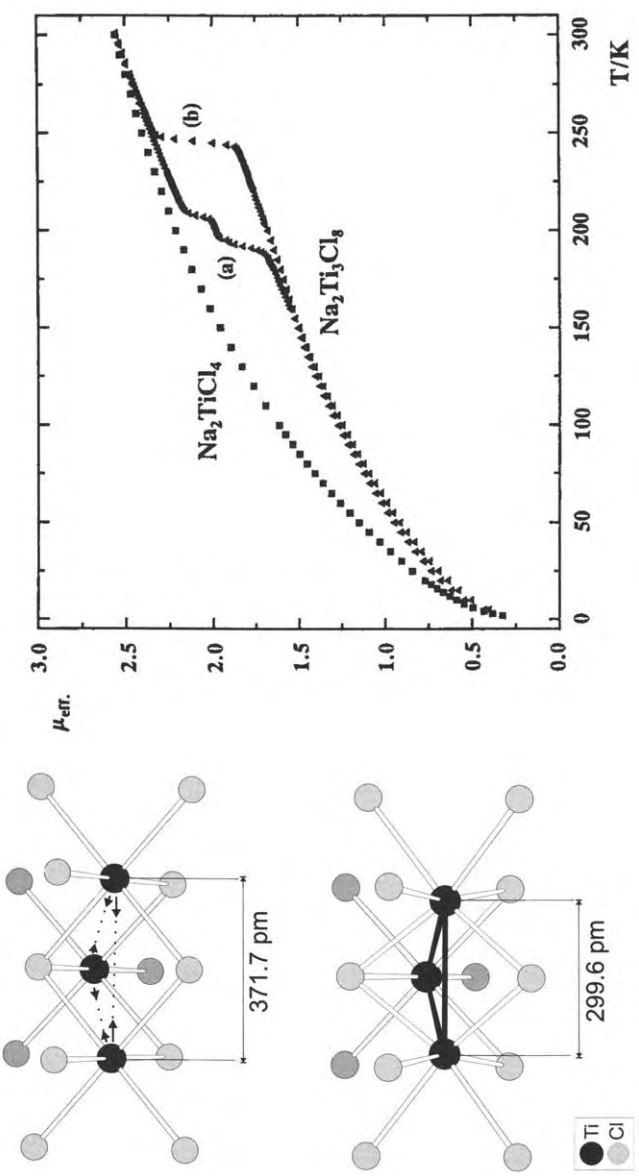

Fig. 47. Left: the formation of $[Ti_3]Cl_{13}$ clusters from equidistant Ti^{2+} ionic layers in $Na_2Ti_3Cl_8$. Right: the effective magnetic moment *versus* absolute temperature for $Na_2Ti_3Cl_8$ and, for comparison, for Na_2TiCl_4 exhibiting the phase transition in the former and its ample hysteresis: (a) cooling and (b) heating curve.

faces, for example in $[Th_6H_7]Br_{15}$ (Simon et al. 1991b) or in $[YH_{0.67}]Se$ (Schleid and Meyer 1992), would not contribute sufficiently to $[R_3H]$ bonding so that other possibilities like condensed clusters with hydrogen in tetrahedral interstices are preferred.

Transition elements that form triangular clusters in halides are titanium, niobium, molybdenum, tungsten and rhenium. $[Ti_3]$ clusters were first seen in Ti_7Cl_{16} (Schäfer and Laumanns 1981, Krebs and Henkel 1981). According to $(Ti^{4+})_{0.5}[(Ti^{4+})_3(e^-)_6](Cl^-)_8$ it has like $(Na^+)_2[(Ti^{4+})_3(e^-)_6](Cl^-)_8 \equiv Na_2Ti_3Cl_8$ (Hinz et al. 1995) the "right" number of 6 electrons to form three 2e–2c bonds with a Ti–Ti distance of 295 pm. Like Nb_3Cl_8 (Simon and von Schnering 1966) that has 7 electrons (see for an explanation H.-J. Meyer 1994) both contain $[M_3]Cl_{13} \equiv [M_3](\mu_1\text{-Cl})_9(\mu_2\text{-Cl})_3(\mu_3\text{-Cl})$ units. In $Na_2Ti_3Cl_8$ these triangular clusters are only formed below about 200 K, above this temperature it is a "normal" ternary titanium(II) chloride (fig. 47).

When two such $[Ti_3]Cl_{13}$ units are combined via $2\times[Ti_3]Cl_{13} \equiv [Ti_6(\mu_3\text{-Cl})_2]Cl_{12}Cl_{12}$, there are two possibilities:

- When the triangles are put in *staggered* conformation on top of each other, twelve chloride ligands are shared and the two μ_3-Cl are substituted by a carbon interstitial, the above-mentioned $[Ti_6C]Cl_{14}$ is formed which is isostructural with $[Zr_6C]Cl_{14}$ and $[Nb_6]Cl_{14}$ (Simon et al. 1965).
- When in the case of $[Nb_3]Br_{13}$ units the triangles are put in *eclipsed* conformation on top of each other, 12 bromide ligands are shared and a sulfur atom is put into the so-formed trigonal prism, the anionic unit $[Nb_6S]Br_{18}^{4-}$ is obtained that is now known from the salt $Rb_3[Nb_6S]Br_{17}$ (Womelsdorf and Meyer 1994).

In both cases new bonds are formed because the number of electrons set free through the removal of halide atoms and the addition of an interstitial reduces the cluster. On the other hand, triangular clusters may be oxidized and then may, in general, share common corners, edges or faces.

Two triangular clusters sharing *one* common corner are not known. They may, however, share two common corners, thereby forming a linear chain. $Pr_2Br_5 \equiv [Pr_{2/2}Pr_{1/1}]Br_5$ may serve as an example (Schleid and Meyer 1987b) (fig. 48). It is a semiconductor with a mixture of ferro- and antiferromagnetic ordering at not too low temperatures (below 50 K) (Krämer et al. 1991). Subject to band-structure calculations, the excess electron with respect to the formulation $[(Pr^{3+})_2(e^-)](Br^-)_5$ has d character and forms a 1e–3c bond with Pr–Pr distances around 417 pm (Meyer and Meyer 1992).

Two triangles sharing one common edge are known from $Cs[Nb_4]Cl_{11}$ (Broll et al. 1969). The four niobium atoms form a (planar) butterfly with five 2e–2c bonds (10 electrons) in accord with the five edges of that "polyhedron", see also box 5.

5.4. *Tetrahedra, $[R_4]$*

The addition of two more electrons to the $[R_4]$ butterfly could lead to a tetrahedron via a bent butterfly when finally six like edges are formed. Twelve electrons seem, however, to be too much for an isolated tetrahedral cluster.

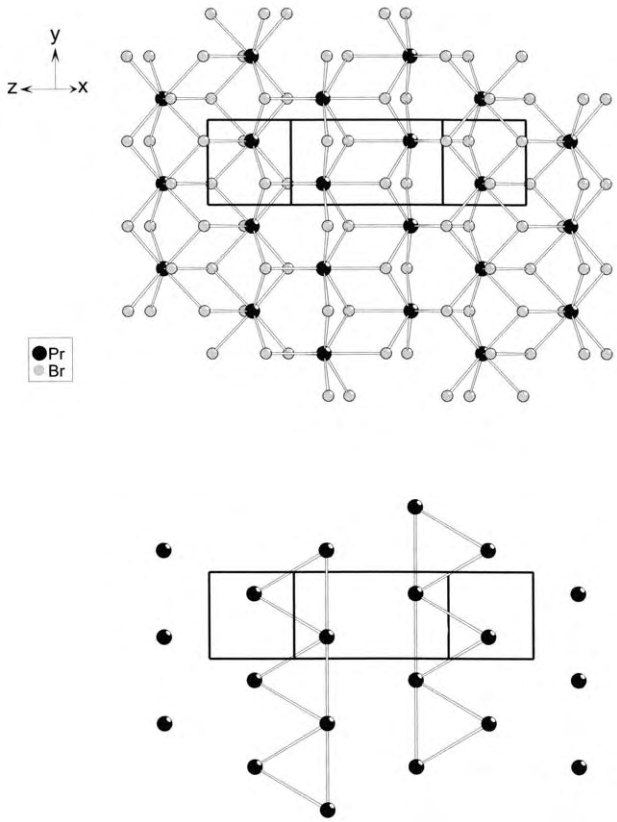

Fig. 48. One layer in the structure of Pr_2Br_5: (top) with bromide ligands; (bottom) without bromide ligands and emphasizing the 1e–3c bonds.

A truly isolated tetrahedron is known from one of the many modifications of PrI_2 (Warkentin and Bärnighausen 1979). According to $[Pr_4](\mu_3\text{–}I)_4(\mu_1\text{–}I)_{12}$, sixteen iodide ligands surround the tetrahedron (fig. 49) and, of course, connect the tetrahedra to a three-dimensional structure. There are only four electrons left which occupy low-lying d states (a_1, e), see fig. 49. The Pr–Pr distances (387 pm) are similar to those found in Pr_2Br_5.

Isolated tetrahedra are known with oxygen or nitrogen as interstitial atoms. The oxyhalides with the divalent lanthanides europium, ytterbium and samarium, $[R_4O]X_6$, are prominent examples (Schleid and Meyer 1987a–c). Very nicely, these divalent lanthanides show analogous behaviour as the group 2 elements calcium (H.-J. Meyer et al. 1991), strontium and barium (Frit et al. 1970). Figure 50 exhibits the $[R_4O](\mu_3\text{–}X)_3(\mu_2\text{–}Cl)_6(\mu_1\text{–}X)_{3+3\times2}$ unit in the structure of these compounds which is also known as an *anti*-type, for example for $K_6[HgS_4]$ (Sommer et al. 1976, Sommer and Hoppe 1978).

These lanthanide and alkaline-earth oxyhalides can be easily understood by an ionic description, for example $[Yb_4O]Cl_6$ as $[(Yb^{2+})_4(O^{2-})](Cl^-)_6$ (Schleid and Meyer 1987d).

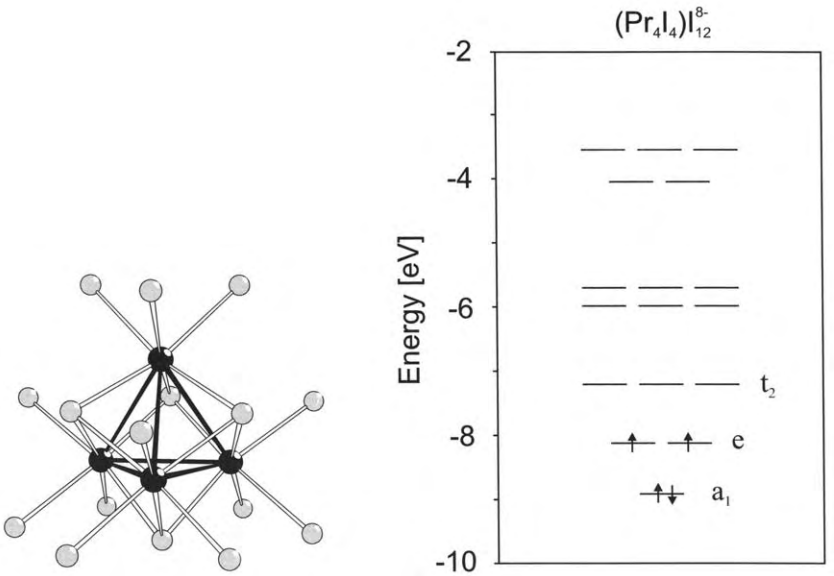

Fig. 49. The $\{[Pr_4](\mu_3\text{-}I)_4(\mu_1\text{-}I)_{12}\}^{8-}$ unit in PrI_2-V (left) and a *d* block splitting diagram for the low-lying d states.

On the other hand, there are 8 electrons for intra-cluster covalent bonding when one counts as $(4\times2)+(1\times6)-(6\times1)=8$. Sulfide-chloride derivatives, $[R_4N]S_3Cl_3$ of this structure type may be obtained with the trivalent lanthanides R = La–Nd, Gd (Lissner and Schleid 1994). Again, these may be "understood" with the ionic or the covalent view, according to, for example, $[(La^{3+})_4(N^{3-})](S^{2-})_3(Cl^-)_3$ *vs.* $(4\times3)+(1\times5)-(3\times2)-(3\times1)=8$.

Two tetrahedra sharing one common *corner* are not known in rare-earth element cluster chemistry. In contrast, two tetrahedra sharing one common *edge* and a common *face*, respectively, are now well known. The latter will be discussed in the following chapter, as they are normally addressed as trigonal bipyramids.

Two tetrahedra with one common edge were first observed with Gd_3NCl_6 (Simon and Koehler 1986). From this nitride-chloride $(Gd^{3+})_3(N^{3-})(Cl^-)_6$, with the connection pattern $[(Gd_{2/1}Gd_{2/2})(N)]_2Cl_2^iCl_6^{i-a}Cl_{2/2}^{i-i}Cl_{2/2}^{a-a}Cl_{6/3}^{a-a}$ one is directly led to such with linear chains of *trans* edge-connected $[R_4N]$ tetrahedra, analogous to the chains known from the structure of SiS_2(*anti*-type).

The nitride-chlorides $[R_2N]Cl_3$ with R = La–Nd, Y, and Gd (Uhrlandt and Meyer 1995b, H.-J. Meyer et al. 1989, Schwanitz-Schüller and Simon 1985) exhibit two slightly different but essentially like structures according to the connection pattern $[(R_{4/2})(N)]Cl_{2/2}^{i-i}Cl_{2/2}^{i-a}Cl_{2/2}^{a-i}$. The tetrahedra are distorted in that the connecting edge is shortest, for example 351 vs. 390 and 397 pm (two times each) in Pr_2NCl_3 (fig. 51).

Similar chains are also observed in the polynaries $Na_2Pr_4O_2Cl_9$ (Mattfeld and Meyer 1994) and $Na_2Pr_4NOBr_9$ (Lulei and Corbett 1995). The connection pattern in the former

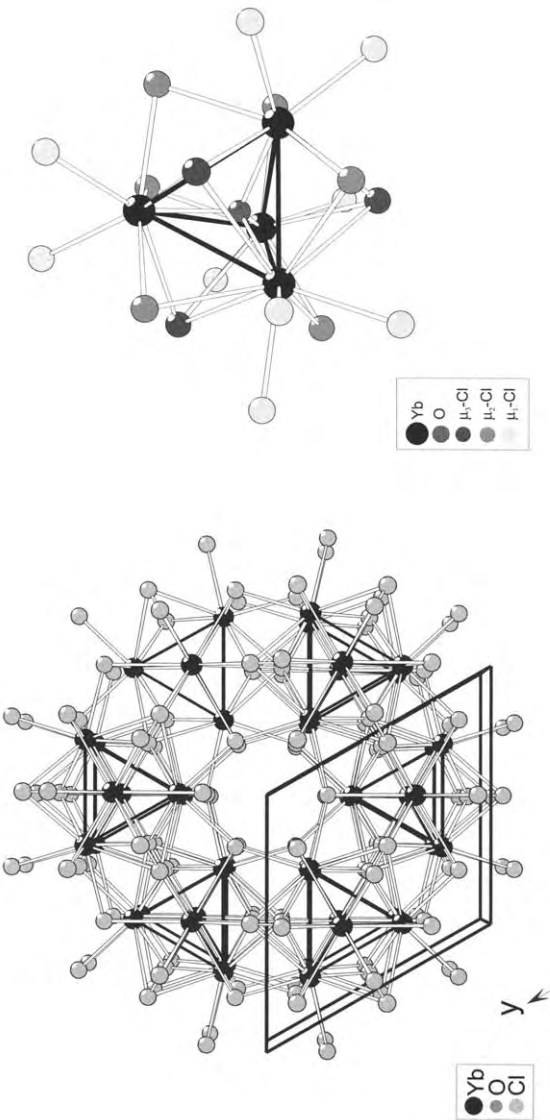

Fig. 50. The $[R_4O](\mu_3\text{-}X)_3(\mu_2\text{-}Cl)_6(\mu_1\text{-}X)_{3+3\times2}$ unit in the crystal structure of $[R_4O]X_6$-type oxyhalides with R = *Ca*, Sr, Ba, Yb, Eu, Sm and X = Cl, Br, (I).

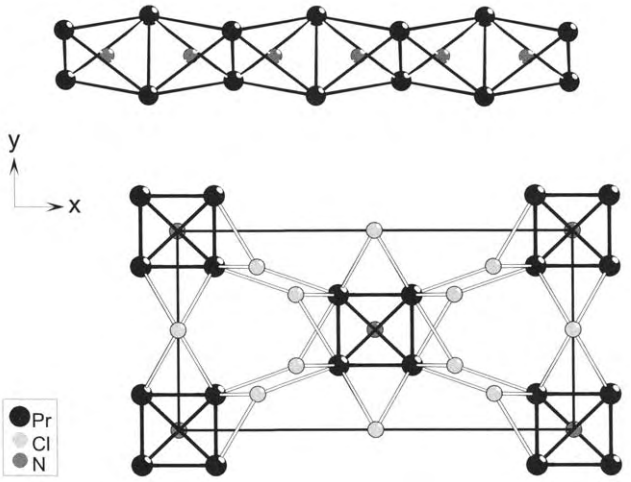

Fig. 51. (top) The anti-SiS_2 analogous chain of *trans* edge-connected $[R_4N]$ tetrahedra in Pr_2NCl_3; (bottom) a projection of the crystal structure on (001) with only the Cl^{i-i} and Cl^{i-a} bridges exhibited.

may be formulated as $Na[Pr_{4/2}O]Cl_1^iCl_2^{i-i}Cl_{2/2}^{i-a}Cl_{1/2}^{a-a}$. Apparently, there may both N^{3-} or O^{2-} be incorporated as interstitials giving them either one excess electron per formula unit as in $Na_2Pr_4O_2Cl_9$ (metallic lustre) or none as in $Na_2Pr_4NOBr_9$ which is transparent. Figure 52 gives a projection of the unit cell showing the chains running parallel to [010]

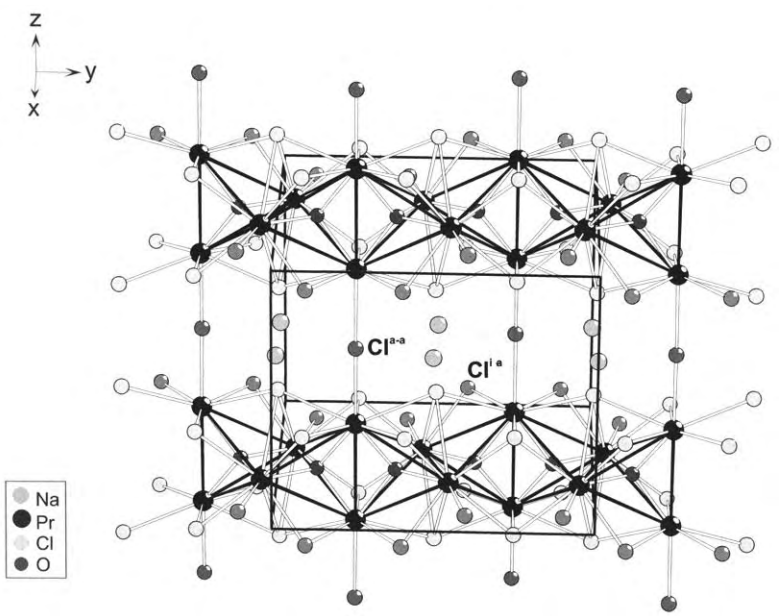

Fig. 52. Perspective view of the crystal structure of $Na_2[Pr_4O_2]Cl_9$.

and their connection via Cl4 (i–a bridges) to layers and their connection via Cl3 (a–a bridge) and the location of Na^+ between the sheets.

5.5. *Hexa(delta)hedra, [R_5]: trigonal bipyramids*

When two tetrahedra share one common face they produce a so-called trigonal bipyramid. This is in fact a hexa(delta)hedron: six triangular faces, five corners and nine edges. Only recently, the existence of such clusters, all with a C_2 unit as the interstitial, [$R_5(C_2)$], was established. $Rb[Pr_5(C_2)]Cl_{10}$ was the first example (Meyer and Uhrlandt 1993). Figure 53 shows the $[Pr_5(C_2)]Cl^i_9Cl^a_{12}$ unit as observed therein. So far, only the compositions $[R_5(C_2)]X_9$ and $A[R_5(C_2)]X_{10}$ have been observed with the lighter and bigger rare-earth elements R = La, Ce, Pr, Nd and with A = K, Rb and X = Cl, Br (Uhrlandt and Meyer 1994, 1995a, Uhrlandt et al. 1995, Heuer et al. 1996) only.

There are compounds, however, with the heavier and smaller rare-earth elements with the same stoichiometry, for example $Gd_5(C_2)Cl_9$, but they contain double octahedra which becomes obvious when their formulae are doubled, e.g., $[Gd_{10}(C_2)_2]Cl_{18}$ (Simon et al. 1981). It is also surprising that [$R_5(C_2)$] clusters cannot be stabilized with iodide. In the Rb–Pr–C–I system $[Pr_{12}(C_2)_3]I_{17}$ is obtained instead with chains of *cis* and *trans* edge-connected octahedra (fig. 54) (Uhrlandt and Meyer 1995c).

While octahedral clusters are surrounded by 8 inner and 6 outer or by 12 inner and 6 outer ligands only, the ligand sphere of [$R_5(C_2)$] clusters appears to be much more flexible. At present, we know

(1) [$R_5(C_2)$] units surrounded by 7 to 10 inner ligands. With 7 to 9 they are edge capping (μ_2). In $[La_5(C_2)]Br_9$ and $[Ce_5(C_2)]Br_9$ there is, in addition, one face-capping ligand (μ_3) (Heuer et al. 1996) (fig. 55).
(2) The total number of halide ligands is 19 to 22.

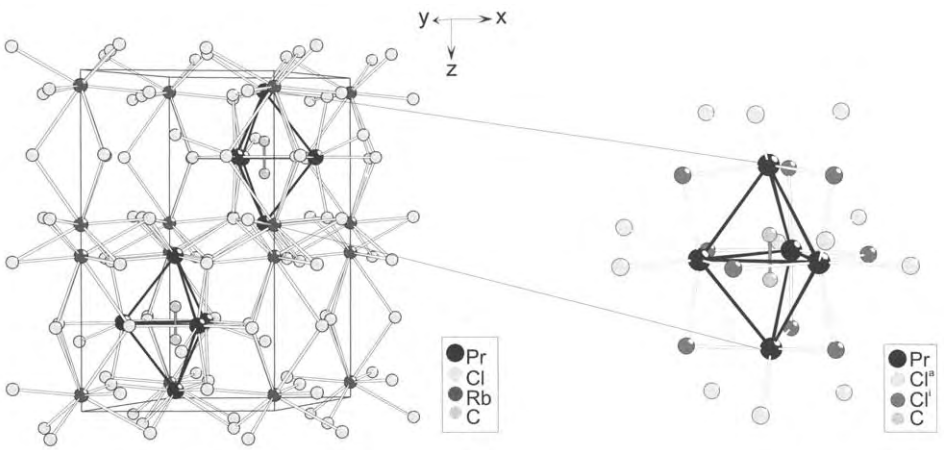

Fig. 53. The $[Pr_5(C_2)]Cl^i_9Cl^a_{12}$ unit in the crystal structure of $Rb[Pr_5(C_2)]Cl_{10}$.

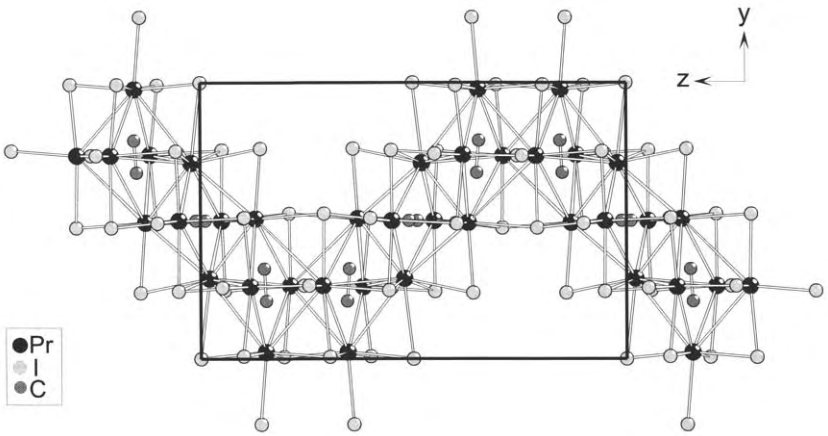

Fig. 54. Part of the chain of *cis* and *trans* edge-connected $[Pr_6(C_2)]$ octahedra as observed in $[Pr_{12}(C_2)_3]I_{17}$.

(3) All ligands bridge the $[R_5(C_2)]X_{19-22}$ units via a wide variety of connectivities (box 6) giving rise to coordination numbers of the halide anions from 2 to 4 (Box 7 and fig. 56).

(4) R–R distances in the $[R_5(C_2)]$ units are as in isolated $[R_6(C)]$ or $[R_6(C_2)]$ units; for R = Pr, one finds edge lengths between, roughly, 380 and 410 pm. There is one exception: In $[Pr_5(C_2)]Br_9$ one finds one edge of a length of 440 pm which is not capped by a bromide ligand (fig. 55).

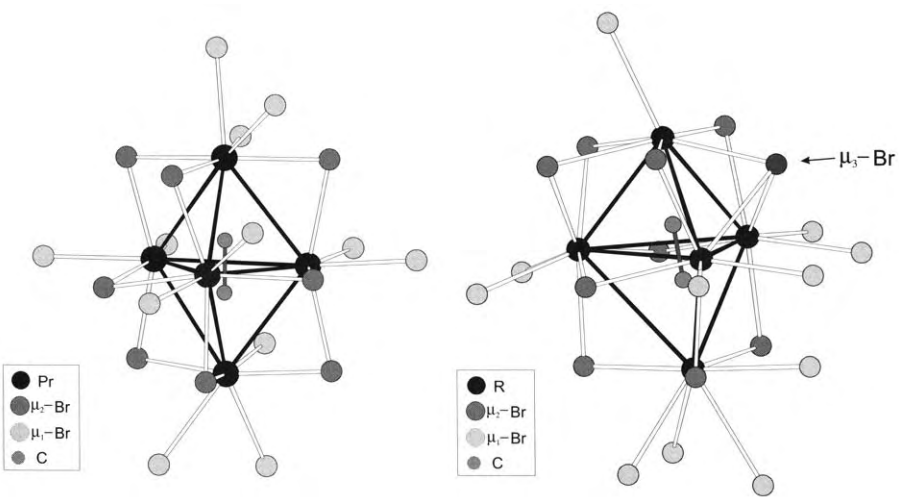

Fig. 55. (left) The $[Pr_5(C_2)]Br_{20}$ unit in $[Pr_5(C_2)]Br_9$ with *eight* edge-capping μ_2-Br ligands only; (right) the $[R_5(C_2)]Br_{21}$ unit in $[R_5(C_2)]Br_9$ (R = La, Ce) with *nine* μ_2-Br ligands and *one* additional face-capping μ_3-Br.

Box 6
Connectivities in $[R_5(C_2)]X_9$ and $A[R_5(C_2)]X_{10}$-type compounds with A = K, Rb; R = La, Ce, Pr, Nd; X = Cl, Br

	a–a	i–a	a–i	a–a–a	i–i	i–a–a	a–a–i	a–a–a–a
$[R_5(C_2)]Cl_9$ (R = La, Ce, Pr)	3/2	6/2	6/2	3/3	1/2			
$[R_5(C_2)]Br_9$ (R = La, Ce)		4/2	4/2	3/3	4/2	2/3	4/3	
$[Pr_5(C_2)]Br_9$		7/2	7/2	3/3		1/3	2/3	
$K[R_5(C_2)]Cl_{10}$ (R = La, Ce)		9/2	9/2					4/4
$K[Pr_2(C_2)]Cl_{10}$, $Rb[R_5(C_2)]Cl_{10}$ (R = Pr, Nd)		9/2	9/2	3/3				

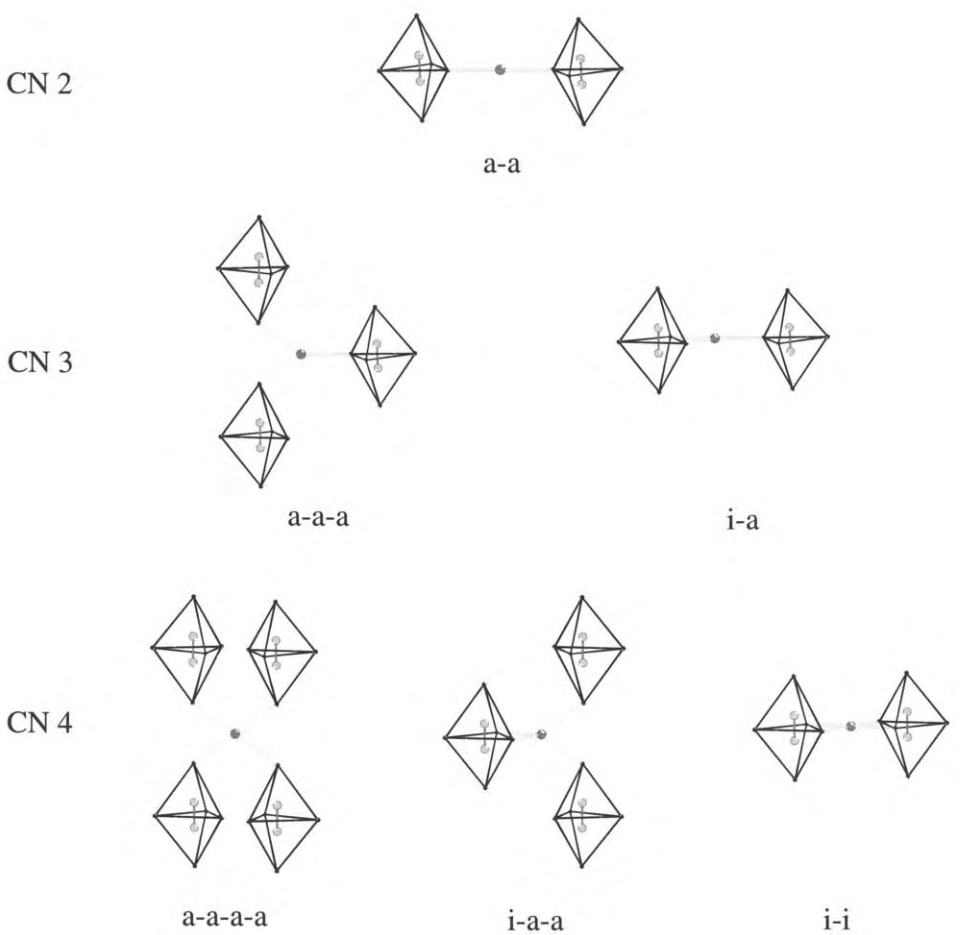

Box 7. Coordination numbers and connectivities of the ligands X in $[R_5(C_2)]X_9$ and $A[R_5(C_2)]X_{10}$-type compounds with A = K, Rb; R = La, Ce, Pr, Nd; X = Cl, Br.

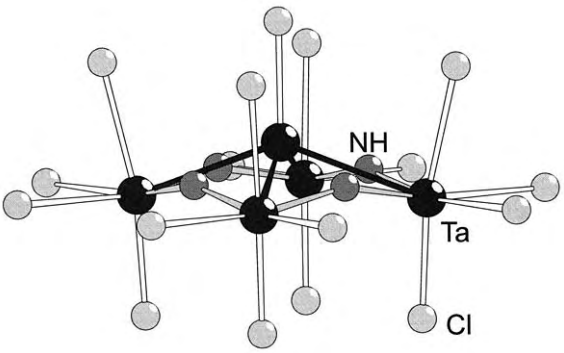

Fig. 56. The $\{[Ta_5(NH)_4]Cl_{17}\}^{6-}$ anion in the crystal structure of the green $(NH_4)_6[Ta_5(NH)_4]Cl_{17}$.

Electronically, all chlorides and bromides containing the "isolated" $[R_5(C_2)]$ cluster ("condensed" clusters with hexadeltahedra are not known!) with the formula types $[R_5(C_2)]X_9$ and $A[R_5(C_2)]X_{10}$ may be grasped

(1) either in a purely *ionic* view: According to $[(R^{3+})_5(C_2^{6-})](X^-)_9$ and $(A^+)[(R^{3+})_5(C_2^{6-})](X^-)_{10}$, there are no excess electrons. The red colour and transparency of the crystals is in accord with this observation. Preliminary magnetic susceptibility measurements exhibit a Curie–Weiss paramagnetism with a magnetic moment of $\mu_{eff} = 1.51\mu_B$ (300 K; 10 KOe). Although this value is smaller than expected for Pr^{3+} (around $3.5\mu_B$), i.e., the $4f^2$ electronic configuration, it is close to $\mu_{eff} = 1.8\mu_B$ as observed for $[Pr_4Ru]I_5$ (Uhrlandt 1994, Payne and Corbett 1991).

(2) or in a rather *covalent* view: With the single-bonded C_2 unit contributing six electrons to *intra*-cluster bonding, one counts a total of 12 electrons. Naively, these could be thought to form six 2e–3c bonds. They also obey Wade's $2n+2$ skeletal-electrons rule for *closo*-clusters.

The five-corner polyhedron "trigonal bipyramid" (hexa-delta-hedron) has as an alternative the pentahedron "square pyramid", see box 4. Examples are extremely rare. None are known for rare-earth halides. The only true example is known for molybdenum $(Bu_4N)_2[Mo_5]Cl_{13}$ (Jödden et al. 1975). With tantalum, the rather complicated imide-chloride $(NH_4)_6[Ta_5(NH)_4]Cl_{17}$ is obtained from ammonium chloride and tantalum at 380°C (Simon and Meyer 1993). It contains the isolated $\{[Ta_5(NH)_4]Cl_{17}\}^{6-}$ unit (fig. 56). With $(6\times1)+(5\times5)-(4\times2)-(17\times1)=6$ electrons for cluster-based metal–metal bonding states it is a B_5H_9 analogue with 1.5 electrons each for the four Ta–Ta apical-basal bonds. A detailed account of the electronic structure of the $[Ta_5(NH)_4]$ cluster has been given recently (Lawler and Hoffmann 1996).

5.6. *Octa(delta)hedra, [R_6], monomers and dimers*

Owing to the ample contributions of the groups of Corbett and Simon, one must have the impression that the so-called reduced halide chemistry of the rare-earth elements is that of interstitially stabilized $[R_6Z]$ clusters. It is certainly dominated by these units when *condensed metal clusters* are considered. This chemistry has been reviewed several times (Corbett 1992, Simon 1995, Meyer 1988).

Box 8
Electron counts n for *intra*-cluster bonding and connectivities of the isolated $[R_6(Z)]X^i_{12}X^a_6$ cluster units of some quaternary halides

n		i	i–a	a–i	a–a	a	Reference(s)
9	$Cs_2Lu[Lu_6C]Cl_{18}$	12				6	[1]
11	$Cs[Er_6C]I_{12}$	6	6/2	6/2			[1,2]
14	$Cs_2[Pr_6(C_2)]I_{12}$	6	6/2	6/2			[3]
13	$Cs_4[Sc_6(C)]Cl_{13}$	8	4/2	4/2	2/2		[4]
15	$Cs_4[Pr_6(C_2)]I_{13}$						

References
[1] Artelt et al. (1992)
[2] Artelt and Meyer (1992)
[3] Artelt and Meyer (1993)
[4] Artelt et al. (1994)

When it comes to isolated or oligomeric clusters, there is only a limited number of examples. They may all be derived from $[R_6(Z)]X^i_{12}X^a_6$ units (fig. 46). The most oxidized example is $Cs_2Lu[Lu_6(C)]Cl_{18}$ with only 9 electrons for *intra*-cluster bonding. It forms red transparent crystals. Other quaternary halides with isolated octahedra all with a single carbon atom or the dicarbon unit have 11 to 15 cluster-based electrons (box 8).

The examples of $Cs_4[Sc_6(C)]Cl_{13}$ and $Cs_4[Pr_6(C_2)]I_{13}$ (Artelt et al. 1994) are particularly interesting because they were the missing link of the connectivities of $[R_6(Z)]X^i_{12}X^a_6$ units between the compositions $[R_6(Z)]X_{18}$ and $[R_6(Z)]X_{10}$. Box 9 gives an overview.

The first step of condensation of $[R_6(Z)]$ octahedra is the formation of $[R_{10}(Z)_2]$ double octahedra through connection via one common edge. The only interstitial Z that has been incorporated in such a double octahedron is the dicarbon unit, $(C_2)^{6-}$. Figure 57 exhibits the $[Y_{10}(C_2)_2]$ cluster as observed in $[Y_{10}(C_2)_2]I_{18}$ and the reduced $Cs[Y_{10}(C_2)_2]I_{18}$ (Hinz and Meyer 1995a,b). The double octahedron is surrounded by 18 inner and 8 outer ligands.

Edge-connected double octahedra $[R_{10}(C_2)_2]$ were first observed for $[Gd_{10}(C_2)_2]Cl_{18}$ and $[Gd_{10}(C_2)_2]Cl_{17}$ (Warkentin et al. 1982) and for $[Gd_{10}(C_2)_2]I_{16}$ as well (Simon 1985). Formal derivatives of these three ternary ethanide-halide compounds have now been found as quaternary compounds where from one up to four moles of alkali halide are added (box 10).

Electronically, these cluster units contain either two ($[R_{10}(C_2)_2]X_{16}$-type and derivatives), one ($[R_{10}(C_2)_2]X_{17}$) or zero ($[R_{10}(C_2)_2]X_{18}$) excess electrons when the ionic model is used, or 26, 25 and 24 cluster-based electrons, respectively, in the covalent model. See for theoretical calculations Satpathy and Andersen (1985).

Connections between the $[R_{10}(C_2)_2]I^i_{18}I^a_8$ units can be rather complicated and are certainly not as symmetric and straightforward as in simple octahedral $[R_6(Z)]X^i_{12}X^a_6$ units. Figure 58 gives one example.

The next step of condensation would be a triple octahedron. This is not known as an oligomer. Infinite chains are formed instead. Gd_2Cl_3 contains chains of *trans*-connected

Box 9

Regular connectivities of $[R_6(Z)]X^i_{12}X^a_6$ cluster units, examples and electron counts n for intra-cluster bonding in $A_x[R_6(Z)]X_z$-type compounds

z	i	i–i	i–a	a–i	a–a	a	example	n	Ref.
18	12					6	$K_4[Nb_6]Cl_{18}$	16	[1]
							$Cs_2Lu[Lu_6C]Cl_{18}$	9	[2]
17	12				2/2	4	$Ba_2[Zr_6B]Cl_{17}$	14	[3]
16	12				4/2	2	$Cs_3[Zr_6C]Cl_{16}$	15	[4]
15	12				6/2		$[Nb_6]F_{15}$	15	[5]
							$K_2[Zr_6C]Cl_{15}$		[6]
14	10		2/2	2/2	4/2		$[Nb_6]Cl_{14}$	16	[7]
							$[Ti_6C]Cl_{14}$	14	[8]
13	8		4/2	4/2	2/2		$Cs_4[Sc_6C]Cl_{13}$	13	[9]
							$Cs_4[Pr_6C_2]I_{13}$	15	
12	6		6/2	6/2			$Sc[Sc_6N]Cl_{12}$	14	[10]
							$Ho[Ho_6C]I_{12}$	13	[11]
11	4	2/2	6/2	6/2			$[Sc_6C_2]I_{11}$	13	[12]
10	2	4/2	6/2	6/2			$[Y_6Ru]I_{10}$	16	[13]

References

[1] Simon et al. (1968)
[2] Artelt et al. (1992)
[3] Zhang and Corbett (1989)
[4] Ziebarth and Corbett (1989)
[5] Schäfer et al. (1965)
[6] Ziebarth and Corbett (1987)
[7] Simon et al. (1965)
[8] Hinz and Meyer (1994)
[9] Artelt et al. (1994)
[10] Hwu and Corbett (1986)
[11] Hohnstedt (1993)
[12] Dudis and Corbett (1987)
[13] Hughbanks and Corbett (1989)

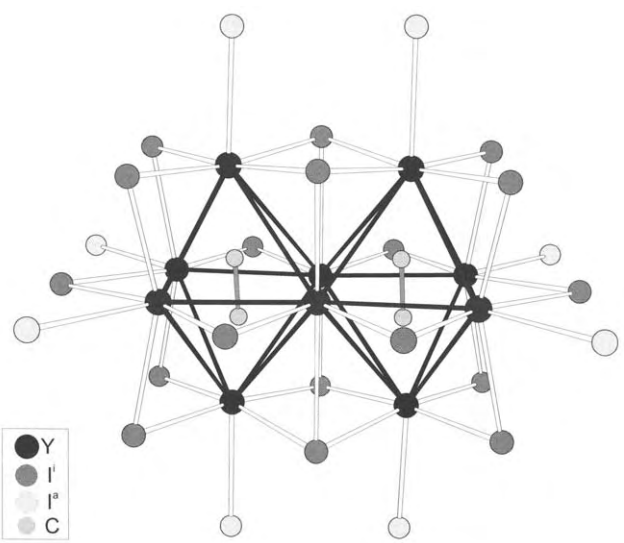

Fig. 57. The $[Y_{10}(C_2)_2]I^i_{18}I^a_8$ unit as observed in $[Y_{10}(C_2)_2]I_{18}$ and $Cs[Y_{10}(C_2)_2]I_{18}$ and the compounds as summarized in box 10.

Box 10

Ternary and quaternary halides containing the $[R_{10}(C_2)_2]$ double octahedron with two, one and zero excess electrons, respectively

$[Gd_{10}(C_2)_2]I_{16}$ [1]	$[Gd_{10}(C_2)_2]Cl_{17}$ [2]	$[Gd_{10}(C_2)_2]Cl_{18}$ [2,3]
	$Cs[Y_{10}(C_2)_2]I_{18}$ [4]	$[Tb_{10}(C_2)_2]Cl_{18}$ [6]
	$Cs[Er_{10}(C_2)_2]I_{18}$ [5]	$[Gd_{10}(C_2)_2]Br_{18}$ [7]
		$[Tb_{10}(C_2)_2]Br_{18}$ [7]
		$[Er_{10}(C_2)_2]Br_{18}$ [5]
		$[Y_{10}(C_2)_2]I_{18}$ [8]
	$K_2[Gd_{10}(C_2)_2]Br_{19}$ [9]	
	$Rb_2[Gd_{10}(C_2)_2]Br_{19}$ [9]	
	$Rb_2[Tb_{10}(C_2)_2]Br_{19}$ [9]	
	$Cs_2[Gd_{10}(C_2)_2]Cl_{19}$ [9]	
		$K_2[Gd_{10}(C_2)_2]Br_{20}$ [9]
		$Cs_3[Tb_{10}(C_2)_2]Cl_{21}$ [10]

References

[1] Simon (1985)
[2] Warkentin et al. (1982)
[3] Simon et al. (1981)
[4] Hinz and Meyer (1995b)
[5] Uhrlandt et al. (1994)
[6] Uhrlandt (1994), Payne and Corbett (1991)
[7] Steffen et al. (1995)
[8] Hinz and Meyer (1995a)
[9] Ließ et al. (1997)
[10] Artelt and Meyer (1994)

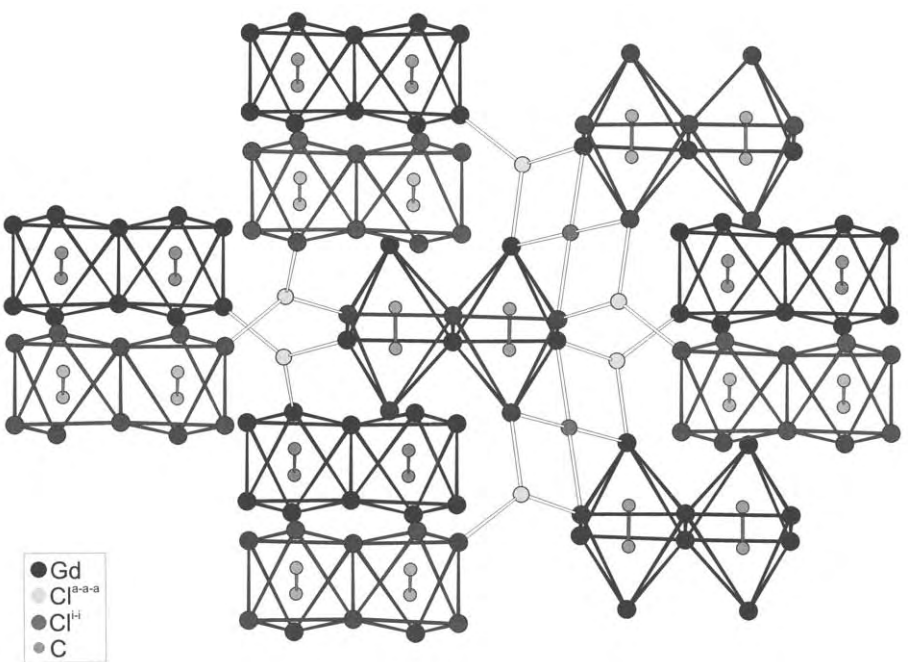

Fig. 58. Cl^{i-i} and Cl^{a-a-a} bridges between $[Gd_{10}(C_2)_2]Cl^i_{18}Cl^a_8$ units (most of the ligands have been omitted for clarity) in $Cs_2[Gd_{10}(C_2)_2]Cl_{19}$. The entire connection pattern may be formulated as follows: $Cs_2[Gd_{10}(C_2)_2]Cl^i_{14}Cl^{i-i}_{2/2}Cl^{i-a}_{2/2}Cl^{a-i}_{2/2}Cl^{a-a-a}_{6/3}$.

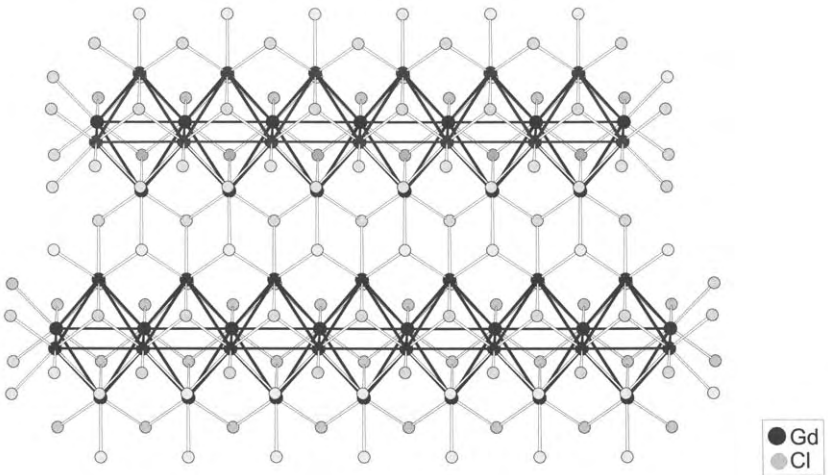

Fig. 59. The *trans* edge-connected chains of empty $[Gd_6]$ octahedra derived from $[Gd_6]Cl_8^i$ clusters in Gd_2Cl_3.

$[Gd_6]$ octahedra without interstitials, see fig. 59. This may be rationalized by the fact that they may be derived from $[Gd_6]Cl_8^i$ cluster units (Lokken and Corbett 1973, Simon et al. 1979). Gd_2Cl_3 has been amply investigated, it is a semiconductor with a band gap of 0.85 eV and orders antiferromagnetically at 26.8 K (Simon 1995).

Octahedral clusters derived from the 6–12 type are, as usual, interstitially stabilized. Two types of *trans* edge-connected octahedral chains are now known both with the dicarbon unit as the interstitial. The chains are, however, distorted in both cases:

In the heteroleptic $[Gd_4(C_2)]X_6$ (Ließ et al. 1996), for example, with X being Cl^- and I^- approximately 50% each, two octahedra are elongated along the (pseudo)C_4 axis as usually in $[R_{10}(C_2)_2]$ double octahedra and the third one is compressed with the C_2 unit in the octahedral base statistically distributed over two orientations, see fig. 60.

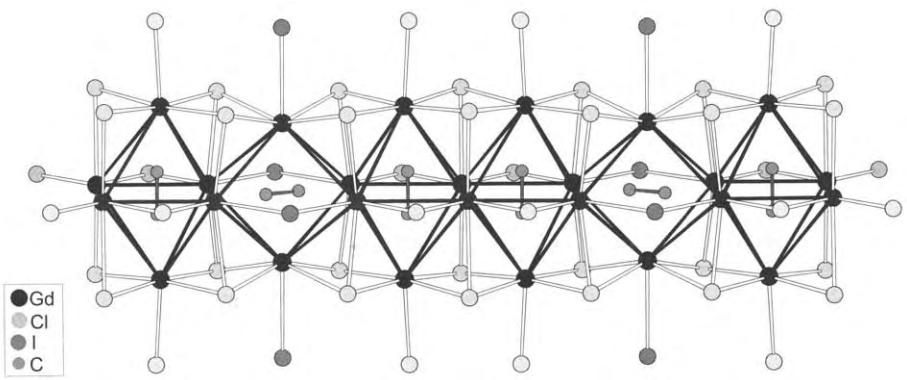

Fig. 60. *Trans* edge-connected chains of $[Gd_6(C_2)]$ octahedra in the crystal structure of the heteroleptic $Gd_4(C_2)X_6$ (X = Cl, I).

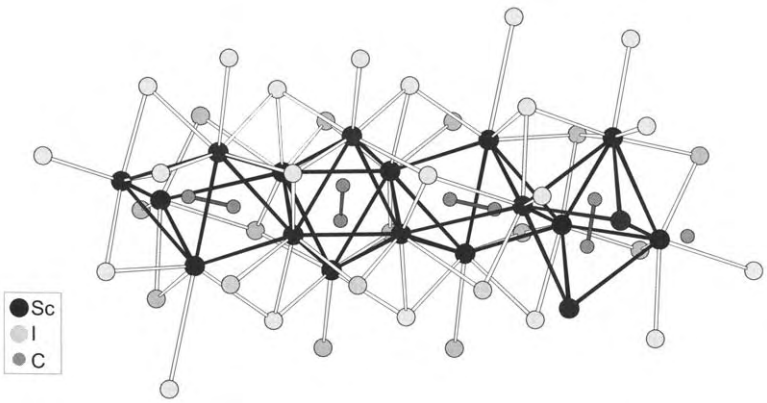

Fig. 61. Part of the chain of edge-connected $[Sc_6(C_2)]$ clusters in the crystal structure of $[Sc_4(C_2)]I_6$. Note that every second octahedron is distorted to a trigonal prism.

In $[Sc_4(C_2)]I_6$ (Dudis and Corbett 1987), every second octahedron $[Sc_6(C_2)]$ is distorted to a trigonal prism, see fig. 61. In both compounds and in $Na[Mo_4]O_6$ as well (Torardi and McCarley 1979) the octahedral chains are arranged as is shown in fig. 62.

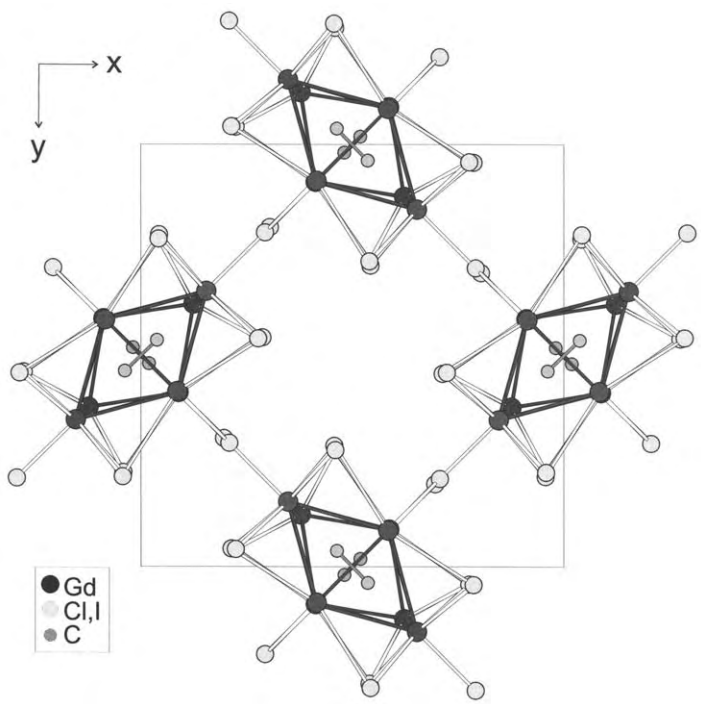

Fig. 62. Projection of the crystal structure of $[Gd_4(C_2)]X_6$ onto (001). The chains are arranged in the same way as in $[Sc_4(C_2)]I_6$ and $Na[Mo_4]O_6$.

Cis–trans edge connection of octahedral chains as in $[Pr_{12}(C_2)_3]I_{17}$ has already been mentioned above, see fig. 54.

5.7. *Combinations of deltahedra*

It appears that atoms of the second-row elements, B, C, N, O, some of which are truly ubiquitous, prefer as interstitials different polyhedra. Oxygen and nitrogen atoms (or O^{2-} and N^{3-}) prefer tetrahedra, single carbon atoms are found in octahedra (see above) or in tetragonal pyramids as in the recently observed boride-carbides, for example in $Gd_4C_2BBr_3$ (Mattausch and Simon 1995). Dicarbon units are found in octahedra, trigonal prisms and in trigonal bipyramids as shown above. Boron atoms enter octahedra in zirconium clusters and in the mentioned boride-carbide trigonal prisms.

When carbon and oxygen/nitrogen are involved, one observes oligomers built from $[R_6(C/C_2)]$ octahedra and $[R_4(O/N)]$ tetrahedra. An oligomer built from two octahedra and two tetrahedra connected via common trans edges was observed for the iodides $[R_{14}(C_2)_2(N)_2]I_{24}$ with R = Y, Ho (Mattausch et al. 1995a) and Er (Steffen and Meyer 1995), see fig. 63. Nitrogen may be, at least partly, substituted by oxygen. The change of colour from red-brown to black with metallic lustre in $[Er_{14}(C_2)_2(O)_2]I_{24}$ (Meyer and Steffen 1995) accounts for the excess electron(s) in the oxide.

Octahedra and tetrahedra are also known from the chain compounds R_4CNX_6 (R = Gd, La; X = Br, I) and $Y_6C_2NI_9$ (Mattausch et al. 1995b) and from a number of compounds with corrugated layers, essentially $[Y_9(C)_4(O)]I_8$ (compounds with Ho, Er, Lu are isotypic) (Mattfeld et al. 1993) and $[Y_7(C)_3(O)]I_6$ (Mattausch et al. 1993), see fig. 64.

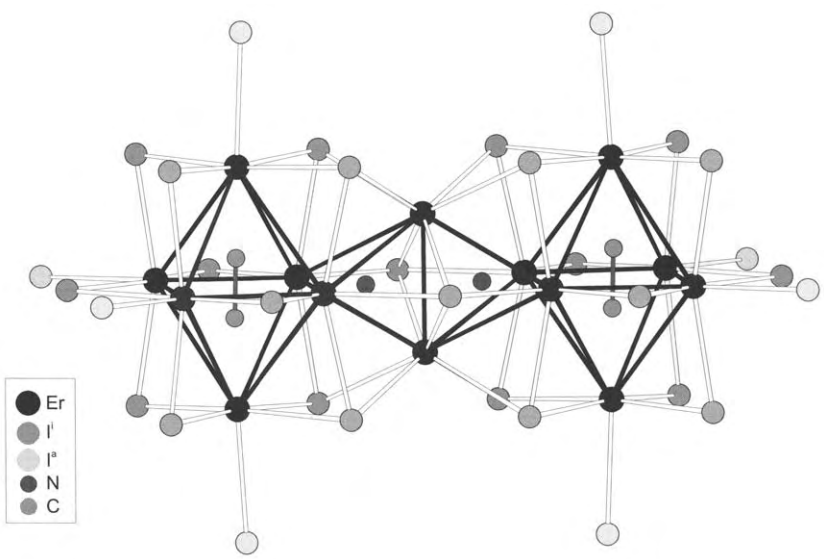

Fig. 63. The $[Er_{14}(C_2)_2(N)_2]I^i_{24}I^a_8$ unit in the crystal structure of $[Er_{14}(C_2)_2(N)_2]I_{24}$.

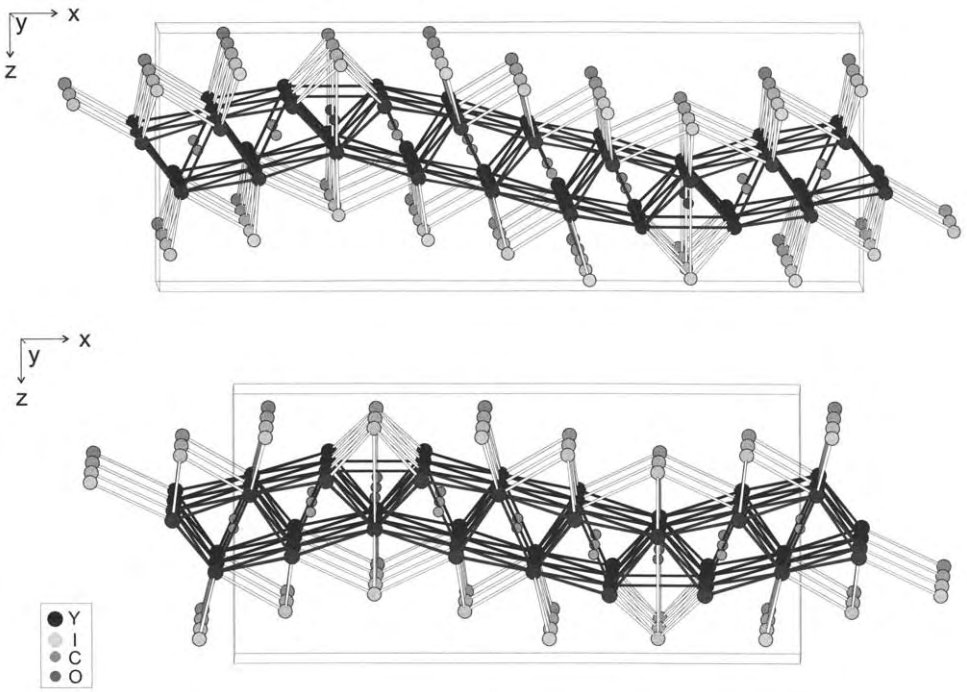

Fig. 64. Projections of the crystal structures of (top) $[Y_9(C)_4(O)]I_8$ and (bottom) $[Y_7(C)_3(O)]I_6$ exhibiting a side-view on the corrugated layers built from four and three $[Y_6(C)]$ octahedra, respectively, separated by $[Y_4(O)]$ tetrahedra, all connected via common edges.

Acknowledgements

Our own work as summarized in this article was aided by ample support from the Deutsche Forschungsgemeinschaft, Bonn, and the Fonds der Chemischen Industrie, Frankfurt am Main.

References

Aléonard, S., D. Gonzales, M.F. Gorius and M.T. Roux, 1975, Mater. Res. Bull. **10**, 1185.

Aléonard, S., Y. le Fur, L. Pontonnier, M.F. Gorius and M.T. Roux, 1978, Ann. Chim. Sci. **3**, 417.

Aléonard, S., Y. le Fur, M.F. Gorius and M.T. Roux, 1980, J. Solid State Chem. **34**, 79.

Allenspach, P., A. Furrer, H.U. Güdel and H. Büttner, 1997, Physica B **234**, 744.

Amilius, Z., B. van Laar and H.M. Rietveld, 1969, Acta Crystallogr. B **25**, 400.

Anderson, S., 1976, U.S.P. 3948798 [1969/] C.A. 84 Nr. 188582.

Aronsson, B., M. Backman and S. Rundqvist, 1960, Acta Chem. Scand. **14**, 1001.

Artelt, H.M., and G. Meyer, 1992, J. Chem. Soc., Chem. Comm. **460**.

Artelt, H.M., and G. Meyer, 1993, Z. Anorg. Allg. Chem. **619**, 1.

Artelt, H.M., and G. Meyer, 1994, Z. Anorg. Allg. Chem. **620**, 1527.

Artelt, H.M., Th. Schleid and G. Meyer, 1992, Z. Anorg. Allg. Chem. **618**, 18.

Artelt, H.M., Th. Schleid and G. Meyer, 1994, Z. Anorg. Allg. Chem. **620**, 1521.

Babel, D., 1962, Acta Crystallogr. **15**, 1098.

Balz, D., and K. Plieth, 1955, Z. Elektrochem., Ber. Bunsenges. Phys. Chem., **59**, 545.

Beck, H.P., and H. Bärnighausen, 1971, Z. Anorg. Allg. Chem. **386**, 221.

Beck, H.P., and E. Gladrow, 1983, Z. Anorg. Allg. Chem. **498**, 75.

Beck, H.P., and W. Milius, 1986, Z. Anorg. Allg. Chem. **539**, 7.

Beck, H.P., and M. Schuster, 1992, J. Solid State Chem. **100**, 301.

Benachenhou, F., G. Mairesse, G. Nowogrocki and D. Thomas, 1986, J. Solid State Chem. **65**, 13.

Bergerhoff, G., and O. Schmitz-Dumont, 1956, Z. Anorg. Allg. Chem. **284**, 10.

Bevan, D.J.M., and A.W. Mann, 1975, Acta Crystallogr. B **31**, 1406.

Bevan, D.J.M., O. Greis and J. Strähle, 1980a, Acta Crystallogr. A **36**, 889.

Bevan, D.J.M., O. Greis and J. Strähle, 1980b, Acta Crystallogr. A **37**, 266.

Blachnik, R., and J.E. Alberts, 1982, Z. Anorg. Allg. Chem. **490**, 235.

Blachnik, R., and E. Enninga, 1983, Z. Anorg. Allg. Chem. **503**, 133.

Blachnik, R., and A. Jäger-Kasper, 1980, Z. Anorg. Allg. Chem. **461**, 74.

Blachnik, R., and D. Selle, 1979, Z. Anorg. Allg. Chem. **454**, 90.

Blachnik, R., G. Alberts and E. Enninga, 1985, Z. Anorg. Allg. Chem. **522**, 207.

Bochkova, R.I., Y.N. Saf'yanov, E.A. Kuz'min and N.V. Belov, 1973, Dokl. Akad. Nauk. SSSR **211**, 357.

Böcker, M., 1996, Dr. rer. nat. Thesis (Universität Hannover).

Bode, H., and E. Voss, 1957, Z. Anorg. Allg. Chem. **290**, 1.

Bohnsack, A., and G. Meyer, 1996a, Z. Kristallogr. **211**, 326.

Bohnsack, A., and G. Meyer, 1996b, Z. Anorg. Allg. Chem. **622**, 173.

Bohnsack, A., and G. Meyer, 1997, Z. Anorg. Allg. Chem. **623**, 837.

Bohnsack, A., M.S. Wickleder and G. Meyer, 1996, Z. Kristallogr. **211**, 394.

Bohnsack, A., F. Stenzel, A. Zajonc, G. Balzer, M.S. Wickleder and G. Meyer, 1997a, Z. Anorg. Allg. Chem. **623**, 1067.

Bohnsack, A., G. Balzer, M.S. Wickleder, H.U. Güdel and G. Meyer, 1997b, Z. Anorg. Allg. Chem. **623**, 1352.

Bridgman, P.W., 1925, Proc. Am. Acad. Arts Sci. **60**, 303.

Broll, A., A. Simon, H.G. von Schnering and H. Schäfer, 1969, Z. Anorg. Allg. Chem. **367**, 1.

Brunton, G., 1969, Acta Crystallogr. B **25**, 600.

Burns, J.H., 1965, Inorg. Chem. **4**, 881.

Burnus, R., D.J. Hinz and G. Meyer, 1994, Z. Kristallogr. **209**, 544.

Burrow, J.H., C.H. Maule, P. Strange, J.N. Tothill and J.A. Wilson, 1987, J. Phys. C **20**, 4115.

Corbett, J.D., 1973, Rev. Chim. Minér. **10**, 239.

Corbett, J.D., 1983, Inorg. Synth. **22**, 31.

Corbett, J.D., 1991, Conproportionation route to reduced lanthanide halides, in: Synthesis of Lanthanide and Actinide Compounds, eds G. Meyer and L.R. Morss (Kluwer, Dordrecht) p. 159.

Corbett, J.D., 1992, Pure Appl. Chem. **64**, 1395.

Druding, L.F., and J.D. Corbett, 1961, J. Am. Chem. Soc. **83**, 2462.

Dudis, D., and J.D. Corbett, 1987, Inorg. Chem. **26**, 1933.

Eick, H.A., 1994, in: Handbook on the Physics and Chemistry of Rare Earths, Vol. 18, eds K.A. Gschneidner Jr and L. Eyring (North-Holland, Amsterdam) p. 365.

Faget, H., J. Grannec, A. Tressaud, V. Rodriguez, T. Roisnel, I.N. Flerov and M.V. Gorev, 1996, Eur. J. Solid State Inorg. Chem. **33**, 893.

Fasiska, E.J., and G.A. Jeffrey, 1965, Acta Crystallogr. **19**, 463.

Fink, H., and H.J. Seifert, 1980, Z. Anorg. Allg. Chem. **466**, 87.

Friedrich, G., H. Fink and H.J. Seifert, 1987, Z. Anorg. Allg. Chem. **548**, 141.

Frit, B., B. Holmberg and J. Galy, 1970, Acta Crystallogr. B **26**, 16.

Gaebell, H.C., and G. Meyer, 1984, Z. Anorg. Allg. Chem. **515**, 133.
Geller, S., 1955, Acta Crystallogr. **8**, 15.
Goodenough, J.B., 1984, Proc. R. Soc. London A **393**, 215.
Greis, O., 1982, Rev. Inorg. Chem. **4**, 1245.
Greis, O., and J.M. Haschke, 1982, in: Handbook on the Physics and Chemistry of Rare Earths, Vol. 5, eds K.A. Gschneidner Jr and L. Eyring (North-Holland, Amsterdam) p. 387.
Haschke, J.M., 1979, in: Handbook on the Physics and Chemistry of Rare Earths, Vol. 4, eds K.A. Gschneidner Jr and L. Eyring (North-Holland, Amsterdam) p. 89.
Hawthorne, F.C., and R.B. Ferguson, 1975, Can. Miner. **13**, 377.
Hehlen, M., H.U. Güdel, Q. Shu, J. Rai and S.C. Rand, 1996, J. Chem. Phys. **104**, 1232.
Heuer, Th., F. Steffen and G. Meyer, 1996, Eur. J. Solid State Inorg. Chem. **33**, 265.
Hinz, D., 1994, Dr. rer. nat. Thesis (Universität Hannover).
Hinz, D.J., and G. Meyer, 1994, J. Chem. Soc., Chem. Commun., p. 125.
Hinz, D.J., and G. Meyer, 1995a, Z. Kristallogr. **210**, 957.
Hinz, D.J., and G. Meyer, 1995b, Z. Kristallogr. **210**, 958.
Hinz, D.J., G. Meyer, Th. Dedecke and W. Urland, 1995, Angew. Chem. Int. Ed. Engl. **34**, 71.
Hohnstedt, C., 1993, Dr. rer. nat. Thesis (Universität Hannover).
Hohnstedt, C., and G. Meyer, 1993, Z. Anorg. Allg. Chem. **619**, 1374.
Hoppe, R., 1980, personal communication.
Hoppe, R., and K.M. Roedder, 1961, Z. Anorg. Allg. Chem. **313**, 154.
Hughbanks, T., and J.D. Corbett, 1989, Inorg. Chem. **28**, 631.
Hughes, J.M., and J.W. Drexler, 1994, Can. Miner. **32**, 563.
Hwu, S.-J., and J.D. Corbett, 1986, J. Solid State Chem. **64**, 331.
Hyde, B.G., and S. Andersson, 1989, Inorganic Crystal Structures (Wiley, New York).
Hyde, B.G., A.N. Bagshaw, S. Andersson and M. O'Keeffee, 1974, Annu. Rev. Mater. Sci. **4**, 43.
Imoto, H., and J.D. Corbett, 1981, Inorg. Chem. **19**, 1241.
Imoto, H., J.D. Corbett and A. Cisar, 1981, Inorg. Chem. **20**, 145.
Jeitschko, W., and P.C. Donohue, 1975, Acta Crystallogr. B **31**, 1890.
Jödden, K., H.G. von Schnering and H. Schäfer, 1975, Angew. Chem. Int. Ed. Engl. **14**, 570.
Kasten, A., P.H. Müller and M. Schienle, 1984, Solid State Commun. **51**, 919.
Keeling, R.O., 1957, Acta Crystallogr. **10**, 209.
Keller, H.L., 1976, Z. Naturforsch. B **31**, 885.
Krämer, K., and H.U. Güdel, 1995, J. Alloys & Compounds **207**, 128.
Krämer, K., and G. Meyer, 1990, Z. Anorg. Allg. Chem. **589**, 96.
Krämer, K., G. Meyer, P. Fischer, A.W. Hewat and H.-U. Güdel, 1991, J. Solid State Chem. **95**, 1.
Krämer, K., P. Fischer, Th. Hauß, M.S. Wickleder and H.U. Güdel, 1997, unpublished.
Krebs, B., and G. Henkel, 1981, Z. Anorg. Allg. Chem. **474**, 149.
Lange, Th., 1992, Dr. rer. nat. Thesis (Universität Karlsruhe).
Laptev, D.M., V.M. Kulagin, T.S. Astakhoven and N.V. Tolstoguzov, 1981, Russ. J. Inorg. Chem. **26**, 553.
Lawler, K.A., and R. Hoffmann, 1996, Inorg. Chem. **35**, 1431.
Le Fur, Y., S. Aleonard, M.F. Gorius and M.T. Roux, 1982, Acta Crystallogr. **38**, 1431.
Lerch, K., and W. Laqua, 1990, Z. Anorg. Allg. Chem. **591**, 47.
Ließ, H., H.-J. Meyer and G. Meyer, 1996, Z. Anorg. Allg. Chem. **622**, 494.
Ließ, H., F. Steffen and G. Meyer, 1997, J. Alloys & Compounds **246**, 242.
Lissner, F., and Th. Schleid, 1994, Z. Anorg. Allg. Chem. **620**, 1998.
Lissner, F., K. Krämer, Th. Schleid, G. Meyer, Z. Hu and G. Kaindl, 1994, Z. Anorg. Allg. Chem. **620**, 444.
Löchner, U., and R. Blachnik, 1988, Z. Kristallogr. **183**, 207.
Lokken, D.A., and J.D. Corbett, 1973, Inorg. Chem. **12**, 556.
Lösch, R., and C. Hebecker, 1976, Rev. Chim. Minér. **13**, 207.
Lösch, R., C. Hebecker and Z. Ranft, 1982, Z. Anorg. Allg. Chem. **491**, 199.
Lulei, M., and J.D. Corbett, 1995, Inorg. Chem. **34**, 2671.
Lumpp, A., 1988, Dr. rer. nat. Thesis (Universität Karlsruhe).
Lutz, H.D., K. Wussow and P. Kuske, 1987, Z. Naturforsch. **42B**, 1379.

Makovicky, E., and B.G. Hyde, 1981, Struct. Bonding **46**, 101.

Mann, A.W., and D.J.M. Bevan, 1972, J. Solid State Chem. **5**, 410.

Marsh, R.E., and F.H. Herbstein, 1988, Acta Crystallogr. **44**, 77.

Martin, J.B., and J.D. Corbett, 1995, Angew. Chem. Int. Ed. Engl. **34**, 242.

Massa, W., 1980, Z. Kristallogr. **153**, 201.

Masse, R., and A. Simon, 1981, Mater. Res. Bull. **16**, 1007.

Masselmann, S., and G. Meyer, 1998a, Z. Anorg. Allg. Chem. **624**, 551.

Masselmann, S., and G. Meyer, 1998b, Z. Anorg. Allg. Chem. **624**, 357.

Mattausch, Hj., and A. Simon, 1995, Angew. Chem. Int. Ed. Engl. **34**, 1633.

Mattausch, Hj., H. Borrmann and A. Simon, 1993, Z. Naturforsch. **48B**, 1828.

Mattausch, Hj., H. Borrmann, R. Eger, R.K. Kremer and A. Simon, 1995a, Z. Naturforsch. **50B**, 931.

Mattausch, Hj., H. Borrmann, R. Eger, R.K. Kremer and A. Simon, 1995b, Z. Anorg. Allg. Chem. **620**,.

Mattfeld, H., and G. Meyer, 1992, Z. Anorg. Allg. Chem. **618**, 13.

Mattfeld, H., and G. Meyer, 1994, Z. Anorg. Allg. Chem. **620**, 85.

Mattfeld, H., K. Krämer and G. Meyer, 1993, Z. Anorg. Allg. Chem. **619**, 1384.

Meyer, G., 1978, Naturwissenschaften **65**, 258.

Meyer, G., 1980, Z. Anorg. Allg. Chem. **469**, 149.

Meyer, G., 1981, unpublished results.

Meyer, G., 1982, Prog. Solid State Chem. **14**, 141.

Meyer, G., 1983a, Inorg. Synth. **22**, 1.

Meyer, G., 1983b, Inorg. Synth. **22**, 10.

Meyer, G., 1983c, J. Less-Common Met. **93**, 371.

Meyer, G., 1984a, Z. Anorg. Allg. Chem. **511**, 193.

Meyer, G., 1984b, Z. Anorg. Allg. Chem. **517**, 191.

Meyer, G., 1988, Chem. Rev. **88**, 93.

Meyer, G., 1989, Inorg. Synth. **25**, 146.

Meyer, G., 1991a, Binary lanthanide(III) halides, MX_3 (X = Cl, Br, I), in: Synthesis of Lanthanide and Actinide Compounds, eds G. Meyer and L.R. Morss (Kluwer, Dordrecht) p. 135.

Meyer, G., 1991b, Complex lanthanide(III) chlorides, bromides and iodides, in: Synthesis of Lanthanide and Actinide Compounds, eds G. Meyer, L.R. Morss (Kluwer, Dordrecht) p. 145.

Meyer, G., 1994, The ammonium ion for synthesis, in: Advances in the Synthesis and Reactivity of Solids, Vol. 2, ed. T.E. Mallouk (JAI Press, Greenwich) p. 1.

Meyer, G., and P. Ax, 1982, Mater. Res. Bull. **17**, 1447.

Meyer, G., and E. Hüttl, 1983, Z. Anorg. Allg. Chem. **497**, 191.

Meyer, G., and H.J. Meyer, 1992, Chem. Mater. **4**, 1157.

Meyer, G., and L.R. Morss, eds, 1991, Synthesis of Lanthanide and Actinide Compounds (Kluwer, Dordrecht).

Meyer, G., and Th. Schleid, 1986, J. Less-Common Met. **116**, 187.

Meyer, G., and Th. Schleid, 1991, Action of alkali metals on lanthanide(III) halides: an alternative to the conproportionation route to reduced lanthanide halides, in: Synthesis of Lanthanide and Actinide Compounds, eds G. Meyer and L.R. Morss (Kluwer, Dordrecht) p. 175.

Meyer, G., and F. Steffen, 1995, Z. Kristallogr., Suppl. **9**, 201.

Meyer, G., and S. Uhrlandt, 1993, Angew. Chem. Int. Ed. Engl. **32**, 1318.

Meyer, G., P. Ax, A. Cromm and H. Linzmeier, 1984, J. Less-Common Met. **98**, 323.

Meyer, G., P. Ax, Th. Schleid and M. Irmler, 1987, Z. Anorg. Allg. Chem. **554**, 25.

Meyer, G., Th. Schleid and K. Krämer, 1989, J. Less-Common Met. **149**, 67.

Meyer, H.-J., 1994, Z. Anorg. Allg. Chem. **620**, 81.

Meyer, H.-J., N.D. Jones and J.D. Corbett, 1989, Inorg. Chem. **28**, 2635.

Meyer, H.-J., G. Meyer and M. Simon, 1991, Z. Anorg. Allg. Chem. **596**, 89.

Michaelis, C., Hj. Mattausch and A. Simon, 1992a, Z. Anorg. Allg. Chem. **610**, 23.

Michaelis, C., Hj. Mattausch, H. Borrmann, A. Simon and J.K. Cockcroft, 1992b, Z. Anorg. Allg. Chem. **607**, 29.

Michaelis, C., W. Bauhofer, H. Buchkremer-Hermanns, R.K. Kremer, A. Simon and G.J. Miller, 1992c, Z. Anorg. Allg. Chem. **618**, 98.

Morss, L.R., 1974, J. Inorg. Nucl. Chem. **36**, 3876.

Müller, B.G., 1991, Lanthanide fluorides, in: Synthesis of Lanthanide and Actinide Compounds, eds G. Meyer and L.R. Morss (Kluwer, Dordrecht) p. 55.

Noël, H., M. Potel and J. Padiou, 1976, Acta Crystallogr. B **32**, 605.

Payne, M.W., and J.D. Corbett, 1991, Inorg. Chem. **30**, 1467.

Poeppelmeier, K., J.D. Corbett, T.P. McMullen, D.R. Torgeson and R.G. Barnes, 1980, Inorg. Chem. **19**, 129.

Pollnau, M., W. Lüthy, H.P. Weber, K. Krämer, H.U. Güdel and R.A. McFarlane, 1996, J. Appl. Phys. B **62**, 1339.

Potel, M., C. Perrin, A. Perrin and M. Sergent, 1986, Mater. Res. Bull. **21**, 1239.

Reed, J.B., B.S. Hopkins and L.F. Audrieth, 1939, Inorg. Synth. **1**, 28.

Reshetnikova, L.P., I.B. Shaimuradov, V.A. Efremov and A.W. Novoselova, 1974, Dokl. Akad. Nauk. SSSR **215**, 877.

Reuter, G., J. Sebastian and G. Frenzen, 1996, Acta Crystallogr. C **52**, 1859.

Reuter, G., J. Sebastian, M. Roffe and H.J. Seifert, 1997, Thermochim. Acta **296**, 47.

Riedener, T., K. Krämer and H.U. Güdel, 1995, Inorg. Chem. **34**, 2745.

Riedener, T., Ph. Egger, J. Hulliger and H.U. Güdel, 1997, Phys. Rev. B **56**, 1800.

Rundqvist, S., and F. Jellinek, 1959, Acta Chem. Scand. **13**, 425.

Ryan, R.R., S.H. Mastin and M.J. Reisfeld, 1971, Acta Crystallogr. B **27**, 1270.

Satpathy, S., and O.K. Andersen, 1985, Inorg. Chem. **24**, 2604.

Schaart, D.R., P. Dorenbos, C.W.E. van Eijk, R. Visser, C. Pedrini, B. Moine and N.M. Khaidukov, 1995, J. Phys.: Condens. Matter **7**, 3063.

Schäfer, H., and R. Laumanns, 1981, Z. Anorg. Allg. Chem. **474**, 135.

Schäfer, H., and H.G. von Schnering, 1964, Angew. Chem. **20**, 833.

Schäfer, H., H.G. von Schnering, K.-J. Niehues and H.G. Nieder-Vahrenholz, 1965, J. Less-Common Met. **9**, 95.

Schäfer, H., H.G. von Schnering, J.V. Tillack, F. Kuhnen, H. Woehrle and H. Baumann, 1967, Z. Anorg. Allg. Chem. **353**, 281.

Schilling, G., and G. Meyer, 1996, Z. Anorg. Allg. Chem. **622**, 759.

Schilling, G., C. Kunert, Th. Schleid and G. Meyer, 1992, Z. Anorg. Allg. Chem. **618**, 7.

Schleid, Th., and G. Meyer, 1987a, Z. Anorg. Allg. Chem. **554**, 118.

Schleid, Th., and G. Meyer, 1987b, Z. Anorg. Allg. Chem. **552**, 97.

Schleid, Th., and G. Meyer, 1987c, Z. Anorg. Allg. Chem. **553**, 231.

Schleid, Th., and G. Meyer, 1987d, J. Less-Common Met. **127**, 161.

Schleid, Th., and G. Meyer, 1990, Z. Anorg. Allg. Chem. **590**, 103.

Schleid, Th., and G. Meyer, 1994, Z. Kristallogr. **209**, 826.

Schleid, Th., and H.-J. Meyer, 1992, J. Alloys & Compounds **189**, 75.

Schwanitz-Schüller, U., and A. Simon, 1985, Z. Naturforsch. **40B**, 705.

Seifert, H.J., and D. Büchel, 1998, Z. Anorg. Allg. Chem. **624**, 342.

Seifert, H.J., and J. Sandrock, 1990, Z. Anorg. Allg. Chem. **587**, 110.

Seifert, H.J., and J. Sandrock, 1997, Z. Anorg. Allg. Chem. **623**, 1525.

Seifert, H.J., and G. Thiel, 1982, J. Chem. Thermodyn. **14**, 1159.

Seifert, H.J., H. Fink and G. Thiel, 1985, J. Less-Common Met. **110**, 139.

Seifert, H.J., J. Sandrock and G. Thiel, 1986, J. Therm. Anal. **31**, 1309.

Seifert, H.J., J. Sandrock and J. Uebach, 1987, Z. Anorg. Allg. Chem. **555**, 143.

Seifert, H.J., H. Fink and J. Uebach, 1988, J. Therm. Anal. **33**, 625.

Seifert, H.J., J. Sandrock and G. Thiel, 1991, Z. Anorg. Allg. Chem. **598/**, 307.

Seifert, H.J., J. Sandrock and J. Uebach, 1995, Acta. Chem. Scand. **49**, 653.

Simon, A., 1967, Z. Anorg. Allg. Chem. **355**, 311.

Simon, A., 1985, J. Solid State Chem. **57**, 2.

Simon, A., 1995, J. Alloys & Compounds **229**, 158.

Simon, A., and T. Koehler, 1986, J. Less-Common Met. **116**, 279.

Simon, A., and H.G. von Schnering, 1966, J. Less-Common Met. **11**, 31.

Simon, A., H.G. von Schnering, H. Wöhrle and H. Schäfer, 1965, Z. Anorg. Allg. Chem. **339**, 155.

Simon, A., H.G. von Schnering and H. Schäfer, 1968, Z. Anorg. Allg. Chem. **361**, 235.

Simon, A., N. Holzer and Hj. Mattausch, 1979, Z. Anorg. Allg. Chem. **456**, 207.

Simon, A., E. Warkentin and R. Masse, 1981, Angew. Chem. Int. Ed. Engl. **20**, 1013.

Simon, A., Hj. Mattausch, G.J. Miller, W. Bauhofer and R.K. Kremer, 1991a, in: Handbook on the Physics and Chemistry of Rare Earths, Vol. 18, eds K.A. Gschneidner Jr and L. Eyring (North-Holland, Amsterdam) p. 365.

Simon, A., F. Böttcher and J.K. Cockcroft, 1991b, Angew. Chem. Int. Ed. Engl. **30**, 101.
Simon, M., and G. Meyer, 1993, J. Chem. Soc., Chem. Commun., p. 460.
Sommer, H., and R. Hoppe, 1978, Z. Anorg. Allg. Chem. **443**, 201.
Sommer, H., R. Hoppe and M. Jansen, 1976, Naturwissenschaften **63**, 194.
Staffel, Th., and G. Meyer, 1988, Z. Anorg. Allg. Chem. **557**, 40.
Staffel, Th., and G. Meyer, 1989, Z. Anorg. Allg. Chem. **574**, 107.
Steffen, F., and G. Meyer, 1995, Z. Naturforsch. **50B**, 1570.
Steffen, F., H. Ließ and G. Meyer, 1995, unpublished research.
Stenberg, E., 1961, Acta Chem. Scand. **15**, 861.
Stenzel, F., and G. Meyer, 1993, Z. Anorg. Allg. Chem. **619**, 652.
Thiel, G., and H.J. Seifert, 1988, Thermochim. Acta **133**, 275.
Torardi, C.C., and R.E. McCarley, 1979, J. Am. Chem. Soc. **101**, 3963.
Uhrlandt, S., 1994, Dr. rer. nat. Thesis (Universität Hannover).
Uhrlandt, S., and G. Meyer, 1994, Z. Anorg. Allg. Chem. **620**, 1872.
Uhrlandt, S., and G. Meyer, 1995a, Z. Anorg. Allg. Chem. **621**, 1466.
Uhrlandt, S., and G. Meyer, 1995b, J. Less-Common Met. **225**, 171.
Uhrlandt, S., and G. Meyer, 1995c, Z. Kristallogr. **210**, 361.
Uhrlandt, S., H.M. Artelt and G. Meyer, 1994, Z. Anorg. Allg. Chem. **620**, 1532.
Uhrlandt, S., Th. Heuer and G. Meyer, 1995, Z. Anorg. Allg. Chem. **621**, 1299.
van 't Spijker, J.C., P. Dorenbos, J.Th.M. de Haas, C.W.E. van Eijk, H.U. Güdel and K. Krämer, 1995, personal communication.
van 't Spijker, J.C., P. Dorenbos, C.W.E. van Eijk, M.S. Wickleder, K. Krämer and H.U. Güdel, 1996, unpublished results.
von Schnering, H.G., W. May and K. Peters, 1993, Z. Kristallogr. **208**, 368.
Warkentin, E., and H. Bärnighausen, 1979, Z. Anorg. Allg. Chem. **459**, 187.
Warkentin, E., R. Masse and A. Simon, 1982, Z. Anorg. Allg. Chem. **491**, 323.
Wells, A.F., 1975, Structural Inorganic Chemistry, 4th Ed. (Clarendon Press, Oxford).
Wickleder, M.S., 1994, Dr. rer. nat. Thesis (Universität Hannover).
Wickleder, M.S., and G. Meyer, 1995a, Z. Anorg. Allg. Chem. **621**, 457.
Wickleder, M.S., and G. Meyer, 1995b, Z. Anorg. Allg. Chem. **621**, 546.
Wickleder, M.S., and G. Meyer, 1998a, to be published.
Wickleder, M.S., and G. Meyer, 1998b, Z. Anorg. Allg. Chem. **624**, 1577.
Wickleder, M.S., H.U. Güdel, Th. Armbruster and G. Meyer, 1996a, Z. Anorg. Allg. Chem. **622**, 785.
Wickleder, M.S., A. Bohnsack and G. Meyer, 1996b, Z. Anorg. Allg. Chem. **622**, 675.
Wickleder, M.S., P. Egger, T. Riedener, N. Furer, H.U. Güdel and J. Hulliger, 1996c, Chem. Mater. **8**, 2828.
Womelsdorf, H., and H.-J. Meyer, 1994, Angew. Chem. Int. Ed. Engl. **33**, 1943.
Zajonc, A., 1996, Dr. rer. nat Thesis (Universität Hannover).
Zhang, J., and J.D. Corbett, 1989, J. Less-Common Met. **156**, 49.
Ziebarth, R.P., and J.D. Corbett, 1987, J. Am. Chem. Soc. **109**, 4844.
Ziebarth, R.P., and J.D. Corbett, 1989, J. Solid State Chem. **80**, 56.

Handbook on the Physics and Chemistry of Rare Earths
Vol. 28
edited by K.A. Gschneidner, Jr. and L. Eyring

Chapter 178

SOLID ELECTROLYTES

R. Vasant KUMAR[1] and Hiroyasu IWAHARA[2]
[1] *Department of Materials Science and Metallurgy, University of Cambridge, Cambridge CB2 3QZ, UK*
[2] *Centre for Integrated Research in Science and Engineering, Nagoya University, Nagoya 464, Japan*

Contents

List of symbols and abbreviations

A/F	air/fuel ratio	R	universal gas constant
AFC	alkaline fuel cell	SOFC	solid oxide fuel cell
HCs	hydrocarbons	SPFC	solid polymer fuel cell
emf	electromotive force	TWC	three-way catalyst
EVD	electrochemical vapor deposition	YBCO	$YBa_2Cu_3O_{7-y}$
F	Faraday's constant	YSZ	yttria stabilized zirconia
ISE	ion selective electrode	λ	operating A/F / stoichiometric A/F
Nasicon	Na super ionic conductor	σ	conductivity
PAFC	phosphoric acid fuel cell		

1. Introduction

One of the early applications of solid electrolytes was the Nernst glower proposed by Nernst as a new form of electric light (Nernst 1900). Zirconia doped with a rare-earth oxide (such as yttria) can become a conductor of oxygen ions at elevated temperatures resulting in emission of light when passing electric current through it. Interest in doped zirconia solid electrolytes intensified in the 1950s, following the launching of rockets for space research, for application in fuel cells.

Solid electrolytes have also been variously described as Fast Ionic Conductors or Superionic conductors and may cover ionic conductivities within the range of 10^{-5} to 1 S/cm with activation energies of 0.1 to 2 eV/atom. The levels of ionic conductivity achieved in many of these solid electrolytes are well below their melting points and the values are more typical of liquids than solids. In contrast to liquid electrolytes such as the aqueous electrolytic solutions or molten salts, the mobile ions in a solid are limited to one sublattice such that one ionic component can move through a rigid framework provided by the other components.

Fast ionic transport in solids has become a major area of both scientific investigations and technological applications. Until a few decades ago, solid-state ionic conductors were considered as exceptions in materials science and their discovery was seen as a fortuitous event. More recently, however, fast ionic conduction has been discovered or rediscovered, observed, studied and introduced synthetically in several hundreds of solid materials ranging from ceramics to glass and polymers (Geller 1977, Hagenmuller and Van Gool 1978, Chandra 1980, Tuller and Moon 1988, Laskar and Chandra 1991 and Iwahara 1995). Considerable research has focussed on the theory of ionic transport and its implication for solid state reactions such as corrosion, oxidation and sintering. Scientific interest has mainly been driven by applications in many technological areas such as fuel cells, batteries, sensors, electrolysis, electrochromics and displays, optical materials and environmental protection. Development of practical devices has in turn raised many interesting scientific and technological questions relating to transport of ions in solids, resulting in the emergence of the field of *solid-state ionics* as a major scientific area.

2. Ionic transport in solid electrolytes

Solid electrolytes are characterized by a high ionic conductivity with a low activation energy relative to "normal" defective solids. This requires the presence of a large concentration of charge carriers with high mobilities, such that the coulombically charged particles move rapidly among near-equivalent atomic sites or within a disordered host medium. High ionic conductivity in solids is achieved in a variety of ways as described below.

Some solid electrolytes such as α-AgI are characterized by a high degree of intrinsic disorder in the Ag^+ ion sublattice, resulting in a random distribution of Ag^+ ions over an excess number of equivalent sites, leading to ion hopping between crystallographic sites. Another striking feature of many such soft ionic crystals is the high entropy increase of a solid–solid phase transition which brings the material to a good conductivity phase. The values of entropy changes and the diffusion coefficient of the mobile ions are closer to those found in molten salts. A number of solid electrolytes such as β-alumina and CaF_2, on the other hand, reach high conductivity values without passing a first-order solid–solid phase transition.

In some other solid electrolytes, the intrinsic disorder is created as a consequence of forming a metastable phase, e.g. by rapid solidification of a melt to form a glass. Polymeric and glassy solid electrolytes comprise some of the most recent additions to solid-state ionics. Although there is no long-range order of any type, disorder in glasses and polymers far exceeds that in crystals. The entropy of the glassy state (supercooled liquid) is high and such electrolytes are deemed to have liquid-like properties.

In another group of materials, fast ionic conductivity is introduced extrinsically by doping. For example, addition of aliovalent Y_2O_3 to ZrO_2, not only stabilizes the cubic fluorite structure, but also leads to the formation of oxygen vacancies to compensate for the charge difference between Zr^{4+} and Y^{3+}. At high concentrations of the dopant, typically at 8–15 mol%, a considerable disorder is created in the oxygen sublattice, leading to ionic conductivity. A special case of extrinsic doping occurs in composite materials where high levels of charge carriers are created only at interfaces owing to the limited solubility of the insulating phase in the matrix of the ionically conducting phase, for example in the CaF_2–Al_2O_3 composite electrolyte.

3. The role of rare earths in solid electrolytes

In order for an ion to move easily in a solid, a special array of atoms (or ions) in the material is necessary. This array requires either several large clearances for the mobile ions or a number of lattice defects through which a certain ion can move. The former structure can be constructed by large ions as host constituents and the latter can be induced by the introduction of some dopants. Rare-earth ions act as host ions of the crystal lattice in the former case and as dopants in the latter.

In general, ionic radii of multivalent ions are small. The ionic radii of rare-earth elements, however, are relatively large, even if they are tri- or tetravalent and, furthermore,

Table 1
Typical solid electrolytes containing rare earth elements

Mobile ion	Solid electrolytes[a]	Notes: crystal structure etc.
O^{2-}	ZrO_2–Ln_2O_3, HfO_2–Ln_2O_3, CeO_2–Ln_2O_3, ThO_2–Ln_2O_3, CeO_2–MO (M = Ca, Sr, etc.)	Fluorite-type tetravalent oxide
	Bi_2O_3–Ln_2O_3,	Fluorite-type, rhombohedral-type bismuth sesquioxide
	$Zr_2Gd_2O_7$, $Zr_2Sm_2O_7$, $Ti_2Y_2O_7$, $Ti_2Sm_2O_7$	Pyrochlore-type
F^-	CaF_2–LnF_3, SrF_2–LnF_3, BaF_2–LnF_3	Fluorite-type
	LnF_3–MF_2 (M = Ca, Sr, etc.)	Tysonite-type
	La_2O_3–CaF_2, LaOF, ZrO_2–LnF_3	Oxyfluorides
H^+	(NaH) $GdSi_4O_{12}$	Nasicon-type
	$SrCe_{1-x}Ln_xO_{3-\delta}$, $BaCe_{1-x}Ln_x0_{3-\delta}$	Perovskite-type, in H_2 or H_2O at high temperature
Li^+	YPO_4–Li_3PO_4	Zircon-type
Na^+	Na_2SO_4–$Ln_2(SO_4)$	High-temperature phase
	$Na_3GdSi_4O_{12}$, $Na_3Sc_2P_3O_{12}$	Nasicon-type
Eu^{2+}	Eu–β″-alumina	Layer structure
Gd^{3+}	Gd–β″-alumina	Na^+-conductor? layer structure

[a] Ln, rare-earth element.

their valency in general is very stable. Rare-earth ions as the constituent of solid electrolytes have the following features: (1) they behave as stable trivalent cations with large ionic radii; (2) they provide different sizes of trivalent ions; (3) their electronegativity is rather small and they function as a constituent with strong ionicity; (4) they provide a variety of ions, for example, tetravalent or divalent ions which are stable under given conditions; and (5) they exhibit characteristics expected of 4f electrons. As rare-earth elements are all quite similar in their chemical properties, it may be possible to select the most appropriate ion for optimum properties such as conductivity and most favorable practical usage, without significantly affecting the chemical properties.

Rare-earth elements are vital constituents of many prominent solid electrolyte systems such as the oxygen-ion conductor in fluorite structures (Dell and Hooper 1978), the fluorine-ion conductor in tysonite-type trifluorides (Reau and Portier 1978), the protonic conductor in doped perovskite phases (Iwahara et al. 1981a), and the trivalent cationic conductor in hexagonal β-alumina-type compounds (Verstegen et al. 1973). Typical solid electrolytes containing rare-earth elements are listed in table 1. It is worth noting that rare-earth elements have a high profile in conferences directly concerned with solid electrolytes. If we consider the last two International Conferences on Solid State Ionics (held every two years in various locations around the world), of the 190 oral presentations and 260 posters in the last Conference, held in Singapore in December 1995, and the 360 oral presentations in the more recent conference held in Hawaii in November 1997,

more than one-third of the papers were directly concerned with solid-state ionic systems containing rare-earth elements.

4. Oxide ion conductors

4.1. *Extrinsic oxide ionic conductors*

Inorganic crystalline materials which exhibit oxygen-ion conduction are mainly found among the oxides of tetravalent cations which crystallize with the fluorite structure (e.g. CeO_2) or distorted fluorite structure (e.g. ZrO_2). Introduction of divalent or trivalent cations into the lattice stabilizes the cubic fluorite structure and also leads to the formation of oxygen-ion vacancies in order to retain charge neutrality. Oxygen-ion conduction occurs as a result of this defect structure.

4.1.1. *Zirconia electrolytes*

In a fluorite-type oxide, whose chemical formula is expressed as MO_2, the structure type is named after CaF_2, in which the cation/anion radius ratio is such that the anions achieve a simple cubic packing with the cations occupying half the available sites with 8-fold coordination. The packing of the anions is not as compact as those found in other oxides such as spinel or corundum-type structures, which have closest packing of oxide ions.

Pure zirconia has a distorted fluorite (monoclinic) structure at room temperature, which transforms to a tetragonal structure at above 1200°C and finally to a cubic form at >2300°C. The cubic fluorite form has a crystal structure as shown in fig. 1a. The exact transformation temperature and behavior are probably very sensitive to any impurity present and also influenced by hysteresis. If the Zr is partially replaced by a divalent or trivalent cation with relatively large ionic radius, the fluorite structure can be stabilized at lower temperatures. This "stabilized zirconia" is often metastable at room temperature and does not decompose to the thermodynamically stable phases.

Rare-earth elements are the most commonly used stabilizers in the zirconia electrolytes. Rare-earth oxides can dissolve in relatively large amounts in zirconia, and can thus substitute for tetravalent zirconium ions resulting in a large concentration of oxide-ion vacancies in order to compensate for the charge imbalance. In this "defect fluorite structure", the oxygen ions are mobile at elevated temperatures by an oxygen vacancy mechanism as shown in fig. 1b. Therefore the rare-earth stabilized zirconia is a good oxygen-ion conductor at elevated temperatures. In summary, the rare-earth elements dissolved in zirconia serve both as a stabilizer for the cubic fluorite structure and as a dopant to create oxygen-ion vacancies which are indispensable for ionic conduction.

When a rare-earth oxide, e.g. Y_2O_3, is dissolved in ZrO_2, the following defect equilibria can be expressed, using Kröger–Vink notation:

$$Y_2O_3 \leftrightarrow 2Y'_{Zr} + V^{\bullet\bullet}_O + 3O^x_O . \tag{4.1}$$

The addition of rare-earth oxides thus introduces oxygen-ion conductivity by affecting the defect equilibria. Increasing the concentration of dopant leads to an increase in the

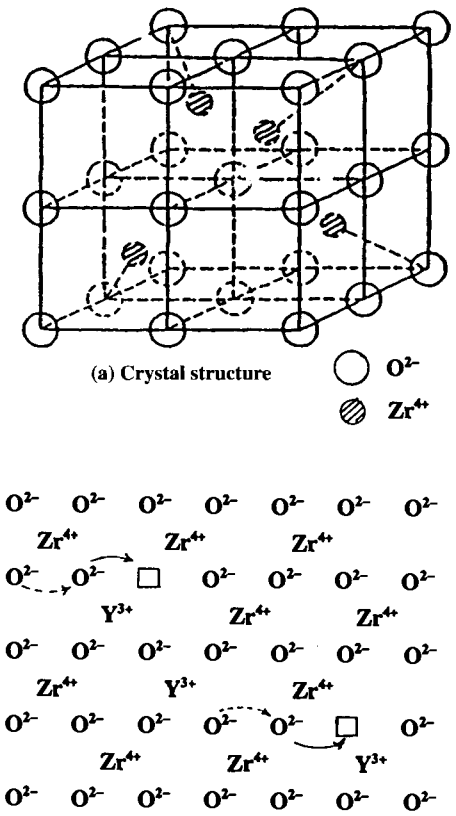

Fig. 1. Fluorite-type ZrO_2, its crystal structure; and oxide ion vacancies.

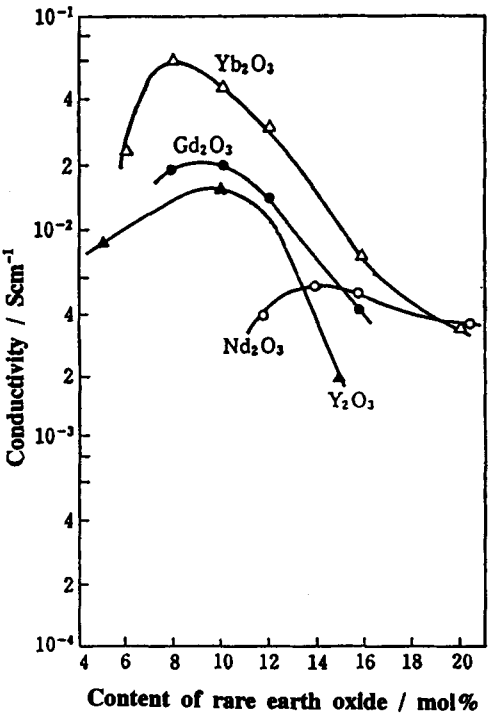

Fig. 2. Conductivities of rare-earth doped zirconias.

conductivity until a maximum is reached after which the conductivity begins to decrease, either limited by the solid solution range or due to the formation of vacancy clusters with lower mobility. This onset of substantial ordering in the defect structure not only leads to a decrease in the conductivity but also to an increase in the activation energy values. Ionic conductivity data at 1073 K for several rare-earth–zirconia systems are shown in fig. 2 (Tannenberger et al. 1965). The ionic radius of the dopant rare-earth element directly affects the value of ionic conductivity in zirconia as shown in fig. 3 (Adachi 1988). As the ionic radius is increased from that of Sc^{3+} at 1.12 Å to Nd^{3+} at 1.25 Å, the ionic conductivity at 1273 K is observed to decrease by almost an order of magnitude from 0.32 S/cm to 0.04 S/cm.

In the stabilized zirconia doped with a rare-earth oxide such as yttria, the vacancy concentration is determined by the dopant concentration, for a wide range of temperature and partial pressure of oxygen, as given by the equation

$$[V_O^{\bullet\bullet}] = \tfrac{1}{2}[Y]. \tag{4.2}$$

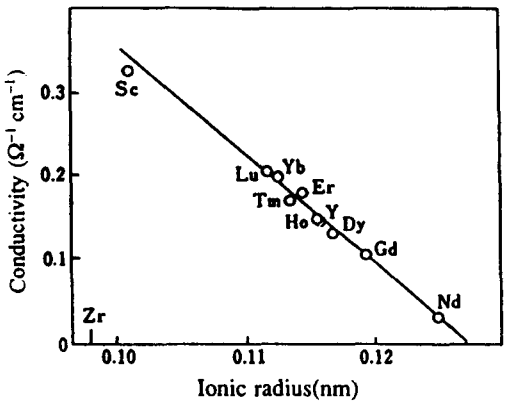

Fig. 3. Conductivity of rare-earth doped zirconia as a function of ionic radius. (Reprinted from Adachi 1988 by permission of the publisher, Elsevier Science Ltd.)

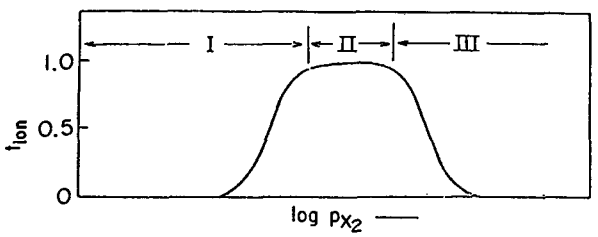

Fig. 4. A schematic representation of ionic transference number vs $\log p_{O_2}$.

At higher temperatures and low P_{O_2} values, n-type electronic conductivity may appear as a result of the following equilibria:

$$O_O^x \leftrightarrow \tfrac{1}{2}O_2(g) + V_O^{\bullet\bullet} + 2e', \tag{4.3}$$

while at high P_{O_2} values, p-type electronic conductivity may dominate as a result of the following equilibria:

$$\tfrac{1}{2}O_2(g) + V_O^{\bullet\bullet} \leftrightarrow O_O^x + 2h^{\bullet}. \tag{4.4}$$

Since electronic mobilities are usually much higher than ionic mobilities, the ionic conductivity can be dominant only when a very large concentration of ionic defects are present in the solid. For a given temperature, there is a range of P_{O_2} values within which eq. (4.2) is dominant, and the conductivity, predominantly ionic, is independent of oxygen pressures, as shown in fig. 4. This P_{O_2} range is referred to as the electrolytic or ionic domain of the solid electrolyte at that temperature. As the temperature is increased the electrolytic domain is diminished. A schematic representation of the electrolytic domain as a function of temperature for a typical oxide-ion conductor is represented in fig. 5. In order to operate a given oxygen-ion conductor as an useful solid electrolyte, it is important to know the ionic domain of the material. Areas close to the domain boundary represent mixed ionic and electronic conduction.

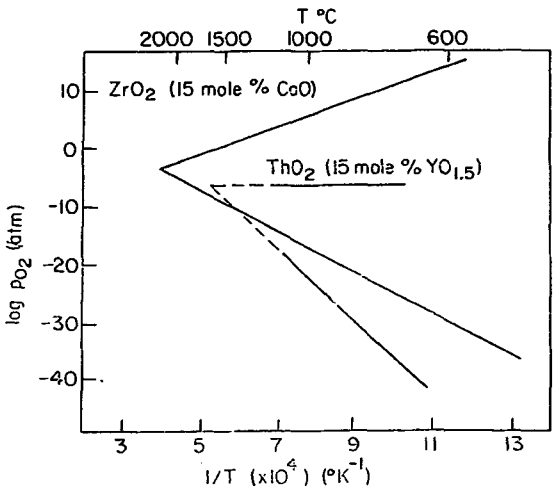

Fig. 5. Electrolytic domain of typical oxygen conducting electrolytes.

Among the zirconia systems, yttria-stabilized zirconia is the most familiar oxygen-ion conductor, with widespread practical applications in sensors (Seiyama 1988–94), oxygen pumps (Fouletier et al. 1975), fuel cells (Minn and Takahashi 1995), and steam electrolysers (Donitz and Erdle 1985). At a dopant concentration of around 8 mol% of Y_2O_3, the zirconia solid electrolyte can achieve a conductivity value of 10^{-1} S/cm at 1273 K with an activation energy of 0.8 eV.

4.1.2. *Ceria-based electrolytes*

The tetravalent cerium ion is large (1.01 Å) in ionic size compared to the zirconium ion (0.8 Å), and its dioxide CeO_2 crystallizes to a fluorite-type structure even at room temperatures and without the need for any stabilizers. Ceria can also dissolve a large concentration of trivalent rare-earth oxides, while retaining the fluorite structure. In the solid solution, when the trivalent rare-earth ions partially replace the tetravalent Ce^{4+}, a corresponding concentration of oxygen vacancies is created in a manner as described for the zirconia solid electrolytes. As shown in table 2, the conductivity of doped ceria is, in general, higher than that of stabilized zirconia. Figure 6 shows Arrhenius plots of conductivity of various ceria-based solid electrolytes, also comparing them with pure ceria and yttria-stabilized zirconia systems (Eguchi et al. 1992). It should be pointed out that the activation energies for the fluorite-type oxide ionic conductors fall within the range 0.6 to 1.4 eV and are relatively high in comparison with the truly fast ion conductors such as AgI-based electrolytes and some β-aluminas which exhibit room-temperature conductivities of 0.12 and 0.03 S/cm with activation energies of 0.07 and 0.15 eV, respectively.

The maximum value of conductivity for ceria-based electrolytes is attained at a certain concentration of the dopant oxides, in a manner similar to the zirconia electrolytes. As shown in fig. 7 (Takahashi and Iwahara 1966), the conductivity of CeO_2 doped with

Table 2
Conductivity of fluorite-type solid oxide electrolytes

Electrolyte	σ at 1273 K (S/cm)	Activation energy (eV)	Electrolyte	σ at 1273 K (S/cm)	Activation energy (eV)
10 mol% Y_2O_3–ZrO_2	0.1	0.8	8 mol% Y_2O_3–ThO_2	0.0048	1.1
10 mol% Sm_2O_3–ZrO_2	0.058	0.95	10 mol% La_2O_3–CeO_2	0.08	0.9
8 mol% Yb_2O_3–ZrO_2	0.088	0.75	15 mol% CaO–CeO_2	0.025	0.75
10 mol% Sc_2O_3–ZrO_2	0.25	0.65	10 mol% Gd_2O_3–CeO_2	0.5	0.7

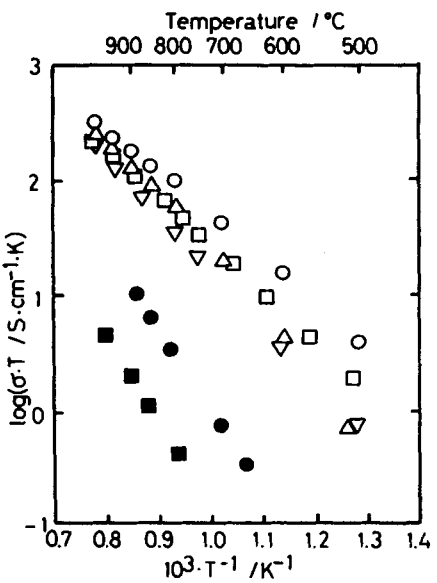

Fig. 6. Arrhenius plots for ionic conductivities of ceria-based oxides. (Reprinted from Eguchi et al. 1992 by permission of the publisher, Elsevier Science Ltd.)

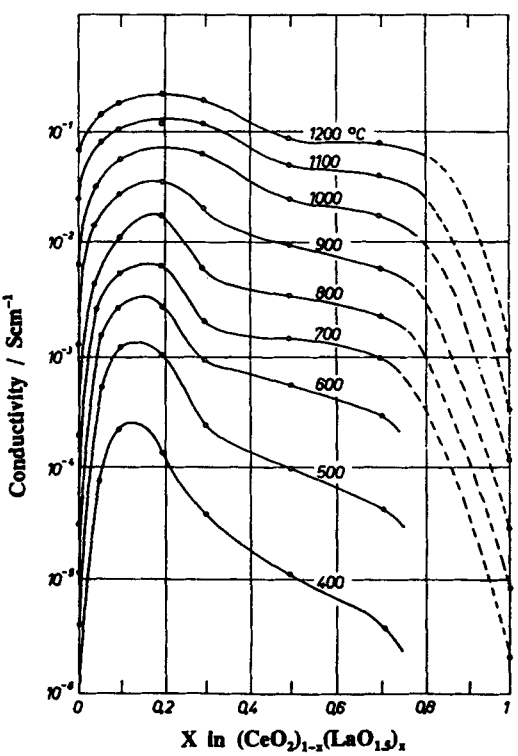

Fig. 7. Conductivities of $(CeO_2)_{1-x}(LaO_{1.5})_x$ in air.

$LaO_{1.5}$ reaches a maximum value at about 20 mol% of the dopant concentration, although the upper limit of solid solution formation range extends far beyond this value. The association of oxide-ion vacancies at high concentrations leads to a decrease in the mobility of the vacancies, which in turn diminishes progressively the effect of increased concentration (Anderson et al. 1983). The lattice parameters of defect fluorite-type CeO_2 change monotonously with the dopant content, i.e. with the concentration of oxygen vacancies. It is possible to change the lattice parameter of the defect fluorite CeO_2, at

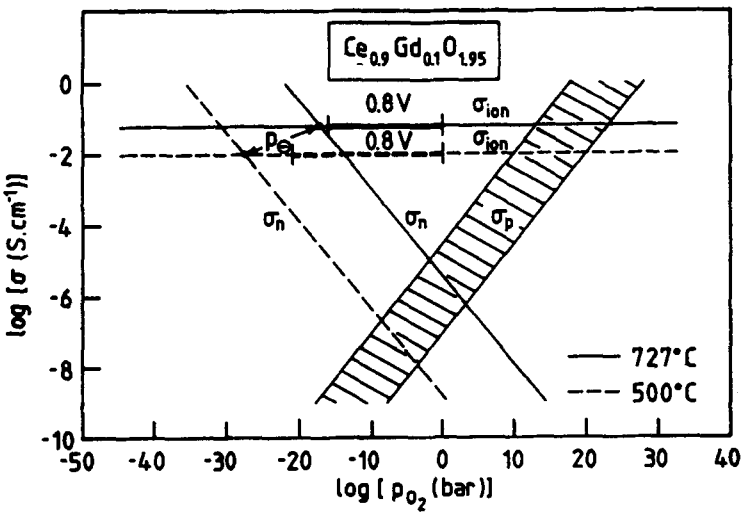

Fig. 8. Ionic and electronic conductivities of CeO_2–$GdO_{1.5}$ (10 mol%) at 773 and 1000 K. (Reprinted from Steele et al. 1994 by permission of the publisher, The Institute of Energy, London.)

a fixed concentration of vacancies, by using different rare-earth ions. For example, in the ternary system $(CeO_2)_{1-(x+y)}(GdO_{1.5})_x(YO_{1.5})_y$, the lattice parameter can be controlled by changing the contents of Gd and Y respectively. An increase in Gd content (x) results in an increase in the lattice constant, while an increase in Y content (y) leads to a decrease in the lattice constant. It was found that at $x = 0.09$ and $y = 0.01$, the lattice constant of the doped CeO_2 is identical to that of the non-doped (pure) CeO_2 and that the conductivity exhibits a maximum value in this system (Zhen et al. 1987). This opens up the prospect of designing the size of crystal lattice and the concentration of defects in the oxide-ionic conductors by using a combination of trivalent rare-earth ions with similar chemical properties. Ceria can also dissolve divalent alkali-earth oxides such as SrO and CaO resulting in ionic conductivity at elevated temperatures (Yahiro et al. 1986).

The electrolytic domain for a ceria-based electrolyte, at any given temperature, is narrower than that of a zirconia-based electrolyte, such that electronic conductivity is acquired in reducing atmospheres. As shown in fig. 8 (Steele et al. 1994), the electrolytic domain of CeO_2–$GdO_{1.5}$ (10 mol%) at 1000 K is such that the electrolyte is not suitable for use at oxygen pressures below 10^{-10} atm. The high ionic conductivity, however, makes the electrolyte of considerable interest at low temperatures and/or in environments of moderate oxygen potential.

4.2. *Intrinsic oxygen ionic conductors*

4.2.1. *Bi_2O_3-based electrolytes*

Bi_2O_3 is monoclinic at room temperature, and exhibits electronic conductivity. On heating to 1050 K, Bi_2O_3 undergoes a phase change to a cubic fluorite structure (δ-Bi_2O_3), which

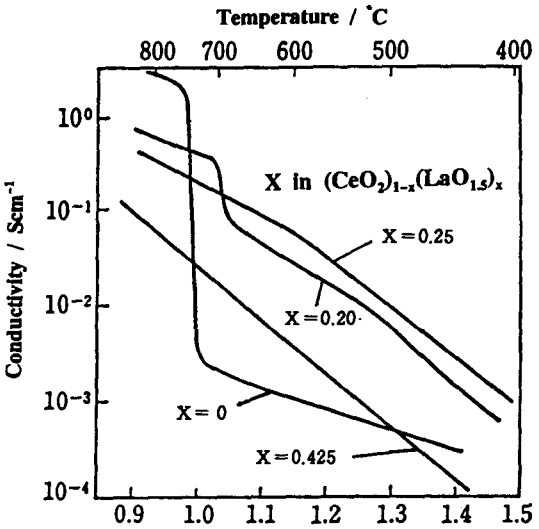

Fig. 9. Conductivities of $(Bi_2O_3)_{1-x}(Y_2O_3)_x$.

is highly disordered with $\frac{1}{4}$ of the oxygen lattice sites vacant. It is this high concentration of defects which is directly responsible for the high oxygen-ionic conductivity of >1 S/cm at $T > 1050$ K. The formation of δ-Bi_2O_3 can be expressed as $BiO_{1.5}\square_{0.5}$ (where $\square$ represents a vacancy in the oxygen site). The conductivity of this phase is the highest of all known oxygen-ion conductors. However, at $T < 1050$ K, the monoclinic phase of pure Bi_2O_3 has a low conductivity, at least three orders of magnitude lower than that of the high-temperature cubic phase.

Addition of heavy-rare-earth or yttrium oxides stabilizes the high-temperature cubic phase of Bi_2O_3 and, as shown in fig. 9 for the Bi_2O_3–Y_2O_3 system, the oxide-ion conductivity can be kept at a high level even at temperatures far below 1050 K (Takahashi et al. 1975a, Harwig and Gerards 1978 and Verkerk et al. 1982). Even if trivalent rare-earth ions are partially substituted for Bi, $\frac{1}{4}$ of the oxygen-ion sites in the fluorite-type lattice is still vacant as in the case of pure Bi_2O_3. In order to maintain this structure at low temperatures, it is necessary for the array of ions to distort. By partially replacing some of the Bi with Y, it has been shown, using neutron diffraction analysis, that the oxygen ions are shifted from their ideal position of the fluorite sublattice towards the oxygen vacancy site (Infante et al. 1987).

Addition of 10–30 mol% of light-rare-earth cations with large ionic radii to Bi_2O_3 produces a solid solution phase with a rhombohedral crystal structure called "sillenite". This kind of solid solution exhibits relatively high conductivity at elevated temperatures (Takahashi et al. 1975b, Iwahara et al. 1981b). The crystal structure is formed by slightly squashing the defect fluorite-type structure along the diagonal axis, and the conduction is based on a vacancy mechanism similar to that of the defect fluorite oxides. Substitution of Bi by rare-earth cations of medium ionic radii also leads to the formation of the rhombohedral phase in the 10–30 mol% composition range, but at

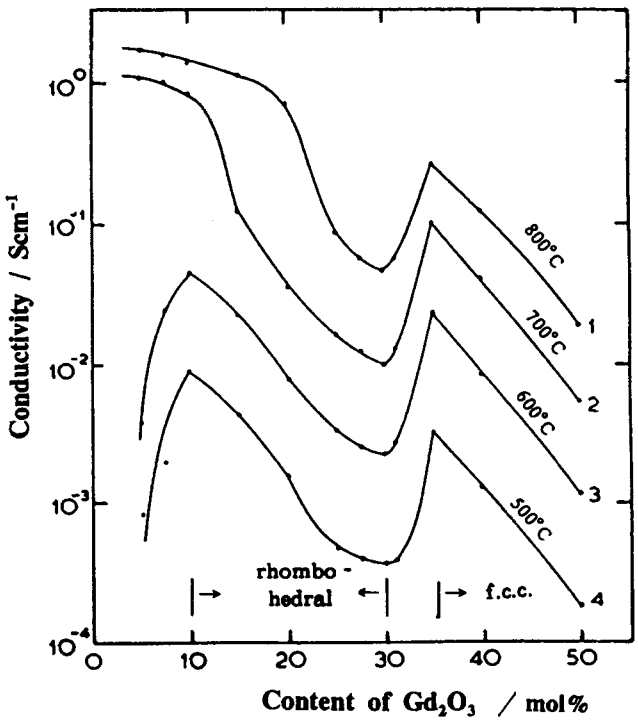

Fig. 10. Conductivities of sintered oxides of the system Bi_2O_3–Gd_2O_3. (Reprinted from Takahashi et al. 1975a by permission of the publisher, Kluwer Academic Publishers.)

higher concentration a face-centred cubic solid solution phase is formed. Both phases exhibit oxygen-ion conductivity, and the conductivity is a function of the composition, achieving a maximum value near the lower solubility limit within each phase, as is shown in fig. 10 for the Bi_2O_3–Gd_2O_3 system (Takahashi et al. 1975a). Within each of the solid solution phases, the conductivity decreases with increasing concentration of rare-earth element, suggesting that the rare-earth ions themselves do not directly contribute to the movement of oxygen ions, but serve as a constituent to support the framework which makes the oxide ion mobile. The stable regions of both the rhombohedral and the face-centred cubic solid solutions are shown in fig. 11 as a function of composition and ionic radius of the rare-earth cations (Iwahara et al. 1981b).

Despite their high ionic conductivity, the Bi_2O_3-based solid electrolytes are not widely used in practice, as they are easily reduced under a reducing atmosphere to form Bi metal, especially at higher temperatures, and because of their poor mechanical properties. However, their application in oxygen sensing at high oxygen pressures, and for oxygen extraction from air has been considered (Vinke et al. 1989). Mischmetal rare-earth oxide as a dopant component has also been considered (Hu et al. 1988).

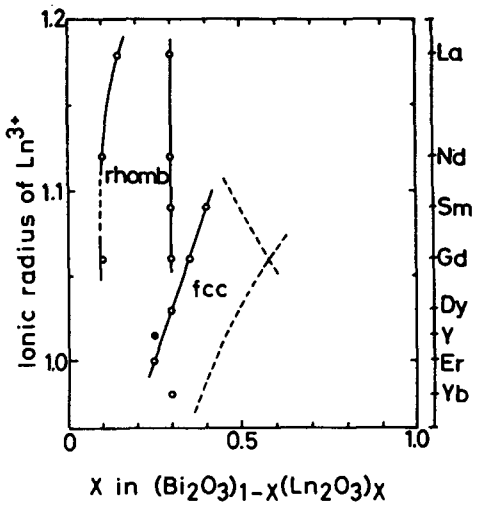

Fig. 11. Formation range of the rhombohedral and fcc phases in the ionic radius of Ln^{3+} versus composition diagram. (Reprinted from Iwahara et al. 1981b by permission of the publisher, Academic Press.)

4.2.2. *Pyrochlore-type oxide*

The pyrochlore structure has a cubic unit cell with a lattice constant of ~10 Å and the general formula $A_2B_2O_7$. It forms a superstructure of the defect fluorite structure with ordering on both the cation and anion sublattice. A map of the $(A^{3+})_2(B^{4+})_2O_7$ pyrochlore stability field has been constructed as a function of the radii of the A^{3+} and B^{4+} cations using IR spectroscopy data (Moon and Tuller 1987) as shown in fig. 12. A particularly interesting example of a pyrochlore oxygen-ion conductor is the $Gd_2(Zr_xTi_{1-x})_2O_7$ system as it exhibits a large increase in conductivity as the composition is varied from $Gd_2Ti_2O_7$ to $Gd_2Zr_2O_7$. This is attributed to structural disorder which results in an increased mobile oxygen vacancy concentration (Tuller and Moon 1988). At $x > 0.4$, the structure acquires substantial intrinsic disorder. The $Gd_2(Zr_xTi_{1-x})_2O_7$ system varies from extrinsic ionic conductivity at low Zr contents, where doping is required to produce substantial oxygen defects, to an intrinsic oxygen ionic conductivity at high Zr content, where conductivity is unaffected by doping. If the composition shifts from the stoichiometric ratio, the number

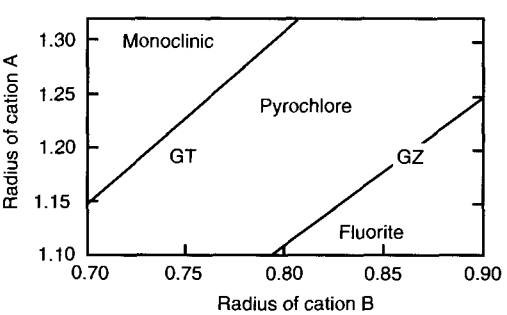

Fig. 12. The pyrochlore structure stability as a function of cation radii. (Redrawn after Moon and Tuller 1987 by permission of the publisher, Elsevier Science Ltd.)

of vacancies changes and the ordering of oxygen vacancies breaks down. As a result, the vacancies can occupy various sites in the lattice resulting in disordered state of oxide ions. This implies that oxide ions can move easily among the oxygen sublattice. It is reported that in systems such as TiO_2–Y_2O_3 and ZrO_2–Gd_2O_3 such a shift in the composition resulted in increasing conductivity due to the appearance of mobile oxygen vacancies (Mizutani et al. 1976, Miyauchi et al. 1981, van Dijk et al. 1980).

4.3. *Mixed oxygen-ion/electron conductors*

A perovskite-type oxide ABO_3 consists of a large cation A and a small cation B, such that the sum of the valences of A and B is 6. Either both A and B are trivalent cations, e.g. $LaAlO_3$, or A is divalent and B is tetravalent, e.g. $CaZrO_3$. The large cation A can combine with the oxygen ions to form a close-packed cubic structure, with the smaller (and perhaps more highly charged) B ions in the octahedral interstices, as shown in fig. 13 (Kingery 1980), coordinated to 6 oxygen ions. The large A cation, on the other hand, has 12-fold oxygen coordination. If either A or B cation is partially substituted by a cation of lower valency, and if the host ions cannot increase their valence to restore electrical neutrality, then it is most likely that oxygen-ion vacancies are created, giving rise to oxygen-ion conductivity. Several perovskite-type mixed oxides have been investigated in the last three decades, and in general, pure ionic conductivity is observed only under reducing conditions, and the oxides exhibit p-type and oxygen-ion mixed conductivity at most oxygen partial pressures (Takahashi and Iwahara 1967, Iwahara 1992). For example, the ionic conductivity in Sr-doped La cobaltite (such as $La_{0.7}Sr_{0.3}CoO_3$) is comparable to that of stabilized zirconia, while the p-type electronic conductivity is 3–4 orders of magnitude higher than the oxygen-ion conduction. A series of alkali-earth-doped rare-earth cobaltites and manganites belong to this class of conductors.

Another class of mixed perovskite oxides, such as Ca-doped $LaAlO_3$ (for instance, $La_{0.7}Ca_{0.3}AlO_3$), exhibits ionic conductivity $>10^{-2}$ S/cm at 1273 K, comparable to the above system, while the electronic conductivity is not as high. The transport number of ionic transport is >0.5 in air at 1273 K, which increases as oxygen partial pressure is decreased. Recently, $LaGaO_3$-based solid solutions were reported to be highly conductive oxygen-ion conductors, conductivities being higher than that of stabilized zirconias (Ishihara et al. 1994). A typical example is $La_{0.9}Ca_{0.1}Ga_{0.9}Mg_{0.1}O_3$ which has a wide ionic domain ranging from air to $P_{O_2} = 10^{-20}$ atm at 1273 K (Ishihara et al. 1996).

Another interesting defect perovskite material exhibiting large shifts in the electronic/ionic character is $YBa_2Cu_3O_{7-y}$, the first material to exhibit superconductivity at temperatures above the boiling point of liquid nitrogen (Wu et al. 1987). In the superconducting phase, which is orthorhombic, seven out of the nine oxygen sites of the perovskite structure may be occupied if the structure was filled up completely. Two-thirds of the copper (Cu II) atoms form sheets of corner-shared square planes, while the remaining 33% of the copper (Cu I) atoms form chains of corner-shared square planes along the longer orthorhombic direction, as shown in fig. 14. Transition to the non-superconducting tetragonal phase occurs by removing O from the Cu–O chain, leaving

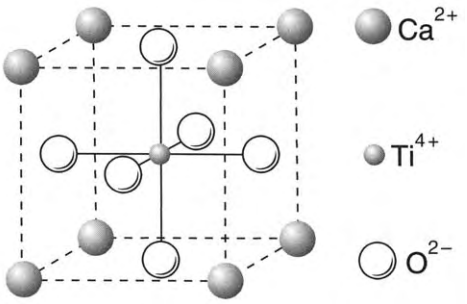

Fig. 13. An idealized perovskite structure. (Redrawn after Kingery 1980 by permission from the publisher, John Wiley & Sons, Inc.)

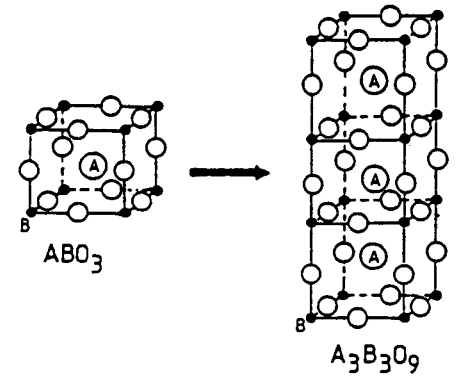

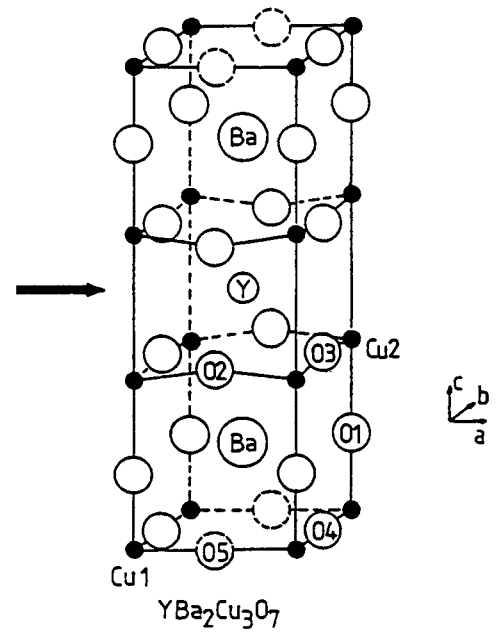

Fig. 14. The (123) crystal structure of YBCO from the simple perovskite structure.

Cu(I) in two-fold coordination. The redox chemistry occurs in the Cu(I) plane by a formal change of the oxidation state of Cu(I) between Cu^{3+} ($y=0$) and Cu^{+} ($y=1$). $YBa_2Cu_3O_{7-y}$ is a highly disordered ionic crystal with a high oxygen-ionic conductivity at $T > 750\,K$, accompanied by a large shift of electronic character from semiconducting to metallic properties (Kumar et al. 1993).

5. Fluoride-ion conducting solid electrolytes

The small size of the F^- ion as well as its single charge make it a good candidate for an ionic conductor. Rare-earth elements can act as a dopant or a host cation for

halide-ion conducting solid electrolytes. The fluorite-type fluorides doped with rare-earth elements, and trifluorides of rare-earth element with tysonite-type structure are known to be fluoride-ion conductors. Since O^{2-} and F^- ions have similar ionic radii, oxygen ions can readily substitute for the fluoride ions in an ionic lattice, resulting in non-stoichiometry which can affect the transport properties. Therefore it is important to carefully control the composition of the fluoride electrolytes.

5.1. *Fluoride solid electrolytes with fluorite-type structure*

It is well known that difluorides of alkali-earth elements doped with monovalent cations are good fluoride-ion conductors at elevated temperatures. CaF_2 doped with NaF (e.g. at 5 mol%) is a typical example (Nagel and O'Keeffe 1976). In this material, the fluoride ions can move via vacancies in the fluorine site, in a manner analogous to oxygen transport in stabilized zirconia electrolytes. Trivalent rare-earth ions can also act as dopants. CaF_2 doped with up to 25 mol% of YF_3 is an example of a such a solid electrolyte (Nagel and O'Keeffe 1976), which achieves a fairly high conductivity at elevated temperatures as shown in fig. 15.

Replacing divalent calcium ions with trivalent yttrium ions in the cationic sublattice results in excess fluoride ions, which are situated in the interstitial sites of the anionic sublattice. The interstitial fluoride ion thus generated can move through both the normal and the interstitial sites, leading to an increase in ionic conductivity with increasing concentrations of the rare-earth fluoride dopant. As the mobility of the interstitial fluoride

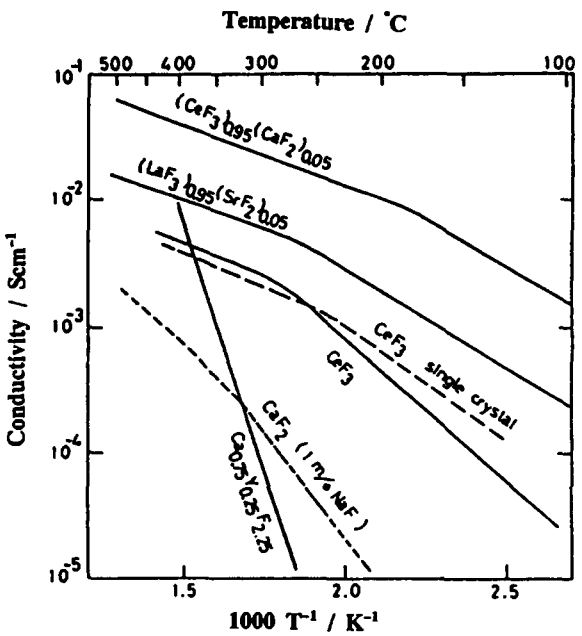

Fig. 15. Conductivities of rare-earth fluorides.

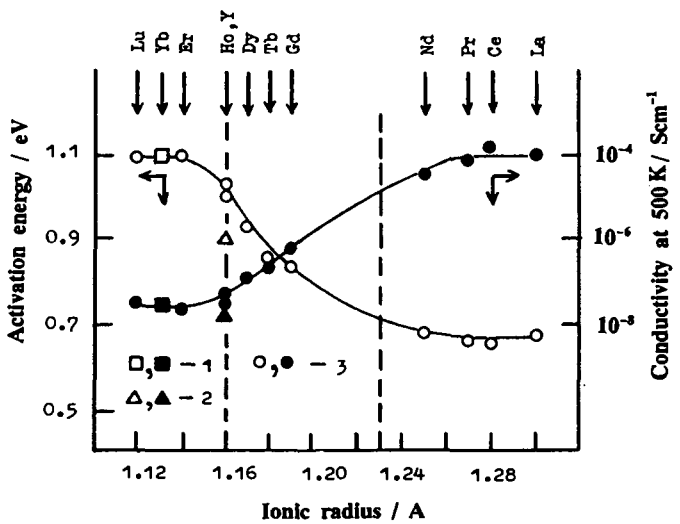

Fig. 16. Fluoride ion conductivity and activation energy as a function of ionic radius of Ln in $Sr_2Ln_{0.2}F_{2.2}$.

ions is lower than that of fluoride ions through vacancies, the activation energy for the interstitial mechanism is higher than that for the vacancy mechanism. The total ionic conductivity of a solid electrolyte is a product of charge, mobility and the concentration of the charge carriers. The number of charge carriers in rare-earth doped fluorides with the fluorite structure is much larger than in monovalent fluoride-doped fluorites, as the solubility for the rare-earth fluorides is much higher than for the monovalent-doped fluorides in the CaF_2. As a result, the conductivity of rare-earth doped CaF_2 can be higher than in the case of monovalent-doped CaF_2, especially with increasing temperatures.

Solid solutions based upon SrF_2 or BaF_2 with rare-earth fluoride as a dopant are also known to be good fluoride-ion conductors. Fluoride-ion conductivity and the corresponding activation energy have been investigated for $Sr_{1-x}R_xF_{2+x}$ as a function of the ionic radius of R (Ivanov-Shits et al. 1989). As shown in fig. 16, relatively high and almost identical conductivity values are obtained for light rare-earth dopants La to Nd ($\sigma = 10^{-4}$ S/cm at 500 K) with correspondingly low activation energy value at ~0.7 eV. In contrast, with the heavier rare-earth dopants Er to Lu, the conductivity of SrF_2 is lower by two orders of magnitude, while the activation energy is higher at 1.1 eV. The intermediate rare-earth dopants Gd–Ho and Y produce effects which are in between the above values.

5.2. *Rare-earth fluorides*

Rare-earth fluorides exist either as hexagonal (LaF_3) or as orthorhombic structures (β-YF_3), as shown in fig. 17 for rare-earth fluorides with La to Lu (Thomas and Brunton 1966). Fluorides of the rare-earth elements La to Nd crystallize in the tysonite structure at all temperature ranges below the melting point. SmF_3 to GdF_3 are orthorhombic at lower

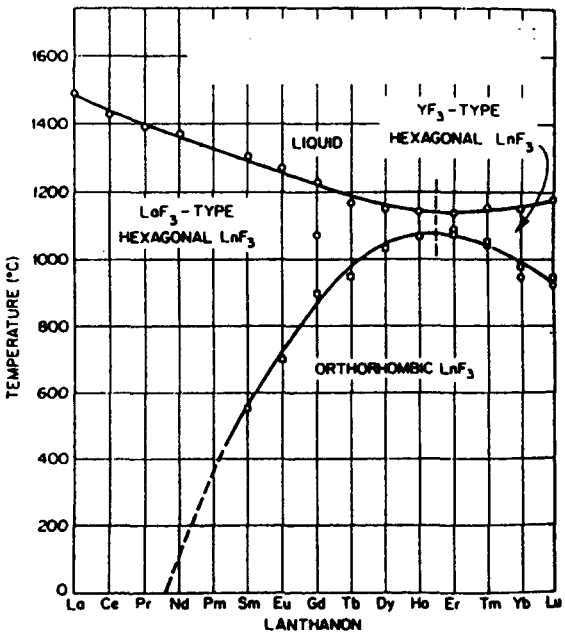

Fig. 17. Dimorphism among the rare-earth trifluorides.

temperatures and undergo a phase transition to the tysonite structure on heating. The tysonite stability ranges for TbF_3, DyF_3 and HoF_3 are very narrow (10–20 K) between the orthorhombic and the liquid phase. From Er to Lu (and Y), the β-YF_3 form changes to a hexagonal α-YF_3 form at a temperature just below the melting point. It has been found that only rare-earth fluorides in the hexagonal form are good fluoride-ion conductors (Adachi and Imanaka 1995).

5.2.1. *Tysonite-type fluorides*

As described in the previous section, trifluorides of light rare-earth elements such as LaF_3 and CeF_3 crystallize to a tysonite-type structure and are stable from room temperature to their respective melting points at 1480 and 1410 K. The tysonite structure has a hexagonal symmetry, the coordination number being 11 for the cations. All the fluoride ions are not equivalent, in fact 3 types of fluoride ions have been identified in the structure. As shown in fig. 18 the packing of fluoride ions is somewhat sparse and therefore can readily form vacancies due to Schottky-type lattice defects. Thus, this type of fluoride can exhibit fluoride-ion conduction at elevated temperatures even in the pure, non-doped state. Conductivity studies have revealed a strong dependence upon the frequency in the range 400–800 K, which has been ascribed to the electrode contribution (Reau and Portier 1978). Enhancement in conductivity is obtained when some difluoride is added to the tysonite rare-earth trifluoride, due to increase in vacancy concentrations (Takahashi et al. 1977, O'Keeffe 1973). As shown in fig. 15, the conductivities of CeF_3 and LaF_3 increase by several orders of magnitude as a result of doping with 5 mol% of CaF_2 or SrF_2.

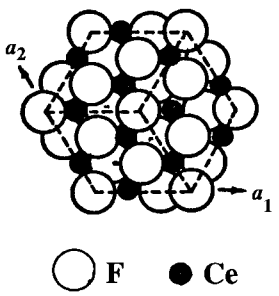

Fig. 18. Crystal structure of a tysonite-type fluoride.

5.3. *Oxyfluoride solid electrolyte*

Oxyfluorides can be prepared by reacting an oxide and a fluoride at elevated temperatures in air. For example, LaOF readily forms on heating La_2O_3 and LaF_3 in air at 1100 K. Ionic conductivity appears on doping LaOF with difluorides. Ionic conductivity is also reported for solid solutions of fluoride–oxide systems such as CaF_2–La_2O_3 (Pelloux et al. 1973, Iwahara and Esaka 1984). It is still not clear to what extent oxygen-ion conduction is significant in the total ionic conduction otherwise dominated by fluoride-ion conduction (Takashima and Kano 1987). Following experimental work with these materials, it was concluded that fluoride ions are the charge carriers and can mask any oxygen-ion conductivity due to the difference in mobility between fluoride oxygen ions (Iwahara and Esaka 1984). However, recently, $Nd_2Eu_2O_3F_6$ was reported to be an oxide-ion conductor, although it was readily hydrolyzed to form $Nd_2Eu_2O_4F_4$ at elevated temperatures in humid air (Takashima et al. 1996).

6. Cation conductors

It has usually been assumed that trivalent ionic transport in solid electrolytes will be insignificant and therefore rare-earth cationic conductors may not be readily observed in solid materials. Although ionic conductivity for the trivalent lanthanides is very low at room temperature, significant values are reported at higher temperatures for rare-earth-containing β-aluminas (Verstegen et al. 1973, Farrington et al. 1983, Warner et al. 1996, Kumar 1997), $LaNb_3O_9$ (George and Virkar 1988) and $Sc_2(WO_4)_3$ (Imanaka et al. 1995).

At this stage solids with trivalent rare-earth ionic conduction should be considered as exceptions. On the other hand, rare-earth elements are effective as a constituent of cationic solid electrolytes, serving either as a large-size framework ion in the lattice or as an aliovalent dopant ion.

6.1. *Proton conductors*

Since the discovery of conductivity in ice in the last century, proton transport in solids has aroused great scientific interest. Synthesis of Nafion Perfluorocarbon sulphonic acid poly-

mers with fast protonic conduction [$\sigma(300\,K) = 0.05$ S/cm] for the Gemini-Fuel cell program in 1972 has led to a major research and technological interest in proton conductors. In recent years proton transport has been discovered in several dozens of solid materials comprising inorganic crystalline, amorphous, polymeric, gels and hydrated solids (Colomban 1992). Rare-earth elements are important constituent of several proton conductors.

Protonic conduction is a particular case of ionic conduction, except that the small dimension of the proton might suggest some similarities with electronic conduction. In solids, protons can react strongly with the surrounding environment due to the absence of electron shells surrounding the nucleus. For example, in metals, protons interact with conduction electrons such that proton transport is associated with polarization of electrons. In electronic insulators and semiconductors, protons can penetrate the valence shell to form covalent bonds. Protons can also be solvated by oxygen, water or ammonia to form ions such as OH^-, H_3O^+ or NH_4^+. Therefore, the conducting species in protonic conductors may be protons, oxonium, ammonium, hydrazinium or hydroxyl groups.

An accepted classification of proton conductors is based upon the conductivity mechanism: (i) defect mechanism in anhydrous compounds, e.g. in KH_2PO_4; the activation energy is high and proton conduction occurs by interstitial or vacancy mechanisms; (ii) ionic jumps in loosely packed structures, e.g. in H_3O^+ or NH_4^+ β-aluminas. Such materials also are associated with high activation energies and acquire considerable conductivity at higher temperatures: although the rigid lattice is not much affected, the dynamic disorder of mobile species takes over; (iii) quasi-liquid state bulk conduction inside the structure (e.g. Hydrogen Uranyl Phosphate) or surface conduction at interfaces (as in gels or particular hydrates). In many systems, several mechanisms can operate simultaneously.

6.1.1. *Low-temperature protonic conductors*

Protonic conductors which may operate at temperatures lower than ~450 K include hydrates of cerium oxide (Slade et al. 1987), cerium hydrogen phosphate hydrates (Casciola et al. 1988), hydroxides of rare-earth elements (Yamamota et al. 1985, Yamashita et al. 1988), and rare-earth doped Nasicon-type compounds (Gulens et al. 1988). These are typically surface conductors, involving quasi-liquid state conduction. In these systems, where a surface film of "water" is responsible for the conductivity, the materials have been described as "particle hydrates". The partial pressure of water vapor (p_{H_2O}) has a strong influence on both the water content in the hydrates as well as the conductivity. In the case of $CeHPO_4 \cdot nH_2O$ for example, the value of n changes from 0 to a maximum of 4, while the specific conductivity (σ) increases almost exponentially from 10^{-7} to 10^{-3} S/cm as p_{H_2O} changes from dry atmosphere to 100% relative humidity at room temperature. The conductivity values remain low ($<10^{-5}$ S/cm) until a relative humidity of 80% is achieved.

6.1.2. *Protonic defects in oxides*

As early as 1966, Stotz and Wagner reported the existence of protons in Cu_2O, NiO and ZrO_2 at high temperatures in presence of water vapor (Stotz and Wagner 1966). Such

defects have also been reported in other oxides such as Sn-doped ThO_2 (Shores and Rapp 1972), SiO_2 (White 1970), $LaYO_3$ (Takahashi and Iwahara 1980) and hydroxyapatites (Takahashi et al. 1978). When the source of hydrogen is water vapor in the atmosphere, the following equilibrium is assumed:

$$H_2O(g) + V_O^{\bullet\bullet} \leftrightarrow 2H_i^{\bullet} + O_O . \tag{6.1}$$

The protons can be bonded to oxygen ions on normal lattice sites and the corresponding defects are either hydroxide ions, $OH^{\bullet}$ or interstitial protons, $H_i^{\bullet}$. In stoichiometric oxides, protons may determine the charged defects and be counterbalanced by electrons or any other negatively charged point defects. When protons dominate, the defect-related properties such as electrical conductivity, hot corrosion, sintering and creep are likely to be water-pressure dependent.

These studies on the above materials did not however, provide a direct evidence for high-temperature protonic conduction in oxide materials. A conclusive demonstration for high-temperature protonic conduction in oxides was first reported in 1981 by Iwahara et al. (1981a) for rare-earth doped perovskite oxides.

6.1.3. *High-temperature proton conductors*

The discovery of proton conduction in $SrCeO_3$ doped with rare earths such as trivalent Yb, when treated in hydrogen and/or water vapor (Iwahara et al. 1981a), opened up a new class of ionic conductors in which protons, present only as a minor constituent, can migrate by a simple hopping mechanism, in contrast with the low-temperature protonic conductors in which hydrogen is a major constituent and its transport involves complex mechanisms.

Undoped $SrCeO_3$, $BaCeO_3$, $SrZrO_3$ or $CaZrO_3$ perovskite materials which are normally low-conductivity electronic semiconductors, acquire extended oxygen-ion conduction when doped with aliovalent cations of rare earths such as Nd(III), Yb(III) or Gd(III) (Iwahara et al. 1981b, Iwahara 1992). The electrolytic domain for oxygen-ion conductivity is fairly narrow, such that, depending upon the temperature and the dopant concentration, n-type semiconductivity is exhibited at low P_{O_2} and p-type at high P_{O_2} values (such as in air for example). Remarkably, when these doped materials are exposed to hydrogen or water vapor gaseous atmosphere at elevated temperatures, protonic conductivity is introduced at the expense of electronic conductivity through the following mechanisms:

In hydrogen:

$$V_O^{\bullet\bullet} + \tfrac{1}{2}O_2(g) \leftrightarrow 2h^{\bullet} + O_O , \tag{6.2}$$

$$H_2 + 2h^{\bullet} \leftrightarrow 2H_i^{\bullet} . \tag{6.3}$$

In water vapor:

$$H_2O(g) + V_O^{\bullet\bullet} \leftrightarrow 2H_i^{\bullet} + O_O \quad \text{or} \tag{6.4}$$

$$H_2O(g) + 2h^{\bullet} \leftrightarrow 2H_i^{\bullet} + \tfrac{1}{2}O_2(g) . \tag{6.5}$$

Protons, because of their small size, do not occupy lattice positions, but rather attach themselves to negative ions. The conduction mechanism of proton in these oxides is

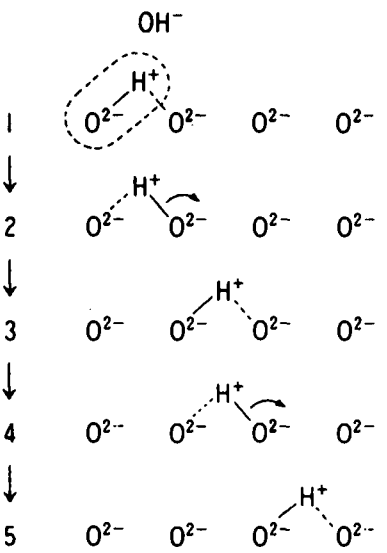

Fig. 19. Proton migration in a perovskite-type oxide. (Reprinted from Uchida et al. 1983 by permission of the publisher, Elsevier Science Ltd.)

considered to be hopping mechanism of protons moving from one oxygen to the next as illustrated in fig. 19. H_i is in fact better described as $(OH)_O$. Since the hole concentration in the doped perovskite appears to directly influence the protonic conductivity, it may be important to choose a dopant which increases the p-type conductivity. Of the rare-earth elements Yb, Y, Sc, Nd and Gd, the element Yb^{3+} has a ionic radius closest to that of Ce^{4+} and therefore it has been suggested that Yb might be the best candidate for doping (Uchida et al. 1983). Several investigators have reported results from dc transport number determination (Kosachi and Tuler 1995, Iwahara 1992), ac conductivity (Iwahara et al. 1991a), impedance spectroscopy (Bananos et al. 1988), and open circuit voltage measurements (Sutija et al. 1995). These results confirm the presence of protonic conductivity in doped perovskites under hydrogen or water vapor atmospheres at $T > 750$ K. At temperatures >1100 K, electronic conductivity may become significant.

The conductivities of typical perovskites of this type in a hydrogen atmosphere are presented in fig. 20 (Iwahara 1995). Of these, $BaCeO_3$-based perovskites show the highest conductivity, but oxygen ions contribute to the conduction as the temperature is raised, and the transport number of protons decreases with increasing temperatures (Iwahara et al. 1991a, 1993). For example, when a ceramic disc of $BaCe_{0.9}Nd_{0.1}O_{3-\alpha}$ is exposed to hydrogen on one side of the disc and air on the other (fuel cell conditions), the transport number of protons changes from 0.8 at 973 K to 0.2 at 1273 K. Although the conductivity of $SrCeO_3$-based perovskites is relatively low (~0.01 S/cm at 1273 K), the transport number of protons is higher than that of $BaCeO_3$-based systems. The increase in activation energy at approximately 1100 K, as indicated by the change in slope in Arrhenius plots of conductivity for both the above systems, may be associated with a transition from protonic to oxygen ion conduction (Kumar et al. 1996).

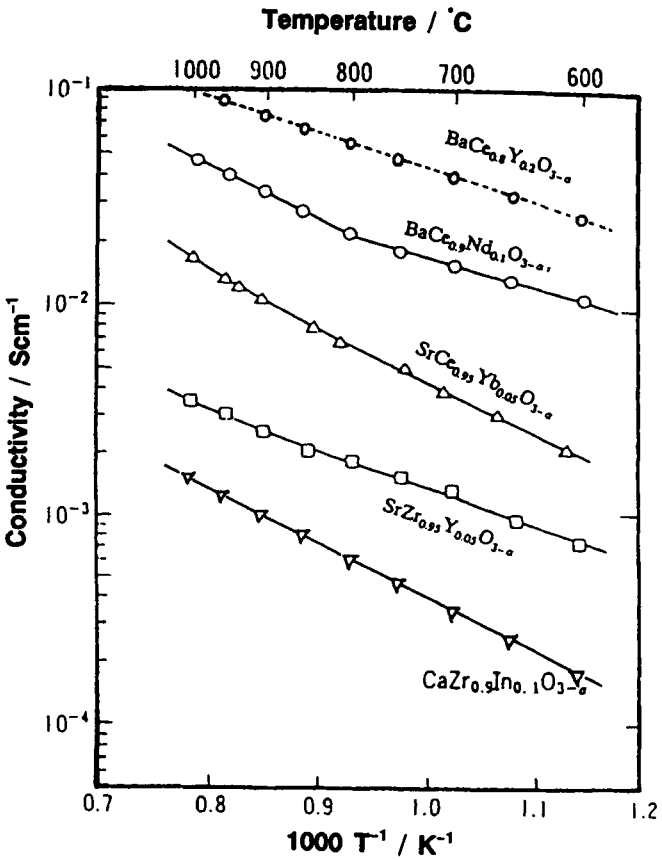

Fig. 20. Conductivities of typical perovskite-type oxide protonic conductors in hydrogen. (Reprinted from Iwahara 1995 by permission of the publisher, Elsevier Science Ltd.)

From a fundamental point of view, the behavior of this class of materials has raised a number of interesting questions. One of the problem has been the large number of variables available in the experimental studies reported in the literature. The following four perovskites have been extensively investigated in recent years: $SrCeO_3$, $BaCeO_3$, $SrZrO_3$ and $CaZrO_3$ perovskite materials doped with rare-earth elements selected from Yb, Y, Sc, or Nd, at concentrations ranging from 1 to 10 mol% under a wide range of temperatures, 300–1300 K, and partial pressures of hydrogen, water vapor and oxygen. In addition to the native oxygen-ion conduction, n-type and p-type electronic conduction and proton conduction are observed. The protonic species in turn may be comprised of protons, hydroxyl ions or hydronium ions. Conductivity measurements have been carried out in dc, fixed-frequency ac or variable-frequency impedance spectroscopy experiments.

Using the perovskite $SrCeO_3$ (doped with 5 mol% Yb) as an example, it can be seen from table 3 that different activation energy values have been reported in humid gaseous

Table 3
Comparison of activation energy for conduction in $SrCeO_3$ (5 mol% Yb)

Atmosphere	Temperature (K)	Activation energy (eV)	Reference
H_2O/air	873–1273	0.95	Iwahara et al. (1981b)
H_2O/air	300–473	0.63	Scherban et al. (1989)
H_2O/air	873–1273	0.62	Yajima and Iwahara (1992)
Air	473–873	0.65	Bananos et al. (1988)
H_2O/nitrogen	500–1273	0.55	Zheng and Zhu (1995)
Air	773–1073	0.57	Zheng and Zhu (1995

atmosphere (Kumar et al. 1996). In humid air, at temperatures over 1073 K, activation energy values >0.8 eV are most frequently reported (Iwahara et al. 1981b, Kumar et al. 1996), which is in fact comparable to values of 0.7–0.9 eV for ceria-based oxide-ion conductors (Turillas et al. 1988). In the pioneering work on these materials, Iwahara et al. estimated the activation energy to be 0.9 eV from their high-temperature conductivity data. The authors did suggest that the oxide ion vacancies in the doped perovskites can react with oxygen in the air to form electronic holes. If the temperature is sufficiently high and/or p_{H_2O} is not adequate, it is likely that oxide-ion and/or hole conduction may dominate. Scherban et al. (1989), critical of Iwahara's data, using measurements at a single frequency (10 kHz), reported a lower value of 0.63 eV in the lower temperature range of 298–473 K. These measurements were made, however, after equilibrating the samples in argon gas saturated with moisture at 1173 K for 10 hours, which may have helped freeze a fixed concentration of protons in the sample (Scherban et al. 1989). More recent measurements using ac impedance spectroscopy in the frequency range 1 Hz–10 MHz have suggested activation energies around 0.55 eV in the 600–1050 K temperature range (Bananos et al. 1988, Yajima and Iwahara 1992, Zheng and Zhu 1995, Kumar et al. 1996).

Conductivity measurements in air/H_2O atmospheres over a wide range of temperatures from 450 to 1123 K, reported by Kumar et al. (1996), have indicated 3 activation energy values in 3 different temperature ranges, as shown in fig. 21. The activation energy was observed to vary from 0.88 eV at 1073–1123 K, corresponding to oxygen-ion conduction, to 0.55 eV at 600–1073 K, corresponding to H^+ conduction, and 0.43 eV at 450–600 K, postulated as OH^- conduction. Shin et al. (1995) also reported a change in slope in the Arrhenius plot for $SrCeO_3$ as well as $SrZrO_3$ (both were doped with 5 mol% Y) single crystals at approximately 773 K in air/H_2O atmospheres. At temperatures below 773 K, the activation energy for the $SrZrO_3$ system was observed to be relatively low at 0.45 eV, increasing to 0.54 eV at higher temperatures. Using IR measurements, the authors reported that the low value of activation energy is closely related to the value of the OH binding energy.

According to the report by Kumar et al. (1996) the temperature at which the Arrhenius slope exhibits a change corresponds well to the emf measurements, as shown in table 4: the polarity of open circuit voltage measurements changes in steam concentration cells

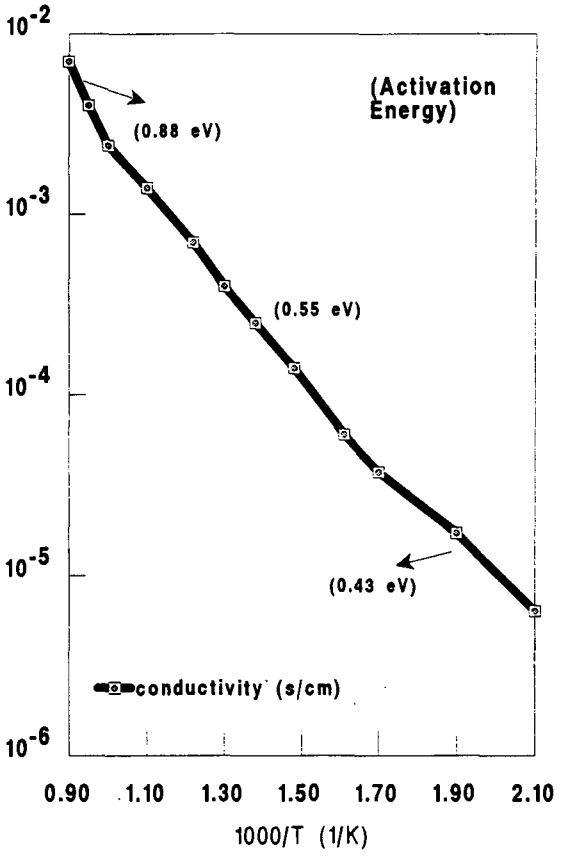

Fig. 21. Conductivity of $SrCeO_3$ (5 mol% Yb) in steam/air. (Reprinted from Kumar et al. 1996 by permission from the Institute of Ionics.)

Table 4
Emf of steam concentration cell[a]

Temperature (K)	emf (mV)		Remarks
	measured	calculated	
500	28	25	OH^- conduction
573	27	28	OH^- conduction
623	−20	31 (for OH^-) −31 (for H^+)	transition from OH^- to H^+ conduction
700	−27	34 (for OH^-) −34 (for H^+)	transition from OH^- to H^+ conduction
773	−36	−38	H^+ conduction

[a] Cell characteristics: (−) H_2O (0.023 atm), Pt|$SrCeO_3$ (5 mol% Yb)|Pt, H_2O (0.073 atm) (+)
Carrier gas: Air in both electrodes.

with air as the carrier gas. The authors have speculated that this may indicate a change in the mode of ionic transport from protons to hydroxyl ions.

6.2. *Metal-ion conductors*

In several cationic conductors, for example sodium-ion conductors based upon Na_2SO_4 and perovskite-type lithium-ion conductors, rare-earth elements are important constituents, which directly or indirectly aid the ionic conduction in such solids. Somewhat unexpectedly, rare-earth elements in oxidation state (III), despite their large size and high charge, themselves may be the mobile component in solid electrolytes such as β-alumina, $LaNb_3O_9$ and $Sc_2(WO_4)_3$ oxides.

6.2.1. *Sodium-ion conductors*

Pure Na_2SO_4 undergoes a phase transformation at 510 K from a low-temperature II- or V-type orthorhombic phase to a high-temperature I-type hexagonal phase, which exhibits substantial Na-ion conductivity (Jacob and Rao 1979). The solid–solid transition is associated with an abrupt transition in the conductivity data (fig. 22), whose entropy is of the same order of magnitude as the melting entropy (van Gool 1973). Addition of selected rare-earth sulphates can directly affect the total ionic conductivity as well as the phase stability field of the conducting phase (fig. 22). For example, an addition

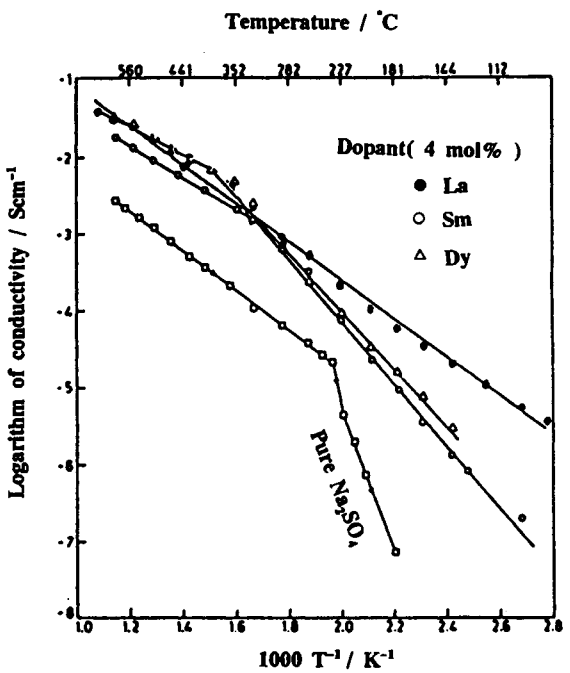

Fig. 22. Sodium-ion conductivities of Ln-doped Na_2SO_4. (Reprinted from Prakash and Shahi 1987 by permission of the publisher, Elsevier Science Ltd.)

of up to 4 mol% of $La_2(SO4)_3$ to Na_2SO_4 has the effect of both stabilizing the high-conductivity phase and increasing the total conductivity (Prakash and Shahi 1987), thus making this system attractive for developing solid-state galvanic sensors for measuring SO_x (Imanaka et al. 1987a, 1988). Additions of sulphates of Dy(III), Sm(III), Eu(III) and Y(III) also increase the conductivity of Na_2SO_4, although not to the same extent as that of La, especially at lower temperatures (Prakash and Shahi 1987, Imanaka et al. 1986, 1987b). The phase transition to a lower-conductivity phase is not eliminated, in fact the temperature at which the solid–solid transition can take place is raised by over 100 K.

The discovery of fast ion conduction in skeleton structures has led to considerable interest in the Na Superionic Conductor called Nasicon (Goodenough et al. 1976). The nominal formula of Nasicon is $Na_3Zr_2P_3O_{12}$ with the existence of a spontaneous "natural non-stoichiometry" (Hong 1976). The structure of Nasicon can be described as groups of two zirconium octahedra ZrO_6 separated by 3 phosphorus/silicon tetrahedra with which they share corner oxygen, resulting in a loosely packed 3D quasicubic framework. The transport properties of Nasicon are comparable to that of Na β-aluminas and therefore Nasicons are seen as promising materials for use in battery applications. Rare-earth elements (such as Nd and Gd) have been frequently added to Nasicon structures in order to influence the transport properties as well as to minimise the presence of second phases (Collin et al. 1988, X.H. Wang et al. 1988). However, the conductivities are worse than the values reported for the original Nasicon.

6.2.2. *Lithium-ion conductors*

Microelectronics-based high-value consumer products requiring portable primary or secondary batteries have led to intense research and development in lithium-ion conducting solid electrolytes for applications particularly in rechargeable batteries. Lithium-based cells derive their interest from the ability to deliver higher cell potentials, higher energy density and longer charge retention than other systems. At present the available practical batteries are based upon non-aqueous solutions and polymers, which may not be adequate to meet the needs of size compactness, integration and stability at high temperatures (Sato et al. 1997). Oxide lithium-ion conductors, containing rare-earth elements have attracted considerable attention in recent years for potential applications in batteries (Inaguma and Itoh 1996, Sato et al. 1997).

Yttrium phosphate, YPO_4, is a zircon-type phosphate with orthorhombic crystal structure and it dissolves lithium phosphate up to 20 mol% to form a solid solution in the system YPO_3–Li_3PO_4. On sintering, the above solid solution ceramics exhibit Li-ion conduction at elevated temperatures. As shown in fig. 23 (Esaka et al. 1989), the conductivity of the solid solutions is much higher than that of pure YPO_4, and this conduction was experimentally demonstrated to be associated with lithium ions. The zircon-type crystal structure has appropriate size interstitial sites in which lithium ions can be inserted, and hence they can move easily among the PO_4 tetrahedra.

$Li_3Sc_2(PO_4)_3$ in its orthorhombic form (γ-phase) was reported as a new lithium-ion conductor (Bykov et al. 1990) at temperatures over 518 K. The lithium sites in the γ-phase

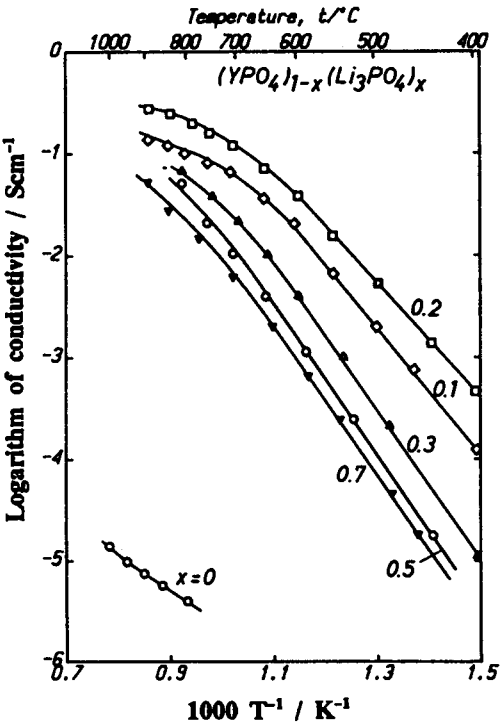

Fig. 23. Conductivity of $(YPO_4)_{1-x}(Li_3PO_4)_x$. (Reprinted from Esaka et al. 1989 by permission of the publisher, Elsevier Science Ltd.)

are only partially occupied, in a manner similar to Nasicon (Aono et al. 1990). By partially substituting Zr^{4+} ions for Sc^{+3} ions, the superionic conducting γ-phase has been shown to be stable at room temperature, with a corresponding increase in the conductivity (Sato et al. 1997). The increase in conductivity was ascribed to the stabilization of the high-temperature disordered phase by the introduction of more polarizable zirconium ions and the formation of a higher concentration of vacancies for charge compensation.

Lithium-ion conducting oxides with perovskite structure exhibit relatively high ionic conductivity in the range 10^{-5} to 10^{-3} S/cm at room temperature (Inaguma et al. 1995, Ito et al. 1994). The high conductivity arises due to the migration of lithium ions via vacancies among the A-sites, one-third of which are deficient, in the ABO_3-type perovskites. The host material can be expressed as $R_{2/3}TiO_3$, in which the lanthanide ions, R(III), can be partially replaced by Li^+ ions to form substitutional solid solutions $R_{2/3-x}Li_{3x}O_{3-\delta}$ ($x < 0.5$), in which ($\frac{1}{3} - 2x$) of the A-sites are vacant. A typical composition might be $R_{0.51}Li_{0.34}O_{2.94}$, the conductivity of which is $>10^{-3}$ S/cm at 300 K, one of the highest conductivity reported for a lithium-ion conducting solid electrolyte. The lithium ion can migrate from one vacant A-site to another across a bottleneck formed with four oxygen ions as illustrated in fig. 24 for the (100) plane of (R, Li)TiO_3 (Ito et al. 1994, Inaguma and Itoh 1996). R^{3+} serves as a prop for keeping the A-site empty, and the size of the bottleneck through which the lithium ion can pass, increases with the ionic size of

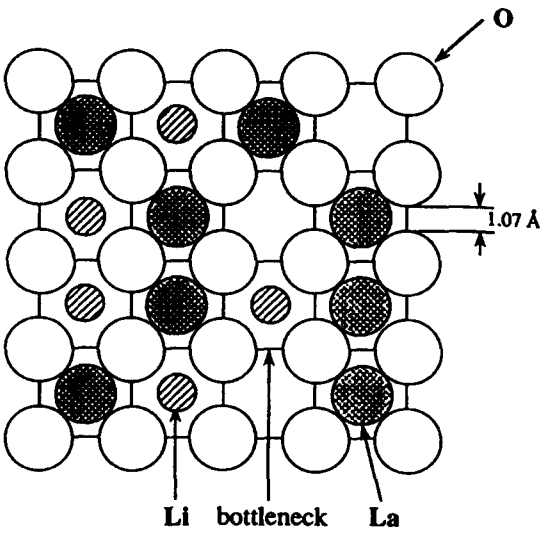

Fig. 24. Schematic structure of lanthanum lithium titanate. (Reprinted from Inaguma et al. 1995 by permission of the publisher, The Electrochemical Society Inc.)

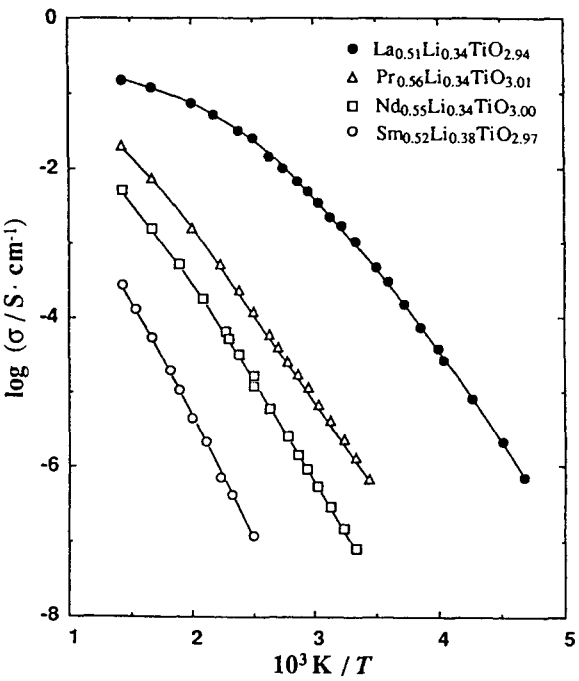

Fig. 25. Bulk conductivities of lanthanum lithium titanates. (Reprinted from Ito et al. 1994 by permission of the publisher, Elsevier Science Ltd.)

the lanthanide ion. There is a corresponding increase in the ionic conductivity with the increase in the size of the lanthanide ions as shown in fig. 25 (Ito et al. 1994).

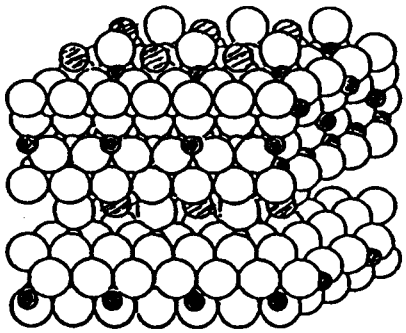

Fig. 26. Crystal structure of a β-alumina.

6.2.3. *Rare-earth-ion conductors*

Na β-alumina, with nominal formula $Na_2O{\cdot}11Al_2O_3$, and the related β″-alumina are well-known sodium-ion conductors. Since the discovery of high Na-ionic conductivity in the Na β- and β″-alumina (Yao and Kummer 1967), a variety of solid-state electrochemical devices have been developed for applications in batteries and sensors (Staikov 1991). In the β-alumina structure, the unit cell is composed of two spinel blocks of oxygen and aluminum atoms, separated by a mirror as show in fig. 26. The sodium ions can easily move two-dimensionally along the layer between two spinel blocks. In the case of β″-alumina, the structure is the result of the stacking of three spinel blocks, and is usually stabilized by the addition of MgO or Li_2O. The sodium in the β-alumina type of phases can be ion-exchanged not only for monovalent cations of Ag, K and Li (Kummer 1972) and divalent cations of Ca, Sr and Pb (Dunn and Farrington 1980), but also for trivalent cations of rare-earth elements such as La, Nd, Gd, Sm, Tb and Eu (Farrington et al. 1983, Dunn and Farrington 1983). Ion exchange has usually been carried out by immersing Na β″-alumina in a molten salt of rare-earth element at high temperatures. Eu β″-alumina thus prepared was reported to be a good conductor of divalent Eu(II) ions, the conductivity of which is shown in fig. 27 (Ghosal et al. 1983). It has been reported that in general, for the trivalent β″-aluminas, only low conductivity is observed (typically $<10^{-5}$ S/cm at 573 K) since the trivalent rare-earth cations are highly charged, making the Coulombic force between oxygen and the rare-earth ions too strong to allow rapid mobility especially at relatively low temperatures. Since the trivalent rare-earth ions inserted in the β″-aluminas behave as luminescent centers, attention is mostly focused on application in fluorescent or laser material (Shriver and Farrington 1985).

The rare-earth-containing β-alumina type of phases can also be directly synthesized at elevated temperatures (Verstegen et al. 1973, Mizuno et al. 1974, Kumar and Kay 1985, Warner et al. 1996); they are of considerable interest not only as optical materials for laser and phosphor hosts (Abraham et al. 1987) but also in electrochemical cells at elevated

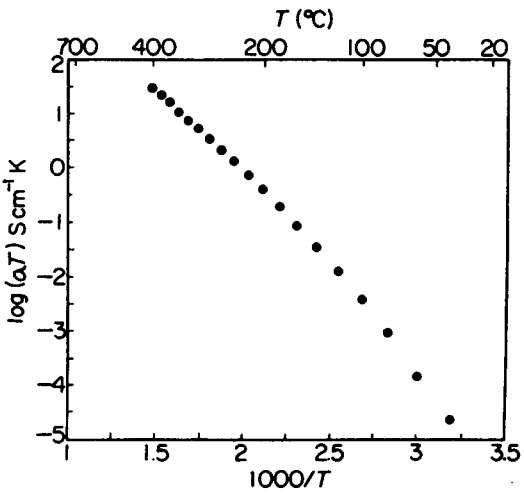

Fig. 27. Conductivity of Eu^{2+} β-alumina single crystal. (Reprinted from Ghosal et al. 1983 by permission of the publisher, Elsevier Science Ltd.)

temperatures (Kumar 1984, Kumar and Kay 1985, Warner et al. 1997). Various phases that have been identified and reported range from the β-phase in a narrow composition range near $R_2O_3 \cdot 11Al_2O_3$ (Sun et al. 1991) to the more densely packed but distorted magnetoplumbite (MP) $R_2O_3 \cdot 12Al_2O_3$ (W.S. Wang et al. 1988). It is possible to stabilise the MP structure by introducing divalent oxides such as MgO. Even for the β-phase, which has a higher conductivity than the MP-phase, adequate values ($>10^{-4}$ S/cm) are achieved only at $T > 1600$ K (Kumar 1997, Warner et al. 1996).

The possibility of trivalent-ion conduction has also been reported for β-$LaNb_3O_9$ (George and Virkar 1988), and was experimentally demonstrated by electrolysis which resulted in a significant increase of the La content at the cathodic surface. The possibility of oxide decomposition at the cathode cannot, however, be unambiguously ruled out.

Imanaka et al. (1995) demonstrated direct evidence for trivalent-ion conduction in $Sc_2(WO_4)_3$. They purposely chose this material due to its large tunnel size of 2.2 Å, relative to the ionic size of 1.8 Å for Sc^{3+}. By combining results from polarization experiments (both dc and ac) with emf measurements the authors provided confirmation for trivalent-Sc-ion conduction in a solid oxide material. At 823 K, the conductivity value was greater than 10^{-5} S/cm, and the transport number for Sc^{3+} was estimated to be 0.92. The same laboratory reported that $Y_2(WO_4)_3$ also exhibits trivalent ion conduction for Y^{3+} ions (Adachi and Imanaka 1996).

7. Technological applications of rare-earth-containing solid electrolytes

7.1. *Fuel cells*

Fuel cells are potentially attractive for converting chemical energy directly into electrical energy, as their performance is dictated by the Gibbs function rather than the Carnot

cycle. Fuel cells based upon aqueous electrolytes have been successfully used in manned space craft and space shuttle and in the military domain, thus demonstrating the principle in the form of an engineered product. Low-temperature fuel cells suffer significant efficiency penalties through the need for external reforming of fuel. Because a fuel cell based on solid oxide electrolyte can only operate at high temperatures, internal reforming of the fuel is possible and the prospect of operating at high efficiencies (>60%), especially at low current density, can be practically realized (Steele 1990).

7.1.1. *Solid oxide fuel cells*

The Solid Oxide Fuel Cell (SOFC) is a solid-state device that can generate electricity in an electrochemical cell by combining fuel and oxidant gases across an oxygen-ion conducting solid electrolyte. The current technological applications of SOFCs are based upon the oxygen-ion conducting yttria-stabilized zirconia solid electrolyte with special electrodes for operating in the temperature range 1200–1300 K. Use of solid-state materials provides simplicity in the electrolyte management unlike the fuel cells based on liquid electrolytes such as aqueous phosphoric acid, aqueous alkaline hydroxide or molten alkali carbonate (Steele 1990). The high operating temperatures not only promote rapid reaction kinetics, eliminating the need for expensive precious-metal catalysts [as in phosphoric acid fuel cells (PAFC), alkaline fuel cells (AFC) or solid polymer electrolyte fuel cell (SPFC)] but also allow in-situ reforming of hydrocarbon fuels,

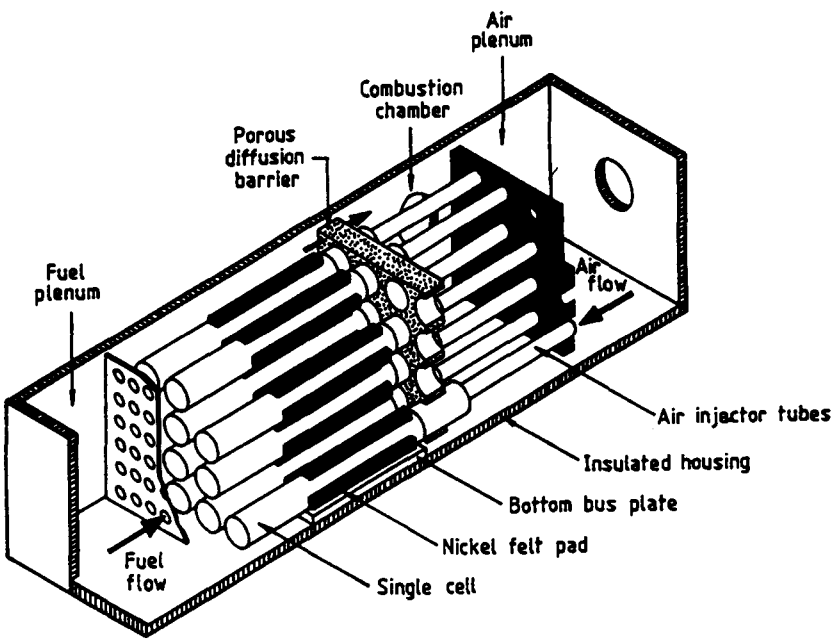

Fig. 28. Tubular Solid Oxide Fuel Cell. (Reprinted from Steele 1990 by permission from the publisher, Elsevier Science Ltd.)

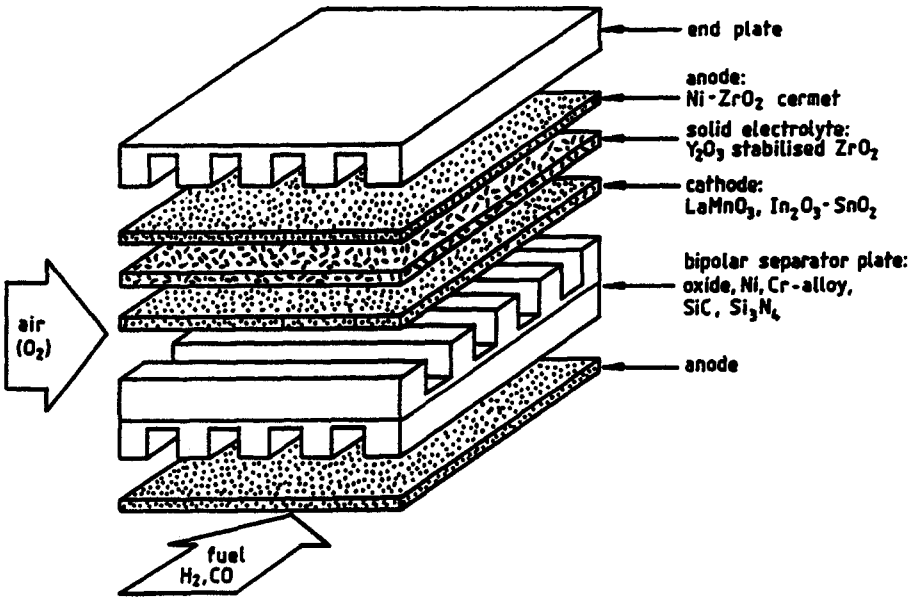

Fig. 29. Planar Solid Oxide Fuel Cell. (Reprinted from Steele 1990 by permission from the publisher, Elsevier Science Ltd.)

while producing high-quality heat as a by-product. SOFCs are considered particularly suitable for use in combined heat and power applications or for high-efficiency power generation (approaching 60%) in combination with steam and/or gas turbines. Since the mid-1980s there has been a considerable world wide interest in SOFCs, with research and development, pilot scale and semi-commercial activities in USA, Europe and Japan.

Two different types of stack designs are generally used – the tubular design and the self-supporting planar design. In the tubular design, as shown in fig. 28, a porous cathode, an impermeable electrolyte, and a porous anode followed by an impermeable interconnector layer are deposited sequentially by electrochemical vapor deposition (EVD) on a porous support tube of calcia-stabilized zirconia (Pal and Singhal 1990, Haydock 1994). In a more recent version, the support tube has been replaced by a thick tube of porous cathode material based upon La(Sr)MnO_3 (Singhal 1997).

During cell operation, air is injected into the cell near the closed end, while the fuel flows on the outside of the support tube. Individual cells are bundled together to form a power generating module. Due to the disadvantages of low power density and high-cost manufacturing process, the planar configuration design as shown in fig. 29 has received increasing attention (Haydock 1994). In this design, the cell is made up of thin electrodes deposited on a self-supporting flat yttria-stabilized zirconia electrolyte fabricated by tape casting or extrusion to a thickness of 150 μm. The anode and the cathode are connected in series by flat interconnect plates, with ribs on both sides to form channels for the gaseous fuel and oxidant to generate a monolith module.

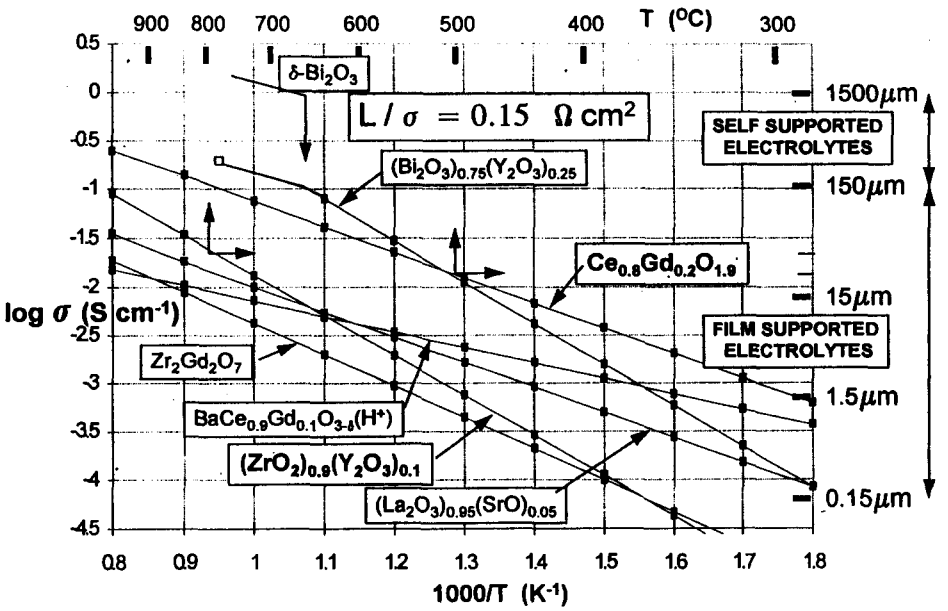

Fig. 30. Ionic conductivity vs $1/T$ for selected oxide electrolytes. (Reprinted from Steele et al. 1994 by permission of the publisher, The Institute of Energy, London.)

The porous cathode is generally made of Sr- and/or Co-doped $LaMnO_3$ perovskite mixed conductors. The $LaCoO_3$ (Sr-doped) material exhibits a high oxygen diffusivity and is therefore very attractive from an electrochemical point of view, but unfortunately suffers from an unacceptably high reactivity with zirconia and high coefficient of thermal expansion. The $LaMnO_3$ electrode (doped with Sr) on the other hand, is predominantly an electronic conductor. Various compositions are being considered to optimise the required properties.

The anode is usually a thin layer of Ni-YSZ cermet. At temperatures over 1173 K, the kinetics of steam reforming reactions are faster than the electrochemical oxidation of hydrogen or carbon monoxide. The other principal component is the bipolar plate, which is commonly fabricated from $LaCrO_3$ (Mg-doped) which is predominantly an electronic conductor and is compatible with other cell components at 1273 K. It is however relatively brittle and expensive, and there is a continuous effort to replace it with other materials preferably with a metallic system.

In order to reduce the capital costs of SOFC systems, Steele has suggested operating a SOFC at lower temperature, 800–1050 K, such that the expensive bipolar ceramic plate can be replaced by a metallic alloy or stainless steel (Steele et al. 1994, Steele 1996). In order to select a suitable electrolyte, for any given operating temperature, Steele has provided a comparison of the electrolyte area resistance:

$$R_0(\text{ohm cm}^2) = L/\sigma\,, \tag{7.1}$$

where L is the thickness of the electrolyte (in cm) and σ is the oxygen-ion conductivity (in S/cm), for different electrolytes. For a practical fuel cell, the minimum value of area resistance that would be required is 0.15 ohm cm^2. As shown in fig. 30, in order to satisfy the minimum value of area resistance the practical thickness required for a self-supported electrolyte would be 150 μm; the ceria-based electrolyte could be used at 1050 K, although they are not sufficiently mechanically strong. As a supported thick film (10 μm), Gd-doped ceria may be used at temperatures as low as 800 K.

7.1.2. *High-temperature fuel cells based upon protonic conductors*

Recent developments using high-temperature oxide protonic conductors as electrolytes in fuel cells, as demonstrated by Iwahara and co-workers (1983) must be regarded as a next-generation device after SOFC. As shown in fig. 31, when a protonic conductor is used instead of an oxygen-ion conductor, and provided the conduction is purely protonic, with hydrogen as the fuel, circulation of the fuel is not necessary, since no water molecules will be generated at the fuel electrode. Another advantage as with the SOFC systems is that a hydrocarbon fuel can be reformed in-situ at the anode due to the high operating temperatures (1100 K), and furthermore since only hydrogen is consumed, the residual component will be available as useful reformed products, e.g. ethylene from ethane (Iwahara et al. 1991a).

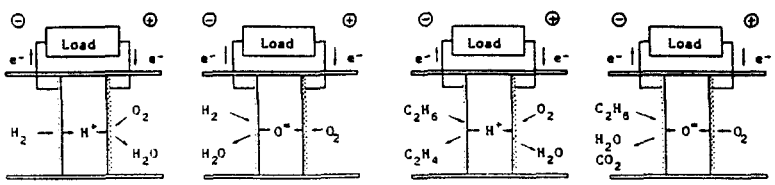

(a) Hydrogen fuel cells (b) Ethane fuel cells

Fig. 31. Comparison of a protonic conductor with an oxide ionic conductor in the case of hydrogen and ethane fuel cells. (Reprinted from Colomban 1992 by permission of the publisher, Cambridge University Press.)

7.2. *Chemical sensors*

Solid electrolytes interfaced with suitable electrodes can quantitatively transduce the ratio of activities of the ionically conducting component at the two electrodes directly into an electrical potential. This forms the basis of using solid electrolytes in the development of "chemical sensors" for monitoring and/or controlling chemical components in gaseous, liquid and solid systems. Chemical sensing based upon solid electrolytes is indeed now a well-established field, with considerable examples of highly successful commercial applications related mainly to oxygen (Goto 1988, Dell and Hooper 1978, Soejima and Mase 1985, Dietz 1982, Wiedenmann et al. 1994) and fluorine measurements (Reau and Portier 1978). Discoveries of new solid electrolytes have led to new areas of development and applications such as hydrogen monitoring (Colomban 1992, Kumar and Fray 1988a,

Yajima et al. 1993) and sodium measurements in molten metals (Kumar and Fray 1989, 1993). In recent years there has been a considerable increase in research, development and applications of solid-electrolyte-based chemical sensors for the detection of gases such as CO_2, SO_x, H_2O, NO_x, HCl, CO and hydrocarbons (HCs). It is interesting to note that rare-earth elements are prominent components of many of the above sensors.

7.2.1. *Oxygen sensors*

The yttria-stabilized zirconia (YSZ) oxygen sensors are one of the most successful applications of solid electrolytes. The most prominent applications are in the control of air/fuel ratio (A/F) in automobile exhaust gases and industrial combustion. Several millions of oxygen sensors are produced each year and the demand continues to grow.

Reduction of pollutant gases of CO, HCs and NO_x from automobile emissions is currently achieved by the use of three-way catalysts (TWC), which can oxidise CO and HCs into CO_2 and H_2O, while simultaneously reducing NO_x into N_2, provided the TWC is operated at stoichiometric air/fuel ratio, as shown in figs. 32 and 33. The air/fuel ratio is normally defined in terms of lambda (λ):

$$\lambda = \frac{\text{operating air/fuel ratio}}{\text{stoichiometric air/fuel ratio}}. \tag{7.1}$$

The stoichiometric point is defined at $\lambda = 1$, at which the engine is supplied with the exact quantity of air required for complete combustion. Even if a stochiometric air/fuel ratio is maintained, because the conditions within the engine are not perfect, a number of products of incomplete combustion, such as CO and HCs, are present. The main source of NO_x, which is a mixture of NO, NO_2 and N_2O, is the reaction between nitrogen and oxygen at the high combustion temperature. As shown in fig. 34, a fuel-rich mixture ($\lambda < 1$) produces high concentrations of CO and HCs (including H_2), while lean-burn ($\lambda > 1$) mixtures

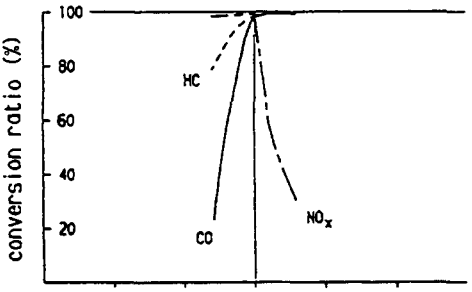

Fig. 32. Conversion rates for CO, NO and HCs in a TWC converter. (Reprinted from Wiedenmann et al. 1994 by permission of the publisher, The McGraw-Hill Companies.)

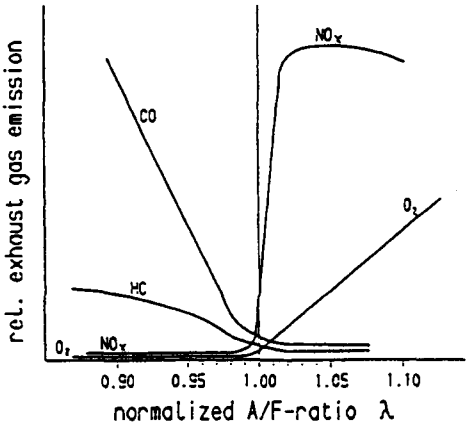

Fig. 33. Typical curve for exhaust gas composition downstream from a TWC converter. (Reprinted from Wiedenmann et al. 1994 by permission of the publisher, The McGraw-Hill Companies.)

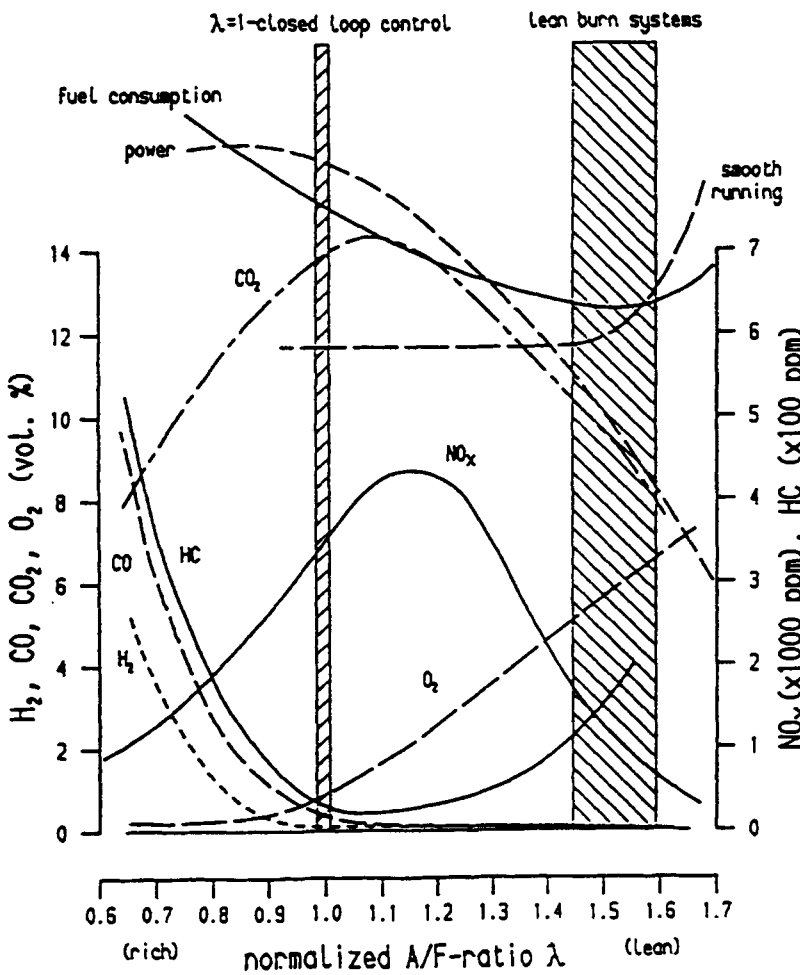

Fig. 34. Composition of exhaust gases relative to lambda in a spark-ignition system. (Reprinted from Wiedenmann et al. 1994 by permission of the publisher, The McGraw-Hill Companies.)

generate higher levels of NO_x and free O_2. However at $\lambda > 1.2$, the temperature in the combustion chamber decreases which results in a reduction of NO_x levels.

Since TWC catalytic conversion is most efficient at $\lambda = 1$, it is necessary to use an oxygen sensor in the exhaust stream to maintain the air/fuel ratio as close to the stoichiometry as feasible. A TWC combined with a closed-loop control system featuring an oxygen sensor has been successfully employed in achieving adequate reduction in all 3 pollutants with high conversion rates for CO, NO_x and HCs as shown in fig. 33 (Wiedenmann et al. 1994).

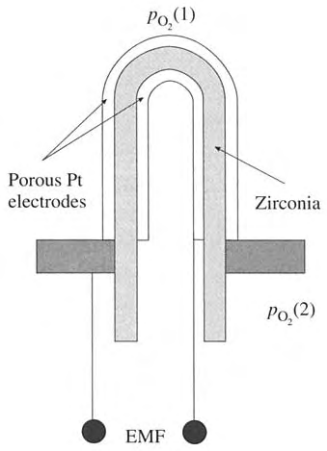

Fig. 35. Design of a lambda sensor.

7.2.2. *Mechanism of air/fuel control*

The YSZ solid electrolyte is effectively used as a galvanic cell in the form of an oxygen concentration cell. The Y_2O_3 concentration in the solid electrolyte is usually 2–5 mol%, at which partial stabilization of ZrO_2 is achieved, a factor contributing to obtaining adequate mechanical and thermal shock resistance properties. In the construction of the oxygen sensor, as shown in fig. 35, a gas-impermeable YSZ solid electrolyte tube separates the exhaust gas from the reference atmosphere, containing air. Both electrode compartments make use of platinum as electrocatalysts to promote the following electrochemical equilibrium:

$$\text{Reference (cathodic)}: \quad O_2\ (\text{air}) + 4e^- = 2O^{2-}. \tag{7.2}$$

$$\text{Exhaust (anodic)}: \quad 2O^{2-} = O_2\ (\text{exhaust}) + 4e^-. \tag{7.3}$$

The oxygen concentration difference results in an emf E given by

$$E = \frac{RT}{4F} \ln \left\{ \frac{p_{O_2}(\text{air})}{p_{O_2}(\text{exhaust})} \right\}, \tag{7.4}$$

where R is the universal gas constant, F is Faraday's constant, T is temperature, and p_{O_2} is the partial pressure of oxygen.

7.2.3. *Operation of the λ oxygen sensor*

One of the great advantages of using the oxygen sensor in the stoichiometric mode to control the air/fuel ratio at $\lambda = 1$, is that there is a step change of emf at stoichiometric air/fuel ratio, as shown in fig. 36. This arises due to the fact that p_{O_2} changes sharply at $\lambda = 1$, the main reason for referring to the sensors as lambda sensors.

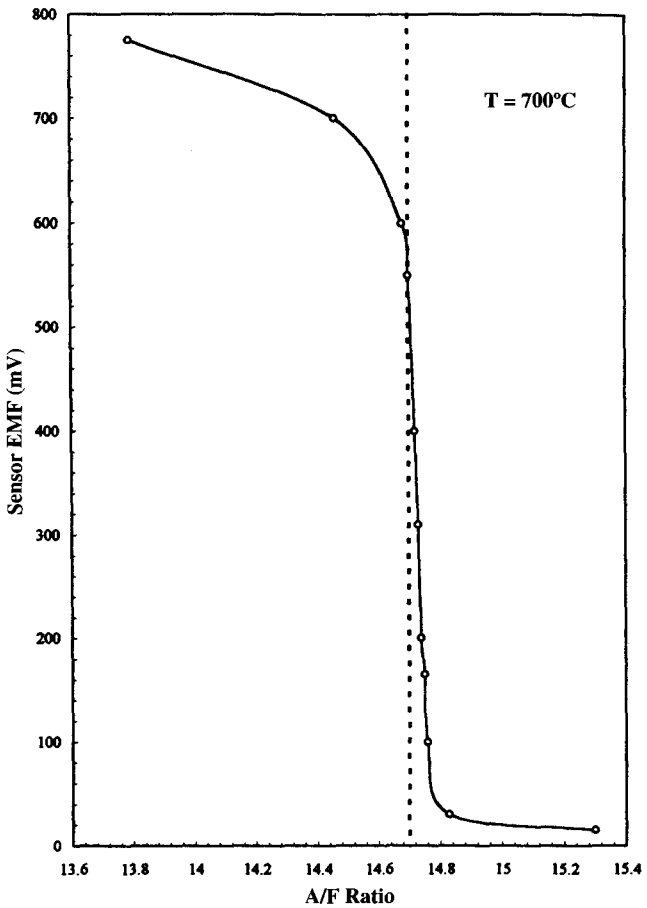

Fig. 36. Emf from a lambda sensor as a function of air/fuel ratio in a petrol engine.

7.2.4. *Planar-type lambda oxygen sensors*

Planar technology is increasingly seen as more attractive than tubular techniques for developing oxygen sensors for gas monitoring. In the planar version, the design is similar to multilayer technology for ceramic capacitors and high-density electronics circuit boards: all the components are formed in layers in plain consecutive surfaces by using tape-casting and screen-printing processes. Cost reduction arises from volume production, single-step sintering and integration of a heater in one of the surfaces. In the planar design, the thermal mass is much lower, hence resulting in miniaturization, low power requirement and rapid response (Wiedenmann et al. 1994).

7.2.5. *Sensors for lean-burn combustion*

Low emissions can also be achieved by operating the engine in a lean-burn mode at $\lambda = 1.2–1.7$ for petrol engines and $\lambda = 1.1–7$ for diesel engines. This has the considerable benefit of achieving improved fuel economy and good driving performance at low emissions. Further pollutant reduction, as may be demanded in the next generation of legislation, can be achieved by using oxidation catalysts for reducing CO and HCs emissions and DeNOx catalysts or traps.

However, the lambda sensors in the potentiometric mode, due to their log dependence on oxygen partial pressure, cannot be used in lean-burn conditions, as deviations of a few mV are sufficient to produce unacceptable errors in the control of air/fuel ratio. This has led to the development of amperometric sensors, in which current is measured which has a linear dependence upon oxygen concentration (Kaneko et al. 1987, Maskell and Steele 1988).

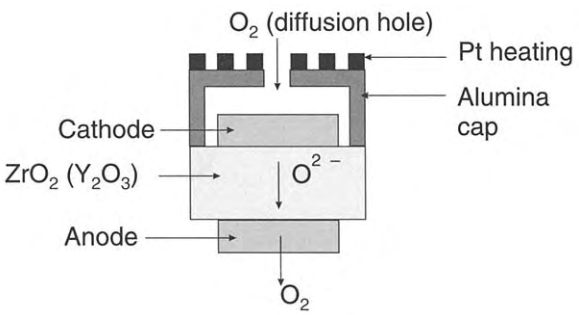

Fig. 37. Schematic diagram of a limiting current sensor with a pin-hole for limiting diffusion.

In this type of amperometric sensors, an external electrical potential is applied between 3 platinum electrodes on a YSZ electrolyte in order to pump oxygen ions from the exhaust gas (used as a cathode) to the anode. If the flow of oxygen to the electrolyte is sufficiently impeded, either by the use of a pin-hole aperture (fig. 37) or by the use of carefully controlled porous ceramics (fig. 38), the current is proportional to the concentration of oxygen in the exhaust gas:

$$I = 4FD\frac{Q}{L}c_O, \tag{7.4}$$

where I is the limiting current, F is Faraday's constant, D is the diffusion coefficient of oxygen, Q is the effective diffusion cross section, L is the effective diffusion length, and c_O is the concentration of oxygen in the exhaust gas. The proportionality occurs as a result of diffusion-limited flow of oxygen through the restriction. When the rate of oxygen diffusion is identical to the rate of electrochemical oxygen pumping, a limiting current is reached (fig. 39), such that its value is directly proportional to the concentration of oxygen in the exhaust gas.

The limiting current sensor is suitable for use only in lean-burn gases. It is also critical to maintain a stable operating temperature at near 1100 K. In order to obtain reproducible

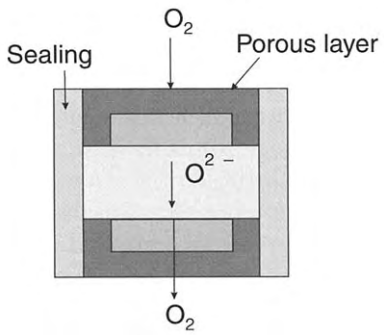

Fig. 38. Schematic diagram of a limiting current sensor with a porous ceramic diffusion barrier.

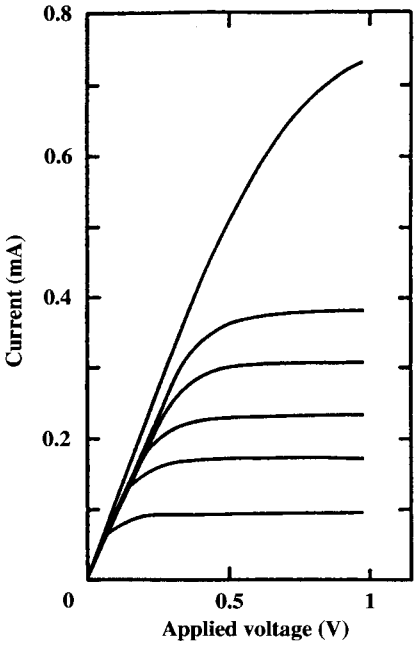

Fig. 39. Current–voltage characteristics in the limiting current type sensor.

results, it is necessary to achieve a standard diffusion gap during manufacturing and it is also vital to maintain the pore size during operation. Considerable test work has been carried out with amperometric oxygen sensors in one or several modified versions (Ioannou and Maskell 1992, Maskell 1997, Wiedenmann et al. 1994), and commercial application has taken place only to a limited extent.

7.2.6. *A new type of oxygen sensors*

In a novel variation on the currently available potentiometric and amperometric sensors, a new approach has been developed (Fray and Kumar 1997, Gibson et al. 1999). The method is based upon applying a potential to an oxygen-conducting solid electrolyte such as stabilized zirconia, and measuring the current, reapplying the same potential in the reverse direction and re-measuring the current. The current ratio obtained from the above two measurements has been found to be strongly and linearly dependent upon the concentration of oxygen in the high concentration range. Complications such as pin-hole or porous ceramic layer diffusion barriers for limiting current are not required in this approach. In fact it is possible to use an identical construction to that developed so successfully for the currently available potentiometric Nernstian sensors.

The proposed sensors can also operate over the whole range of gas compositions. By choosing appropriate values of the applied potential, it is possible to obtain a peak current ratio value at any predetermined oxygen concentration and therefore can be used to control oxygen in the entire range from parts per billion to 100%. Using this concept, it is possible

to use a standard solid-electrolyte oxygen sensor to cover fuel-rich, stoichiometric and lean-burn combustion modes in one sensor with maximum sensitivity appropriate to each range, making the sensors attractive for applications to automotive engines and other combustion systems. A wide-range oxygen sensor is appropriate to situations where the engine may be switched between lean-burn to stochiometric for maximizing power, and to fuel-rich periodically to decompose nitrates formed in NOx traps.

In this concept using air as the reference on one side of the electrolyte and the test gas on the other, a potential is applied across the electrolyte, current is measured, then direction of the potential is reversed and the current is measured again. The observed current magnitude is different in the two directions, even if the magnitude of applied potential (V_{appl}) is the same. The ratio of the currents in the forward (I_{for}) and the reverse (I_{rev}) direction is quantitatively related to the partial pressure of oxygen in the test gas through the following equations:

$$\frac{I_{for}}{I_{rev}} = \frac{V_{appl} + emf}{V_{appl} - emf}, \tag{7.5}$$

where

$$emf = 2.303\frac{RT}{4F}\log\left[\frac{p_{O_2}(reference)}{p_{O_2}(test)}\right]. \tag{7.6}$$

It has been assumed that the resistance ratio is unity, which is valid only for small currents, when the activation and concentration overpotentials due to polarization of the electrodes can be neglected. The ionic resistance of the electrolyte is identical for both forward and reverse currents. By carefully choosing the magnitude of the applied potential, the current ratio dependence on oxygen concentration can be shown to be virtually linear at high concentrations.

A typical result is shown in fig. 40 for an applied potential of 35 mV. The current ratio (I_{for}/I_{rev}) is almost linearly dependent upon oxygen concentration. At higher concentrations, a linear response is more sensitive than the logarithmic dependence obtained with potentiometric Nernstian mode of operation. The small departure from linearity is not seen as a problem, since the main issue is that of sensitivity at the appropriate range of concentrations, and eqs. (7.5) and (7.6) describe the response quantitatively. Sensitivity, in fact, is related to the rate of change of the signal with respect to the oxygen concentration, given by $d(I_{for}/I_{rev})/dp_{O_2}$, higher values representing higher sensitivity. A linear response is observed in the concentration range where the sensitivity factor $d(I_{for}/I_{rev})/dp_{O_2}$ is constant. In many applications, higher sensitivity rather than linearity may be desirable.

The sensitivity factor at any given oxygen concentration is clearly a function of the applied potential, as can be deduced from the results shown in fig. 41 for oxygen in the 2–14% concentration range. Lower applied potentials (e.g. 5 mV) have resulted in greater sensitivity, while higher values (e.g. 50 mV) have produced a linear response.

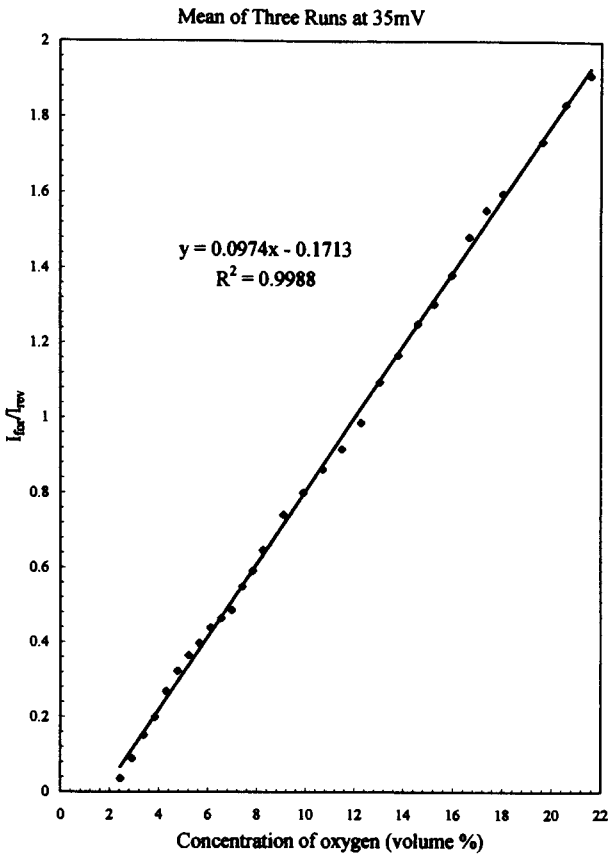

Fig. 40. Measured current ratio vs % oxygen at 35 mV.

The experimentally measured values are compared with the calculated values in fig. 42, using eqs. (7.5) and (7.6), and the agreement at all values of V_{appl} is excellent.

Using eq. (7.5), one can predict that the maximum sensitivity is expected at $V_{appl} \rightarrow$ emf, such that $I/I_0 \rightarrow \infty$. Results are shown in fig. 43, where applied potentials were purposely selected at a value equal to the expected emf for 1.4% oxygen, in order to obtain a I_{for}/I_{rev} peak at this concentration. It is possible to obtain a current peak at any selected oxygen concentration and therefore this new concept can be applied to developing sensors that can be used to control oxygen at any level in the entire range from 1 part per billion to 100%. No such oxygen instrument is currently available except the "lambda" sensor, which operates with a step change for just precisely one value of $\lambda = 1$, representing the transition between a reducing and an oxidizing atmosphere (Fray and Kumar 1997, Gibson et al. 1999).

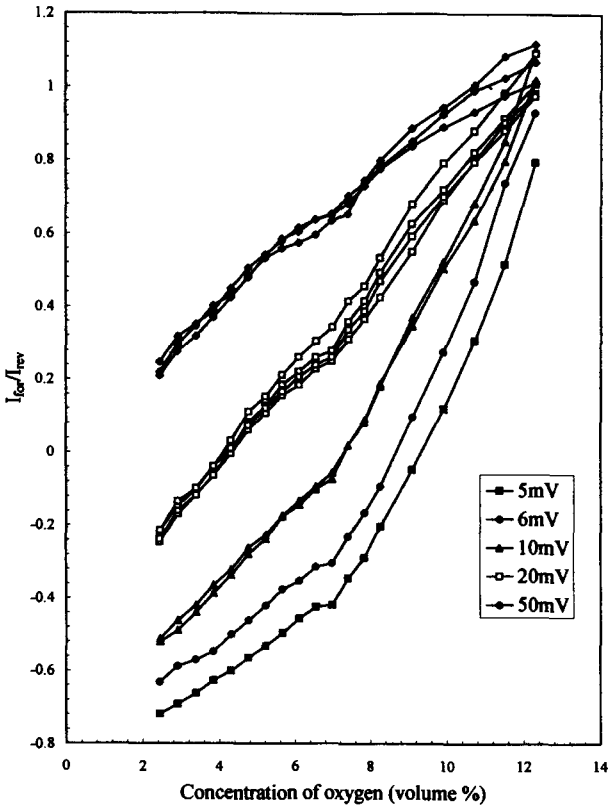

Fig. 41. Measured current ratio vs % oxygen at 5–50 mV.

7.3. *Fluorine sensors*

Rare-earth fluorides are good fluorine-ion conductors (see sect. 5.2). Addition of aliovalent cations significantly increases the fluorine-ion conductivity even further. For example, single crystals of LaF_3 doped with EuF_2 are widely used in commercial applications of ion-selective electrodes (ISE) as F^- specific electrodes (Frant and Ross 1966). In the field of ISE, only the pH-sensing glass electrode is more widely used. Fluoride-ion detection is important in sea water, water minerals, rocks, fossils and minerals, biomedical applications, potable water and plant and animal metabolism.

In an operating sensor, which works as a concentration cell, the potential difference between a reference solution containing a known concentration of fluoride ion and the unknown fluoride concentration test solution is proportional to the logarithm of the ratio of the concentrations, as described by the Nernst equation. Interference from most anions is insignificant, except from hydroxide ions. The specifications for making the actual measurements are normally specified within a certain pH range, usually 5.5 to 6.0.

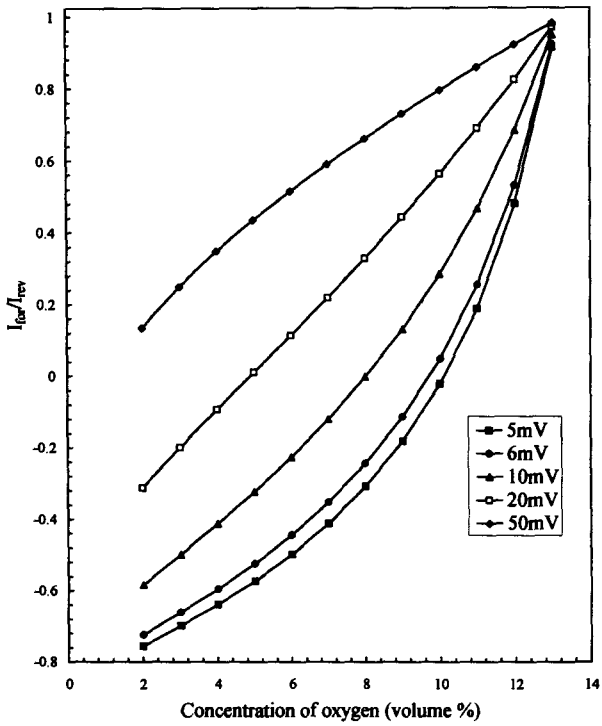

Fig. 42. Calculated values of current ratio vs % oxygen at 5–50 mV.

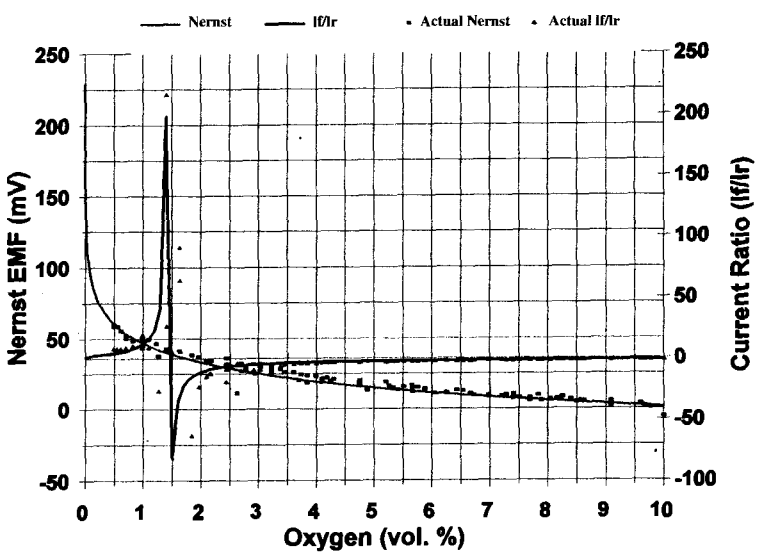

Fig. 43. Current ratio peak at 1.4% oxygen.

7.4. *Sensors based on protonically conducting oxides*

7.4.1. *Hydrogen sensors*

Quantitative detection of hydrogen is of considerable importance in a variety of industrial situations, such as the synthesis of ammonia, methanol and other chemicals, petroleum refining, the manufacture of semiconductors, chemical reduction, power station coolant, corrosion control and general metallurgical reactions (Kumar and Fray 1988b). Gas sensors based upon solid electrolytes have a remarkable potential for meeting the demanding criteria of selectivity. Using low-temperature solid electrolytes such as hydrogen uranyl phosphate or nafion, a number of hydrogen sensors have been developed (Kumar and Fray 1988a, Morris et al. 1989, Miura et al. 1987) and subsequently commercialized. Iwahara et al.'s discovery of proton conduction in oxides at elevated temperatures have led the way for new hydrogen sensors at elevated temperatures (Iwahara et al. 1981b).

After a considerable amount of systematic work with different oxide and dopant systems (see sect. 6.1.3), Iwahara and his team have developed a high temperature hydrogen sensor using $BaCe_{0.9}Nd_{0.1}O_{3-\alpha}$ as a solid electrolyte and hydrogen gas as a reference electrode. They demonstrated that galvanic cells with hydrogen gas at 1 atmosphere as the reference, could be used to measure hydrogen rapidly from $< 1\%$ to 100% in the temperature range 473–1173 K (Iwahara et al. 1991b). As shown in fig. 44, the emf signal was linear against log p_{H_2} (fig. 44a), and the response speed was rapid (fig. 44b).

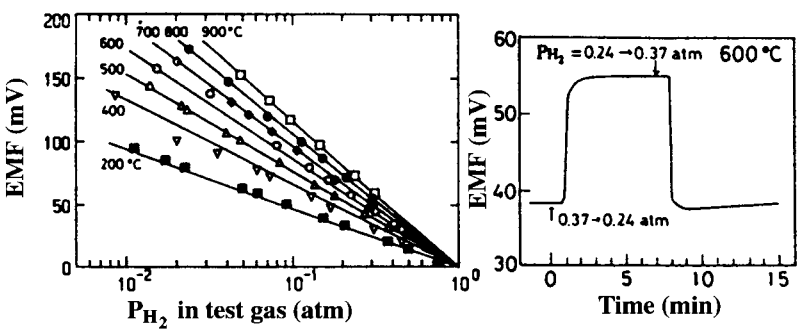

Fig. 44. Performance of a hydrogen sensor using a $BaCeO_3$-based ceramic as a solid electrolyte. (Reprinted from Iwahara et al. 1991b by permission of the publisher, The Electrochemical Society Inc.)

Another interesting application of perovskite-based hydrogen sensors, which has now been commercialized, is for monitoring hydrogen in molten metal such as aluminium, zinc and copper (Yajima and Iwahara 1992). As cerates were not entirely suitable, the investigators used $CaZrO_3$ doped with indium oxide as the solid electrolyte (Iwahara 1996).

7.4.2. *Humidity sensors*

A humidity sensor based upon a galvanic cell has also been demonstrated by Iwahara et al. (1983); a schematic illustration is shown in fig. 45. $SrCeO_3$, doped with aliovalent rare-

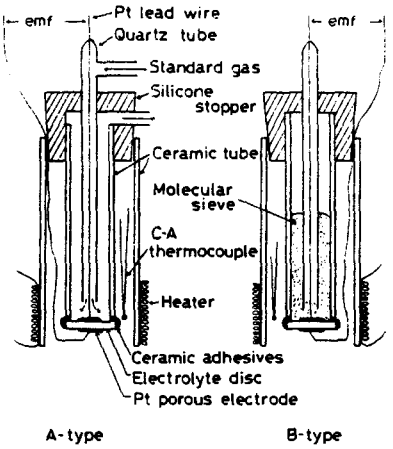

Fig. 45. Schematic illustration of the galvanic cell-type humidity sensors. (Reprinted from Iwahara et al. 1983 by permission of the publisher, Kluwer Academic Publishers.)

earth elements such as Y or Yb, is a p-type mixed O^{2-}/electronic conductor at elevated temperatures. On subjecting the material to water vapor, holes are replaced by hydrogen ions in the structure:

$$H_2O + 2h^{\bullet} = 2H_i^{\bullet} + \tfrac{1}{2}O_2\,, \tag{7.7}$$

$$H_2O + V_O^{\bullet\bullet} = 2H_i^{\bullet} + O_O^{x}\,. \tag{7.8}$$

Thus the material can behave as a proton conductor. The electrode reactions for a humidity concentration cell can be written as

$$\text{Anode}: \quad H_2O(g) = 2H^+ + \tfrac{1}{2}O_2 + 2e^-\,. \tag{7.9}$$

$$\text{Cathode}: 2H^+ + \tfrac{1}{2}O_2 + 2e^- = H_2O(g)\,. \tag{7.10}$$

Combining the two half reactions, the theoretical emf is obtained by the following equation:

$$E = \frac{RT}{2F}\ln\left(\frac{p_{H_2O}(I)}{p_{H_2O}(II)}\sqrt{\frac{p_{O_2}(I)}{p_{O_2}(II)}}\right). \tag{7.11}$$

If the oxygen pressures are maintained identical in the two electrodes, then the equation is simplified. If one of the humidity values is known, the other can be measured from the emf signal.

In a modified version, a perovskite electrolyte ($SrCeO_3$ doped with 5 mol% Yb) in the form of a tube was coated with a layer of impermeable Au–Pd alloy to allow access to oxygen gas on the outer surface, while impeding H_2O transfer. The inner surface coated with platinum is exposed to both H_2O and oxygen (Kumar et al. 1996, Cobb et al. 1996, Fray et al. 1995, Kumar 1997).

7.5. *Potential application of rare-earth-containing solid electrolytes in novel gas sensors*

In general, application of solid electrolytes in gas sensing has been limited to those species, such as oxygen, fluorine and hydrogen, for which suitable solid electrolytes are available. By using auxiliary phases to provide chemical coupling between the species being measured and the species which is ionically mobile in the electrolyte, applicability has been extended to species which are not components of the electrolyte (Kumar and Fray 1988b, 1989, 1993, 1997, Fray and Kumar 1994, Hotzel and Weppner 1986, Weppner 1987, Adachi and Imanaka 1995).

More recently, another novel approach of interfacing two or more electrolytes has led to significant progress in the sensing of molecular species such as CO_2, SO_2, HCl and H_2O in the gas phase (Kumar 1996, 1997, Cobb et al. 1996, Ahmad et al. 1996, Slater et al. 1996, Fray et al. 1995). Many practical gas sensors based on solid electrolytes have used separate compartments for the reference electrode, usually a gas containing a known concentration of the gas to be measured. This requires stringent design, impervious materials and seals and the inconvenience of flowing a reference gas in the electrolyte.

In this new approach, both electrodes are exposed to the same test gas, and separation of the working compartment from the reference compartment is not required. Sensors are fabricated by combining more than one solid electrolyte in an electrochemical chain and/or by using semi-permeable coating to allow one component (or impede the target component) for an alternate electrode reaction.

7.5.1. *SO_x sensors*

Since the ionic form of SO_x is SO_4^{2-}, it is unlikely that a solid electrolyte for transporting the sulphate ions will be easily available. Therefore the idea of using a cationic conductor, such as the alkali-metal sulphates, containing sulphate ions has been considered. The most prominent examples are based upon sodium sulphate (Jacob and Rao 1979, Imanaka et al. 1983), potassium sulphate (Gauthier and Chamberland 1977) and lithium sulphate (Worrell 1983, Liu and Worrell 1988). As discussed in sect. 6.2.1, the electrical properties of sodium sulphate are considerably improved by doping with a rare-earth element. For example, the ionic conductivity of Y_2O_3-doped Na_2SO_4 can be 2 orders of magnitude higher than that of the undoped material (Saito et al. 1984).

Sensors are typically based upon SO_2 concentration cells with a reference SO_2 gas circulation (Imanaka et al. 1986, Adachi and Imanaka 1995). The principle of sensing is based upon equilibrium being achieved between the conducting cation, Na^+ and the gas phase containing SO_3 and O_2. In fact the emf is related to the concentration in the gas phase of the two electrodes by the following equation:

$$\text{Emf} = \frac{RT}{2F} \ln \left[\frac{(p_{SO_3} \sqrt{p_{O_2}})^{\text{test gas}}}{(p_{SO_3} \sqrt{p_{O_2}})^{\text{reference}}} \right]. \tag{7.12}$$

The sensor was adapted for measuring SO_2 by providing platinum mesh as a catalyst for promoting oxidation of SO_2 in both the test and the reference gas. Further simplification

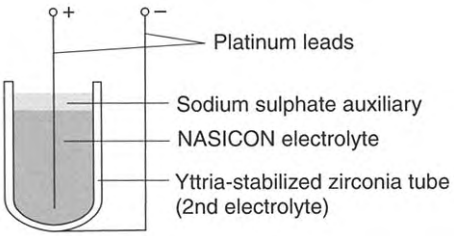

Fig. 46. Schematic diagram of a SO_x sensor.

was obtained by maintaining oxygen partial pressure at the same level in the two compartments.

Since it may not be practical to use a gaseous reference, the authors modified the sensor by providing a solid reference by equilibrating a metal sulphate with its oxide in order to provide a constant p_{SO_3} value at a fixed temperature

$$MSO_4 = MO + SO_3 . \tag{7.13}$$

Nickel or cobalt proved useful candidates for providing the reference system (Imanaka et al. 1987a). The sensors, operating at 900–1000 K, were shown to respond to sulphur dioxide concentrations in the 30 ppm to 1% range. Such sensors have been developed further towards commercial application (Adachi and Imanaka 1991, Adachi and Imanaka 1995).

More recently, SO_x sensors have been developed using solid electrolytes with substantially higher conductivity such as β-alumina (Itoh et al. 1984, Itoh and Kozuka 1985, Sugimoto and Kozuka 1988) and Nasicon (Saito et al. 1983, Maruyama et al. 1985, Akila and Jacob 1988), by applying a surface layer of sodium sulphate on the electrolyte, such that there is a chemical coupling between the gas phase and the conducting sodium ions in electrolyte through the sulphate auxiliary phase. In all the above examples, catalysis has been necessary in order to achieve SO_2/SO_3 equilibria. Emf is dependent upon the oxygen partial pressure, if not maintained identical in both electrode compartments.

In a novel approach, YSZ has been interfaced with either Nasicon or Na β-alumina and the same test gas is exposed to both the electrode such that the two compartments are not separated (fig. 46), which greatly simplifies the design and the operation of the sensors in practice (Slater et al. 1996). The arrangement of the cell can be described as

$$\text{Test gas, Pt} \mid \text{YSZ} \mid \text{Nasicon} \mid Na_2SO_4 \mid \text{Pt, Test gas.}$$

Electrode reactions for SO_3 sensing can be expressed as

$$Na_2SO_4 = 2Na^+ + SO_3(g) + \tfrac{1}{2}O_2(g) + 2e^-, \tag{7.14}$$

$$\tfrac{1}{2}O_2(g) + 2e^- = O^{2-}, \tag{7.15}$$

$$2Na^+ + O^{2-} = Na_2O \quad \text{(YSZ/Nasicon interface).} \tag{7.16}$$

Oxygens involved in both anodic and cathodic reactions cancel out of the final emf–gas composition relationship. Using the known values of free energy of formation of Na_2SO_4 and the activity of Na_2O in Nasicon, it can be shown that

$$\text{emf} = \text{const.} + \frac{RT}{2F} \ln p_{SO_3}. \tag{7.17}$$

The sensor has been modified to measure SO_2 by providing a Pt/alumina catalyst for in-situ catalysis of SO_2 oxidation to an equilibrium concentration of SO_3 at a temperature near 1000 K (Slater et al. 1996, Kumar 1997).

Using the above principles, other gas sensors have been developed, with K_2CO_3 as solid electrolyte (Gauthier and Chamberland 1977) or Nasicon/Na_2CO_3 (Saito and Maruyama 1988, Yao et al. 1990, Kale et al. 1996, Fray et al. 1995, Kumar and Fray 1997) for CO_2 sensing.

7.5.2. *HCl sensors*

A novel solid-state electrochemical sensor for monitoring HCl has been recently developed by interfacing the protonically conducting $SrCeO_3$ doped with 10 mol% of Nd, and $SrCl_2$, a chloride-ion conductor (Ahmad et al. 1996, Fray et al. 1995, Kumar 1997, Kumar and Fray 1997). $SrCl_2$ is melted into the cerate tube to form a compact plug as

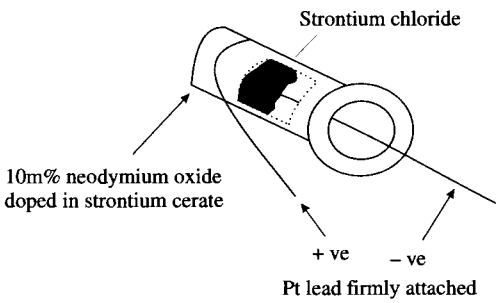

Fig. 47. Schematic diagram of a HCl gas sensor. (Redrawn after Ahmad et al. 1996 by permission from the publisher, Elsevier Science Ltd.)

shown in fig. 47. The variation of emf with HCl concentration in argon gas is shown in fig. 48. The emf is related to the HCl concentration as

$$\text{Emf} = \frac{RT}{2F} \ln p_{HCl} + \text{const.} \tag{7.18}$$

This concept has also been applied for detecting HF, H_2O and H_2S (Kumar 1997).

8. Concluding remarks

The rare-earth elements consist of scandium, yttrium and the fifteen lanthanoids usually associated with a stable valency of three and similar ionic radii as a result of the lanthanide

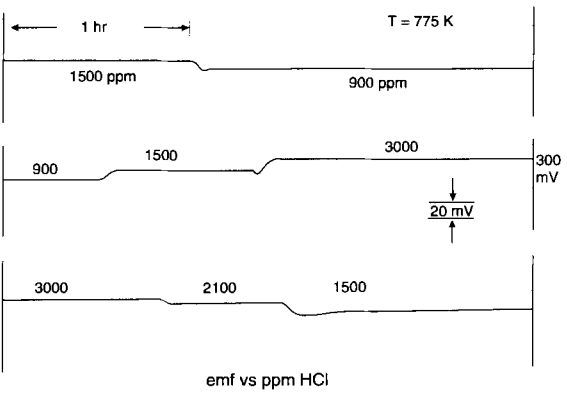

Fig. 48. Emf vs ppm HCl in argon using the sensor shown in fig. 47. (Redrawn after Ahmad et al. 1996 by permission from the publisher, Elsevier Science Ltd.)

contraction. Some of the elements exhibit di- or tetravalency in addition to trivalency, which can alter the ionic radius. The above properties allow a wide choice of components either as base material, as dopant, and in some cases even as the conducting component.

Rare-earth elements are vital constituents of several prominent high-temperature solid electrolytes ranging from oxygen- or fluoride-ion conductors in the fluorite structures to protonic conductors in the doped perovskite phases and trivalent-ion conduction in $Sc_2(WO_4)_3$ and β-alumina-type compounds. Solid electrolytes are considered as important for scientific studies and technological applications in vital areas such as fuel cells, batteries, sensors, process control and environmental protection.

References

Abraham, S.C., P. Marsh and C.P. Brandle, 1987, J. Chem. Phys. **86**, 4221.

Adachi, G., 1988, Sermikkusu **23**, 435.

Adachi, G., and N. Imanaka, 1991, Chem. Sens. Tech. **3**, 131.

Adachi, G., and N. Imanaka, 1995, in: Handbook on the Physics and Chemistry of Rare Earths, Vol. 21, eds K.A. Gschneidner Jr. and L. Eyring (Elsevier, Amsterdam) p. 179.

Adachi, G., and N. Imanaka, 1996, in: Proc. 14th IUPAC Conf. On Chemical Thermodynamics, Osaka, p. 519.

Ahmad, N.N., G.M. Kale, R.V. Kumar and D.J. Fray, 1996, in: Proc. 10th Int. Conf. on Solid State Ionics, Singapore, p. 1013.

Akila, R., and K.T. Jacob, 1988, J. Appl. Electrochem. **18**, 245.

Anderson, M.P., D.E. Cox, K. Halperin and A.S. Nowick, 1983, Solid State Ionics **9**, 953.

Aono, H., E. Sugimoto, Y. Sadoka, N. Imanaka and G. Adachi, 1990, J. Electrochem. Soc. **137**, 1023.

Bananos, N., B. Ellis and M.N. Mahmood, 1988, Solid State Ionics **28–30**, 579.

Bykov, A.B., A.P. Chirkin, L.N. Demyanets, S.N. Doronin, E.A. Genkina and A.K. Ivanov-Shits, 1990, Solid State Ionics **38**, 31.

Casciola, M., U. Costantino and S. D'Manico, 1988, Solid State Ionics **28**, 617.

Chandra, S., ed., 1980, Superionic Solids – Principles and Applications (North-Holland, Amsterdam).

Cobb, L.J., R.V. Kumar and D.J. Fray, 1996, Ionics **2**, 231.

Collin, G., R. Comes, J.P. Boilot and P. Colomban, 1988, Solid State Ionics **28–30**, 427.

Colomban, P., ed., 1992, Proton Conductors (Cambridge University Press, Cambridge).

Dell, R.M., and A. Hooper, 1978, in: Solid Electrolytes, eds P. Hagenmuller and W. van Gool (Academic Press, New York) p. 291.

Dietz, H., 1982, Solid State Ionics **6**, 175.
Donitz, W., and E. Erdle, 1985, Int. J. Hydrogen Energy **10**, 291.
Dunn, B., and G.C. Farrington, 1980, Mater. Res. Bull. **15**, 1773.
Dunn, B., and G.C. Farrington, 1983, Solid State Ionics **9/**, 223.
Eguchi, K., T. Setoguchi, T. Inoue and H. Arai, 1992, Solid State Ionics **52**, 165.
Esaka, T., Y. Kobayashi, H. Obata and H. Iwahara, 1989, Solid State Ionics **34**, 287.
Farrington, G.C., B. Dunn and J.O. Thomas, 1983, Appl. Phys. **32A**, 159.
Fouletier, J., G. Vitter and M. Kleitz, 1975, J. Appl. Electrochem. **5**, 111.
Frant, M.S., and J.W. Ross Jr, 1966, Science **154**, 1553.
Fray, D.J., and R.V. Kumar, 1994, in: Ceramics in Energy Applications, Proc. 2nd Int. Conf. Inst. Energy (The Institute of Energy, London) p. 191.
Fray, D.J., and R.V. Kumar, 1997, British Patent Application, File No. 9713953.9.
Fray, D.J., R.V. Kumar and G.M. Kale, 1995, British Patent Application 9521169.4.
Gauthier, M., and A. Chamberland, 1977, J. Electrochem. Soc. **124**, 1579.
Geller, S., ed., 1977, Solid Electrolytes (Springer, Berlin).
George, A.M., and A.N. Virkar, 1988, J. Phys. Chem. Solids **49**, 743.
Ghosal, B., E.A. Mangle, M.R. Topp, B. Dunn and G.C. Farrington, 1983, Solid State Ionics **9**, 273.
Gibson, R.W., R.V. Kumar and D.J. Fray, 1999, Solid State Ionics **121**, 43.
Goodenough, J., H.Y.-P. Hong and J.A. Kafalas, 1976, Mater. Res. Bull. **11**, 203.
Goto, K.S., 1988, Solid State Electrochemistry and its Applications to Sensors and Electronic Devices (Elsevier, Amsterdam).
Gulens, J., T.H. Longhurst, A.K. Kuriakose and J.D. Canaday, 1988, Solid State Ionics **28**, 622.
Hagenmuller, P., and W. Van Gool, eds, 1978, Solid Electrolytes (Academic Press, New York).
Harwig, H.A., and A.G. Gerards, 1978, J. Solid State Chem. **26**, 265.
Haydock, H., 1994, in: Ceramics in Energy Applications, Proc. 2nd Int. Conf. Inst. Energy, London (The Institute of Energy, London) p. 79.
Hong, H.Y.-P., 1976, Mater. Res. Bull. **11**, 173.
Hotzel, G., and W. Weppner, 1986, Solid State Ionics **18/**, 1223.
Hu, K., C. Chen, D. Peng and G. Meng, 1988, Solid State Ionics **28**, 566.
Imanaka, N., G. Adachi and J. Shiokawa, 1983, Chem. Lett., p. 287.
Imanaka, N., Y. Yamaguchi, G. Adachi and J. Shiokawa, 1986, Solid State Ionics **20**, 153.
Imanaka, N., S. Kuwabara, G. Adachi and J. Shiokawa, 1987a, Solid State Ionics **23**, 15.
Imanaka, N., Y. Yamaguchi, G. Adachi and J. Shiokawa, 1987b, J. Electrochem. Soc. **134**, 725.
Imanaka, N., G. Adachi and J. Shiokawa, 1988, Chem. Lett., p. 1133.
Imanaka, N., Y. Kobayashi and G. Adachi, 1995, Chem. Lett., p. 433.
Inaguma, Y., and M. Itoh, 1996, in: Proc. 10th Int. Conf. on Solid State Ionics, Singapore, December 1995, ed. B.V.R. Chowdhury (North-Holland, Amsterdam) p. 257.
Inaguma, Y., J. Yu, Y.-S. Shan, M. Ito and T. Nakamura, 1995, J. Electrochem. Soc. **142**, L8.
Infante, C.E., C. Gronomeyer and F. Li, 1987, Solid State Ionics **25**, 63.
Ioannou, A.S., and W.C. Maskell, 1992, Solid State Ionics **53–56**, 85.
Ishihara, T., H. Matsuda, Y. Mizuhara and Y. Takita, 1994, Solid State Ionics **70/**, 234.
Ishihara, T., H. Matsuda and Y. Takita, 1996, Solid State Ionics **86**, 197.
Ito, M., Y. Inaguma, W.H. Jung, L. Chen and T. Nakamura, 1994, Solid State Ionics **70/**, 203.
Itoh, M., and Z. Kozuka, 1985, Trans. Jpn. Inst. Met. **26**, 17.
Itoh, M., E. Sugimoto and Z. Kozuka, 1984, Trans. Jpn. Inst. Met. **25**, 504.
Ivanov-Shits, A.K., N.I. Sorokin, P.P. Fedorov and B.P. Sobolev, 1989, Solid State Ionics **31**, 1154.
Iwahara, H., 1992, Solid State Ionics **52**, 99.
Iwahara, H., 1995, Solid State Ionics **77**, 289.
Iwahara, H., 1996, in: Proc. 10th Int. Conf. on Solid State Ionics, Singapore, December 1995, ed. B.V.R. Chowdhury (North-Holland, Amsterdam) p. 9.
Iwahara, H., and T. Esaka, 1984, J. Appl. Electrochem. **14**, 687.
Iwahara, H., T. Esaka and T. Sato, 1981a, J. Solid State Chem. **39**, 173.
Iwahara, H., T. Esaka, H. Uchida and N. Maeda, 1981b, Solid State Ionics **3/**, 359.
Iwahara, H., H. Uchida and N. Maeda, 1983, Solid State Ionics **9**, 1021.

Iwahara, H., T. Yajima, H. Uchida and K. Morimoto, 1991a, in: Proc. 3rd Int. Symp. on Solid Oxygen Fuel Cells, Athens, p. 229.

Iwahara, H., H. Uchida, K. Ogaki and H. Nagato, 1991b, J. Electrochem. Soc. **138**, 295.

Iwahara, H., T. Yajima, T. Hibino and H. Uchida, 1993, J. Electrochem. Soc. **140**, 1687.

Jacob, K.T., and D.B. Rao, 1979, J. Electrochem. Soc. **126**, 1842.

Kale, G.M., A.J. Davidson and D.J. Fray, 1996, in: Proc. 10th Int. Conf. on Solid State Ionics, Singapore, December 1995, ed. B.V.R. Chowdhury (North-Holland, Amsterdam) p. 1107.

Kaneko, H., W.C. Maskell and B.C.H. Steele, 1987, Solid State Ionics **22**, 161.

Kingery, W.D., 1980, Introduction to Ceramics (Wiley, New York).

Kosachi, I., and H.C. Tuler, 1995, Solid State Ionics **80**, 223.

Kumar, R.V., 1984, Ph.D. Thesis (McMaster University, Canada).

Kumar, R.V., 1996, in: Proc. Asian Conf. on X-rays and Related Techniques in Research and Industry, Malaysia (University Sains, Malaysia) p. 171.

Kumar, R.V., 1997, J. Alloys & Compounds **250**, 501.

Kumar, R.V., and D.J. Fray, 1988a, Sensors Actuators **15**, 185.

Kumar, R.V., and D.J. Fray, 1988b, Solid State Ionics **28–30**, 1688.

Kumar, R.V., and D.J. Fray, 1989, in: Extractive Metallurgy '89, ed. D.S. Flett (IMM, London) p. 315.

Kumar, R.V., and D.J. Fray, 1993, Solid State Ionic Lett. **4**, 8.

Kumar, R.V., and D.J. Fray, 1997, in: Proc. Symp. on the Applications of Sensors and Modelling to Materials Processing, 126th Annual Meeting of the TMS, Orlando, FL, eds S. Viswanathan et al. (TMS) p. 317.

Kumar, R.V., and D.A.R. Kay, 1985, Metall. Trans. B **16**, 107.

Kumar, R.V., D.J. Fray, H. Williams, A. Misson and J. Evetts, 1993, J. Electrochem. Soc. **140**(10), 2895.

Kumar, R.V., L.J. Cobb and D.J. Fray, 1996, Ionics **2**, 162.

Kummer, J.T., 1972, in: Progress in Solid State Chemistry, Vol. 7, eds H. Reiss et al. (Pergamon Press, New York) p. 141.

Laskar, A.L., and S. Chandra, eds, 1991, Superionic Solids and Solid Electrolytes (Academic Press, New York).

Liu, Q., and W.L. Worrell, 1988, Solid State Ionics **28–30**, 1668.

Maruyama, T., Y. Saito, Y. Matsumoto and Y. Yano, 1985, Solid State Ionics **17**, 281.

Maskell, W.C., 1997, in: Proc. 1997 Sensor and Transducer Conf., ed. R. Bogue (MTEC, NEC, Birmingham) ch. 3.

Maskell, W.C., and B.C.H. Steele, 1988, Solid State Ionics **28–30**, 1677.

Minn, N.Q., and T. Takahashi, 1995, Science and Technology of Ceramic Fuel Cells (Elsevier, Amsterdam).

Miura, N., J. Hisamoto, S. Kuwata and N. Yamazoe, 1987, Chem. Lett., p. 1477.

Miyauchi, N., N. Mizutani and M. Kato, 1981, Nippon Kagaku Kaishi, p. 516.

Mizuno, M., J. Yamada and T. Noguchi, 1974, Yogyo-Kyo-Kaishi **82**, 631.

Mizutani, N., Y. Tajima and M. Kato, 1976, J. Am. Ceram. Soc. **59**, 168.

Moon, P.K., and H.L. Tuller, 1987, in: Proc. 6th Int. Conf. on Solid State Ionics, Garmisch Partenkirchen, September, eds W. Weppner and H. Schultz (North-Holland, Amsterdam) p. 470.

Morris, D.R., R.V. Kumar and D.J. Fray, 1989, Ironmaking Steelmaking **16**(6), 429.

Nagel, L.E., and M. O'Keeffe, eds, 1976, Fast Ion Transport in Solids (North-Holland, Amsterdam) 165 pp.

Nernst, W., 1900, Z. Electrochem. **6**, 41.

O'Keeffe, M., 1973, Science **180**, 1276.

Pal, U.B., and S.C. Singhal, 1990, J. Electrochem. Soc. **137**(9), 2937.

Pelloux, A., P. Fabry and C. Deportes, 1973, C.R. Acad. Sci. Paris **C276**, 241.

Prakash, G., and K. Shahi, 1987, Solid State Ionics **23**, 151.

Reau, J.M., and J. Portier, 1978, in: Solid Electrolytes, ed. P. Hagenmuller and W. Van Gool (Academic Press, New York) p. 313.

Saito, Y., and T. Maruyama, 1988, Solid State Ionics **28–30**, 1644.

Saito, Y., T. Maruyama, Y. Matsumoto and Y. Yano, 1983, in: Proc. Int. Meeting on Chemical Sensors, Bordeaux, eds J.-L. Aucouturier et al., p. 326.

Saito, Y., T. Maruyama and K. Kobayashi, 1984, Solid State Ionics **14**, 265.

Sato, M., T. Suzuki, K. Yoshida, K. Uematsu, K. Toda and Z. Ye, 1997, J. Alloys & Compounds **250**, 510.

Scherban, T., W. Lee and A.S. Nowick, 1989, Solid State Ionics **35**, 189.

Seiyama, T., ed., 1988–94, Chemical Sensor Technology, Vols. 1–5 (Kodannsha, Tokyo).

Shin, S., H.H. Huang and M. Ishigame, 1995, Solid State Ionics **40/**, 910.

Shores, D.A., and R.A. Rapp, 1972, J. Electrochem. Soc. **119**, 300.

Shriver, D.F., and G.C. Farrington, 1985, Chem. Eng. News (May 20), p. 42.

Singhal, S.C., 1997, in: Proc. 5th Int. Symp. On Solid Oxide Fuel Cells, Aachen, pp. 37–50.

Slade, R.C.T., J. Barker and T.K. Halstead, 1987, Solid State Ionics **24**, 147.

Slater, D.J., R.V. Kumar and D.J. Fray, 1996, in: Proc. 10th Int. Conf. on Solid State Ionics, Singapore, December 1995, ed. B.V.R. Chowdhury (North-Holland, Amsterdam) p. 1063.

Soejima, S., and S. Mase, 1985, SAE Congress 850378, Detroit.

Staikov, G., ed., 1991, β-Alumina and β Batteries (Trans Tech Publications, Aedermannsdorf, Switzerland).

Steele, B.C.H., 1990, Mater. & Design **11**(1), 4.

Steele, B.C.H., 1996, in: Proc. 10th Int. Conf. on Solid State Ionics, Singapore, December 1995, ed. B.V.R. Chowdhury (North-Holland, Amsterdam) p. 1223.

Steele, B.C.H., J.A. Lane, K. Zheng and J. Bae, 1994, in: Proc. 2nd Int. Conf. on Ceramics in Energy Applications (The Institute of Energy, London) p. 109.

Stotz, S., and C. Wagner, 1966, Ber. Bunsenges., Phys. Chem. **70**, 781.

Sugimoto, E., and Z. Kozuka, 1988, Nippon Kogyo Kaishi **104**, 89.

Sun, W.Y., T.S. Yen and T.Y. Tien, 1991, J. Solid State Chem. **95**, 424.

Sutija, D.P., T. Norby and B. Bjornbom, 1995, Solid State Ionics **77**, 579.

Takahashi, T., and H. Iwahara, 1966, Denki Kagaku **34**, 906.

Takahashi, T., and H. Iwahara, 1967, Denki Kagaku **35**, 433.

Takahashi, T., and H. Iwahara, 1980, Rev. Chim. Miner. **17**, 243.

Takahashi, T., H. Iwahara and T. Arao, 1975a, J. Appl. Electrochem. **5**, 187.

Takahashi, T., T. Esaka and H. Iwahara, 1975b, J. Appl. Electrochem. **5**, 197.

Takahashi, T., H. Iwahara and T. Ishikawa, 1977, J. Electrochem. Soc. **124**, 280.

Takahashi, T., S. Tanase and O. Yamamoto, 1978, Electrochim. Acta **23**, 369.

Takashima, M., and C. Kano, 1987, Solid State Ionics **23**, 99.

Takashima, M., S. Yonezawa and N. Horita, 1996, J. Mater. Chem. **6**, 795.

Tannenberger, H., H. Schacher and P. Kovas, 1965, in: Proc. J. Int. d'Etude des Piles a Combustible, Brussels, p. 19.

Thomas, R.E., and G.D. Brunton, 1966, Inorg. Chem. **5**, 1937.

Tuller, H.L., and P.K. Moon, 1988, Mater. Sci. Eng. B **1**, 171.

Turillas, X., A.P. Sellara and B.C.H. Steele, 1988, Solid State Ionics **28–30**, 465.

Uchida, H., N. Maeda and H. Iwahara, 1983, Solid State Ionics **11**, 117.

van Dijk, T., K.J. de Vries and A.J. Burggraaf, 1980, Phys. Status Solidi A **58**, 115.

van Gool, W., 1973, in: Solid Electrolytes, eds P. Hagenmuller and W. van Gool (Academic Press, New York) p. 9.

Verkerk, M., G.M.H. van de Velde and A.J. Burggraaf, 1982, J. Phys. Chem. Solids **43**, 1129.

Verstegen, J.M.P.J., J.L. Sommerkdijk and J.G. Verviet, 1973, J. Lumin. **6**, 425.

Vinke, I.C., K. Seshan, B.A. Boukamp, K.J. de Vries and A.J. Burggraaf, 1989, Solid State Ionics **34**, 235.

Wang, W.S., L. Rao, Z. Lu and X. Yi, 1988, Solid State Ionics **28–30**, 424.

Wang, X.H., A.M. Lejus, D. Vivien and R. Collongues, 1988, Mater. Res. Bull. **23**, 43.

Warner, T., D.J. Fray and A. Davies, 1996, Solid State Ionics **92**, 99.

Warner, T., D.J. Fray and A. Davies, 1997, J. Mater. Science **32**, 279.

Weppner, W., 1987, Sensors Actuators **12**, 107.

White, S., 1970, Nature **225**, 375.

Wiedenmann, H.-M., G. Hotzel, H. Neumann, J. Riegel and H. Weyl, 1994, in: Automotive Electronics Handbook, p. 6.1.

Worrell, W.L., 1983, in: Proc. Int. Meeting on Chemical Sensors, Bordeaux, eds J.-L. Aucouturier et al., p. 332.

Wu, M.K., J.R. Ashburn, C.J. Tong, P.H. Hor, R.L. Meng, L. Gao, Z.J. Huang, Y.Q. Wang and C.W. Chu, 1987, Phys. Rev. Lett. **58**, 908.

Yahiro, H., K. Eguchi and H. Arai, 1986, Solid State Ionics **21**, 37.

Yajima, T., and H. Iwahara, 1992, Solid State Ionics **50**, 281.

Yajima, T., K. Koide, N. Fukatsu, T. Ohashi and H. Iwahara, 1993, Sensors and Actuators **13–14**, 697.

Yamamota, O., Y. Takeda, R. Kano and M. Fushimi, 1985, Solid State Ionics **17**, 107.

Yamashita, K., H. Owada, T. Umegaki and T. Futagami, 1988, Solid State Ionics **28**, 660.

Yao, S., Y. Shimizu, N. Miura and N. Yamazoe, 1990, Chem. Lett., p. 2033.

Yao, Y.F.Y., and J.T. Kummer, 1967, J. Inorg. Nucl. Chem. **29**, 2453.

Zhen, Y.S., S. Milne and R.B. Brook, 1987, Sci. Ceram. **14**, 983.

Zheng, M., and B. Zhu, 1995, Solid State Ionics **80**, 59.

Handbook on the Physics and Chemistry of Rare Earths
Vol. 28
edited by K.A. Gschneidner, Jr. and L. Eyring

Chapter 179

ACTIVATED THERMOLUMINESCENCE (TL) DOSIMETERS AND RELATED RADIATION DETECTORS

A. HALPERIN
Racah Institute of Physics, Hebrew University, Jerusalem 91904, Israel

Contents

List of abbreviations

AG	afterglow
BES	bound exciton states
CB	conduction band
CC	color centers
CL	cathodoluminescence
EEE	exoelectron emission
EPR	electron paramagnetic resonance
ESR	electron spin resonance
eV	electronvolt
GC	glow curve
Gy	Gray (SI unit for absorbed dose, 1 Gy = 100 rad)
ir	initial rise
IR	infrared
LET	linear energy transfer
LNT	liquid-nitrogen temperature
OA	optical absorption
OSL	optically stimulated luminescence

OSTL	optically stimulated thermoluminescence	SIU	standard international units
PC	photochromic centers	SXR	soft X-rays
PL	photoluminescence	TL	thermoluminescence
PM	photomultiplier	TLD	TL dosimeter
PSL	photostimulated luminescence	TSC	thermally stimulated conductivity
PSTL	photostimulated thermoluminescence	TSL	thermally stimulated luminescence (= TL)
PTTL	phototransferred thermoluminescence	TSEE	thermally stimulated electron emission
REM	Roentgen equivalent man	VB	valence band
RPL	radio photoluminescence	XL	X-ray induced luminescence
SD	standard deviation	UV	ultraviolet

List of symbols

A_m	recombination probability	N	concentration of electron traps N
A_n	retrapping probability	n	concentration of electrons in the N traps
b	general kinetic order	n_c	concentration of electrons in CB
E	thermal trap depth (thermal correction energy)	M	concentration of hole traps M
		m	concentration of holes in the M traps
E_d	thermal decay (or quenching) energy	R	lanthanides (rare earths)
E_g	forbidden gap energy	s	pre-exponential (or frequency) factor
F, F′, F_i etc.	color centers due to electron trapped at various imperfections	T	temperature on absolute scale
		T_m	temperature at the maximum of a TL peak
	V, V_K, V_i etc.: color centers related with trapped holes	Z	atomic number
		ω, τ, δ	shape factors of a TL peak (see fig. 4)
	Z, Z_1 etc.: color centers formed in crystal containing divalent impurities	μ_g	shape factor: $\mu_g = \delta/\omega$
K	temperature on absolute scale		
k	Boltzmann constant		

1. Introduction

Insulators and semiconductors exposed at a temperature T_0 to ionizing radiation or light will often emit characteristic light when warmed up above T_0. This effect is conventionally called *thermoluminescence* (TL). Some investigators prefer to call it *thermally stimulated luminescence* (TSL), which stresses the fact that the thermal energy supplied during warming only stimulates the emission potentially excited by the irradiation.

TL was first reported in 1663 when Robert Boyle presented to the Royal Society in London his observation of a *glimmering* light emitted by a diamond warmed up in the dark. Wiedemann and Schmidt (1895) explained the above effect as the release, in the form of light, of energy stored in the crystal by irradiation. Later, Urbach (1930) suggested that TL can be used for the investigation of the nature and characteristics of charge-carrier trapping levels, which act as energy storage levels in TL emitting crystals.

The TL can be described as filling up, usually only partly, of metastable levels by charge carriers, let us say electrons, by the irradiation. On subsequent warming the trapped electrons are raised by the thermal energy to levels from which they can recombine radiatively with charge carriers of the opposite sign, positive *holes* in the present case, at the so-called *luminescence centers.* The concentration of traps and luminescence centers, and with it the storage capacity and the TL intensity, can be increased by introducing suitable point defects, e.g. impurities, into the sample. Such doping that gives intense TL emission is called *activation* of the sample. The activated samples are commonly called *phosphors.*

The quality of phosphors and their suitability for practical devices, e.g. radiation dosimeters, depend on the dopants used, on their concentration and on other factors as will be shown below. The lanthanides, R, play a unique role in the production of high-sensitivity reliable TL dosimeters. The present article will give a review of the advance in the investigation of the properties of R-containing phosphors and in the TL dosimeters based on these phosphors.

More than a thousand original papers in this field have been published in the last 30 years. Obviously, not all of them can be included in the present article. In selecting the papers for the review, emphasis has been placed on their contribution to the advances in the field. In addition, papers published in recent years, naturally containing more advanced theoretical and practical new results, were given higher priority. Reviews of older papers can be found in published monographs on these topics cited below. Still, good and seminal older work was included, especially when needed for a clearer view on the progress in the field.

Section 2 will give an introductory presentation of the essence of TL and of dosimetry. For deeper understanding the reader will be referred to monographs on these topics. The rest of the article will review the progress in the field and future trends. For the benefit of investigators who work in the field of R-activated phosphors the review will be ordered according to the host compounds.

2. Background

2.1. *Introduction to TL*

2.1.1. *Energy bands in solids*

The band theory, given in every text book on solid state, shows that electrons in a solid are restricted to allowed energy bands and energy levels. Each energy band can accommodate a given number of electrons. The deep-lying bands are filled with electrons up to a given energy band for which no more electrons are available. For insulators, the highest electron-containing energy band is filled with electrons and the next energy band is separated from the lower one and contains no electrons. Of these two energy bands the filled one is named the *valence band* (VB) and the empty one is the *conduction band* (CB). To make a good insulator the energy gap, E_G, between the VB and the CB should be high

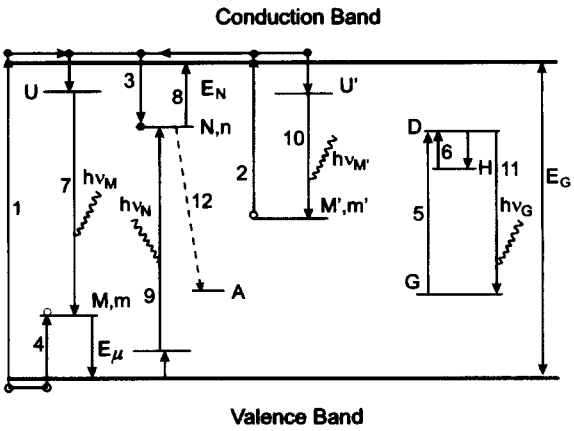

Fig. 1. A schematic diagram of the forbidden gap (E_G) of an insulating phosphor. Various defect levels are shown. The arrows show possible transitions during the excitation, trapping and emission (see text).

compared to the thermal energy at the ambient temperature, $E_G \gg kT$, where k is the Boltzmann constant and T is the ambient temperature on the absolute temperature scale. In a perfect crystal there are no allowed energy levels in the forbidden gap. In the case of semiconductors things are somewhat more complicated as shown in solid-state text books. Many semiconductors can still be treated, as far as TL is concerned, in a way similar to that for insulators.

Incorporation of impurities or other defects into the host crystal introduces allowed energy levels in the forbidden gap. A schematic diagram showing such defect levels is given in fig. 1. Levels in the forbidden gap close to the CB (levels N) act as electron traps. Electrons at the N levels cannot drop down to the completely full VB and so they remain trapped. Possible ways by which some of the trapped electrons can leave the N levels without warming the sample will be given when discussing the *fading* of TL in sect. 2.1.5 below. Defect levels in the lower half of the forbidden gap (M and M′ levels in fig. 1) are usually filled with electrons.

Exposing the sample to ionizing radiation raises VB electrons to the CB leaving behind holes (missing electrons) in the VB (transition 1). CB electrons are free to move, and some of them will get trapped at N levels (transition 3). Some M electrons will now get accommodated at the VB states emptied by the irradiation, leaving holes in the M levels. For the analogy between the CB electrons and the VB holes it is convenient to describe the later transitions as the trapping of VB holes at the M hole traps (transition 4). The ionizing radiation has thus resulted in the trapping of the excited electrons, at a concentration n, at N traps and trapping of the VB-radiation-produced holes, at a concentration m, at M traps. Let us note that both the VB and the CB are involved in this process.

Near-UV or visible light cannot produce ionization by transitions across the forbidden gap when E_G is greater than about 6 eV. Yet, excitation of electrons up to the CB and their trapping in N traps is still possible. UV or even visible light can excite electrons from defect levels in the lower half of the forbidden gap up to the CB. This is shown in fig. 1 for comparatively high-lying M′ levels (transitions 2). The excited electrons will

get trapped at N traps as before, leaving behind m′ holes at M′ centers. In this case the CB is involved in the transitions but not the VB.

Transitions in which neither the CB nor the VB are involved in the excitation and trapping processes are the so-called *localized transitions* shown schematically at the right in fig. 1. In this case G is the ground state of an impurity and D and H are excited and metastable states, respectively, of the same impurity. All these states are located in the forbidden gap of the host crystal. The irradiation (often by light) excites the ground-state electron to the D state, from where it relaxes and remains trapped at the metastable state H. Obviously both the VB and CB are not involved in the transitions in this case.

Figure 1 shows only one type of electron traps involving transitions up to the CB (N), and two types of hole traps (M and M′).

2.1.2. *Thermal release of trapped charge carriers and the TL emission*

A full treatment of the theory, the experimental set-ups and TL measurements is beyond the scope of this article. These can be found in monographs in this field, such as those by Chen and Kirsh (1981), McKeever (1985) and Vij (1993). References to earlier books on TL can also be found in the above monographs. Books on dosimetry also give an introductory chapter on TL. In the following an outline is given of the basic principles of TL. Results of mathematical and experimental methods in TL research will be given in as much as needed for the understanding of the results presented in papers reviewed in the course of the article.

We begin with a sample containing only one type of electron traps (in short – one electron trap) and one hole trap (N and M in fig. 1). The characters N and M will be taken also to stand for the concentrations of the respective electron and hole traps in the sample. We assume that the sample has been exposed to radiation which filled up the N and M traps to concentrations n and m, respectively. After the termination of the excitation the concentration of electrons in the CB (n_c) and holes in the VB (m_v) will drop down to values very small compared to n and m, respectively, when practically all the electrons excited to the CB are trapped at the N traps and all the holes left behind in the VB are at the M traps, so we have $n = m$.

By thermodynamics, the probability per second for an electron to be released thermally from N traps (and analogously for M traps) will be given by

$$p = s\mathrm{e}^{-E/kT}, \tag{1}$$

where s is the *frequency factor,* which depends only slightly on temperature, E is the trap depth, k is the Boltzmann constant and T is the absolute temperature. On warming the sample, p rises exponentially with temperature, and at a given temperature emptying of the N traps will become significant and continue until the full exhaustion of the N traps. When $p_N \gg p_M$ the N electrons will be released and recombine with the holes at the M centers. When the recombination is radiative a TL peak emitting the photon energy $h\nu_M$ will be observed. $h\nu_M$ corresponds to the energy drop either from the CB or from an excited level (U in fig. 1) to the luminescence center M. The analogous case of release of

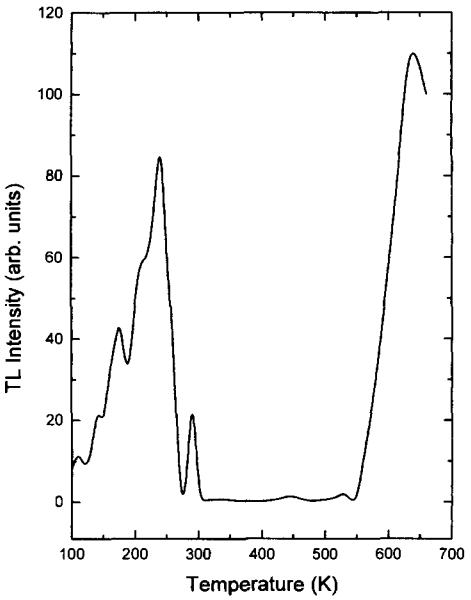

Fig. 2. A glow curve obtained for a quartz crystal exposed to about 3×10^3 Gy of X-rays (50 kVp, 20 mA). Heating rate 10 K min^{-1}.

holes from M and recombination at an electron containing luminescence center will take place when $p_M \gg p_N$. In this case recombination will take place at the N levels, serving now as luminescence centers, with the emission $h\nu_N$ (fig. 1).

In practice, phosphors have more than a single trap and a single recombination center, which results in a curve of TL intensity versus temperature exhibiting a variety of TL peaks spreading over a wide temperature range. Such a curve is called a *glow curve.* An example of a glow curve is shown in fig. 2. It is of course possible that some of the TL peaks in the glow curve are related to electrons released from traps and recombining with holes at luminescence centers and others are obtained by the release of holes followed by recombination with electrons.

Back to the case of a single trap (N) and a single luminescence center (M) we assume that the N electrons will be released during the warming and recombine radiatively with holes at M centers. The TL intensity (I) will go up with the concentration of electrons in the CB (n_c) and holes at M (m). If the probability of a radiative transition is A_m we obtain

$$I = -\frac{dm}{dt} = A_m m n_c. \tag{2}$$

The rate of change of the electron concentration at N will be given by the balance between those excited up to the conduction band given by np and the retrapping at N of CB electrons given by $n_c(N-n)A_n$, where A_n is the probability for retrapping (transitions 8 and 3 in fig. 1). This gives:

$$-\frac{dn}{dt} = np - n_c(N-n)A_n. \tag{3}$$

Similarly the kinetic balance of electrons in the CB is given by transitions 3,7 and 8 in fig. 1, which gives:

$$\frac{dn_c}{dt} = np - [mA_m + (N-n)A_n]. \tag{4}$$

The three differential equations (2–4) have to be integrated. To obtain I as a function of temperature we have to introduce the heating rate β. Practically all TL measurements are taken at a constant heating rate $\beta = dT/dt$. Under these conditions there is no exact solution of the set of differential equations. It can of course be calculated numerically. An Appendix at the end of Chen and Kirsh (1981) gives a full treatment including a computer program for the numerical analysis of thermally stimulated processes. Most investigators, however, use approximate solutions of the differential equations. For the case treated above, the approximate solution by Halperin and Braner (1960) gives:

$$I = -\frac{dm}{dt} = pn\frac{A_m m}{A_m m + A_n(N-n)}. \tag{5}$$

In case of dominant recombination, or $A_m m \gg A_n(N-n)$, eq. (5) gives $I = pn$. This is the case of *first-order kinetics* called also *monomolecular kinetics*. For $A_n(N-n) \gg A_m m$, i.e. for the situation in which retrapping is dominant, I is nearly proportional to n^2, which is the case of *second-order kinetics* or *bimolecular kinetics*.

The treatment of localized transitions (fig. 1) is somewhat simpler. It can be found in Halperin and Braner (1960), which also gives detailed analyses of both the above cases. Chen (1969) has extended this treatment for a general order of kinetics given by b, where $I \propto n^b$. The main results of this treatment are given also in Chen and Kirsh (1981), pp. 163–167.

2.1.3. *TL measurements and experimental set-ups*

Basically TL measurements and instrumentation are very simple. For the excitation one needs a source, which according to the specific measurement could be a light source, X- or γ-rays, or suitable energetic particles. For measurements limited to above RT the sample has to be mounted in a suitable oven programmed for linear heating, preferably enabling various heating rates. When the measurements start below RT the sample has to be kept in a cryostat fitted with suitable windows for the excitation and for the TL-emission measurements. Most set-ups use a photomultiplier as a detector. The output can be recorded on a chart recorder or be stored in a computer which can be programmed to produce a full analysis of the results.

The heating rate used for the TL emission is of importance. When the sample is a single crystal, often a good heat insulator, high heating rates will give a lag between the measured temperature and the actual temperature of the sample; more than that, a temperature gradient will be formed within the sample. The use of bulky samples is therefore limited to heating rates of about 1 deg s^{-1}.

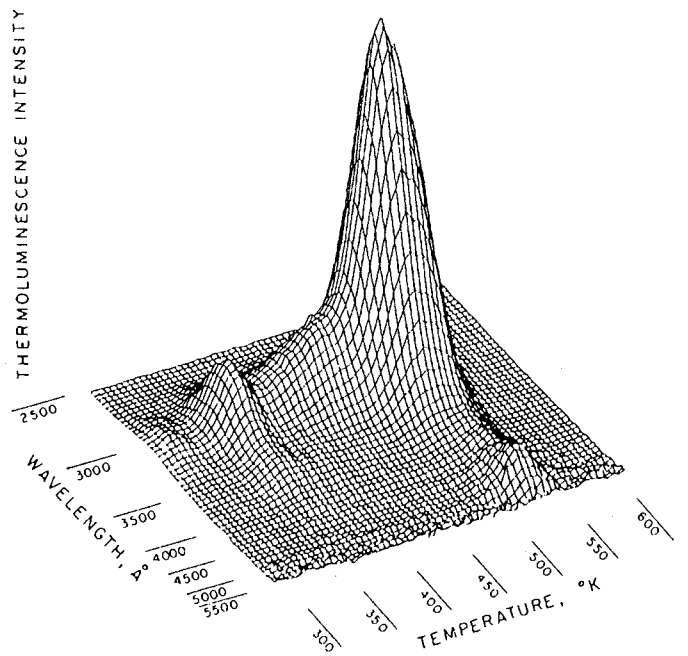

Fig. 3. A *three-dimensional plot* for a KCl:Tl crystal. The plot gives the TL intensity for the temperature range 300–600 K and emission wavelengths in the range 2500–5500 Å (250–550 nm).

Higher heating rates are however of advantage because fast emptying of traps gives higher TL peak intensities, rising nearly linearly with the heating rate. This is important when measuring weak signals. Powder samples spread on a heat-conducting metal plate enable higher heating rates. Such powders are used often for dosimetry, where the powder is mixed with gold dust, graphite dust or other conducting binders. This enables heating rates of more than 10 deg s^{-1}. Further improvement was reached by the hot fluid method and by infrared radiation. In the later case, developed by Yasuno et al. (1980), heating rates up to 300 deg s^{-1} are possible. Laser heating developed by Gasiot et al. (1982) and recently by Justus et al. (1996) enables heating rates up to 10^4 deg s^{-1}. In this case the extremely high temperatures are limited to a defect point of interest, with the bulk temperature rising only by a few tens of degrees.

Conventional TL measurements record glow curves giving the total emission or a narrow spectral band passed by a monochrometor. A better highlight on the emitted TL is obtained by the *three-dimensional* presentation. In this case glow curves covering a wide temperature range are taken over a wide wavelength range. The data are processed by a computer and presented as a plot of TL intensity against both temperature and wavelength (or photon energy). Figure 3 shows such a plot published by Mattern et al. (1970).

Automatic computerized glow curve analyzers were developed for large-scale monitoring of the output of TL dosimeters as described by Vana et al. (1988), by Sahre and Schonmuth (1993) and by others.

2.1.4. *Determination of TL parameters*

Equation (5) shows two parameters characteristic of a given TL peak for a measured sample. These are the frequency factor s and the trap depth E. Another characteristic parameter is the order of kinetics, which is not shown explicitly in eq. (5) but appears in the general order equation (see at end of sect. 2.1.2). There are several methods for the determination of the TL parameters:

(1) *The initial-rise (ir) method.* From eq. (5) it is clear that at the very beginning of a TL peak, when n and m remain practically unchanged, the TL intensity should rise exponentially with T, $I \propto p = s \exp(E/kT)$. A plot of $\log I$ as a function of the reciprocal temperature (T^{-1}) should then give a straight line from which E can be determined.

Care has to be taken in ir measurements to have the low-temperature tail of the measured TL peak clean from weak satellite TL peaks. This can be done by pre-warming the sample up to a temperature on the tail of the measured peak, which bleaches away the satellite peaks in this region. One has also to make sure that no thermal decay of the emission takes place in the relevant temperature range. If such a decay takes place (at a thermal activation energy E_d), this has to be added to the measured ir value of E. Similarly, if the frequency factor is temperature dependent, it will affect the measured E values. The later effect is, however, usually neglected.

Extension of the plot of $\log I$ beyond the ir region will, of course, give a deviation from the straight line. A plot of $\log(I/b)$, where b is the general kinetic order as a function of T^{-1}, should then give a straight line. Computer fitting of the experimental points to a straight line will give the order of kinetics of the measured TL peak. Once E and b are known s can easily be determined.

(2) *The TL peak-shape method.* A schematic diagram of a TL peak is shown in fig. 4. It peaks at a temperature T_m, where the intensity is I_m. T_1 and T_2 are the half-intensity ($I_m/2$) temperatures on both sides of T_m. ω, τ and δ are the total half-intensity width ($T_2 - T_1$), the lower-temperature halfwidth ($T_m - T_1$), and that at the higher-temperature side ($T_2 - T_m$), respectively. As shown by Halperin and Braner (1960), the peak shape depends on the order of kinetics. Thus for $n = m$ one gets for the symmetry $\mu = \delta/\omega$:

$$\mu_1 = e^{-1}(1 + \Delta); \qquad \mu_2 = 0.5(1 + \Delta), \tag{6}$$

where μ_1 and μ_2 are the symmetry factors (δ/ω) for first- and second-order kinetics, and $\Delta = 2kT_m/E$. A typical value for Δ is 0.6 when $\mu_1 \approx 0.39$ and $\mu_2 \approx 0.53$. Halperin and Braner (1960) have also shown that from the shape of the TL peak one can get the activation energies for first- and second-order peaks, E_1 and E_2 respectively. These can be obtained as functions of ω, δ or τ. However the first two cases require

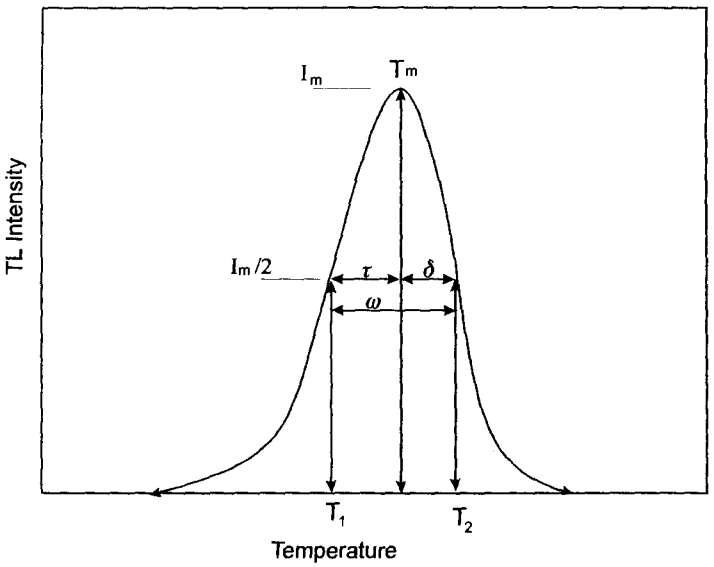

Fig. 4. A schematic presentation of a single TL peak (of first-order kinetics).

exact knowledge of T_2, which is difficult to determine because it is almost impossible to clean the high-temperature side of a TL peak. The expressions obtained using τ as given by Halperin et al. (1960) (for $n=m$) are

$$E_1 = \frac{1.72}{\tau} kT_m^2(1-2.58\Delta); \qquad E_2 = \frac{2}{\tau} kT_m^2(1-3\Delta). \tag{7}$$

For an improved version of the latter equations and an extension to the case of general-order kinetics, see Chen and Kirsh (1981), pp. 159–165.

(3) *Various-heating-rates method.* This method is based on the fact that T_m of a given TL peak depends on the heating rate. Measurements of the same peak at two different heating rates will then give the value of E. This method is given in Chen and Kirsh (1981), pp. 167–171. For a first-order kinetics peak, one gets approximately

$$E = \frac{kT_{m1}T_{m2}}{T_{m2}-T_{m1}} \ln\left[\frac{\beta_2}{\beta_1}\left(\frac{T_{m1}}{T_{m2}}\right)^2\right], \tag{8}$$

where T_{m1} and T_{m2} are the peak temperatures for the two heating rates β_1 and β_2. The difference $T_{m2}-T_{m1}$ is usually small and can thus affect the accuracy of the measured E values. It has therefore been suggested to use several heating rates. The plot of $\log T_m^2/\beta$ versus $1/T_m$ should then yield a straight line, from the slope of which E can be calculated. One should still make sure that the measured T_m values are not affected by satellite peaks and that there is no temperature lag in the measured peak temperatures even at the highest heating rates used.

Other methods used for the determination of the parameters of TL peaks are given in Chen and Kirsh (1981), ch. 6.

Much care has to be taken in practical determination of the TL parameters. Practically all the methods include approximations and limitations. Thus, for example, the expressions given in eq. (7) were obtained for a single trapping level and a single recombination center. We also did not take into account the degree of filling of the traps, or the dose of excitation. One has also to make sure that the measured TL is a well-isolated single TL peak. Temperature gradients across the sample and temperature delays caused by bad thermal contacts and by too fast heating rates have also to be avoided. The general computer best-fit methods which give the parameters providing the best fit between the numerically integrated TL equations and the measured GC do not include the approximations which appear in most of the other methods. Still the computed parameters depend on the data fed into the computer containing the number of TL peaks in the GC etc. Temperature gradients or temperature lags and other experimental artifacts may of course also affect the computed parameters. Some recently developed generalized expressions from which more accurate TL parameters can be derived are briefly described in sect. 4 below.

2.1.5. *TL-related phenomena*

Studies using TL in combination with other techniques should provide more information on the nature of the defects and transitions involved in the measurement. Thus, electron spin resonance (ESR) provides information on the chemical nature of defects that can not be obtained by TL alone. The present subsection gives a brief description of phenomena related to TL and used by researchers working on TL as an additional technique. The following discussion centers on electron transitions, but can easily be extended to the analogous hole transitions. Figure 1 and the transition numbers indicated therein will be used here.

(a) Phenomena taking place during TL excitation.

(1) *Photoluminescence* (PL). Using UV or visible light for excitation (fig. 1, transition 2 or 5), some of the excited electrons will return radiatively to the M′ (transition 10) or G (transition 11) levels. These transitions produce PL during the excitation. The spectra that describe the intensity of the PL as a function of the wavelength or photon energy of the exciting light are called *excitation spectra.* They provide information on the energy levels involved in the PL excitation. The excitation spectra are related to the optical *absorption spectra.* PL spectra give information on the energy levels involved in the emission.

(2) *X-ray-induced luminescence* (XL) and luminescence induced by other ionizing radiation are presented in fig. 1 by transition 1. It will, however, also produce transitions like 2 and 5. This will yield more complex excitation and emission spectra.

(3) *Photoconductivity* (PC). This term is used for excitation by UV or visible light in which the transitions involve the VB, the CB or both. In such cases the mobile

charge carriers contribute to the conduction of the sample in an electric field. This enhanced conduction is called PC.

(4) *Radiation-induced conductivity,* similar to PC but induced by other ionizing radiation.

(b) Effects depending on the standing time after the excitation.

(1) *Phosphorescence.* This term is commonly used for the thermal release of electrons (holes) from traps followed by radiative recombination at luminescence centers. From eq. (1) we see that the phosphorescence should rise exponentially with T and decrease exponentially with the trap depth E. Depending on the probability for retrapping of the released electrons, the phosphorescence is described as monomolecular or bimolecular.

(2) *Fading* of TL. The longer a phosphor stands after the excitation, the more trapped carriers will leave the traps, and the subsequently measured TL peaks will be weaker. This is called *thermal fading* or *normal fading.* Trapped electrons can also be released by exposure to light, in which case we call the decay of the TL *optical fading.* Fading occurs in some samples even when kept in the dark and even for deep-lying traps when the above-described fading processes should not occur. This has been named *anomalous fading.* It is temperature independent. It has been assigned by Garlick and Robinson (1972) and by others to tunneling. Tunneling recombination decreases very quickly with the distance between the trapped carrier and the recombination center and becomes negligible for distances above a few lattice units. Transition 12 in fig. 1 indicates the tunneling. Anomalous fading can also occur in localized transitions not involving excitation to the D level (fig. 1).

Fading is very disturbing in archeological and geological dating, as well as in dosimetry. Among other essential features of a good phosphor for dosimetry, one is negligible fading.

(c) Effects taking place during the TL emission.

(1) *Thermally stimulated conductivity* (TSC). Electrons in the CB (or holes in VB) will show enhanced conductivity in an electric field. During the warming of an excited phosphor this conductivity will rise with the concentration of CB electrons n_c (and m_v). The resulting TSC peaks may have correlated TL peaks. It can happen that one type of carriers, for example holes, will have a very low mobility in the temperature range of the TL peak, when the corresponding TSC peak may not be detected. TL peaks related to localized transitions will, of course, not have corresponding TSC peaks.

(2) *Thermally stimulated electron emission* (TSEE). This is a special case of exoelectron emission (EEE). In EEE an insulating or semiconducting sample is put between two electrodes with a potential difference. One electrode is connected to the sample and the other (the collecting plate) is separated from the sample and is connected to an electrometer. The sample is kept under vacuum and is exposed to high-energy radiation when electrons are emitted from its surface and collected by the collecting plate. In TSEE, trapped electrons excited to the CB are collected

by the collecting plate and show a TSEE peak. No TSEE will appear when trapped holes are excited to the valence band, because holes cannot be freed out of the crystal. The TSEE thus provides a method to distinguish between TL peaks due to released electrons and those due to released holes.

There are more techniques used by TL investigators. For example, *phototransferred TL* (PTTL) and *optically stimulated luminescence* (OSL). These will be dealt with when discussing papers using such techniques.

2.1.6. *Irradiation and thermal treatment effects on the TL*

It is well known that the properties of a phosphor, including its TL, depend on its preparation methods. More than that, even samples prepared apparently in the same way may differ from each other in their properties. The preparation of a good phosphor seems sometimes to be a magic art. Differences in the glow curves are observed even for the same sample after repeated radiations or heating and cooling cycles. Most of these effects can be traced back to differences in the degree of filling and emptying of various traps. In some cases defects can be frozen-in by fast quenching. Energetic particles can even produce new defects. To overcome these difficulties, a new phosphor has to be examined carefully by its producer, and limits such as the highest allowed temperature and suggested controlled procedures during the measurements have to be given.

Controlled pre-treatment of a phosphor can sometimes be of advantage. An example is the *pre-dose dating* technique. It involves exposure of the sample to a given radiation dose followed by heating to a given temperature when the intensity of the TL peak used for the dating is found to increase in intensity. Fleming (1973) has developed the pre-dose technique as a new dating method. He used the sensitization of a TL peak at 110°C in quartz by a pre-irradiation dose of about 10^3 rad followed by heating to 500°C, when the intensity of the 110°C peak exposed to a small probe dose was enhanced by a factor of 6 compared to that before the pre-treatment. Further details on pre-dose dating can be found in the monographs cited above in sect. 2.1.2.

2.2. *Introduction to TL dosimetry*

2.2.1. *Characteristics and applications of radiation dosimeters*

Dosimeters have to measure accurately radiation intensities. Their applications include personnel monitoring, environmental monitoring, radiation therapy, diagnostic radiology and other radiation measurements.

Ionization chambers measure directly intensities of ionizing radiation. For many applications, such as personnel and environmental monitoring, the absorbed energy has to be stored for long periods. This is done by a suitable storing element. The intensity is then measured at the end of the period by the measuring system or the *reader*. The latter is essentially technical in nature while the features of the storing element are crucial. Care has to be taken in comparing the TL intensities of various phosphors. The readings may be affected by the wavelength dependence of the detector and by other factors.

Historically, the photographic emulsion which darkens on exposure to radiation served as a storing element for radiation dosimetry. It suffers from nonlinearity of the darkening with the radiation dose, and there are also problems related to the developing of the photographic image. It has therefore been replaced by the more accurate, more sensitive and more convenient TL phosphors. These are called *TL dosimeters* (TLD). A good TLD has to possess the following main features:

(1) High sensitivity – to enable measurements of very low radiation doses.
(2) Linearity – It is convenient to have a linear relation between the measured TL intensity and the absorbed energy dose over a wide range of exposures.
(3) Negligible fading – otherwise part of the stored energy will get lost during the period of accumulation and will not show up in the TL.
(4) Energy independence – The phosphor has to measure the correct energy absorption independently of the type of energy distribution of the radiation source.
(5) Tissue equivalent phosphors – In most cases the TLDs have to provide warning from hazardous radiation. For this, their energy absorption has to fit that of the human body. In other words, they have to be tissue equivalent ($Z = 7.4$).

When using a phosphor for TLD the measurements are usually limited to a specific TL peak which has optimal features and appears in a temperature range fitting for the measurement, usually in the range of about 150–350°C. Most research of TLD concentrates on the development of new phosphors exhibiting improved performance and of measuring set-ups based on such phosphors. Still, no ideal phosphor exists, and efforts are being made to improve the function of phosphors by choosing proper grain sizes, using the right binding materials and filters which will reduce the energy dependence of the phosphor. Thus, embedment of the phosphor in thin cards of teflon (less than 0.1 mm thick) was found by Lakshmanan et al. (1990b) to give higher sensitivity for β radiation, better re-usability, and enabled large-scale production of $CaSO_4$:Dy TLDs. Raves and Stoebe (1990) describe a personnel monitoring TLD for mixed radiation fields that contains 3 filters which eliminate the phosphor's energy dependence. This system also enables the use of the energy dependence for discrimination between doses of different energies in mixed radiation fields. Numerous papers in the literature deal with more sophisticated methods applied to improve the performance of TLDs.

Details on the features and construction of TLDs can be found in monographs on radiation dosimetry such as: Becker (1973), Kase and Nelson (1978) which give a theoretical approach to radiation dosimetry, *Thermoluminescence and Thermoluminescent Dosimetry* edited by Horowitz (1984a), and McKeever et al. (1995).

A review of commercially available and some "home made" TLDs was given by Azorin et al. (1993). The review describes preparation methods and dosimetric properties, and gives measured TL parameters for the various TL peaks of the phosphor.

2.2.2. *R-containing TLDs*

The R-containing TLDs are based on a phosphor that contains R impurities acting as activators enhancing the TL emission of the phosphor. A review on the chemistry and

physics of R-activated phosphors was published in this Handbook by Blasse (1979). It contains energy diagrams for the main R used as activators in phosphors and discusses the allowed optical transitions in R-activated phosphors. It also describes various processes related to the emission of R-activated phosphors like energy transfer, optical excitation and emission, thermal and concentration quenching of the luminescence and other features of these phosphors. The main merits of TLDs based on R-activated phosphors are:

(1) Efficient emission in direct excitation of the R-activator.
(2) Characteristic R emission by *energy transfer.* This is possible when the R activator has an energy level fitting the excited energy level of the host, and an interaction exists between the excited host atom and the R, for example by overlapping wave functions or by Coulomb interaction.
(3) R change valencies easily; for example, Eu ions show the transitions $Eu^{3+} \leftrightarrow Eu^{2+}$. This corresponds in fact to the trapping of electrons or holes by the R activators in phosphors, which occurs in the processes of excitation and emission of TL in R-activated phosphors.

2.2.3. *Units used in dosimetry*

Historically, the aim of radiation measurements was mainly to protect the human body from hazardous radiation. The system of units was therefore adjusted to give the doses absorbed by human tissue. In addition, the conventional system of units was in general different from the now-accepted Standard International (SI) Units. This situation is confusing since many authors continue to use conventional units. A conversion table for the various units can be found in Handbooks, for example in the Handbook of Chemistry and Physics, 1st Student Edition, 1987, CRC Press, Boca Raton, Florida, p. F208. The table presents quantity names, symbols, expressions and special names for both the SI and the conventional systems. It also gives the values of the conventional units in SI units. The data given in the Table should help to overcome the difficulties arising from the use of the various unit systems.

The meaning of most units given in the above-mentioned Table is simple. Yet, a few of them need clarification:

(1) *Roentgen* – Is a unit of *exposure.* It is defined as the quantity of X or γ radiation such that the associated corpuscular emission per 0.001293 gram of dry air (at normal conditions) produces in air ions carrying 1 esu of electric charge of either sign. This definition requires that all electrons liberated by the photons in a mass element of air and all the ions produced by these electrons are stopped in the air.
(2) *REM* (Roentgen Equivalent Man) – Is defined as the amount of any type of ionizing radiation that produces the same damage to man as 1 roentgen of about 200 kV radiation. The quantity of such biological units is named *dose equivalent.*
(3) *Kerma* – Is the quotient dE_k/dm, where dE_k is the sum of the initial kinetic energies of all the charged particles liberated by indirectly ionizing particles in a mass element of the specified material. This unit is used mainly in neutron irradiation.

(4) *Linear Energy Transfer* (LET) – Is used for charged particles in a medium. It is given by dE_L/dl, where dE_L is the average energy locally imparted to the medium by a charged particle of specified energy traversing a distance dl. The LET can affect strongly the glow curves of phosphors, and consequently also the function of dosimeters. The LET affects the intensity ratios of the various TL peaks and the supralinearity of the peaks as shown by Rassow et al. (1988). The LET effect on the TL is stronger for heavy particles, like n, p and α radiation. More on the effects of high LET on dosimetry will be presented in the review of papers dealing with such effects.

Radiation protection standards and solid-state dosimetry standards are referred to in published papers on the subject. The symbols for the standards are very often national and vary from one country to another. Becker (1996) describes the various standards and gives references to earlier papers on the standards.

Julius (1996) discusses various problems related to the operational quantities H(0.07) and H(10) introduced by ICRU (International Commission on Radiological Protection) for measurements in personnel dosimetry.

3. R-activated TLDs and their characteristics

This is the bulk section of the present article. It will present the main results of published papers and follow the progress achieved in the understanding and characterization of R-phosphors. The first commercial R-activated phosphors were reported in the 1960s. The merits of R as activators were recognized and by now a variety of high-sensitivity R-containing phosphors suitable for various dosimetric needs are available commercially. Investigations continue with the attempt of further improvement of the characteristics of existing TLDs and the introduction of new R-phosphors.

The review of the published work in this field will be divided into subsections according to the various chemical host compounds.

3.1. *Alkali-metal compounds*

A review on the TL of alkali-halide phosphors, including R-activated, ones was given by Sastry (1993).

3.1.1. *Lithium halides*

LiF:Mg,Ti was the first commercial phosphor, named TLD-100, introduced by the Harshaw Co. more than 30 years ago. Its preparation was under highly controlled conditions. It served for many years as the main TLD and is still widely used. A more sensitive LiF:Mg:Cu:P was developed by Nakajima et al. (1978) and has been developed later as a commercial TLD by Wang et al. (1986) under the label GR-200. It is claimed to give sensitivities up to 50 times those of TLD-100.

Taking into account the merits of the R as efficient activators, one would have expected to obtain ultrasensitive R-activated LiF TLDs. As yet this is still not the case. Ayappan et al. (1981) have developed a LiF:Mg:Dy phosphor embedded in teflon. It is claimed to have identical properties as TLD-100 and to be convenient for personnel monitoring. More controlled work exploring various R activators and co-activators can be expected to result in more sensitive LiF:R phosphors. It should be noted that Li-including mixed crystals, such as $LiNaSO_4$:Eu, gave highly sensitive TLDs. These will be dealt with in a separate subsection below.

3.1.2. *Sodium halides*

Work on R-activated sodium halides was more intensive than that on lithium halides. Still the number of published papers is low.

Bhan (1982) has investigated the TL and other optical properties of undoped and Ce^{3+}-doped NaF. The NaF:Ce^{3+} has been found to add a TL peak at 183°C in addition to four peaks in the temperature range 73–223°C observed in undoped NaF. The authors deal with the thermal stability of the various TL peaks and give the related optical absorption and the PTTL. They also give the calculated TL parameters for all the TL peaks. For the Ce^{3+}-related 183°C TL peak they have obtained $E = 1.40$ eV and $s = 0.4 \times 10^{14}$ cm^3 s^{-1}. This peak was found to be characterized by second-order kinetics. The authors do not relate to the dosimetric characteristics of the Ce^{3+}-doped samples.

The TL of NaCl:Eu^{2+} was investigated by Aguirre de Carcer and coworkers. Aguirre de Carcer et al. (1988) found a close relation between the AG (afterglow), the PC and the TL of Eu^{2+}-doped NaCl, KCl, KBr and KI host crystals after exposure of the samples to UV at LNT. The TL spectra were found to match the Eu^{2+} spectrum in the samples. Thermal quenching from high temperatures was found to reduce the TL intensity, indicating the existence of Eu precipitates. They suggested for the TL emission the process

$$Eu^{3+} + e^- \rightarrow (Eu^{2+})^* \rightarrow Eu^{2+} + h\nu, \tag{9}$$

which means that an electron released from a trap recombines with a hole at an Eu^{3+} center leaving behind an excited Eu^{2+} ion which relaxes with the emission of a photon $h\nu$.

Aguirre de Carcer et al. (1991) have studied NaCl:Eu^{2+}, concentrating on its applicability as a UV dosimeter for the hazardous actinic range (200–300 nm). The UV radiation was found to excite the Eu^{2+} to levels in the CB of the host alkali halide, where the excited electrons could get trapped in electron traps. The most effective UV wavelength in this process was 240 nm. Warming the UV-excited crystal emitted the TL according to eq. (9). The NaCl:Eu^{2+} phosphor was found by these authors to be a promising material for UV dosimeters. Its low sensitivity limit was 0.2 μJ cm^{-2} when using an experimental 4 nm wide band at 240 nm. This value is an order of magnitude lower compared with the actinic UV phosphors reported by Mehta and Sengupta (1978).

Lopez et al. (1991) used freshly quenched NaCl:Eu in which the Eu^{2+} gets dissolved in the lattice and forms Eu–vacancy dipoles. The TL of samples X-irradiated at 77 K was found to fit well that of samples excited at the same temperature by UV. EPR

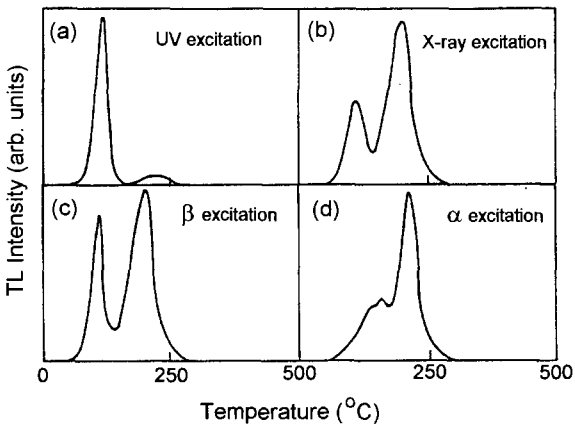

Fig. 5. Glow curves of NaCl:Eu^{2+} after UV (250 nm), X-ray, β and α irradiation at RT (curves a–d, respectively).

measurements helped in the analysis of the processes. They conclude that the TL is connected with tunneling processes of electron–V_k pairs. Espana et al. (1992) also report on the TL of NaCl:Eu^{2+} and its use as a TLD for the UV.

The work by Aguirre de Carcer et al. (1993) on dosimetric properties of NaCl:Eu^{2+} irradiated by UV, X, β and α radiations will be described in some detail.

The glow curves obtained by these authors for single crystals of NaCl:Eu^{2+} exposed at RT to UV(250 nm), X, β and α radiation is shown in fig. 5, curves (a)–(d) respectively, at a heating rate of 3.3°C s^{-1}. The main TL peaks appear at 100 and 225°C. The α-irradiated sample gives an additional weak peak near 150°C. The variation in intensity ratios between the two main peaks in the different curves is attributed by the authors to different radiation damage by the different sources. The excitation process is given (for UV) by

$$Eu^{2+} + h\nu_{UV} \rightarrow Eu^{3+} + e_{trapped}. \tag{10}$$

Figure 6, also taken from Aguirre de Carcer et al. (1993), gives three-dimensional plots of the TL intensity as a function of temperature and wavelength for the UV and X-irradiated crystals (curves a and b, respectively). A strong peak appears at 460 nm and a weak one at 600 nm. Close examination shows structure in both TL peaks. Inspection of the 600 nm band reveals components that can be ascribed to traces of Mn^{2+} in NaCl as shown by Jaque et al. (1991). Similarly, the overlapping components of the 460 nm band were identified as the emission of different Eu precipitates. This leads to the following two-way formula for the TL emission:

$$\begin{aligned} Eu^{3+} + e^- &\rightarrow (Eu^{2+})^* \rightarrow Eu^{2+} + h\nu_{460\,nm}. \\ &\downarrow \\ &(Mn^{2+})^* \rightarrow Mn^{2+} + h\nu_{600\,nm} \end{aligned} \tag{11}$$

Thus, the 600 nm emission is obtained by energy transfer from the excited Eu^{2+} to a near-by Mn^{2+}. The later relaxes to the ground state with the emission of the 600 nm band.

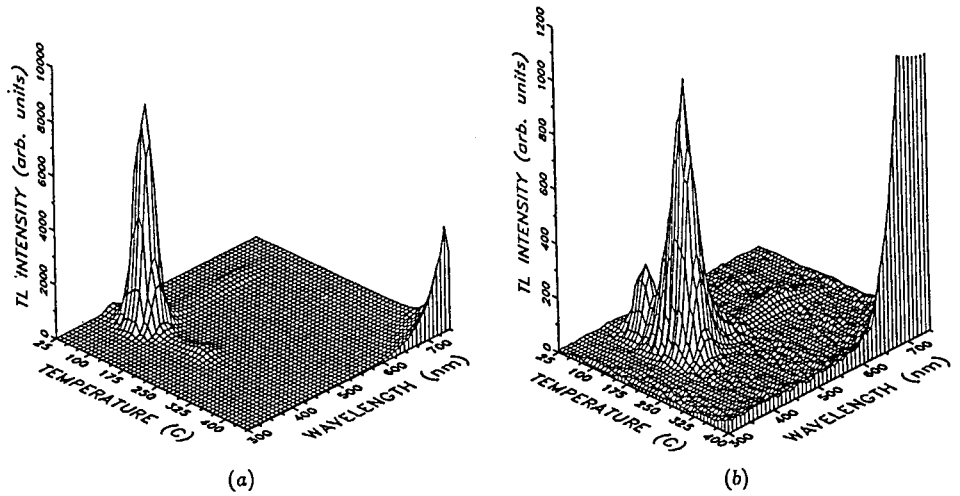

Fig. 6. Three-dimensional plots of the TL of (a) UV-irradiated and (b) X-ray-irradiated NaCl:Eu^{2+} crystal.

Another interesting effect reported by the same authors is that annealing at 500°C and then keeping the sample for 24 hours in the dark at RT resulted in a shift (~20 K) of the TL peaks to higher temperatures and an increase in the TL intensities. This was observed in both UV and X excitations. The authors suggest that these changes are related to precipitation of Eu^{2+} during the stay of the sample in the dark.

The authors found good linearity over a wide range of irradiation doses. Only the β-irradiated samples showed a slight sublinearity above 5 Gy.

The sensitivity limits for the various radiation sources, not taking into account the increase in TL after annealing and keeping in the dark, was 0.2 μJ cm^{-2} for UV(250 nm), 1 mGy for β, and 1.5 mGy for α radiation. The authors conclude that NaCl:Eu^{2+} has good characteristics to make a high-grade personnel dosimeter for the above radiation sources.

Reddy et al. (1982) explored the TL and optical absorption of Z_1 centers in γ-irradiated Sm-doped NaCl. TL peaks have been observed at 60, 90, 130 and 180°C. Quenching from higher temperatures affected the various peaks in different ways; some were enhanced and others were suppressed. Bleaching X-irradiated crystals with light absorbed by F^- centers also enhanced some TL peaks and reduced others, though not in the same way as by quenching from high temperatures. The above experiments, combined with measurements of optical absorption, led to the conclusion that the 180°C peak is related to Z_1 centers. None of the TL peaks could be related directly to the Sm ions. It is claimed that the glow curve is affected by the dispersion of the impurity. More direct evidence is needed to clarify the effect of the Sm impurity on the glow curve of NaCl.

$NaYF_4$ was found by Hund (1950) and others to be isomorphous with CaF_2. It was therefore hoped that $NaYF_4$:R would make good phosphors comparable with CaF_2:R (see sect. 3.2.2 below). Pol and Rau (1973) studied the UV-excited fluorescence of $NaYF_4$:Eu. The emission spectrum was found to be characteristic of Eu^{3+} and the fluorescence

increased with the Eu concentration up to 10 wt%. Reddy et al. (1988) prepared $NaYF_4$:Gd by firing the mixture at 900–1000°C, then grinding to a fine powder and pressing it into pellets. The RT $\gamma(^{60}Co)$-irradiated samples showed 3 TL peaks at 120, 130 and 180°C (at 0.5°C s^{-1}). The fading of the irradiated samples was high. The authors present E and s values for the TL peaks. These are unfortunately incorrect. Thus, the s-values for the 180°C peaks were found to be of the order of 10^2 s^{-1} (!) probably caused by miscalculation.

3.1.3. *Potassium halides*

Several authors of papers published in the 1960s and 1970s came to the conclusion that divalent impurities, including R ions, form in alkali-halide hosts impurity–vacancy (I–V) dipoles. Kao and Perlman (1979) have also accepted the I–V dipole model for KCl:Eu^{2+}. They studied the relaxation and aggregation processes in these dipoles. It has been observed that X-irradiation destroys the dipoles and reduces the Eu^{2+} to Eu^{1+}. References to earlier papers dealing with the I–V dipole model are cited in the above paper.

Opyrchal et al. (1982) have measured the TL, the EPR and other optical properties of γ-irradiated KCl:Eu^{2+} (80–100 ppm). The glow curves showed TL peaks at 373, 460 and 553 K. The 553 K peak was very weak compared to the others. In a later paper, Opyrchal et al. (1986) report the observation of only two TL peaks, at 363 and 453 K in KCl:Eu^{2+} (heating rate not specified). The integrated area under the glow curve was found to rise with the Eu^{2+} concentration, just as the F-center concentration does. For a sample containing 18 ppm Eu the 453 K TL peak was the stronger one in the glow curve, while with 140 ppm Eu the 363 K peak took over.

Rubio et al. (1982a,b) studied Eu^{2+}-doped NaCl and KCl. They have ascertained that the Eu^{2+} ions change valency during X-irradiation by capturing an electron or a hole. On warming the RT-irradiated sample, they observed a strong TL emission which glowed up to about 600 K. The spectral emission of this glow was in the range 400–500 nm, where detectors (such as PMs) give high sensitivity. These authors also remark that KCl:Eu crystals are cheap and easy to obtain commercially and can therefore be expected to serve as good practical dosimeters.

Camacho et al. (1988) have undertaken a study of the dosimetric properties of KCl:Eu^{2+} single crystals. Prior to the TL excitation the samples were kept for one hour at 870 K and then quenched quickly to RT. After the quenching the samples were X-irradiated (at 300 K) at a dose rate of 0.4 rad min^{-1} and heated at a rate of 4 K min^{-1}. A sample containing 113 ppm Eu and excited by a dose of 12 rad gave TL peaks at 350, 386 and 453 K. The calculated TL parameters were as follows: The activation energies E were 0.74, 0.92 and 1.11 eV, the s-values were 2.6×10^9, 4.1×10^9 and 8.1×10^9, and the kinetic orders were 1, 1 and 2 for the three peaks, respectively. A very good linear dose response of the 453 K peak was observed up to 180 rad. The fading of this peak was 20% in 45 days. The emission spectra were the same for the 3 peaks and showed a broad band peaking at 427 nm. It was found to be composed of two bands at 424 and 442 nm. The 424 nm band is very similar to that obtained for the PL of UV-illuminated KCl:Eu^{2+}. The 442 nm band

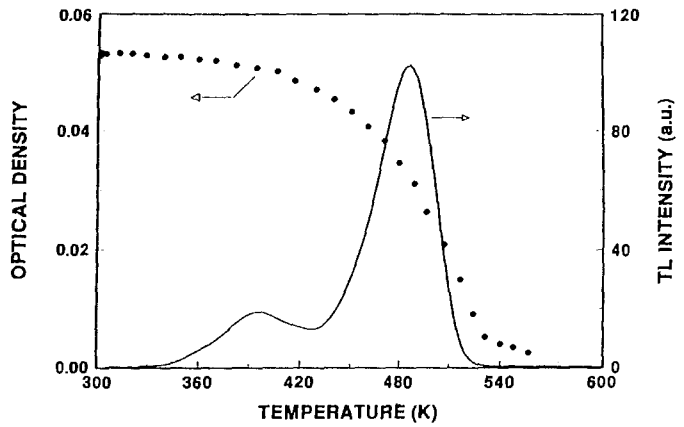

Fig. 7. The GC (full line) and the thermal bleaching of the F-center absorption (circles) of X-ray-irradiated KCl:Eu^{2+}.

was observed by earlier investigators in pure and in alkaline-earth doped KCl, and was found to be associated with F-centers. The mechanism suggested for the excitation and emission of the TL in KCl:Eu^{2+} was the same as that given for NaCl:Eu^{2+} (eqs. 10 and 9 above).

Novosad et al. (1995) report on the TL of X-irradiated KCl:Eu crystals with the Eu introduced as Eu_2O_3. The emission spectra were characteristic of the Eu. Irradiation at 290 K gave a very high TL intensity. It is concluded that the phosphors can make a very good TLD for ionizing radiation.

Perez-Salas et al. (1993) have observed a *new TL phenomenon* in KCl:Eu crystals. They noticed that crystals kept for a long time in the dark emit TL without excitation. This effect was later studied and reported in a few papers by Perez-Salas and coworkers which show that the TL of the non-irradiated potassium halides can be traced back to the *self-irradiation* due to the radioactive ^{40}K isotope present in natural potassium at an abundance of 0.0177%. This irradiation and its effect on the TL of potassium halides was studied by Barboza-Flores et al. (1994) and by Pashchenko et al. (1995a). The self-irradiation was found to affect not only the TL but also the measured fading of TLDs based on potassium-containing phosphors. As shown by the above authors, the measured fading of potassium-containing phosphors has to be corrected for the self-irradiation in long time exposures or measurements of very low doses. A simple dosimetric calibration procedure for the self-irradiation effect has been suggested by Pashchenko et al. (1995b).

Aceves et al. (1994) studied the TL of KCl:Eu^{2+} excited at RT by X-rays and by non-ionizing 250 nm UV. X-irradiation gave a glow curve with the main peaks at 395 and 490 K and much weaker peaks in the range 530–670 K. The relation between the 490 K peak and the F-centers is shown in fig. 7. It shows that the F-absorption band bleaches thermally just at the temperature range of the 490 K TL peak. 250 nm excitation gives the main TL peak at 380 K with shoulders at about 360 and 415 K. The UV excitation did not produce a measurable F-band. An irradiated sample in which the

low-temperature TL was eliminated by warming to 450 K was found by Aceves et al. to exhibit PTTL by F-light illumination at RT. The originally X-excited sample exhibited then the regeneration of the 395 K peak. UV-excited samples showed under the same conditions two regenerated peaks at about 380 and 420 K. It seems that the 395 K peak is complex and its components are excited differently by different sources. This may explain the discrepancy in the TL peak temperatures reported by Aceves et al. (1994), by Camacho et al. (1988) and by Opyrchal et al. (1982, 1986). Aceves et al. concluded that the TL at 490 K is related to F-center electrons. Illumination with light of F_z center absorption was found to bleach the 380 and 415 K peaks indicating their relation to the F_z centers.

Optical bleaching with F-light produced F_z centers. It was interpreted by Aceves et al. as detrapping of electrons from vacancies far away from Eu^{2+}–vacancy dipoles and their retrapping at shallower traps related to vacancies in the neighborhood of I–V dipoles.

Cusso et al. (1991) stress that Eu^{2+}-doped alkali-halides suit well as personnel protection dosimeters and as a tool for studying biological effects at low UV doses.

In a recent paper Melendrez et al. (1996a) show that the glow-curve structure of KCl:Eu^{2+} (150 ppm) is similar for RT α, β, γ, X and UV (200–300 nm) irradiations with differences only in relative peak intensities. Heating rates were 2–5 K s^{-1}. A well-marked difference in the relative TL peak intensities was obtained for the UV-excited glow curve which gave the main peak at 380 K compared to the 480 K as main peak in excitation by the other sources. This agrees with the results by Aceves et al. (1994) given above. The dose response of the integrated area under the glow curve was found to show good linearity for all the sources. The fading was fast in the first few minutes and stabilized at a fairly low fading rate of about 50% in 45 days for all the above radiation sources. For UV the fading was somewhat faster at 240 nm excitation. The authors stress the suitability of KCl:Eu^{2+} phosphors as dosimeters for all the above sources along with the simple dosimetric calibration procedure accounting for the self-irradiation due to the ^{40}K given by Pashchenko et al. (1995b). It is very likely that the fading is thermal and can be eliminated by preheating to a suitable temperature before measuring the integrated TL intensity.

Almost all the published work on R-activated KCl deals with Eu activators, and very little was done on other KCl:R phosphors. Balraj and Veeresham (1992) describe the optical absorption and the TL of KCl:Pr (1062 ppm). The glow curve of RT X-irradiated crystals exhibited TL peaks at 358, 393 and 453 K (heating rate 30 K min^{-1}). These peaks were also observed in pure KCl and so they are not related to Pr. It seems from the results that the Pr enhances the TL, an effect that has to be confirmed by additional measurements. The TL of KCl:Gd^{2+} was studied by Vijayan and Murti (1989). It showed peaks at 381, 407 and 478 K and an emission band at 2.61 eV with a shoulder at 2.76 eV. All the TL peaks were found to be related to Z_1 centers.

Very little was published on the TL of KBr:R until the 1990s. Radhakrishna and Chowdari (1972) presented a glow curve for KBr:Yb^{2+} which shows only TL peaks related to F and Z_1 centers.

Buenfil and Brandan (1992) found for KBr:Eu^{2+} annealing conditions, which gave a strong TL peak near 100°C. This annealing gave good linearity with doses up to 10 cGy and sensitivities up to 10 times that of TLD-100.

Interest in KBr:Eu^{2+} increased in 1996 when its features raised hope that it can make a good phosphor for many applications.

Melendrez et al. (1996b) studied the dosimetric properties of UV(200–300 nm)- and X-ray excited KBr:Eu^{2+} (200 ppm). The crystals were pre-treated by annealing for one hour at 773 K, followed by fast quenching to RT. This procedure prevented aggregation of Eu^{2+}–cation vacancy dipoles. Irradiation took place at RT and the heating rate for the TL emission was $5\,K\,s^{-1}$. Assuming first-order kinetics, the glow curves were resolved into six TL peaks at 337, 384, 402, 435, 475 and 510 K, with the main peak at 384 K. The results resemble those obtained by Melendrez et al. (1996a) for KCl:Eu^{2+}.

The fading at RT of the various TL peaks of KBr:Eu^{2+} phosphors was found to be smallest for the 438 K peak. Still, the more intense 380 and 510 K peaks were chosen as the best for UV dosimetry. These peaks show fast fading for the first few minutes, after which they stabilize. All TL peaks showed good linearity with dose and good stability and reproducibility. The highest efficiency with UV light was found in the range 190–230 nm. Melendrez et al. conclude that the KBr:Eu^{2+} phosphor is suitable for dosimetric applications for UV, X and α radiations.

In another paper from the same laboratory, Perez-Salas et al. (1996) deal with RT effects of UV radiation in KBr:Eu^{2+} crystals. There is very little new in this paper compared to the former one. The similarities between the UV and X-ray excited glow curves is stressed again. A correlation was observed between the 384 K TL peak and the F-center bleaching. It is also stressed that the non-ionizing UV radiation induces the formation of F_z centers.

Rosete et al. (1996a,b), working on KBr:Eu^{2+} (50 ppm) X-irradiated at RT, have observed only three TL peaks at 355, 370 and 398 K. The spectral emission was the same for all the peaks and showed bands at 419 and 460 nm. The 419 nm band exhibited Eu^{2+} characteristics. The authors give a complicated model for the TL excitation and emission processes. It involves Eu^{2+}–vacancy dipoles and their aggregates as well as additional partners like Cl_3, H and V_K centers.

Buenfil et al. (1997) added Mg as a codopant to KBr:Eu. A sample containing 0.01% of Eu and Mg respectively was subjected to heat treatment and its sensitivity to 254 nm UV light was examined. Optimal heat treatment gave an increase by a factor of 3 in the UV sensitivity. The Mg was found to improve the reproducibility of the GCs. The codoped phosphor exhibited the main TL peaks at 170 and 245 °C. Practically the same GCs were obtained for UV and $\gamma(^{60}Co)$ irradiations.

Barland et al. (1982) observed a strong AG in Eu^{2+}-doped KI X-irradiated at 11 K. Its intensity increased with the application of an electric field across the crystal. The authors suggest that the emission involves trapping in domains of high Eu^{2+} concentration, a process which depends on thermal pretreatment.

3.1.4. *Rubidium halides*

Most of the published work on R-doped rubidium halides was done by Sastry and co-workers. It was summed up (together with work on other alkali halides) by Sastry (1993). The summary gives TL characteristics, models and mechanisms. A Table (pp. 135–138)

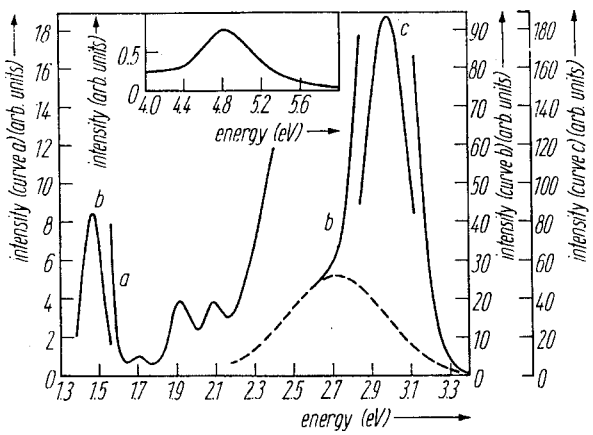

Fig. 8. The TL emission spectra of RbCl:Eu^{2+} recorded at 440 K. The 1.7, 1.9 and 2.1 eV bands emission is characteristic of Eu^{3+}.

lists TL peak temperatures, emission spectra and mechanisms for the TL of the various phosphors.

Sastry and Sapru (1978) presented preliminary results on the TL of RbCl:Eu^{2+} (800 ppm) obtained after γ-irradiation at RT. Peaks appear (at a heating rate of 6.6 K min^{-1}) at 330 and 380 K. The TL of the Eu-doped samples gave intensities about 30 times those of pure RbCl crystals. Sastry and Sapru (1981) obtained, for RbCl doped with 250 ppm Eu and after γ-irradiation at RT and a heating rate of 120 K min^{-1}, TL peaks at 390 K (very weak), 450 K (main peak) and 470 K. The glow curves were resolved into three peaks using the total-curve-fitting method. All peaks were found to fit first-order kinetics. The TL parameters of the 450 K peak gave an E-value of 1.94 eV and an s-value of 10^{21} s^{-1} compared with 0.92 eV and 0.7×10^{9} s^{-1}, respectively, for the 470 K peak. The extremely high s-value does not seem to be real and has to be rechecked using an additional method and a lower heating rate. One has also to make sure that the peak is a real single TL peak.

From PL, EPR and optical absorption spectra, the authors concluded that during the irradiation a positive hole gets trapped at the Eu^{2+} resulting in Eu^{3+} as expressed by eq. (10) above. During the TL emission, an electron released from a trap recombines with a hole at the Eu^{3+} (eq. 9 above). An interesting observation was the appearance of spectral bands in the range 1.5–2.7 eV in the TL emission spectra, in addition to the main peak at 3 eV characteristic of Eu^{2+} (fig. 8). Three sharp bands at 1.7, 1.9 and 2.1 eV were found to fit the Eu^{3+} emission. This was explained by assuming that during the irradiation, Eu^{3+} can trap another hole thus forming Eu^{4+}. During the TL emission we then get

$$Eu^{4+} \xrightarrow{\text{heating}} (Eu^{3+})^{*} \rightarrow Eu^{3+} + h\nu \quad (1.7,\ 1.9,\ 2.1\,\text{eV}). \tag{12}$$

Gadolinium is mostly three-valent. However, in alkali halides it is known to enter in the divalent form. Sastry and Muralidharan (1988a) have studied the optical absorption, PL spectra, PSL and TL emission spectra of RbCl:Gd^{2+}. The crystals were quenched

by fast cooling from 400°C to RT prior to the irradiation. The experimental procedures were the same as those in Sastry and Sapru (1981) except for the heating rate which was reduced to 120 K min^{-1}. TL peaks appeared at 373, 405 and 450 K (very weak), with the 373 K peak dominating. F-light reduced the 373 K peak and enhanced that at 405 K. The TL emission gave three well-resolved bands at 2.1, 2.8 and 3.96 eV. Z_1 centers were formed during the irradiation. The TL was associated with release of F-electrons and their recombination at the Gd^{3+} with the emission of a 4 eV band. Sastry and Muralidharan (1988b) observed only one TL peak, at 380 K, which after F-light bleaching has revealed another component at 355 K. The latter was suggested to be associated with Z_1 centers. The TL mechanism was found to be the same as for RbCl:Gd^{2+}. The presence of hydroxyl reduced strongly the TL in both RbCl:Gd^{2+} and RbBr:Gd^{2+}.

RbI:Eu^{2+} was studied by Sapru and Sastry (1981). From various optical measurements, it was concluded that the processes of TL excitation and emission were compatible with the model given in eqs. (10) and (9). The Eu was found to increase the integrated TL by a factor of about one hundred compared to that of undoped RbI.

Sastry and Muralidharan (1988c) found for RbI:Gd^{2+}, under similar conditions as above, one TL peak at 365 K which shifted to higher temperatures with radiation dose. This TL peak was shown to be due to recombination of F-electrons with holes at V centers. A TL emission band at 2.9 eV was characteristic of the Gd^{2+} ions.

Thoms et al. (1994) studied RbI with various bivalent dopants including Eu^{2+}. Samples were X-irradiated at 80 K and the TL was measured in the range 80–400 K at a heating rate of 6 K min^{-1}. RbI:Eu^{2+} gave two peaks at 325 and 345 K with E-values of 1.1 and 1.4 eV, respectively, and emitting at 430 nm.

3.1.5. *Cesium halides*

Cesium halides differ from other alkali halides crystallographically. They are simple cubic while the other alkali halides have a face-centered cubic structure. Because of this, R ions occupy the interstitial sites in cesium halides instead of the substitutional sites in the other alkali halides.

No work on the TL of R-activated cesium halides seems to have been published until 1994. Radhakrishnan and Selvasekarapandian (1994) studied CsCl:Eu phosphors. The same authors (in 1995) dealt with the TL of CsCl:Sm, and Christober Selvan et al. (1996), from the same laboratory, have investigated CsCl:Tb crystals. These three papers will be referred to below as (a), (b) and (c), respectively. All these works used the same experimental procedures. It included the growth of the crystals using the same slow evaporation from solution method. The samples were quenched to RT after four hours of annealing at 400°C (300°C in the Eu doped crystals), and γ-irradiated at RT. The samples were then left standing for two hours at RT after which the TL was recorded at a heating rate of 60 K min^{-1}. The measurements covered optical absorption and excitation spectra, TL and TL emission spectra. Three main TL peaks appear in (a), (b) and (c) roughly at the same temperatures, at about 360, 380 and 415 K. The TL peak at about 415 K [418, 408 and 415 in (a)–(c), respectively] is the only one of the three that does not appear

in undoped CsCl, and is ascribed to the R dopant. In paper (a) the main TL emission at 425 nm is characteristic of Eu^{2+}. The authors assume that in the case of the 415 K peak the Eu^{2+} is converted to Eu^{3+} during the irradiation and during the TL emission an F-electron recombines at Eu^{3+} whence we get $Eu^{2+} + h\nu$. Strangely, all the other TL peaks also emit the same 425 nm band characteristic of Eu^{2+}. This is suggested to result from a recombination of an F-electron with a hole at a V-type center combined with a transfer of the recombination energy to a neighboring Eu^{2+} ion. The emission is then obtained during the relaxation of the excited Eu. Similarly also in (b) and (c) the emission of all the TL peaks is characteristic of the R ions. In (c) it is characteristic of Tb^{3+}. In this case the authors assume energy transfer from an excited V center to a Tb^{3+} neighbor.

The TL peaks at about 415 K in (a), (b) and (c) may be of some interest in dosimetry. These peaks become dominant at higher doses. In the case of CsCl:Eu the authors show its linear dose response and conclude that it may suit for radiation dosimetry. In (b) and (c) the dose response is sublinear. This conclusion seems however to have resulted from overlap with other peaks. Proper resolution of the peaks by prewarming to a temperature close to 400 K or by total-glow-curve computer fitting may show linear dose dependence also for the Sm- and Tb-doped phosphors.

3.1.6. *Other alkali-metal compounds*

Sahare and Moharil (1989) have observed a peculiar effect in non-irradiated $LiNaSO_4$:Eu powders. The as-received sample gave, during the first heating up from RT, a TL-like intense glow curve showing peaks at 365 and 405 K with the 365 K peak in the form of spikes. During the cooling back to RT spikes appeared again below about 400 K at an intensity about 10 times that obtained during the first heating. Heating after the first cycle gave a smooth glow curve with peaks at 365 and 405 K. Subsequent cooling continued to show the high-intensity spikes. The authors suggested that the emission during the heating, in the cycles following the first one, was real TL excited by the intense spikes during the previous cooling. To check this, they mixed the $LiNaSO_4$:Eu with $CaSO_4$:Dy powder, and the glow curve indeed exhibited an additional peak at 525 K characteristic of $CaSO_4$:Dy as shown in fig. 9. The TL of the $LiNaSO_4$:Eu powder was found to have an intensity 50 times that of the undoped powder. The spikes were suggested to be due to a pyroelectric effect related to a structure transition. In a later paper Sahare and Moharil (1990a) report that the 405 K TL peak emits at 412 nm and it gives a TLD material with high sensitivity, excellent reusability and moderate fading. Moharil et al. (1995) present $LiNaSO_4$:Eu as a phosphor more sensitive than the widely used $CaSO_4$:Dy phosphor.

Somaiah et al. (1990a) studied the X-ray luminescence (XL) and TL of $LiBaF_3$:Eu(1%). They claim that the incorporation of the Eu adds to the glow curve of the undoped RT X-irradiated sample a TL peak at 420 K (at a heating rate of 0.5 K s^{-1}).

Furetta et al. (1996) studied the TL of $Li_2B_4O_7$:Eu powder samples β-irradiated at RT in comparison to that of the undoped and Cu-doped samples. The Eu-doped sample showed two intense TL peaks at 150 and 220°C and a weak one at 310°C. The total TL intensity of

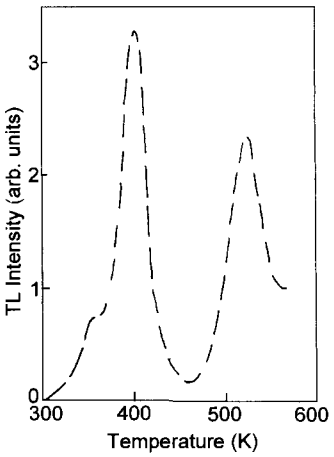

Fig. 9. GC of a mixture of $LiNaSO_4$:Eu and $CaSO_4$:Dy preheated to 550 K, cooled down to RT when the GC was obtained in heating. The excitation was only by the intense spikes from the $LiNaSO_4$:Eu during the cooling.

these samples was lower than that of the Cu-activated one, and its linear dose dependence was limited to the dose range 0.45–1.5 Gy, which limits its use for dosimetry.

The TL of X-irradiated Gd-doped $NaMgF_3$ was examined by Venkata Narayana and Somaiah (1990). X-irradiation at RT gave three well-defined TL peaks at 360, 495 and 548 K, and a shoulder at 585 K. Comparison with the glow curve of an undoped crystal showed that only the 495 K TL peak was related to Gd. The others were enhanced and shifted to higher temperatures by the doping. This effect was pronounced after X-irradiation at 77 K, when all the peaks below RT were enhanced and shifted to higher temperatures. No Gd-related TL peaks appeared up to RT. The 495 K peak was ascribed to $Gd^{2+} \rightarrow Gd^{3+}$ during the excitation and $Gd^{3+} \rightarrow (Gd^{2+})^*$ when the TL is emitted on relaxation to the ground state.

Castaneda et al. (1996) found that the mixed crystal $KCl_{1-x}Br_x:Eu^{2+}$ exhibits high sensitivity to UV in the actinic 200–300 nm region. Its optimal sensitivity was obtained for $KCl_{40}Br_{60}:Eu^{2+}$. A maximum was found at 230 nm. The limit of detection under the optimal conditions was 0.01 $\mu J\,cm^{-2}$ which is better by more than an order of magnitude compared to either Eu-doped KCl or KBr. The enhancement of the TL of the mixed crystal compared to each of the components was attributed by the authors to variations in the vacancy concentration with the change in composition. The fading of the TL of the mixed crystal at RT has also improved compared to that of the components. It dropped fast for about 200 s and then it stabilized. It is recommended by the authors as a high-sensitivity TLD for UV in the actinic region.

The TL of K_2SO_4, Rb_2SO_4 and Cs_2SO_4 doped with Dy was studied by Kumar et al. (1993). The as-grown crystals did not show any absorption in the range 200–800 nm at low irradiation γ-doses. Only above 2.5 MRad was observed a weak absorption in the range 1.5–2.7 eV. This absorption disappeared after warming which bleached away the TL. Each of the three phosphors gave three TL peaks after RT irradiation. They were located at 365, 430 and 480 K for K_2SO_4:Dy, at 370, 395 and 445 K for Rb_2SO_4:Dy, and

at 375, 405 and 440 K for Cs_2SO_4:Dy. K_2SO_4:Dy exhibited stronger TL compared to the other two phosphors. The TL emission spectra gave two bands at 2.16 and 2.6 eV for all the three phosphors. K_2SO_4:Dy exhibited two distinct weak additional bands at 1.66 and 1.88 eV. The weak absorption observed at very high doses of γ-irradiation was attributed to a conversion $Dy^{3+} \rightarrow Dy^{2+}$ and fitted the Dy^{2+} transition $4f^{10} \rightarrow 4f^9d$ observed in many Dy-doped phosphors. The TL peaks were assigned to the release of holes trapped at anion radicals produced during the irradiation and their recombination at Dy^{2+}. The TL emission was characteristic of Dy^{3+} transitions from $^4F_{9/2}$ levels to the 6H manifold. All TL peaks exhibited first-order kinetics. E-values are given for the three phosphors. Those for K_2SO_4:Dy were found to be 0.89, 1.11 and 1.24 eV for the 364, 431 and 482 K peaks respectively.

Chryssou (1987) studied the TSEE of K_2SO_4. The undoped crystals exhibited TSEE peaks in the range 60–380°C with the main one at 180°C. Annealing at 1100°C shifted the main peak to 160°C. Dy (or Sm) doping only changed the intensity of the TSEE peaks which increased with the Dy (or Sm). After UV-light excitation the TSEE decreased with rising concentration of the dopant. This was interpreted to be caused by small depth of penetration of the UV light and by assuming that the R dopant increases the concentration of the bulk traps and decreases that of the surface states.

Somaiah et al. (1990b) studied the TL of $KCaF_3$:Gd. The Gd was found to have only a marginal effect on the observed TL.

$K_2Ca_2(SO_4)_3$:Eu has been investigated in several papers by Sahare and coworkers and was found promising as a high sensitivity stable TLD phosphor. Sahare et al. (1989) found for $K_2Ca_2(SO_4)_3$:Eu γ-ray excited at RT a very strong TL peak at 720 K (at a heating rate of 150 K min^{-1}). It also showed higher sensitivity compared to LiF TLD-100. It was found to rise monotonously with the dose, though sublinearly. The authors recommend it as a useful TLD phosphor for high-temperature environmental conditions.

In another paper Sahare and Moharil (1990b) reported on a new high-sensitivity phosphor for TLD – $K_2Ca_2(SO_4)_3$:Eu (0.1 mol%). It has been used as a powder of grain sizes 100–125 μm. An important pre-treatment was pre-annealing for one hour at 970 K after which the phosphor was quenched to RT. The TL (at 150 K min^{-1}) was excited by γ-irradiation and measured after 2 hours standing at RT. The glow curve exhibited peaks at 375 and 410 K for a sample quenched from about 500 K. When quenched from 970 K the 375 K peak disappeared and the 420 K was enhanced by more than two orders of magnitude. Under these conditions the sensitivity was at least five times that of the widely used $CaSO_4$:Dy TLD. No change in the glow-curve features was found for γ-doses of 10^{-3}–3 C kg^{-1}. Figure 10 gives the dose–response curves for $K_2Ca_2(SO_4)_3$:Eu (curve B) and for $CaSO_4$:Dy (curve A). Both curves show perfect linear dose response. The fading of the $K_2Ca_2(SO_4)_3$:Eu was found to be negligible after 10 days standing under ambient conditions. The TLD peak (420 K) emission at 415 nm fits well for the widely used PM detectors. The re-usability and stability were also found to be excellent. The authors recommend its use as a replacement of the $CaSO_4$:Dy TLD for ionizing radiation. No mention is made in their paper of the 720 K and other TL peaks observed in the glow curves of $K_2Ca_2(SO_4)_3$:Eu. It seems likely that the changes in the glow curves were due

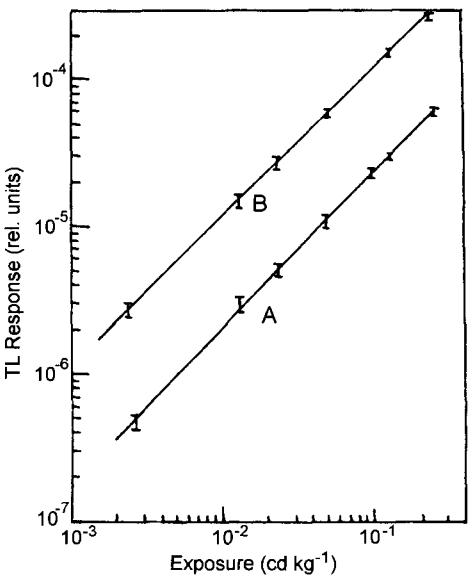

Fig. 10. Dose dependence (A) of the dosimetric TL peak of $CaSO_4$:Dy and (B) of the 420 K peak of $K_2Ca_2(SO_4)_3$:Eu.

to differences in the preparation of the samples and in their pre-treatments before the TL measurements.

A paper by Dhopte et al. (1991a) is dedicated to the effects of preparation procedures on the TL of $K_2Ca_2(SO_4)_3$:Eu phosphors. This paper is limited to TL up to about 600 K. It describes various effects of preparation procedures on the glow curves and on the TL and PL emission spectra. It is beyond the scope of the present article to give in detail all the effects. One important general conclusion is that in order to obtain high-sensitivity $K_2Ca_2(SO_4)_3$:Eu phosphors one has to follow a given path in the mixing of the components. One of the examples given in the paper compares the TL obtained after annealing for 24 hours at 1000°C (above the melting point), when a weak TL peak appears at 375 K, to that obtained after quenching of the sample annealed at about 970°C. The latter treatment gives a TL peak of 410 K at an intensity more than two orders of magnitude higher compared to that obtained by the former treatment. To get the intense TL peak the mixed components have to be subjected to a solid-state diffusion procedure at a high temperature without reaching the melting point.

Another phosphor more sensitive than the $CaSO_4$:Dy was reported by Dhoble et al. (1993). This is the Eu-doped (0.1 mol%) $K_3Na(SO_4)_2$ mixed crystal. After melting and slow cooling to RT the molten mass was crushed and sieved to obtain 72–200 μm grain sizes. The powder samples were excited at RT by γ-radiation, and the glow curves were taken at 150 K min^{-1}. A very strong TL peak appeared at 475 K with weak shoulders on both sides. The 475 K peak gave excellent linear dose response over the measured range 2.5×10^{-3}–0.25 C kg^{-1}, and negligible fading in 10 days. Its sensitivity was more than five times that of $CaSO_4$:Dy at low doses and more than three times of that at high

doses. The kinetics of this TL peak was of first order, its E-value was 1.32 eV, and the s-value was $10^{-14}\,s^{-1}$.

A few papers deal with $KMgF_3:Eu^{2+}$ phosphors. Two of them, by Furetta et al. (1990) and Bacci et al. (1993), both from the same laboratory, stress the good dosimetric properties of the above phosphor. The RT γ- and β-irradiated samples exhibited a prominent TL peak at 613 K. Its sensitivity remained constant over the range of 4×10^{-3}–1 sv. It exceeded the sensitivity of TLD-700 discs by a factor of nearly three and that of LiF:Mg,Ti pellets by a factor of five. Its fading is described to be negligible and it is claimed to show no interfering effects. In the 1993 paper the authors studied the optical absorption and emission spectra. From this they concluded that in spite of the introduction of Eu as three-valent $EuBr_3$, only Eu^{2+} was incorporated in the host material. The high-temperature TL peak was found to shift to lower temperatures and to increase in intensity with the concentration of the Eu dopant.

Two other papers describe the TL of X- and UV-irradiated $KMgF_3:Eu^{2+}$ crystals. These are by Gektin et al. (1995) and Shiran et al. (1995), again both from the same laboratory. They have observed that the TL depends on the type of chemical Eu compound added to the melt of the host. With Eu_2O_3 the glow curve showed a very intense dominant TL peak at 390°C (at $0.28°C\,s^{-1}$). This TL peak increased with the Eu_2O_3 up to concentrations of 0.5%. The Eu concentration in the host compound, when introduced in the form of Eu_2O_3, was several times higher compared to that obtained with EuF_3. The intense 390°C TL peak is suggested to be associated with oxygen in the neighborhood of the Eu^{2+} ions. The main drop in the F-center absorption occurred in this sample just at 390°C. Gektin et al. (1995) stress that the sensitivity of $KMgF_3:Eu^{2+}$ to ionizing radiation is related to the presence of oxygen impurities. It is concluded that $KMgF_3:(Eu_2O_3)$ is an effective TLD phosphor. Moharil et al. (1996) mark that in order to obtain effective $KMgF_3:Eu^{2+}$ phosphors the preparation of the material has to be carried out in a solid-state diffusion process at a temperature *below* the melting point [see Dhopte et al. (1991a) above]. This seems to disagree with the process of growing $KMgF_3:(Eu_2O_3)$ from the melt which has been shown to give efficient TL phosphors.

Gd-doped $KMgF_3$ has been studied by Venkata Narayana et al. (1990). RT X-irradiation followed by warming (at $0.5\,K\,s^{-1}$) gave, in addition to the TL of undoped $KMgF_3$, a TL peak at 430 K. The presence of Gd was found to suppress a TL peak at 350 K when irradiated at RT. When X-irradiated at 80 K the Gd was found to reduce the intensity of all the TL peaks below RT and to shift them towards higher temperatures. $KMgF_3$:Gd does not seem suitable for TL dosimetry. Venkata Narayana and Somaiah (1990) did similar work on $NaMgF_3$:Gd.

Deshmukh et al. (1986) studied Sm(0.1 mol%)-doped $K_2Cd_2(SO_4)_3$. Samples were prepared by the solid-state diffusion method with the mixture of components kept at 873 K for six days. The product was powdered, melted at 1048 K and cooled down *slowly* to RT. γ-irradiated samples were warmed (at $50\,K\,min^{-1}$). The glow curve exhibited a prominent peak at 430 K. The TL of the doped sample was higher by a factor of forty compared to the undoped $K_2Cd_2(SO_4)_3$. No discontinuous changes occurred in the glow curves near the transition point of the host (428 K).

Komar et al. (1996) studied R-doped $KMgF_3$ single crystals. It was found that proper variation of the oxygen content in these crystals makes them effective scintillators and phosphors for TLDs highly sensitive to ionizing radiation and for UV. It was also found to make good laser material.

Summing up sect. 3.1 we can say that some alkali-metal compounds can make high-sensitivity phosphors showing also other good dosimetric features. For example the K_3Na:Eu crystals showed a sensitivity three times higher than the widely used $CaSO_4$:Dy TLDs as shown by Dhoble et al. (1993). Similarly $K_2Ca_2(SO_4)$:Eu was shown by Sahare and Moharil (1990b) to give a TL sensitivity 5 times that of $CaSO_4$:Dy. The sensitivity of these compounds was shown to depend drastically on the method of preparation. It seems that further investigation of the alkali-metal compounds may yield more efficient TL phosphors.

Two specific results are worth mentioning. One is the self-irradiation effect observed by Perez-Salas and coworkers in K-containing phosphors. The self-irradiation was traced to be due to the radioactive ^{40}K isotope present in natural potassium at a concentration of only 0.0177%. This effect gives a feeling of the high sensitivity of the phosphors. A peculiar effect was observed by Sahare and Moharil (1989) in $LiNaSO_4$:Eu. This phosphor was shown to give pyroelectric spikes which proved to be very efficient in exciting the TL.

3.2. *Alkaline-earth compounds*

This section will be divided into subsections according to the various alkaline-earth metals. No work seems to have been published on Be compounds, so magnesium compounds will be dealt with in the first subsection. Ca compounds and heavier alkaline-earths will follow. The R-doped Ca compounds, and especially CaF and $CaSO_4$, have been studied extensively. Therefore each will be described in a separate subsection.

3.2.1. *Magnesium compounds*

MgS has been considered for many years as a high-sensitivity phosphor. The main investigation of R-doped MgS started only in the 1980s. The reason for this delay was the chemical instability of MgS against atmospheric CO_2 and H_2. This difficulty has been removed by Rao (1986a) who developed protective methods for single crystals, polycrystalline powders, films and pellets of MgS phosphors.

Most of the work on R-activated MgS has been carried out by the same research groups in various author combinations and in a few locations like Montpellier, France; Karaikuchi, India; and Silver Spring, MD, USA. The studies in all the published work were mainly on doubly activated samples ($MgS:R_1,R_2$). In such cases one activator served as an electron trap and the other as a hole trap. The work concentrated on the TL and on the related OSL of the phosphors. Rao et al. (1984) gave preliminary results on the OSL of MgS:Eu,Sm. They reported good sensitivity of the phosphor.

Mathur et al. (1986) studied MgS:Ce,Sm using UV and γ-rays for excitation of the TL (at RT). The glow curves showed two dominating peaks at 346 and 449 K. The latter

peak was found suitable for OSL dosimetry. The OSL was stimulated at 1317 nm by an InGaAsP diode laser subsequent to UV or γ-irradiation. The high sensitivity and linear dose dependence is claimed to be promising for UV and γ dosimetry.

Rao (1988) studied MgS doped by Eu, Sm, Ce and Tb and their doubly activated combinations. The activators were incorporated into the host at about 900°C. Films of the product were grown on a glass substrate and coated with a Dow Corning 805 polymeric binder for protection from the ambient atmosphere. Standing for a year did not affect at all the characteristics of the protected films. The TL was excited by UV, X-rays or daylight. Warming (at $2°C\,s^{-1}$) gave dominating peaks near 200°C in the glow curves of MgS:Ce, MgS:Sm and MgS:Ce,Sm. MgS:Eu,Sm gave the dominating TL peak near 270°C. These peaks were found to be most suitable for dosimetry. Some of the above phosphors were studied earlier by Rao (1986b) where details on the fading and dose response were given.

Chakrabarti et al. (1988a) concentrated on the OSL of MgS:Ce,Sm and MgS:Eu,Sm. From the OSL and TL emission spectra it has been concluded that the process involved in the OSL differs from that in the TL emission; in OSL, Ce (or Eu) acts as the recombination center and Sm as electron trap, whereas in TL emission, Sm acts as the recombination center and Ce (or Eu) as the hole trap.

Chakrabarti et al. (1988b) studied mainly a TL peak which appears in MgS singly doped by Sm^{3+}, Ce^{3+} and Tb^{3+}. X-irradiation at RT gave the main TL peak near 70°C (60–80°C for the three dopants). The authors suggested that during the excitation the R dopants serve as electron traps, and cation vacancies with a next-neighbor sulfur ion form V-centers which act as hole traps. On warming, holes are released from the V-centers and give the 80°C TL peak by recombination with the trapped electrons at the R ions.

Terbium-activated magnesium orthosilicate is known as a high-sensitivity phosphor since the early 1970s. Nakajima (1971), Toryu et al. (1973), Jun and Becker (1975), Lakshmanan et al. (1978a) and others have observed a very strong TL peak near 200°C in Mg_2SiO_4:Tb phosphors. Its sensitivity was estimated to exceed that of LiF TLD-100 by a factor of 40. The 200°C peak was also found to show excellent dose–response linearity, excellent stability, very low fading, low photon energy dependence and good annealing characteristics. Toryu et al. (1973) studied the relation between the phase composition of the fixed MgO and SiO_2 components and the TL peaks of a Mg_2SiO_4:Tb phosphor obtained by firing at temperatures up to 1400°C. A ratio of about three to one of the MgO to SiO_2 gave an optimal high-intensity TL peak at 190°C (obtained by γ-irradiation and a warming rate of $3°C\,s^{-1}$). The intensity of this peak increased with the firing temperature of the phosphor, and its optical fading dropped drastically when approaching a firing temperature of 1400°C. Bhasin et al. (1976) prepared a Mg_2SiO_4:Tb phosphor by firing the components at 2750°C (compared to up to 1700°C by other investigators). Under these conditions the dominant TL peak appeared at 300°C and its sensitivity was 80 times that of TLD-100. Other dosimetric characteristics were also good.

In spite of its excellent dosimetric qualities very little work has been done on Mg_2SiO_4:Tb phosphors after the successful start in the 1970s. The few papers published more recently deal mainly with arrangements for special practical uses of the phosphor. Nakajima (1988) has fitted two filters, one of lead and another of Lucite, to eliminate

the energy dependence of the phosphor. Kato et al. (1991) and Li et al. (1995) describe the calibration and other fittings of the Mg_2SiO_4:Tb phosphor for diagnostic X-ray dose measurements. The phosphor (in pellets) is described as a precise, small and sensitive dosimeter.

A review of magnesium silicate phosphors was given by Nakajima (1993).

R-activated magnesium tetraborates make stable high-sensitivity phosphors. The MgB_4O_7:Tb has been studied more extensively compared to the Mg_2SiO_4:Tb, though not enough. Prokic (1993) has reviewed the published work on magnesium borate phosphors. He also gives details on the preparation of the phosphors and on their applications.

Toryu et al. (1973) studied the effects of the composition of the various components fired to produce the phosphor, and the effect of the temperature of firing. They observed that generally there appear, in addition to MgB_4O_7, also other phases like monoclinic and triclinic $Mg_2B_2O_5$ and $Mg_3(BO_3)_2$. The glow curve obtained after RT γ-irradiation and at a heating rate of $3°C\,s^{-1}$ exhibited a TL peak at 170°C related to MgB_4O_7:Tb which was enhanced by the presence of $Mg_2B_2O_5$. This TL peak also increased in intensity with the firing temperature. It also displayed strictly linear dose dependence up to 50 Gy.

Paun et al. (1977) studied the dosimetric properties of various borates including Sm- and Ce-activated MgB_4O_7. The Sm-activated phosphor gave a main TL peak at 260°C and the Ce-activated one gave a single TL peak at 150°C (γ-irradiation, heated at $5°C\,s^{-1}$). The maximum intensities of these peaks were obtained with 0.5 mol% of the R. The peaks gave high sensitivity, linear dose dependence (up to 50 Gy) and negligible fading. The optimal firing temperature was found by these authors to be 900°C. The authors also note an advantage of these phosphors giving nearly tissue equivalence.

Lakshmanan et al. (1979) prepared MgB_4O_7:Dy by firing a mixture of $MgCO_3$, H_3BO_3 and Dy_2O_3 (0.5 mol%) at 950°C for two hours and quenching to RT. Powder samples of 105–210 μm grain size were γ-irradiated at RT. The glow curves exhibited a strong peak at 200°C. It gave good linearity with doses up to 40 Gy. The TL sensitivity for γ-rays was slightly higher than that of TLD-100. Its fading was 40% in 17 days. The authors consider this phosphor promising as a good TLD, but note that its fading and hygroscopicity need improvement.

Barbina et al. (1981) give preliminary results of the dosimetric properties of sintered discs of MgB_4O_7:Dy after annealing at 500°C. The phosphor showed a single TL peak at 170–190°C. Its fading was about 30% in 15 days. It gave linear dose response and low photon energy dependence (in the range of 30–300 keV). The phosphor's TL sensitivity was 4 times that of TLD-100.

Prokic (1980) prepared discs of pressed MgB_4O_7:Dy,Tm sintered at 950°C. The double R activation and the sintering resulted in higher sensitivity and better performance. A single TL peak appeared in the glow curve at about 210°C. Its sensitivity was about seven times that of TLD-100, and its fading was 10% in 60 days. In addition, the sintered discs were not hygroscopic. The TL emission was characteristic of Dy and Tm. Prokic (1982) describes an improved graphite mixed MgB_4O_7:R sintered disc phosphor. Using the TL sensitization technique the phosphor sensitivity was five times that of the regular powder phosphor. Prokic (1986) and Prokic and Christensen (1983, 1986) prepared

a graphite-mixed sintered disc MgB_4O_7:Dy phosphor. It exhibited high sensitivity and was found attractive for β-radiation dosimetry. Its low transparency has greatly reduced the optical fading. A review article describing the performance of the improved magnesium borates up to the middle of the 1980s and their applications was given by Christensen and Prokic (1986). Prokic (1990) reports on further improvements in the dosimetric characteristics of various TLD phosphors embedded in graphite mixed sintered MgB_4O_7:Dy. The improved MgB_4O_7:Dy phosphor exhibits a dominating TL peak at 270°C up to 12 times more sensitive compared to TLD-100. No fading was observed after 5 months storage at RT and very little fading on storage at 200°C. The optical fading was also very low. Suitable introduction of graphite (about 2%) gave a flat β-energy dependence for the range 0.1–2.3 MeV. A more recent improved R-activated MgB_4O_7 was reported by Prokic and Botter-Jensen (1993). The improved phosphors reduced the sensitivity to light. The fading of the new MgB_4O_7:Dy,Tm phosphor was about 2% per month.

It is important in the measurements of skin tissues to have control of the depth of penetration of the measuring beam. The ICRU regulations [ICRU Report 39 (1985)] require measurements of skin doses at beam penetrations of 0.07 mm (H_s 0.07). Christensen and Prokic (1986) have shown that thin graphite-mixed sintered pellets of MgB_4O_7:Dy can be fitted to satisfy the H_s 0.07 requirements and give accurate β-ray doses for β energies above 0.2 MeV. A flat β-energy dependence can be obtained by introducing a Mylar filter of suitable thickness.

Fukuda et al. (1989) studied the TL and the TSEE of Dy- and Tm-doped MgB_4O_7 X-irradiated at 77 K. The dopants (0.06 wt% $DyCl_3$, 0.03 wt% Tm_2O_3) were mixed in the powder materials and sintered at 980°C. Most TSEE peaks had corresponding TL peaks shifted towards lower temperatures compared to the TL peaks, except for a peak near 330°C which appeared at a higher temperature compared to the corresponding TL peak. The unexpected shift of the TSEE peaks to lower temperatures was explained by the authors to be due to surface states and contamination of the surface by vapors, that affected the TSEE which comes from the surface of the sample. The main dosimetric TL peak appeared (at 20°C min^{-1}) at 158°C for the Dy-doped sample, and that of the TSEE peaked at 148°C. Fukuda and Takeuchi (1989) give the glow curve obtained after X-irradiation at RT of MgB_4O_7:Dy. The strongest TL peak appeared near 150°C for both the Dy- and Tm-doped samples. The peak of the Tm-doped sample was weaker by a factor of five compared to the Dy-doped one.

Shahare et al. (1993) prepared a MgB_4O_7:Dy phosphor by firing a mixture of magnesium-nitrate hexahydrate, ammonium tetrahydrate and dysprosium oxide at 800°C. The material was then cooled slowly to RT and crushed to a fine powder. The powder was annealed at 500°C and quenched to RT before taking the TL measurements. The excitation was by γ-rays (at RT) and the heating rate was 150°C min^{-1}. A strong peak at 187°C similar to that obtained by Campos and Filho (1990) appeared in the GC. Its TL sensitivity was about 50% of that of $CaSO_4$:Dy. The authors claim that the good TLD characteristics together with the good tissue equivalence ($Z = 8.4$) of the MgB_4O_7:Dy phosphor make it a good practical phosphor for β measurements. It should be noted that

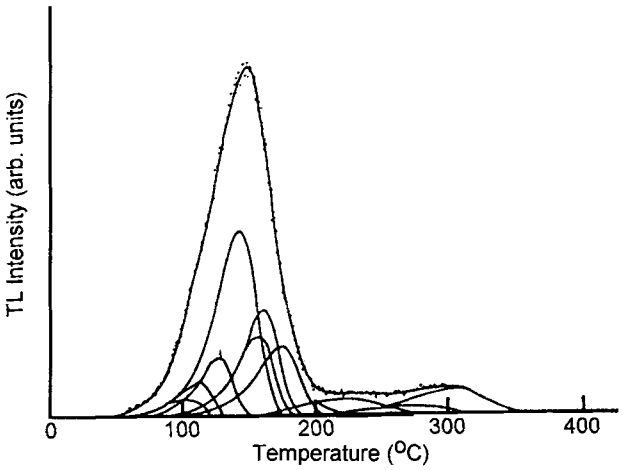

Fig. 11. Experimental GC of MgB_4O_7:Dy and the peaks separated by a best-fit computer program.

the Dy concentration in this case was considerably lower than the 0.5 mol% found by Paun et al. (1977) and by other investigators to give the highest dosimetric sensitivity of MgB_4O_7:Dy phosphors.

Under various conditions of preparation, the GC of the MgB_4O_7:Dy phosphor is often described as showing one dominating TL peak which is reported by various authors to appear somewhere in the range of about 160 to 220°C. These deviations can only partly be explained by variations in the heating rate. Souza et al. (1990) in preliminary examination of these deviations concluded that the dominating TL peak of MgB_4O_7:Dy is not a single TL peak. Further work by Souza et al. (1993a,b) was done on MgB_4O_7:Dy graphite mixed discs (1 mm thick and 4.2 mm in diameter). ^{60}Co γ-rays were used for excitation. The TL peaks were separated using a computer program with general-order kinetics. The heating rate was $1°C\,s^{-1}$. After irradiation the phosphor was heated to different temperatures T_{stop} in the range 50–500°C. The peak temperature obtained with different T_{stop} values changed rapidly for T_{stop} values above about 140°C. Another set of GCs at a wide range of doses rising up to 2.5 Gy did not show any shift in the peak temperature. This indicated that the dosimetric peak is composed of individual first-order kinetics peaks. The computer program gave a fitted combination of 11 peaks in the range 100–304°C as shown in fig. 11. As the authors note, the low s-values of some of the separated component peaks may not be real, and further experiments on thinner samples are necessary to validate the parameters of the individual peaks. That the dosimetric TL peak of MgB_4O_7:Dy has a complex structure was already indicated by Oduko et al. (1984).

Abtahi et al. (1985, 1987) examined the behavior of the MgB_4O_7:Dy under CO_2 laser heating at heating rates of about 500–4000°C s^{-1}. They assumed second-order kinetics for the high-temperature peak and obtained accordingly $E = 1.5$ eV and $s = 1.75 \times 10^{11}$. The assumption of second-order kinetics is of course not necessarily correct, but it was enough

for checking the behavior of the phosphor under the high heating rates. The TL efficiency and the TL emission spectra were found to remain unchanged under the extremely high heating rates. Using pre-annealing at 200°C for 10 min the TL peak did not show any thermal fading after 4 months at RT, and very low optical fading. It was also found to be up to 4 times more sensitive than TLD-100.

Richmond et al. (1987) examined the possibility of using the PTTL excited by UV (254 nm) illumination following γ-irradiation of a MgB_4O_7:Dy phosphor. The γ-irradiation produced a TL peak at 180°C. UV illumination showed two TL peaks, at about 60 and 210°C. The authors have shown that a good correlation exists between the PTTL and the prior γ-ray dose.

Ranogajec-Komor and Osvay (1986) have compared the dosimetric characteristics of MgB_4O_7:Dy, CaF_2:Mn, Al_2O_3:Mg,Y and LiF:Mg,Ti. The dosimetric peak of the examined MgB_4O_7:Dy phosphor appeared at 150°C and not in the range 180–210°C (see above). It seems that it was not one of the improved forms of the MgB_4O_7:Dy phosphors cited above. Still, the sensitivity of the MgB_4O_7:Dy was comparable to that of CaF_2:Mn and higher by a factor of 4–8 compared to the other examined phosphors. Its linearity was excellent and its energy dependence was lower than those of CaF_2:Mn and Al_2O_3:Mg,Y. The fading was higher compared to that of the other phosphors (30% in 21 days) which is also high compared to that of the improved phosphors described above. An important advantage of the MgB_4O_7 phosphor is its close tissue equivalence.

Vekic et al. (1990) compared the β- and α-energy dependence of TLD-700, LiF:Mg,Ti, MgB_4O_7:Dy, CaF_2:Mn, CaF_2:Cu and Al_2O_3:Mg,Y TLDs. Various radio-isotopes differing in energy have been used as radiation sources. All these phosphors showed very low energy dependence at 364 keV (from a ^{131}I source). At 140 keV (from $^{99}Tc^m$) only the first three phosphors, which are nearly tissue equivalent, showed low energy dependence. It was concluded that these three phosphors are suitable for TLDs used in nuclear medicine, where the $^{99}Tc^m$ radio-isotope is applied.

3.2.2. *Calcium fluoride hosts*

CaF_2 can accommodate most of the R ions. This has contributed to the large number of publications on CaF_2:R phosphors. Merz and Pershan (1967) give results of some optical properties of single crystals of R-activated CaF_2 including TL. Samples were excited by X-rays at 77 K and the glow curves were taken at a heating rate of 2 K min^{-1} up to above 400 K. Figure 12 shows the GCs for the undoped and R-doped crystals. The vertical dashed lines in the figure give the average peak temperatures for each of the six TL peaks appearing in the various GCs. It can be seen that the TL peaks appear at almost identical temperatures, independent of the particular R ion. It is also interesting to note that for most R ions the doping enhanced the TL, except for Eu and Yb which seem to have suppressed the TL. The authors also present curves and tables of the TL peak temperatures, E-values and emission spectra for the individual TL peaks and for the various R dopants. Analogous work carried out on RT-irradiated samples and presenting the TL up to 700 K would have been of more value for dosimetric work. In the following

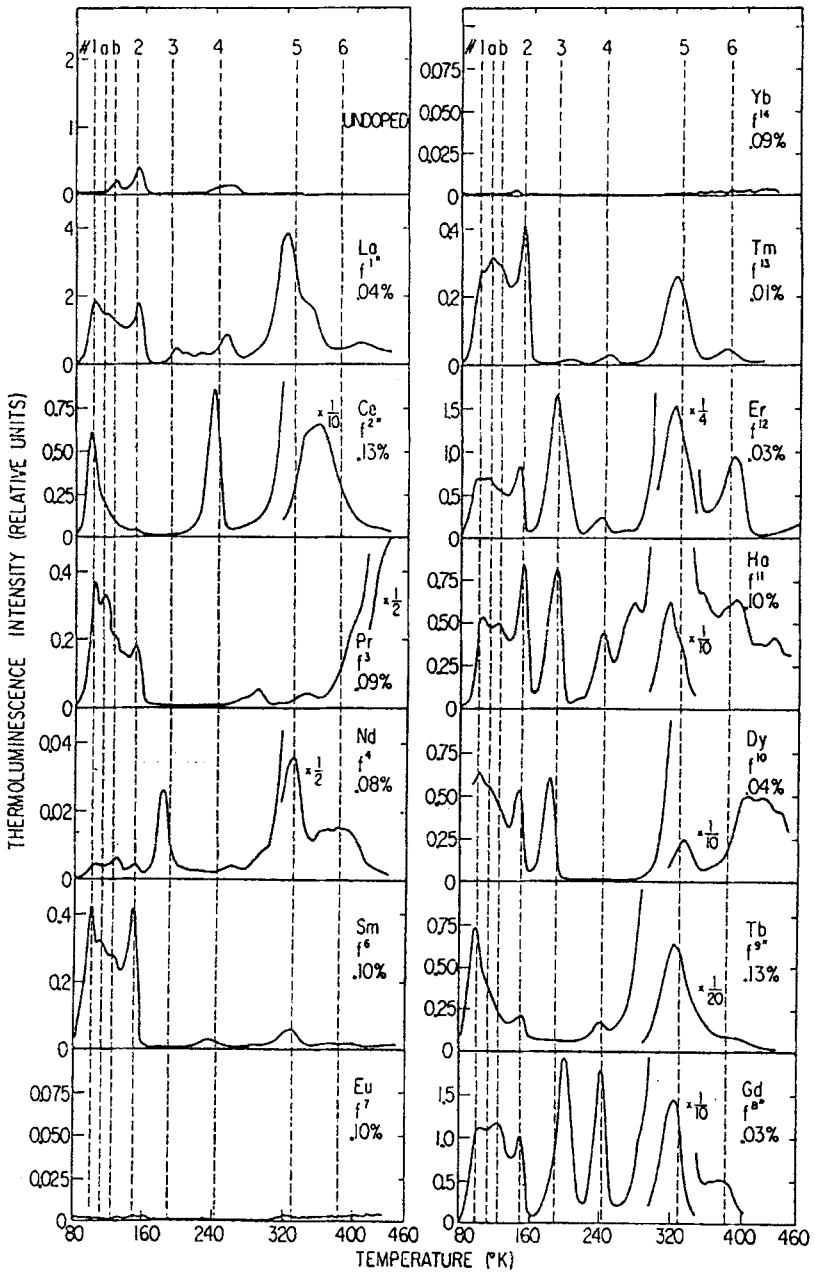

Fig. 12. GCs for an undoped CaF_2 crystal and a CaF_2 crystal doped by various R ions. Excitation by X-rays at 77 K.

paragraphs the review of the published work on R-doped CaF_2 will be presented separately for each of the R dopants.

CaF_2:Dy phosphors. CaF_2:Dy is available commercially as TLD-200. It has been described in some detail by Binder and Cameron (1969). Its sensitivity to RT γ radiation was found to be up to 30 times that of TLD-100. The GC showed four overlapping main TL peaks at 120, 140, 200 and 240°C. Preheating at 100°C eliminated the two low-temperature peaks and with them, the fast fading of the TL, which was now about 10% per month. TL dose response was found to be linear up to about 6 Gy. Pre-annealing at 600°C for one hour extended the linear dose response to higher doses but reduced the sensitivity by a factor of two. The phosphor showed dependence on the photon energy for γ energies below 250 keV.

Hsu and Weng (1994) used a CaF_2:Tm phosphor as a TLD for UV radiation. It was pre-exposed to β radiation and then to UV. A linear UV dose response was observed up to above 25 $J\,m^{-2}$.

Takeuchi et al. (1976) while working on MgO have noted that heating of CaF_2:Dy at 900–1000°C in the open air enhanced remarkably its RT-excited TL. The heating makes the CaF_2:Dy phosphor a very sensitive and convenient TLD for UV light. This enhancement of the UV sensitivity of the TLD-200 phosphor has been investigated by Bassi et al. (1975–1977). The increased UV sensitivity by pre-heating to 900–1000°C was found to rise up to a maximum at about 3 hours of heating. At longer heating times the sensitivity dropped sharply. The sensitivity at the maximum was about 500 times that of the untreated TLD-200. The heat treatment was observed to leave a white layer on the surface of the ribbon-TLD-200 phosphor which looked like an oxide. This layer was believed to be responsible for the sensitivity enhancement. It was supported by the fact that heating in an inert atmosphere did not show any enhancement. The maximum sensitivity was for light in a narrow band peaking at 254 nm. Treated phosphors were insensitive to visible light and to UV above about 300 nm. The fading was fairly high (30–40% in 12 days). In addition, the enhanced phosphor suffered from changes in the sensitivity during the regular annealing between successive measurements (5 min at 600°C). This had to be corrected using a reference detector. Pradhan and Bhatt (1981a) observed that the above pre-heating UV sensitization is accompanied by a sharp drop in sensitivity to ionizing radiation.

Charalambous and Hasan (1983) and Kitis and Charalambous (1988) observed a strange effect of regenerated TL (R-TL) in TLD-200, TLD-900 ($CaSO_4$:Dy) and TLD-100 phosphors. Exposure to high-dose ^{60}Co γ-rays (a few Mrad) followed by heating to a high temperature (about 300°C) bleached of course away all TL below this temperature. Subsequently storing the sample at low temperatures for a long enough time gave regenerated TL peaks upon heating. Figure 13 shows such an R-TL GC obtained after 3 Mrad γ-irradiation at RT followed by heating to 300°C and 10 hours storing in the dark at 77 K. It shows R-TL peaks at 40 and 83°C which were absent in the original GC measured during the heating to 300°C. The authors carried out various sets of experiments on this effect. Based on the results of their measurements they propose a model for R-TL. In this model the high-dose irradiation is assumed to generate new damage defects. These

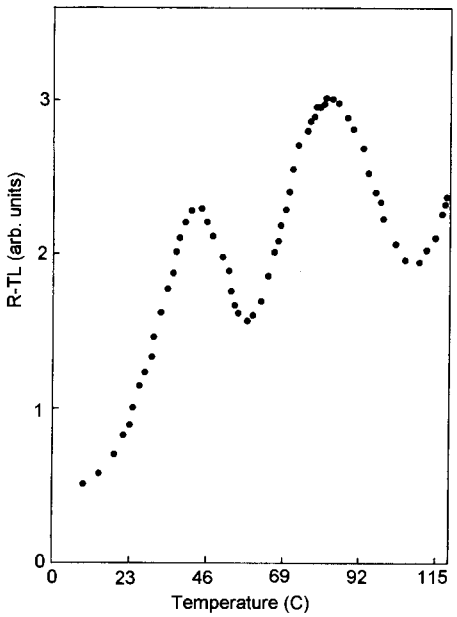

Fig. 13. Regenerated TL obtained after 3 Mrad γ-irradiation at RT of a TLD-200 phosphor followed by heating to 300°C and 10 hours storing in the dark at 77 K.

defects diffuse slowly in the crystal during the storage in the dark. Approaching deep traps of electrons (holes) not emptied during the heating at 300°C the damage-defects get trapped, thus forming composite defects. The trap depths E and frequencies s of the composite defects will of course be different from those of the original "deep" traps. Subsequent heating will then exhibit the regenerated TL peaks. Similar R-TL has been observed by Hasan et al. (1985) also in $CaSO_4$:Dy phosphors.

Hasan and Charalambous (1983) studied the effect of the radiation dose on the behavior of Harshaw ribbons of CaF_2:Dy (TLD-200). Three TL peaks at 127, 140 and 340°C show supralinearity in the range 10^2–10^5 rad. Two others at 188 and 234°C do not. The TL parameters were measured using the ir method. The E-values obtained were 1.01, 1.05, 1.23, 1.34 and 1.64 eV and the s-values were 3, 47, 10, 7 and $7(\times 10^{12})\,s^{-1}$ for the 124, 140, 188, 234 and 340°C TL peaks, respectively. The halflives of the 5 TL peaks range from 26 h for the 124°C peak up to about 10^8 years for the one at 340°C.

Hsu and Wang (1986) checked a variety of pre-measurement annealings of CaF_2:Dy phosphors. They found that annealing for 20 min or more at 450°C results in little residual TL and highly stable sensitivity.

Dielhof et al. (1988) explored effects of the energy of fast neutrons and of the encapsulating materials on the sensitivity of CaF_2:Dy phosphors to neutron radiation. Comparison of sensitivities to fast neutrons of the TL peaks of Tm-, Dy- and Mn-doped CaF_2 showed the superiority of CaF_2:Tm. Encapsulating in A-150 (Shonka tissue-equivalent plastic) gave higher TL sensitivity compared to teflon encapsulation. The authors relate this to a contribution of the recoil protons to the TL. The Mn-doped

phosphor showed very low TL sensitivity. On the other hand, the TL sensitivity was highest for the 272°C TL peak of CaF_2:Tm. Increasing the neutron energy from 0.5 to 14.8 MeV increased the intensity of the 270°C peak by about a factor of 3. This was attributed to a decrease in the LET of the secondary particles produced by the neutrons, confirming that high LET of the secondary particles produced by the neutrons reduces the TL response.

The XL and TL of CaF_2:Dy (0.1 mol%) at low temperature (15–300 K) has been investigated by Chakrabarti et al. (1991). Single-crystal samples were X–irradiated at 15 K and heated at a rate of 12 K min^{-1}. The GCs exhibited overlapping TL peaks covering the range of 80–250 K. The TL emission spectrum was found to be similar to that reported by Merz and Pershan (1967). The TL near 100 K was assumed to be due to V_K centers. The Dy^{3+} characteristic emission was found to be most intense near 300 K.

The XL, PL and TL of single crystals of CaF_2:Tm X-irradiated at 80 K has been compared by Figura and Nepomnyashchikh (1991). The XL showed Tm-characteristic emission structures at 2.5, 3.5 and 4.3 eV. The TL peak at 140 K showed only the 2.5 and 3.5 structures truncated on the high-energy side of each structure. This indicated the missing of transitions from the high-energy P levels in the TL.

Semenov et al. (1992) studied the enhancement of the TL of CaF_2:Dy crystals by helium. Annealing of the crystals under vacuum at elevated temperatures reduced the intensity of the high-temperature TL peaks. Subsequent saturation with He gave rise to an increase of the TL above 300 K. A peak at 625 K hardly observable before the He treatment was enhanced most markedly. The enhancement of the TL increased with the helium concentration up to 1×10^{14} cm^{-3} and remained unchanged for higher He concentrations. The He sensitization resulted in an increase in the high-temperature TL by more than a factor of 10 compared to the untreated CaF_2:Dy. The effect seems to be unique to CaF_2:Dy, and was assumed by the authors to be due to a change in the state of the Dy. Stabilization of anionic vacancies resulted then in an increase in the concentration of the deep traps and hence the enhanced TL.

The TL excited by soft X-rays (SXRs) in CaF_2:Dy has been studied by Pietrikova et al. (1993). SXRs in the range 1–22.2 keV were used. The irradiation at RT and subsequent heating at 2 K s^{-1} produced TL peaks at 293, 413, 473, 523, 613 and 673 K, peaks P_1–P_6 respectively. The peaks were separated and analyzed numerically using a least-squares computer program. An interesting effect was that the curves describing the ratios of the intensities P_1/P_3 and P_2/P_3 as function of the SXR photon energies showed an abrupt change in slope at 2.6 keV. This was assumed to be related to the effective absorption by the Dy M level electrons in the range 1.33–2.05 keV.

Carrillo et al. (1996) studied the response of CaF_2:Dy to photons in the range 0.275–2.55 keV. Chips of the phosphor were irradiated with monoenergetic photons of synchrotron radiation. GCs for He and open air anneal showed the adverse effect of the air annealing. The authors concluded that the He anneal maintained the sensitivity of the CaF_2:Dy chips independently of the photon energies and the number of times used. It thus allows the proper use of TLD-200 to monitor synchrotron exposures to integrated circuits.

Sastry and Kennedy (1993) investigated the effect of a Pb co-activator added to CaF_2:Dy phosphors. The TL after γ-irradiation at RT exhibited six peaks in the range 300–700 K. The emission was characteristic of Dy^{3+}, and the 420 K peak was found strongest with 0.1 mol% of Dy. The excited Pb was found to transfer its energy to nearby Dy^{3+}.

Budzanowski et al. (1996) studied, among other TLDs, the background and the cosmic-ray component of CaF_2:Dy (TLD-200). Care was taken in the background measurements to omit any terrestrial and cosmic ray effects. For this, the phosphor was put in a steel cage and was located 775 m below sea level [in the Hasse mine (Germany)]. The fading of the TLD was less than 5% per year, at the ambient temperature (33°C) in the mine. The intrinsic background or the "self-dose" background of TLD-200 was less than 4 nGy h^{-1}. Assuming a reference dose of 37 nGy h^{-1} over an artificial lake at sea level, TLD-200 gave a relative response of 0.81 to cosmic rays.

Pradhan et al. (1994) describe a simple fast method for measurement of energy and homogeneity of high-energy electron beams using transmitted radiation through lead sheets and two TLDs on both sides of the lead sheet. The authors chose a LiF(TLD-700) on the upstream side and a CaF_2:Dy (TLD-200) for the downstream side. This enables an energy determination better than 0.1 MeV. The homogeneity of the beam energy and the absorbed dose were measured by using a jig with TLDs in the desired order on both sides of a lead plate of suitable thickness.

CaF_2:Tm phosphors. The research of these phosphors started at the Harshaw Company. It resulted in a patent by Lucas et al. (1977) and was given the commercial name TLD-300. Some characteristics of this phosphor were published by Lucas and Capsar (1977). The patented phosphor contained 0.1–0.5 mol% of Tm. Its GC displayed two main TL peaks, at 150 and 250°C. The latter peak showed high sensitivity to neutrons (n) and the 150°C peak was more sensitive to γ-rays, which enabled simultaneous measurements of both n and γ radiation in a mixed field using just one phosphor sample. Rank and Theus (1979) studied the dosimetric characteristics of the TLD-300 phosphor. They used the 14 MeV cyclotron at the NRL. The phosphor showed the main TL peaks at 140 and 250°C and a weaker peak on the low-temperature tail of the 140°C peak. The fading of the 250°C peak was less than 2% in 40 days. The 140°C peak showed comparatively high fading which was due to the weak low 110°C peak. A 15 min anneal at 70°C reduced the fading to a few percent in 40 days. Both TL main peaks show linear dose response, at least up to 16 Gy which was the limit of the measurements. The effect of the holder was also checked. Aluminum and teflon holders affected similarly the 140 and 250°C peaks. Polystyrene increased the response of the TLD by nearly 50% for both the peaks. The energy response of the phosphor has been checked by using 7 and 14 MeV beams. The 250°C peak gave an increase of 40% in the response at 14 MeV when using a teflon holder and an increase of 75% with polystyrene.

Morato and Nambi (1977) have shown that diffusion of hydrogen into CaF_2:Tm increases the sensitivity of its 250°C TL peak to fast neutrons. Hydrogen concentrations of 10^{19} cm^{-3} are needed to make it suitable for fast neutron personnel monitoring.

Lakshmanan et al. (1982a,b) observed that an increase in the X-ray photon energy from 29 to 100 keV gives a decrease by a factor of 4 in the sensitivity of the 250°C TL peak of CaF_2:Tm, while the ratio of the 250 and 150°C TL peaks decreased only by 16%. This superiority of the *double-peak method* was found to be kept over a wide range of photon energies.

The different relative sensitivities to fast neutrons of the various TL peaks of CaF_2:Tm were discussed by Hoffmann and Prediger (1984), and by Apostolova et al. (1985). It has been attributed to the high LET of the neutrons. These authors assumed that the different LET effects for different TL peaks come from a radiation-induced annealing by phonon interaction caused by elastic collisions at high LET radiation. This annealing should affect more the low temperature TL peaks related to the shallower traps.

This explanation did not agree with the experimental results by Pradhan and Rassow (1987) according to which the low-temperature TL peak of CaF_2:Tm at 110°C was less affected by the high LET neutron radiation compared with that of the 250°C peak. In addition, the sum of the TL response of the 150 and 250°C peaks showed that the γ-ray-produced trapped carriers were not affected by the neutron radiation. These results led to the assumption that the traps and the recombination centers together form complex defects. The different LET dependencies of the various TL peaks were then proposed to be due to different dimensions of the related defect complexes. The high LET radiation was assumed to produce a faster saturation of the smaller defect complexes, and hence the differences in the LET effects on the various TL peaks. It seems that to confirm the above assumption a method has to be developed to measure the dimensions of the defect complexes.

Hoffmann (1996) has reviewed the dosimetric behavior of different materials in heavy charged particle and fast neutron fields. These particles exhibit high LET fields which in most TLD materials reduces the TL sensitivity. The heavy particles are used in therapy and the high LET then may lead to incorrect biological effects. CaF_2:Tm (and LiF) behave differently. In one TL peak in these materials the sensitivity does not decrease up to comparatively high LET values. The different behavior of the two TL peaks near 150 and 250°C in CaF_2:Tm allows the separation of the low and high LETs of the radiation field. This enables one to measure the biological equivalent in a single irradiation.

In a recent paper Pradhan (1996) used the two-peak method as a tool for simultaneous estimation of low and high LET radiation in a mixed field and measured the influence of the heating rates on the measurements. Comparison is given between TLD-300, Al_2O_3:C and LiF TLD-700 (similar to TLD-100 but with differences in the ratio of lithium isotopes). The two peaks used for TLD-300 were the 240–260 K peaks together and the 150°C peak. Similarly the ratio of two peaks was used for Al_2O_3:C and TLD-200 phosphors. The ratio of the areas under the pair of peaks for TLD-300 changed by less than 10% with an increase of the heating rate from 1 to 50°C s^{-1} compared to a change of 55% under analogous conditions for TLD-700. In the case of the Al_2O_3:C TLD the change in the area ratios by the same increase in heating rates was a factor of 3.5. It is concluded that the stability with changes in heating rate exhibits the superiority of the CaF_2:Tm over the other two TLDs. This in addition to the established superiorities

of TLD-300 which has well separated peaks, comparable intensities of the pair of peaks and lower supralinearity of the high-temperature peak.

Ben-Shachar and Horowitz (1988) used a computerized deconvolution program in an investigation of the high-temperature peaks of CaF_2:Tm and LiF:Mg,Ti phosphors. They concluded that CaF_2:Tm is superior to LiF:Mg,Ti for γ-dosimetry when using the double-peak method, especially with energy-dependence compensating filters. The use of the ratio of the sum of the 240–260°C TL peaks to the 150°C peak is suggested as a good method for γ-dosimetry. Ben-Shachar (1989) concluded that CaF_2:Tm is not sensitive enough for use as a UV dosimeter. This without sensitization by hydrogen diffusion suggested by Morato and Nambi (1977).

Bacci et al. (1989) explored the behavior of TLD-300 (and TLD-200) in dry and humid air (up to 80% relative humidity) and at temperatures up to 46°C. TLD-300 remained stable up to 900 hours of storing under the above conditions. They found TLD-300 to be a good stable phosphor for environmental monitoring insensitive to the ambient conditions. Bacci et al. (1990) studied the TL peaks of the GC of Harshaw TLD-300 phosphors using a computerized deconvolution program assuming general-order kinetics. The samples were annealed at 400°C before the irradiation, then γ-irradiated (10^{-2} Gy) and heated at $2\,K\,s^{-1}$. The program gave 6 TL peaks at 361, 394, 417, 447, 497 and 528 K. It is somewhat strange that the 361 K peak gave a kinetic order of $b = 1.42$, the four intermediate peaks gave first order ($b = 1$) and the 528 K peak gave $b = 1.22$. The E-values ranged from 0.81 to 1.44 eV for the six peaks, and the s-values were about 10^9 for the 361 K peak, 10^{11}–$10^{14}\,s^{-1}$ for the other peaks. Repeating the measurements for other irradiation doses may enable one to estimate the accuracy of the measured parameters.

Furetta and Tuyn (1985) have checked various pre-treatments for CaF_2:Tm phosphors. They found that 2 hours at 400°C resulted in good stability and high-sensitivity TLD phosphors.

Meissner et al. (1988a, 1988b) used an IR-sensitive silicon photodiode detector, which revealed, in addition to the TL emission of CaF_2:Tm in the visible, TL emission at 800 nm. The IR TL exhibited the same TL peaks as the visible TL but at higher intensities. The increase in the TL intensities in the IR was by factors of 24, 16 and 6 for the 100, 150 and 240°C peaks, respectively. The same investigators (Jacob et al. 1990) have verified that the visible and IR TL peaks are related to the same trapping levels.

The IR TL emission of CaF_2:Tm was also observed by other investigators. Rasheedy et al. (1991) observed an intense emission at 805 nm in addition to bands at 375, 460 and 655 nm. The 805 nm band was much more intense compared to the visible bands. Figure 14a shows a three-dimensional plot of the TL. In this uncorrected figure the 805 nm peak looks only a little stronger compared to the visible bands. The emission spectra obtained for the 145°C peak after the calibration of the system is shown in fig. 14b, where the visible emission is shown on an $\times 10$ ordinate. It is obvious that the 805 nm emission intensity of the 145°C peak exceeds by more than one order of magnitude that of the visible peaks. Bos et al. (1995) investigated the TL of CaF_2:Tm excited by X, γ, α and n radiations. They show the effects of the high LET of the heavy α-particles on the TL. The TL emission spectra show also the intense band at 803 nm.

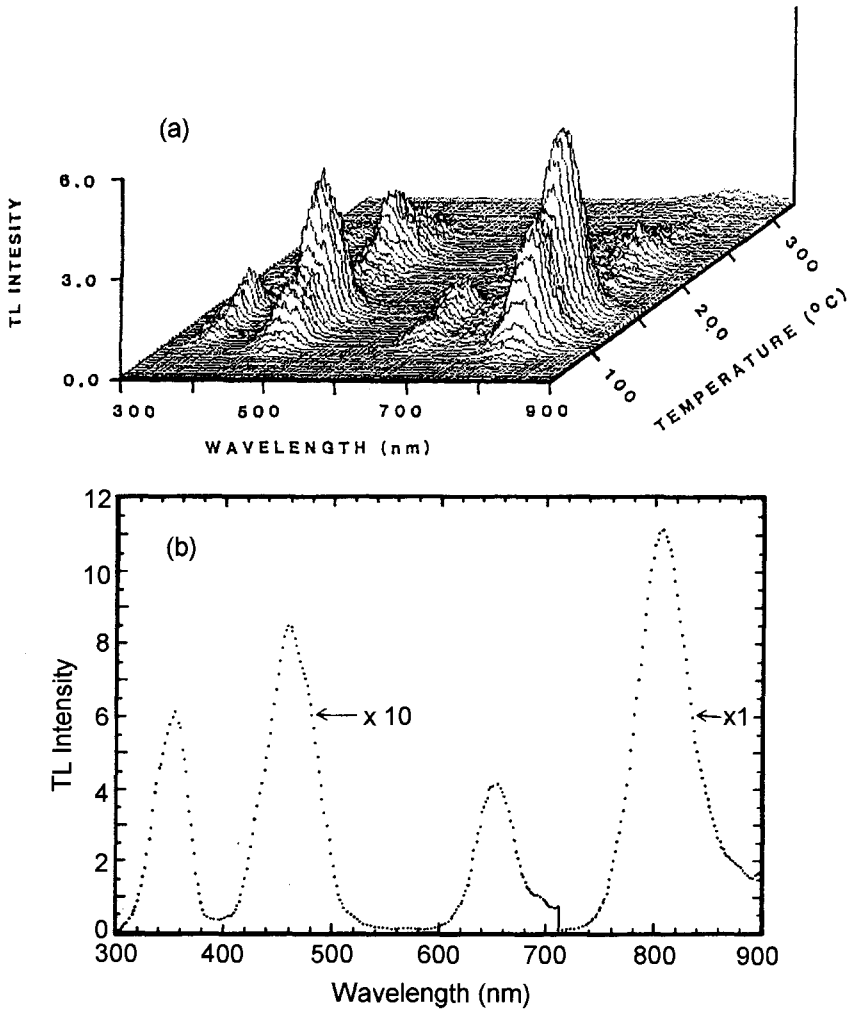

Fig. 14. (a) A three-dimensional plot of the TL of CaF_2:Tm (not corrected for wavelength response). (b) TL emission spectrum of CaF_2:Tm corrected for wavelength response. The 805 nm emission is shown on a reduced ($\times 0.1$) scale.

Bos and Dielhof (1991) have determined the E- and s-values for the TL peaks of single crystals of CaF_2:Tm. They found that increasing the dose of excitation did not show any shift in the TL peak, which indicated that the kinetics is of first order. They have therefore assumed first-order kinetics in the separation of the individual TL peaks by a computer deconvolution program. It gave 6 peaks at about 350, 370, 420, 468, 515 and 530 K (peaks 1–6, respectively). The four most intense peaks (2, 3, 5 and 6) gave E-values of 0.66, 1.15, 1.54 and 1.14 eV and s-values of about 10^{14}, 4×10^{12}, 10^{14} and

3×10^9, respectively. Azorin et al. (1989) used 11 different methods for the determination of the *E*- and *s*- parameters of the 3 main TL peaks at 390, 438 and 523 K (peaks 1, 3 and 5) of CaF_2:Tm ribbon phosphors. The samples were γ-irradiated and heated at a rate of $2°C\,s^{-1}$, except, of course, in the variable heating rate method (sect. 2.1.4). The agreement between the parameters obtained by the various methods was good (a spread of 4% in the *E*-values). The average *E*-values were 0.72, 1.16 and 1.78 eV, and the *s*-values were 2.6×10^8, 4×10^{12} (not including the computer fitting value which was about two orders of magnitude higher) and 6×10^{16} for peaks 1, 3 and 5, respectively. Those obtained by the computer fitting methods deviated considerably from those derived by the other methods. There are also considerable disagreements with the parameters obtained by Bos and Dielhof (1991), Bacci et al. (1990) and others.

The wide spread in the calculated parameters of the TL peaks of TLD-300 reported by different investigators was emphasized by Lin and Weng (1995) and Lin et al. (1996). They have therefore taken more precautions in the measurements. These included post-irradiation annealing at various temperatures in order to bleach away low-temperature peaks. Various sources (protons and γ-rays) were also applied at various energies. The measuring methods included the generalized-peak-shape, the general-order and the Levenberg–Marquardt algorithm adapted to GC analysis (described by Press et al. 1989). For peak 5 of TLD-300 at 550 K ($21.5\,K\,s^{-1}$) they obtained fractional kinetic orders (between 1 and 2). The values were found to vary during the read-out and were affected also by the post-irradiation annealing and by long storage at RT. The trap depth (*E*) was also affected by these treatments. Some effects influencing the TL parameters are suggested to be due to invalidity of the general-order equations and due to increase in retrapping probability by treatments. Such effects may indeed affect the parameters. However to validate the above suggestions it is necessary to make sure that the measured TL is indeed a single TL peak.

Aleshin and Karelin (1991) studied the TL of single crystals of CaF_2:Tm (0.01–4 mol%) and of phosphors co-activated by various R ions (0.01–5 mol%). The TL was excited at RT by β-rays and recorded at a heating rate of $2\,K\,s^{-1}$ passing only a narrow wavelength range fitting the maximum of a TL emission band. This method eliminated the thermal radiation and thus allowed records of the TL up to 550°C. The GC of CaF_2:Tm showed new high-temperature peaks at 390 and 450°C. The doubly doped phosphors showed also high-temperature peaks of the co-activator. The TL spectra showed emission bands in the spectral range 250–800 nm. The authors show that the interstitial fluorine atom (F_i^0) acts as a charge carrier in the TL peaks of CaF_2:Tm up to above 200°C. The 240°C high-sensitivity TL is suggested to be related to double-hole centers $(F_i^0)_2$.

Wang et al. (1989) studied the effects of high-temperature annealing on the TL of TLD-300 response to α, β, γ and X radiations. The results indicated possible identification of the radiation source in the range 0.05-0.3 MeV for β-radiation and in the range 0.006–10 MeV for γ and X. α-radiation could be identified from differences in the GC structure. The authors claim that the energy range which can be discriminated with TLD-300 is much wider than that obtained with TLD-200 (CaF_2:Dy). Hsu et al. (1985) and Hsu and Li (1990) found that pre-irradiation annealing at temperatures up to 800°C affects the

TL sensitivity, the residual TL and the GC distribution of TLD-300. The TL sensitivity did not change up to 400°C and decreased after annealing at higher temperatures. The low-temperature peak shifted towards lower temperatures and the 250°C peak shifted to higher temperatures with the increase in the annealing temperature.

The sensitivity of TLD-300 to UV light was found by Li et al. (1991) to depend strongly on the pre-treatment temperature. Annealing at 1000°C enhanced the TL by a factor of 2000 compared with the untreated phosphor. The optimal stability, however, was obtained by 1 hour annealing at 800–900°C, when the TL enhancement was only by about a factor of 50. Hsu et al. (1993) showed that the enhanced UV sensitivity obtained by annealing at high temperatures can be stabilized by an additional annealing at medium temperatures (about 300°C). The stabilized TLD gave linear response over a wide range of doses and was not sensitive to visible light. Weng et al. (1995) found that the response of TLD-300 to protons is similar to that to α-particles.

Lakshmanan and Tiwari (1993) studied the optical absorption, the TL and the PTTL of RT γ-irradiated CaF_2:Tm. They concluded that TL peaks at 160, 180 and 280°C are due to the release of hole-trapping centers, giving rise to absorption near 310 nm, and their recombination with electrons at Tm^{2+}, resulting in Tm^{3+}-characteristic emission. The dominating peak near 280°C is suggested to be related with an OH-associated trap and recombination with a Tm^{2+} as before. The suggested model is still not quite clear and needs further clarification.

Ludemann et al. (1995) studied the response of TLD-300 to 14.1 MeV neutrons. Simultaneous measurements of the n and photon doses by means of the two main TL peaks showed a systematic deviation with the depth in the phantom. It was found that the deviation can be reduced by the addition of a second n component from scattered neutrons (n_s) about half the energy of the original n. The observed inconsistency was found to be suppressed by using a 1.5 mm thick teflon instead of the A-150 encapsulator.

Bhatt et al. (1995) measured the relative efficiencies of the dosimetric TL peaks of fine grains (1–8 μm) of CaF_2:Tm, CaF_2:Dy, $CaSO_4$:Tm and $CaSO_4$:Dy. The peak temperatures were at 518, 473, 493 and 495 K and the measured relative TL efficiencies were 0.78, 0.41, 0.26 and 0.28 for the four phosphors respectively. The very high efficiency of the 518 K peak of CaF_2:Tm was assumed by the authors to support a speculation suggesting the capture of more than one carrier by the trap during the irradiation.

Meijvogel et al. (1996) used a simple model for the trapping, transfer and recombination to calculate the theoretical intrinsic efficiencies for various phosphors. The upper theoretical limit for the efficiency was 14%. Experimental values were 0.017% for crystalline LiF, 0.031% for LiF (TLD-100), 0.91% for LiF (GR200A), and 0.84% for Al_2O_3:C. CaF_2:Tm gave only 0.29% while CaF_2:Dy (TLD-200) showed the highest efficiency, namely 4.1%. These efficiencies are not necessarily characteristic of the various phosphors and may change with the method of preparation of the phosphors and other factors.

CaF_2:Ce phosphors. Not much has been reported on CaF_2:Ce phosphors, and most of the few published papers deal with co-activated CaF_2:Ce.

Merz and Pershan (1967) present among other R-doped CaF_2 the GC of CaF_2:Ce obtained after excitation at 77 K. The GC up to 400 K shows a strong TL peak at 360 K. Bangert et al. (1982a,b) studied the TL produced by ion implantation in CaF_2 and the TL emission spectra. The TL of the Ce-implanted CaF_2 showed for the shallower traps above RT an emission near 360 nm. Re-excitation of the Ce-implanted sample revealed selective emission affected by thermal pre-treatment and effects of impurities and intrinsic defects on the TL peaks. A combination of ion implantation and thermal anneal cycles led to the conclusion that the TL peak at 90°C is related to a Ce^{3+} ion linked to an interstitial fluorine ion. Perturbation of this center by other defects was found to shift the TL peak to 110°C. The peaks at 180, 220 and 350°C are assumed to involve intrinsic defect clusters.

Jassemnejad and McKeever (1987) studied the optical absorption and the TL emission spectra of RT γ-irradiated CaF_2:Ce. Two major TL peaks appeared at 130 and 350°C (at 2°C s^{-1}). Based on the thermal stability of the various radiation induced absorption bands and on the TL emission spectra, the authors suggested that the 130°C TL peak is due to recombination of electrons released from Ce^{2+} ions at cubic (O_h) sites and perturbed V_k centers, resulting in 290 nm emission. The 350°C peak was assumed to involve re-absorption of part of the 290 nm emission by overlapping absorption bands related to Ce^{3+} ions at C_{4V} sites resulting in $(Ce^{3+})^*$ excited ions. The Ce^{3+} doublet at 320, 340 nm is then emitted on the relaxation of the excited ions.

The TL of CaF_2:Ce,Mn was described in a few papers by McKeever and co-workers. The measurements included PL, XL, optical absorption and TL emission spectra. The TL excitation was generally performed at RT by γ-rays. McKeever et al. (1986) claim that the optical measurements suggest pairing of Mn^{2+} and Ce^{3+} ions in C_{4V} sites, where the Ce^{3+} ion is usually charge compensated by an interstitial fluorine ion (F_i^-). The irradiated samples did not show energy transfer from Ce^{3+} to Mn^{2+} ions. The tetragonal Ce^{3+} sites dominated in the irradiated samples, and the Ce-related absorption bands completely dominate the Mn-related ones as observed by Jassemnejad et al. (1986). A more detailed description of the processes involved in the TL emission of CaF_2:Ce,Mn was given by Jassemnejad et al. (1988). The process in the dominant TL peak above 100°C (at 2°C s^{-1}) involved re-absorption of the ($e^- - V_K$) recombination emission by Ce- and Mn-related defects with the Ce dominating in the competition. The authors stress that their results disagree with those reported by Sunta (1984) who assumed energy transfer from Ce to Mn ions in the irradiated CaF_2:Ce,Mn phosphors.

CaF_2:Eu phosphors. Merz and Pershan (1967) found no enhancement of the CaF_2:Eu TL by the dopant (see fig. 12). Their model for the TL of R-doped CaF_2 included capture of an electron by the three-valent R, $R^{3+} \rightarrow R^{2+}$, during the irradiation, and a process involving $R^{2+} \rightarrow R^{3+}$ during the TL emission. The low interest in the dosimetric properties of CaF_2:Eu seems to lie in its low TL intensity. The few publications on this phosphor try to explain its low TL intensity.

Sangeeta et al. (1990) worked on single crystals of CaF_2:Eu. The GCs of this phosphor after γ-irradiation at RT and heating at a rate of 100 K min^{-1} showed five peaks in the range 50–350°C with the strongest peak at 80°C. The TL emission was characteristic

of Eu^{2+}. From optical absorption spectra and TL emission spectra the authors conclude that there is no conversion of the Eu^{2+} during the whole process of the TL excitation and emission. This of course disagrees with the Merz and Pershan model. The 80°C TL intensity was found to depend strongly on the rate of cooling of the annealed crystal. A maximum was reached at a cooling rate of about $500°C\,h^{-1}$. Sangeeta et al. (1991) concentrated on the OSTL of CaF_2:Eu single crystals. The experimental procedures were similar to those in Sangeeta et al. (1990). The OSTL was obtained by exposure of the sample to room light after partial bleaching of the TL by heating at temperatures up to 250°C, when the TL peaks at lower temperatures were regenerated. The OSTL was not obtained after heating to higher temperatures which bleached away the TL including the peak above 300°C.

Dhopte et al. (1992) prepared Eu-doped CaF_2 by mixing a solution of the compounds, then drying the mixture at 100°C. The resulting powder samples were subjected to annealing at 400, 700, 1000 and 1400°C in the open air. One sample was heated to 700°C under vacuum. Samples were exposed to γ-rays at RT and heated at a rate of $150\,K\,min^{-1}$. All samples showed a prominent TL peak at 600 K. The TL intensities of all the samples were lower by at least a factor of 50 compared with the TL intensity of the $CaSO_4$:Dy phosphor. The TL emission differed for the various heat-treated samples. Open-air treated samples showed transitions $Eu^{3+} \leftrightarrow Eu^{2+}$. The TL emission of these samples was characteristic of Eu^{3+}. It is interesting that no Eu^{3+} was observed in the vacuum-treated sample. The authors stress that besides the $R^{3+} \rightarrow R^{2+}$ transitions F- and V-type centers are also formed. The V-type centers are stabilized by the R ions and stay stable above RT. When heated, the V- and F-centers recombine with a recombination energy of 4.1 eV. If the R^{3+} ions occupy a site with an excited level of about 4.1 eV and at which effective energy transfer takes place, one will obtain an efficient TL activation. This is the case for Dy- and Tm-activated CaF_2, but not for Eu.

The fact that Eu^{3+} was obtained in thermal treatment in the open air but not in vacuum-treated samples suggests that diffusion of oxygen into the sample enables the $Eu^{2+} \rightarrow Eu^{3+}$ transition. This diffusion should be much more effective in powder samples compared to single crystals, which may explain the failure to observe Eu^{3+} by Sangeeta et al. (1990).

In another paper of the same group, Upadeo et al. (1994) used the PL and ESR techniques to study the mechanism of the TL in CaF_2:Eu (and $CaSO_4$:Eu). The sample preparation and experimental arrangements were generally the same as in the first paper. PL spectra showed that in CaF_2:Eu the Eu was exclusively in the three-valent state. No ESR signals were observed in the unirradiated state, which indicated three-valent state of the Eu. The γ-irradiated sample showed an ESR signal with a g-value expected for Eu^{2+}. PL measurements showed no correlation between the $Eu^{3+} \leftrightarrow Eu^{2+}$ conversion and the TL. These and other experiments favored the model by which the TL arises from a transfer of the energy of an electron–hole recombination to a Eu ion resulting in characteristic Eu emission. The authors suggest the same model for the $CaSO_4$:Eu TLD phosphor.

Other CaF_2:R phosphors. De Melo et al. (1997) studied the TL of $CaF_2:La^{3+}$ and of $CaF_2:Al^{3+}$ for dopant concentrations of 0.01–1 mol%, using powder samples

of 0.078–0.149 μm grains. The authors found the Al-doped samples to be more sensitive than the La-doped ones. On the other hand, the TL intensity of the Al-doped samples reached its maximum at an Al concentration of 0.02 mol% while that of the La-doped samples continued to rise up to 0.1 mol%. The authors did not check the TL above 0.1 mol%.

Subramanian and Mukherjee (1986) studied the XL and TL of CaF_2:Nd single crystals X-irradiated and heated at a rate of 45 K min^{-1}. After RT irradiation the major TL peak appeared at about 340°C and a weaker peak was observed at 120°C. Very weak TL could be detected near 200°C. The TL increased with the Nd concentration up to a maximum at 0.049 wt% Nd. X-irradiation at 77 K showed additional TL peaks up to RT. γ-irradiation at RT gave the main TL peaks at 97 and 315°C. Their E- and s-values were 1.15 eV, 2×10^{14} s^{-} and 1.70 eV, 10^{13} s^{-1}, respectively. Subramanian and Mukherjee (1987) measured the 340°C TL peak emission spectra which exhibited bands at about 300, 600 and 830 nm. All the emission bands reached a maximum with a concentration of 0.049 wt% Nd. The intensity of the 830 nm band was higher by an order of magnitude or more compared to the UV and visible emission bands. The authors state that the origin of the 300 nm emission is uncertain but the 600 and 830 nm bands are characteristic of Nd^{3+}. The XL shows the same emission bands as the TL, which indicates a common recombination center.

Holgate et al. (1994) also worked on the TL and XL of CaF_2:Nd (0.01, 0.1 and 1.0 wt%). The XL showed emission bands at 285, 525 and 700 nm, decreasing with increasing Nd concentration. The emission intensity as function of the Nd concentration gave an inverse log–log relationship, which was explained by the authors to be due to the production of nonradiative transitions of the Nd. The TL emission showed a line structure which fitted the Nd energy scheme. The 350°C TL peak emission showed a band at 490 nm. An emission band at 870 nm expected from the Nd energy scheme was indeed detected in the emission spectra. Pre-annealing at 500°C followed by very slow cooling and by rapid cooling showed differences in the emission spectra which was suggested to be due to clustering of Nd ions during the slow cooling. It still remains unclear how the trapping and energy transport operates in CaF_2:Nd phosphors.

Sinha and Mukherjee (1981) studied the kinetics of the TL peak at 530 K (at 40 K min^{-1}) of RT X-irradiated CaF_2:Pr. The intensity of this peak increased with the Pr concentration up to 0.06 wt% and decreased slowly at higher concentrations. The peak shifted to higher temperatures with an increase in temperature of the thermal pre-treatments. Thus, preheating to 505 K shifted the peak to 545 K. The kinetic order of the peak was found to be 1.5 and E and s were 1.68 eV and 10^{14} s^{-1}, respectively. The RT phosphorescence of the irradiated phosphor was also investigated.

Becker et al. (1973) measured the TL of single crystals of CaF_2:Sm (0.01 wt% of SmF_3) X-irradiated at 77 K. The GC (at 25 K min^{-1}) showed at least six peaks in the range 140–350 K. The TL emission showed a line structure characteristic of Sm^{3+} in the range of 550–700 nm, and a broad band at 700–800 nm due to Sm^{2+}. UV excitation gave only two peaks at 275 and 312 K. The 275 K peak emitted a broad band at 650–850 nm and showed no emission in the range 550–650 nm. The excitation efficiency increased sharply

at wavelengths below 400 nm and no TL was excited by light above 500 nm. The authors suggest that the presence of both Sm^{3+} and Sm^{2+} before the irradiation may be responsible for the differences between the X- and UV-excited TL. Kiessling and Scharmann (1975) also worked on single crystals of CaF_2:Sm. They studied the PSTL. In this technique the crystals were first X-irradiated at 77 K and then exposed to UV and heated (25 K min^{-1}) to 600 K. The PSTL GC showed 7 peaks in the range 77–600 K. Annealing the X-irradiated crystal at 600 K followed by UV radiation showed all, but one, glow peaks. The missing glow peak was the one at 380 K. Excitation spectra also differed for the different peaks. The 275 K peak showed efficient excitation at all wavelengths below 420 nm, while the 380 K peak was quite low down to 350 nm and increased sharply below this wavelength. The 275 K peak bleached readily by visible light below 650 nm while the other TL peaks were not affected at all by visible light. The authors conclude that the effects arise from differences in the charge-transfer mechanism which involves deep traps.

Ohtaki et al. (1994) and Fukuda et al. (1996) estimated the sensitivity of CaF_2:Tb as a UV TLD. The phosphors were prepared by mixing CaF_2 with Tb_4O_7 (0.06 wt%), pressing into pellets and sintering the pellets for five hours at 1100 or 1250°C. After exposure to UV (300 nm) or to daylight the GCs (at 20 K min^{-1}) showed two overlapping peaks at 100 and 180°C. The TL intensity of samples sintered at 1100°C had a maximum at 235 nm of UV excitation, and the excitation spectrum of the samples sintered at 1250°C showed a maximum at 260 nm. The TL sensitivity in both cases dropped to practically zero at 320 nm. The TL increased with the third power of the dose. The authors attribute this fast increase with the dose to a triple-stage excitation.

Schlesinger and Whippey (1969) studied the TL of CaF_2:Ho single crystals grown from the melt of CaF_2 and HoF_2 (0.05%) by Harshaw. Crystals were X-irradiated at 77 K and heated at a rate of 11 K min^{-1}. The GCs (up to 350 K) showed peaks at 155, 206, 256 and 333 K. The E-values of the four peaks ranged between 0.30 and 0.95 eV. The TL emission spectra were characteristic of Ho^{3+} in sites of different symmetries. The relative intensities of the spectral lines differed from one peak to another, especially near RT. This was attributed by the authors to charge compensators near the Ho ions which become mobile near RT.

The near-IR TL of CaF_2 single crystals doped with Tm, Gd, Nd, Er and Eu was studied by Jacob et al. (1993). As the sensitivity of most PMs is low in the IR a photodiode detector has been used for the measurements. The R concentrations were about 1 wt% of the R oxide. γ-rays (^{60}Co) were used for the TL excitation. The heating rate was 3.4°C s^{-1}. The R-doped crystals, except for the Eu-doped ones, showed IR-TL. The main high-temperature IR dosimetric peaks appeared at 270, 150 and 200°C and their intensities were higher compared to the visible TL peak by factors of 5, 160 and 8.3 for the Tm, Nd and Er oxide dopings, respectively. CaF_2:Gd showed only a low-temperate (105°C) peak 2.1 times stronger than the visible peak.

A review of the progress in the understanding and applications of the TL of R-doped (and Mn-doped) CaF_2 phosphors was given by Jain (1990). It also discusses effects of the radiation doses and of the LET on the GCs. Optical absorption ESR and TL emission spectra which lead to the identification of traps and luminescence centers are also given.

3.2.3. *$CaSO_4$:Dy*

The vast amount of material published on $CaSO_4$:Dy and $CaSO_4$:Tm justifies separate subsections for each of these phosphors.

$CaSO_4$:Dy was introduced by Yamashita et al. (1968, 1971) who extracted the phosphor by evaporation from sulfuric acid containing a mixture of $CaSO_4 \cdot 2H_2O$ and Dy_2O_3 (0.1 mol%). The resulting $CaSO_4$:Dy crystals were dried at 600–700°C and ground to a fine-grain powder. The phosphor was found to be of high sensitivity and practically free from fading. The commercial $CaSO_4$:Dy (TLD-900) was produced by Harshaw.

General features of the GCs and the TL peaks of $CaSO_4$:Dy. McDougall and Axt (1973) measured the dosimetric features of $CaSO_4$:Dy powders using the main TL peak at 220°C. The photon energy response was found to be constant down to about 1 MeV. The high energy dependence at lower energies was attributed to the high Z of $CaSO_4$ compared to that of air. The dose dependence was linear up to 15 Gy and the fading was about 1–2% per month. A preliminary study of the dosimetric properties of Harshaw TLD-900 was done by Bacci et al. (1980). Their GCs contained two main peaks at 140 and 212°C. To reduce the effect of the fast fading of the 140°C peak, the sample ribbons were annealed for 5 min at 100°C after the X-irradiation at RT. This was not enough to eliminate most of the 140°C peak, and the fading was reduced to 10% per month. A few minutes annealing at 140°C would have resulted in a much lower fading rate. 10 min at 400°C between measurements was found suitable for the elimination of the effects of previous exposures. The phosphor showed linear response up to above 0.1 Gy and photon-energy independence down to about 1 MeV.

Becker (1972) studied $CaSO_4$:Dy and $CaSO_4$:Tm powders. For γ-irradiation $CaSO_4$:Dy had advantages over $CaSO_4$:Tm. It exceeded the sensitivity of TLD-100 by a factor of 30–40 and showed low fading (1.5% in 6 weeks). $CaSO_4$:Tm showed higher sensitivity to thermal neutrons and is suggested for use in mixed radiation fields.

Nambi et al. (1974) studied the TL, TL spectra and ESR spectra of RT γ-irradiated $CaSO_4$:R, for all the anthanides. They noticed that the main TL peaks appeared at about the same temperatures for almost all R ions. Dy- and Tm-doped samples were found the most efficient phosphors. The γ-irradiation was found to produce various radicals like SO_4^-, SO_3^-, O_3^-, etc. The TL emission spectra were characteristic of the R^{3+} ions. Step bleaching recording the partial GC after each step discerned 11 TL peaks in the range 85–510°C as shown in fig. 15. The trap depths E of the various TL peaks were found to be proportional to the peak temperatures T_m (fig. 16). This indicates one s-value common to all the peaks and suggests also the same order of kinetics for the various TL peaks. The most likely model for the TL suggested by the authors involves trapping of electrons by the R^{3+} ions and of holes by the sulfate radicals during the γ-irradiation, and recombination of the thermally released holes with the electrons at the R ions during the TL emission.

Souza et al. (1993a) observed that the peak temperatures of all the TL peaks in $CaSO_4$:Dy do not shift with the radiation dose at least in the range 0.1–3 Gy. They concluded from this that the TL kinetics (10 peaks in the range 128–400°C) is of

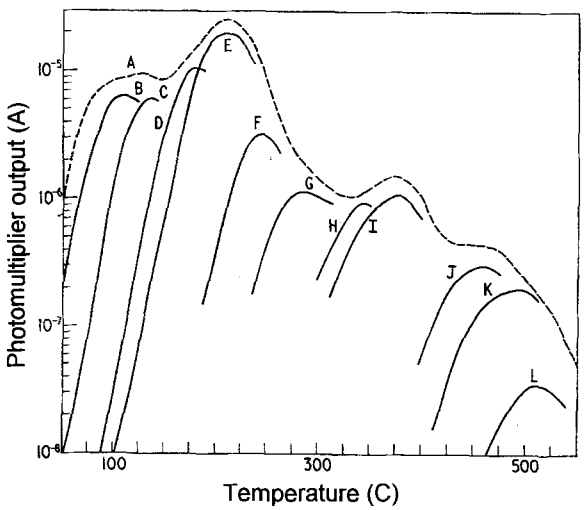

Fig. 15. The GC of $CaSO_4$:Dy (curve A) and its step resolution showing individual peaks (B through L).

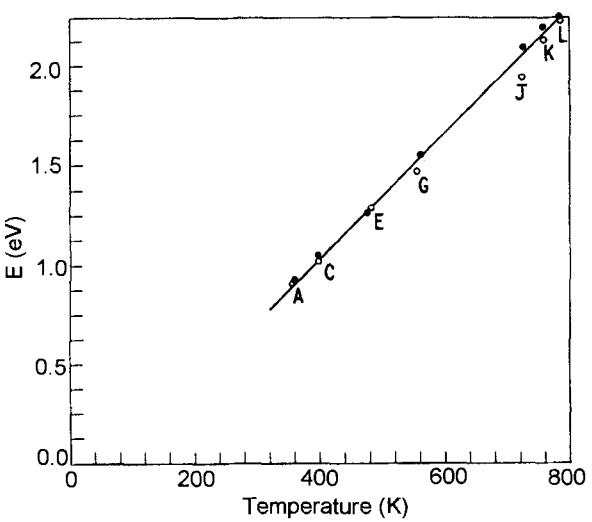

Fig. 16. Activation energies (E) as a function of peak temperature for $CaSO_4$ doped with Dy (open circles) and Tm (solid circles).

first order. The GCs obtained by Souza et al. (1993b) and by Nambi et al. (1974) showed 10 or more overlapping peaks. To make a good phosphor it is desirable to have one dominating TL peak having good dosimetric properties. The relative intensities of the various peaks in the GC depend on the purity of the chemicals used, on the preparation methods, on heat pre-treatments, on activator (and co-activator) concentrations, on grain sizes and on the binders used for the phosphor powders. Kasa (1990) has studied the effects of the quality of the starting materials, activator concentrations and grain sizes on the GCs of $CaSO_4$:Dy (and $CaSO_4$:Tm).

Dependence of the TL on grain size. Using high-purity chemicals, 0.18% (w/w) Dy and grain sizes of 63–200 μm, Kasa (1990) obtained, after γ-irradiation at RT, a strong TL peak near 220°C with only very weak shoulders on both sides. The intensity of the main peak increased from 0.85 for grain sizes of 1000 μm to 1 for 200 μm grains, and then decreased, with further reduction in the grain size, to 0.54 for 0–30 μm grains. Similar dependence of the TL on grain size of $CaSO_4$:Dy were reported by Prokic (1991), Pradhan et al. (1979) and Felszerfalvi et al. (1979). Chandra et al. (1976) have also observed a decrease of the TL of γ-irradiated $CaSO_4$:Dy when decreasing the phosphor grain size. For UV irradiation however, the TL response increased by a factor of 3 when decreasing the grain size from 108–210 μm to 0–37 μm.

Lakshmanan et al. (1988) observed that the TL of $CaSO_4$:Dy for γ-irradiation increased by a factor of 2 upon increasing the grain size from 0–37 μm to 250–420 μm. Grinding reduced the grain size but not the TL. This has been explained by the authors to result from an increase in the Dy concentration with the grain size, which was also confirmed by neutron activation analysis. In light of the Burlin cavity theory given below one has to assume that the Dy-concentration effect proposed by Lakshmanan is taking place in addition to the cavity effect. Lakshmanan et al. (1988) have also observed that the TL sensitivity for UV increases with a decrease in the grain sizes, which may result from the UV TL resulting mainly from near surface states.

Shastry and Kher (1979) used $CaSO_4$:Dy powders of a constant grain size (65–74 μm). They examined the TL for grains sieved after various grinding times. For γ-irradiated samples the TL increased with the grinding time up to about 90 min and remained unchanged for longer grinding times. With UV-irradiated samples the TL again increased with grinding time, this time only up to 40 min and decreased steeply for longer grinding times. The authors concluded that the grinding creates new bulk traps and degrades surface traps, forming an inactive surface layer on the grains. The difference in behavior of the UV-irradiated samples compared to the γ-irradiated ones seems to have resulted from the comparatively higher effect of the surface traps on the UV-excited TL compared to the γ-excited TL.

The TL dependence on grain sizes was also studied theoretically. Burlin (1966) and Burlin and Chan (1966) have developed the *Cavity theory.* By this theory a powder phosphor is looked at as particles in a medium of air. A missing grain forms a cavity in the medium. The TL due to the phosphor grain will then be given by the balance between the energy absorbed by the phosphor grain and that absorbed by the cavity (air in our case, can also be a binding medium). As a specific example the authors calculated the TL response as a function of the cavity size for $FeSO_4$.

Zanelli (1968) observed that the TL of X- or γ-irradiated LiF depended on the grain sizes and to some extent also on the photon energy of the irradiation. The two main TL peaks were examined. The 120°C peak increased with the particle size. The dependence of the intensity ratio $I_{210°C}/I_{120°C}$ on particle size is shown in fig. 17, presented as a function of grain size for 22.9 keV and 1230 keV photons. Zanelli has attributed these effects to inactive surface layers of the grains. These effects were analyzed theoretically by Burlin et al. (1969). With photon energies above 0.18 MeV the dominating effect is due to

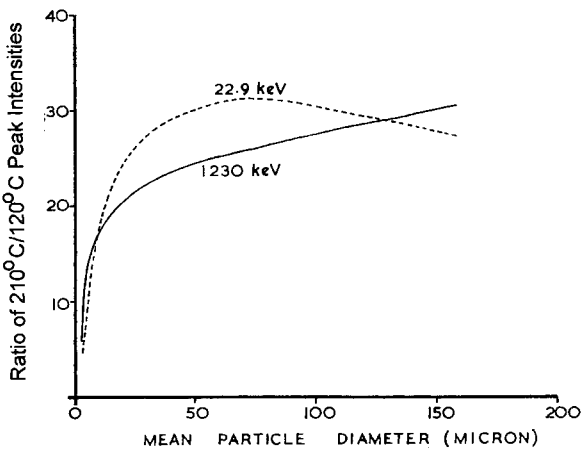

Fig. 17. The ratio of 210°C/120°C TL peak intensities of LiF as a function of mean particle diameter, for 22.9 and 1230 keV photons.

Compton absorption which is independent of Z. The energy entering and leaving a given grain will then be independent on the material in the cavity, and hence independent on the grain sizes. At 0.03 MeV, the photoelectric absorption takes over. It is sharply dependent on Z and the different effective Z of LiF compared to air will result in an energy loss, which will be comparatively higher the smaller the particles are, resulting in a lowering of the TL. At photon energies as low as 0.01 MeV the range of the photoelectrons is small, which results in lower dependence of the TL on grain size. In addition to the above effects which give the photon energy dependence of the TL, there exists the regular Cavity effect (Burlin 1966), which in the case of LiF is expected to give a decrease in the TL which increases with the grain sizes.

Some modification in the Burlin Cavity theory was offered by Horowitz and Dubi (1982) and Horowitz et al. (1983). Kearsley (1984) has compared the theoretical grain size effects obtained by the Burlin Cavity effect and those obtained by the modified Horowitz et al. model (1983) to experimental results obtained by Ogunleye et al. (1980) for TLD-100. He found that the modified model does not give any improvement compared to the original Burlin model. Azorin and Gutierrez (1988) applied the Cavity theory to $CaSO_4$:Dy bound in KBr for particle sizes in the range 50–300 μm. The authors concluded that the modified Cavity theory fitted the experimental data better.

Dependence of phosphor characteristics on thickness. The photon energy dependence of the TL response to β and γ-irradiated phosphors rises with the thickness of the phosphor pellets. $CaSO_4$:Dy teflon discs 0.8 mm thick were commonly used. These are good for high energies, for example ^{60}Co γ-rays. At low energies these discs suffer from high energy dependence. Nagpal et al. (1992) produced 0.4 mm thick detectors as tapes which fit for large-scale manufacturing. A personal monitoring TLD based on the above tapes is described by Nagpal et al. (1994). It includes energy-dependence compensating filters, and a dose-computation algorithm developed to give body and skin doses. Campos and Lima (1987) used teflon pellets 0.2 mm thick which fitted well

for β-ray detection. da Rosa et al. (1986) produced ultrathin, 20 μm thick, pellets of $CaSO_4$:Dy and found them useful for low-energy β and γ dosimetry. Pradhan and Bhatt (1977) pointed out that the use of graphite or other strongly absorbing additives can serve as effectively thin pellets because only TL light from a thin surface layer can then reach the light detector. The addition of graphite was also found to give sharper GCs and to reduce the background TL signals. $CaSO_4$:Dy teflon discs including 10% graphite showed little energy dependence down to 0.4 MeV. A set of filters enabled energy-independent measurements down to 0.18 MeV. This TLD is claimed to be attractive for β and mixed-field β and γ measurements. Pradhan and Bhatt (1979a,b) reported on a significant reduction in the photon energy dependence by using small phosphor grains, below 1 μm, for the pellets. A combined filter of 0.50 mm Sn + 0.35 mm stainless steel reduced the range of energy independence down to 0.08 MeV (with the stainless steel on the side closer to the pellet). Adding another filter (1.6 mm plastic + 0.8 mm Al) gave an energy independence down to 0.027 MeV.

Liu et al. (1986) used teflon discs containing 20% graphite which further reduced the low energy limit. Without filters it was energy independent over the range 0.225–2.274 MeV. It is claimed to show high-sensitivity, low-background TL, good durability and long-term stability. The low energy detection limit was 0.1 mGy.

A metal filter combination for a $CaSO_4$:Dy TLD which enables energy independent measurements down to 0.029 MeV is also described by Lakshmanan and Bhatt (1982) and Lakshmanan et al. (1989a). The TLD was constructed to fit the recommended ISO/SEC standards. The same authors (Lakshmanan et al. 1990a) describe a $CaSO_4$:Dy TLD designed for personal and environmental monitoring, giving an estimate of the ambient dose equivalent H(10). It makes use of a combination of metal filters and perspex.

Recently Prokic (1996) developed a system of detection for environmental monitoring. The system consists of three sintered $CaSO_4$:Dy pellets and one MgB_4O_7:Dy,Na detector. Two Ca sulfate detectors are filtered by 2 and 1.5 mm Cu respectively and the third is only covered by plastic. The low-Z ($Z = 8.55$) Mg borate detector is covered by only a plastic filter. The Mg borate detector showed one TL peak near 190°C. It was prepared from very pure materials and a special preparation method. Its TL sensitivity exceeded that of TLD-100 by a factor of 6–15. The low-dose limits were 2 and 3 μGy for the Ca sulfate and Mg borate detectors respectively. The detector with the 2 mm Cu filter was used for the determination of the ambient dose equivalent $H^*(10)$ and that with the 1.5 mm Cu served for the determination of $H'(0.07)$ for photons. The ratio of the readings of the unfiltered and the 2 mm Cu filtered detectors provided information of the spectral distribution of the radiation. Wernli (1990) developed a TLD system very similar to the above, to measure the ICRU dose quantities H(10) and H(0.07) in evironmental dosimetry.

da Silva et al. (1995) constructed a system containing four $CaSO_4$:Dy phosphors with different filters. The system was calibrated for use in γ and X fields in the range 0.017–1.25 Mev. It enabled dose equivalent evaluation of H(10) for incidence angles of 0–60° with an accuracy better than 30%.

The TL response is lowered in teflon-embedded discs, often by more than an order of magnitude. Lakshmanan and Jose (1993) observed that much of this effect can be

removed by passing a nitrogen flow. The fast fading due to the low-temperature TL peak can be eliminated by post-irradiation annealing at a temperature close to and below the dosimetric peak. The authors have also compared the relative sensitivities of $CaSO_4$:Tm and $CaSO_4$:Dy produced in Hungary to that of $CaSO_4$:Dy produced in India. The relative sensitivities were 1.5, 1.26 and 1.00 respectively. Beregic et al. (1993) describe the characteristics of a $CaSO_4$:Dy teflon phosphor developed in Romania. Azorin and Furetta (1989) found, for Mexican $CaSO_4$:Dy teflon phosphors, pre-annealing for 30–60 min at 300°C to give optimal performance. Niewiadomski et al. (1996) and Niewiadomski (1996) reviewed the work on TL dosimetry carried out in the Institute of Nuclear Physics in Krakow, Poland. The only phosphor relevant to the present article is $CaSO_4$:Dy, which was described in detail by Niewiadomski and Ryba (1983). The detector consists of 30 mg of $CaSO_4$:Dy spread as a thin layer on an Al base. Besides its high sensitivity and low background it gives the highest α and γ response ratio. It was used for simultaneous radon and radon-daughter measurements. The system consists of two parts. The passive radon part is a diffusion chamber with electrostatic collection of ^{218}Po ions. The active part measures the concentration of potential α energy. Such measurements are important in mines where radon-daughter concentrations are often high.

Sintered TL phosphor pellets. Teflon-based dosimeters soften and change their optical properties when heated. Besides, they melt at about 320°C which prevents annealing at 350–400°C desired for their operation. These difficulties can be overcome by sintering at high temperatures. The advantage of sintered pellets in the case of LiF TLDs was already recognized in 1968 when Shambon and Condon (1968) prepared sintered phosphor pellets of LiF powder with a drop of a sodium silicate solution. Cold pressing squeezed out most of the sodium silicate solution. The annealed pellet showed good linearity, good reproducibility and reliable TL response. Improved phosphors obtained by sintering are described in sect. 3.2.1 for Mg_2SO_4:Tb and other TLDs.

Prokic (1978) prepared sintered $CaSO_4$:Dy and $CaSO_4$:Tm pellets in a way similar to that described by Shambon and Condon. The pressed pellets were sintered for 1 hour at 750°C. The phosphors showed excellent precision and stability. Shastry et al. (1980) prepared $CaSO_4$:Dy following the method of Yamashita et al. (1968). They used 0–37 μm Dy grains. The binder was magnesium borate and SiO_2 powder moistened by a little water. The mixture was pressed (2 tons cm^{-2}) and sintered at 750°C. The GCs showed one dominating TL peak at about 220°C, which shifted to higher temperatures with the thickness of the pellets. The optimal sensitivity was obtained with pellets of 345 mg cm^{-2}. The optical absorption and the scattering of the sintered pellets resulted in an effective thickness (from which the TL light could reach the detector) of about 28 mg cm^{-2}, which did not change much over a wide range of real thicknesses. The TL compared with the phosphor powder was enhanced by a factor of 2.8 for β-rays and about 2.0 for γ-rays, both for 345 mg cm^{-2} pellets. For β-rays there was also a considerable reduction in energy dependence down to about 0.25 MeV.

Campos (1993) reported on 0.2 mm thick $CaSO_4$:Dy teflon pellets mixed with up to 10% graphite. The author calls them *sintered* phosphors. The sintering temperature is not given in the paper. Campos described these phosphors as attractive for β and mixed β–γ

dose measurements. They do not differ considerably from other thin or effectively thin $CaSO_4$:Dy teflon–graphite pellets described above.

Furetta and Tuyn (1986) studied the TL response of various sintered $CaSO_4$:Dy pellets including Harshaw TLD-900. Annealing at 400°C gave a low threshold dose of 1 μGy, and a pre-readout annealing at 100°C for 10 min eliminated the fast fading due to the low-temperature TL.

Drazic and Trontelj (1983, 1984) sintered a powder mixture of $CaSO_4$ and Dy_2O_3 with an inorganic binder at 900°C. The sintered phosphor showed a TL peak at 300°C in addition to the 150 and 200°C peaks. 25 hours of sintering at 900°C enhanced the 300°C peak, especially when using small phosphor grains of 10 μm. These sintered pellets exhibited high mechanical strength and were found to be suitable for high-temperature dosimetry. Drazic and Trontelj (1986) measured the characteristic parameters of the 300°C peak. They obtained $E = 1.61$ eV, $s = 5 \times 10^{13}$ s^{-1} and a kinetic order of 2 ($b = 2.0$). The authors suggest that this TL peak is related to centers at the grain boundaries. The obtained second-order kinetics of the peak contradicts a conclusion by Souza et al. (1993a) which suggests that all the TL peaks of $CaSO_4$:Dy are of first order (see above).

TL sensitization. This term is used only for the increase in the TL sensitivity of finished and ready-to-use phosphors. The sensitization is defined as S/S_0, where S is the TL intensity after the sensitization and S_0 is that of the virgin TL phosphor. The sensitization can be achieved by high-dose pre-irradiation followed by annealing at a suitable temperature or by special heat treatment. In the first case the high-dose exposure fills up competing deep traps, thus increasing the efficiency for trapping at the levels related to the dosimetric TL peak. Thermal pre-treatment can change the trapping structure or the concentration of traps, in a way which enhances the dosimetric TL. A more detailed discussion of the TL sensitization was given by Horowitz (1984b).

Lakshmanan et al. (1978b) observed that a high γ-exposure followed by annealing at temperatures below 600°C induced TL sensitization in $CaSO_4$:Dy by a factor of 2.3. The sensitization vanished by annealing above 600°C which empties the deep traps and thus restores the competition. The sensitization was retained up to γ pre-exposures of 2.7×10^3 Gy and decreased for higher exposures. Lakshmanan and Bhatt (1979) give additional arguments to support the competing model for the sensitization of $CaSO_4$:Dy phosphors. The increased supralinearity accompanying the sensitization was attributed to the increased trapping efficiency. Chandra et al. (1981) found a close relation between the sensitization and the residual 400°C TL intensity. The shape of the dosimetric TL in the range 200–300°C was also strongly dependent on the residual 400°C TL peak.

Pradhan and Bhatt (1982) used TLD discs of $CaSO_4$:Dy with 75% teflon. Grain sizes were below 74 μm and disc thicknesses 0.2 and 0.8 mm. Phosphors were sensitized by prolonged γ pre-irradiation followed by 1 hour annealing at 350°C. The treatment has increased the TL response by a factor of 2.3 at 1.25 MeV and came down to 1.4 for 8 keV X rays. The reduction in the TL enhancement at low photon energies was attributed to the high LET effects at these photon energies.

TL peaks, their structure and parameters. Nambi et al. (1974) observed that the trap depths (E) of the various TL peaks of $CaSO_4$:Dy are proportional to the peak temperatures

(fig. 15, above). For the dosimetric peak at 210°C they obtained $E = 1.28$ eV. Souza et al. (1993a) concluded (see above) that all the TL peaks are of first-order kinetics. Yeh (1986) found for the dosimetric TL peak of $CaSO_4$:Dy (self-made) a shape symmetry factor $\mu_g = 0.52$, which fits second-order kinetics, and $E = 0.87$ eV from shape analysis. The variable-heating-rate method gave, for the same peak, $E = 1.19$ eV.

It should be noted that all the shape symmetry factors were calculated by Yeh (1986) from an uncleaned TL peak showing shoulders on both sides (Yeh's fig. 1). The μ_g-value as well as the E-values calculated from the peak shape are therefore wrong. A clean TL peak would have given higher E-values, probably around 1.20 eV.

Furetta and Gennai (1981) obtained for the dosimetric peak 0.8 eV from the initial rise and 0.94 eV from the *variable heating rate* method.

Azorin and Gutierrez (1986) used three different methods for the determination of E. They obtained second-order kinetics and $E = 0.88 \pm 0.02$ eV by all the methods used, and s-values of the order of $10^{10}\,s^{-1}$. It should be noted that the clean dosimetric TL peak given in fig. 1 of the paper by Azorin and Gutierrez (1986) does not look as a pure single TL peak. This may explain the wide spread in measured E, s and b values.

A few investigators have shown that the TL of $CaSO_4$:Dy is composed of a distribution of traps. Srivastava and Supe (1979) worked on crystalline powders of $CaSO_4$:Dy (0.05 mol%) of 100–200 mesh grains. The γ-irradiated samples exhibited a dominating TL peak above 200°C (at $6.2°C\,s^{-1}$) with a symmetry factor $\mu_g = 0.52$ fitting second-order kinetics. Between 1 and 5×10^2 Gy the GCs showed a structure spreading towards higher temperature (about 220°C). At 5×10^3 Gy, μ_g decreased to 0.42 which fits first-order kinetics. μ_g dropped down to 0.38 in the range 10^4–10^6 Gy. Srivastava and Supe (1980) extended the measurements to include various irradiation sources differing in their stopping powers (LETs). For low-LET sources (^{60}Co γ-rays) the GCs showed considerable shoulders on the high-temperature side of the main TL peak spreading above 220°C for dose ranges of 1–100 Gy. The structure decreased with the increase of the LET of the sources. For the high-LET α particles (from ^{241}Am) the GC exhibited practically a single TL peak at 220°C. This peak remained unshifted over the whole range of 0.1–100 Gy as shown in fig. 18. The build-up of shoulders and the accompanying variations in the halfwidth of the peak and in the supralinearity of the dose response were inversely related to the LET of the source. The authors propose a quasi-continuous distribution of traps to explain the spread in the GC. The model is based on the fact that the density of electron–hole pairs under irradiation increases with the LET when deeper traps start to saturate. This reduces the competition for charge carriers and thus enhances the filling of the shallower traps. Eventually the filling of traps becomes limited to the range of the 222°C TL peak. In a later publication Srivastava and Supe (1983) show by the fractional glow technique that the GC of $CaSO_4$:Dy indeed gives a distribution of trap depths ranging from 1.15 to 2.39 eV over the temperature range 340–740 K. A TL emission band at 1.40 eV was found to be linked with the dosimetric 222°C peak. Srivastava and Supe (1984, 1986) show that high-LET radiation, e.g. α particles, involves an anomalous fading of the TL at high doses. The work by Srivastava and Supe seems to explain the

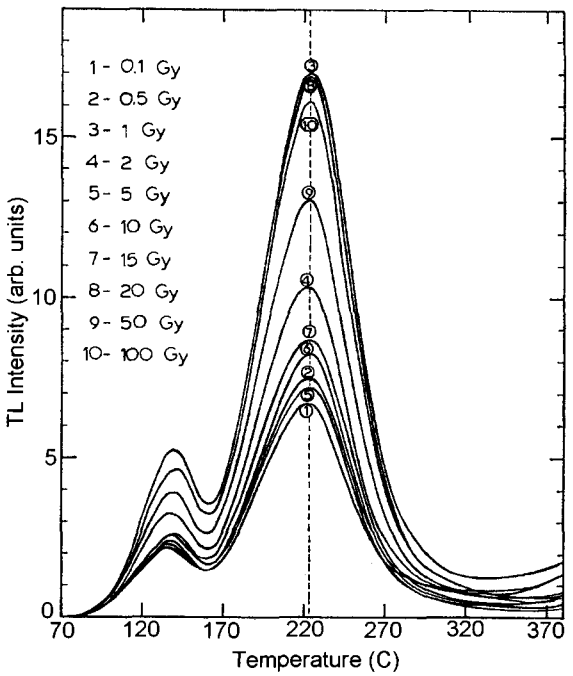

Fig. 18. GCs of $CaSO_4$:Dy obtained after high LET α irradiation at doses in the range 0.1–100 Gy.

disagreement in the parameters obtained by various authors for the TL parameters of $CaSO_4$:Dy, and shows how much care has to be taken in measuring these parameters.

Lewandowski et al. (1996) found a clear temperature correlation between the 360 nm lattice defect emission of Dy- and Tm-doped $CaSO_4$ and Dy^{3+} (Tm^{3+}) emissions. They concluded from this that the same traps are involved in the Dy- and Tm-doped samples, and the different R dopants do not affect the nature of the traps. Only the luminescence efficiencies are changed. The excitation bands for the Dy^{3+} and Tm^{3+} samples increased markedly over the temperature range of the observed TL, possibly due to an increase in the R^{3+} concentration resulting from the conversion $R^{2+} \rightarrow R^{3+}$ during the TL emission.

Lewandowski and Mathur (1996) explored the dose effect of ^{60}Co γ-rays in the range 1–100 kGy for the GCs of $CaSO_4$:Dy (0.1 mol%). The spread towards higher temperatures of the GC on the high-temperature side of the 222°C TL peak observed by these authors was higher than that obtained by Srivastava and Supe described above. This may have resulted from differences in the preparation, impurities and thermal treatments. If true, it may suggest methods which will give GCs closer to real single TL peaks.

Fiorella et al. (1976, 1978) used post-irradiation isothermal annealing at gradually rising temperatures. From the changes of the peak, its gradual shift to higher temperatures and its agreement with a theoretically constructed glow peak assuming $s = 3 \times 10^{12}\ s^{-1}$ they concluded that the TL peaks of $CaSO_4$:Dy are indeed composed of a continuous distribution of trap depths.

Bacci et al. (1988) studied the fading of various TLDs including TLD-900 and $CaSO_4$/LiF:Dy. The phosphors were stored at 20°C and 40°C. They have not used pre-readout annealing. All the examined phosphors showed high fading due to the low-temperature TL. A point of interest in these results is that the low-temperature TL of $CaSO_4$:Dy TLDs was found to be composed of three overlapping TL peaks. The TL peaks near 200°C showed very low fading. Guelev et al. (1994) have shown that 10 min pre-readout annealing at 120°C of $CaSO_4$:Dy results in only 5% fading in 6 months.

TL mechanisms and emission spectra. Nambi et al. (1974) and Nambi and Bapat (1980) proposed that the R^{3+} ions in a phosphor trap electrons during excitation, $R^{3+} + e^- \rightarrow R^{2+}$. Simultaneously, sulfate radicals trap holes. The trapped holes are released during the warm-up when the TL is emitted during the recombination with electrons at the R^{2+} ions, or $R^{2+} + h^+ \rightarrow R^{3+} + h\nu$. Las et al. (1980) propose that the charge transfer occurs between the R ions and V-type centers, V^0, V^{1-} and V^{2-}, where V^0 is a cation vacancy which captured two holes and serves as the hole trap related with the dosimetric TL peak. In $CaSO_4$:Dy the main emission bands appear at 478 and 571 mm, and are characteristic of Dy^{3+} transitions. Pradhan (1993) has also reported on TL emission in the regions 440–480 and 500–580 nm for $CaSO_4$:Dy. Different mechanisms for TL of $CaSO_4$:Dy (and other $CaSO_4$:R phosphors) were proposed by Mathews and Stoebe (1982) who studied the optical absorption (OA), ESR and TL spectra of $CaSO_4$:Dy. Again the same emission bands at 478 and 570 mm characteristic of Dy^{3+} have been observed. Supported by the OA and ESR results they offered the following two possible mechanisms:

(1) The first mechanism assumes for the dosimetric TL peak of $CaSO_4$:Dy a process similar to that offered by Huzimura (1979) and Huzimura et al. (1980). In this model the irradiation reduces the Dy^{3+} to Dy^{2+} which follows from the OA measurements. During the heating the electron is released from the Dy^{2+} and recombines with SO_4^- thus forming an excited $(SO_4^{2-})^*$. The excitation is then transferred to the Dy^{3+} which relaxes with the emission of $h\upsilon$, $(Dy^{3+})^* \rightarrow Dy^{3+} + h\nu$. Another possibility is the dissociation of the $(SO_4^{2-})^*$ into $SO_3^- + O_i^-$, where O_i^- is an interstitial oxygen ion. During this dissociation the energy is transferred to the Dy^{3+} forming $(Dy^{3+})^*$. The TL is then emitted during the de-excitation as above.

(2) The second offered mechanism is given schematically by

$$\begin{array}{c} Dy^{3+} \\ | \\ SO_3^- + O_i^- \end{array} \xrightarrow{\text{irrad}} \begin{array}{c} Dy^{3+} \\ | \\ (SO_4^{2-})^* \end{array} \longrightarrow \begin{array}{c} (Dy^{3+})^* \\ | \\ SO_4^{2-} \end{array} \xrightarrow{\text{warming}} \begin{array}{c} Dy^{3+} + h\nu \\ | \\ SO_4^{2-} \end{array} . \qquad (13)$$

This mechanism will take place when an interstitial O_i^- is present as a charge compensator at the Dy^{3+}.

Barkyoumb et al. (1997) studied the low-temperature TL of $CaSO_4$:Dy. The TL emission spectra taken after irradiation at 20 K showed the main bands at 490 and 580 nm related to the Dy transitions from the $^4F_{9/2}$ level to $^6H_{15/2}$ and $^6H_{13/2}$ respectively. The spectra taken at 200 K also showed the above main bands but with a structure of weak

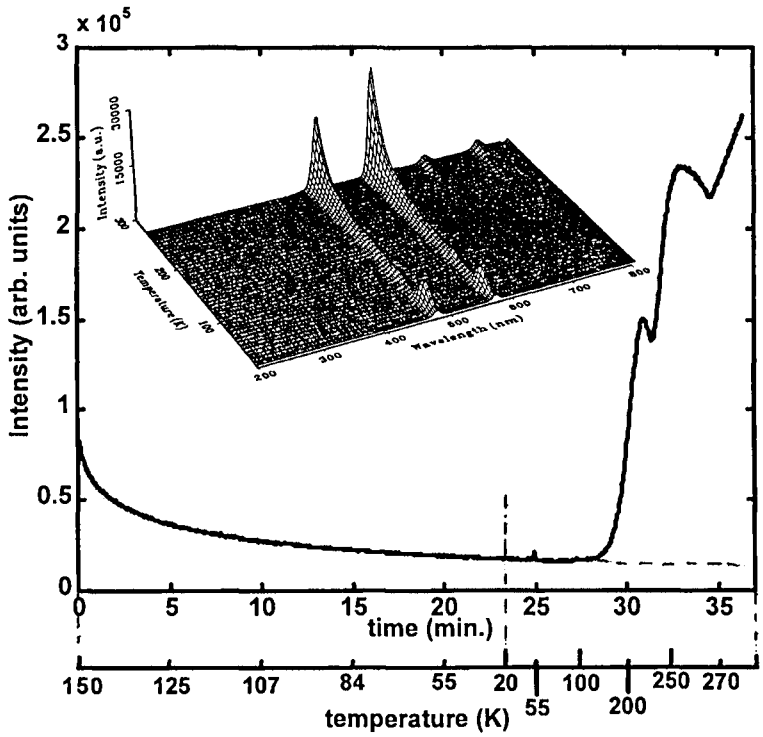

Fig. 19. The TL intensity of $CaSO_4$:Dy after X-ray irradiation at 150 K, cooling to 20 K and then heating to RT (above 23 min on the time scale). The inset gives the low-temperature TL spectrum after irradiation at 20 K.

bands near the main bands. Figure 19 shows results of another experiment. The three-dimensional plot (the inset) gives the low-temperature TL spectrum after 20 K irradiation. It shows a constant temperature-independent emission in the range below about 200 K with superimposed TL peaks. This suggests a tunneling process. The continuous curve in fig. 19 shows results of a sample irradiated at 150 K, which did not excite any TL peaks below 150 K. The sample was now cooled down to 20 K as shown on the temperature scale and warmed up to RT. No TL is observed up to nearly 200 K. Still the temperature-independent emission appears between 23 and 28 min on the time scale. This supports the tunneling hypothesis. The authors conclude that in the process involving O_i^- ions the local lattice symmetry is destroyed, thus allowing forbidden transitions responsible for the extra bands, while at low temperatures only the allowed transitions appear. The emission thus involves both of the models proposed by Mathews and Stoebe (1982), depending on the experimental conditions.

Morgan and Stoebe (1986) observed four new paramagnetic centers in the ESR of $CaSO_4$:Dy single crystals. Analysis of the g- factors and $\boldsymbol{g}$-tensors indicated that these ESR centers are related to various sulfate ions. The authors propose models for all the

four centers, when the decay temperatures of these centers enables their correlation with observed TL peaks.

In two later papers Morgan and Stoebe (1990a,b) continue the study of the TL mechanism of $CaSO_4$:Dy single crystals. The ESR indicated the presence of several variations of distorted SO_4^- centers stabilized by a nearest-neighbour Ca vacancy. The presence of Dy increases the concentration of Ca vacancies required for charge neutrality. As a result, the intensities of the 220 and 350°C TL peaks increase. Holes captured at the various V_{Ca}^{2-}–SO_4^- complexes during the irradiation are released during the warming, and the energy of the recombination is eventually transferred to the Dy ions with the emission of the various TL peaks. The structure of the various centers involved seems to be quite complex. We shall mention here only the processes involved in the formation of the 220 and 350°C TL peaks. The V_{Ca} can trap two holes. There exist four such two-hole centers as indicated by the ESR spectra. The irradiation provides the pairs of holes for these centers. These are trapped at the oxygens adjacent to the calcium vacancy. The center with the two holes is not paramagnetic and cannot be observed in ESR. Only after the first hole is released can one observe the new paramagnetic ESR center. The second hole is released at about 350°C and is related with the emission of the 350°C TL peak. Centers related with other TL peaks are also quite complex, and the behavior of these centers and their relation to the TL peaks emphasizes the complexity of the system.

Mauricio et al. (1996) also studied the relation between the ESR and TL of $CaSO_4$:Dy. They concluded that SO_3^-, SO_4^- and Ca vacancy centers are responsible for the ESR signals. Step annealing measurements enabled them to relate ESR signals with some of the TL peaks.

Gerome et al. (1996) studied the influence of the preparation method on the TL of $CaSO_4$:Dy (0.1%). Five preparation methods are described. In all the methods the GCs showed the same 7 TL peaks but differing in the relative intensities. The TL showed emission near 480 nm characteristic of Dy^{3+}. The intensity of the emission is claimed to be related with Na ions. The high-temperature peaks at 400 and 450°C varied in intensity with the preparation method.

UV-emitting TL was observed by Portal et al. (1980). Two high-temperature TL peaks were observed at 540 and 605°C in GCs of $CaSO_4$:Dy (0.05 mol%). The 605°C peak emitted at about 325 nm and the 540°C peak emitted near 350 nm. These peaks are recommended for high-temperature dosimetry. High-temperature TL has also been studied by Goyet et al. (1993) and by Lapraz et al. (1996). In the latter paper the UV was found to show a combination of bands at 288, 341 and 360 nm characteristic of the most intense transitions of Tm^{3+}. These were observed indeed to be very strong in $CaSO_4$:Tm, and their appearance in $CaSO_4$:Dy is attributed to traces of Tm (about 0.004 mol%).

Codoping of $CaSO_4$:Dy. Codoping sometimes enhances the TL sensitivity but it can also reduce it. In the latter case it can still be useful when it improves other features of the phosphor, for example the range of its linearity. It also provides information on the mechanism of the TL. Ayyangar et al. (1974a) investigated the TL with ^6Li (as $^6Li_2SO_4$) as a charge-compensating codopant in $CaSO_4$:Dy. They have shown that the 210°C TL peak decreases with the increase of the ^6Li concentration. With 0.2 mol% of Dy the 210°C

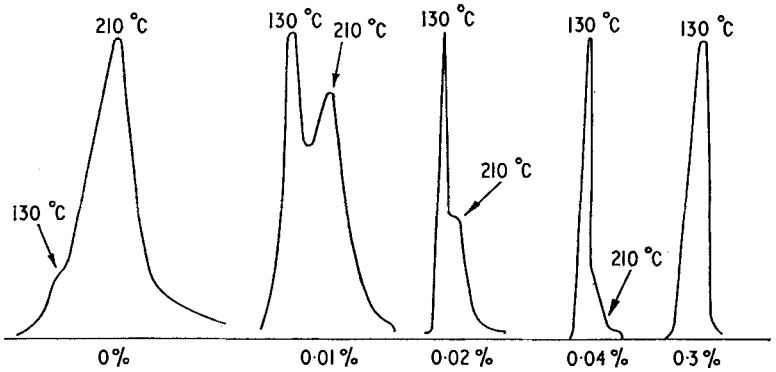

Fig. 20. GCs of $CaSO_4$:Dy codoped by various concentration of ^6Li.

peak practically disappeared when adding 0.3 mol% of ^6Li. Under these conditions only the 131°C peak remained in the GC as shown in fig. 20. Similar effects with Na_2SO_4 as codopant were described by Pawar (1978) and by Mulla and Pawar (1979). The effect of Li and Na ions on the TL of $CaSO_4$:Dy has been investigated in more detail by Chandra et al. (1986, 1987). They used various concentrations of Dy and Li (or Na). $CaSO_4$:Dy,Li (0.05, 1.13%) gave a reduction by a factor of 25 in the 225°C TL peak and a factor of 7 in the 370°C peak compared to $CaSO_4$:Dy. Qualitatively similar results were obtained with Na as the codopant. The authors concluded that Ca^{2+} vacancies are involved in the formation of both the 228 and 375°C TL peaks and that both the peaks are related to traps similar in nature. The work by Morgan and Stoebe (1990a,b) discussed above supports the above conclusions. The 131°C TL peak was found by Chandra et al. to be enhanced by Li (Na) codoping. Li was also found to induce new TL peaks around 300 and 450°C. The appearance of the latter peaks was found to enhance the PTTL of the phosphor.

Rao et al. (1993) studied the defect centers formed in $CaSO_4$:Dy,Na using ESR. The phosphors were pre-annealed at 600°C, and $\gamma(^{60}Co)$-irradiated at RT. They found the 130°C peak to be correlated with the Na^+ codopant which increases the formation of SO_4^-. The SO_4^- center was found to be characterized by an axial $\boldsymbol{g}$–tensor with $g_\perp > g_{11}$. An SO_3^- center was found to be affected by the Na^+ but no TL could be assigned to these centers. Bhatt et al. (1996) also investigated Na-codoped $CaSO_4$:Dy (and $CaSO_4$:Tm) as well as the effects of P^{5+} and Zr^{4+} as codopants. The correlation of the 130°C TL peak with the SO_4^- radical was established again using ESR and PL. Figure 21 shows the dependence on Na concentration of the 130°C TL peak (curve A), that of the ESR signal (curve B) and that of the Dy^{3+} 576 nm emission (curve C). The relation between the three is evident. Phosphorus codoping of $CaSO_4$:Dy was also found to enhance the 130°C peak (by 40%). Zr^{4+} reduced the intensity of the SO_3^- and SO_2^- radicals by about a factor of 2.

Atone et al. (1993) investigated $CaSO_4$:Dy codoped by P or Ce. The $CaSO_4$:Dy,P when excited by γ-rays from ^{60}Co showed a 50% enhancement in the TL compared with $CaSO_4$:Dy. The GC of the phosphor did not change by the P codoping. This enhancement

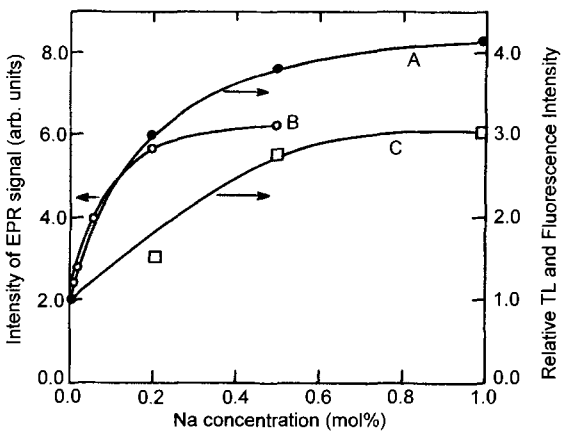

Fig. 21. Dependence on Na concentration of (A) the 130°C TL peak intensity, (B) the ESR signal, and (C) the 576 nm emission of $CaSO_4$:Dy.

was attributed to incorporation of Dy concentrations above 0.2 mol% with no quenching effects, enabled by the P doping. The PL under the same P codoping was enhanced by 150%. Ce codoping enhanced the PL, which resulted from additional Ce absorption lines introduced by the Ce in the region 265–295 mm. The TL was not enhanced by the Ce. In a more recent paper by Atone et al. (1995a) the enhancement by P was shown again. The authors have now examined also the effects of Mo and SO_3 codoping. The TL enhancement by the Mo was 60% (in $CaSO_4$:Tm,Mo it was 150%). This enhancement was found to result from the production of more hole traps in the Mo-codoped phosphor. No change was observed in the GC and in other dosimetric properties by the Mo codoping. SO_3 codoping enhanced the TL by 80%. This enhancement, however was not stable and disappeared after two weeks of storing at RT. The effect was attributed to the instability of $CaSO_3$ which by absorption of oxygen from the atmosphere gives $CaSO_4$.

$CaSO_4$:Dy,Mn (1:4) was found by Li and Hsu (1990a) to give high sensitivity, low fading and a linear dose response over a wider range compared to the singly doped $CaSO_4$:Dy. The TL and especially the low-temperature peak was found to be strongly influenced by the Mn concentration. The optimal performance was obtained after 30 min of annealing at 350–400°C. The high-temperature annealing experiments were extended by Hsu et al. (1990) and Li and Hsu (1990b) up to 800°C, for $CaSO_4$:Dy containing Mn and Na. Treatments up to 400°C did not affect the TL at all. At higher temperatures, 400–600°C, the 110°C TL peak decreased in samples with high Na content while the high-temperature peak (near 200°C) increased. Above 600°C the high-temperate TL peak decreased sharply. The sample returned to the original behavior after a regular anneal at 400°C.

Srivastava et al. (1991) explored the effect of Cu^{2+} codoping of $CaSO_4$:Dy. The Cu was found to suppress efficiently the 350°C TL. The dosimetric TL peak is affected only slightly by the Cu. It becomes narrower with no reduction in its intensity. The addition of Cu was found to extend the range of linear dose response from about 1 Gy in $CaSO_4$:Dy to 10–100 Gy. With Cu concentration above 0.2 mol%, the $CaSO_4$:Dy,Cu was found to be

a sensitive TLD for UV. Kasa et al. (1996) have also examined the TL of $CaSO_4$:Dy,Cu. They stress that the elimination of the 350°C TL peak by the Cu is responsible for the extension of the range of linearity. The authors feel that the small reduction of sensitivity by the Cu codoping is practically not important. The optimum dopant concentration suggested by the authors is 0.20 mol% Dy and 0.25 mol% Cu. The extension of the range of linearity enables the use of $CaSO_4$:Dy,Cu for accident dosimetry.

$CaSO_4$:Dy,Cu was also studied by Peto et al. (1997). The Dy concentration was 0.2 mol% and the Cu was varied in the range of 0.1–0.3 mol%. After excitation by 4 MeV electrons the emission showed, in addition to the Dy-characteristic emission bands, an additional band at 350 nm whose intensity increased with the Cu concentration. The decay time of the Dy emission was 1 ms, while that of the 350 nm band was about 60 ms. It was therefore concluded that the 350 nm band has no direct relation with the Dy emission. The reduction in the TL intensity by the codoping with Cu was ascribed by the authors to the absorption of part of the excitation energy by the Cu centers.

Improvement in the $CaSO_4$:Dy phosphors can be obtained by mixing with suitable inorganic compounds that also act as binders. Morato et al. (1982) have mixed the phosphor with NaCl, and Azorin et al. (1986) used KBr. Care was taken in both cases using high purity compounds, and comparatively small grains (about 100 μm). The mixtures were cold-pressed into pellets. The Dy concentration in the phosphor was close to the optimal, about 0.2 mol%. The optimal ratio of the concentration of the $CaSO_4$:Dy to that of the mixed binder was about 1:2 by weight. The mixtures were preheated for 30–60 min at 600°C. This treatment has increased the intensity of the dosimetric TL peak at about 220°C and decreased the other peaks. It also produced mechanically strong and good-reusability pellets. The γ-irradiated pellets gave good linearity, a detection threshold below 10^{-5} Gy, negligible thermal fading, low optical fading and good zero point stability and repeatability. The dosimeters were sealed in plastic sheets to protect them from moisture. With suitable filters including 0.8 mm lead the range of energy independence was extended down to below 0.02 MeV.

Dosimetric properties of $CaSO_4$:Dy. Some dosimetric properties were discussed throughout this subsection.

The sensitivity of $CaSO_4$:Dy to γ-rays is high. Ayyangar et al. (1974a) reported for $CaSO_4$:Dy (0.05 mol%) a γ-sensitivity nearly a hundred times that of TLD-100, when corrected for the spectral response of the PM of the reader. Since then, improvements in the preparation methods, purity of the chemicals used, optimal Dy concentrations (0.2 mol%), high-temperature sintering, sensitization, high-temperature annealing, codoping and mixing with suitable binding compounds have further increased the phosphor sensitivity. Prokic (1978) has shown that non-activator impurities can affect adversely the sensitivity of $CaSO_4$:Dy. This effect is demonstrated in fig. 22, where samples 1 and 6 having the lowest impurity content are seen to have the strongest dosimetric 220°C TL peak. On the other hand, sample 4 with the highest impurity concentration gives only a weak TL near 200°C appearing as a shoulder to the strong peak near 100°C. Prokic also showed that 0.2 mol% Dy gives the highest sensitivity of $CaSO_4$:Dy phosphors. The same optimal Dy concentration was observed by Eid et al.

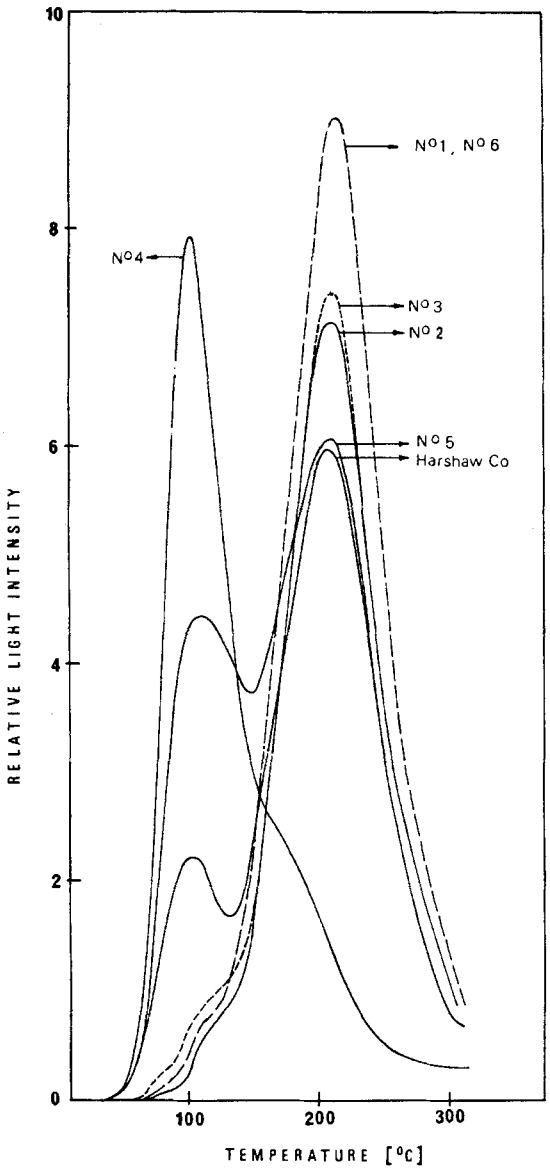

Fig. 22. Intensities of the 100°C (x) and 215°C (o) for $CaSO_4$:Dy containing various concentrations of alkali-metal impurities.

(1992) and by others. Ayyangar et al. (1974a) have shown that the relative sensitivity of $CaSO_4$:Dy (0.05 mol%) to thermal neutrons is only 0.38 compared to about 1500 for the Harshaw LiF TLD-700. It has to be noted that while the γ-sensitivity of $CaSO_4$:Dy drops quite sharply above 0.2 mol% Dy, that for thermal neutrons rises steeply at and above 3 mol% Dy.

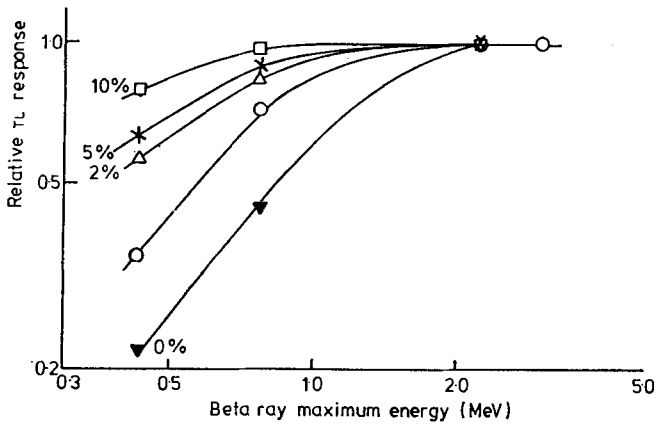

Fig. 23. β energy response of $CaSO_4$:Dy pellets containing various concentrations of graphite (as indicated). Results by Pendurkar et al. (1971) for a 0.13 nm thick teflon TLD (open circles) are shown for comparison.

A few methods have been developed for high-sensitivity detection of radiation by $CaSO_4$:Dy phosphors in a mixed radiation field. Hsu et al. (1978) developed a method of self-activation for thermal neutrons and γ dosimetry. They covered the $CaSO_4$:Dy phosphor with ^{113}Cd which has an extremely high cross section for thermal neutron absorption. The Dy, S and Ca of the phosphors were activated by the thermal neutrons to ^{165}Dy, ^{35}S and ^{45}Ca, all β emitters. This makes the $CaSO_4$:Dy a very sensitive thermal neutron detector. In addition it is quite sensitive to γ-radiation. The TL due to the ^{165}Dy is shown to be proportional to the γ-exposure. As shown by Hsu and Chen (1975) the self-dose method makes the phosphor a high-sensitivity detector for thermal neutrons and γ-rays in a mixed field. The sensitivity to γ-radiation was found to be two orders of magnitude higher compared to TLD-100. Majchrowski et al. (1994) also reported on the results of an activated $CaSO_4$:Dy. They made use of the $^{32}S(n,p)^{32}P$ fast neutron conversion. Their preliminary results show a high sensitivity and good linearity.

Not much has been reported in the literature on the β-sensitivity of $CaSO_4$:Dy phosphors. Pradhan et al. (1978) also used the fast neutron reaction $^{32}S(n,p)^{32}P$. To increase the efficiency, the phosphor was mixed with sulfur powder and pressed into pellets. After the neutron irradiation the pellets were heated on an Al planchette and the accumulated TL due to the ^{32}P activity was used for the β dosimetry. The sensitivity is reported to be 100 times that of the conventional $CaSO_4$:Dy phosphors.

In β-radiation measurements using a $CaSO_4$:Dy phosphor there is usually a very strong β-energy dependence especially for low-β-energy particles for which the penetration range is smaller than the pellet thickness. To overcome this difficulty Pradhan and Bhatt (1977) have used graphite-mixed $CaSO_4$:Dy. Teflon discs also reduced the effective thickness of the phosphor. The effect of the graphite is shown in fig. 23. One notes that with 10% graphite the β-energy independence range is reduced to 0.8 MeV compared to about 2 MeV in the graphite-free discs. A different method was used by Lakshmanan

et al. (1980) who produced 0.1 mm thick $CaSO_4$:Dy teflon films and bonded them thermally on 0.7 mm teflon discs. The obtained pellets were rigid and gave β-energy independence down to 0.76 MeV. Spurny and Votockova (1993a) examined the sensitivity of $CaSO_4$:Dy to protons in the energy range 2.9–8.4 MeV in comparison with other TLDs like Al_2O_3 and LiF-TLDs. They found the sensitivity to be comparable to that of the other TLDs examined and to depend to some extent on the proton energy.

Luguera et al. (1996) developed a dosimeter for β radiation using the EGS4 code for simulation described by Nelson et al. (1985) to estimate the dosimetric response. The dosimeter consists of a layer of 50–100 μm grain sizes of $CaSO_4$:Dy (0.1 mol%) 60 mg cm^{-2} thick, pressed to an Al foil and covered by a 5 mg cm^{-2} thick polyethylene filter. The dosimeter has a flat response in the β-energy range 0.76–2.27 MeV and almost flat for angles 0–40°. The authors have shown that simulation using EGS4 is an efficient tool for studying the behavior of dosimeters in radiation fields.

The response of $CaSO_4$:Dy to α-particles was studied by Spurny and Votockova (1993b, 1994). They found the $CaSO_4$:Dy phosphor to give an α-sensitivity comparable to other phosphors, though somewhat lower than that of Al_2O_3. The $CaSO_4$:Dy phosphor was almost energy independent in the range 2.5–5 MeV.

The UV sensitivity of $CaSO_4$:Dy is quite low and rises sharply only near 200 nm. Chandra et al. (1976) have used the 215°C TL peak for UV dosimetry. It showed negligible fading and linearity over the range 400–4×10^4 erg mm^{-2}. The TL increased by a factor of 300 from 250 to 200 nm. The sensitivity above 350 nm was practically zero. The UV sensitivity increased with the decrease of the phosphor grain sizes.

The linearity of $CaSO_4$:Dy was discussed above. It was observed by Morato et al. (1982) that the supralinearity at high exposures results from the high-temperature TL peaks at about 350°C. Elimination of these TL peaks has been shown by Morato et al. to increase the linearity range from about 1 G to 30 Gy. Srivastava et al. (1991) reported that Cu codoping extends the range of linearity up to 100 Gy. The same limit of linearity was also reported by Abubakar et al. (1990). Srivastava and Supe (1985) have also shown that the linearity upper limit of $CaSO_4$:Dy increases with the LET.

Morato et al. (1982) report on a detection threshold below 10^{-5} Gy observed for cold sintered $CaSO_4$:Dy–NaCl phosphor pellets. An extremely low detection limit of β-radiation by $CaSO_4$:Dy was reported by Benko (1990). The technique consists of spreading a thin layer (0.1 g spread on a circle 1.5 cm in diameter) of the phosphor powder directly on the heating plate. After heating to 350°C the phosphor can be re-used with no change in sensitivity, provided that the detector has not been exposed to high doses. Under certain conditions the TLD is claimed to give reliable β-measurements down to doses of 0.1 μGy.

The reported thermal fading rates of $CaSO_4$:Dy vary widely. Values as high as 15% per month have been observed by Aypar (1978), rates as low as a few percent per 6 months have been reported by Guelev et al. (1994), and practically zero fading is claimed by Becker et al. (1973). In some cases it is not clear that the fading rates were measured in the dark. In such cases the data include an unknown contribution of optical fading. Another contribution of quite high fading is obtained when the low-temperature TL in the range

up to 140°C is not eliminated at all or is only partly eliminated by pre-read annealing at temperatures between 100 and 140°C. An almost full elimination of the low-temperature TL was obtained by Guelev et al. (1994) who pre-annealed the phosphor at 140°C. The fading rate is also affected by the LET and dose of the irradiation as shown by Srivastava and Supe (1986) and by others. Chemical impurities may also contribute to the fading. Nambi (1982) has shown that this results from radioactivity of some of the impurities. He has even estimated the self-dose fading rates from analysis of the radioactivity of the phosphors. It is certain that the intrinsic fading of pure $CaSO_4$:Dy phosphors due to only the 220°C dosimetric peak is very low.

$CaSO_4$:Dy suffers from a high effective Z which differs considerably from tissue equivalence. This can be reduced by mixing with low-Z compounds. $^6Li_2SO_4$ makes the phosphor almost tissue equivalent.

Phototransferred TL (PTTL) and related phenomena in $CaSO_4$:Dy. The term PTTL is used for the TL induced by light which releases charge carriers from deep traps from where they get trapped at shallower traps. This involves population of the deep traps by pre-irradiation, let us say by γ-rays. In order to be able to determine the intensity of the PTTL one has to empty the shallow traps excited directly by γ-irradiation. This is done by warming the sample after γ-irradiation to a temperature above the range of the part of the GC related to the shallow traps and measurements of the GC after the exposure to the PTTL-inducing light at a low temperature. The PTTL will, under suitable conditions, be proportional to the γ pre-exposure for a constant inducing light dose or to the inducing light when the pre-exposure is kept constant. It is of course also possible to carry out the pre-irradiation at a comparatively high temperature, say at 300°C. This irradiation will fill up effectively the deeper traps. Irradiation by light at low temperature will then transfer charge carriers from the deeper traps to shallower ones, when the PTTL will appear during the warming up of the sample. The PTTL enables high-temperature and high-dose measurements, UV dosimetry and other applications. A review article on PTTL and related phenomena is by Jain (1984).

Caldas and Mayhugh (1976) have done preliminary work on the PTTL of $CaSO_4$:Dy. They showed that it enables determination of X-ray exposures up to 10^6 Gy without saturation compared to only 10^3 Gy by direct TL measurements. The main PTTL peak is the dosimetric peak at about 220°C. UV excited PTTL is also much more sensitive compared to the conventional direct TL measurements of UV doses. Nagpal et al. (1980) used $CaSO_4$:Dy (0.05 mol%) of grain size 74–100 μm, γ pre-irradiation from ^{226}Ra and ^{60}Co sources, and UV 365 nm light from a mercury lamp. The annealing preceding the UV illumination was at 460°C. The study revealed two deep traps at 500 and 570°C. The PTTL (220°C peak) obtained after γ-irradiation followed by a 460°C anneal and a fixed UV (365 nm) dose at 95°C was found suitable for γ dosimetry. Pradhan and Bhatt (1985) used ^{60}Co γ-rays for the pre-dose and the 254 nm mercury line for the charge transfer. The PTTL was measured in the range 10^2–3×10^5 Gy γ doses. They have observed only one deep-trap TL peak at 420°C. Their results showed that the intensity of the transferred TL was considerably higher compared to the reduction in the 420°C peak intensity. The authors concluded that the PTTL originated not only from the radiative

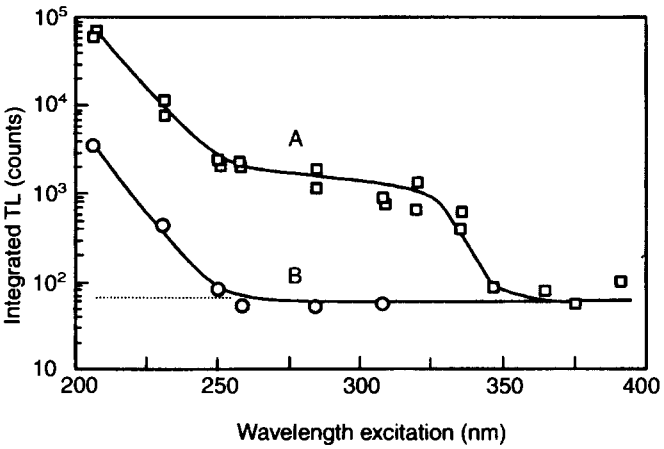

Fig. 24. (A) Integrated PTTL of $CaSO_4$:Dy as a function of the exciting UV wavelength. (B) UV-excited TL.

deep trap but also from non-luminescent centers. This conclusion looks unjustified, and indeed Shinde et al. (1988) observed TL peaks at 420 and 520°C. These authors have still missed TL peaks at higher temperatures, e.g. the peak at 570°C observed by Nagpal et al. (1980) mentioned above (the measurements by Shinde et al. (1988) were carried out up to about 550°C) which explains why the intensity of the transferred TL was still higher compared to the reduction in the two high-temperature peaks together. Shinde et al. (1988) have also found that the intensity of the 420 and 520°C peaks depended on the grain sizes of the phosphor. The 420°C peak decreased and the 520°C peak increased in intensity with a decrease in grain size. This effect was attributed partly to the short penetration depth of the UV light into the phosphor grains and partly to the higher concentration of Dy in the larger grains. Goyet et al. (1993) have shown that the PTTL of $CaSO_4$:Dy phosphors can be applied for high-temperature dosimetry. This work has been extended by Goyet et al. (1996). They stress that the strong decrease in sensitivity of the peak of $CaSO_4$:Dy at 140–150°C observed by Nagpal and Pendurkar (1979) and by Lakshmanan et al. (1983) originated from strong fading. Goyet et al. have therefore looked for TL peaks at higher temperatures which by PTTL allows measurements of the dosimetric peak at 220°C. Their GC measurements were extended to 700°C. The $CaSO_4$:Dy samples contained 0.1 mol% Dy and had 36–50 μm grains. They were pre-irradiated by X-rays, annealed at 500°C and then exposed to 206 nm UV at RT. To enable TL measurements up to 700°C, the GCs were taken through a 340 nm transmitting filter. The heating rate was $1°C\,s^{-1}$. Under these conditions the high-temperature TL consisted of practically one peak at 600°C. Figure 24 shows the integrated PTTL as a function of the UV wavelength using a constant UV energy fluence (curve A). Curve B shows for comparison the TL directly excited by UV. The PTTL is seen to drop strongly with wavelength above 200 nm and to disappear near 350 nm. The emitted TL was measured through a 480 nm filter and is characteristic of Dy^{3+} emission. On increasing the annealing temperature the

PTTL started to decrease above 500°C following the decrease in the 600°C peak and approaching zero above 650°C, confirming that the PTTL is directly related to this TL peak and that no TL peaks related to the PTTL exist above 700°C. For the X-irradiated samples the PTTL was limited to 10^2 Gy. Lewandowski and Mathur (1996) studied the PTTL of Dy- (and Tm-) doped $CaSO_4$. They found that elimination of 260 nm from the UV sources reduced the PTTL to zero. This contradicts the observations described above. No details are given which could help in the evaluation of this strange observation. Potiens and Campos (1996) report in "preliminary" results on the use of $CaSO_4$:Dy for high-dose UV dosimetry. The results do not look reliable. Part of the failure may have resulted from using the teflon-embedded phosphor up to 360°C when the teflon is unstable mechanically.

Some investigators studied the PSL (photostimulated luminescence) of $CaSO_4$:Dy. It differs from PTTL only in the measurement after the pre-irradition, when the luminescence during the following illumination is measured instead of the induced TL. Pradhan et al. (1980) and Pradhan and Bhatt (1981b) studied the PSL of $CaSO_4$:Dy. They stress the identical emission spectra observed in PSL and PTTL, which of course results from the identical recombination centers in both cases. The sensitivity limit is lower in PTTL compared to that in PSL. The advantage of the PSL is that the measurements do not require cooling and heating cycles needed in TL. In addition the PSL measurements can be repeated a few times after which the PTTL can still be measured with almost no reduction in the intensity.

Miscellaneous investigations on the TL of $CaSO_4$:Dy. This subsection will deal with topics on which very few investigations were published in literature.

The simultaneous estimation of the TL and of the time elapsed since an abnormal exposure took place is based on the fact that the fading of the TL appearing at low temperatures is faster than that of high-temperature TL peaks. The ratio of the quantities will then depend on the elapsed time after the abnormal exposure. Some work on this topic was carried out almost thirty years ago by Sidran (1968), by Spurny (1971) and others. More recently Wang et al. (1987) have attempted to use the ratio of intensities $R = P_2/P_1$, where P_2 is the intensity of the dosimetric peak at about 220°C and P_1 is that of the lower peak (about 100–140°C), for the estimation of the elapsed time t_e. The results showed that $R(t)$ depends on the ambient temperature, which is difficult to estimate accurately, especially in case of an accident. Lakshmanan et al. (1989b) have taken the ratio of the areas under the glow curve in the range 180–300°C (P_2) and in the range 25–80°C (P_1). They worked with a $CaSO_4$:Dy,Na phosphor under γ-ray exposure. The area P_2 was taken to estimate the γ-ray dose and the ratio $R = P_2/P_1$ was used to give an estimate of t_e. They concluded that R is affected by the ambient temperature, by the radiation dose and by the LET of the radiation. Furetta and Azorin (1989) measured both the ratio of the heights of the two peaks, $R_H = H_2/H_1$, and the ratio of the areas under the glow curve in the two temperature ranges, $R_\phi = \phi_2/\phi_1$. The irradiation was by X-rays of various energies. Figure 25 shows the dependence on t of both R_ϕ and R_H for the phosphors $CaSO_4$/KBr:Dy and $CaSO_4$:Dy in a teflon binder. Their theoretical calculations show also differences between first-order and second-order kinetics TL peaks. They also

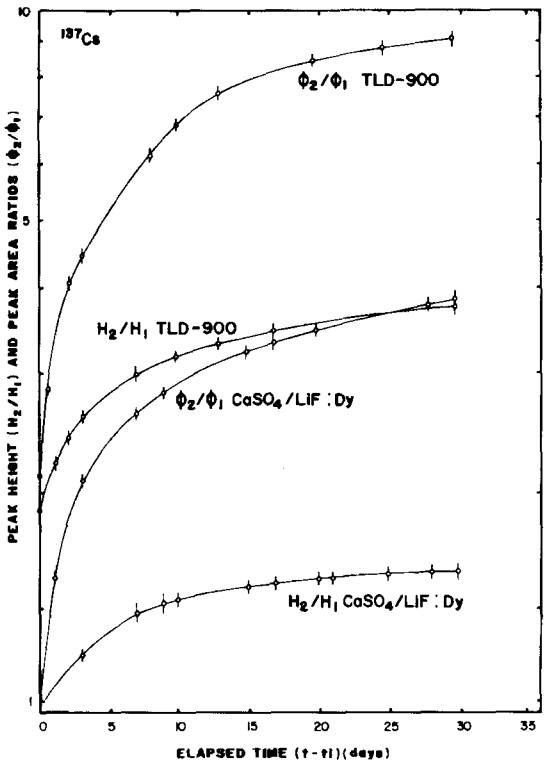

Fig. 25. The dependence on the elapsed time of the ratios of the peak heights $R_\phi = \phi_2/\phi_1$ and the areas under the peaks H_2/H_1 in the temperature regions 180–300 and 25–180°C, for the $CaSO_4$:Dy and $CaSO_4$:LiF, Dy phosphors.

found that for the above phosphors the R-values are not applicable above 12 days, when the P_1 becomes very weak. They claim that the error in the measured t_e is ± 2 days. It seems however that under accident conditions, when the ambient temperature is difficult to estimate, the error in the measured t_e may be much higher.

Lakshmanan (1992) has fitted a $CaSO_4$:Dy badge for simultaneous measurements of peak voltages, half-value layer thickness and exposure to diagnostic X-rays. This TLD badge is used in India for β, γ and X-ray personnel monitoring.

Sahre (1987) describes a computerized $CaSO_4$:Dy teflon TLD. It was applied for fading-independent dose evaluation and for estimation of the time that has passed since the occurrence of a short high-intensity exposure. The computer unfolds the GC into the main peak and sub-peaks. Using only the main peak area the error due to fading is reduced to only 5%. The fading of the low-temperature peak gives the elapsed time since the high exposure. Of course this estimation can be given for a known constant temperature.

Energetic particles may induce damage in phosphors, which can be reversible or even irreversible. This may involve the production of interstitials or vacancies or affect the TL in another way. The work by Aguirre de Carcer et al. (1993) described in sect. 3.2.1. has shown that the GC obtained for NaCl:Eu^{2+} was different for α-irradiation compared to

that obtained after UV, X- and β-irradiation (fig. 5). These changes have been assigned by the authors to radiation damage. Bhatt et al. (1988) studied the radiation damage in $CaSO_4$:Dy (and various LiF TLDs). γ doses of $1-3\times10^6$ Gy followed by annealing at 650°C for 1 hour changed the TL sensitivity of $CaSO_4$:Dy by less than 5%. It seems that the high temperature (650°C) has annealed the reversible damage induced by the γ-irradiation. The reversible and irreversible radiation damage has been studied in some detail by Srivastava et al. (1991). The $CaSO_4$:Dy phosphor was γ- and α-irradiated. The main effect on the TL resulted from residual TL and was restored by high-temperature annealing. Some irreversible damage was found to set in when the doses exceeded 10^3 Gy. γ-irradiation induced both reversible and irreversible effects, while high-LET α radiation induced mainly reversible effects. The reversible effects were found to be closely related to the radiation-induced TL sensitization. The irreversible component was ascribed to changes in the capture probability of the traps, and it was preferential via the deeper traps. The permanent change in the capture rates was attributed by the authors to radiation-induced dislocation edges or loops, which were assumed to compete destructively with the filling of normal traps.

Many papers deal with clinical applications of the TL dosimeters using $CaSO_4$:Dy. These papers describe the adjustment of the TLD for specific applications and system calibration. Only a few of these papers will be included in the present article. Hsu et al. (1986) and other related publications by the same group deal with exposure measurements in computerized topography. The reader's stability was found by these authors to give a standard deviation (SD) of less than 1%, while the total SD of the system amounted to nearly 3%. Zarand and Polgar (1983, 1984) gave an expression for the SD of TLD systems. It includes various factors which affect the SD. Comparison with published experimental measurements supported the theoretical expression. The SD at low exposures will of course be affected by the sensitivities of the phosphor and of the reader, and by the geometrical matching. Zarand (1996) has put much effort in the calibration and measurements of the accuracy of several dosimeters, including $CaSO_4$:Dy, in his physical research laboratory in Budapest. The measurements included the long-run behavior in many repeated measuring cycles of the TLD systems. Unfortunately some of the measurements were erratic and the SD for the $CaSO_4$:Dy system was 5% or even higher. The authors attributed this failure to bad thermal contacts and electrical instabilities of the (old) Harshaw 2000 reader used. Part of the error was suggested by the authors to have originated from the 600°C annealing of the $CaSO_4$:Dy dosimeters.

$CaSO_4$:Dy is a very sensitive phosphor which is of importance in many medical applications. It is however not tissue equivalent. It is therefore necessary to make corrections for obtaining the right values of the energy absorbed in the tissue and to account for the energy dependence of the phosphor. Niroomand-Rad and Dewerd (1983) describe a TLD-900 fitted for low exposures in diagnostic X-rays which permitted measurement down to 10^{-6} Gy with an accuracy better than 20%. The authors found TLD-900 of advantage over TLD-900/LiF at very low doses. Lakshmanan et al. (1989c) studied the diagnostic X-ray (50–120 kVp) response characteristics of $CaSO_4$:Dy teflon badges. The badge consisted of three TLDs with different filters: the first with a

Cu + Al filter, the second with a perspex filter, and the third with an open window (D_1, D_2 and D_3, respectively). Each of the detectors showed dependence on the X-ray photon energies. The values $D_3 - D_1$ however were nearly constant over the whole range of 50–120 kVp X-rays. Another method was using D_1 with a correction factor ($D_1 \times$CF). The study also included measurements at various incidence angles (0–90°). The authors concluded that the $D_1 \times$CF method is preferable over the $D_3 - D_1$ method in mixed radiation fields such as X, γ or β, γ. The $D_3 - D_1$ method was found preferable in direct incidence diagnostic and low-energy X-rays. Pradhan et al. (1992, 1993) also describe a $CaSO_4$:Dy teflon disc system designed for measurements in diagnostic X-ray installations. The TLD was fitted for large-scale measurements of the incidence and exit beams. The authors show that conventional calibration of the detectors using X-rays up to 80 kVp can give an error of 30–40%. In the work by Pradhan et al. the discs were put in specially designed holders. The measurements are based on the decrease of the TL under a filter of 1 mm Cu + 0.5 mm plastics compared with the open discs. The ratio of the two gave an estimate of the quality of the X-rays (the half-value thickness). The two sets of calibration of the entrance and exit beams proved to be superior compared with the conventional calibration.

A system similar to the above, involving two $CaSO_4$:Dy teflon discs, one with and the other without composite filters, was also described by Pradhan et al. (1990). TLDs are often introduced into a patient's body in the form of capsules including $CaSO_4$:Dy powder. These TLDs give a measure of the internal radiation in the body of a patient treated by radioactive or nuclear radiation. In other radiation treatments the TLD is used to measure internal distribution at tumor sites. An example of the use of $CaSO_4$:Dy in radiotherapy or nuclear medicine is given in Yao et al. (1981). The discussion of this and many other papers dealing with the medical applications of $CaSO_4$:Dy TLDs is beyond the scope of the present review article.

$CaSO_4$:Dy TLDs are often used for measurements of radiation in various locations. As an example, Hsu et al. (1991) describe the ratio of the radiation above the ground and that below the ground in various locations in Taiwan due to Rn diffusion. They found, for example, in a given location that the radiation two meters below the ground level was 50% higher compared to that one meter above the ground level. Results of local measurements carried out in various locations in many countries can also be found in the literature.

Laser heating has been discussed shortly above (see Gasiot et al. (1982) and Justus et al. (1996) in sect. 2.1.3, and Abtahi et al. (1985, 1987) in sect. 3.2.1). Its main advantages are the high heating rates of about 10^4°C s^{-1}, which can be achieved with no problems of bad heat contacts, and its local heating which is limited to points in the range of 0.025–0.5 mm. Abtahi et al. (1986) used special techniques to obtain a CO_2 laser with uniform intensity profiles and high reproducibility. This enabled them to measure the TL efficiencies of $CaSO_4$:Dy (and LiF:Mg,Tc) over the range of 4–5500°C s^{-1} heating rates. The point heating enables scanning of surfaces of TLD films. This was done by Serviere et al. (1991). The dosimeter was constructed as a few mg cm^{-2} thin $CaSO_4$:Dy film on a 50 μm thick polyimide substrate. The grain sizes of the phosphor were 25–50 μm.

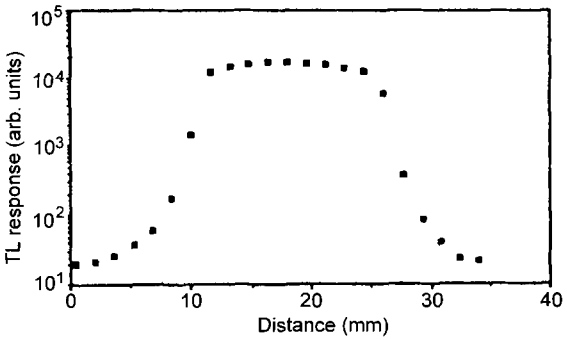

Fig. 26. Absorbed dose in a $CaSO_4$:Dy film exposed to $^{90}Sr/^{90}Y$ β-rays measured along the axis in the center of the dosimeter. The TL was obtained by laser heating at about 10^4 K s^{-1}.

A computer-controlled set-up including a 10 W CO_2 laser and a scanning device enabled to scan a phosphor film of 80×80 mm^2, which was mapped by 10^4 points in about 30 min. Figure 26 gives the absorbed dose in the detector relative to an axis in the center of the dosimeter. The excitation source in this case was β-rays from $^{90}Sr/^{90}Y$. The dose ranges used were 10^{-3}–10^3 Gy. The emitted light was proportional to the dose over the whole range. The laser-heated TLD also enabled measurements in a mixed field, for instance n–γ radiations.

Setzkorn et al. (1996) used laser heating on thin (0.1 mm) β-sensitive $CaSO_4$:Dy phosphors. The foils were irradiated by β-rays from ^{147}Pm, ^{204}Tl and $^{90}Sr/^{90}Y$ sources and were laser scanned. The authors present various dose profiles of the scanned foils. They conclude that the laser-heated TLD foils give a good alternative to the conventionally heated TL detectors and they offer an efficient method to visualize large-size radiation fields with a good resolution.

Bhatt et al. (1994) describe the results of intercomparison of $CaSO_4$:Dy teflon discs as personal monitoring TLDs. The work was conducted independently in Japan and Australia. The irradiations were performed free in the air and on the surface of water and PMMA-equivalent composite phantoms. The performance of the analysis was according to the ANSI-N13-1983 criteria. Results were also analyzed according to the trumpet curve analysis with the requirements of ICRP-35 and ICRP-60. The results showed satisfactory performance of the TLDs which fell within the limits of the requirements.

3.2.4. *$CaSO_4$:Tm*

Comparison with $CaSO_4$:Dy. $CaSO_4$:Tm behaves much like the Dy-activated phosphor. This is why many papers dealing with $CaSO_4$:Dy include also some information on the Tm-activated phosphor. Nambi et al. (1974) observed similar GCs almost equal in intensity for the two phosphors. This can be seen in fig. 27 where GCs are given for all the $CaSO_4$:R for the temperature range from RT to 500°C, obtained after irradiation at RT. Nambi et al. have also shown that the relative TL sensitivity as a function of the R concentration is nearly the same for both activators as shown in fig. 28. More than that, the thermal activation energies (E) for the phosphors as a function of the peak temperatures, were found to lie on the same straight line (fig. 16). Both phosphors

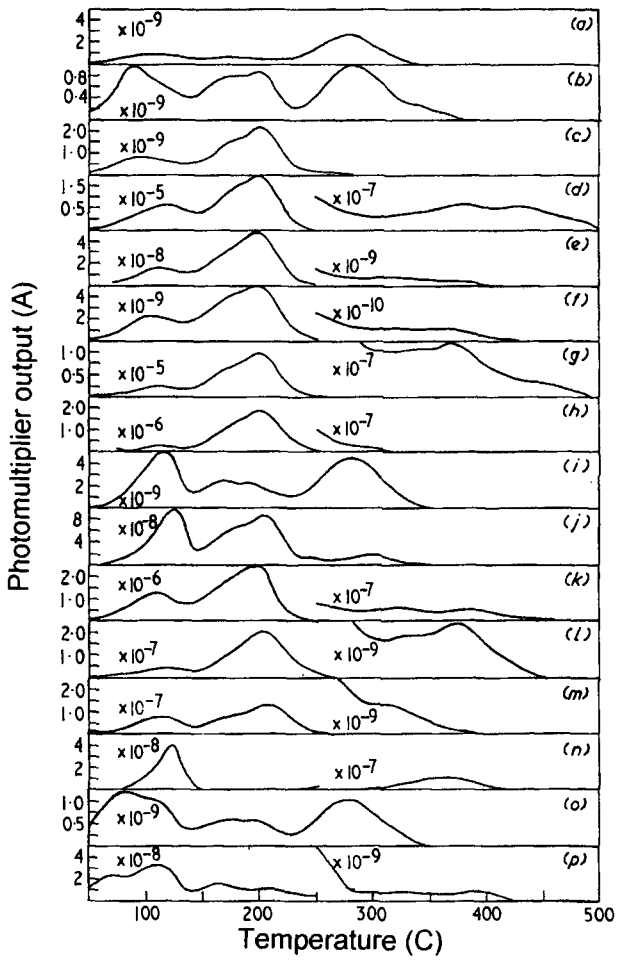

Fig. 27. GCs for RT γ-irradiated $CaSO_4$ doped by various R ions: (a) Y, (b) Lu, (c) Yb, (d) Tm, (e) Er, (f) Ho, (g) Dy, (h) Tb, (i) Gd, (j) Eu, (k) Sm, (l) Nd, (m) Pr, (n) Ce, (o) La, and (p) undoped.

also show the maximum TL sensitivity at about 0.2 mol% activator concentrations. The TL emission spectra are of course different as each activator exhibits its characteristic emission. We shall mention here only the UV emission of $CaSO_4$:Tm at about 350 nm, which does not appear in high-purity Dy-activated phosphors. Both phosphors suffer of course equally from the considerable departure from tissue equivalence of the $CaSO_4$ host ($Z_{eff} = 15.4$). Both $CaSO_4$:Dy and $CaSO_4$:Tm were first reported as sensitive phosphors by Yamashita et al. (1968, 1971). Burgkhardt et al. (1977) found for both the phosphors a TL peak above 100°C (peak I) and the dosimetric peak above 200°C (peak II). Peak II of $CaSO_4$:Tm looks a composite peak, a fact which was also observed in $CaSO_4$:Dy as described above. Both peak I and peak II of $CaSO_4$:Tm became narrower and both

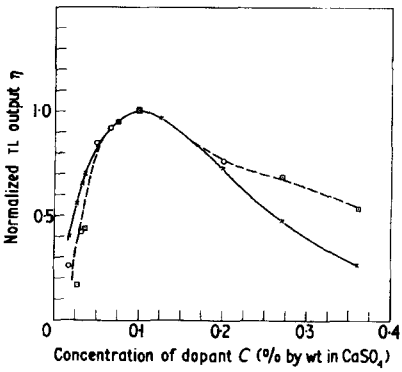

Fig. 28. Normalized TL intensities for Dy-doped (squares) and Tm-doped (circles) $CaSO_4$ as a function of the dopant concentration.

shifted to lower temperatures with γ-radiation dose. The ratio of their intensities varied as a result of an increase in the intensity of peak II. The supralinearity of $CaSO_4$:Tm is also similar to that of $CaSO_4$:Dy. It seems however to start at a somewhat lower dose of about 3 Gy. Chandra et al. (1981) studied the supralinearity and the sensitization of Dy and Tm doped $CaSO_4$. They have also examined the residual TL (RTL) which remains after γ-irradiation followed by annealing. The annealing at temperatures above the RTL peaks was found to remove the sensitization completely. The experiments showed that the sensitization of both phosphors is directly related to the RTL intensities. Other observations showed that the shape of the dosimetric peak in both phosphors also depends on the RTL intensities. In addition, UV illumination caused a decrease in the sensitization in parallel with the decrease in the RTL intensity. Prokic (1978) observed that the GCs of $CaSO_4$:Tm depended on the purity of the chemicals used in the preparation just in the same way as those of $CaSO_4$. Namely, with high-purity chemicals the low-temperature TL peaks disappear, leaving almost a pure dosimetric peak (see fig. 22). Similar results were reported by Kasa (1990) who found that the dosimetric TL peaks of both the Dy- and Tm-doped phosphors grow in intensity with the purity of the chemicals of the phosphors. Prokic (1991) working with sintered pellets has also obtained similar GCs and similar dependence of the TL on the grain sizes for the two phosphors. This result was in agreement with Felszerfalvi et al. (1979) who concluded that the decrease in the TL with the decrease in the grain sizes was directly related to the lower activator concentration in the smaller-grain phosphor. The sensitivity of the Tm-doped phosphor was found by Prokic (1991) to be almost twice that of the Dy-doped one. It is possible that at least part of this difference in sensitivity originated from differences of the readers' response to the different emission spectra. The TL emission of $CaSO_4$:Dy showed the strongest bands at about 480 and 570 nm, other bands at 688, 700 and 732 nm, and a broad weak band at about 360 nm. $CaSO_4$:Tm had its strongest emission band at 455 nm, other bands at 515, 655, 700, 733 nm, and a band near 360 nm. The broad emission band of the Dy phosphor at about 360 nm is assigned by the authors to the recombination of radiation-induced defects in the $CaSO_4$ lattice. This band did not appear in $CaSO_4$:Dy

emission reported by Yamashita et al. (1968). Lapraz et al. (1996) have observed very weak UV-emission bands in $CaSO_4$:Dy which they attributed to traces of Tm.

Chakrabarti et al. (1990, 1992) worked on Dy- and Tm-doped phosphors sintered for 12–20 hours at 1000°C. The phosphors exhibited high stability and both had the dosimetric peaks near 220°C (at 2°C s^{-1}). UV or γ-irradiation of both the sintered phosphors showed high-temperature TL near 330°C. The authors suggest that the sintering, as well as annealing at high temperatures, produce a UV-absorption band, in $CaSO_4$:Tm. Illumination in this band induces the 330°C TL by the release of charge carriers and their trapping at the deep traps related to the 330°C TL. The authors also show that sintering at 1000°C breaks up the $CaSO_4$ into sulfates, thiosulfates and sulfides which produce the UV absorption. This effect is more pronounced in high-dose X-irradiated samples. Just as $CaSO_4$:Dy, the Tm phosphors also exhibit strong energy dependence. Stammers and Kingston (1991) have fitted for the $CaSO_4$:Tm phosphors combinations of metal filters which flatten the energy response of the phosphor. Azorin and Gutierrez (1989) and Azorin and Furetta (1989) designed a sealed-system method for growing single crystals of Dy-and Tm-doped $CaSO_4$. The crystals were tested and were found to comply well with the ANSI N-545-1975 requirements. The phosphors were suitable for long-term γ-radiation monitoring in low- and variable-dose-rate areas. Abdul Ahad et al. (1990) used $CaSO_4$:Tm TLDs for continuous environmental monitoring of γ radiation. They give radiation dose rates for various locations in Iraq. Nikl (1996) used $CaSO_4$:Tm for a survey of radon in Hungarian homes. Zhang et al. (1993) used $CaSO_4$:Tm TLDs for measuring radiation doses in space aboard a satellite. They report on radiation dose rates below 0.2 mGy per day. The response of environmental $CaSO_4$:Tm TLDs to high-energy photons was studied by Saez-Vergara et al. (1993). Energy dependence of the phosphors under different radiation conditions has been measured in the range 0.6–6.5 MeV. Data indicated that corrections of the TLD readouts have to be made to account for the high energy range. The authors suggest the use of special dose-calculation algorithms for the high-energy measurements. The specific corrections of TLDs for high-energy (4–7 MeV) photon radiation is of special importance around nuclear power plants and high-energy accelerators during operation.

Matsuda and Minato (1991) studied the response of $CaSO_4$:Tm (UD 100, M8) TLDs to α radiation from ^{241}Am. They suggest estimation of the α energy absorbed in the TLD by measuring the radiation daughters. Their measurements gave very good proportionality between the measured values and the absorbed α energies.

The effect of codopants on the TL of Tm-doped phosphors is similar to that of the Dy-doped $CaSO_4$. Atone et al. (1995a) studied the effect of P, Mn and SO_3 codopants in Dy- and Tm-doped $CaSO_4$. The effect of the dopants in $CaSO_4$:Dy was described in sect. 3.2.3. The main difference between the two phosphors was that the enhancement of $CaSO_4$:Tm,P by the codopant was 150% compared to only 60% in $CaSO_4$:Dy,P. It is possible that part of the difference in the enhancement arose from the difference in the TL emission spectra of the two phosphors, and from differences in the spectral response of the reader in the two emission ranges. This has still to be checked by detailed emission spectra measurements in phosphors with and without the P codopant.

Kitahara (1987) studied the self-irradiation of a commercial $CaSO_4$:Tm (UD-200 S) TLD. This is a high-sensitivity TLD. Ten samples, one of each of 10 batches, were used for the measurements. The samples were kept in a lead brick enclosure located underground for 20 days. The average self-irradiation obtained was $2.6 \pm 0.36\ \mu Rad\ h^{-1}$. This radiation was found to be due to the cap of the holder which served as a Sn–Pb alloy for energy compensation. Tokuyama et al. (1990) studied the self-dose and the cosmic ray dose of a UD-200 S TLD. The self-dose was measured in a tunnel where the cosmic rays are attenuated. A self-dose of $0.26\ nC\ kg^{-1}\ h^{-1}$ was measured with and without the Sn–Pb filter of the TLD. The dose of the cosmic rays at sea level was $0.74\ nC\ kg^{-1}\ h^{-1}$.

3.2.5. *$CaSO_4$ activated by other R*

Not much has been done on $CaSO_4$:R phosphors with R different from Dy and Tm. The reason for this is the low TL sensitivity of such phosphors to γ- and X-rays. This has been shown by Nambi et al. (1974) for γ-irradiation. An illustration of these differences is shown in fig. 29 which is based on results by Nambi et al. The figure roughly gives TL intensities integrated over the dosimetric range of 150–300°C for the undoped (ud) and R-activated $CaSO_4$ as obtained after 2.5×10^3 Gy γ-irradiation at RT. The TL of Tm- and Dy-doped samples is seen to be the strongest, and that of Sm is weaker by a factor of

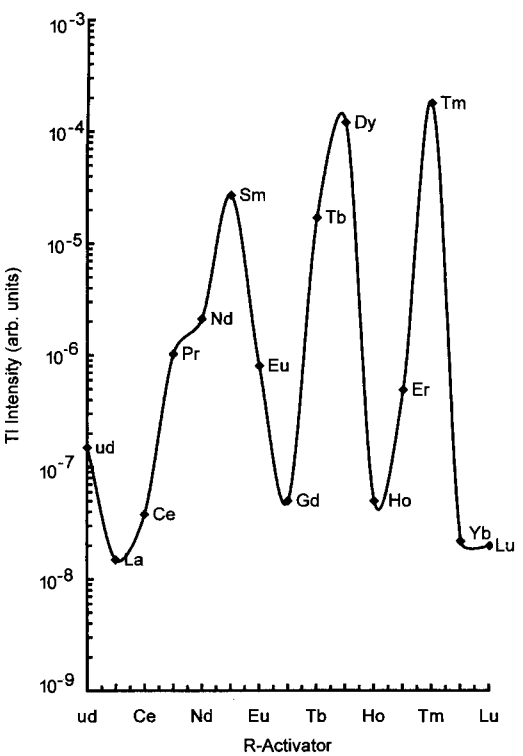

Fig. 29. Relative TL intensity integrated over the range 150–300°C for $CaSO_4$ doped by various R ions.

about 5. We note also that the sensitivity of La- Ce- Gd- Ho- Yb- and Lu-doped phosphors is lower by nearly four orders of magnitude compared to that of $CaSO_4$:Tm, and is even lower than that of the undoped (ud) sample. As will be shown below, $CaSO_4$:Eu makes a very sensitive UV phosphor, which indicates different processes involved in the TL of γ and UV radiations.

$CaSO_4$:Eu phosphors. Nambi et al. (1974) suggested that during the irradiation of $CaSO_4$:R the R ions are reduced, $R^{3+} \rightarrow R^{2+}$, by capturing an electron. During the warming for the TL emission $R^{2+} \rightarrow R^{3+}$ takes place by thermal release of holes and their recombination at the R^{2+}, leaving the R^{3+} in an excited state. To check this model Bapat (1977) studied the PL of UV(254 nm)-excited $CaSO_4$:Eu (0.1 wt%). The irradiated sample showed PL emission at 385 nm characteristic of Eu^{2+} and at 600–700 nm emission bands characteristic of Eu^{3+}. Exposure at RT to a $\gamma(^{60}C)$ dose of 10^3 Gy enhanced the Eu^{2+} emission and reduced the Eu^{3+} bands. Annealing at 500°C, which bleached away the TL, reduced the Eu^{2+} emission and enhanced the Eu^{3+} bands to the original values, which supports the above model. Danby (1988) studied the UV reduction $R^{3+} \rightarrow R^{2+}$ in $CaSO_4$:Eu. He found it to proceed by a charge-transfer transition of the Eu^{3+}–O complex followed by trapping of the hole generated by the charge transfer. He proposed a kinetic model for the process. The UV-induced TL of $CaSO_4$:Eu was found to be correlated with the rate of the Eu^{2+} conversion, but only for UV wavelengths above 230 nm. The exceptionally high TL sensitivity of $CaSO_4$:Eu to UV light is also assumed to be related with the charge transfer, again only for wavelengths above 230 nm. The author presents a full description of the kinetics of the $R^{3+} \rightarrow R^{2+}$ process. The results support the model suggested by Nambi et al. (1974). Calvert and Danby (1984a) studied the TL and the radio PL (RPL) of Eu- and Sm-doped $CaSO_4$ excited at RT by X- and UV radiation. X-irradiated $CaSO_4$:Eu exhibited TL peaks at 110 and 200°C (at 25°C min^{-1}). UV-irradiated Eu-doped samples showed only one peak at 200°C. The X-excited TL of $CaSO_4$:Eu was significantly lower compared to that of the Sm- and Dy-doped samples, while the UV-excited TL of $CaSO_4$:Eu was stronger than that of either the Sm-doped or the Dy-doped samples. The authors stress the possibility of combining a TL and RPL dosimetry system which should provide good sensitivity to both X- and UV radiations using either TL or RPL.

Calvert and Danby (1984b) studied the ESR of single crystals of $CaSO_4$:Eu after X-irradiation. The ESR spectra showed that only one Eu^{2+} site is produced by the reduction of the Eu^{3+}. This site was found to be of orthorhombic symmetry and there was no charge compensation at the Eu ions which occupied substitutionally Ca^{2+} sites. Both Eu^{3+} and Eu^{2+} PL emission were present. Comparison with the results on $CaSO_4$:Eu suggested that the process giving rise to the TL in Gd differs from that in Eu. Dhopte et al. (1991b) used various methods for the preparation of $CaSO_4$:Eu. The PL excitation and emission spectra as well as GCs of the sample were measured. They were able to separate the excitation spectra of Eu^{2+} from those of Eu^{3+}. This is shown in fig. 30 where curves a and b give the emission spectra of Eu^{2+} and Eu^{3+}, respectively, and curves c and d give the respective excitation spectra. Selecting 320 nm for the excitation resulted in practically only the Eu^{2+} (385 nm) emission and excitation at 254 nm gave the Eu^{3+}

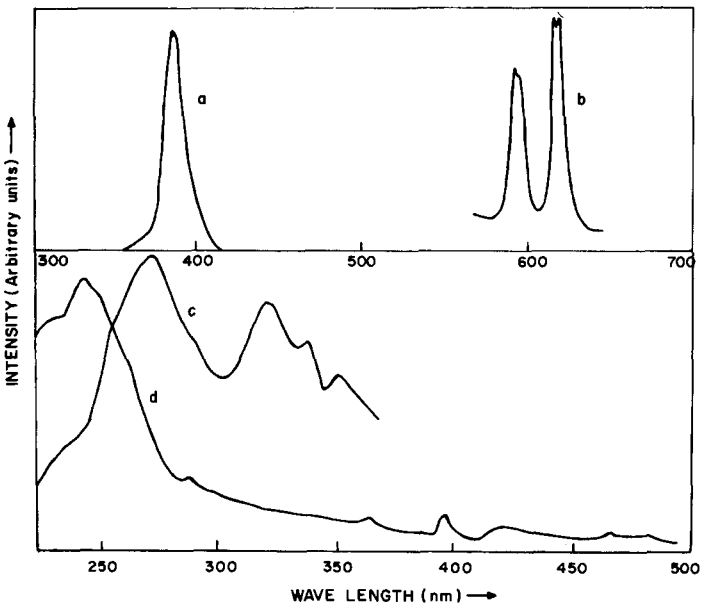

Fig. 30. (a) Eu^{2+} and (b) Eu^{3+} emission spectra of $CaSO_4$:Eu and (c, d) the respective excitation spectra.

emission (near 600 nm). Variously prepared samples behaved differently. Thus sample P-400 (dried at 400°C) before exposure to γ-radiation showed mainly Eu^{3+} emission. Exposure to γ-rays (42.3 C kg^{-1}) reduced the Eu^{3+} and enhanced the Eu^{2+} PL. At the end of the TL run mainly the Eu^{2+} decreased. The P-700 sample (same as P–400 but dried at 700°C) gave very strong Eu^{2+} emission and no Eu^{3+} emission. The authors concluded that samples can be prepared containing predominantly Eu^{2+} or Eu^{3+}. From the excitation spectra it was concluded that Eu^{2+} can be incorporated in several sites. After reading the TL the Eu^{2+} is not fully converted to Eu^{3+}. The results are claimed to support the model given by Nambi et al. (1974) and indicate that the mechanism of γ-induced TL is different from that of UV-induced TL. Upadeo et al. (1994) extended the work by Dhopte et al. (1991b). They worked in parallel on $CaSO_4$:Eu and CaF_2:Eu and measured the temperature dependence, including the remaining areas under the 135°C and the 253°C TL peaks as well as that under the entire glow curve. These were also compared with the Eu^{2+}-related PL. From these and other experiments it was concluded that there is no correlation between the GC above RT and the $Eu^{3+} \rightarrow Eu^{2+}$ and $Eu^{2+} \rightarrow Eu^{3+}$ conversions in both $CaSO_4$:Eu and CaF_2:Eu. This can be explained by a model which attributes the TL to a transfer of the electron–hole recombination energy to the R ion followed by characteristic R-ion emission. It is suggested that this model may be valid for other R-doped $CaSO_4$:Eu and CaF_2 systems.

Upadeo and Moharil (1995, 1997) extended the study of the Eu conversion to various phosphors. They found that compounds that resemble $CaSO_4$:Eu and CaF_2:Eu exhibit

high $Eu^{3+} \rightarrow Eu^{2+}$ conversion. They also observed that no conversion was noticed in stoichiometric Eu^{3+} compounds. The above work has been extended by Nair et al. (1997) of the same research group. The TL and ESR of RT-irradiated $CaSO_4$:R were studied. The TL excitation was either by γ-rays (^{60}Co) or by UV light. The highest Eu incorporation in $CaSO_4$ without formation of aggregates was 0.05 mol%. Aggregates of Eu were found to break by irradiation producing Eu^{2+}. The TL mechanism for γ-irradiated samples was found to fit the model suggested by Morgan and Stoebe (1986, 1990a,b) according to which the electron–hole recombination energy is transferred to the Eu^{3+} ions. The TL is then emitted on relaxation of the excited ions. The UV-excited TL, on the other hand, fitted the $Eu^{3+} \leftrightarrow Eu^{2+}$ reaction. The incorporation of the Eu and the defects produced in $CaSO_4$:Eu differed from those produced in $CaSO_4$:Dy. The various sites of the Eu and Dy in the radiation produced centers and the thermal stabilities of the centers are also described.

$CaSO_4$:Sm phosphors. The TL induced by γ-irradiation at RT of $CaSO_4$:Sm was presented by Nambi et al. (1974) together with GCs of other R-doped $CaSO_4$. These are shown in fig. 27. The relative dosimetric TL intensities for the various $CaSO_4$:R phosphors are shown in fig. 29. The sensitivity of the Sm-doped phosphor is seen to be about one quarter of that of the Dy-doped one. Detailed research even reveals conditions under which the Sm-doped phosphor shows a sensitivity close to that of $CaSO_4$:Dy. Still, only a little work was done on $CaSO_4$:Sm. Its GC as measured by Nambi et al. (1974) contains two main peaks above RT, at about 110 and 200°C. The latter one seems to be composed of overlapping components in a way similar to that shown by the dosimetric TL peaks of the Dy- and Tm-doped phosphors. The TL emission spectrum of $CaSO_4$:Sm gives two bands, at 560 and about 595 nm. Sabnis and Pawar (1980) studied a mixture of $CaSO_4$:Sm with Na_2SO_4. After X-irradiation at RT the GC of the $CaSO_4$:Sm phosphors showed main peaks at 110 and 230°C (at 50°C min^{-1}) with shoulders on the sides of each peak. Mixing with Na_2SO_4 exhibited only the peak at 230°C but broadened by a tail towards higher temperatures. The authors used various methods to determine the thermal depth (E) of this peak. Their results are generally too low, which was caused by the complex broad peak. This explains also the measured high shape factors (up to $\mu_g = 0.60$). Calvert and Danby (1984a) compared the GCs of $CaSO_4$:Sm obtained after RT X-irradiation to those obtained by UV. In the later case the main TL peak appeared near 300°C. The emission spectrum of the peak near 200°C showed four bands in the range 530–660 nm. The authors found the sensitivity to ionizing radiation of $CaSO_4$:Sm to be comparable to that of $CaSO_4$:Dy.

3.2.6. *Other Ca compounds*

This section will not include the calcium compounds discussed in earlier sections.

R-activated CaS. Lehmann (1972) studied calcium sulfide activated by almost all the R elements. His measurements included absorption and emission spectra but not TL. All measurements were made at RT. He found CaS:R phosphors to be poorly luminescent, but the addition of co-activators was found to make them well luminescent. The PL of

the CaS:R phosphors was generally characteristic of R-ion emission. CaS:Nd however did not show any measurable PL. The investigation of the CaS phosphors has been neglected for many years before the 1970s, undeservedly so according to Lehmann. It seems that the reason for this was the chemical instability of CaS which tends to decompose with water, forming H_2S. Jain and Bhawalkar (1975) measured the TL of triply activated CaS. They found that the co-activators do not introduce new trapping levels but change the distribution of traps. Their measurements were limited to 300–400 K and showed the main TL peak at 340–360 K. Vij and Mathur (1975) observed only one peak near 300 K for CaS:Ce. Pandey and Ghosh (1981) worked on the TL of CaS:Ce,Cl in the range 300–450 K. They prepared the phosphor by firing a mixture of the chemicals at 1000°C for 1 hour. The TL excitation was by low-energy (20 kV) electrons, which has limited the excitation to a thin surface layer of the phosphors. The GC exhibited two peaks at 340 and 371 K (at $1.87\,K\,s^{-1}$). The Cl concentrations were fixed (4 wt%) and the Ce varied in the range 0.03–1.25 mol%. The sample with 0.08 mol% of Ce exhibited the strongest TL at 371 K. This peak decreased and practically disappeared at 1.25 mol% of Ce. The trap depths were 0.66 and 1.13 eV and the s-values were 10^8 and $10^{12}\,s^{-1}$ for the 340 and 371 K peaks respectively. It is not certain that the parameters were obtained for isolated single peaks, which makes the calculated parameters doubtful. Patil and Lawangar (1981) worked on CaS:Dy,Ag at various concentrations of both Ag and Dy. The measurements were limited to 300–443 K. The undoped CaS showed one TL peak at about 400 K and the activation added another peak near 330 K (at $0.64\,K\,s^{-1}$). The GCs were affected by both the Dy and the Ag concentrations. The Ag changed the relative intensities of the two TL peaks in such a way that at low Ag concentrations the 335 K peak increased with the Ag concentration, while above 0.05 wt% Ag it decreased with Ag concentration. Variation in the Dy concentrations gave the opposite effect. The kinetic order for the 335 K peak was $b = 1.6$, and the measured E-values varied in the ranges 0.7–0.85 and 0.8–1.0 eV for the 345 and 400 K peaks respectively.

Ghosh and Pandey (1982) examined the role of Cl in CaS:Ce,Cl. They extended the range of the TL measurements to low temperatures. Samples were excited at 100 K by UV from a high-pressure Hg lamp. The GCs contained four peaks at 157, 226, 317 and 349 K (at $0.107\,K\,s^{-1}$) and four more satellite peaks. The TL intensity was quite low, which did not allow emission spectra measurements. The intensity ratio of the integrated TL excited at RT to that excited at 100 K was found to decrease with the Ce concentration from $R > 1$ at 10^{-4} mol% Ce to $R = 0.17$ at 0.9 mol%. This was caused by a comparatively higher concentration quenching of the RT-excited TL. Singh et al. (1982) investigated the effects of Fe, Co, Ni and Cd as codopants in CaS:Ce. Excitation was by laser light. The study is claimed to shed light on the nature of the luminescence centers and on the association of the traps with the dopants. In contrast with earlier work, Ni and Fe were found to act as efficient luminescence killers especially at the short-wavelength (high-energy) Ce emission bands. Ghosh et al. (1986) observed that the TL after X-irradiation of a CaS:Ce sample prepared by the "sulfurizing flux" method showed a TL peak near 470 K. Its intensity however was lower by an order of magnitude compared to the lower-temperature TL. The 470 K peak parameters were found to be $E = 1.42$ eV

and $s = 1.6 \times 10^{14}\ s^{-1}$. The peak could be bleached away by 650 K annealing for 30 min. The 470 K peak appeared only in the first TL run and UV pre-excitation was necessary to obtain it in subsequent runs. This peak is recommended by the authors for TL dosimetry. This seems doubtful because of its low TL sensitivity and the necessity of the pre-irradiation by UV light. Sweet and Rennie (1987) discuss the use of CaS:Ce in UV, X and γ TL dosimetry. The samples were prepared by firing for 3–4 hours at 1000°C. Exposure dose response was not strictly linear. The authors admit that the TL characteristics of the phosphor are not perfect, but express hope to be able to produce an efficient and sensitive CaS:Ce dosimeter in further work. In Sweet and Rennie (1988) the results of the earlier work on CaS:Ce are given in some more detail. They also add results on CaS:Cd,Na as a promising phosphor.

Sweet and Liddell (1990) studied the TL of single crystals of CaS:Ce in the temperature range 8–300 K. UV excitation from a high-pressure mercury lamp gave no TL up to 80 K. Irradiation at 77 K gave four overlapping TL peaks in the range 108–261 K. The authors determined the parameters of these peaks. The E- and s-values and the kinetic orders obtained for the TL peak do not look reliable, presumably because of the complexity of the GCs. Rennie et al. (1990) compared the GCs of single crystals, powders and thin films of CaS:Ce. The TL of the thin films was found to be dramatically different from that of the single crystals and the powders. Bushtruk et al. (1990) have shown that the GCs of CaS:Ce change from fairly defined peaks at low Ce concentrations to a broad cluster at high Ce concentrations (1 at%). Adding an alkali-metal (1 at%) codopant brings back the GC to fairly defined peaks. The TL peaks still differ in peak temperatures and in intensity for added Li, Na or K.

CaS:Ce,Cu (at concentrations 0.01 and 0.001 respectively) phosphors were studied by Green et al. (1988a). Samples were prepared by different methods and were characterized by X-ray diffraction. PL, PL excitation spectra, TL and ESR techniques were applied. Broad overlapping peaks characterized the GC in the range 100–400 K, showing maxima at about 220 K. The phosphors do not seem to be suitable for dosimetry. Green et al. (1988b) extended the earlier work by changes in the sample preparation methods. Increasing the Ce concentration was found to increase and broaden the TL peaks. The authors assign the various TL peaks to particular defects. Chakrabarti et al. (1989) studied the PL and TL of CaS:Ce,Sm UV-irradiated at RT. The GC showed an isolated peak near 100°C and a much weaker peak at 330°C. Both Sm^{3+}- and Ce^{3+}-characteristic bands were observed in the TL emission. The authors suggest a "likely" model for the TL. Optically stimulated luminescence (OSL) was observed in an infrared band at 1100 nm.

The work on CaS:Ce added little to our understanding of the processes involved in the TL emission, and did not contribute positively to TL dosimetry. The reason for this is not only the chemical instability of the host, but also the poor TL emission of the Ce ion. Nambi et al. (1974) have found very weak TL emission in $CaSO_4$:Ce (see fig. 29). It seems that the same is true in the case of CaS:Ce.

Ca borates. Fukuda et al. (1986) studied the TL of CaB_4O_7:Dy and CaB_4O_7:Eu sintered at 950°C. The samples were X-irradiated and heated at 20°C min^{-1}. The TL peaks were divided into three groups: (1) 75–110°C, (2) 170–190°C and (3) 200–275°C. The

TL did not show any supralinearity up to about 100 Gy. The peaks in groups (2) and (3) showed low fading. In a further paper Fukuda et al. (1987) extended the above work by comparing the TL to the TSEE (sect. 2.1.5). The samples contained 0.08 wt% of the activator (Dy or Eu) and were X-irradiated at 77 K. The GCs were recorded up to nearly 400°C. The $CaB_4O_7:Eu^{3+}$ sample showed many TL peaks up to about 50°C and two high-temperature peaks at 190 and about 325°C. Only two TSEE peaks appeared, at 130 and 357°C. $CaB_4O_7:Dy^{3+}$ showed the main TL peaks at 110 and at 250°C and TSEE peaks at 128 and 315°C. The authors suggest that TL peaks not accompanied by TSEE peaks are related to hole traps. Nakamura et al. (1992) examined the PL and TL of sintered $CaB_5O_9Cl:Eu^{2+}$ excited by UV light or by X-rays. The TL emission spectra were characteristic of Eu^{2+} which is assumed to be due to the recombination of free electrons at Eu^{3+} centers. On the other hand, the PL was found to be related to the optical excitation of Eu^{2+} ions.

Calcium phosphates. Little, if any, has been published on the TL of calcium phosphates until 1990. Meijerink and Blasse (1990) studied the TL and PL of $Ca_2PO_4Cl:Eu^{2+}$. Eu^{2+} can occupy two different sites in the host, one with C_2 symmetry and the other with C_s symmetry. The main difference between the two is that the C_s site is considerably larger than the C_2 site. The vibronic coupling strength of the $4f^7 \rightarrow 4f^6$ transition of Eu^{2+} was found to be quite sensitive to the size of the site. RT X-irradiation of $Ca_2PO_4Cl:Eu^{2+}$ (1 wt%) gave two TL peaks at 350 and 412 K (at 0.17 K s^{-1}) and weak peaks at higher temperatures. The 350 K peak emitted at 452 nm, which is also the Eu^{2+} emission under UV excitation at RT. The trap depths obtained by the initial-rise and peak-shape methods are 0.83 and 1.13 eV, and the *s*-values are 1×10^{10} and 6×10^{11} s^{-1} for the 350 and 412 K peaks, respectively. Both peaks gave first order kinetic. During X-irradiation the transition $Eu^{2+} \rightarrow Eu^{3+}$ takes place by trapping a hole. Electrons were assumed to get trapped at halide vacancies. The reverse takes place during the TL emission. It is suggested that the two TL peaks are related with the two available sites.

Fukuda and coworkers studied the TL and TSEE of $Ca_3(PO_4)_2$ doped by various R ions. Fukuda (1990) studied CeO_2-doped samples. The samples were X-irradiated at RT and heated at a rate of 20°C min^{-1}. The GC showed peaks at 100, 128, 230, 320 and 350°C. The peaks appeared in the α-phase of the host obtained by heating in the β-phase. The TSEE showed peaks at 120, 250 and 340°C corresponding to the second, third and fifth peaks in the GC given above. The TL emission of all the peaks is suggested to be due to the process $Ce^{4+} + e \rightarrow (Ce^{3+})^* \rightarrow Ce^{3+} + h\nu$ (350 nm). Fukuda et al. (1992) worked on Sm(0.06 wt%)-doped $Ca_3(PO_4)_2$. The experimental conditions were the same as in the above work. The GC showed peaks at 110, 230 and 320°C emitting at 568, 590 and 640 nm. The authors find β-$Ca_3(PO_4)_2$:Ce,Sm, suitable for TL dosimetry. Fukuda et al. (1993) studied β-$Ca_3(PO_4)_2$:Ce. The peak at 210°C was weak in these samples. Codoping with Tm gave a strong 210°C peak, considered by the authors to be usable for dosimetry. Ohtaki et al. (1993) of the same group worked on Dy-doped $Ca_3(PO_4)_2$, again under the same experimental conditions. TL peaks appeared at 100, 132, 210 and 315°C. The peaks gave a linear dose response at X-ray doses up to 100 C kg^{-1} when saturation starts.

With the Dy concentration the TL was found to rise almost linearly up to 0.2 mol%. The emission was characteristic of Dy^{3+}. After X-irradiation the ESR showed a doublet structure due to H atoms. It disappeared at 130°C, suggesting relation to the 132°C TL peak.

The TL and PL of Eu-doped calcium halosphosphate $Ca_4(PO_4)_2(F,Cl)$:Eu, was investigated by Quang et al. (1996). The powder samples were prepared by a solid-state reaction at 1200°C in air. They were annealed at 400°C for 30 min before the X-irradiation. The non-irradiated samples exhibited PL spectra characteristic of Eu^{3+}, which turned to Eu^{2+} characteristic spectra by X-irradiation. The GC showed a few peaks including high-temperature peaks at 250 and 360°C. Nd^{3+} and Er^{3+} gave similar GCs but with different relative intensities of the various peaks. The high-temperature peaks of the Nd doped samples had their strongest TL peaks at 250 and 360°C. X-irradiation produced in the Eu-doped samples absorption bands at 550–650 nm. Illumination in these bands gave PSL characteristic of Eu^{2+}. This PSL makes the phosphor suitable for medical radiography. The fading of the high-temperature TL peaks was found to be low.

In spite of some suggestions to use the R-doped calcium phosphates for dosimetry it is still far from competing with the high-quality TLDs like the Tm- and Dy-doped $CaSO_4$.

R-doped calcium tungstates. Very little has been published on these phosphors. Grasser et al. (1988) investigated Sm-doped $CaWO_4$ crystals X-irradiated at 77 K. The TL in these crystals was weak. The pure $CaWO_4$ gave a weak TL peak at 280 K and Sm doping did not change this considerably. Adding Nb^{5+} as a compensating codopant resulted in high sensitivity to X-rays due to a strong TL peak at 320 K.

3.2.7. *Sr and Ba compounds*

Some mixed crystals, containing Sr or Ba, for example $LiBaF_3$:Eu, have been dealt with in sect. 3.1.6. These will not be included in the present section. The review in thia section will be divided according to the type of host compound.

Strontium halide hosts. Somaiah and coworkers published three papers on the TL of SrF_2:Eu at Eu concentrations in the range 0.004–42 mol%. The GCs obtained for the various Eu concentrations are given in Somaiah et al. (1991). There are about a dozen TL peaks which the authors divide into three groups: (340, 360–370 K), (460–474, 540–575 K) and (615–635, 680, 720 K). The crystals seem to contain various impurities responsible for some of the TL peaks. It seems that the main valuable result is that the three TL groups appear only in samples containing low Eu concentrations. At medium concentrations the third, high-temperature group disappears and at high Eu concentrations (close to 42 mol%) only the low-temperature TL appears as one broadened peak. Sharma and Somaiah (1992) calculated the TL parameters for the peaks for this wide range of Eu concentrations. The results do not look reliable. The E-values vary largely and range from 0.13 up to 1.15 eV for peaks in the range 400–580 K, and the s-values range from about 10^3 (!) to 10^{11} s^{-1}. The failure seems to have resulted from the complexity of the overlapping peaks. Sharma et al. (1995) measured the radiation-induced optical absorption and the TL emission spectra. They concluded that some of the TL peaks are related with

impurities and others with the SrF_2 lattice. The TL peaks at 460 and 475 K are assigned to electrons released from F-centers and their recombination with holes at Eu-containing recombination centers.

Strontium fluorohalide hosts doped with Yb or Eu were studied by Schipper and Blasse (1991). The paper deals mainly with the PL of Yb-doped SrFBr and SrFCl. The phosphors were prepared by keeping the mixture of chemicals at 980°C for seven days. For the TL measurements the samples were X-irradiated at RT and heated at 10°C min^{-1}. The main TL appeared at 320–340 K, with weaker peaks up to about 480 K. The Eu doping gave a TL sensitivity nearly 3 times that of Yb. The weak TL of the Yb-doped samples is not surprising and fits qualitatively the results for $CaSO_4$:Yb (see fig. 29). The authors stress the similarity of the glow curves of the Yb- and Eu-doped phosphors and conclude that the excitation and TL emission mechanisms are the same for both phosphors.

Strontium sulfide hosts. Shaver and Krongaus (1990) studied the TL of doubly activated SrS:Sm,Tb. The GC was divided into two temperature regions: (1) around 130°C and (2) in the 220–390°C range. The intensity ratio of the light sums in (1) and (2) was found to be of the order of 10^3 after γ-irradiation and only 10^{-2} after visible-light excitation. The authors discuss this effect and suggest its use for selective dosimetry in mixed fields.

Strontium sulfate hosts. Dy-doped $SrSO_4$ (and $BaSO_4$) was studied by Dixon and Ekstrand (1974). The phosphors were prepared by dissolving the high-purity component chemicals in hot H_2SO_4. The deposited small crystals were ground and sieved to obtain 75–180 μm grains. A concentration of 0.4 mol% of Dy was found to give the highest TL sensitivity. The X-irradiated phosphors gave a single TL peak at 140°C (at 1°C s^{-1}). The TL emission appeared at 478 and 568 nm characteristic of Dy^{3+}. The TL sensitivity to 1.25 MeV γ-rays was found to be practically equal to that of Harshaw TLD-900. For 50 keV irradiation the sensitivity of the $SrSO_4$:Dy phosphor exceeded that of TLD-900 by a factor of nearly 7. A 15 min post-irradiation annealing at 90°C reduced the fading of the phosphor to 5% in 10 days storage in the dark at RT. The dose response was found to be linear over a dose range of five orders of magnitude. The phosphor was found to remain energy independent down to about 0.7 MeV. The authors found $SrSO_4$:Dy most promising for dosimetry. The behavior of the Tm-doped phosphor was similar to that of the Dy-doped one.

Shrivastava et al. (1986) studied the TL of RT X-irradiated $SrSO_4$:Dy. The PL before irradiation was characteristic of Dy^{3+} and the emission was at 478, 491 and 572 nm. The strongest TL peak appeared at 57°C (at 70°C min^{-1}), and other peaks showed up at 140, 180 and 220°C. The 57°C peak reached a maximum at 60 s X-irradiation, dropped to a minimum at 90 s irradiation, and grew monotonously at higher doses. The other TL peaks did not show this anomaly. The authors attribute the anomalous behavior of the 57°C peak to structural defects. With Dy concentration the 57°C peak increased up to 0.5 mol%. The 140 and 180°C peaks reached the highest intensity near 0.05 mol% and the 220°C peak at 0.001 mol% of Dy. At this Dy concentration the 220°C peak was prominent in the GC and at a Dy concentration of 0.1 mol% the 57°C peak was practically the only peak in the GC. The GCs obtained for $SrSO_4$:Dy by Shrivastava et al. (1986) differ considerably

from those obtained by Dixon and Ekstrand (1974). The differences possibly originated from various impurities in the chemicals used.

Strontium haloborates. Pu et al. (1995) present a kinetic analysis of Eu^{2+}-doped alkaline-earth haloborates including $Sr_2B_5O_9X:Eu^{2+}$ (X = Cl or Br). The phosphors were synthesized at temperatures close to 1000°C. GCs were obtained after RT X-irradiation and heating at a rate of $0.16°C\,s^{-1}$. The Eu^{2+}-doped Cl haloborate showed its main TL peak at 317 K and a weaker peak at 427 K, while the Br haloborate showed one TL peak at 360 and another at 488 K. The authors present tables of the TL parameters for the various TL peaks. It seems however that the TL peaks were not clean single peaks, which resulted in wrong parameters.

Strontium aluminates. Abbruscato (1971) studied the TL, PL, and optical reflection spectra of $SrAl_2O_4:Eu^{2+}$. The phosphor was prepared by three hours firing at 1700°C in the open air and was deposited as thin layers on a copper substrate. UV (366 nm) was used for the irradiation at 77 K. The GC, up to 300 K showed three overlapping peaks with the maximum at about 200 K. Phosphors with an excess of strontium oxide showed a dominating peak at 120 K (at $10\,K\,min^{-1}$). Other optical properties also depended on the stoichiometric composition of the phosphor. The authors suggest that the PL and TL involve charge transfer. Matsuzawa et al. (1996) studied Dy- and Nd-co-activated $SrAl_2O_4:Eu^{2+}$. The phosphor was prepared by firing at 1300°C with B_2O_3 as a flux and in a mildly reducing atmosphere. Grain sizes were 20–30 μm. Addition of Dy or Nd as codopants resulted in strong phosphorescence. After exposure to UV at RT and heating at a rate of $2°C\,s^{-1}$, the Eu^{2+}(1 mol%)-activated phosphor showed peaks at 30, 80 and 145°C. Adding 2 mol% Dy as codopant gave a broad TL peak at 60°C. Nd^{3+} as codopant gave a broad TL peak at 75°C. The co-activators were found to act as hole traps and to create dense trapping levels. The bright and lasting phosphorescence resulted from thermal release of charge carriers from the shallow trapping levels at RT.

Nakazawa and Mochida (1997) measured the trap depths in $SrAl_2O_4:Eu,R$ using the transient (thermo-) luminescence (TRL, TTL), method. By this method, the temperature was allowed to change slowly. Every 2 seconds the sample was excited for about one second by 365 nm light. The intensities of the AG were then measured at several delay times after the excitation from which the trap depths were calculated. Figure 31 shows the ionization potentials (IP) and the system difference (SD), which means, the energy differences between the $4f^n$ and $4f^{n-1}$ 5d configurations of the divalent R ions. The open circles give the trap depths for Nd, Dy, Ho and Er. Trap depths of other R ions were either too deep or being filled by other ions (Ce, Pr, Gd and Tb). Trap depths of Eu, Sm, Tm and Yb do not appear because they are too shallow to be included in the measured temperature range (80–430 K) or they may be located in the valence band and so do not capture holes. Mochida et al. (1996) used the above method to explain why the strong AG was observed only in Nd- and Dy-codoped $SrAl_2O_4:Eu$ phosphors.

Antonyak and Pidzyrailo (1995) studied the TL of $SrCl_2:Ce$ crystals in the temperature range 77–450 K. At high Ce concentrations (up to 1 mol%) they observed that most of the holes appearing after high-energy irradiation are trapped at the photochromic PC^+ centers. The 400 K TL peak was found to be related with the release of holes from the PC^+ centers

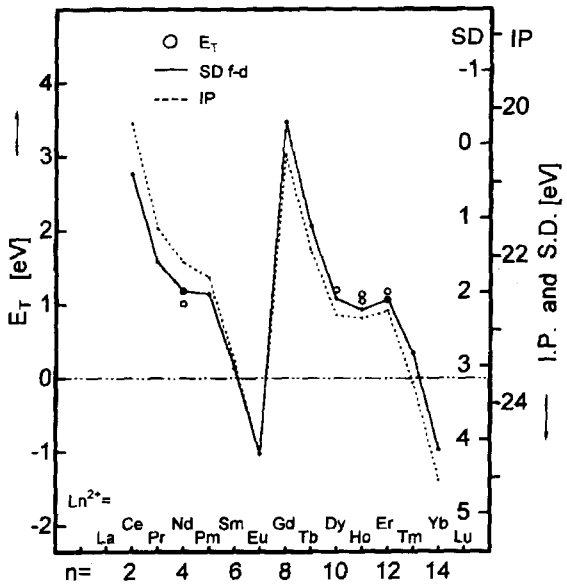

Fig. 31. Ionization potentials, system differences (SD) and trap depths (E_T) of divalent R^{2+} ions in a series of R-codoped $SrAl_2O_4:Eu^{2+}$.

and recombination with Ce^{2+} centers, thus producing $Ce^{3+} + h\nu$. The emission appeared at 365 and 386 nm.

Strontium molybdates and tungstates. Pilipenko et al. (1982) studied the PL and TL of $SrMO_4$:Eu (M=Mo or W). The Eu concentrations were up to about 25 mol%. Specimens were obtained by the solid-state method in air at 1100°C. Irradiations were by X-rays and UV light. At low Eu concentrations the TL peaks for the molybdates appeared at 140, 210, 390 and 400 K. For tungstates the four TL peaks appeared at somewhat different temperatures. At high dopant concentrations the TL decreased and only the low-temperature peak remained. The TL is assumed to be due to electrons released from MO_4^{3-} centers and recombination with holes at luminescence centers. The decrease in the TL at high Eu concentrations was assumed by the authors to be due to the formation of competing Eu^{3+} and other defects in the cation and oxygen sublattices.

Barium compound hosts. More has been published on R-activated Ba compounds compared to Sr compounds. The two host compounds do not vary much in their properties as R-activated phosphors. In fact many papers deal with both Ba and Sr phosphors. The high effective Z of the Ba compounds turns these phosphors further away from tissue equivalence compared to the Sr compounds. There are some variations in the energy dependence and in the TL intensities of the two phosphors. The R ions substitute for the alkaline earths in the lattice. The considerable difference between the ionic radius of Ba (0.153 nm) and that of Sr (0.112 nm) may explain the changes in the GCs of the two compounds. As before, the review will deal separately with the various host compounds.

Barium fluorohalide compounds. Somaiah and Hari Babu (1984) studied the TL and optical absorption of RT $\gamma(^{60}Co)$- or X-irradiated Gd activated (0.5 mol%) BaFCl

single crystals. The strongest TL peaks appeared at 340 and 370 K (at 25 K min^{-1}). The Gd-activated crystals showed a TL sensitivity about 100 times that of the undoped crystal. Ten minutes of X-irradiation showed also peaks at 410, 455 and 560 K. The TL emission exhibited bands at 315 and 450 nm. The 315 nm emission was found characteristic of Gd^{3+}. The parameters were calculated to be about 0.92 and 1.2 eV, 3×10^{8} and 2×10^{9} s^{-1} for the 455 and 560 K peaks, respectively. Standing for 90 days at RT after the irradiation was found to alter the GC, which showed now a prominent TL peak at 430 K. This was accompanied by a change in the irradiation-induced optical absorption. A strong double absorption band at 540–560 nm almost disappeared after the 90 days RT storage. Inabe et al. (1986) studied RT X-irradiated BaFCl:Dy (0.1 mol%). The GC (at 15 K min^{-1}) showed peaks at 320 and 370 K and a weak peak at 410 K. It looked similar to that of BaFCl:Gd except for the high-temperature peaks which were not observed in the BaFCl:Gd crystals. This was perhaps caused by the lower irradiation times (2 min compared with 10 min) and perhaps also by the lower sensitivity of the set-up in the BaFCl:Dy measurements.

Somaiah and Nambi (1987) investigated the TL of BaFCl:Eu^{2+} powders γ-irradiated at RT. The Eu-doped sample showed a TL sensitivity higher by one order of magnitude compared to the undoped sample. The dominating TL peak was at 400 K. Much weaker peaks appeared at 435, 480, 510 and 580 K. The peaks shifted to lower temperatures with irradiation time. All the TL peaks were found to give first-order kinetics. Trap depths ranged from 0.86 eV for the 435 K peak up to 1.25 eV for that at 580 K. All the TL peaks gave the same s-value of about 2×10^{10} s^{-1} and emitted at 390–400 nm characteristic of Eu^{2+}. Zhao and Su (1993) deal mainly with PSL of BaFX:Eu^{2+} (X = Cl or Br) which is of importance for X-ray screens. GCs for RT X-irradiated BaFCl:Eu^{2+} show peaks at 350, 380 and 412 K, with the 350 K peak dominating. The BaFBr:Eu^{2+} sample gave the strongest peak at 412 K and another peak at 370 K. From the decay with time at various temperatures it was concluded that the process of recombination of the TL (and PSL) is monomolecular.

Chen et al. (1997) investigated the TL and PSL of BaFCl:Eu^{2+}. They suggest that the electrons released from F centers get retrapped by other F centers and other defects. This effect lowers the X-ray image-plate sensitivity, which results in a higher exposure to X-rays involved in the PSL energy storage process. To avoid this difficulty the authors suggest the use of single crystals which show lower retrapping, or to anneal the phosphors prior to each exposure at temperatures up to 600°C. The GCs observed by these authors exhibited the main peaks at 400, 540 and 640 K and spectral emission at 540, 670, 865 and 975 nm. Illumination in the 540 nm band gave the strongest PSL. Chen and Su (1995) observed three new high-temperature TL peaks up to 770 K in the GCs of BaFCl:Eu^{2+} and BaFBr:Eu^{2+}. The authors suggest that these high-temperature TL peaks arise from the release of electrons from F-center aggregates, F_2, F_3 and F_4. Meijerink (1996) studied the effect of the chemical composition on the PSL and TL of BaFBr:Eu^{2+}. A stoichiometric BaFBr:Eu^{2+} showed the strongest TL peak at 430 K (at 0.17 K s^{-1}), a weaker peak at 537 K and very weak peaks as shoulders below 430 K. Replacing 12% of the Ba by Sr enhanced a TL peak at 350 K. An excess of fluorine suppressed the high-temperature

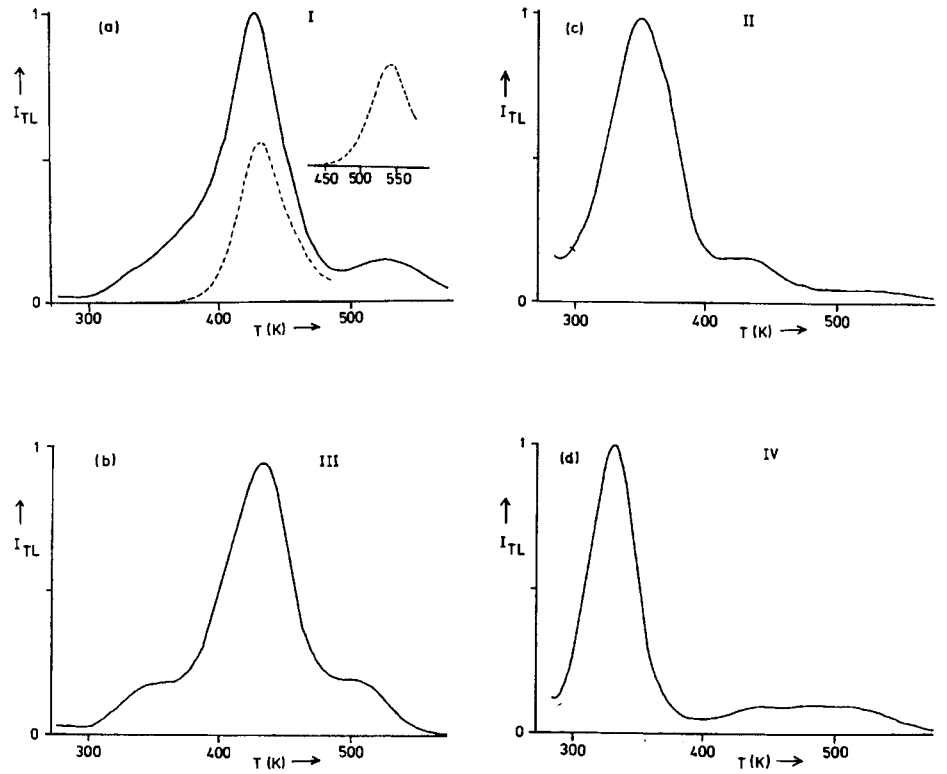

Fig. 32. Glow curves for barium fluorohalides: (a) BaFBr–Eu^{2+}; (b) $Ba_{0.88}Sr_{0.12}FBr:Eu^{2+}$; (c) $BaF_{1.12}Br_{0.88}:Eu^{2+}$ and (d) $Ba_{0.88}Sr_{0.12}F_{1.09}Br_{0.91}:Eu^{2+}$.

peaks leaving the 350 K dominating. The $SrFBr:Eu^{2+}$ with an excess of fluorine left the 330 K peak dominating. The GCs for the above four cases of chemical composition are shown in fig. 32a–d. Analysis of the results suggested that the TL peaks are related with F centers. Harrison et al. (1991) used the TL of BaFBr:R (R = Ce, Eu, Tb, Dy and Yb) to study the PSL mechanism. RT β- or γ-irradiation showed GCs with distinct peaks at 350 and 520 K, and weaker peaks in the range 600–750 K. The TL sensitivity was highest for the Eu-doped samples, one order of magnitude lower for the Ce- and Tb-doped samples, and lowest for the Dy- and Yb-doped samples. These intensity ratios have not been corrected for the spectral response of the reader. Still, the relative sensitivities of the various R-doped samples are much different from those obtained for $CaSO_4$:R (fig. 29). The authors conclude that BaFBr:R phosphors should be suitable as sensitive storage phosphors for the retention of images implanted by ionizing radiation. Luminescence properties like PL, TL, XL and PSL were found by Starick et al. (1993) to depend strongly on the phosphor composition, which depends on the preparation method. X-ray powder diffraction has shown that the BaFBr matrix is affected in the course of evaporation of

the $BaBr_2$–BaF_2 suspension. Firing at 700–900°C proved to be of great importance in the formation of the matrix as an efficient storage phosphor. The PSL efficiency and the TL efficiency were affected strongly by the heating and cooling. The highest PSL intensities were obtained at the lowest cooling rates from 700–900°C. Other effects of the preparation methods are also described in the paper.

The mechanism involved in the emission of the PSL in BaFBr:Eu has been studied by several groups. Von Seggern et al. (1988) accepted the monomolecular mechanism. It assumes the existence of complexes of F-center electron traps together with Eu^{3+} as recombination centers at close proximity. Optical excitation is assumed to transfer the F-electron by tunneling to the neighboring Eu^{3+}, converting it into Eu^{2+} with the characteristic 390 nm emission. The model is claimed to explain quantitatively the short-time behavior and qualitatively the long-time behavior of the PSL. Bradford et al. (1997) found a power-law dependence of the PSL decay for longer duration and a weak dependence of the laser-stimulated PSL on temperature. These results support the monomolecular mechanism. On the other hand, Takahashi et al. (1984), Iwabuchi et al. (1991) and others present evidence for the bimolecular mechanism in BaFBr:Eu (and BaFCl:Eu). The strongest arguments for this model are that the PSL was found to be accompanied by PC, indicating excitation of the electrons to the CB, and that the spectra of the PSL, PC, OA and ESR decay correspond with one another. These results are in disagreement with the tunneling mechanism.

Miyahara et al. (1986) have developed an excellent X-ray storage detector. It is based on a He–Ne laser used in the reading of the PSL of an X-ray storage BaFBr:Eu^{2+} screen. The detector has a 100% efficiency for X-rays of 8–17 keV and a spatial resolution of better than $0.2 \times 0.2\,mm^2$. The X-ray dose needed with this detector was found to be smaller by several orders of magnitude compared with high-sensitivity photographic X-ray films. It also showed a linear dose dependence over more than 5 orders of magnitude of the X-rays.

Upadeo et al. (1998) studied the PL, TL and PSL of BaFCl:Eu. They used two types of powder samples. After the precipitation, washing and drying one type was heat-treated at 973 K under vacuum. The other type was treated in the open air, thus introducing oxygen impurities as charge compensators. The vacuum-treated samples showed strong Eu^{2+} PL while the PL of the oxygen-including samples did not show any Eu-characteristic PL. The GCs of the two types of samples also differed from each other. The TL emission spectrum, however, was characteristic of Eu^{2+} in both types. From these and other results including ESR spectra the authors concluded: (a) The reduction $Eu^{3+} \rightarrow Eu^{2+}$ is more probable than the opposite conversion $Eu^{2+} \rightarrow Eu^{3+}$. (b) The $Eu^{3+} \rightarrow Eu^{2+}$ conversion takes place at sites close to F-centers. (c) The Eu^{2+} acts as an efficient luminescence center. (d) The TL process differs from that of the PSL. The TL involves migration of holes to F centers and the PSL involves migration of F centers to holes.

The applications and mechanisms of PSL phosphors for X-ray imaging were described by Crawford and Brixner (1991). The paper depicts the requirements and the mechanisms of high PSL efficiency phosphors. It deals mainly with BaFCl:Eu^{2+} and BaFBr:Eu^{2+}.

Hydrogen ions are assumed to play an important role in these phosphors as is clearly demonstrated in the paper.

Xia and Shi (1997) studied the ESR, TL and PSL of $BaLiF_3:Eu^{2+}$. They concentrated on the PSL and on the possible application of the phosphors as energy storage plates for X-ray diagnostics. The maximum for PSL excitation appeared at 660 nm which is convenient for the He–Ne laser, and the PSL emission spectrum at 415 nm is at a wavelength of high sensitivity of PMs. Taking into account also the comparatively high effective atomic number of $BaLiF_3$ (50.9) and the resulting high X-ray absorption, the authors conclude that $BaLiF_3:Eu^{2+}$ should make an efficient phosphor for X-ray diagnostics which can be expected to reduce the patients exposure dose to X-rays.

Barium sulfate hosts. Dixon and Ekstrand (1974) have compared the TL sensitivities of $SrSO_4$:Dy and $BaSO_4$:Dy (see Sr sulfates above). The sensitivity of $BaSO_4$:Dy to 1.25 MeV γ-rays was about 0.25 compared to Harshaw TLD-900. Yet, for 50 keV radiation it was nearly 3 times that of Harshaw TLD-900. Paun et al. (1977) found the TL sensitivity of $BaSO_4$:Sm (and $BaSO_4$:Ce) the lowest of all the MSO_4:Sm compounds (M = Mg, Ca, Sr and Ba). The $MgSO_4$:Sm phosphor gave the highest sensitivity. Taking into account that it is also closer to tissue equivalence, $MgSO_4$:Sm proves to be superior to the other alkaline-earth sulfate TLDs. Atone et al. (1995b) have incorporated Eu in $BaSO_4$ as Eu^{2+} or Eu^{3+}. They observed that the $Eu^{3+} \rightarrow Eu^{2+}$ conversion is of importance in UV-induced TL in $BaSO_4$:Eu. The low UV efficiency in this phosphor is attributed by the authors to poor $Eu^{3+} \leftrightarrow Eu^{2+}$ conversions. This is in contrast with the high efficiency of conversion in the analogous $CaSO_4$:Eu phosphor.

Okamoto et al. (1986) developed a TL detector sheet for the study of hadronic electromagnetic cascade showers in ultra-high energy interactions. It is based on $BaSO_4$:Eu powders fixed with NH_4Cl and NH_4SO_4 fluxes. High-purity chemicals were used. The shape of the GC and the TL sensitivity was found to change drastically with the concentration of the two fluxes. The concentrations of Eu and of the fluxes were varied to give optimal characteristics needed for a shower detector. The GC showed one dominating TL peak at 200°C. The final detector showed good dose linearity over seven orders of magnitude and low fading. Sheets of $BaSO_4$:Eu were used by Wada et al. (1995) for the detection of super-slow 1–16 keV massive particles of Ar^+. The ion micro analyzer was used for the readout. More energetic 0.8 MeV Ar^+ was also measured. The authors conclude that the $BaSO_4$:Eu sheets are efficient for low energy ions.

Azorin et al. (1991) developed a $BaSO_4$:Eu TLD. It was embedded in a polytetra fluoroethylene sheet. Discs cut from the sheet were used for TL dosimetry. Its GC showed one TL peak at 540 K of nearly first-order kinetics. Its dose response was linear in the range 4 mGy–50 Gy, and its TL sensitivity to γ-rays was nearly 4 times that of $CaSO_4$:Dy. It is recommended as a successful TLD. Azorin and Rubio (1994) studied the optical absorption and the TL of RT γ-irradiated $BaSO_4:Dy^{3+}$ (0.05 mol%). It showed TL peaks at 407, 420, 442 and 487 K (at 10 K s^{-1}). The emission of all TL peaks was the same and was characteristic of Dy^{3+}. The 420 K peak showed second-order kinetics, other peaks showed first-order kinetics. The four TL peaks gave E-values of 2.35, 2.43, 3.36 and 1.92 eV as obtained by total-GC fitting. These results do not look reliable. The dose response was

linear over the range 10 mGy–20 Gy. The absorption spectra taken after the γ-irradiation helped to identify SO_4^-, SO_3^- and O^- centers responsible for the TL. The authors suggest the application of the phosphor as a useful TLD.

Rao et al. (1995) studied the TL, PL and ESR of $BaSO_4$:Eu and $BaSO_4$:Eu,P. $BaSO_4$:Eu gave the maximum sensitivity at a Eu concentration of 0.2 mol%. The P-codoped samples contained 0.5 and 0.2 mol% Eu and P respectively. The P codoping enhanced the TL by a factor of 5–6 and its sensitivity to γ-rays was 3 times that of $CaSO_4$:Dy. The TL enhancement by P was found to be linked with P^{5+} charge compensators and increased incorporation of Eu into the $BaSO_4$ lattice. The ESR showed two types of SO_2^- radicals. Thermal bleaching of the two ESR spectra was found to coincide with the temperature of the two main TL peaks at 170 and 250°C. The two SO_2^- defects were thus related each to one of these TL peaks.

Shinde et al. (1996) explored further the dosimetric properties of $BaSO_4$:Eu,P using various preparation methods. The co-precipitation method followed by 1 hour at 900°C gave the most suitable results. $BaSO_4$:Eu,P (0.5 and 0.05 mol%) gave the highest TL sensitivity (5.3 times that of $CaSO_4$:Dy (0.05)). The γ-sensitivity of $BaSO_4$:Eu,P (0.5 and 0.2 mol%) was only 2.8 times that of $CaSO_4$:Dy. Yet it gave a better GC structure. Its UV sensitivity was 640 times that of $CaSO_4$:Dy. This phosphor showed good dose linearity in the range 0.1–10 Gy and only a slight deviation from linearity in the range 10–100 Gy. Its fading was found to be 5% in 30 days. $BaSO_4$:Eu,P (0.5, 0.2 mol%) is suggested for application in personnel and environmental dosimetry. The higher-sensitivity phosphor (with 0.05 mol% of phosphorus) is recommended as an X-ray storage phosphor.

Rao et al. (1996) concentrated on the correlation between the ESR, TL and PL of the P-codoped phosphor. The study revealed an almost one to one correlation in the growth of the dosimetric TL peak (at 215°C) and that of the SO_2^- radical. Both increased linearly with the dose in the range $1–10^3$ Gy. The TL, ESR and the PL all behaved similarly upon annealing and all reached a maximum after annealing at 1173 K as shown in fig. 33. These results of Rao et al. support the earlier assumption that the TL enhancement (by a factor of 5.3) by the addition of the P codopant results mainly from an increased intake of Eu^{2+} into the lattice.

Bhatt et al. (1997) compared the dosimetric characteristics of (I) $BaSO_4$:Eu and (II) $CaSO_4$:Dy, both as teflon discs of the same dimensions punched out from the phosphor sheets. The TL dosimetric peaks appeared at about 220°C for both the phosphors. The TL sensitivity of phosphor I was 5.8, i.e. 11 times that of phosphor II when measured with an EMI 9524A and 6255S PMs respectively. The photon energy dependence of phosphor I was considerably higher than that of phosphor II. Both phosphors showed linear dose response. The UV(254 nm) response of phosphor I was about 3400 times that of phosphor II. The optical fading on exposure to 200 nm light was 14% and 8% in 8 hours for phosphors I and II respectively.

Vlasov and Karezin (1993) report on a strange effect of wave-like fading of a $BaSO_4$:Eu phosphor as a function of the Eu concentration. They interpret this effect to be due to clusters of 8–9 atoms when the Eu exceeds 1.5 mol% and electron retrapping processes

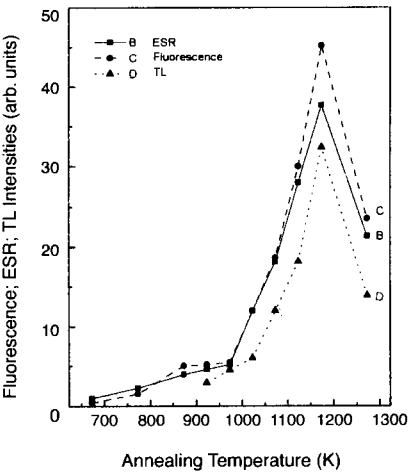

Fig. 33. Dependence of the ESR (B), PL (C) and TL (D) of $BaSO_4$:Eu,P on the annealing temperature.

take place in the clusters. It seems however that the effect has to be investigated more deeply to make sure that it is not caused by an experimental artifact.

Kawada and Sakaguchi (1990a) compared the TL and the ESR of the SO_3^- radical in La- and Eu-doped $BaMg(SO_4)_2$ powders (115–170 mesh). Samples were prepared by two methods: (A) preparation of $BaMg(SO_4)_2$ by solid-state reaction of a mixture of $BaSO_4$ and $MgSO_4$ carried out at 500°C. The $BaMg(SO_4)_2$ powder was then mixed with $R_2(SO_4)_3$ powder (R = La or Eu) and subjected to a solid-state reaction at 700°C. The second method (B) was a solid-state reaction of all the components at 1000°C followed by annealing at 750°C. The main TL peak appeared at 150°C. The effect of the dopants was found more significant in samples (B) compared to (A). The effect of the dopants on the ESR and TL in $BaMg(SO_4)_2$:R was weaker compared to that in $K_2Mg_2(SO_4)_3$:R and especially $K_3Na(SO_4)_2$:R measured by Kawada and Sakaguchi (1990b). The behavior was qualitatively similar for all the above compounds. For example, the TL intensity in the Eu-doped samples was higher than that with La doping. In contrast with this the ESR increased with La doping and decreased in the Eu-doped samples.

Iwata et al. (1993) describe a $BaSO_4$:Eu phosphor fitted for measurements of spatial dose distribution around radioactive sources. The phosphor is embedded in a flexible teflon sheet about $40 \times 50\,cm^2$ and $200\,\mu m$ thick. Its dose response was found to be linear in the range 2×10^{-5}–$50\,Gy$ and it was insensitive to room light. The phosphor is either wrapped around or rolled and put into the radiation field to be measured and the distribution is printed out with a digital readout system. The phosphor sheet has many clinical applications.

Borchi et al. (1991) used an improved deconvolution method allowing general-order kinetics to determine the TL parameters from a GC obtained for a $BaSO_4$:Eu (heating rate $7\,K\,s^{-1}$). The GC deconvolution was into six TL peaks and the TL parameters are given for all the peaks. In spite of the care taken in the treatment of the phosphor and the

improvements in the deconvolution program the TL parameters seem not to be accurate. Repeating the measurements on a GC obtained at a much lower heating rate (say 0.5 $K\,s^{-1}$) should give an indication of the accuracy of the method.

Other Ba-compound hosts. Under this heading will be included R-activated Ba compounds on which only little work has been published. Natarajan et al. (1986) studied the TL of $BaCO_3$:Eu and $BaCO_3$: ^{241}Am. ESR was used for the identification of the radiation-produced defects involved in the TL. RT γ-irradiated $BaCO_3$:Eu indicated the formation of O_2^- and CO_3^- radicals. The TL showed peaks at 383 and 430 K. Na helped to stabilize Na^+–O_2^- complexes with an important role in the TL process. The $BaCO_3$:^{241}Am phosphor exhibited TL peaks at 357, 420 and 500 K and showed only CO_3^- radicals. The authors suggest that the missing of the oxygen radicals was caused by internal heating of the sample by the α-radiation from the ^{241}Am. It seems that this assumption can be checked by lowering the temperature, say to 250 K, or by utilizing samples with a lower concentration of Am.

Little has been published on the TL of R-activated BaS. Thomas and Nampoori (1988) did some work on the TL of BaS doubly activated by Ca, Ce and by Cu, Ce. The TL of BaS:Ce was enhanced considerably by Cu as coactivator. It emitted in the blue. The main peak appeared near 350 K. It seems to be a complex of at least two overlapping peaks, which reduces the reliability of the measured E- and s-values (about 0.5–0.6 eV and $10^6\,s^{-1}$).

A short description of the TL and ESR of $Ba_3(PO_4)_2$:Eu was given by Gavrilov and Krongauz (1975). It showed a paramagnetic ESR signal whose intensity was directly related to that of the TL. The main TL peak in the GC appeared near 150°C.

Schipper et al. (1993) studied the La^{3+}-codoped $Ba_3(PO_4)_2$:Eu^{2+} stressing its efficiency as a storage phosphor. After RT X-irradiation it showed an intense TL at 335 K which was stronger by two orders of magnitude compared with the non-codoped sample. The TL energy remained when the sample was stored in the dark for several days (temperature not specified). Na^+ and K^+ were found to suppress the TL. The trap depth of this peak was about 0.75 eV. Its shape factor was found to be $\mu_g = 0.46$. The stimulated optical emission was characteristic of Eu^{2+}. In addition there appears a broad emission band ascribed to a phosphate group close to the La^{3+} ion. The EPR reveals the presence of H^0 after the irradiation which indicates that the addition of La^{3+} in a Ba^{2+} site introduces H^+ into the lattice which acts as an electron trap. The TL is obtained by thermal release of the electrons at the H^0 centers. The obtained storage capacity was found to be comparable to that of BaFBr:Eu^{2+}. In a more recent paper Schipper et al. (1994) studied the X-ray storage of $Ba_3(PO_4)_2$ doped with various R^{3+} ions. All the studied phosphors showed high efficiency as X-ray storage phosphors. The TL mechanism however was not the same for all the dopants. Ce- and Gd-doped phosphors showed after X-irradiation the presence of H^0 in a way similar to that observed in $Ba_3(PO_4)_2$:La^{3+} but the EPR signal disappeared at a temperature below that of the TL emission. Pr- and Tb-doped phosphors did not show the H^0 centers. The TL emission spectra were characteristic of R^{3+} emission. Codoping with Eu^{2+} of all the above phosphors changed the GCs, and the Eu^{2+} took up the recombination energy.

Meijerink and Blasse (1989, 1991) studied the Eu^{2+}-activated phosphors $Ba_5SiO_4Br_6$ (in the 1989 paper), $Ba_2B_5O_9Br$ and $Ba_5GeO_4Br_6$ (in 1991). The investigation concentrated on the PSL of the phosphors and their possible use as X-ray storage phosphors for scanning in computerized radiography using a He–Ne laser (633 nm). The three phosphors behaved similarly. The TL of the first phosphor showed an emission band near 440 nm, characteristic of Eu^{2+} ions. Its PSL excitation spectrum exhibited one band below 500 nm and a second at 610 nm. The latter is suited for stimulation by the He–Ne laser. With the Eu concentration the PSL increased linearly up to 0.25% of Eu. A short response time is essential for fast scanning. This was 0.64 μs compared to 0.8 μs for BaFBr:Eu^{2+} used as an efficient storage phosphor. The $Ba_2B_5O_9Br$:Eu^{2+} phosphor showed a TL emission at 420 nm which consists of two bands at 411 and 434 nm characteristic of Eu^{2+} at two lattice sites. The PSL excitation showed bands at 510 and 620 nm; the latter is suitable for He–Ne laser excitation. This phosphor was found to be comparable with $Ba_5SiO_4Br_6$ as an X-ray storage phosphor. The $Ba_5GeO_4Br_6$:Eu^{2+}PSL was found to be similar to the other two phosphors. The replacement of Si by Ge was found to lower the stimulating laser light needed to deplete the phosphor.

Summing up sect. 3.2 one can say that the alkaline-earth compounds, and particularly the $CaSO_4$:Dy phosphor, make excellent phosphors for TLD. The $CaSO_4$:Dy phosphor has been improved and it serves practically as a very high-sensitivity and high-stability TLD. It seems, however, that other alkaline-earth phosphors have been neglected. For example, the Mg-compound phosphors seem to have better properties than $CaSO_4$:Dy. They are extremely close to being tissue equivalent, and they show better energy independence than $CaSO_4$:Dy. The sensitivity of some of the Mg-compound phosphors is also very high. Thus, Bhasin et al. (1976) have reported for a Mg_2SiO_4:Tb phosphor a sensitivity 80 times that of the LiF TLD-100 phosphor. Further study of these and other alkaline-earth phosphors can be expected to lead to further improvements.

3.3. *Other phosphors*

In this section we will discuss phosphors not dealt with in sections 3.1 and 3.2.

3.3.1. *Zn and Cd compounds*

The PL and TL of Zn compounds, especially ZnS, has been studied extensively. Very little was published, however, on R-activated Zn compounds. Anderson et al. (1965) worked on the PL of Tb-, Nd-, Tm- and Dy-doped ZnS. They found a strong tendency of the R ions to pair with other lattice defects in the presence of excess S. At least four distinct sites were observed for the R ions in the ZnS lattice. Tripathi et al. (1980) studied the TL of doubly doped ZnS:Tb,Cu and ZnS:Tb,Ag. The phosphor powders were fired for 40 min at 1020°C. The TL was studied up to 420 K and the main peaks above RT appeared near 300 K for the Tb,Cu activators and at about 310–320 K for the silver codoping. The trap depths for the main peaks were about 0.6 eV. Tripathi et al. (1991) worked on the TL of ZnS:Dy and ZnS:Dy,Mn excited by 365 nm mercury light. The GCs above RT exhibited maxima at about 310–320 K. Trap depths E calculated for the main peaks were

0.6–0.8 eV in the range 300–380 K, and s-values were of the order of $10^9\ s^{-1}$. Tripathi et al. (1993) studied ZnSe:Pr and ZnSe:Pr,Sm. Again the TL parameters were calculated and were found to vary with the activator concentrations. So far, the Zn compounds do not look promising as TLD phosphors.

Most of the published work on R-doped Cd compounds deal with Eu-activated CdF_2. Godlewski et al. (1981) studied the TL of CdF_2:Eu crystals. A combination of OA, ESR and electrical conductivity measurements enabled them to give a model for the TL. The main TL peak of CdF_2:Eu appeared at about 170 K. Its activation energy was 0.35 eV. The ESR spectrum and the OA related to Eu^{2+} decayed thermally with the emission of the 170 K TL peak. Resistivity measurements by Trautweiler et al. (1968) suggested the existence of a Eu level 0.33 eV below the conduction band of CdF_2:Eu. Based on the above results Godlewski et al. proposed a model for the mechanism of the 170 K TL peak. In this model electrons are released from Eu^{2+} combinations and recombine with interstitial F^- or substitutional oxygen ions nonradiatively. The recombination energy is then transferred to a nearby Eu^{3+} with the emission of the 170 K TL characteristic of Eu^{3+}. Similar conclusions were reached by Hommel et al. (1975) and by deMurcia et al. (1982). The TL peaks appeared in the range 100–300 K with the main peaks below 200 K. The TL was accompanied by TSC peaks appearing at about 10 K above the corresponding TL peaks. The TL (and TSC) maxima depended on the Eu concentration. The measured activation energy for the 170 K TL peak was 0.35 eV. The suggested TL model is essentially the same as that proposed by Godlewski et al. (1981). Hommel et al. (1975) stress that the electrical resistivity of CdF_2:Eu is stronger by several orders of magnitude compared to that of all other R-activated CdF_2 crystals.

Benci et al. (1990) studied the effect of annealing on the glow curve of CdF_2:Eu (0.1–0.2 mol%). Excitation was by X-rays or by UV at liquid-nitrogen temperature. The heating rate was $0.1\ K\ s^{-1}$. Five seconds after the irradiation the GC exhibited a complex of two peaks at 210–230 K. After an hour standing the 230 K peak disappeared, leaving a peak at 210 K. Quenching from 600–700°C gave a TL peak at 160–170 K. X-irradiation resulted in a peak at 160–170 K with a shoulder above 200 K. The latter disappeared after one hour standing. The effect of quenching from 600–700°C was attributed to dissolution of Eu^{3+}–F_i aggregates. Thermal activation energies were obtained by the fractional TL method. In this method the heating is done by short heating and cooling cycles, when the E-values are calculated from each cycle. The 160–170 K TL gave $E = 0.33$ eV and that at 210–240 K gave $E = 0.43$ eV. The low s-values of 10^7–$10^9\ s^{-1}$ were assigned to strong retrapping. In another paper from the same laboratory (Nagornyi and Pospisil 1990) the low s-values are explained by the dependence of the probability of energy transfer on intercenter distances.

Przybylinska et al. (1992) proposed a model for the TL of CdF_2:Eu. It is based on extensive studies using OA, PL and TL. Out of 17 types of complex centers of various symmetries only two were found to take part in the TL. These were the Eu^{3+}–O_s^{2-} and Eu^{3+}–F_i^- complexes (O_s^{2-} stands for a substitutional oxygen and F_i^- is an interstitial fluorine ion). Annealing of the crystal at 500°C in fluorine was found to show an OA and PL emission at 290 nm and annealing in oxygen resulted in a band at 260 nm. These

annealings produced the Eu^{3+}–F_i^- and Eu^{3+}–O_s^{2-} complexes of symmetries C_{3v} and C_{4v}, respectively. These two centers were found to be excited easily by UV. For the TL the crystal was excited by UV at 100 K. The strongest TL was obtained for 1 mol% of Eu. In the proposed TL model the above complexes act as sources for electrons and as recombination centers and the Eu^{3+} at a cubic symmetry site acts as an electron trap. The allowed transitions in fluoride (or oxygen) are assumed to take part in the TL excitation process. The TL in CdF_2:Eu is assumed to be activated by a charge-transfer process from the C_{3v} and C_{4v} Eu^{3+} complexes to isolated Eu^{3+} forming Eu^{2+}. The electrons are assumed to be autoionized from the coactivator-excited states through lattice relaxation-induced potential barriers. The barriers for the ionized F and O coactivators are shown to be responsible for the activation energies of 0.36 and 0.44 eV for the C_{3v} and C_{4v} complexes resulting in the 165 and 185 K TL peaks, respectively. The model is claimed to explain all the experimental results. A deeper analysis of the results is, however, needed to tell if the proposed model is the only one which fits the experimental results.

Insulating CdF_2:R crystals are converted into n-type semiconductors after annealing (at 500°C) in Cd vapors. DeMurcia et al. (1980) studied the transfer through the conduction band of electrons from shallow hydrogen-like Sm^{3+} donor states to Sm^{3+}–F^0 complexes in n-type CdF_2:Sm^{3+} crystals. TL and TSC curves were taken simultaneously for these measurements. A broad dominating TL peak near 115 K, missing in the TSC of CdF_2:Eu^{3+} and undoped CdF_2, was taken to be due to thermal release of electrons from Sm^{3+} donors. The activation energy for electron capture in non-cubic F^0 sites was found to be 0.032 eV.

3.3.2. *Zr compounds*

Kirsh and Townsend (1987) and Chee et al. (1988) studied the TL of natural zircons ($ZrSiO_4$). They found in the natural zircons (and in some synthetic crystals) that the TL emission spectra are dominated by lines near 380, 480 and 580 nm characteristic of R impurities. Dy^{3+}, Tb^{3+} and Eu^{3+} lines were observed. Their intensities varied in samples from different locations. The Dy emission in zircons spread from 470 to above 800 nm and the GC after X-irradiation at RT showed composite peaks at about 110°C and in the range 200–400°C. Kirsh and Townsend (1987) present results of determination of the TL parameters for each of the resolved TL peaks. The Dy^{3+}-related TL was attributed to recombination at the Dy^{3+} sites. The TL emission spectra of $ZrSiO_4$:R near 100°C were found to cover the whole recorded spectrum while the emission of the higher temperature peaks was more limited. Chee et al. (1988) present three-dimensional plots and contour maps for zircons from various locations. The TL peaks and relative intensities of the various peaks in green zircons were found to alter with the storage after X-irradiation. The authors relate these effects to anomalous fading. Defect models for some of the centers are given.

Zircon is often present in geological and archaeological materials. The mineral can therefore be used for dating. Templer (1985) suggested using the intense TL peak near 100°C for dating. The mineral is often found in U-rich minerals, when its TL reaches saturation under the intense radioactivity. Under these conditions Amin and Durrani

(1985) observed a shift of the emission to long wavelengths, where the sensitivity of readers is low. Jain (1977) observed that zircon grains from beach-sand heated to 1500°C show a considerable increase in their TL sensitivity. The TL emission of the sand-zircon was found by Jain to be characteristic of Tb^{3+} ions.

Arsenev et al. (1980) studied the XL and TL of R-doped mixed crystals of $0.9ZrO_2$–$0.1Y_2O_3$. For the TL measurements the crystals were X-irradiated at RT. The concentration of the various R dopants was 1%. The obtained GCs exhibited two or three peaks in the range 300–600 K. Hsieh and Su (1994) describe the UV-induced TL of ZrO_2:Er (1–20 mol%). Pellets of various thicknesses sintered at 1100 and 1300°C as well as thin films were used. The heating rate for the TL was 20°C s^{-1}. The GC showed three peaks, at 40, 90 and 210°C. The same peaks appeared in the GC of undoped ZrO_2, but at a much lower intensity. The TL of the pellets sintered at 1100°C was higher compared to that of the pellets sintered at 1300°C.

Su and Yeh (1996a) describe the TL of ZrO_2:Er pellets sintered at temperatures in the range 1000–1500°C. The main TL peak appeared below 90°C (at 15°C s^{-1}) with weaker peaks at 60 and ~180°C. Mixing with LiF strongly reduced the TL. Su and Yeh (1996b) used water-resistant ZrO_2:Er sintered pellets as a detector for measurements of the attenuation coefficients in water of UV light in the range 253–365 nm.

3.3.3. *Yttrium compounds*

Hersh and Forest (1970) studied the storage efficiency of various phosphors including Y_2O_3:Eu^{3+} and YVO_4:Eu^{3+}. The X-ray storage efficiency of Y_2O_3:Eu^{3+} was found to be about 4 times that of YVO_4:Eu^{3+}, but considerably lower compared to ZnS:Ag^{1+} and ZnS:Cu^{2+}. The proposed model for the TL in the above Eu^{3+} phosphors is trapping of an electron by Eu^{3+} during the X-irradiation, converting it to Eu^{2+}. During the TL emission a hole is assumed to recombine with the electron at Eu^{2+}, converting it to (Eu^{3+}). The excited Eu^{3+} then relaxes with Eu^{3+}-characteristic emission. Tsukuda (1981) studied black Y_2O_3:Eu (0.1 mol%). The black phosphor was obtained by annealing at temperatures above 200°C in an H_2 atmosphere, and under high pressure. The black phosphor was found to contain ion vacancies serving as electron traps, and the main TL peak appeared at 210 K (at 0.05 K s^{-1}). Mikho (1981) found in preliminary work on the TL of Y_2O_3:(Eu,Tb) (8 and 6%, respectively) excited by UV, GCs which covered the whole temperature range of 20–350°C. A high conversion efficiency was found in the TL, PL, XL and CL (cathodoluminescence) of Y_2O_2S:Eu and Y_2O_2S:Tb powder phosphors by Bolshukhin et al. (1986). It was associated with effective energy transfer from the lattice to the activator. The main TL peak appears near 100 K; the second one appears at 170 K for the Tb-doped phosphor and at 220 K for the Eu-doped phosphor. TL parameters are given for the above peaks and a model for the TL is proposed. Duclos et al. (1994) describe the defects involved in the emission of the AG obtained at liquid-nitrogen temperature in X-ray-excited transparent sintered Y_2O_3:Eu ceramics. The TL of the phosphors was measured over the range 150–350 K, and the TL parameters

were determined. The paper deals mainly with the possible use of the phosphor as a scintillator.

Yeh and Su (1996a) found Y_2O_3:Eu (and Gd_2O_3:Eu) to possess prominent TL. This includes a stable TL peak at 380°C (at 5°C s^{-1}). The phosphor was prepared from the powder by pressing into small pellets and sintering at 1500°C. It was found suitable for UV-radiation dosimetry. Its TL sensitivity was lower than that of the Gd_2O_3:Eu phosphors. Lower-temperature TL peaks of Y_2O_3:Eu appear at 70 and 170°C. Su and Yeh (1996a) found that mixing with LiF enhances all the TL peaks of Y_2O_3:Eu by promoting the incorporation of the Eu_2O_3 into the phosphor. Changing the sintering temperature of the Y_2O_3:Eu phosphor in the range 1000–1500°C did not affect its sensitivity.

Dorenbos et al. (1993) explored the growth-induced defects in $YAlO_3$:Ce. This phosphor is known as a quick efficient scintillator, and the investigation concentrated on the effect on the scintillator efficiency. The growth methods used were the Czochralski and the horizontal directed crystallization methods. Differences in the distribution of the Ce valences between 2 and 4 and the color centers (CC) affected the properties of the crystals. The reactions were $CC \leftrightarrow Ce^{3+}$. Thus, in the GC of the Czochralski-grown crystals there appeared a strong TL peak at 283 K which was unstable at RT. This peak was missing in the crystals grown by the horizontal directed crystallization method, which improved the scintillation of the crystal.

A significant improvement in the TL intensity of Y-compound hosts was obtained by Erdei et al. (1996). They present three-dimensional plots of the TL spectra of Eu- and Ce-doped YVO_4 and $YV_{0.4}P_{0.6}O_4$ phosphors. The phosphors were prepared by a hydrolyzed colloid reaction at about 80°C and then fired at high temperatures. The defect structure was found to depend on the parameters of the hydrolyzed colloid reaction. The phosphors showed TL peaks at about 85°C and 135°C. The TL intensities of these two peaks were highest for the mixed $Y_{0.96}O_{0.4}P_{0.6}O_4$:$Eu^{3+}$ (0.04): 6800 and 4600 compared to 100 and 80 for the 80°C and 130°C peaks of the YVO_4:Eu phosphor, respectively. The authors relate this improvement to an increased defect concentration in the anion sublattice by the introduction of the PO_4^{3-}.

Pode et al. (1996) studied the TL of γ-irradiated YVO_4:Yb. The doping showed only a small increase in the TL. The GC of the undoped sample showed one TL peak at 360 K. The doping added another peak at 475 K. The TL of the doped sample reached a maximum at a concentration of 0.25 mol% Yb. The thermal activation energy of the 360 K peak of the doped sample was 0.45 eV compared with 0.60 eV for the undoped sample. The difference seems to be an artifact caused by the broadening of the TL peak by satellite peaks.

The PL, CL (cathodoluminescence), TL and PSL spectra of Sm^{3+} doped Y_2SiO_5 and of Sm^{3+}- and Tb^{3+}-codoped Y_2SiO_5 was studied by Meiss et al. (1994a). Figure 34 shows TL spectra of Y_2SiO_5:Sm (0.02) and those of phosphors codoped by 0.1 and 0.001 Tb^{3+} in curves 1 to 3, respectively. The spectra were taken at 350 K after X-irradiation. The spectrum in curve 1 is characteristic of Sm^{3+}, and those with 0.1 Tb (curve 2) and with 0.001 Tb (curve 3) give mainly Tb^{3+} emission. The PSL of the X-irradiated phosphor obtained by illumination in the 380 nm band gives two intense PSL bands, at 650 and

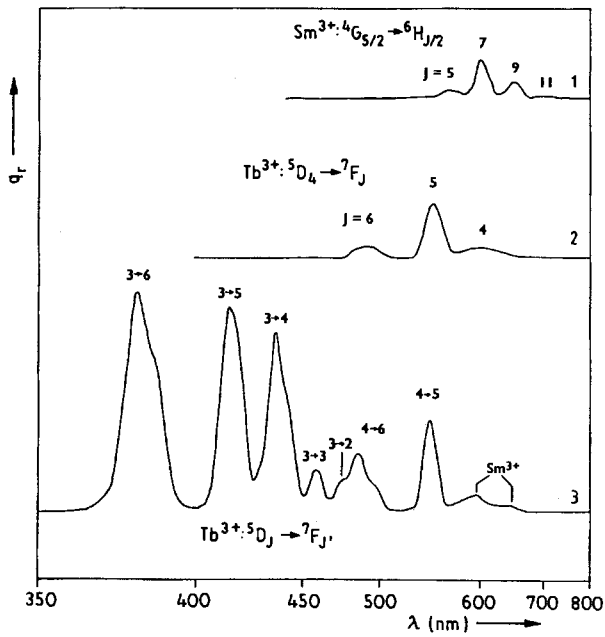

Fig. 34. TL emission spectra (at 350 K) of X-ray-irradiated Y_2SiO_5:$Sm_{0.01}$,Tb_y for different values of y: (1) –0, (2) –0.1 and (3) –0.001. The ordinate q_r denotes the relative quantum output.

850 nm. The 850 nm band is ascribed to recombination of a hole trapped at an oxygen-vacancy complex with an electron at the Sm^{3+}. That at 650 nm is attributed to a hole trapped at a Tb^{3+} and recombining with a Sm^{3+} trapped electron.

Meiss et al. (1994c) have observed that addition of Zr^{4+} to Y_2SiO_5:Ce,Tb increases the efficiency of the phosphor. The process is generally similar to that described above for Y_2SiO_5:Sm^{3+},Tb^{3+}. The improvement by Zr^{4+} codoping is ascribed to the large ionic radius of Zr^{4+} compared to that of Si^{4+}. The Zr^{4+} is therefore incorporated interstitially and serves as an electron trap. The optimal storage was found for a Y_2SiO_5:Sm^{3+},Tb^{3+},Zr^{4+} at codopant concentrations of 0.001 and 0.00075 respectively. The PSL excited in the X-irradiated phosphor by 380 nm illumination showed a broad band peaking at 550 nm. The PSL and TL of powders of $LiYSiO_4$, Ce^{3+} (0.5 mol%) was studied by Knitel et al. (1997). After RT irradiation the GC showed a dominating peak at 530 K. The TL emission showed a broad band peaking at 405 nm. The PSL spectrum consisted of a broad band with a maximum below 450 nm. Practically the same GC shape and PSL spectrum were obtained by excitation with X-rays, γ-rays, α particles, thermal neutrons or UV(254 nm). The TL and the PSL bleached away by annealing at 673 K. UV irradiation followed by illumination with photons in the visible (420–700 nm) resulted in a weaker TL peak shifted to higher temperatures.

The TL of Nd-activated (1 mol%) yttrium–aluminum garnet (YAG, or $Y_3Al_5O_{12}$) is reported in many papers. In the present subsection, however, only the results of papers dealing primarily with yttrium-compound hosts will be discussed.

Niklas (1984) studied the TL of YAG:Nd. In spite of the high-purity chemicals used for the preparation of the garnet, other R ions were present at low concentration. Of these, Tb^{3+} present at a concentration of only 0.001 mol% showed up in the TL spectra. The GCs after X-excitation at 80 K showed the main peak at 170 K and weaker peaks at 210, 290 and 340 K. After RT irradiation the TL peaks appeared at 320, 380, 445 and 525 K, all at a heating rate of 0.8 K s^{-1}. The TL spectra ranged from the UV up to the near IR. At low temperatures the main energy transfer to the R^{3+} ions was through the bound exciton states (BES). The UV emission was ascribed to transitions from the high energy levels of Nd^{3+} (at 4.66 eV) to the lower states. The BES transfer diminished with rising temperature, and above 200 K lines characteristic of transitions from medium energy levels of Nd^{3+} became more intense. At and above RT the Tb^{3+} transitions took over. The hypothesis of energy transfer through BES agreed with earlier suggestions by Robbins et al. (1979) and others. Janusz et al. (1982) concentrated on a possible relation between the observed facets and striations of YAG:Nd^{3+} crystals and their TL topographies. The existence of such a correlation is claimed by the authors to exist. Bernhardt (1980) studied the OA, PL and TL of YAG:Nd^{3+}. The results are similar to those obtained by Niklas. Bernhardt found that the TL peaks at 140 and 180 K appear also in pure undoped crystals and concluded that they are intrinsic to the host crystal. At Nd^{3+} concentrations of 1 mol% or higher the above peaks show also Nd^{3+}-characteristic emissions. The TL peaks above 180 K were found to be connected with the Nd ions. Garmash et al. (1986) report on studies of the TL of YAG:Nd^{3+} in the range 77–300 K. They assign the TL of undoped YAG below 150 K, emitting at 350 nm to radiative decay of auto localized excitons. The peaks above 150 K, emitting at 400 nm, are assumed to be associated with radiative recombination at defects. In YAG:Nd^{3+} the TL emission is assigned to localized holes at oxygens in the vicinity of Nd^{3+} ions. Weak TL peaks at 190 and 210 K are assumed to be related with iron impurities. Garmash et al. (1988) found that the diffusion coefficient of oxygen in YAG:Nd^{3+} crystals in a field of ionizing γ-radiation is six orders of magnitude higher than that of the thermal diffusion in the same crystals.

Smolskaya et al. (1987) studied the XL and TL of YAG crystals activated by Ce^{3+}, Sm^{3+}, Dy^{3+}, Tm^{3+} and Er^{3+}. Ce- and Sm-doped YAGs gave the highest XL sensitivity. The low decay time of the YAG:Ce^{3+} (of the order of 10^{-7} s) and its comparatively high XL sensitivity make it the best X-ray storage phosphor compared to the other R^{3+} doped YAGs. The GCs of the various YAG:R^{3+} measured phosphors X-irradiated at RT showed TL peaks mainly in the temperature range 370–580 K (at 2 K min^{-1}). In this range the Sm^{3+}-doped YAG peak at 560 K had the highest intensity. The highest TL intensity of peaks above 560 K was shown by the Ce^{3+}-doped phosphor. The intensity of its peak at 680 K was 7 times that of the 560 K peak of the Sm^{3+}-doped phosphor. The Ce^{3+}-doped YAG is therefore believed to be the most promising XL and TL phosphor. The high mechanical and thermal stability of the YAG crystals make YAG:Ce^{3+} most promising as a phosphor to be used at high temperature.

Ermakov et al. (1988) studied the TL of Ce-doped YAG crystals. After X- or UV(360 nm) excitation at 77 K the GC exhibited (at a heating rate of 0.13 K s^{-1}) peaks at 90, 130, 150, 190 and 360 K. The authors suggest possible (unproven) models for the various TL peaks. The TL emission fitted the Ce^{3+} transitions. All the traps were found to be filled up by X-rays or by light with energies higher than the forbidden gap. The authors attributed this to the location of the Ce^{3+} 5D level in the conduction band.

Some cathode-ray phosphors suffer from degradation of the luminescence caused by the electron bombardment. Yamamoto and Matsukiyo (1991) present a review of the phosphors for projection tubes emphasizing the problem of the degradation by electron bombardment. Some original impurities were found to reduce the degradation. Thus in YAG:Tb^{3+} and in $Y_3(Al,Ga)_5O_{12}$:Tb^{3+}, in which part of the Al was replaced by Ga, the degradation is reduced by codoping with 10–100 ppm of Yb^{3+}, Eu^{3+} and Si^{4+}. The authors suggest that the reduction in the degradation may be ascribed to competition between these ions and existing traps in the phosphor in capturing free electrons. Uehara et al. (1995) reported that Sc^{3+} ions are more effective in reducing the degradation in the high-sensitivity $Y_3(Al,Ga)_5O_{12}$:Tb^{3+} phosphor. Matsukiyo et al. (1997) showed that no new TL peaks are formed by the introduction of the Sc ions. The TL of the phosphor was found to decrease by annealing in the open air, indicating a close relation of the TL to oxygen vacancies. The TL also decreased with the Sc concentration. Electron bombardment was found to form a new TL peak at 480 K, ascribed to a color center. It is concluded that Sc doping prevents the formation of the color centers, presumably by more dense packing of the lattice by replacing small Ga ions (ionic radius 0.62 Å) by the larger Sc ions (0.81 Å).

Meijerink et al. (1991) studied the PSL of Y_2SiO_5:Ce^{3+} and Y_2SiO_5:Sm^{3+}. The advantage of these PSL phosphors lies in their short response and decay times, 35±10 ns, which enables fast laser scanning of the γ-ray stored energy in the phosphor. In spite of the lower storage efficiency compared with the BaFBr:Eu^{2+} phosphor, the above Ce^{3+}- and Ce^{3+},Sm^{3+}-doped phosphors are recommended as fast scanning X-ray storage phosphors. The authors present a model for the recombination mechanism of the PSL and TL of these phosphors.

3.3.4. *R-containing hosts*

Lanthanum (La) compound hosts. Dhoble (1996) studied the defect formation in LaF_3 and in LaF_3:Eu^{3+}. The phosphors were prepared by solid state diffusion and fired at 800°C in the open air for 24 hours. RT X-irradiated LaF_3 showed the main TL peak at 580 K and at an intensity lower by about 300 times compared with the $CaSO_4$:Dy^{3+} TLD. The Eu-doped crystal showed a weaker TL peak (at 500 K), about one fifth in intensity compared to the undoped LaF_3. The TL emission of the doped phosphor was in the red, characteristic of Eu^{3+} in LaF_3. The dose response of the Eu-doped phosphor was sublinear. Kuzakov (1990) studied pure and Dy^{3+}-, Pr^{3+}- and Sm^{3+}-doped $LaCl_3$ single crystals. The crystals were grown by the Stockbarger–Bridgman method. The crystals were excited by X-rays or UV light. A high-purity (0.0001% total impurities)

crystal showed a TL peak at 111 K (at 0.2 K s^{-1}). This peak was taken as a single TL peak and consequently was concluded to be of second-order kinetics. This seems to be in doubt as the peak seems to be complex, having a weak component at its high-temperature side. The R-doped GCs had characteristic TL peaks at 117, 142 and 156 K for Pr, Dy and Sm, respectively. X-irradiation at RT gave pronounced TL peaks at about 400 and 570 K for Dy^{3+}- and Sm^{3+}-doped crystals and at about 400 and 470 K for the Pr^{3+}-doped crystals. The high-temperature peaks exhibited linear dose dependence over the range 10^{-4}–10^{1} Gy. These peaks are suggested by the authors to be suitable for TL dosimetry. No information is given on the TL sensitivity of the crystals.

Blasse and Bril (1967) reported on the luminescence of many Tb activated phosphors including LaOCl:Tb and LaOBr:Tb. Samples were prepared by firing the mixture of chemicals at 1000–1100°C in a nitrogen atmosphere with a Tb concentration of 5 at%. Low emission efficiencies were obtained for the above La–oxyhalides. Rabatin (1969) obtained for well prepared LaOBr:Tb high luminescence efficiency under UV excitation. With Tb concentrations below 0.01 mol the emission was blue and fitted the $^5D_3$–^7F_j Tb transitions. At a Tb concentration of 0.03 mol the blue emission was completely quenched and was replaced by a green Tb emission from the transitions $^5D_4$–^7F_j. A later paper, (Rabatin, 1975), describes the luminescence of LaOBr:Tm (0.002 mol), which was found more efficient compared with the Tb-doped phosphor. The disagreement between Rabatin and Blasse and Bril (1967) may have arisen form the much higher Tb concentrations in the Tb oxyhalides used by Blasse and Bril. Brixner (1987) in a review of "new" X-ray phosphors describes the above disagreement to have resulted from differences in the preparation methods of the phosphors. He speaks highly of the LaOBr:Tm as a superb X-ray storage phosphor. The main TL peaks of the LaOBr:Tm phosphor appeared at 320 and 380 K (at 0.5 K s^{-1}). Somaiah et al. (1990c) worked on the commercial LaOBr:Tm manufactured by Du Pont Co. (USA) and known at Quanta III. Their work was preliminary and they gave only some information on the GCs of the phosphor and their excitation.

Gadolinium-containing hosts. Gd_2O_3:Eu was reported by Bril and Wanmaker (1964) as a high-efficiency phosphor under cathode-ray excitation. Very little was published on this phosphor until 1996. Yeh and Su (1996a) studied the TL of Gd_2O_3:R^{3+} (R = Tb, Dy or Eu) after UV irradiation at RT. A high-temperature TL peak at 345°C (at 5°C s^{-1}) appeared in the GC, with other main peaks at 50 and 130°C. The latter peaks had higher UV sensitivity but lower thermal stability. The Dy- and Tb-activated Gd_2O_3 showed peaks near and below 110°C much weaker compared with the Gd_2O_3:Eu. The 345°C peak of the Gd_2O_3:Eu showed a linear dose response up to about 100 mJ cm^{-2} after 254 nm irradiation. With longer wavelengths the linearity was limited to somewhat lower doses. Only the Eu-doped phosphors are recommended by the authors as a promising phosphor for UV dosimetry. Yeh and Su (1996b) and Su and Yeh (1996a) found that mixing the Gd_2O_3:Eu phosphor with LiF followed by sintering at 1000–1500°C enhanced its 345°C TL peak by an order of magnitude. This enhancement is ascribed by the authors to a promotion of the incorporation of the Eu into the phosphor by the sintering. The LiF was found to eliminate the monoclinic structure of the phosphor and to enhance the cubic structure.

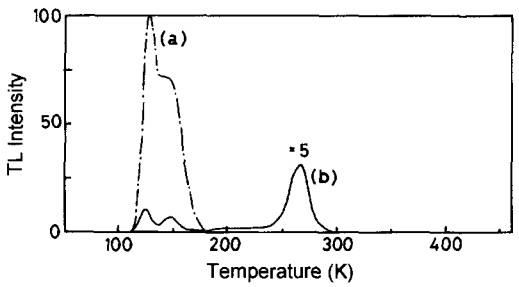

Fig. 35. GCs of Gd_2O_2S:Pr: (a) with 90 ppm F doping and (b) without F doping.

Giakonmakis and Pallis (1989) found Gd_2O_2S:Tb to be an efficient phosphor under cathode-ray and X-ray excitation. Chatterjee et al. (1991) report that the GC of Gd_2O_2S:Tb excited by UV at 77 K exhibits 5 TL peaks in the range 90–320 K. The highest-temperature peak was at 319 K (at 0.52 K s^{-1}). The emission was characteristic of Tb ions. The TL parameters E and s measured by three different methods were spread widely, resulting presumably from the complex overlapping peaks in the GC.

Yamada et al. (1989) studied codoped Gd_2O_2S:Pr,Ce,X (X = F or Cl) phosphors. Their goal was to develop an efficient phosphor for an X-ray computerized tomography (CT) apparatus. Phosphors were prepared by heating a mixture of the chemicals at 1300°C in an iron capsule sealed under vacuum. The Pr-doped sample when UV excited at 77 K showed a TL peak near RT (at 5 K min^{-1}) as shown in fig. 35b. This peak is responsible for a disturbingly strong AG. The addition of 90 ppm fluorine quenched the RT peak by about one order of magnitude and enhanced the low-temperature TL as shown by fig. 35a, thus reducing the AG. Adding Ce further reduced the AG, but it also reduced the sensitivity of the phosphor. The optimal Ce concentration was chosen as a compromise between the two effects. A high output was measured under X-ray and under UV(254 nm) excitation. The final phosphor was suitable for a high-quality CT apparatus.

$(YGd)_2O_3$ ceramic samples doped with Eu, Sm or Dy were examined by Kostler et al. (1993). Samples X-irradiated at low temperatures showed 3 TL peaks in the range 150–250 K. The AG soon after the termination of the X-irradiation showed decay times of about 1 ms. TL and AG of $(YGd)_2O_3$:Eu^{3+} and of Pr^{3+}-codoped samples were investigated in more detail by Kostler et al. (1995). The samples contained 3% Eu^{3+}. Figure 36 shows the GC of $(YGd)_2O_3$:Eu^{3+} (solid line) and the AG as a function of temperature (dashed line). The curves show some similarity, but with quite strong AG around RT. Codoping with Pr^{3+} changed the GC and reduced the AG by a few orders of magnitude depending on the Pr concentration. The authors present a detailed model explaining these effects. In short: (1) Eu^{3+} is known to tend to convert into Eu^{2+}, thus serving as an electron trap; (2) the AG in $(YGd)_2O_3$:Eu^{3+} is related to a hole in the Eu-doped sample; (3) Pr^{3+} serves as a hole trap when it is converted to Pr^{4+}; and (4) the Pr^{3+} hole traps are stable up to about 700 K thus competing with the hole traps related to the AG, which results in the sharp drop in the AG. This model can be of help in elimination of disturbing AG in computerized scanning in X-ray storage devices.

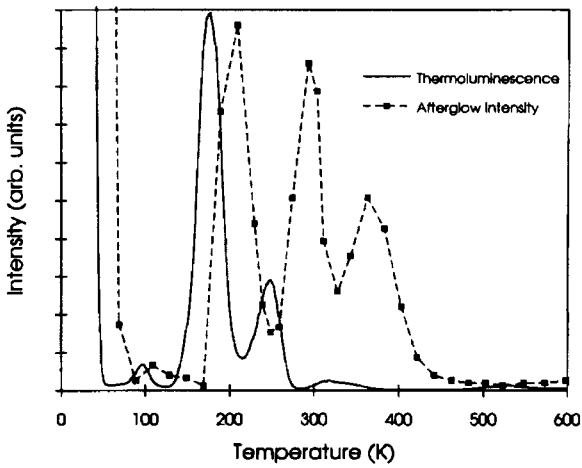

Fig. 36. GC of $(YGd)_2O_3:Eu^{3+}$ (solid line) and the AG (dashed line) as a function of temperature.

Ashurov et al. (1985) studied the effect of Cr^{3+} ions on the formation of color centers in various garnets. They used TL as a tool in the measurements of the temperature at which trapping defects are destroyed. Out of the investigated garnets two contained Gd, namely the Gd–gallium garnet (GGG) and the Gd–Sc–Ge garnet (GSGG). They were activated by Nd^{3+}. γ-rays served for the excitation of the TL. Induced absorption spectra and TL were recorded. GGG:Nd^{3+} irradiated at 77 K showed a complex GC over the range 140–370 K with the main peak at 140 K. GSGG:Nd^{3+} exhibited a GC covering the range 150–400 K. Cr^{3+} codoping completely changed the GCs which now showed a broad TL peak near 210 K. The effect was explained as due to a competition for charge carriers between the Cr^{3+}-related defects and those present before the codoping. Miersch et al. (1996) explored a few radiation resistant fast scintillators and their use as heavy ion detectors. These included $GdSiO_5$:Ce(GSO:Ce) crystals. GCs were recorded 5 days after 3×10^{14} ^{32}Si irradiation at RT. Three overlapping TL peaks appeared at 195, 280 and 380°C. The GSO:Ce was found to be an excellent radiation-resistant heavy-ion detector with high light output and high time resolution (life time of 30 ns). The properties as a TLD were not studied. Some TL measurements of $Sr_3Gd_2Si_6O_{18}:Pb^{2+},Mn^{2+}$ were presented by Chapoulie et al. (1991) in an investigation dealing mainly with the degradation in the green luminescence of the phosphor caused by 185 nm light. The TL measurements presented in this paper include GCs of undoped and doped samples after illumination at RT by 185 + 254 nm light. The undoped sample showed a distinct TL peak at 80°C (at 0.54°C s^{-1}) and a broad weak peak at 230°C. Pb^{2+} (2%) and Mn^{2+} (2.5%) doping suppressed the 80°C peak and showed a very strong TL peak near 220°C. The TL intensity was now about 10 times that in the undoped sample. Replacing 25% of the Gd by Zr^{4+} further enhanced the 220°C peak by a factor of 3.

Lutetium-containing hosts. The high density (7.4 g cm^{-3}), fast decay time (40 ns) and high light yield make $Lu_2(SiO_4)O:Ce^{3+}$ (LSO:Ce^{3+}) suitable as a fast high-energy γ-ray detector as shown by Melcher and Schweitzer (1992). The TL of this phosphor

was investigated by Dorenbos et al. (1994a,b). Two types of crystals were grown, which differed mainly in the growth rate: 2 mm h^{-1} for one type of crystals, 0.5 mm h^{-1} for the others. The GCs varied from one type to the other. Those grown at 2 mm h^{-1} showed, after illumination at RT by UV (Hg lamp), 4 TL peaks limited to the range 320–560 K, while those grown at a rate of 0.5 mm h^{-1} showed 6 or 7 peaks covering the range 340–650 K. The fast-grown crystal also showed a low scintillation yield and a non-exponential decay of the scintillation pulses, which was assigned to quenching of the Ce^{3+} luminescence by energy transfer of the excited Ce^{3+} ions to unidentified defects. The slow-growth crystals showed a high light yield and exponentially decaying scintillations at an activation energy of 1.0 eV, which makes them suitable as fast scintillation crystals. The shape of the low-temperature TL peak at about 380 K of these crystals was found to fit first-order kinetics. The E and s TL parameters were calculated assuming first-order kinetic for all the peaks. Not all the calculated parameters seem to be reliable. The traps of the different TL peaks are assumed by the authors to be related to various configurations of oxygen ions. No clear evidence was given for this assumption.

The TL of $LuAlO_3$:Ce (0.1 mol%) excited by X-, γ- or UV irradiation at RT and heated at a rate of 5 K s^{-1} was studied by Drozdowski et al. (1997). The GCs excited by the three sources contained practically the same TL peaks at about 370, 520 and 640 K. E- and s-values were calculated using the Hoogenstraaten method. The phosphor is described by the authors as a fast and efficient scintillator.

Abdurazakov et al. (1980) studied the TL of $Lu_{0.4}Y_{0.5}R_{0.1}ScO_3$ with R = Er, Ho or Tm. After X-irradiation at RT and at a heating rate of 0.8 K s^{-1} the three phosphors showed 3 TL peaks each at about 400, 530 and above 600 K. The Er-doped crystal showed the highest TL. The TL of the Ho-doped crystal was weaker by a factor of 7 and that of the Tm-doped one was 50 times weaker compared to the Er-doped sample. The authors present rough values for the thermal depths of the various traps. The above work has been extended by Antonov et al. (1981) of the same group, who measured the TL of the above scandates doped by Nd. The work included changes in the crystal composition and in the radiation doses. These variations were found to affect the TL intensities and the position of the TL peaks. Meiss et al. (1994c) studied the $Lu_{2-x}Y_x$:Ce^{3+} codoped by Zr^{4+} (0.075%) or by Sm^{3+}. The codoping introduced additional defects enabling to store more charge carriers during RT X-irradiation. The work deals mainly with PL and CL emission and excitation spectra. Measurements of the TL and PSL showed differences between Zr^{4+}- and Sm^{3+}-codoped samples. The Zr^{4+}-doped samples warmed to 350 K showed an unresolved Ce^{3+} doublet at 400–440 nm and a corresponding PSL band at 550 nm. Samples coactivated by Sm^{3+} (0.1%) showed Ce^{3+} TL emission and two PSL bands at 650 and 850 nm.

4. Past advances and future trends

The present article reviewed the advance gained in the characteristics and in the function of radiation detectors based on TL and related phenomena. The large number of

original papers published in this field did not allow the inclusion of all of them in the review. Papers not easily available and those not adding much new information or not concentrated directly on the subject were therefore left out. Glass detectors deserve a separate treatment and were not included in the present review. Numerous R-activated phosphors have been developed and advanced during the last 30 years. Many of them are produced commercially. The most extensively investigated was the $CaSO_4$:Dy phosphor known commercially as TLD-900. It is a high-sensitivity stable detector showing good dosimetric characteristics. Its γ-ray sensitivity was shown by Ayyangar et al. (1974b) to exceed by two orders of magnitude that of the still widely used TLD-100. The sensitivity of $CaSO_4$:Dy has since then improved further. Research concentration on the "favorite" $CaSO_4$:Dy phosphor hindered the investigation and advance of other promising phosphors. For example, the sensitivity of $K_2Ca_2(SO_4)_3$:Eu was shown by Sahare and Moharil (1990b) to exceed that of $CaSO_4$:Dy by a factor of 5 (fig. 10). Further extensive investigation may result in further improvements. R-activated $MgSiO_4$ and MgB_4O_7 phosphors were also found to equal or exceed $CaSO_4$:Dy in sensitivity (see sect. 3.2.1). The MgB_4O_7:R phosphors have the additional advantage of being tissue equivalent, and also show better energy independence compared to $CaSO_4$:Dy. It should be stressed that the comparatively high fading of these phosphors reported by some authors can be eliminated easily by pre-reading annealing at a suitable temperate below the dosimetric TL peak.

The development of large phosphor films enabled many applications. The X-ray storage films, for example, were shown by Miyahara and Moharil (1986) to enable the reduction of the X-ray exposure of a patient by several orders of magnitude compared to that needed for an X-ray image obtained by a photographic X-ray film. Further research may lead to the development of ultrasensitive phosphors. Such phosphors may enable, for example, almost continuous personal monitoring of exposure to radiation without long waiting for the accumulation of doses high enough with the existing TLDs.

The advance in the dosimetric properties of phosphors was mostly empirical. More theoretical work on the effects involved in the preparation of phosphors and in the TL emission may lead to more efficient phosphors. In the present situation it happens that minor changes in the preparation of a phosphor lead to changes by orders of magnitude in the intensity of the dosimetric TL peak (see, for example, Dhopte et al. 1991a). Burlin and co-workers have developed the cavity theory (sect. 3.2.3) to explain the effect of the grain sizes on the sensitivity of TL detectors. Unfortunately, the use of this theory was limited presumably because of additional effects which masked the cavity effect.

The sensitivity of phosphors depends strongly on the activator. This effect was shown by Nambi et al. (1974) for $CaSO_4$:R and is illustrated in fig. 29. The TL sensitivity can be seen to change by up to four orders of magnitude from one R activator to another. This behavior seems to be characteristic of the host. Measurements of the effects of the various R ions on the TL in other hosts should help in the explanation of the drastic variation in the TL sensitivity. Of interest are also the measurements made by Nakazawa and Mochida (1997). They showed that trap depths in $SrAl_2O_4$:Eu^{2+} codoped by other R ions are related to the ionization potentials and to the $4f^n \rightarrow 4f^{n-1}$ 5d transition energies of the R^{2+} ions.

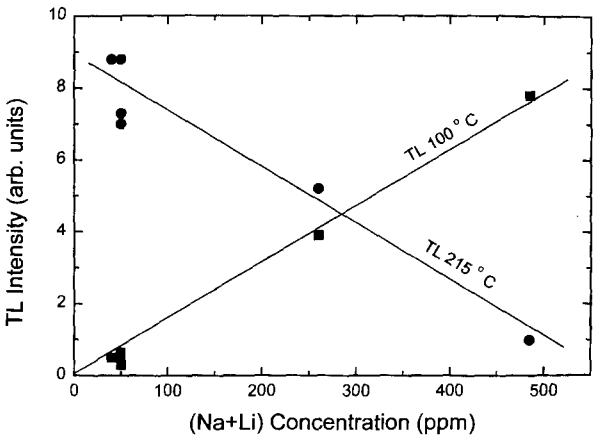

Fig. 37. The dependence of the intensities of the TL peaks of $CaSO_4$:Dy at 100°C and 215°C on the concentrations of Na+Li impurities (in ppm).

Extension of such measurements to wider temperature ranges and to other host phosphors might also give a better insight into the processes involved in the emission of the various TL peaks of a phosphor.

Various impurities have been shown to affect differently the TL peaks of a phosphor. Some $CaSO_4$:Dy phosphors showed a GC consisting of many overlapping TL peaks covering a wide temperature range (see fig. 15). Using ultrahigh-purity chemicals for the preparation of the phosphor eliminated most of the peaks, leaving two main peaks at about 110 and 220°C. Even these two peaks were affected differently by alkali-metal impurities. Prokic (1978) measured the TL of $CaSO_4$:Dy phosphors containing various concentrations of "non-activating" alkali-metal impurities. He found that the alkali metals enhance the 100°C TL peak and quench the 215°C peak (fig. 22). The main effect seems to be due to the Na and Li concentrations. This is shown in fig. 37 which is based on Prokic' data. It shows the enhancement of the 100°C peak and the quenching of the 215°C peak as a function of the sum of the Na and Li concentrations. Both TL peaks seem to be affected linearly by the Na + Li concentrations.

A similar effect obtained by introduction of ^6Li was described by Ayyangar et al. (1974a), as shown in fig. 20. On the other hand, some impurities were found to enhance the TL sensitivity. Meiss et al. (1994b) showed that adding 0.0075% Zr^{4+} to Y_2SiO_5:$Ce^{3+}Tb^{3+}$ boosts the TL sensitivity by production of additional electron traps which take part in the TL emission.

The results of some of the reviewed papers imply that the traps as well as the luminescence centers of a phosphor may be complicated, including complexes of activators, coactivators and various other impurities. Azorin et al. (1993) stressed the importance of obtaining a deeper knowledge on the structure of the defects responsible for the light emission of phosphors. Townsend and Kirsh (1989) stressed the importance of measuring the TL emission spectra which helps in understanding the defects involved in the TL emission. Townsend and White (1996) stress the complexity of defects in phosphors and conclude that a significant defect interaction takes place over distances

of about 10 lattice spacings. They concluded that the simplistic model of isolated single lattice sites is unexceptable and that this has a bearing on the charge transfer involved in the TL. They also suggest that direct association of traps and recombination sites may be commonplace. The defects in phosphors seem indeed to be complex. Still, further work is needed before we will be able to estimate the effective defect dimensions and to assess how common are the high-complexity defects. In most cases the release of charge carriers from traps takes place through the CB (or the VB). This indicates that the traps are separated from the luminescence centers, and are not part of one complex.

The determination of the TL parameters seems to be problematic. In most cases not enough care has been taken to work on isolated single peaks. There are also other limitations in the various approximate methods. Some authors have taken care to eliminate as much as possible the disturbing effects and have obtained reliable TL parameters. Nambi et al. (1974) determined the E values for more than 10 overlapping TL peak of $CaSO_4$:R (see fig. 15). For Dy- and Tm-doped samples they obtained a linear relation between the TL peak temperatures T_m and the trap depth E. More than that, the same curve fitted for both Dy- and Tm-doped phosphors (fig. 16). This suggests that the E-values are quite accurate. Azorin and Gutierrez (1986) obtained for a TL peak of $CaSO_4$:Dy $E = 0.88 \pm 0.01$ eV, which fits well on the curve in fig. 16. Azorin et al. (1989) used 11 different methods for the determination of E-values of 3 peaks in the GC of CaF_2:Tm. All the methods gave the same E-values within a few percent, except for one value obtained by the general-curve-fitting method which deviated by 15% from the E-value obtained by the other methods. The above examples show that under careful experimental measurements practically all the methods used give reliable TL parameters.

Attempts have been made to develop generalized expressions eliminating some of the approximations and limitations of the simplified expressions for the determination of the TL parameters. Mentel et al. (1992) have presented a method to overcome the random and systematic errors met with in measurements of microcrystalline luminescent powders. In such cases even an isolated TL peak looking as a single peak is in fact composed of overlapping components. The generalized method allows sets of systems differing in their TL data which cover the undisturbed region of the TL peak. Comparison with experimental TL peaks showed the advantage of the overall evaluation method over the conventional methods. Mandowski and Swiatek (1996) present a generalized initial rise (ir) method. It involves the adding of a correction term $\phi(T)$ to the conventional ir expression. By this method the whole TL peak is included in the measurements and not only the ir. The authors present numerical tests which show that the generalized ir method enables E-determinations with high accuracy. Lewandowski and McKeever (1991) presented mathematical expressions including the TL and TSC without the restrictions of quasi-equilibrium and kinetic-order approximations. The expressions are given for a single active trap but in the presence of many deep thermally disconnected traps and recombination centers. From the mathematical expressions of the generalized description the authors were able to derive simpler approximations like the Hoogenstraaten (1958) equations and the generalized ir description mentioned above. The Lewandowski–McKeever equations present a general TL–TSC relationship. As a by-

product the results provide a justification for the fact that first-order kinetics dominates in nature.

Summarizing, remarkable progress has been made in the past in the quality of TL detectors and in our understanding of the kinetics involved in the TL of phosphors. Future research is expected to focus on a better understanding of the complexity in the structure of the defects and of the role of the various components in the complex defect structures. For an optimal TL phosphor one has to insure high storage capacity, efficient energy transfer to the luminescence center and efficient radiative recombination. This can be achieved by well-designed experimental work in close combination with theoretical advances, which should bring us closer to the goal of high-quality ultrasensitive TLDs.

References

Abbruscato, V., 1971, J. Electrochem. Soc. **118**, 930.

Abdul Ahad, Y.K., H.H. Ali and M.M. Abadalla, 1990, Radiat. Prot. Dosim. **34**, 215.

Abdurazakov, A.A., V.A. Antonov, P.A. Arsenev, W. Jelenski, A.M. Kevorkov, D.I. Korolev, A. Niklas and J. Wiechula, 1980, Phys. Status Solidi A **59**, K227.

Abtahi, A., P. Braunlich, P. Kelly and J. Gasiot, 1985, J. Appl. Phys. **58**, 1626.

Abtahi, A., P. Braunlich and T. Haugan, 1986, Radiat. Prot. Dosim. **17**, 313.

Abtahi, A., T. Haugan and P. Kelly, 1987, Radiat. Prot. Dosim. **21**, 211.

Abubakar, R., S. Untung and M. Oberhofer, 1990, Radiat. Prot. Dosim. **33**, 95.

Aceves, R., R. Perez-Salas and M. Barboza-Flores, 1994, J. Phys.: Condens. Matter **6**, 10397.

Aguirre de Carcer, I., F. Cusso and F. Jaque, 1988, Phys. Rev. B **38**, 10812.

Aguirre de Carcer, I., G. Lifante, F. Cusso, F. Jaque and T. Calderon, 1991, Appl. Phys. Lett. **58**, 1825.

Aguirre de Carcer, I., F. Cusso, F. Jaque, E. Espanat, T. Calderon, G. Lifante and P.D. Townsend, 1993, J. Phys. D **26**, 154.

Aleshin, V.I., and V.V. Karelin, 1991, Opt. Spectrosk. **70**, 211.

Amin, Y.M., and S.A. Durrani, 1985, Nucl. Tracks Radiat. Meas. **10**, 55.

Anderson, W.W., S. Razi and J. Welsh, 1965, J. Chem. Phys. **43**, 1153.

Antonov, V.A., P.A. Arsenev, Kh.S. Bagdasarov, D.I. Korolev, A.M. Kevorkov, A. Niklas, V. Elenski and E. Viekhula, 1981, Zh. Prikl. Spektrosk. **34**, 430.

Antonyak, O.T., and M.S. Pidzyrailo, 1995, Ukr. Fiz Zh. **40**, 550 [1996, Ukr. J. Phys. **40**].

Apostolova, M., G. Burger, D. Combecher, D. Eckerl and P. Kneschaurek, 1985, in: Proc. 5th Symp. on Neutron Dosimetry (EUR 9762 EN), Munich-Neuberberg, Germany, 17–21 September 1984 (Commission of the European Communities, Luxembourg) Vol. 2, pp. 817–822.

Arsenev, P.A., Kh.S. Bagdasarov, A. Niklas and A.D. Ryazantsev, 1980, Phys. Status Solidi A **62**, 395.

Ashurov, M.Kh., E.V. Zharikov, V.V. Laptev, I.N. Nasyrov, V.V. Osiko, A.M. Prokhorov, P.K. Khabibullaev and I.A. Scherbakov, 1985, Dokl. Akad. Nauk. SSSR **282**, 1104 [Sov. Phys. Dokl. **30**, 490].

Atone, M.S., S.J. Dhoble, S.V. Moharil, S.M. Dhopte, P.L. Muthal and V.K. Kondawar, 1993, Phys. Status Solidi A **135**, 299.

Atone, M.S., S.V. Moharil and T.K.G. Rao, 1995a, J. Phys. D **28**, 1263.

Atone, M.S., S.J. Dhoble, S.V. Moharil and V.K. Kondawar, 1995b, Radiat. Eff. Defects Solids **127**, 225.

Ayappan, P., A.K. Gopalakrishnan, S.M.D. Rao and K.S.V. Nambi, 1981, Indian J. Pure Appl. Phys. **19**, 323.

Aypar, A., 1978, Int. J. Appl. Radiat. Isot. **29**, 369.

Ayyangar, K., B. Chandra and A.R. Lakshmanan, 1974a, Phys. Med. Biol. **19**, 656.

Ayyangar, K., A.R. Lakshmanan, B. Chandra and K. Ramadas, 1974b, Phys. Med. Biol. **19**, 665.

Azorin, J., and C. Furetta, 1989, Nucl. Sci. J. **26**, 512.

Azorin, J., and A. Gutierrez, 1986, Nucl. Tracks **11**, 167.

Azorin, J., and A. Gutierrez, 1988, Rev. Mex. Fis. **34**, 199.

Azorin, J., and A. Gutierrez, 1989, Health Phys. **56**, 551.

Azorin, J., and J. Rubio, 1994, J. Phys.: Condensed Matter **6**, 3831.

Azorin, J., A. Gutierrez and C.G. Martinez, 1985, Radiat Eff. **84**, 263.

Azorin, J., A. Gutierrez and T. Niewiadomski, 1986, Radiat. Prot. Dosim. **17**, 53.

Azorin, J., C. Furetta and A. Gutierrez, 1989, J. Phys. D **22**, 458.

Azorin, J., C. Furetta, P. Gonzalez and A. Gutierrez, 1991, Appl. Radiat. Isot. A **42**, 861.

Azorin, J., C. Furetta and A. Scacco, 1993, Phys. Status Solidi A **138**, 9.

Bacci, C., A. Calicchia, L. Pugliani, P. Salvadori and C. Furetta, 1980, Health Phys. **38**,21.

Bacci, C., C. Furetta, B. Rispoli, G. Roubaud and J.W.N. Tuyn, 1988, Radiaot Prot. Dosim. **25**, 43.

Bacci, C., V. Draghi, C. Furetta and B. Rispoli, 1989, IEEE Trans. Nucl. Sci. **NS-36**, 1154.

Bacci, C., P. Bernardini, A. Domenico, C. Furetta and B. Rispoli, 1990, Nucl. Instrum. Methods A **286**, 295.

Bacci, C., S. Fioravanti, C. Furetta, M. Missori, M. Ramogida, G. Rossetti, R. Sanipoli and C. Scacco, 1993, Radiat. Prot. Dosim. **47**, 277.

Balraj, K., and P. Veeresham, 1992, Cryst. Res. Technol. **27**, 863.

Bangert, U., K. Thiel, D. Ahmed and P.D. Townsend, 1982a, Radiat. Eff. **64**, 143.

Bangert, U., K. Thiel, D. Ahmed and P.D. Townsend, 1982b, Radiat. Eff. **64**, 153.

Bapat, V.N., 1977, J. Phys. C **10**, 2465.

Barbina, V., G. Contento, C. Furetta, M. Malisan and R. Padovani, 1981, Radiat. Eff. Lett. **67**, 55.

Barboza-Flores, M., R. Perez-Salas, R. Aceves, L.P. Pashchenko, L.L. Medvedev and T.M. Piters, 1994, Appl. Phys. Lett. **64**, 1789.

Barkyoumb, J.H., V.K. Mathur, A.C. Lewadowski, A. Tookey, P.D. Townsend and I. Giblin, 1997, J. Lumin. **72–74**, 629.

Barland, M., E. Duval and A. Nouailhat, 1982, J. Phys. **43**, 1413.

Bassi, P., G. Busuoli and O. Rimondi, 1975, Health Phys. **28**, 470.

Bassi, P., G. Busuoli and O. Rimondi, 1976, Health Phys. **31**, 179.

Bassi, P., G. Busuoli and O. Rimondi, 1977, Nucl. Instrum. Methods **143**, 195.

Becker, K., 1972, Nucl. Instrum. Methods **104**, 405.

Becker, K., 1973, Solid State Dosimetry (CRC Press, Cleveland, OH).

Becker, K., 1996, Radiat. Prot. Dosim. **66**, 9.

Becker, M., J. Kiessling and A. Scharmann, 1973, Phys. Status Solidi A **15**, 515.

Ben-Shachar, B., 1989, Appl. Radiat Isot. **40**, 687.

Ben-Shachar, B., and Y.S. Horowitz, 1988, Radiat Prot. Dosim. **22**, 87.

Benci, S., F. Fermi and A. Nagornyi, 1990, Phys. Status Solidi A **120**, 635.

Benko, L., 1990, Radiat. Prot. Dosim. **34**, 225.

Beregic, V., I. Lengyel, I. Beregic, A. David and C. Busunioc, 1993, in: SIEN 93, Proc. Int. Symp. on Nuclear Energy, Bucharest, Romania, 3–4 December 1993 (Romanian Nuclear Energy Association) Vol. 1, pp. 36–40.

Bernhardt, H.J., 1980, Phys. Status Solidi A **61**, 357.

Bhan, S., 1982, Phys. Status Solidi B **110**, 399.

Bhasin, B.D., R. Sasidharan and C.M. Sunta, 1976, Health Phys. **30**, 139.

Bhatt, B.C., A.R. Lakshmanan, S.S. Shinde and R.C. Bhatt, 1988, Radiat. Prot. Dosim. **25**, 37.

Bhatt, B.C., J.K. Srivastava, S.S. Sanaye, S.S. Shinde, A.S. Petill and S.J. Supe, 1994, Radiat. Prot. Dosim. **57**, 343.

Bhatt, B.C., P.S. Jyer and K.S.V. Nambi, 1995, Radiat Prot. Dosim. **62**, 175.

Bhatt, B.C., S.S. Shinde, J.K. Srivastava and T.K.G. Rao, 1996, Radiat. Prot. Dosim. **65**, 287.

Bhatt, B.C., S.S. Sanaye, S.S. Shinde and J.K. Srivastava, 1997, Radiat. Prot. Dosim. **69**, 105.

Binder, W., and J.R. Cameron, 1969, Health Phys. **17**, 613.

Blasse, G., 1979, Chemistry and physics of R-activated phosphors, in: Handbook on the Physics and Chemistry of Rare Earths, Vol. 4, eds K.A. Gschneidner Jr and L. Eyring (North-Holland, Amsterdam) pp. 237–274.

Blasse, G., and A. Bril, 1967, Philips Res. Rep. **22**, 481.

Bolshukhin, V.A., A.M. Malova and M.P. Soshkhin, 1986, Izv. Akad. Nauk SSSR, Seri. Fiz. **50**(3), 599 [Bull. Acad. Sci. USSR, Phys. Ser. **50**, 171].

Borchi, E., M. Bruzzi and C. Furetta, 1991, IEEE Trans. Nucl. Sci. **NS-38**, 877.

Bos, A.J.J., and J.B. Dielhof, 1991, Radiat. Prot. Dosim. **37**, 231.

Bos, A.J.J., R.W. de Jong and K. Meijvogel, 1995, Radiat Meas. **24**, 401.

Bradford, M., D.A. Andrews, A. Harrison, S.G. Ruden and T.A. King, 1997, J. Lumin. **72–74**, 742.

Bril, A., and W.I. Wanmaker, 1964, J. Electrochem. Soc. **111**, 1363.

Brixner, L.H., 1987, Mater. Chem. Phys. **16**, 253.

Budzanowski, M., B. Burgkhardt, P. Olko, W. Pesara and M.P.R. Waligorski, 1996, Radiat. Prot. Dosim. **66**, 135.

Buenfil, A.E., and M.E. Brandan, 1992, Health Phys. **62**, 341.

Buenfil, A.E., A. Flores and M.E. Brandan, 1997, J. Phys. D **30**, 1399.

Burgkhardt, B., D. Singh and E. Piesch, 1977, Nucl. Instrum. Methods **141**, 363.

Burlin, T.E., 1966, Br. J. Radiat. **39**, 727.

Burlin, T.E., and F.K. Chan, 1966, in: Proc. Symp. on Solid State Chemical Radiation Dosimetry in Medical and Biological Radiation Dosimetry, Vienna, 1966, pp. 393–405.

Burlin, T.E., F.K. Chan, G.D. Zanelli and F.W. Spiers, 1969, Nature **221**, 1047.

Bushtruk, I.Ya., S.V. Demishev and A.N. Gruzintsev, 1990, Cryst. Reas. Technol. **25**, 957.

Caldas, L.V.E., and M.R. Mayhugh, 1976, Health Phys. **31**, 451.

Calvert, R.L., and R.J. Danby, 1984a, Phys. Status Solidi A **83**, 597.

Calvert, R.L., and R.J. Danby, 1984b, Radiat. Prot. Dosim. **6**, 55.

Camacho, Q.A., H.G. Munoz, O.J. Rubio, M.J. Garcia, S.H. Murrieta and A.J.H. Hernandez, 1988, J. Phys. Mater. Sci. Lett. **7**, 437.

Campos, L.L., 1993, Radiat. Prot. Dosim. **48**, 205.

Campos, L.L., and O.O.F. Filho, 1990, Radiat. Prot. Dosim. **33**, 111.

Campos, L.L., and M.F. Lima, 1987, Radiat. Prot. Dosim. **18**, 95.

Carrillo, R.E., D.W. Pearson, P.M. Deluca Jr, J.F. Mackay and M.G. Lagally, 1996, Radiat. Meas. **26**, 75.

Castaneda, B., R. Aceves, T.M. Piters, M. Barboza-Flores, R. Melendrez and R. Perez-Salas, 1996, Appl. Phys. Lett. **69**, 1388.

Chakrabarti, K., V.K. Mathur, J.F. Rhodes and R.J. Abbundi, 1988a, J. Appl. Phys. **64**, 1363.

Chakrabarti, K., V.K. Mathur, L.A. Thomas and R.J. Abbundi, 1988b, Phys. Rev. B **38**, 10894.

Chakrabarti, K., V.K. Mathur, L.A. Thomas and R.J. Abbundi, 1989, J. Appl. Phys. **65**, 2021.

Chakrabarti, K., V.K. Mathur, R.J. Abbundi and M.D. Hill, 1990, Radiat. Prot. Dosim. **33**, 35.

Chakrabarti, K., V.K. Mathur, R.J. Abbundi, N. Kristianpoller and W.F. Hornyak, 1991, J. Lumin. **48–49**, 828.

Chakrabarti, K., J. Sharma, V.K. Mathur and R.J. Abbundi, 1992, Nucl. Instrum. Methods B **69**, 322.

Chandra, B., K. Ayyangar and A.R. Lakshmanan, 1976, Phys. Med. Biol. **21**, 67.

Chandra, B., R.C. Bhatt and S.J. Supe, 1981, Nucl. Instrum. Methods **184**, 549.

Chandra, B., A.R. Lakshmanan, S.S. Shinde and R.C. Bhatt, 1986, Radiat. Prot. Dosim. **17**, 451.

Chandra, B., S.S. Shinde, A.R. Lakshmanan and R.C. Bhatt, 1987, Phys. Status Solidi A **103**, 599.

Chapoulie, R., S. Dubernet and M. Schvoerer, 1991, Mater. Chem. Phys. **30**, 47.

Charalambous, S., and F. Hasan, 1983, Phys. Lett. **95A**, 259.

Chatterjee, S., V. Shanker and P.K. Ghosh, 1991, Solid State Commun. **80**, 877.

Chee, J., H.L. Oczkowski, Y. Kirsh, A. Scott, W.C. Siyanbola and P.D. Townsend, 1988, Nucl. Tracks Radiat. Meas. **14**, 35.

Chen, R., 1969, J. Electrochem. Soc. **116**, 1254.

Chen, R., and Y. Kirsh, 1981, Analysis of Thermally Stimulated Processes (Pergamon Press, New York).

Chen, W., and M. Su, 1995, Chin. Sci. Bull. **40**, 599.

Chen, Wei, Q. Song and M. Su, 1997, J. Appl. Phys. **81**, 3170.

Christensen, P., and M. Prokic, 1986, Radiat. Prot. Dosim. **17**, 83.

Christober Selvan, P., S. Selvasekarapandian and P. Neelamegam, 1996, Phys. Status Solidi B **194**, 747.

Chryssou, E., 1987, Phys. Status Solidi A **99**, K103.

Crawford, M.K., and L.H. Brixner, 1991, J. Lumin. **48–49**, 37.

Cusso, F., I. Aguirre de Carcer, A.G. Lifante and T. Calderon, 1991, Health Phys. **60**, 579.

da Rosa, L.A.R., L.V.E. Caldas and P.G. Cunha, 1986, Radiat. Prot. Dosim. **14**, 329.

da Silva, T.A., L.A.R. da Rosa and L.L. Campos, 1995, Radiat. Prot. Dosim. **58**, 17.

Danby, R.J., 1988, J. Phys. C, **21**, 485.

De Melo, A.P., J.F. deLima, A.M.G. Figueredo, A.V. Chadwick and M.E.G. Valerio, 1997, Mater. Sci. Forum **239–240**, 749.

deMurcia, M., P. Brounlich, M. Egee and G. Mary, 1980, Solid State Commun. **34**, 732.

deMurcia, M., Y. Yixin, P. Braunlich, J.P. Jouart and H.J. von Bardeleben, 1982, J. Phys. C **15**, 2069.

Deshmukh, B.T., S.V. Bodade and S.V. Moharil, 1986, Phys. Status Solidi A **98**, 239.

Dhoble, S.J., 1996, Phys. Status Solidi A **157**, 181.

Dhoble, S.J., S.V. Moharil, S.M. Dhopte, P.L. Muthal and V.K. Kondawar, 1993, Phys. Status Solidi A **135**, 289.

Dhopte, S.M., P.L. Muthal, V.K. Kondawar, S.V. Moharil and P.D. Sahare, 1991a, J. Phys. D **24**, 1869.

Dhopte, S.M., P.L. Muthal, V.K. Kondawar and S.V. Moharil, 1991b, J. Lumin. **50**, 187.

Dhopte, S.M., P.L. Muthal, V.K. Kondawar and S.V. Moharil, 1992, J. Lumin. **54**, 95.

Dielhof, J.B., A.J.J. Bos, J. Zoetelief and J.J. Broerse, 1988, Radiat. Prot. Dosim. **23**, 405.

Dixon, R.L., and K.E. Ekstrand, 1974, Phys. Med. Biol. **19**, 196.

Dorenbos, P., M.V. Korzhik, A.P. Kudryavtseva, S.V. Lyubetskii, B.I. Minkov, V.B. Pavlenko and A.A. Fyodorov, 1993, Zh. Prikl. Spectrosk. **59**, 226 [J. Appl. Spectrosc. **59**, 633].

Dorenbos, P., C.W.E. van Eijk, A.J.J. Bos and C.I. Melcher, 1994a, J. Lumin. **60–61**, 979.

Dorenbos, P., C.W.E. van Eijk, A.J.J. Bos and C.I. Melcher, 1994b, J. Phys.: Condens. Matter **6**, 4167.

Drazic, G., and M. Trontelj, 1983, Int. J. Appl. Radiat. Isot. **34**, 1633.

Drazic, G., and M. Trontelj, 1984, Radiat. Prot. Dosim. **6**, 344.

Drazic, G., and M. Trontelj, 1986, Appl. Radiat. Isot. **37**, 337.

Drozdowski, W., D. Wisniewski, A.J. Wajtowicz, A. Lempicki, P. Dorenbos, J.T.M. de Haas, C.W.E. van Eijk and A.J.J. Bos, 1997, J. Lumin. **72–74**, 756.

Duclos, S.J., C.D. Greskovich and C.R. Oclair, 1994, in: Scintillator and Phosphor Materials Symp., San Francisco, CA, USA, 6–8 April 1994 (Materials Research Society, Pittsburgh, PA) pp. 503–509.

Eid, A.M., G.M. Hassib, F.A. Koraiem and M. Kenawy, 1992, Isot. Radiat. Res. Egypt **24**, 1.

Erdei, S., L. Kovacs, M. Martini, F. Meinardi, F.W. Ainger and W.B. White, 1996, J. Lumin. **68**, 27.

Ermakov, G.A., V.M. Lynbchenko, S.A. Smirnova and A.A. Shabaltai, 1988, Inorg. Mater. **24**, 682.

Espana, E., T. Calderon, F. Cusso, F. Jaque, G. Lifante and P.D. Townsend, 1992, Nucl. Tracks Radiat. Meas. **20**, 605.

Felszerfalvi, J., P.P. Szabo, J. Pacso and P. Kovacs, 1979, Pact **3**, 311.

Figura, P.V., and A.I. Nepomnyashchikh, 1991, Opt. Spectrosc. **70**, 75. Original: Opt. Spektrosk. **70**, 132.

Fiorella, O., M. Mangia and E. Oliveri, 1976, Radiat. Phys. Chem. **8**, 441.

Fiorella, O., M. Mangia and E. Oliveri, 1978, Radiat. Phys. Chem. **11**, 261.

Fleming, S.J., 1973, Archaeometry **15**, 13.

Fukuda, Y., 1990, Radiat. Prot. Dosim. **33**, 151.

Fukuda, Y., and N. Takeuchi, 1989, J. Mater. Sci. Lett. **8**, 1001.

Fukuda, Y., K. Miziguchi and N. Takeuchi, 1986, Radiat. Prot. Dosim. **17**, 397.

Fukuda, Y., A. Tomita and N. Takeuchi, 1987, Phys. Status Solidi A **99**, K135.

Fukuda, Y., A. Tomita and N. Takeuchi, 1989, Phys. Status Solidi A **114**, K 245.

Fukuda, Y., H. Ohtaki and N. Takeuchi, 1992, J. Mater. Sci. Lett. **11**, 731.

Fukuda, Y., H. Ohtaki, A. Tomita and N. Takeuchi, 1993, Radiat Prot. Dosim. **47**, 201.

Fukuda, Y., H. Ohtaki, A. Tomita and S. Owaki, 1996, Radiat. Prot. Dosim. **65**, 325.

Furetta, C., and J. Azorin, 1989, Nucl. Instrum. Methods A **280**, 318.

Furetta, C., and P. Gennai, 1981, Radiat. Eff. **55**, 23.

Furetta, C., and J.W.N. Tuyn, 1986, Appl. Radiat. Isot. **37**, 935.

Furetta, C., and T.W.N. Tuyn, 1985, J. Appl. Radiat. Isot. **36**, 1000.

Furetta, C., C. Bacci, B. Rispoli, C. Sanipoli and A. Scacco, 1990, Radiat. Prot. Dosim. **33**, 107.

Furetta, C., C. Sanipoli, A. Scacco and K. Somaiah, 1996, Radiat Prot. Dosim. **65**, 339.

Garlick, G.F.J., and I. Robinson, 1972, in: 2nd Moon Symp. International Astronomical Union, 1971, Symp. Int. Astron. Union **47**, 324–329.

Garmash, V.M., G.A. Ermakov, V.M. Lyubchenko and A.A. Filimonov, 1986, Opt. Spectrosc. **61**, 337.

Garmash, V.M., G.A. Ermakov, Yu.P. Konstantinov, V.M. Lyubchenko, V.V. Gromov, N.Yu. Konstantinov and L.G. Karaseva, 1988, Russ. J. Phys. Chem. **62**, 273.

Gasiot, J., P. Braunlich and J.F. Fillard, 1982, J. Appl. Phys. **53**, 5200.

Gavrilov, V.V., and V.G. Krongauz, 1975, Fiz. Tverd Tela. **17**, 3346 [Sov. Phys. Solid State **17**, 2250].

Gektin, A.V., V.K. Komar, N.V. Shiran, V.V. Shlykhturov, N.P. Nesterenko, I.M. Krasovitskaya and V.V. Kornienko, 1995, IEEE Trans. Nucl. Sci. **NS-42**, 311.

Gerome, V., P. Iacconi, D. Lapraz, H. Prevost and A. Baumer, 1996, Radiat. Prot. Dosim. **65**, 309.
Ghosh, P.K., and R. Pandey, 1982, J. Phys. C **15**, 5875.
Ghosh, P.K., H.P. Narang and H. Chander, 1986, J. Lumin. **35**, 99.
Giakonmakis, G.E., and A.J. Pallis, 1989, Solid State Commun. **70** 418.
Godlewski, M., D. Hommel, J.M. Langer and H. Przybylinska, 1981, J. Lumin. **24–25**, 217.
Goyet, D., D. Lapraz, P. Iacconi, G. Portal, J. Barthe, H. Prevost and J. Gasiot, 1993, Radiat. Prot. Dosim. **47**, 147.
Goyet, D., D. Lapraz and P. Iacconi, 1996, Radiat. Prot. Dosim. **65**, 317.
Grasser, R., I. Jeuck, A. Scharmann and J. Strode, 1988, J. Lumin. **40–41**, 389.
Green, A.G.J., B. Ray, I.V.F. Viney and J.W. Brightwell, 1988a, Phys. Status Solidi A **110**, 269.
Green, A.G.J., J.W. Brightwell, I.V.F. Viney and B. Ray, 1988b, J. Cryst. Growth **86**, 639.
Guelev, M.G., I.T. Mischev, B. Burgkhardt and E. Piesch, 1994, Radiat. Prot. Dosim. **51**, 35.
Halperin, A., and A.A. Braner, 1960, Phys. Rev. **117**, 408.
Halperin, A., A.A. Braner, A. Ben-Zvi and N. Kristianpoller, 1960, Phys. Rev. **117**, 416.
Harrison, A., L.C. Lane, R.H. Templer and J.M. Seddon, 1991, Nucl. Instrum. Methods A **310**, 220.
Hasan, F., and S. Charalambous, 1983, J. Phys. C **16**, 5921.
Hasan, F., G. Kitio and S. Charalambous, 1985, J. Phys. C **18**, 1743.
Hersh, H.N., and H. Forest, 1970, Proposed mechanism of cathodoluminescence in some oxygen dominated phosphors, in: Proc. Int. Conf. on Luminescence, Delaware, 1969, ed. W. Ferd (North-Holland, Amsterdam) pp. 862–868.
Hoffmann, W., 1996, Radiat. Prot. Dosim. **66**, 243.
Hoffmann, W., and B. Prediger, 1984, Radiat. Prot. Dosim. **6**, 149.
Holgate, S.A., T.H. Sloane, P.D. Townsend, D.R. White and A.V. Chadwick, 1994, J. Phys.: Condens. Matter **6**, 9255.
Hommel, D., J.M. Langer and B. Brukowska, 1975, Phys. Status Solidi A **31**, K81.
Hoogenstraaten, W., 1958, Philips Res. Rep. **13**, 515.
Horowitz, Y.S., 1984a, Thermoluminescence and Thermoluminescent Dosimetry, Vols. 1–3 (CRC Press, Boca Raton, FL).
Horowitz, Y.S., 1984b, TL dose response, in: Thermoluminescence and Theomoluminescent Dosimetry, ed. Y.S. Horowitz (CRC Press, Boca Raton, FL) Vol. II, pp. 2–41.
Horowitz, Y.S., and A. Dubi, 1982, Phys. Med. Biol. **28**, 867.
Horowitz, Y.S., M. Moscovitch and A. Dubi, 1983, Phys. Med. Biol. **28**, 829.
Hsieh, W.-C., and C.-S. Su, 1994, J. Phys. D **27**, 1763.
Hsu, P.-C., and P.-S. Weng, 1994, Nucl. Sci. J. Taiwan **31**, 65.
Hsu, P.C., and M.N. Chen, 1975, Nucl. Sci. J. **12**, 29.
Hsu, P.C., and S.H. Li, 1990, Radiat. Prot. Dosim. **33**, 189.
Hsu, P.C., and T.K. Wang, 1986, Radiat. Prot. Dosim. **16**, 253.
Hsu, P.C., C.L. Tseng, S.H. Li and P.S. Weng, 1978, Nucl. Instr. Methods **154**, 561.
Hsu, P.C., J.C. Jao and P.S. Weng, 1985, Radiat. Prot. Dosim. **11**, 123.
Hsu, P.C., P.S. Weng and L.N. Su, 1986, Radiat. Prot. Dosim. **15**, 51.
Hsu, P.C., S.H. Li and P.S. Weng, 1990, Nucl. Sci. J. **27**, 173.
Hsu, P.C., P.S. Weng, H.L. Wang and P.W. Tseng, 1991, Health Phys. **61**, 367.
Hsu, P.C., C.D. Wang, P.S. Weng and S.H. Li, 1993, Radiat. Prot. Dosim. **47**, 235.
Hund, F., 1950, Z. Anorg. Chem. **261**, 106.
Huzimura, R., 1979, Jpn. J. Appl. Phys. **18**, 2031.
Huzimura, R., K. Asahi and M. Takenaga, 1980, Nucl. Instr. Methods **175**, 8.
Inabe, K., Y. Utsui and N. Takeuchi, 1986, Phys. Status Solidi B **138**, 493.
Iwabuchi, Y., C. Umemoto, K. Takahashi and S. Shionoya, 1991, J. Lumin. **48–49**, 481.
Iwata, K., H. Yoshimura, T. Tamada, H. Uchida, M. Nakagawa, K. Utsunomiya, I. Yamamoto and T. Wada, 1993, Sensors Actuators A **36**, 127.
Jacob, M., P. Meissner and J. Rassow, 1990, Radiat. Prot. Dosim. **33**, 291.
Jacob, M., B. Spallek, R. Rassow and W. Hoffmann, 1993, Radiat. Prot. Dosim. **48**, 265.
Jain, S.C., and D.R. Bhawalkar, 1975, Indian J. Appl. Pure Phys. **13**, 74.
Jain, V.K., 1977, Indian J. Pure Appl. Phys. **15**, 601.
Jain, V.K., 1984, Photostimulated Tl, in: Thermoluminescence and Thermoluminescent Dosimetry, ed. Y.S. Horowitz (CRC Press, Boca Raton, FL) Vol. II, pp. 173–211.
Jain, V.K., 1990, Radiat. Phys. Chem. **36**, 45.

Janusz, Cz., W. Jelenski and A. Niklas, 1982, J. Cryst. Growth **57**, 593.

Jaque, F., F. Cusso, I. Aguirre de Carcer, G. Lifante and T. Calderon, 1991, Health Phys. **60**, 579.

Jassemnejad, B., and S.W.S. McKeever, 1987, J. Phys. D **20**, 323.

Jassemnejad, B., S.W.S. McKeever, R.J. Abbundi, V.K. Mathur and M.D. Brown, 1986, Radiat. Prot. Dosim. **17**, 469.

Jassemnejad, B., R.J. Abbundi, M.D. Brown and S.W.S. McKeever, 1988, Phys. Status Solidi A **108**, 753.

Julius, H.W., 1996, Radiat. Prot. Dosim. **66**, 1.

Jun, S.J., and K. Becker, 1975, Health Phys. **28**, 459.

Justus, B.L., A.L. Huston and T.L. Jhonson, 1996, Appl. Phys. Lett. **68**, 1.

Kao, K.J., and M.M. Perlman, 1979, Phys. Rev. B **19**, 1196.

Kasa, I., 1990, Radiat. Prot. Dosim. **33**, 299.

Kasa, I., J. Solymosi and A. Molnar, 1996, Radiat. Prot. Dosim. **65**, 313.

Kase, K.R., and W.R. Nelson, 1978, Concepts of Radiation Dosimetry (Pergamon Press, New York).

Kato, K., S. Antoku, S. Sawada and W.J. Kussell, 1991, Med. Phys. **18**, 928.

Kawada, Y., and M. Sakaguchi, 1990a, Radiat. Eff. Defect Solids **114**, 63.

Kawada, Y., and M. Sakaguchi, 1990b, Radiat Eff. Defects Solids **112**, 15.

Kearsley, E.E., 1984, Phys. Med. Biol. **29**, 57.

Kiessling, J., and A. Scharmann, 1975, Phys. Status Solidi A **29**, K177.

Kirsh, Y., and P.D. Townsend, 1987, J. Phys. C **20**, 967.

Kitahara, A., 1987, Radioisotopes Japan **36**, 186.

Kitis, G., and S.T. Charalambous, 1988, Phys. Status Solidi A **105**, K175.

Knitel, M.J., P. Dorenbos and C.W.E. van Eijk, 1997, J. Lumin. **72–74**, 765.

Komar, V.K., A.V. Gektin, N.P. Ivanov, Y.A. Nesterenko and N.V. Shiran, 1996, J. Cryst. Growth **166**, 419.

Kostler, W., E. Bayer, W. Rossner and B.C. Grabmaier, 1993, Nucl. Tracks Radiat. Meas. **21**, 135.

Kostler, W., A. Winnacker, W. Rossner and B.C. Grabmaier, 1995, J. Phys. Chem. Solids **56**, 907.

Kumar, V.S.K., B.S.V.S.R. Acharyulu and S.B.S. Sastry, 1993, J. Lumin. **55**, 43.

Kuzakov, S.M., 1990, Radiat. Prot. Dosim. **33**, 115.

Lakshmanan, A.R., 1992, Radiat. Prot. Dosim. **42**, 41.

Lakshmanan, A.R., and R.C. Bhatt, 1979, Nucl. Instrum. Methods **164**, 215.

Lakshmanan, A.R., and R.C. Bhatt, 1982, Radiat Prot. Dosim. **1**, 125.

Lakshmanan, A.R., and M.T. Jose, 1993, Radiat. Prot. Dosim. **46**, 181.

Lakshmanan, A.R., and S.S. Tiwari, 1993, Radiat. Prot. Dosim. **47**, 243.

Lakshmanan, A.R., S.S. Shinde and R.C. Bhatt, 1978a, Phys. Med. Biol. **23**, 952.

Lakshmanan, A.R., B. Chandra and R.C. Bhatt, 1978b, Nucl. Instrum. Methods **153**, 581.

Lakshmanan, A.R., B. Chandra, A.S. Pradhan and R.C. Bhatt, 1979, Radiochem. Radioanal. Lett. **37**, 377.

Lakshmanan, A.R., B. Chandra, A.S. Pradhan, A.S. Kher and R.C. Bhatt, 1980, Int. J. Appl. Radiation Isot. **31**, 107.

Lakshmanan, A.R., B. Chandra and R.C. Bhatt, 1982a, Int. J. Appl. Radiat. Isot. **33**, 707.

Lakshmanan, A.R., B. Chandra and R.C. Bhatt, 1982b, Radiat. Prot. Dosim. **2**, 13.

Lakshmanan, A.R., W. Hoffmann, J.W.N. Tuyn and C. Raffnsoe, 1983, Radiat. Prot. Dosim. **5**, 251.

Lakshmanan, A.R., S.S. Shinde, R.C. Bhatt and S.J. Supe, 1988, Radiat. Prot. Dosim. **22**, 173.

Lakshmanan, A.R., K.L. Popli and R.K. Kher, 1989a, Radiat. Prot. Dosim. **28**, 263.

Lakshmanan, A.R., B.C. Bhatt and R.C. Bhatt, 1989b, Radiat. Prot. Dosim. **27**, 15.

Lakshmanan, A.R., A.K. Gopalakrishnan and R.K. Kher, 1989c, Radiat. Prot. Dosim. **28**, 263.

Lakshmanan, A.R., K.L. Popli and R.K. Kher, 1990a, Radiat. Prot. Dosim. **32**, 127.

Lakshmanan, A.R., R.K. Kher and U. Madhvanath, 1990b, Radiat. Prot. Dosim. **30**, 179.

Lapraz, D., D. Goyet, V.Gerome.P. Iacconi, H. Prevost, J. Gasiot and A. Baumer, 1996, Phys. Status Solidi A **153**, 239.

Las, W.L., R.J. Matthews and T.G. Stoebe, 1980, Nucl. Instrum. Methods **175**, 1.

Lehmann, W., 1972, J. Lumin. **5**, 87.

Lewandowski, A.C., and V.K. Mathur, 1996, Radiat. Prot. Dosim. **66**, 213.

Lewandowski, A.C., and S.W.S. McKeever, 1991, Phys. Rev. B **43**, 8163.

Lewandowski, A.C., J.H. Barkyoumb and V.K. Mathur, 1996, Radiat. Prot. Dosim. **65**, 281.

Li, L.B., M. Kai and T. Kusoma, 1995, Radiat. Prot. Dosim. **59**, 148.
Li, S.H., and P.C. Hsu, 1990a, Health Phys. **58**, 65.
Li, S.H., and P.C. Hsu, 1990b, Radiat. Prot. Dosim. **33**, 147.
Li, S.H., P.C. Hsu and P.S. Weng, 1991, Health Phys. **61**, 849.
Lin, S.W., and P.S. Weng, 1995, Appl Radiat. Isot. **46**, 1369.
Lin, S.W., P.S. Weng and P.C. Hsu, 1996, Appl. Radiat. Isot. **47**, 83.
Liu, C.-J., S.-H. Yeh and H.-H. Hu, 1986, Nucl. Sci. J. **23**, 185.
Lopez, F.J., P. Colino, M.M. Perez and F. Jaque, 1991, J. Phys.: Conden. Matter **3**, 8127.
Lucas, A.C., and B.M. Capsar, 1977, in: Proc. 5th Int. Conf. on Luminescence Dosimetry, São Paulo, Brazil, ed. A. Scharmann (Physics Institute, Giessen) pp. 68–74.
Lucas, A.C., H.R. Moss and B.M. Kapsar, 1977, US Patent 403 9834 (CL 250-337) GO1 T. 11.
Ludemann, L., B. Heningsen, R. Schmidt and W. Scobel, 1995, Radiat. Prot. Dosim. **59**, 303.
Luguera, E., F. Fernandez, C. Domingo, C. Baixeras and H. Prevost, 1996, Radiat. Prot. Dosim. **65**, 321.
Majchrowski, A., A. Korman, J. Zmija, W. Borys, M. Malecki and S. Warkocki, 1994, Proc. SPIE **2373**, 251.
Mandowski, A., and J. Swiatek, 1996, Radiat. Prot. Dosim. **65**, 55.
Mathews, R.J., and J.F. Stoebe, 1982, J. Phys. C **15**, 6271.
Mathur, V.K., J. Gasiot, R.J. Abbundi and M.D. Brown, 1986, Radiat. Prot. Dosim. **17**, 333.
Matsuda, H., and S. Minato, 1991, Radioisotopes Japan **40**, 455.
Matsukiyo, H., H. Toyama, Y. Uehara and H. Yamamoto, 1997, J. Lumin. **72–74**, 229.
Matsuzawa, T., Y. Aoki, N. Takeuchi and Y. Murayama, 1996, J. Electrochem. Soc. **143**, 2670.
Mattern, P.L., K. Lengweiller, P.W. Levy and P.D. Esser, 1970, Phys. Rev. Lett. **24**, 1287.
Mauricio, C.L.P., E. Bortolin and S. Onori, 1996, Radiat. Meas. **26**, 639.
McDougall, R.S., and J.C. Axt, 1973, Health Phys. **25**, 612.
McKeever, S.W.S., 1985, Thermoluminescence of Solids (Cambridge University Press, Cambridge).
McKeever, S.W.S., B. Jassemnejad, M.D. Brown, V.K. Mathur, R.T. Abbundi and H. Chan, 1986, Radiat. Eff. **99**, 15.
McKeever, S.W.S., M. Moscovitch and P.D. Townsend, 1995, Thermoluminescence Dosimetry Materials (Nuclear Technology Publishing, Ashford, England).
Mehta, S.K., and S. Sengupta, 1978, Phys. Med. Biol. **23, 471.**.
Meijerink, A., 1996, Mater. Chem. Phys. **44**, 170.
Meijerink, A., and G. Blasse, 1989, Mater. Chem. Phys. **21**, 261.
Meijerink, A., and G. Blasse, 1990, J. Phys. Condens. Matter **2**, 3619.
Meijerink, A., and G. Blasse, 1991, J. Phys. D **24**, 626.
Meijerink, A., W.J. Schipper and G. Blasse, 1991, J. Phys. D **24**, 992.
Meijvogel, K., B. van der Burg and A.J.J. Bos, 1996, Radiat. Prot. Dosim. **65**, 117.
Meiss, D., W. Wischert and S. Kemmler-Sack, 1994a, Phys. Status Solidi A **141**, 495.
Meiss, D., W. Wischert and S. Kemmler-Sack, 1994b, Mater. Chem. Phys. **38**, 191.
Meiss, D., R. Reichardt, W. Wischert and S. Kemmler-Sack, 1994c, Phys. Status Solidi A **142**, 237.
Meissner, P., M. Jacob and J. Rassow, 1988a, Phys. Med. Biol. **33**, 1407.
Meissner, P., M. Jacob and J. Rassow, 1988b, Phys. Med. Biol. **33**, 613.
Melcher, C.L., and J.S. Schweitzer, 1992, Nucl. Instrum. Methods **314**, 212.
Melendrez, R., R. Perez-Salas, L.P. Pashchenko, R. Aceves, T.M. Piters and M. Barboza-Flores, 1996a, Appl. Phys. Lett. **68**, 3398.
Melendrez, R., R. Perez-Salas, R. Aceves, T.M. Piters and M. Barboza-Flores, 1996b, Appl. Phys. Lett. **69**, 1068.
Mentel, J., W. Lange, D. Haberland and G. Herzog, 1992, Phys. Status Solidi A **130**, K285.
Merz, J.L., and P.S. Pershan, 1967, Phys. Rev. **162**, 217.
Miersch, G., D. Habs, J. Kenntner, D. Schwalm and A. Wolf, 1996, Nucl. Instrum. Methods A **369**, 277.
Mikho, V.V., 1981, J. Appl. Spectrosc. **32**, 590.
Miyahara, J., K. Takahashi, Y. Amemiya, N. Kamiya and Y. Satow, 1986, Nucl. Instrum. Methods A **246**, 527.
Mochida, T., K. Kamiyama and E. Nakazawa, 1996, Res. Rep. Kogakuin Univ. **81**, 84.
Moharil, S.V., S.V. Bodade, P.D. Sahare and V.K. Kondawar, 1995, Radiat. Eff. Defects Solids **127**, 177.

Moharil, S.V., S.J. Dhoble, S.M. Dhopte, P.L. Muthal and V.K. Condawar, 1996, Radiat. Eff. Defects Solids **138**, 159.

Morato, S.P., and K.S.V. Nambi, 1977, Development of hydrogen doped TL phosphors for fast neutron dosimetry, in: Proc. 5th Int. Conf. on Luminescence Dosimetry, ed. A. Scharmann (Justus-Liebig University, Giessen) pp. 155–161.

Morato, S.P., A.M.P. Gordon, E.N. Dos Santos, L. Gomes, L.L. Campos, L. Prado, M.M.F. Vieira and V.N. Bapat, 1982, Nucl. Instrum. Methods **200**, 449.

Morgan, M.D., and J.F. Stoebe, 1990a, Radiat. Prot. Dosim. **33**, 31.

Morgan, M.D., and J.F. Stoebe, 1990b, J. Phys.: Condensed Matter **2**, 1619.

Morgan, M.D., and T.G. Stoebe, 1986, Radiat. Prot. Dosim. **17**, 455.

Mulla, M.R., and S.H. Pawar, 1979, Pramana **12**, 593.

Nagornyi, A.A., and J. Pospisil, 1990, Czech. J. Phys. **40**, 203.

Nagpal, J.S., and H.K. Pendurkar, 1979, Nucl. Instrum. Methods **159**, 581.

Nagpal, J.S., V.K. Kathuria and P. Gangadharan, 1980, Phys. Med. Biol. **25**, 549.

Nagpal, J.S., K.I. Popli, R.K. Kher and G. Varadharajan, 1992, Radiat. Prot. Dosim. **40**, 45.

Nagpal, J.S., K.I. Popli, G. Varadharajan, R.K. Kher and G. Venkataromen, 1994, Radiat. Prot. Dosim. **51**, 275.

Nair, S.R., V.K. Kondawar, S.V. Upadeo, S.V. Moharil and T.K.G. Rao, 1997, J. Phys.: Condens. Matter **9**, 8307.

Nakajima, T., 1971, in: Proc. 3rd Int. Conf. on Luminescence Dosimetry, Riso Report No. 249 (Danish AEC, Riso) p. 466.

Nakajima, T., 1988, Radiat. Prot. Dosim. **25**, 191.

Nakajima, T., 1993, in: Thermoluminescent Materials, ed. D.R. Vij (PTR Prentice Hall, New Jersey) pp. 322–336.

Nakajima, T., Y. Murayama, T. Matsuzawa and A. Koyano, 1978, Nucl. Instrum. Methods **157**, 155.

Nakamura, S., K. Inabe and N. Takeuchi, 1992, Jpn. J. Appl Phys. **31**, 1823.

Nakazawa, E., and T. Mochida, 1997, J. Lumin. **72–74**, 236.

Nambi, K.S.V., 1982, Nucl. Instrum. Methods **197**, 13.

Nambi, K.S.V., and V.N. Bapat, 1980, J. Phys. C **13**, 1555.

Nambi, K.S.V., V.N. Bapat and A.K. Ganguly, 1974, J. Phys. C 7, 4403.

Natarajan, V., A.G.I. Dalvi and M.D. Sastry, 1986, Radiat Eff. **88**, 45.

Nelson, W.R., H. Hirayama and D.W.O. Rogers, 1985, Stanford Linear Accelerator Report SLAC-256.

Niewiadomski, T., 1996, Radiat. Prot. Dosim. **65**, 1.

Niewiadomski, T., and E. Ryba, 1983, Radiat. Prot. Dosim. **6**, 67.

Niewiadomski, T., P. Bilski, M. Budzanowski, P. Olko, E. Ryba and M. Waligorski, 1996, Nuklionika (Poland) **41**, 93.

Nikl, I., 1996, Radiat. Prot. Dosim. **67**, 225.

Niklas, A., 1984, Appl. Phys. **B34**, 87.

Niroomand-Rad, A., and L.A. Dewerd, 1983, Mod. Phys. **10**, 691.

Novosad, S.S., B.O. Belikovich, S.D. Martiyniv and I.Yo. Kukharskii, 1995, Ukr. Fiz. Zh. **40**, 1206 [Ukr. J. Phys. **40**].

Oduko, J.M., S.J. Harris and J.C. Stewart, 1984, Radiat. Prot. Dosim. **8**, 257.

Ogunleye, O.T., F.H. Attix and B.R. Paliwal, 1980, Phys. Med. Biol. **25**, 203.

Ohtaki, H., Y. Fukuda and N. Takeuchi, 1993, Radiat. Prot. Dosim. **47**, 119.

Ohtaki, H., H. Kido, A. Hiratsuka, Y. Fukuda and N. Takeuchi, 1994, J. Mater. Sci. Lett. **13**, 1267.

Okamoto, Y., S. Kawaguchi, S.Kino.S. Miomo, T. Kitajima, A. Misaki and T. Saito, 1986, Nucl. Instrum. Methods A **243**, 219.

Opyrchal, H., K.D. Nierzewski and B. Macalik, 1982, Phys. Status Solidi B **112**, 429.

Opyrchal, H., K.D. Nierzewski, B. Macalik and M. Mladenova, 1986, Phys. Status Solidi B **135**, 141.

Pandey, R., and P.K. Ghosh, 1981, Solid State Commun. **38**, 647.

Pashchenko, L.P., R. Perez-Salas, R. Aceves and M. Barboza-Flores, 1995a, Appl. Phys. Lett. **66**, 3126.

Pashchenko, L.P., R. Perez-Salas, R. Aceves and M. Barboza-Flores, 1995b, Appl. Phys. Lett. **67**, 3266.

Patil, M.G., and R.D. Lawangar, 1981, Mater. Res. Bull. **16**, 109.

Paun, J., A. Iozsa and S. Jipa, 1977, Radiochem. Radiat. Lett. **28**, 411.

Pawar, S.H., 1978, Indian J. Pure Appl. Phys. **16**, 1034.

Pendurkar, H.K., R. Boulanger, L. Ghoos, W. Nicasi and E. Mertens, 1971, in: Proc. 3rd Int. Conf. on Luminescence Dosimetry, Riso Report No. 249 (Danish AEC, Riso) p. 1089.

Perez-Salas, R., M. Barboza-Flores, A.C. Bayon and R.M. Rodriguez, 1993, Nucl. Tracks Radiat. Meas. **21**, 157.

Perez-Salas, R., R. Melendrez, R. Aceves, R. Rodriguez and M. Barboza-Flores, 1996, J. Phys.: Condens. Matter **8**, 4983.

Peto, A., A. Kelemen and N. Otvos, 1997, J. Lumin. **72–74**, 778.

Pietrikova, M., J. Krasa and L. Juha, 1993, Z. Phys. B **93**, 63.

Pilipenko, G.I., M.Ya. Khodos, M.B. Vidrevich, V.M. Zhukovskii and C.B. Cherlov, 1982, Inorg. Mater. **17**, 1244.

Pode, R.B., A.M. Band, H.D. Juneta and S.T. Dhoble, 1996, Phys. Status Solidi A **157**, 493.

Pol, P.G., and V.J. Rau, 1973, Indian J. Pure Appl. Phys. **11**, 886.

Portal, G., S. Lorrian and G. Valladas, 1980, Nucl. Instrum. Methods **175**, 12.

Potiens Jr, A.J., and L.L. Campos, 1996, Radiat. Prot. Dosim. **66**, 95.

Pradhan, A.S., 1993, Radiat. Prot. Dosim. **47**, 151.

Pradhan, A.S., 1996, Radiat. Prot. Dosim. **65**, 73.

Pradhan, A.S., and B.R.C. Bhatt, 1979a, Nucl. Instrum. Methods **161**, 243.

Pradhan, A.S., and B.R.C. Bhatt, 1979b, Nucl. Instrum. Methods **166**, 497.

Pradhan, A.S., and R.C. Bhatt, 1977, Phys. Med. Biol. **22**, 873.

Pradhan, A.S., and R.C. Bhatt, 1981a, Int. J. Appl. Radiat. Isot. **32**, 179.

Pradhan, A.S., and R.C. Bhatt, 1981b, Phys. Status Solidi A **68**, 405.

Pradhan, A.S., and R.C. Bhatt, 1982, Radiat. Prot. Dosim. **2**, 23.

Pradhan, A.S., and R.C. Bhatt, 1985, J. Appl. Phys. **18**, 317.

Pradhan, A.S., and J. Rassow, 1987, Nucl. Inst. Meth. Phys. Res. **A255**, 234.

Pradhan, A.S., R.C. Bhatt, A.R. Lakshmanan, A.R. Chandra and S.S. Shinde, 1978, Phys. Med. Biol. **23**, 723.

Pradhan, A.S., A. Dere and K. Popli, 1979, Int. J. Appl. Radiat. Isot. **30**, 317.

Pradhan, A.S., R.C. Bhatt and S.J. Supe, 1980, Int. J. Appl. Radiat. Isot. **31**, 671.

Pradhan, A.S., S.P. Gambhir, P.H. Patel, R.C. Bhatt and S.T. Supe, 1990, Health Phys. **59**, 299.

Pradhan, A.S., J.B. Susane, A.K. Gopalakrishnan, V.K. Shirva and P.S. Iyer, 1992, Radiat. Prot. Dosim. **40**, 49.

Pradhan, A.S., V.K. Shirva, P.K. Dash Sharma, V. Jayalakshmi and P.S. Iyer, 1993, Radiat. Prot. Dosim. **48**, 359.

Pradhan, A.S., U. Quast and P.K.D. Sharma, 1994, Phys. Med. Biol. **39**, 1367.

Press, W.H., B.P. Flannery, S.A. Teukolsky and W.T. Vetterling, 1989, Numerical Recipes, The Art of Scientific Computing, 2nd Ed. (Cambridge University Press, Cambridge) ch. 15.

Prokic, M., 1978, Nucl. Instrum. Methods **151**, 603.

Prokic, M., 1980, Nucl. Instrum. Methods **175**, 83.

Prokic, M., 1982, Health Phys. **42**, 849.

Prokic, M., 1986, Radiat. Prot. Dosim. **17**, 393.

Prokic, M., 1990, Radiat. Prot. Dosim. **33**, 99.

Prokic, M., 1991, Radiat. Prot. Dosim. **37**, 271.

Prokic, M., 1993, Radiat. Prot. Dosim. **47**, 191.

Prokic, M., 1996, Radiat. Prot. Dosim. **66**, 153.

Prokic, M., and L. Botter-Jensen, 1993, Radiat. Prot. Dosim. **47**, 195.

Prokic, M., and P. Christensen, 1983, Radiat. Prot. Dosim. **6**, 133.

Prokic, M., and P. Christensen, 1986, Radiat. Prot. Dosim. **17**, 83.

Przybylinska, H., M. Godlewski and D. Hommel, 1992, Phys. Rev. **B46**, 7395.

Pu, Z., M. Su and S. Ruan, 1995, Comput. Chem. **19**, 107.

Quang, V.X., N.M. Son, P.T. Yen, H. Mai, B. Hüttl, U. Troppenz and R.H. Mauch, 1996, Phys. Status Solidi A **156**, 209.

Rabatin, J.G., 1969, Electrochem. Soc., Spring Meeting, New York, Abstract 78, p. 189.

Rabatin, J.G., 1975, Electrochem. Soc., Spring Meeting, Toronto, Abstract 198, p. 467.

Radhakrishna, S., and B.V.R. Chowdari, 1972, Phys. Status Solidi A **14**, 11.

Radhakrishnan, J.K., and S. Selvasekarapandian, 1994, Phys. Status Solidi A **141**, 457.

Radhakrishnan, J.K., and S. Selvasekarapandian, 1995, J. Lumin. **63**, 137.

Rank, E.X., and R.B. Theus, 1979, IEEE Trans. Nucl. Sci. **NS-26**, 1590.

Ranogajec-Komor, M., and M. Osvay, 1986, Radiat. Prot. Dosim. **17**, 379.

Rao, R.P., 1986a, J. Mater. Sci. **21**, 3357.

Rao, R.P., 1986b, Radiat. Prot. Dosim. **17**, 403.

Rao, R.P., 1988, J. Lumin. **40–41**, 848.

Rao, R.P., M. de Marcia and J. Gasiot, 1984, Radiat. Prot. Dosim. **6**, 64.

Rao, T.K.G., B.C. Bhatt, J.K. Srivastava and K.S.V. Nambi, 1993, J. Phys.: Condens. Matter **5**, 1791.

Rao, T.K.G., S.S. Shinde, J.K. Srivastava and K.S.V. Nambi, 1995, J. Phys.: Condens. Matter. **7**, 6569.

Rao, T.K.G., S.S. Shinde, B.C. Bhatt, J.K. Srivastava and K.S.V. Nambi, 1996, Phys. Status Solidi A **157**, 173.

Rasheedy, M.S., F. Nishimura and T. Ichimori, 1991, Nucl. Instrum. Methods B **61**, 67.

Rassow, J., C. Klein and P. Meisner, 1988, Radiat. Prot. Dosim. **23**, 409.

Raves, I.M., and T.G. Stoebe, 1990, Radiat. Prot. Dosim. **32**, 5.

Reddy, Ch.G., N. Pandaraiah and K. Narasimha, 1988, J. Mater. Sci. Lett. **7**, 1225.

Reddy, K.N., M.L. Rao and V.H. Babu, 1982, Phys. Status Solidi A **70**, 335.

Rennie, J., E. Nakazawa and T. Koda, 1990, Jpn. J. Appl. Phys. **29**, 509.

Richmond, R.G., O.T. Ogunleye, B.L. Cash and K.L. Jones, 1987, Appl. Radiat. Isot. **38**, 313.

Robbins, D.J., B. Cockayne, B. Lent, C.N. Duckworth and J.L. Glasper, 1979, Phys. Rev. **19**, 1254.

Rosete, C., A.J. Hernandez, H.G. Munoz and O.J. Rubio, 1996a, Radiat. Eff. Defects Solids **132**, 49.

Rosete, C., A.J. Hernandez, H.G. Munoz and O.J. Rubio, 1996b, Radiat. Eff. Defects Solids **139**, 207.

Rubio, J.O., M.C. Flores, H.S. Murrieta, J.A. Hernandez, F. Jaque and F.J. Lopez, 1982a, Phys. Rev. B **26**, 2199.

Rubio, J.O., M.G. Aguilar, F.J. Lopez, M. Galan, J. Garcia-Sole and H.S. Murrieta, 1982b, J. Phys. C **15**, 6113.

Sabnis, S.G., and S.H. Pawar, 1980, Indian J. Pure Appl. Phys. **18**, 562.

Saez-Vergara, J.C., J.M. Gomez-Ros and A. Delgado, 1993, Radiat. Prot. Dosim. **47**, 327.

Sahare, P.D., and S.V. Moharil, 1989, J. Lumin. **43**, 369.

Sahare, P.D., and S.V. Moharil, 1990a, Radiat. Eff. Defects Solids **114**, 167.

Sahare, P.D., and S.V. Moharil, 1990b, J. Phys. D **23**, 567.

Sahare, P.D., S.V. Moharil and B.D. Bashin, 1989, J. Phys. D **22**, 971.

Sahre, P., 1987, Radiat. Prot. Dosim. **18**, 19.

Sahre, P., and T. Schonmuth, 1993, Radiat. Prot. Dosim. **47**, 353.

Sangeeta, S.C. Sabharwal, B. Ghosh and M.K. Gupta, 1990, Phys. Status Solidi A **121**, 657.

Sangeeta, S.C. Sabharwal and M.K. Gupta, 1991, Phys. Status Solidi A **125**, K121.

Sapru, S., and S.B.S. Sastry, 1981, J. Lumin. **24–25**, 123.

Sastry, S.B.S., 1993, Alkali-halides, in: Thermoluminescent Materials, ed. D.R. Vij (PTR Prentice Hall, NJ) ch. 6.

Sastry, S.B.S., and S.M.M. Kennedy, 1993, Phys. Status Solidi B **180**, 521.

Sastry, S.B.S., and G. Muralidharan, 1988a, Phys. Status Solidi B **150**, 315.

Sastry, S.B.S., and G. Muralidharan, 1988b, Phys. Status Solidi B **146**, 727.

Sastry, S.B.S., and G. Muralidharan, 1988c, Nucl. Instrum. Methods B **32**, 216.

Sastry, S.B.S., and S. Sapru, 1978, Phys. Status Solidi A **48**, K189.

Sastry, S.B.S., and S. Sapru, 1981, Phys. Status Solidi B **103**, 185.

Schipper, W.J., and G. Blasse, 1991, J. Solid State Chem. **94**, 418.

Schipper, W.J., J.J. Hamelink, E.M. Langeveld and G. Blasse, 1993, J. Phys. D **26**, 1487.

Schipper, W.J., J.J. Hamelink and G. Blasse, 1994, Phys. Status Solidi A **141**, 231.

Schlesinger, M., and P.W. Whippey, 1969, Phys. Rev.1969, Phys. Rev. **177**, 563.

Semenov, O.V., A.Ya. Kupryazhkin and S.O. Cholakh, 1992, Pis'ma Zh. Tekh. Fiz. **18**, 17 [Sov. Tech. Phys. Lett. **18**, 695].

Serviere, H., C. Vignolo, H. Prevost and J. Gasiot, 1991, Radiat. Prot. Dosim. **39**, 145.

Setzkorn, R., H. Prevost, J. Gasiot and P. Christensen, 1996, Radiat. Prot. Dosim. **66**, 419.

Shahare, D.I., S.I. Dhoble and S.V. Moharil, 1993, J. Mater. Sci. Lett. **12**, 1873.

Shambon, A., and W. Condon, 1968, Phys. Med. Biol. **13**, 653.

Sharma, T.A.V., and K. Somaiah, 1992, Cryst. Res. Technol. **27**, 279.

Sharma, T.A.V., M. Giovanni and K. Somaiah, 1995, Mater. Chem. Phys. **39**, 214.

Shastry, S.S., and R.K. Kher, 1979, Nucl. Instrum. Methods **159**, 593.

Shastry, S.S., S.S. Shinde and R.C. Bhatt, 1980, Int. J. Appl. Radiat. Isot. **31**, 244.

Shaver, I.Kh., and V.G. Krongaus, 1990, Radiat. Prot. Dosim. **33**, 67.

Shinde, S.S., A.R. Lakshmanan, B.C. Bhatt and R.C. Bhatt, 1988, Nucl. Instrum. Methods B **31**, 592.

Shinde, S.S., B.C. Bhatt, J.K. Srivastava and S.S. Sanaye, 1996, Radiat. Prot. Dosim. **65**, 305.

Shiran, N.V., A.V. Gektin, V.K. Komar, I.M. Krasovitskaya and V.V. Shlyahturov, 1995, Radiat. Meas. **24**, 435.

Shrivastava, N.K., M.N. Bapat, M. Khan and S. Sivaraman, 1986, J. Mater. Sci. **21**, 2540.

Sidran, M., 1968, in: Proc. 2nd Int. Conf. on Luminescence Dosimetry, Gatlinburg, CONF G80 920 (NTIS, Springfield, VA) p. 883.

Singh, N., G.L. Marwaha, S.P. Garg and V.K. Mathur, 1982, Radiat. Eff. **60**, 155.

Sinha, R.K., and M.L. Mukherjee, 1981, Phys. Status Solidi B **105**, 69.

Smolskaya, L.P., E.F. Martynovich, A.G. Davydchenko and S.A. Smirnova, 1987, Zh. Prikl. Spektrosk. **46**, 56 [J. Appl. Spectrosc. **46**, 44].

Somaiah, K., and V. Hari Babu, 1984, Phys. Status Solidi A **82**, 201.

Somaiah, K., and K.S.V. Nambi, 1987, J. Mater. Sci. Lett. **6**, 386.

Somaiah, K., M. Venkata Narayana and L.H. Brixner, 1990a, Mater. Chem. Phys. **26**, 13.

Somaiah, K., M. Venkata Narayana and L.H. Brixner, 1990b, Mater. Chem. Phys. **24**, 353.

Somaiah, K., M. Venkata Narayana and L.H. Brixner, 1990c, Phys. Status Solidi A **117**, K81.

Somaiah, K., T.A.V. Sharma, K.S.V. Nambi and H. Den Hartog, 1991, Cryst. Res. Technol. **26**, 469.

Souza, J.H., L.C. deFreitas and V.A. Ferrari, 1990, Rev. Bras. Eng. **7**, 344.

Souza, J.H., V.A. Ferrari and L.C. deFreitas, 1993a, Radiat. Prot. Dosim. **47**, 239.

Souza, J.H., L.A.R. da Rosa and C.L.P. Mauricio, 1993b, Radiat. Prot. Dosim. **47**, 103.

Spurny, F., and I. Votockova, 1993a, Radiat. Prot. Dosim. **48**, 341.

Spurny, F., and I. Votockova, 1993b, Radiat. Prot. Dosim. **48**, 355.

Spurny, F., and I. Votockova, 1994, Radiat. Meas. **23**, 247.

Spurny, Z., 1971, Health Phys. **21**, 755.

Srivastava, J.K., and S.J. Supe, 1979, Nucl. Instrum. Methods **160**, 529.

Srivastava, J.K., and S.J. Supe, 1980, J. Phys. D **13**, 2337.

Srivastava, J.K., and S.J. Supe, 1983, J. Phys. D **16**, 1813.

Srivastava, J.K., and S.J. Supe, 1984, Radiat. Prot. Dosim. **6**, 45.

Srivastava, J.K., and S.J. Supe, 1985, Phys. Status Solidi A **92**, 573.

Srivastava, J.K., and S.J. Supe, 1986, Nucl. Instrum. Methods A **243**, 567.

Srivastava, J.K., S.J. Supe and R.C. Bhatt, 1991, Phys. Status Solidi A **124**, 401.

Srivastava, J.K., B.C. Bhatt and S.J. Supe, 1992, Radiat. Prot. Dosim. **40**, 271.

Srivastava, N.K., M.N. Bapat, M. Khan and S. Sivaraman, 1986, J. Mater. Sci. **21**, 2540.

Stammers, K., and S.A. Kingston, 1991, Radiat. Prot Dosim. **36**, 23.

Starick, D., A.M. Gurvich, M.G. Myagkova, J. Rudiger and G. Herzog, 1993, Nucl. Tracks Radiat. Meas. **21**, 39.

Su, C.-S., and S.-M. Yeh, 1996a, Radiat. Prot. Dosim. **65**, 89.

Su, C.-S., and S.-M. Yeh, 1996b, Radiat. Meas. **26**, 83.

Subramanian, U., and M.L. Mukherjee, 1986, Phys. Status Solidi B **137**, 675.

Subramanian, U., and M.L. Mukherjee, 1987, J. Mater. Sci. **22**, 473.

Sunta, C.M., 1984, Radiat. Prot. Dosim. **8**, 25.

Sweet, M.A.S., and I.T. Liddell, 1990, J. Mater. Sci. **25**, 2717.

Sweet, M.A.S., and J. Rennie, 1987, Phys. Status Solidi A **100**, K67.

Sweet, M.A.S., and J. Rennie, 1988, J. Cryst. Growth **86**, 942.

Takahashi, K., K. Kohda, J. Miyahara, Y. Kanemitsu, K. Amitani and S. Shionoya, 1984, J. Lumin. **31–32**, 266.

Takeuchi, N., K. Inabe, J. Yamashita and S. Nakamura, 1976, Health Phys. **31**, 519.

Templer, R., 1985, Nucl. Tracks Radiat. Meas. **10**, 789.

Thomas, R., and V.P.N. Nampoori, 1988, Solid State Commun. **68**, 821.

Thoms, M., H. von Seggern and A. Winnacker, 1994, J. Appl. Phys. **76**, 1800.

Tokuyama, H., S. Igarasi and H. Hayakawa, 1990, Radioisotopes Japan **39**, 357.

Toryu, T., H. Sakamoto, I. Hitomi, N. Kotepa and Kh. Yamada, 1973, Izv. Akad. Nauk SSSR, Ser. Fiz. **37**, 795 [Bull. Acad. Sci. USSR **37**(4), 97].

Townsend, P.D., and Y. Kirsh, 1989, Contemp. Phys. **30**, 337.

Townsend, P.D., and D.R. White, 1996, Radiat. Prot. Dosim. **65**, 83.

Trautweiler, F., F. Moser and R.P. Khosla, 1968, J. Phys. Chem. Solids **29**, 1869.

Tripathi, L.N., B.R. Chaubey and C.P. Mishra, 1980, Phys. Status Solidi A **60**, 185.

Tripathi, L.N., S.K. Mishra and U.N. Pandey, 1991, Phys. Lett. A **154**, 312.

Tripathi, L.N., S.K. Mishra and R.N. Singh, 1993, Indian J. Pure Appl. Phys. **31**, 819.

Tsukuda, Y., 1981, Mater. Res. Bull. **16**, 453.

Uehara, Y., H. Toyama, H. Matsukiyo, Y. Kaseki and N. Nakayama, 1995, Electrochem. Soc. 188th Meeting, Extended Abstract **95.2**, p. 1228.

Upadeo, S.V., and S.V. Moharil, 1995, J. Phys.: Condens. Matter **7**, 957.

Upadeo, S.V., and S.V. Moharil, 1997, J. Phys.: Condens Matter **9**, 735.

Upadeo, S.V., T.K.G. Rao and S.V. Moharil, 1994, J. Phys.: Condens. Matter **6**, 9459.

Upadeo, S.V., S.V. Moharil and T.K.G. Rao, 1998, J. Phys.: Condens. Matter **10**, 683.

Urbach, F., 1930, Wiener Ber. **139**, 363.

Vana, N., R. Erlach, M. Fugger, W. Grotzl and I. Reichalter, 1988, Nucl. Tracks Radiat. Meas. **14**, 181.

Vekic, B., M. Ranogajec-Komor and M. Cukman, 1990, Radiat. Prot. Dosim. **33**, 335.

Venkata Narayana, M., and K. Somaiah, 1990, Cryst. Res. Technology **25**, K209.

Venkata Narayana, M., K. Somaiah, V. Hari Babu and L.H. Brixner, 1990, Mater. Chem. Phys. **26**, 99.

Vij, D.R., ed., 1993, Thermoluminescent Materials (PTR Prentice Hall, NJ).

Vij, D.R., and V.K. Mathur, 1975, J. Electrochem. Soc. **122**, 310.

Vijayan, C., and Y.V.G.S. Murti, 1989, Cryst. Lattice Def. Amorphous Mater. **18**, 431.

Vlasov, V.K., and V.V. Karezin, 1993, Nucl. Tracks Radiat. Meas. **21**, 147.

von Seggern, H., T. Voigt, W. Knuper and G. Lange, 1988, J. Appl. Phys. **64**, 1405.

Wada, T., K. Okei, O. Nishikawa, I. Seto, Y. Yamashita, I. Yamamoto, K. Kuga and M. Nakagawa, 1995, Rep. Res. Lab. Surf. Sci. Okayama Univ. **7**, 191.

Wang, S., G. Chen, F. Wu, Y. Li, Z. Zha and J. Zhu, 1986, Radiat Prot. Dosim. **14**, 223.

Wang, T.K., P.C. Hsu and P.S. Weng, 1987, Radiat. Prot. Dosim. **18**, 157.

Wang, T.K., P.C. Hsu and P.S. Weng, 1989, Appl. Radiat. Isot. **40**, 329.

Weng, P.S., P.C. Hsu and Y.H. Chen, 1995, Appl. Radiat. Isot. **46**, 1081.

Wernli, C., 1990, Radiat. Prot. Dosim. **34**, 199.

Wiedemann, E., and G.C. Schmidt, 1895, Ann. Phys. Chem. **54**, 604.

Xia, Chan-Tai, and Chun-Shan Shi, 1997, Mater. Res. Bull. **32**, 107.

Yamada, H., A. Suzuki, Y. Uchida, M. Yoshida and H. Yamamoto, 1989, J. Electrochem. Soc. **136**, 2713.

Yamamoto, H., and H. Matsukiyo, 1991, J. Lumin. **48–49**, 43.

Yamashita, T., N. Nada, H. Onishi and S. Kitamura, 1968, in: Proc. 2nd Conf. on Luminescent Dosimetry, Gatlinburg, USA (U.S. Atomic Energy Commission) p. 4.

Yamashita, T., N. Nada, H. Onishi and S. Kitamura, 1971, Health Phys. **21**, 295.

Yao, Y.A., S.C. Huang, P.C. Hsu and P.S. Weng, 1981, Radiat. Res. **86**, 147.

Yasuno, Y., M. Watari, H. Tsutsui, M. Skedo and O. Yamamoto, 1980, U.S. Patent No. 4 **204**, 119.

Yeh, S.-M., and C.-S. Su, 1996a, Radiat. Prot. Dosim. **65**, 359.

Yeh, S.-M., and C.-S. Su, 1996b, Mater. Sci. Engineering **B38**, 245.

Yeh, S.H., 1986, Radiat. Effects. **88**, 39.

Zanelli, G.D., 1968, Phys. Med. Biol. **13**, 393.

Zarand, P., 1996, Radiat. Prot. Dosim. **66**, 279.

Zarand, P., and I. Polgar, 1983, Nucl. Instrum. Methods **205**, 525.

Zarand, P., and I. Polgar, 1984, Nucl. Instrum. Methods **222**, 567.

Zhang, Z.L., Y.Z. Zheng, Z. Su, K.J. Zhao and C.X. Liu, 1993, Chin. J. Space Sci. **13**, 116.

Zhao, W., and M.-Z. Su, 1993, Mater. Res. Bull. **28**, 123.

Handbook on the Physics and Chemistry of Rare Earths
Vol. 28
edited by K.A. Gschneidner, Jr. and L. Eyring
2000 Elsevier Science B.V.

Chapter 180

ANALYTICAL SEPARATIONS OF THE LANTHANIDES: BASIC CHEMISTRY AND METHODS*

Kenneth L. NASH and Mark P. JENSEN
Chemistry Division, Argonne National Laboratory, 9700 S. Cass Ave., Argonne, IL 60439-4831, USA

Contents

List of symbols and acronyms

AAS	atomic absorption spectroscopy
Aliquat 336	tetraalkyl ammonium extractant with alkyl chains ranging between C_8 and C_{10}
Arsenazo III	2,2′-(1,8-dihydroxy-3,6-disulfonapthalene-2,7-bisazo)-bis(benzenearsonic acid)

* Work performed under the auspices of the U.S. Department of Energy, Office of Basic Energy Sciences, Division of Chemical Sciences under contract number W-31-109-ENG-38

CMPO	octyl(phenyl)-*N,N*-diisobutyl-carbamoylmethylphosphine oxide	HPLC	high-performance liquid chromatography
dcpa	2,6-dicarboxypiperidine-*N*-acetic acid	HPMBP	1-phenyl-3-methyl-4-benzoyl-5-pyrazolone
dcta	*trans*-1,2-diaminocyclohexane-*N,N,N',N'*-tetraacetic acid	ICP/AES	inductively coupled plasma atomic emission spectroscopy
dipic	2,6-dicarboxypyridine	ICP/MS	inductively coupled plasma mass spectrometry
D_m	distribution ratio for metal m	MS	mass spectroscopy
DMSO	dimethylsulfoxide	NAA	neutron activation analysis
DOTA	1,4,7,10-tetraazacyclododecane-*N,N',N'',N'''*-tetraacetic acid	nta	nitrilotriacetic acid
edta	ethylenediamine-*N,N,N',N'*-tetraacetic acid	PAR	4-(2-pyridylazo)resorcinol
GC	gas chromatography	SFC	supercritical fluid chromatography
HDEHP	bis(2-ethylhexyl)phosphoric acid	$S^m_{m'}$	separation factor for metal m from metal m'
HEDPA	1-hydroxyethane-1,1-diphosphonic acid	TBP	tributylphosphate
hedta	*N*-(2-hydroxyethane)ethylenedinitrilo-*N,N',N'*-triacetic acid	thftca	tetrahydrofuran-2,3,4,5-tetracarboxylic acid
hiba	α-hydroxyisobutyric acid	TOPO	trioctylphosphine oxide

1. Introduction

The rare-earth elements are assuming an increasingly important role in modern society (Szymanski 1987). For example, Nd–Fe–B magnets possess the highest field strength of any permanent magnet. Certain rare-earth elements are a basic component of the ceramic 123 high-temperature superconductors. They are widely used in optical materials as special-purpose glasses, including perhaps their largest application in the phosphors of cathode ray tubes for television sets and computer monitors. Rare earths are also now commonly found in metal alloys, for example replacing chromium in bright metal alloys. Rare earths are also employed as catalysts. In medicine, gadolinium compounds are finding increased use as magnetic resonance imaging reagents for diagnosis, and radioactive isotopes of Y, Dy, Er and Sm are applied as radiotherapeutic reagents. Sm and Gd are used as neutron poisons to control unwanted criticality events in the handling of nuclear materials.

In addition to these technological applications, the rare earths have made diverse contributions to science. Several lanthanides are used in nuclear power as fission yield monitors to track the progress of nuclear reactions occurring in power plants. Much of the understanding that modern society has developed about the genesis of the earth has been accomplished through studies of the distribution of rare-earth elements on and in the earth and in meteorites (isotope geology). The disposition of rare-earth elements in the subsurface surrounding the fossil nuclear reactor at Oklo (in Gabon) establishes a baseline for potential migration of certain actinide ions for a nuclear waste

repository. In fact, rare-earth isotopic distribution in Oklo rocks helped confirm the existence of the fossil reactors. Lanthanide shift reagents are important analytical tools in NMR spectroscopy, thus impacting a wide variety of experimentation in chemistry. In this application, substitution of paramagnetic lanthanide ions into biological materials has produced important insights into the structure and function of important biological macromolecules. Fluorescent molecules incorporating Eu are similarly used to study the structure of biomolecules and for immunoassay. Increasingly, lanthanide compounds are finding application as catalysts in organic synthesis.

At some level, it is necessary in all of these scientific and technological applications to quantify the lanthanides present. Choice of an analytical technique is dictated by the type of information required and by the nature of the sample(s) being analyzed. Separation chemistry is central to many of the most successful analytical methods. For the rare earths, two distinct separations are important: (1) separation of the rare earths as a group from the matrix elements, and (2) separation of the individual members of the series. Due to the chemical similarities of the rare earths and the existence of these metal ions in essentially one oxidation state, the latter is one of the greatest challenges in the separation of metal ions.

Depending on the detection technique employed and the purpose of the analysis, it is occasionally sufficient to conduct a relatively simple group separation to isolate the rare earths from the matrix. Neutron activation analysis (NAA), inductively coupled plasma/atomic emission spectroscopy (ICP/AES), and mass spectrometry (ICP/MS) are examples of techniques that have been applied for "simultaneous" detection/quantitation of individual lanthanides in a mixture of lanthanides. Chemical separation techniques are often required prior to application of these methods because of the susceptibility of element-specific techniques to interferences that may compromise the analysis.

Among the most precise and often applied analytical methods are various chromatographic methods. Chromatography is popular partly for its low cost, but also for its sensitivity, particularly when it is applied with a "preconcentration" separation that isolates the lanthanides from matrix elements. The most demanding analytical methods combine chromatographic techniques with element/isotope specific techniques like NAA or mass spectrometry (MS). The separation chemistry of the lanthanides and Y as a group and of individual members of the series, is the subject of this review.

The general topic of analytical separations of the rare earths has been reviewed a number of times in the past ten years (Zhang et al. 1997, Myasoedov et al. 1997, Shao et al. 1997, Bai et al. 1996, Kitazume 1996, Muralidharan and Freiser 1995, Akiba 1995, Oguma et al. 1995, Kumar 1994, Kuroda 1991, Robards et al. 1988). Some of these reviews have focused on specific techniques. Others have presented a broader comparison of the virtues and vices of various techniques, and their suitability for specific analytical tasks. Reviews have appeared in several languages, indicating that important research is being done around the world on both lanthanide science and technology in general, and on analytical methods development for lanthanides. The most recent of the broad-based English-language reviews was published in 1994, discussing the literature through 1992 (Kumar 1994).

Because these fine resources are available to describe which separation techniques have been applied to analyze various types of samples, we have elected to focus in this review primarily on describing the fundamental chemistry that underpins contemporary analytical separation techniques for lanthanides. We intend that this approach will provide the reader with an improved understanding of the advantages and disadvantages of the mainstream separation-based methods for lanthanide analysis, and thus help the analyst identify the optimum techniques for any particular analytical problem. Some portion of this discussion will address developing trends in lanthanide analytical science. We will outline some of the important interfaces between the separation methods and the detection/quantitation techniques employed. We have elected to include Y among the lanthanides, as this separation is often moderately difficult and sometimes problematic. The separation of Sc from the lanthanides is usually more easily accomplished, taking advantage of the substantial difference in size between Sc and the rare earths. We have therefore elected not to include the analytical separations of Sc in the present discussion. This review will also not specifically address analytical separations that target the trivalent actinides, though we will discuss both the Oklo phenomenon and the use of lanthanides as yield tracers for nuclear fission. Finally, our examination of the literature on the organometallic chemistry (for our purposes, those species involving lanthanide bonds to carbon) revealed no examples of analytical separations for these compounds. We therefore have nothing to report on the analysis of lanthanide organometallics by separation techniques.

Our general research interests are in the area of the coordination chemistry and solvation of f-element complexes. We are particularly interested in descriptions of this chemistry that can be developed through studies of the thermodynamics, kinetics, and spectroscopy of complexation reactions. With the excellent general reviews of techniques and applications already available in the literature, we will indulge ourselves in discussions of the fundamental coordination chemistry of rare earths as they impact analytical-scale separations. We will focus primarily on describing the fundamental interactions that lead to a successful separation. Among the topics we will discuss are:

(1) Solvation effects in both aqueous and non-aqueous media.
(2) The impact of complexation reactions on lanthanide separations, both those occurring in aqueous and non-aqueous solutions and in/on ion exchange resins.
(3) Phase transfer reactions and interfacial phenomena in lanthanide analytical separations.
(4) Matrix dissolution effects.
(5) The behavior of yttrium in rare-earth separations.
(6) How detection methods impact the separations chemistry (and are impacted by the separations).
(7) Research needs and future directions.

We have focused principally on the literature from about 1990 to the present, relying on the prior reviews for a description of the literature before 1990. Due to the difficulty in getting translations of foreign language reports, our review will rely primarily on the most accessible English language reports and readily available translations of non-English

journals. Those non-English reports that are not generally available in translation must be evaluated primarily based on English-language abstracts. The contents of the work have therefore been evaluated with this limitation.

2. Description of the methods

Among the analytical-scale separation techniques for lanthanide analysis, the most widely used (and generally successful) methods are ion exchange (for isolation from the matrix) and liquid chromatography (for separation of individual members of the series). However, most available chromatographic methods have been tested for analysis of rare-earth elements, achieving variable success. Solvent extraction has been applied for preconcentration of rare earths from the matrix elements, though it has not been used with the same frequency as it is used for production-scale separations of rare earths. Adaptation of solvent extraction reagents to chromatographic applications has had a more substantial impact in analytical chemistry of the rare earths. Two examples of these techniques are extraction chromatography and centrifugal partitioning chromatography. Precipitation techniques have been applied for preconcentration of lanthanides from certain matrices, but are of little value for analytical separation of series members. Neither gas chromatography nor supercritical fluid chromatography has made substantial impact in rare-earth analysis. We will discuss reasons for this lack of success, emphasizing the basic chemistry of the techniques as they impact the rare earths.

Analysis of lanthanide samples is typically a destructive process. Most commonly, the sample (rock, ceramic, metal/alloy, metal oxide etc.) will be subjected first to a digestion process that completely dissolves the sample (as opposed to selective dissolution of the rare earths). In most cases, the solution resulting from matrix dissolution is too complex to allow a simple direct analysis by ICP/AES or ICP/MS. To improve sensitivity and/or eliminate interferences, a "preconcentration" separation is often needed. Solvent extraction, ion exchange, and precipitation methods have been used, alone and in combination, for lanthanide preconcentration. We will refer to these reactions as group separations in the following discussion. For the most demanding analytical applications such as isotope geology, it is necessary to separate the individual members of the series from their neighbors. Because of the great similarity of the chemistry of the trivalent lanthanides and the wandering behavior of yttrium, these separations are most demanding of the chemistry.

2.1. *Impact of matrix dissolution on analytical separations*

Most analytical procedures for rare-earth analysis require destructive dissolution of the sample. As most analyzed lanthanide samples are often refractory inorganic materials, the initial step of dissolution of the matrix is often the most time-consuming stage of the analysis. Dissolution of rock samples prior to analysis requires either a prolonged high-temperature digestion with mixtures of mineral acids (e.g., HF and $HClO_4$) or a

solid-state fusion reaction. In one report, microwave digestion was applied to dissolve natural samples (Watkins et al. 1995). Occasionally secondary precipitation reactions are needed to eliminate potentially interfering ions. The dissolution of metal alloys is typically accomplished by high-temperature dissolution with mineral acids. This too can require prolonged treatment, as many lanthanide alloys are designed for their resistance to corrosion. In contrast to these samples, pure lanthanide oxides readily dissolve in mineral acids.

The dissolution process typically results in complete digestion of the sample and formation of a stable acidic solution. This solution will contain all of the inorganic components (except for the minimal few that are volatilized). Treatment protocols generally should destroy most organic matter. The subsequent manipulation of the dissolved solution is determined by the requirements of the detection method to be applied. Direct application of multielement detection techniques (radiochemistry, neutron activation analysis, mass spectrometry) may occasionally be applied, but the general characteristics of the sample must be well-known to avoid unexpected problems in conducting the analysis. It is often advisable to apply group-separation techniques to avoid such conflicts. Preparation of the sample for chromatography almost always includes a preconcentration step in which the lanthanides are concentrated and freed of interfering cations and anions (sect. 2.2.2).

2.2. *Separation methods*

The most sensitive analytical methods for rare earths include a group separation followed by a lanthanide separation with subsequent application of ion selective analysis. Preconcentration removes potential problem species and prepares the sample for the subsequent analysis. For most samples, a group separation from matrix ions is desirable. An example of a system perhaps not requiring preseparation might be the analysis of lanthanide impurities in high-purity lanthanide oxides. For most samples, application of a cation-selective separation method and a generic (i.e., non-element specific) detection system provides the appropriate analytical sensitivity. Two-stage chromatographic separation techniques (group separation followed by element separation) are the most commonly employed methods for analysis of individual lanthanide cations. In the following sections, we will describe generically the most common separation methods.

2.2.1. *General aspects of chromatographic analysis*

Chromatographic techniques are well-known and widely used for analysis of all sorts of samples. Most of the common chromatographic methods have been applied for quantitative and qualitative analysis of lanthanides with varying degrees of success. Chromatographic analytical methods share the common characteristic of multiple interactions between the species to be analyzed, generally present in a homogeneous phase, and a counterphase into which the analyte is transferred. In successful separation techniques, the interactions within the homogeneous phase and at interfaces occur reversibly. As the

analyte travels through (or over) the counter medium, these equilibrations are repeated endlessly. Minor differences in the equilibrium behavior of the analyte and competing species (matrix components or other species to be analyzed) are amplified through the repetitive equilibration to accomplish the separation. The relative affinities of the analyte for the solvent, solutes in the solution phase (for those techniques involving liquids), and the counter phase (generally an immiscible liquid or reactive solid) determines the elution time for the solute from the column.

Powell (1961) has described in elegant terms the application of ion-exchange chromatographic separations to analysis and production of lanthanides. The concepts described are not unique to ion-exchange separations, but apply generally to chromatographic analyses, particularly those involving a mobile liquid phase. Gas (GC) and supercritical fluid (SFC) chromatography share some of the same characteristics, but lack certain aspects of the chemistry that are unique to aqueous media.

Powell describes "Displacement Chromatography" and "Elution Chromatography" as the two principal methods for separating lanthanide cations by ion-exchange chromatography. In displacement chromatography, the ions to be separated are first sorbed onto a column of the resin. The analyte metals are eluted from the column by introducing a species that is more strongly bound to the resin, displacing the analyte metal ions. As the analyte metal ions are displaced, they travel down the column at different rates governed by their relative affinity for the resin phase. This results in "banding" of the analyte metal ions as they exit the column. Some overlap between the bands is inevitable in this technique. However, pure samples can be collected by avoiding the band overlap regions. This technique is generally more suitable for production-scale chromatography than for analysis.

In elution chromatography, the analyte ions are adsorbed onto the column as in displacement chromatography. However, the driving ion is sorbed less strongly than the analyte species. In this case, the driving ion is present at a greater concentration than the analyte ions and displaces the latter by mass action. The driving ion overruns and accompanies the analyte ions through the column. Because the displacing ions are weakly sorbed, they are displaced down the column by the more strongly bound analyte ions. The overflow of the solution containing the displacing ions leads to repeated sorption and desorption of the analyte ions. Differentiation of the analyte species is accomplished based on the relative affinity of the ion exchanger for the ions. This approach can result in discrete bands containing the analyte ions without overlap if the chemistry is suitable and the number of re-equilibrations (theoretical plates) is large enough. This approach is most suitable for analysis of rare earths.

In a recent review of analytical separations of the rare earths, Robards et al. (1988) have summarized the column-chromatographic techniques that have been applied for lanthanide analysis using the following categories:

- Displacement chromatography, as described above, is a primarily production-scale technique and is not an important analytical procedure.
- Adsorption and partition chromatography relies on the uptake of lanthanide ions by silica or alumina as a solid-phase transfer medium with aqueous chelating agents used for partitioning.

- Ion-pair chromatography (also called dynamic ion exchange or ion interaction chromatography), as applied for lanthanide analysis, consists of the use of silica phases with long-chain alkyl groups covalently bonded to the silica, creating a hydrophobic layer on the solid sorbent. The eluting solution is an aqueous medium containing a mixture of hydrophilic chelating agent(s) and a sulfonic acid surfactant. The hydrophobic silica column is preconditioned by passage of an aqueous medium containing the sulfonic acid surfactant. The organic tail of the surfactant interacts strongly with the lipophilic layer of the silica to form a solid material analogous to cation-exchange resins. Metal ions are sorbed to the sulfonate groups and separated based on their relative affinity for the chelating agent in the aqueous medium. This method is one of the most consistently successful analytical methods for lanthanide quantitation. The general characteristics of the method and their application for the analysis of nuclear fuels have been summarized by Cassidy et al. (1985).
- Cation-exchange chromatography is based on cation-exchange resins, principally sulfonated polystyrene–divinylbenzene copolymers, as the phase-transfer medium, and aqueous complexants as the eluant. Anion exchange is the comparable technique in which anionic mobile solutes interact with immobile cation sites in the resin phase. Anion exchange is employed less frequently in lanthanide analysis. Ion exchange using resins containing chelating functional groups, which can exhibit greater cation specificity, has also been investigated.
- Ion chromatography is distinguished from cation-exchange chromatography by the application of continuous conductivity detection, and the use of two ion-exchange columns in series. Separation of the analyte solution is achieved in the first column while the second sorbs counter ions that interfere with the conductivity detection system. Recent developments have reduced the need for a secondary (suppression) column, thus blurring the distinction between cation exchange and ion chromatography.
- Extraction chromatography is the application of conventional solvent extraction chemistry in a chromatographic mode. The lipophilic solvent extraction solution is immobilized on a solid support and an aqueous solution containing the analytes is passed through the column. The extraction chromatographic material may serve as a phase transfer medium only (much like cation-exchange resin, exhibiting minimal selectivity) or may engage in selective sorption of lanthanide ions thus achieving separation without the addition of water-soluble chelating agents. Acidic organophosphorus extractants are the most typical reagents for lanthanide analysis by extraction chromatography.

In addition to these techniques, applications of capillary electrophoresis for lanthanide analysis have appeared recently (Corr and Anacleto 1996, Vogt and Conradi 1994). Capillary electrophoretic separations rely on differences in the electrophoretic mobility of analyte species in an electrolyte buffer while under the influence of an applied electric field. For lanthanide analysis, the mobilities of the solvated cations are not adequately differentiated for an effective mutual separation, though separation from transition metals or alkali/alkaline-earth metals should be readily accomplished. Introduction of chelating agents that form complexes with the ions leads to improved separation efficiency through

the altered mobility of the complexes. Vogt and Conradi (1994) describe the relationship between complex formation and electrophoretic mobility using the basic equations we will discuss in sect. 3.4. Robards et al. (1988) also described lanthanide separations by the related techniques of zone electrophoresis and isotachophoresis, both based on the electrophoretic mobility of lanthanide complexes.

2.2.2. *Preconcentration/group separations*

For analysis of lanthanide ions in complex matrices like rocks, it is generally necessary to remove non-lanthanide components of the dissolved sample before conducting the analysis. Preconcentration is often essential for lanthanide analysis by neutron activation, wherein the γ-emission spectra of certain matrix elements overlap with those of the target lanthanides. In mass-spectrometric analysis of samples, some matrix elements can interfere with lanthanide quantitation (for example, barium with lanthanum). Application of a preseparation step gives the added benefit of concentrating dilute solutions of lanthanides to improve detection limits.

A commonly used approach for group separations is to apply cation exchange from concentrated mineral acid solutions. Typically, a column of Dowex 50X8 sulfonic acid resin is prepared and preconditioned by passage of nitric acid of the appropriate concentration followed by a deionized water wash. The sample is then loaded onto the column from dilute acid. The lanthanides and most polyvalent cations are bound to the column while anions and alkali metal ions pass through. A subsequent rinse with 2 M HCl or 2 M HNO_3 is used to elute alkaline-earth metal ions and most first-row transition metals. A second rinse of 4 M HCl or HNO_3 may be applied to remove problematic metal ions like Fe^{3+}. The concentrated lanthanides are eluted with 6 M HCl or 6–8 M HNO_3. This eluant is usually evaporated to prepare the sample for the subsequent ion-selective analysis. Depending on the exact composition of the sample being analyzed, Fe^{3+}, Al^{3+}, Sc^{3+} and Ba^{2+} are common contaminants that may coelute in the group separation and can interfere with lanthanide analysis.

Some authors have used precipitation techniques to concentrate the lanthanides. The most commonly used species are oxalates and fluoride. Rare-earth oxalates ($R_2(C_2O_4)_3$) have solubility products ranging from 10^{-25} to 10^{-29} M^5. Isolation of lanthanide cations as oxalate precipitates is often followed by ignition to the oxide, then acid dissolution of R_2O_3. This procedure can be expected to provide samples suitable for almost any type of detection/quantitation method. The solubility products of the fluorides (RF_3) are found in the range of 10^{-15} to 10^{-19} M^4. Whether precipitation techniques can be applied is partly determined by the concentration of rare-earth ions in the sample, and whether a carrier precipitation is acceptable for those samples in which the lanthanide concentration is too low. The detection method most directly impacts the viability of carrier precipitation techniques.

Solvent extraction is also suitable for group separation and preconcentration in many analyses. The basic technique can be applied in either a liquid–liquid contact mode or using extraction chromatographic techniques. When the sample is not too complex and

the method of analysis is amenable to a group separation without preconcentration, the easiest approach for isolation of the rare earths is often to extract the interfering matrix components, leaving the rare earths in the aqueous phase. This approach has been applied in the analysis of rare earths in nuclear materials (Gopalkrishnan et al. 1997, Carney and Cummings 1995, Sanchez-Ocampo et al. 1991) and also in NAA of high-purity Ni (Yoon et al. 1996). Saiki (1989) used the antibiotic tetracycline in benzyl alcohol to extract U, Th, Fe, Sc, Na, Ta, and Mo from rock samples before NAA of the lanthanides.

When an analysis demands preconcentration of the rare earths, a reagent capable of selectively extracting rare-earth ions must be employed. Extractants from each of the categories discussed in sect. 3.2 extract the rare earths well. For instance, Alimarin et al. (1978) applied cupferron extraction of the rare earths Sc, Th, Hf, and Zr from pH 6–7 volcanic vapor condensates prior to NAA. However, most solvent-extraction based group separations or preconcentrations of the rare earths use one of the extensively studied organophosphorus extractants such as tributylphosphate (TBP) (Shmanenkova et al. 1991), octyl(phenyl)-*N,N*-diisobutylcarbamoylmethylphosphine oxide (CMPO) (Pin et al. 1994) or, most often, bis(2-ethylhexyl)phosphoric acid (HDEHP) (Rehkämper et al. 1996). Extraction by neutral reagents like TBP and CMPO requires high concentrations of counter-anions in the aqueous phase to achieve charge balance of the extracted complex in the organic phase. In these cases the lanthanide cations could be extracted from aqueous phases containing 0.5–10 M HNO_3, 6–10 M HCl, or 0.5 M $Al(NO_3)_3$/3.5 M $LiNO_3$. Stripping is accomplished with dilute (10^{-2}–10^{-1} M) acid. A dilute acid strip has obvious sample preparation advantages for element-specific quantitation in a subsequent step.

Preconcentration by an acidic organophosphorus extractant is also effective, though the lanthanides are extracted from dilute acid solutions (10^{-4}–10^{-1} M) and stripped into acidic (>1 M) solutions when HDEHP is employed as the extractant. A representative application of liquid–liquid extraction to rare-earth preconcentration is the 100 to 200-fold concentration of the rare earths in seawater prior to ICP/MS determination using a mixture of HDEHP and mono-(2-ethylhexyl)phosphoric acids (Shabani et al. 1990, Shabani and Masuda 1991). When the same extractant system was adsorbed on a C_{18} cartridge and used in an extraction chromatographic mode, the rare earths were concentrated 200–1000-fold (Shabani et al. 1992).

2.2.3. *Solvent extraction/extraction chromatography/centrifugal partitioning chromatography*

A liquid–liquid, or solvent, extraction system is composed of two immiscible liquid phases that are free to mix on agitation. One phase is generally aqueous while the other is a water-immiscible organic solvent. The organic medium usually contains lipophilic complexing agents that promote distribution of the analyte into the organic phase by the formation of lipophilic complexes or ion pairs. Aqueous biphasic systems with two distinct aqueous phases, rather than one organic and one aqueous phase, also have been applied to lanthanide separations as reviewed by Rogers et al. (1993). Reagents that form hydrophilic complexes with an analyte can be introduced to hold selected metals in the aqueous

phase. Given the number of different organic solvents, extractants, and aqueous phase compositions, the possibilities for separations of the rare earths by solvent extraction techniques are vast. Moreover, an individual solvent extraction separation itself requires no special equipment, is easily scaled up or down, and can usually be completed in minutes. Alcohols, ketones, neutral or acidic organophosphorus compounds, β-diketones, carboxylic acids, crown ethers, and alkyl amines have all been used as extractants for rare-earth cations.

Solvent extraction has been widely applied for the analysis of many different classes of metal ions, typically using moderately volatile solvents like chloroform. By the nature of the technique, high single-stage extraction efficiency is required for the direct application of solvent extraction to quantifying the metal ion content of a sample. High stage efficiency is typically achieved through the application of selective chelating agents, capable of binding a single metal ion out of a mixture of similar species. Often such analyses rely on differences in the oxidation states of the metal ions to be analyzed. Unfortunately, if more than two or three stages of extraction are required for the analysis, most of the advantages of solvent extraction for analysis are lost. Multiple-stage countercurrent solvent extraction systems are, however, important in the commercial isolation of pure rare earths in >99% purity from ores.

While there are a number of different solvent extraction systems that could be used for rare-earth separations and the procedures are simple and fast, analytical separations of the rare earths usually utilize solvent extraction only for group separations, preconcentration, or for separations based on the different chemistries of the tetravalent (Ce^{4+}) or divalent (Eu^{2+}) oxidation states. The unique chemistry of the trivalent rare-earth cations makes their separation from matrix metal ions a straightforward process that is often achievable in a single extraction cycle (unless trivalent actinides are also present). Conversely, the similarity of the individual rare-earth cations makes their mutual separation difficult. The similar sizes of adjacent trivalent lanthanide cations cause the separation factors (sect. 3) to be much too small to allow separation of individual lanthanides in a single extraction stage. Enrichment of an analyte (e.g. Nd^{3+}) to 99.9% from an equimolar mixture with a contaminant (e.g. Pr^{3+}) in a single stage requires a separation factor of 10^3. The widely used extractant HDEHP has an average separation factor of only 2.5 for adjacent trivalent cations across the lanthanide series (Peppard et al. 1957). These values are among the highest known separation factors for adjacent lanthanides.

Solvent extraction systems incorporating both aqueous complexants and size-selective extractants achieve separation factors approaching 10 for a system comprised of edta (ethylenediamine-*N,N,N′,N′*-tetraacetic acid), trichloroacetate, and crown ethers (Frazier and Wai 1992). These separation factors are much larger than those obtainable in a single-batch equilibration with a typical ion exchange resin. However, they are still small enough that separation of individual rare-earth cations by solvent extraction requires multiple stages.

Like solvent extraction, separations by extraction chromatography and centrifugal partition chromatography (also known as centrifugal countercurrent chromatography depending on the apparatus used), are based on the partitioning of an analyte between

two liquid phases. The same solvents, extractants, and stripping reagents can be used in the three methods. Extraction chromatography and centrifugal partition chromatography differ from solvent extraction in that one liquid phase is stationary, giving the immobile phase the characteristics of a chromatographic material. In extraction chromatography the stationary phase is fixed via sorption on an inert solid such as silica, polystyrene, or even paper. In centrifugal partition chromatography, one liquid phase is held stationary by centrifugal force either in individual partition cells (centrifugal partition chromatography) or in a spiral column (centrifugal countercurrent chromatography).

As compared to solvent extraction, the primary advantage of extraction chromatography or centrifugal partition chromatography for rare-earth separations resides in the presence of multiple equilibration (extraction) stages, or theoretical plates, along the path of the mobile phase. By immobilizing one phase and using it for chromatography, the same reagents used for group separations by solvent extraction become capable of separating individual rare-earth ions from each other. When the same diluents, extractants, and aqueous phases are employed, the separation factors of rare-earth elements obtained by solvent extraction, extraction chromatography, and centrifugal partition chromatography are similar (fig. 1, Pierce et al. 1963, Dietz and Horwitz 1993). Generally, the number of theoretical plates in an extraction chromatographic column or a CPC apparatus is moderate compared to those encountered in conventional chromatography, between 10 and 500 vs. 10000. Nevertheless, separations based solely on the affinity of an extractant for the individual rare earths have been demonstrated with these systems, eliminating the need for aqueous complexants (sect. 3.4). Moreover, Kitazume et al. (1991) report a high-speed counter-current chromatographic separation of the lanthanides with separation factors between 60 and 6000. Unfortunately, extraction chromatography and centrifugal partition chromatography do not scale up as easily as solvent extraction.

2.2.4. *Cation exchange/anion exchange/high-performance liquid chromatography*

Group separations are readily accomplished using cation-exchange or anion-exchange techniques, as we discussed in sect. 2.2.1. Of the two methods, cation exchange is used far more frequently in lanthanide analysis. Anion exchange is less commonly applied for analysis of the rare earths because there are a limited number of realistic or useful systems wherein anionic lanthanide complexes are formed that exhibit an affinity for the resin phase. Though cation-specific ion exchange resins have been synthesized, their performance is often less than acceptable for a successful lanthanide separation. Extraction chromatographic resins based on acidic organophosphorus compounds (for example HDEHP) exhibit much superior performance.

The intrinsic separation of lanthanide ions on sulfonic acid resins is minimal. They typically offer only a few parts-per-thousand separation factors (ratio of distribution ratios or extraction equilibrium coefficients) for adjacent lanthanide ions, as is shown in fig. 2 (Marcus 1983, Surls and Choppin 1957). Values reported for gadolinium numbers (ratio of distribution coefficients normalized to Gd) in 0.01 M $HClO_4$ vary almost linearly across the series while the 0.11 M $HClO_4$ data show better selectivity for the light lanthanides

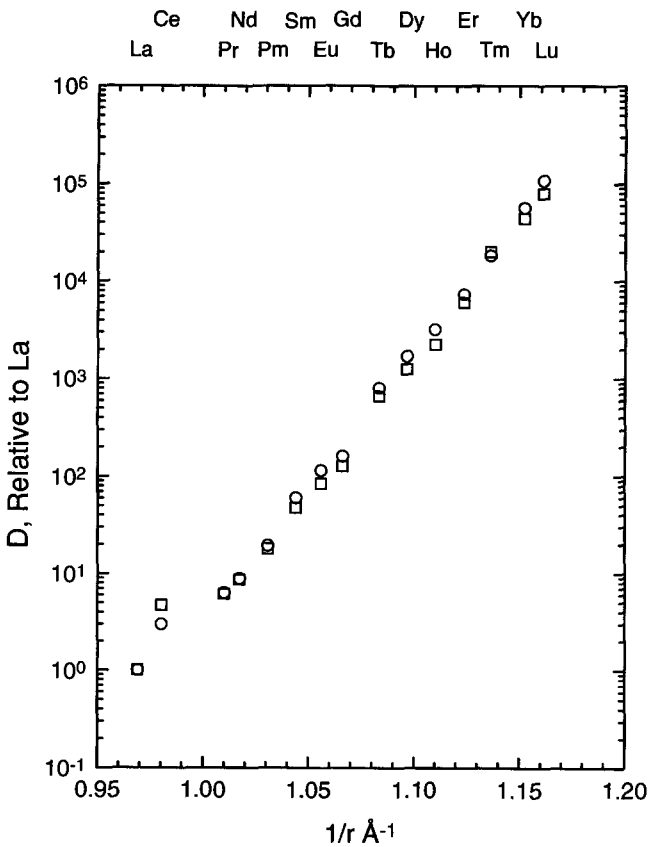

Fig. 1. Cumulative separation factors of lanthanides in $HClO_4$ by HDEHP. Squares: extraction chromatography on a polyvinyl chloride/polyvinyl acetate copolymer at 60°C. Circles: solvent extraction into toluene at 25°C. Data adapted from Pierce et al. (1963).

and almost none for lanthanides heavier than Ho. This general trend has been attributed by Helfferich (1962) (as a first approximation) to differences in cation hydrated radii. Comparison of the Gd numbers with the published values for the hydrated radii at the top of fig. 2 imply that this correlation is not a simple linear relationship. The inner-sphere hydrated radii exhibit a more-nearly linear trend with the Gd numbers, but the relationship is counterintuitive, as the increased electrostatic attraction for the resin as the cation radius decreases results in a weaker interaction with the resin. A complete explanation for trends like these requires careful consideration of all aspects of the solution chemistry of the ions in both homogeneous aqueous media and within the resin pores. We will consider the role of solvation and lanthanide radii in greater detail in sect. 3.1.

In principle, the small separation factors observed in simple cation-exchange systems could be used for separation of macroscopic concentrations of lanthanides on large ion

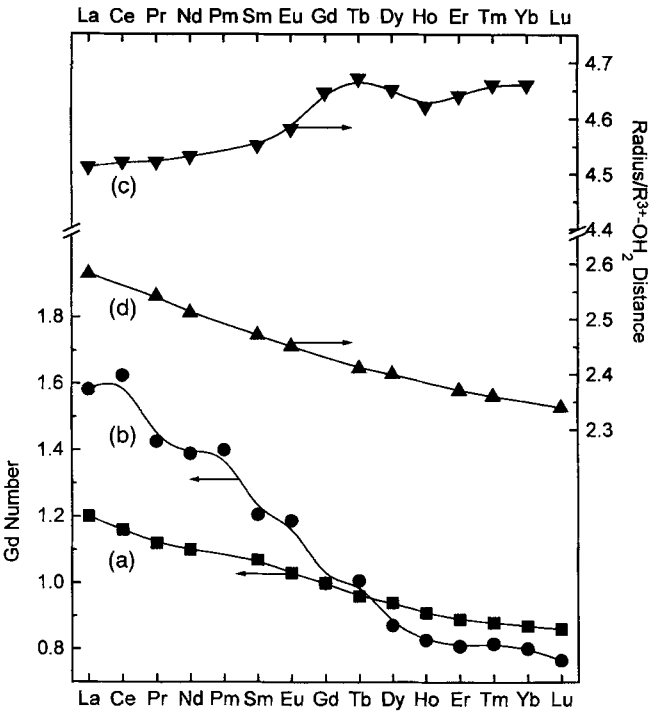

Fig. 2. Comparison of Gd numbers for lanthanide absorption onto Dowex 50 cation exchange resin [(a) Marcus 1983, (b) Surls and Choppin 1957] as compared with (c) cation hydrated radius and (d) R–O distance of hydrated cations.

exchange columns that offer an enormous number of theoretical plates. However, the long contact times required for such separations make them unsuitable for analytical applications. Because they are so inefficient, this approach is not used even for macro-scale applications. This limitation of ion exchange resins was recognized early in the development of ion-exchange separation procedures. It fosters continuing research on the design and synthesis of cation-specific ion exchange resins and extraction chromatographic materials.

The limitations of ion exchange materials for lanthanide separations based on the aquo cations led to the development of separation procedures mediated by aqueous complexants. The first such separations used ammonium citrate as the eluant. The displacement of R^{3+} from the resin by H^+ and NH_4^+ is greatly augmented by the formation of lanthanide–citrate complexes, which tend to enhance transfer of the lanthanide ions to the mobile phase. The relative rates of movement of the rare-earth cations down the column is thus impacted not only by the affinity of the resin phase for the cations, but also by the relative stability of the aqueous citrate complexes. This approach forms the basis of the most useful and successful chromatographic separations of the lanthanides.

Early studies of the separation of lanthanides by ion exchange were done using either gravity-feed or low-pressure elution techniques and chelating agents like lactic acid, citric acid, or edta as eluents. Typically, these separations were done at pH 3–5 in buffered solutions of the ammonium salts of the complexant. Though each chelating agent achieved some success in separating lanthanide ions, these reagents also suffered limitations that reduced their utility. The carboxylic acids often performed well for the light members of the series, but failed to separate the heavy lanthanides adequately. The aminopolycarboxylates gave good separations of individual lanthanides across the series, but were plagued by excessively slow kinetics.

In 1956, the chelating agent α-hydroxyisobutyric acid (hiba) was reported as a superior reagent for separation of individual members of the lanthanide series from a mixture using column chromatography on Dowex 50 cation-exchange resin (Choppin and Silva 1956, Smith and Hoffman 1956). This complexant was actually identified as a unique separations reagent as a part of the development of procedures for discovery of the transplutonium elements that were being synthesized principally at the Lawrence Berkeley Laboratory (Nash and Choppin 1997).

Specifically, it was predicted that lactic acid would be inadequate for a cation-exchange separation of element 101 (Md) based on its performance in separation of the analogous lanthanides (Choppin 1998). The transplutonium actinides (except No) exist predominantly in the trivalent oxidation state and their chemistry parallels that of the lanthanides. Because the new elements were being synthesized in extremely small amounts (a few atoms) and were expected to have very short half-lives for radioactive decay, predictable separation chemistry was required for their identification. Cation-exchange chromatography using hiba satisfied this demand (Choppin et al. 1956). Though many chelating agents have been tested and used in lanthanide chromatographic analyses, hiba remains the premier reagent. The fundamental chemistry that accounts for this pre-eminent role will be discussed in sect. 3.

In modern analysis for lanthanide quantitation, the most common and useful chromatographic methods are those techniques generally classified as High Performance Liquid Chromatography (HPLC). These techniques were developed beginning in the 1960s and were first applied for lanthanide analysis by Sisson et al. (1972). In essence, these methods consist of operation of solid separations media, either as thin plates or (more often) cylindrical columns, in a chromatographic mode. Conduct of column chromatography under pressure leads to substantially improved resolution and efficiency of the separation process. A variety of different interactions between solvents, solutes, and reactive solid phases contribute to such separation systems. With computer-controlled instrumentation, the chemical and physical properties of the solution can be manipulated over a wide range to fine-tune the separation.

The common characteristic of the various HPLC techniques is the reliance on small differences in the strength of interactions between species in the mobile (liquid) phase and the solid material that accomplishes phase transfer. Outside of extraction chromatography, few solid–liquid separation procedures for lanthanides derive their selectivity from the properties of the solid-phase material. For most HPLC separations of the lanthanides,

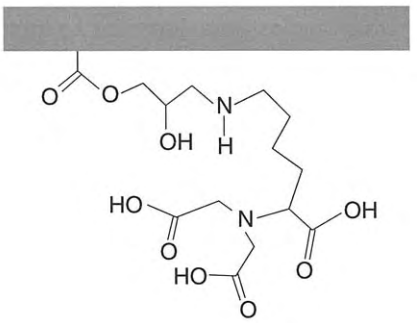

Fig. 3. Functional unit of nitrilotriacetic acid resin. From Inoue et al. (1996).

water-soluble chelating agents that form complexes of steadily varying strength across the series are used to accomplish separation of the individual lanthanide ions. These reagents are often applied using a technique called gradient elution, in which the composition of the eluting solution is changed over the course of the analysis. In some applications, abrupt changes in the reagents or pH are made. Often, a linear ramping of the concentration of one or two complexants is used to accomplish the target separations.

Despite the success of analytical methods based on non-selective solid sorbents and differentiating aqueous solvents, the preparation of ion-selective chelating resins is a continuing goal for those who design chromatographic materials. For example, Inoue et al. (1996) have recently reported on rare-earth separations using a stationary phase consisting of nitrilotriacetic acid chelating groups on a glycidyl methacrylate gel, a macroporous hydrophilic resin. The resin functional group is as shown in fig. 3. Using a nitric-acid gradient elution technique, they report a moderately successful separation of the lanthanides (without Y). The resin fails to separate Eu and Gd, and Sm partially overlaps with the Eu/Gd peak. Dy and Ho also are poorly resolved. However, this resin appears to outperform an earlier polystyrene-based bis(carboxymethyl)amino resin (dtpa functionality bound at the center nitrogen) (Kanesato et al. 1989). Nitrilotriacetic acid has also been applied as a mobile reagent in ion-pair chromatography. The two approaches will be compared in sect. 3.4.

Capillary electrophoresis has also been applied for lanthanide analysis. In this technique, the electro-mobility of ions in an electrolyte buffer under the influence of an applied electric field determines relative separation of the ions. Complexing anions are required for electrophoretic separation of lanthanide ions, as the differences in mobility of the trivalent aquo ions are insufficient for differentiation of individual members of the series. Vogt and Conradi (1994) summarize the mobility of an ion in an electric field in terms of the relative concentrations of complexed ions in solution:

$$\begin{aligned}\mu &= \mu_{eo} + X_{M^{3+}} \cdot \mu_{M^{3+}} + X_{ML^{2+}} \cdot \mu_{ML^{2+}} + X_{ML^{2+}} \cdot \mu_{ML^{2+}} + \cdots \\ &= \mu_{eo} + \sum (X_i \cdot \mu_{ML_i^{3-i}})\end{aligned} \tag{1}$$

where μ_{eo} is the electro-osmotic parameter, and the summation of terms in the mole fractions X_i and electrophoretic mobility ($\mu_{ML_i^{3-i}}$) represent the mobility of each chemical

form of the analyte ion. Thus mobility of the analyte ion is a function of the speciation of the ion in solution. The greater the possible diversity in speciation across the series the greater will be the separation of the ions. We will discuss this aspect further in sect. 3.4 using the term $\bar{n}$ (nbar – the average number of ligands associated with the ion).

2.2.5. *Thin-layer chromatography/gas chromatography/supercritical fluid chromatography*

Chromatographic techniques that do not rely on pressurized aqueous solutions and columns also have been applied for lanthanide analysis. Most of these techniques have achieved only limited success. Paper chromatography and thin-layer chromatography have been applied for lanthanide analysis, but quantitation is somewhat problematic. Though some quantitation is possible for well-separated pairs, thin-layer techniques are useful primarily for qualitative analysis. They must generally be supplemented by some other separation technique for accurate quantitation of the lanthanide ions present. They are also poorly suited to the demands of automated instrumentation, wherein easy detection/quantitation of the ions is desirable. Their greatest utility may be as a screening technique. Mixed organic/aqueous solutions are frequently used for thin-layer chromatographic analyses. Computer-aided experiment design and analysis of plates provide some enhancement in the utility of thin-layer techniques (Wang and Fan 1991).

Gas chromatography (GC) is applied extensively in the analysis of organic compounds. GC analysis requires that the analyte have a measurable volatility at a temperature below its decomposition point in order to conduct the analysis. Though certain classes of chelating agents (e.g., β-diketones) will form potentially volatile complexes with lanthanide ions, these complexes tend, as is true of most lanthanide complexes, to be moderately labile and hence not generally compatible with the demands of gas–solid chromatographic techniques. The lability of lanthanide complexes is largely a result of the predominantly ionic nature of the bonding between lanthanide cations and ligand donor atoms. The general absence of covalent bonding interactions of lanthanides is a common feature of their coordination chemistry. The inherent lability of lanthanide complexes is exacerbated by the elevated temperatures generally needed for gas-chromatographic analysis. Dissociation of the lanthanide complex leads to deposition of the non-volatile lanthanide cation and fouling of columns.

Supercritical fluid chromatography (SFC) relies on the unique solvating properties of supercritical CO_2 (predominantly), CO_2/solute mixtures, or other solvents of suitable properties, like freons. SFC was applied for lanthanide analysis very early in the development of the technique. Though a number of fluorinated β-diketone ligands have been investigated as carrier ligands for lanthanide analysis by SFC, continuing research has yet to provide any truly successful examples of lanthanide analysis by this technique. It has been established that, as is true of gas chromatography, non-labile complexes are highly desirable for a successful SFC separation. The unique solvating properties of supercritical fluids suggest some potential for successful lanthanide separations via this technique. Robards et al. (1988) suggest that supercritical ammonia might be an

interesting solvent for this separation, but no research on this system has appeared. Overcoming the inherent lability of lanthanide complexes may ultimately prove to be an insurmountable obstacle to the successful application of this technique for lanthanide analysis.

2.3. *Detection methods*

Detection methods based on optical properties of the target analyte are perhaps the most commonly employed methods for quantitation of most any species in chromatographic analysis. As the lanthanide cations are only weakly colored, direct detection using standard UV–visible spectrophotometric methods are of minimal applicability. However, selected lanthanide cations exhibit an intrinsic fluorescence which can be used for direct detection of the ions leaving the column. Application of ICP/AES can be used for detection, but the eluants used for HPLC separations of individual lanthanides can compromise the analysis. Sawatari et al. (1995) describe an integrated lanthanide analysis system that combines HPLC separation and ICP/AES detection. They report conditions under which the hiba eluant does not compromise the operation of the detection system. Chemical constituents of the HPLC eluants can also degrade the sensitivity of ICP/MS detection of lanthanides in the analyte. Kawabata et al. (1991) report on the general characteristics of lanthanide analysis using a combination of ion chromatography (IC) and ICP/MS. Ion chromatography is well-suited to mass-spectroscopic detection, as the polishing column is designed to remove contaminants and prepare the sample for analysis.

With the availability of a neutron irradiation source, a research reactor for example, neutron activation analysis accompanied by γ-spectroscopy can be applied for detection of lanthanide ions. This technique can be extremely sensitive. Choppin and Rydberg (1980) tabulate the following detection limits for lanthanide ions for 1 hour irradiation in a neutron flux of $10^{13}\,n\,cm^{-2}\,s^{-1}$: Dy, $1–3\times10^{-6}$ μg; Eu, Ho, Lu, $1–3\times10^{-5}$ μg; Sm, $4–9\times10^{-5}$ μg; Y, $1–3\times10^{-4}$ μg; La, Er, $4–9\times10^{-4}$ μg; Nd, Yb, $1–3\times10^{-3}$ μg; Pr, Gd, $4–9\times10^{-3}$ μg; Ce, Tm, $1–3\times10^{-2}$ μg; Tb, $1–3\times10^{-1}$ μg. Neutron activation analysis for lanthanides is adversely effected by the presence of U, Th, transuranium elements, Fe, and Ta. The actinides undergo neutron-induced fission to produce some of the same lanthanide nuclides as fission products. The γ-ray energy for ^{59}Fe overlaps that for ^{141}Ce, while the γ-emission of ^{182}Ta overlaps ^{170}Tm. Quantitative separation of lanthanides from these elements is therefore of primary importance for application of neutron activation analysis. For the analysis of inherently radioactive samples (e.g., those containing ^{147}Pm), standard radiometric analytical techniques (γ-spectroscopy, liquid scintillation) are applicable.

The far-and-away most widely applied detection method for chromatographic analysis of lanthanides is post-column derivatization with the colorimetric indicator ligands 4-(2-pyridylazo)resorcinol (PAR, fig. 4a) or Arsenazo III (2,2′-(1,8-dihydroxy-3,6-disulfonapthalene-2,7-bisazo)bis(benzenearsonic acid), fig. 4b). These ligands form strongly colored complexes with the lanthanides in dilute acid media. They are typically added to the column effluent after the separation is complete but before the sample passes a single-wavelength, photo-sensitive detector. The principal requirement of the

a

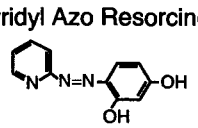

b

c

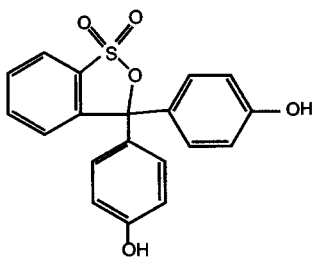

Fig. 4. Structures of several indicators used in chromatographic analysis of lanthanides.

post-column derivatization reagent is that it form complexes with the lanthanide ions that are stronger than those formed by the reagents that accomplish the chromatographic separation (e.g., hiba). This requirement is readily met by these two reagents. A limitation cited by many authors in the application of PAR is its affinity for d-transition-metal ions. Interference by transition metals is less significant if a group-separation step is applied prior to the lanthanide analysis. Arsenazo III is more selective for the lanthanides over divalent transition-metal ions, and so to some degree may reduce the need for the pre-separation step. PAR has been reported to be susceptible to biodegradation, which requires that the reagent be prepared more frequently. The organic debris from this biodegradation can interfere with the analysis of the metal ions (Cassidy et al. 1986, Knight et al. 1984, Cassidy 1988).

Walker (1993) has described an HPLC method for lanthanide analysis based on phenol red (fig. 4c) as the stationary phase complexant and colorimetric indicator in the mobile phase. Lanthanide separation is based on the hiba complexes. The presence of the indicator in the mobile phase eliminates the need for post-column derivatization, as the free indicator absorbance at 490 nm can be monitored in the column effluent to detect the existence of the lanthanide complexes. Overall, the technique is not as effective as

the more conventional post-column derivatization methods, but it offers rapid analysis and decent separation of the heavy lanthanides. The example chromatograms suggest quantitation may be somewhat problematic.

While rare-earth detection by post-column derivatization with colorimetric indicator ligands is the most widely applied detection technique for chromatographic analyses, solvent-extraction methodology is well suited to optical detection of rare earths in the organic phase. Because the rare-earth ion must associate with at least one extractant molecule in the organic phase, the optical properties of either the rare-earth cation or the extractant may be altered, allowing specific detection of the extracted metal ions. As with most elements in the Periodic Table, the formation of intensely colored complexes in an organic phase has been applied numerous times for the quantitation of rare earths by UV–visible absorption spectroscopy (Marczenko 1986). The availability of more sensitive instruments such as ICP/AES and ICP/MS, and the power of the chromatographic methods, has almost stopped research in this once vibrant field, although it remains an easy and powerful approach to analysis of less complex samples containing rare-earth elements (Agrawal and Shrivastav 1997, Chen et al. 1994, Wei and Zhang 1992, Agrawal and Thomaskutty 1993). Other optical methods can also be employed to detect rare earths in the organic phase. A number of the lanthanides fluoresce, and fluorimetric detection of their complexes in an organic phase at 10^{-9} M is possible (Watanabe et al. 1995, S. Liu et al. 1992, Shirakawa et al. 1989, Mishchenko et al. 1977, Taketatsu and Sato 1979). Tran and Zhang (1990) applied thermal lensing to the detection of lanthanides at sub-millimolar concentrations in organic phases, taking advantage of the superior thermo-optical properties of certain organic solvents.

3. Basic chemical principles of lanthanide separations

The separation of metal ions via phase-transfer reactions is determined by many overlapping and often competing processes occurring in the mobile phase, in the immobile phase (or liquid counterphase in solvent extraction), and in the interface between the phases. The processes governing the phase-transfer reactions are outlined schematically in fig. 5. There are clearly many interactions between the analyte and the macroscopic components of the system that contribute to the net reaction. The mutual separation of metal ions is determined by the differences in their response to these chemical processes. The more different the analyte metal ions are, the more readily they will be separated.

The observable parameter that describes the behavior of a metal ion in any separation process is the distribution ratio, simply the ratio of the total metal concentrations in the organic (or resin) phase to that in the aqueous phase. For all systems, therefore, the distribution ratio is

$$D = \frac{[\mathrm{M}]_{\mathrm{org}}}{[\mathrm{M}]_{\mathrm{aq}}}. \tag{2}$$

The specific species represented by $[\mathrm{M}]_{\mathrm{org}}$ and $[\mathrm{M}]_{\mathrm{aq}}$ will be determined by the interaction of the metal ion with solutes in the two phases. For most separations, the difference

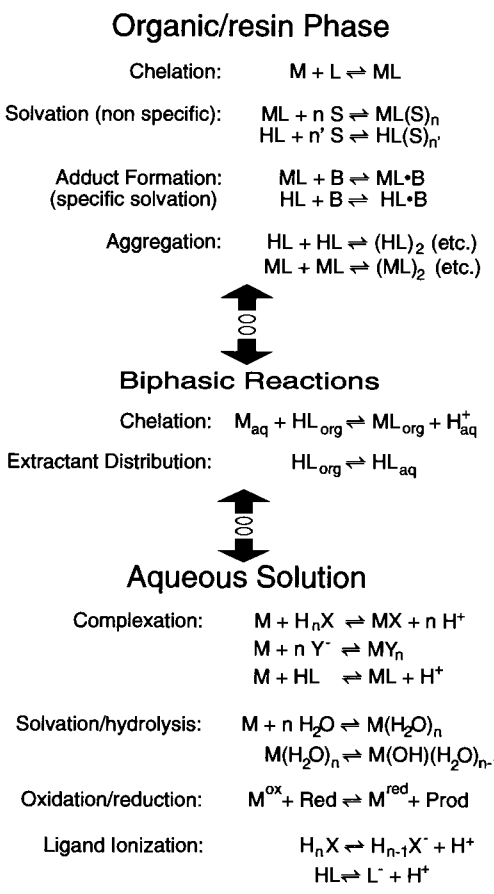

Fig. 5. Generic representation of the equilibria occurring in both aqueous and resin/organic phases that contribute to metal ion separations.

between the phase-transfer equilibrium position of the metal ions to be separated is of greatest interest. The separation factor, $S^{m}_{m'}$, is the ratio of the distribution ratios of the metal ions to be separated:

$$S^{m}_{m'} = \frac{D^{m}}{D^{m'}} = \frac{[M]_{org}/[M]_{aq}}{[M']_{org}/[M']_{aq}} = \frac{[M]_{org} \cdot [M']_{aq}}{[M']_{org} \cdot [M]_{aq}}. \quad (3)$$

The separation factor is a complex function of the chemistries of the metal ions in the two phases. In a strict thermodynamic interpretation, separation factors are also a function of ion activity coefficients in both organic and aqueous phases. However, since $S^{m}_{m'}$ is a ratio of concentrations of closely similar species, the activity coefficient terms in eq. (3) largely cancel. In most cases, it is probably justified to ignore the potential impact of activity changes on the separation efficiency of the lanthanides, particularly for adjacent lanthanide ions.

M_{org} generally represents relatively few charge-neutral thermodynamically stable species. These species may include mixed complexes that combine a lanthanide cation

with anions from the aqueous medium and a lipophilic extractant, as we will describe in sect. 3.2. The aqueous metal species can include the free (hydrated) metal cation and metal complexes with the various ligand species present in the aqueous solution. This general expression can be used to understand the ease of separation of certain classes of metal ions (e.g., lanthanides from first-row d-transition metals) and the challenges represented by others (lanthanides from lanthanides).

Because their interactions with the media are governed principally by electrostatic factors, the separation of individual lanthanides is ultimately based on the chemical effects caused by the decrease in ionic radius with increasing atomic number (Shannon 1976). Trivalent-lanthanide cation radii decline across the series because the valence f electrons compensate relatively poorly for the steadily increasing nuclear charge. The decreasing ionic radii result in increased strength of cation–anion, ion–dipole and ion-induced dipole interactions. Decreasing cation radii therefore lead to stronger bonds between lanthanide ions and ligand donor groups, and simultaneously to stronger interactions with polar solvent molecules like water (via ion–dipole interactions). Because these are competing effects, the overall effect of shrinking cation radii may not be straightforward in lanthanide separation chemistry.

It is important to note that the kinetics of lanthanide complexation reactions in general involve rapid association and dissociation reactions, except for structurally complex ligands like edta. Generally, lanthanide complexation kinetics in aqueous media can be considered sufficiently rapid as to have minimal effect on separations. Phase-transfer rates may be important in some systems, and should be considered in the optimization of an analytical separation procedure. The kinetics of lanthanide complexation reactions has been discussed in a previous report (Nash and Sullivan 1991). There has been some consideration of kinetics-based separations for f-elements (Nash 1994, Merciny et al. 1986), but no useful analytical applications based solely on differences in lanthanide kinetics are known.

The chemical phenomena impacting analytical separations of lanthanide ions include the full array of fundamental interactions between metal ions, chelating agents, solvent molecules, and solid surfaces. In chromatography, these equilibria re-adjust for each of the metal ions repeatedly while the analyte-metal ions traverse the column. The physical and structural chemistry of these varied interactions represent a microcosm of everything that is interesting and unique about lanthanide solution chemistry. We will focus now on several of these interactions with the goal of describing those phenomena that contribute most fundamentally to a successful analytical separation of lanthanide cations.

3.1. *Solvation effects in lanthanide separations*

The three properties of water most significant in the solvation of metal ions and complexes are its high dipole moment (1.84 D), its dielectric constant (78.3 at 25.0°C), and its propensity toward hydrogen bonding. The high dielectric constant of H_2O decreases the need for close association of cations with anions in aqueous solutions. As a result, free hydrated cations and anions diffuse independently through the solution, their movements

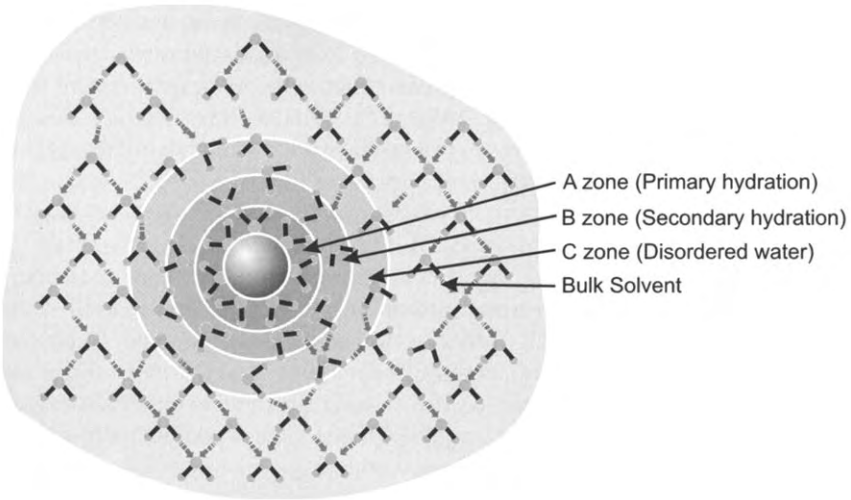

Fig. 6. Hypothetical structure of hydrated cation in water.

impacted by the electrostatic fields of the ions they encounter and the hydration sphere they "carry". Another consequence of the high dielectric constant of water is that, although charge is conserved in the solution, stable metal complexes may carry a formal charge. The high dipole moment contributes to strong ion–dipole interactions, while hydrogen bonding impacts the energetics of all reactions occurring in the medium.

In an aqueous medium, cations are solvated by some number of water molecules, the number of water molecules being determined primarily by the charge and size of the cation. The size of the solvent sheath carried by the cation and its complexes is clearly of significance in predicting the relative mobility of lanthanide ions as they traverse an analytical column, as transport properties are proportional to the "fit" of the analyte into the normal solvent structure. In the following paragraphs, we will explore a few of the more interesting aspects of these phenomena.

The organization of water molecules around a cation has been discussed (conceptually) in terms of 2 or 3 "zones" around the cation, as shown in fig. 6. In the A-zone, water molecules experience the full electrostatic attraction of the cation and are "bound" to the metal ion by ion–dipole interactions. These water molecules exchange with the bulk solvent at a rate that decreases across the series, being measurable only for lanthanides heavier than Dy (Cossy et al. 1989 – the lighter lanthanides exchange their inner-sphere water molecules at near the diffusion-controlled limit)[1]. In addition to this inner solvation shell, all cations in the aqueous medium organize solvent water in a second coordination sphere (B-zone), the volume of which is also strongly a function of the charge/radius ratio of the cation. Weaker electrostatic-induced ordering, order/disorder provided by counter

[1] It has also been demonstrated by NMR spectroscopy that water exchange rates are slower for lanthanide complexes than in the corresponding aquo ions (Powell et al. 1995).

ions, and hydrogen bonding interactions are dominant in this zone. Rizkalla and Choppin (1991) suggest that there is a third, disordered (C) zone of water molecules surrounding the ion wherein water structure is intermediate between the ion–dipole ordered structure and the tetrahedral arrangement that represents the bulk solvent. The necessary anions accompanying the cation are not typically strongly hydrated, though O, N, and F engage in hydrogen bonding interactions that modify water structure.

For d-transition-metal ions, the number of water molecules in the primary coordination sphere (A-zone) is in most cases determined by the strength of orbital overlap between the metal ion and H_2O molecules, crystal field stabilization effects, and cationic charge. Other species (e.g., alkaline earths, rare earths) interact with solvent molecules via ion–dipole forces with minimal orbital overlap contribution to the bonding. Their solvation numbers are determined by a combination of coulombic attraction between cations and water molecules, steric factors, and van der Waals repulsion between the bound water molecules. The larger size and high charge of the lanthanides combine with the absence of directed valence effects to produce primary-sphere hydration numbers above eight for these metal ions.

Rizkalla and Choppin (1991, 1994) have reviewed the hydration of lanthanide ions. They report that experimentally determined values (by electrophoresis and diffusion) for the hydrated radii of the lanthanides increase from La to Dy but apparently level off for the heavier lanthanides (fig. 7). Replicate determinations by different authors place the uncertainty on these experimental values at ±0.02–0.03 Å. The apparent discontinuity near Tb is curious, but is paralleled by the heats and free energies of formation of the aquo cations[2]. The similarity suggests that the observed trend represents a real chemical characteristic of the ions, perhaps related to the change in the inner-sphere coordination number or the balance of inner-sphere/second-sphere hydration. A simple analysis of the ions based on these hydrated radii indicates hydration numbers of 12–15 across the series (Lundqvist 1981). David and Fourest (1997) offer a more detailed interpretation that suggests a larger number of waters associated with the lanthanide cations.

X-ray and neutron diffraction experiments on concentrated lanthanide solutions as simple salts with non-complexing anions indicate that the number of water molecules in the primary coordination sphere, i.e., water molecules in direct contact with the lanthanide cation, is approximately nine for La–Pm, eight for Gd–Lu. The average hydration numbers for Sm^{3+} and Eu^{3+} are intermediate between 8 and 9. The R–O bond distances shown in fig. 2 reflect this fact. The change in the hydration number is a result of the increased crowding of water molecules as the cation radius shrinks. It marks a boundary between the strength of the ion–dipole interactions of the cations with water, and the van der Waals repulsion between the inner-sphere water molecules. The increasing hydrated radius, despite a general decline in the radius of the inner hydration sphere, indicates the substantial organization of second-sphere water molecules that occurs as the charge/radius ratio of the lanthanides increases. It should also be noted that the

[2] The values recorded in Rizkalla and Choppin (1991) for the hydration of Eu appear to be anomalously less exothermic than the other trivalent lanthanides and have been omitted from this plot.

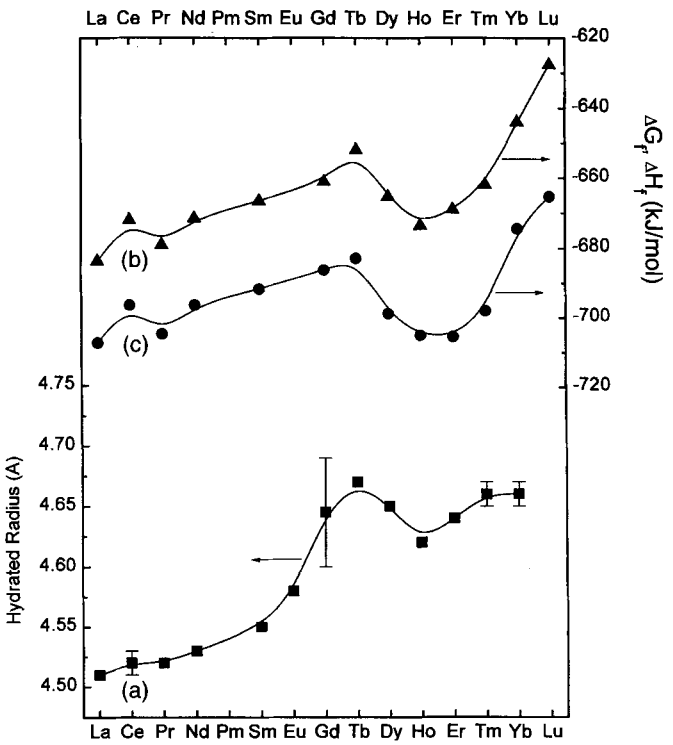

Fig. 7. Hydrated radius of (a) lanthanide cations as compared with (b) free energy and (c) enthalpy of formation of the hydrated cations.

thermodynamic data for formation of the hydrated ions measures the total hydration of the ions, not just the inner-sphere water contribution.

The experimental measurements that provide the hydration number and hydrated radius information are made on lanthanide solutions of moderate concentration with different counter ions. The data in Rizkalla and Choppin (1991) indicate that hydration numbers and Ln–O distances change slightly with both the nature of the counter ion and the concentration of the salt. It appears likely that composition of the primary coordination sphere of the lanthanide ion does not vary appreciably with the concentration (or identity of the counterion) of the lanthanide salts. However, the reduced water activity that occurs in concentrated salt solutions would suggest that overall hydration numbers will be higher in dilute solutions. Thus the values reported for overall hydration and hydrated radii determined in concentrated aqueous salt solutions probably underestimate the hydration of lanthanide cations in the dilute solutions that are typical of analytical applications. It has been suggested that as many as 40 water molecules may feel the presence of a trivalent lanthanide ion in solution (Choppin 1997). Using Lundqvist's (1981) estimate of 30 $Å^3$ for the volume of a water molecule, the radial distance of the lanthanide hydration sphere

would be about 6.6 Å from the center of the lanthanide ion or about 5.6 Å from the ion's "surface".

The solvation of metal complexes in aqueous solutions is substantially more complex than that of the bare cations, and almost certainly is different for every complex. This aspect of lanthanide solution chemistry has been discussed by Choppin and Rizkalla (1994). The general subject of the effect of solutes on the three-dimensional structure of water has been investigated by Choppin and coworkers, who considered the impact of both ionic species and water-miscible non-aqueous solvent on water structure (Choppin 1978). The fundamental conclusion of that research was that solutes of all classes have an impact on the structure of water, and, as a result, on the hydration energies of solutes.

Partial substitution of non-aqueous solvents for water results in a net decrease in the hydration of the cation, thereby reducing the energetic requirements for desolvation and promoting phase transfer. Occasionally, mixed aqueous/organic media have been used to try to improve separation performance. For example, Vera-Avila and Camacho (1992) have applied acetonitrile–water–lactate solutions for lanthanide analysis. Mixed media are also commonly used for thin-layer chromatographic analyses. Lincoln (1986) has discussed both the rates and the solvation numbers of the lanthanide cations, observing that there is a great variety in both solvent exchange rates and coordination numbers in non-aqueous media.

The solutes that make up aqueous solutions can either promote or disrupt the 3D structure of water. Hydrogen ions (H^+) and hydroxide ions (OH^-) are the ultimate structure makers in aqueous solutions, as they fit perfectly into the water structure. Therefore, pH must have an effect on water structure, at least at the extremes, that is, strongly acidic or basic systems. Water-miscible solvents (e.g., methanol, ethanol, acetone, DMSO) generally reduce hydration energies of solutes by interfering with the hydrogen bonding network of pure water. Small, hard-sphere metal cations tend to promote order in the solution, while large cations of low charge tend to disrupt the structure. Among typical anions, fluoride is a strong structure maker, sulfate, phosphate, and nitrate are less efficient structure makers, while the heavy halides and thiocyanate disrupt the water structure. Strongly structure-breaking anions like perchlorate reduce the overall order in water, much like non-aqueous solvents. The resulting increased entropy of the aqueous medium increases the phase-transfer efficiency of strongly hydrated metal ions. The effect of water structuring on selectivity in lanthanide separations is more difficult to predict, particularly as the solvation properties of metal complexes are largely unknown.

Chelating agents of moderate dimensions can be simultaneously structure making and structure breaking in an aqueous solution. The hydrophilic portions of organic complexants are capable of entering into hydrogen-bonding interactions with water molecules and contribute to ordering of the solvent. The aliphatic portions of such compounds can be expected to disrupt water structure. The topology of an organic complexant in solution is also an important factor in this balance between order and disorder, as illustrated by the comparative aqueous solubility of butyl alcohols (*n*-butyl: 7.9 wt%; 2-butyl: 12.5 wt%; isobutyl: 10.0 wt%; *t*-butyl: infinite miscibility with H_2O).

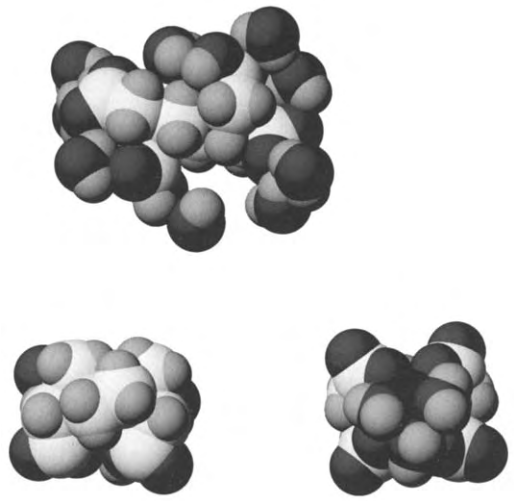

Fig. 8. Molecular mechanics representation (space-filling) of a hypothetical hydrated H_4edta free ligand species and two opposed faces of the trihydrated Eu–edta complex (dominantly organic face left, hydrated face right).

It is also reasonable to assume that the water-structuring effect of an organic chelating agent will be considerably altered by the complexation reaction. Consider, for example, that a multidentate ligand like edta as a free solute in aqueous solution can order water through hydrogen-bonding interactions of the four carboxylate and two amine donor atoms. One would expect that each of the 10 electronegative atoms in edta (8 carboxylate oxygens, 2 amine nitrogens) would form hydrogen bonds with water if steric crowding does not interfere. The backbone methylene groups should have a comparatively minor effect on water structure (and solvation energies). However, when edta is coordinated to a lanthanide cation, the hydrophilic portions of the ligand are less available for hydrogen bonding (and thus ordering) of the solvent. The more hydrophobic CH_2 groups are left in a position that directs them toward the solvent molecules. This structural effect is illustrated in the molecular mechanics shown in fig. 8. It has been determined experimentally that a trivalent lanthanide cation retains only 2–3 of its inner-sphere waters in the edta complexes. The large complexation entropies observed for lanthanide complexes with edta (and similar species) must derive from dehydration of both the cation and the ligand.

The alkali-metal salts of long-chained carboxylic acids exhibit higher solubility limits due to their ability to engage in self-organization. This micellization leads to the formation of lipophilic zones in the aqueous solution surrounded by the hydrophilic opposite ends of the molecules which are stabilized through solvation/hydrogen bonding to solvent water molecules. Such agglomeration accounts for the ability of soaps to solubilize oily substances in water. In organic solutions, certain surfactant molecules form reverse micelles, hydrophilic areas within lipophilic solvents, to allow phase transfer of polyvalent cations. Lipophilic sulfonic acids are particularly important in ion-pair chromatographic analysis of lanthanides.

In the ion-pair chromatographic technique described in sect. 2.2.1, sodium *n*-octylsulfonate (SOS) is combined with an aqueous chelating agent like hiba to allow complete

mutual separation of the lanthanides. The sulfonate molecules help maintain solubility of the lanthanide complexes, but, more importantly, they partition partially to the hydrophobic silica phase which contains a thin organic layer due to covalently bonded alkyl chains. The lipophilic tail of octyl sulfonate dissolves into the alkyl layer of the solid, presenting an active sulfonated layer to the aqueous solution. The water-soluble SOS in the mobile phase constantly replenishes any material that washes out of the solid layer to maintain constant sulfonate coverage. Within limits, the SOS concentration in the aqueous eluant can be varied to increase or decrease the capacity of the resin for cations. Experimental results from a variety of reports do not indicate that the surfactant in the aqueous phase has any direct bearing on the separation efficiency of the lanthanides. However, the sulfonated solid material certainly has kinetic features that contribute to a rapid analysis (as compared with cation-exchange resins).

Solvation of metal ions and complexes in organic solutions is substantially different from that in aqueous media. Interactions between solvent molecules in most organic solvents are much weaker than between water molecules, principally due to the absence of hydrogen-bonding interactions and to the substantially lower dipole moments and dielectric constants. Organic solvent molecules likewise interact comparatively weakly with solutes, mainly via van der Waals forces. Solute–solvent interactions in organic media are generally discussed in terms of the "cavities" created in organic solvents that favor the insertion of solute molecules. Hence, branched alkane solvents are often capable of dissolving higher concentrations of solutes than the corresponding linear-chain alkane. The nature of solvation of complexes in organic media affects the strength and the rates of phase-transfer reactions. Differences between the organic phase solvation of lanthanide complexes should have little impact on interlanthanide separation factors. However, there have been no specific investigations of this potential effect in lanthanide analysis.

3.2. *Solvent extraction and related techniques*

The lipophilic reagents used in solvent extraction, extraction chromatography, and centrifugal partition chromatography may be divided into three categories based on the type of species they extract: acidic extractants (often, but not always, chelating agents) extract cations; basic amine extractants extract anionic species; and neutral, or solvating, extractants solvate neutral molecules or ion pairs in the organic phase. Acidic or basic extractants can also function as solvating extractants if the acidity of the aqueous phase is high or low enough respectively. Regardless of the type of extractant, the extracted species must be charge-neutral due to the low polarity of the organic solvents used in solvent extraction.

Rare-earth extractions by acidic reagents are greatly influenced by a cation-exchange mechanism where H^+ is exchanged for the cation of interest. Depending on the extractant, the organic solvent, and the aqueous phase composition employed, an acidic extractant may exhibit a degree of solubility in the aqueous phase, which can diminish its extraction efficiency both through a loss of extractant from the organic phase and through

formation of water-soluble metal–extractant complexes. The principal equilibria necessary to describe the extraction of trivalent rare-earth cations by an acidic extractant, HL, are:

$$HL_{org} \rightleftharpoons HL_{aq}, \tag{4}$$

$$HL_{aq} \rightleftharpoons H^+_{aq} + L^-_{aq}, \tag{5}$$

$$R^{3+}_{aq} + 3HL_{org} \overset{K_{ex}}{\rightleftharpoons} RL_{3\,org} + 3H^+_{aq}. \tag{6}$$

If Ce^{4+} or Eu^{2+} were extracted instead, the stoichiometry of the extracted complexes would change to maintain charge neutrality in the organic phase. In certain cases, cationic complexes of the rare-earth ions with aqueous soluble ligands (e.g. NO_3^- or $SiO(OH)_3^-$) are extracted by acidic extractants (Ferraro and Peppard 1963, Jensen and Choppin 1996).

The first two equilibria describe the partitioning of the extractant between the organic and aqueous phases and the ionization of the extractant, which is taken to occur in the aqueous phase. The principal equilibrium expression governing the extraction of rare-earth cations is eq. (6). The neutral, lipophilic complex, RL_3, reports to the organic phase, releasing H^+ to the aqueous phase thus maintaining electroneutrality in both phases. When the formation of RL_n complexes in the aqueous phase is not important, the distribution ratio of the metal ion at equilibrium is described by the expression

$$D = \frac{[RL_3]_{org}}{[R^{3+}]_{aq}} = K_{ex}\frac{[HL]^3_{org}}{[H^+]^3_{aq}}. \tag{7}$$

If the distribution of the extractant into the aqueous phase (eq. 4) is not important and the extractant concentration is much larger than the rare-earth concentration, $[HL]_{org}$ may be taken as the total initial concentration of the extractant in the organic phase. At high metal loadings of the organic phase, the extraction equilibria become more complex due to aggregation of the extracted metal complexes, and the failure of the approximation of $[HL]_{org}$ by the total extractant concentration.

Surfactants are a subclass of acidic extractants that are highly aggregated in the organic phase. They form reverse micelles, sequestering metal cations in the hydrophilic inner region of the reverse micelle. These extractants tend to be strongly acidic and function similarly to cation-exchange resins, exchanging H^+, or other less strongly bound cations like Na^+, for rare-earth cations for charge neutralization. With surfactants and other highly aggregated extractants, metal-ion extraction is performed by the aggregated species or micelles, and the concentration of the micelles depends on the total concentration of the extractant in the organic phase. Thus the distribution ratio of a metal ion is linearly dependent on the total concentration of the extractant regardless of the cation's charge, unlike the general case for acidic extractants discussed above. Since metal binding by surfactants is primarily electrostatic, solvent-extraction separations by surfactants are based on the electrostatic potential of cations. Little separation of individual lanthanides is observed due to their similar properties, but surfactants could be applied to group separations of the lanthanides from a simple matrix of dissimilar elements.

Many acidic extractants such as organophosphorus acids or β-diketones are also considered chelating extractants. As such, the stability of the extracted complexes, and thus K_{ex}, is partially determined by the relative sizes of the cation and of the chelate ring. If the cation is a poor match for the extractant, the strain induced in the ligand will reduce the stability of the extracted complexes, as demonstrated with β-diketone extraction of lanthanides (Umetani et al. 1993, Le et al. 1997). The 20% decrease in ionic radii across the lanthanide series might then be exploited to separate adjacent lanthanide ions by solvent-extraction based methodologies. While the differences in the ionic radii between adjacent trivalent rare-earth cations are small, and many other factors interplay, the energies required to achieve a ten-fold separation are small as well, 5.9 kJ/mol, which can be compared to the van der Waals attraction between two Xe atoms, 6.7 kJ/mol (Chashchina and Shreider 1976), or a hydrogen bond between two water molecules, 22 kJ/mol (Greenwood and Earnshaw 1984). In light of this, chelating acidic extractants form the basis of most solvent-extraction based analytical separations of the rare earths.

In contrast to the cation-exchanging properties of acidic extractants, tertiary or quaternary amines extract anionic complexes of the rare earths. Like strongly acidic extractants, these basic extractants tend to aggregate in the organic phase and extract anionic rare-earth complexes based on simple electrostatic attraction. Their chemistry is similar to that of the solid anion-exchange resins like Dowex-1. Any significant discrimination between cations with similar ionic potentials observed in amine extraction arises from differences in the interactions of the cations and the ligands necessary to impart the negative charge to the extracted complex. Amine-solvent extraction systems based on Aliquat 336 that take advantage of softer anions such as Cl^- or SCN^- have been used for the difficult group separation of the trivalent rare earths from trivalent actinides, both for production of pure actinide samples and for analytical purposes (Horwitz et al. 1995).

The general amine extraction equilibrium for rare-earth complexes with singly charged anions (e.g. NO_3^- or Cl^-) can be summarized as

$$R_{aq}^{3+} + 3Y_{aq}^{-} + (A^+Y^-)_{org} \overset{K_{ex}}{\rightleftharpoons} (RY_4A)_{org}. \tag{8}$$

Ignoring the ion-pairing reaction that forms $(A^+Y^-)_{org}$, the distribution ratio can be expressed as

$$D = \frac{[RY_4A]_{org}}{[R^{3+}]_{aq}} = K_{ex}[Y^-]^3[A^+Y^-]_{org} \tag{9}$$

if R^{3+} is the only important aqueous species. However, competing aqueous phase equilibria commonly occur in these systems:

$$R_{aq}^{3+} + nY_{aq}^{-} \overset{\beta_n}{\rightleftharpoons} RY_{n\,aq}^{(3-n)+} \tag{10}$$

changing the distribution ratio expression to:

$$D = \frac{[RY_4A]_{org}}{[R^{3+}]_{aq-tot}} = K_{ex}\frac{[Y^-]^3[A^+Y^-]_{org}}{1 + \sum \beta_n[Y^-]^n}, \tag{11}$$

where β_n is the formation constant of the complex RY_n from R^{3+} and n Y^- molecules.

In the case of tertiary amine extractants, the extractant must be protonated in order to extract anions, making the acidity of the aqueous phase an additional parameter that must be considered. For d-transition-metal ions, the species extracted by amines (i.e., MY_n) are often stable anionic complexes that exist in the aqueous phase in the absence of the lipophilic reagent. For the rare earths, however, the extracted complexes are often not important aqueous species. In this case, the amine is necessary to encourage the net phase-transfer reaction through formation of the anionic complex. Anionic species like $Ce(edta)^-$ can also be extracted by amines, as demonstrated for Ce determination in mineral samples (Chatterjee and Basu 1992).

Neutral extractants constitute the third important class of solvent extraction reagents for the rare-earth elements. Since they have no charge, neutral extractants only extract neutral complexes or charge-balanced ion pairs. They also tend to extract ion-paired acid molecules such as HNO_3. Solvating extractants may be dissolved in an organic diluent, or they may be the organic diluent itself (e.g., diethylether, methylisobutylketone, tributylphosphate). Phase transfer is accomplished by solvation of the complex by the extractant, and a typical equilibrium can be written as

$$R^{3+} + 3Y^- + 2S_{org} \overset{K_{ex}}{\rightleftharpoons} RY_3S_{2\,org} \tag{12}$$

if the extraction of HY is negligible. The distribution ratio of the metal ion would then be

$$D = \frac{[RY_3S_2]_{org}}{[R^{3+}]_{aq}} = K_{ex}[Y^-]^3[S]^2_{org} \tag{13}$$

unless Y^- forms aqueous complexes with R^{3+} as well. In that case, the denominator of the distribution ratio would be the total aqueous phase concentration of R^{3+}, which can be rewritten in terms of the formation constants of the aqueous complexes, as was shown for the amine extractants above (eq. 11). Although nitrate, chloride and perchlorate are the most commonly used anions for this class of extractants, organic anions (Samy et al. 1988, Frazier and Wai 1992), or even hydroxide (Cecconie and Freiser 1990) have been used for lanthanide extraction. Solvating extractants have even been suggested for solvent-extraction based isotopic separations of lanthanide isotopes (Fujii et al. 1998).

Solvating extractants and chelating acidic extractants also may be used together to extract metal ions. The acidic chelating extractant provides the charge neutralization, although K_{ex} will not necessarily be sufficient to extract the metal ion to a significant extent by eq. (7). The neutral extractant can be thought of as assisting in the phase transfer of the neutral complex through eq. (13), with Y^- being the anion of the acidic extractant. By judicious choice of the solvating and acidic extractants, the resulting distribution ratio will be greater than the sum of either extractant functioning alone. Such solvent-extraction systems are termed synergistic or synergic. The solvating extractant improves the extraction by rendering the complex more lipophilic. It accomplishes this either by expanding the coordination sphere, or by replacing water molecules in the

first coordination sphere of the metal ion (Choppin 1981). In addition to improving the solubility of the complex in the organic phase, a favorable entropy contribution to K_{ex} is realized if each bound molecule of the solvating extractant liberates more than one water molecule, as reported for the synergistic extraction of rare earths by 1-phenyl-3-methyl-4-benzoyl-5-pyrazolone (HPMBP) and trioctylphosphine oxide (TOPO) (Wenqing et al. 1986). In the organic phase, some protonated acidic extractants can also function as neutral, solvating extractants replacing water molecules in the extracted metal ion's coordination sphere (Sekine and Dyrssen 1967, and Yoshida 1966).

Synergistic extraction systems have received attention recently for potential applications in lanthanide separations or analysis when size-selective solvating reagents like crown ethers (Saleh et al. 1995, Frazier and Wai 1992, Tran and Zhang 1990) or *o*-phenanthroline (Zahir and Masuda 1997) are employed. Synergistic lanthanide separations incorporating both an acidic chelating agent and amine extractant instead of a solvating extractant have also been investigated (Dukov and Genov 1987, Noro and Sekine 1993). In this case, the chelating reagents form negatively charged species, which are extracted by the amine. As the trends in the separation factors of the chelating and solvating extractants are parallel, synergistic extraction systems should improve intralanthanide separations. However, the effect is not always predictable based on the behavior of individual components. To date, no synergistic extraction system has been identified that will enable intralanthanide separations in a single solvent-extraction stage.

Of these general classes of solvent extraction reactions, only those systems involving the application of lipophilic chelating agents (e.g., alkylphosphoric acids, β-diketones, crown ethers) exhibit any appreciable tendency toward cation selectivity among the trivalent lanthanides. Solvating extractants (e.g., tributylphosphate, TBP), ion-pair forming extractants (e.g., quaternary amines), and micelle-forming extractants typically extract a given class of metal ions indiscriminately (though they are sensitive to the oxidation state of the metal). Such reagents (and their ion-exchange resin equivalents) must rely on changes in aqueous chemistry for selectivity. In effect, such systems serve as "platforms" for selective separations based on differences in the aqueous chemistry of the system. The variation in aqueous chemistry may involve changes in the oxidation state of the metal ion, complexation, or more subtle alteration of the aqueous medium.

3.3. *Ion exchange and HPLC*

As we have noted above, separations based on the application of ion-exchange solids as the phase-transfer reagent rely predominantly on the aqueous chemistry of the rare-earth cations for a successful separation. In analytical applications, the solid material is often a polystyrene–divinyl benzene sulfonic acid resin material. The trivalent aquo cation is the reactive species, interacting with the resin via the following equilibrium:

$$R^{3+} + 3M(\text{resin}) \rightleftharpoons R(\text{resin})_3 + 3M^+, \tag{14}$$

where M^+ typically represents either H^+, NH_4^+, or an alkali-metal cation. The nature of the interactions of the metal with the functional groups in the resin phase is complex,

characterized by multiple reactions between species whose behavior is governed by unique activity coefficients. The most detailed analysis of the thermodynamics and kinetics of such interactions has been offered by Helfferich (1962).

The polystyrene–divinylbenzene backbone of cation-exchange resins can be produced with varying degrees of cross-linking between the linear polystyrene strands. This cross linking produces an internal pore structure within the generally spherical resin beads. Sulfonation of the resin (to create the cation-binding sites) is done after-the-fact and leads to functionalization of both the outer surface and inner pores of the resin beads. In contact with an aqueous solution, the inner pores are hydrated and typically contain simple ionic species from the contacting solution, though typically at a different concentration from that in the bulk solution. Depending on the degree of cross-linking, solute species above a certain size may be excluded from these pore spaces. As a matter of principle, the solute/bead combination must remain electroneutral. Osmotic pressure differences and differences in salt concentrations within the resin bead contribute to substantial differences in ion activity coefficients inside and outside of the resin bead. These activity differences impact metal-ion separation efficiency in sometimes unpredictable ways. In general, the water-soluble metal complexes responsible for separation are not strongly adsorbed by the solid support, and in some cases are too large to penetrate the pores of the resin. It is therefore reasonable to consider the complexation equilibria of the water-soluble metal complexes independently of the solid medium responsible for phase transfer.

Anion-exchange resins behave similarly, relying on the interactions of anionic metal complexes with positively charged functional groups (typically quaternary amine or methyl pyridine) in the resin phase. Resins containing potentially cation-selective chelating groups have also been prepared and evaluated, as we noted in sect. 2.2.4. Resins of this type have the potential for good selectivity in lanthanide separations, but probably cannot exceed the separation efficiency of extraction-chromatographic resins or systems based on aqueous complexes. From an energy balance perspective, the immobilization of an ion-selective chelating agent on a solid backbone removes all translational degrees of freedom possessed by the free ligand and most rotational motions. However, it is doubtful that such restrictions will have substantial impact on cation selectivity.

The nature of the solid sorbent in ion-pair chromatography differs from cation-exchange resins principally in the restriction of the active sulfonate groups to the outer surface of the resin bead. The hydrophobic layer between the sorbed sulfonate group and the silica support repels the water soluble cations. The absence of the polyelectrolyte binding effects and the elimination of functional groups in pores greatly simplifies the fundamental nature of the interaction between the metal ions and the sorbent surface. At a minimum, the kinetics of the phase transfer reaction is improved for this technique. Non-porous silica-based ion-exchange resins containing active functional groups covalently bonded to the silica support have been synthesized (Chiarizia et al. 1996a, Tong et al. 1989). Tong et al. (1989) report a complete separation of 14 lanthanides using a silica-based sulfonic acid cation exchanger combined with an ethylenediamine–hiba isocratic (constant composition) eluant.

3.4. *Lanthanide complexes with water-soluble chelating agents*

The strength of the complexes formed between trivalent lanthanide cations and organic chelating agents in aqueous solution is determined by the balance of hydration of the free metal ion, the free ligand, and the complex, the strength of the coulombic attraction between the acidic cation and the basic ligand donor atoms, cratic entropy (correlated with the change in the number of species diffusing through the solution), and the degrees of translational, rotational, and vibrational freedom lost by the ligand upon coordination to the lanthanide ion. For complex ligands like edta, one ligand combines with one metal ion to form the thermodynamically stable complex. For structurally simpler ligands like hiba, stoichiometries up to RL_3 or even higher are possible. In solutions containing more than one potential chelating agent, mixed complexes (one metal ion with two different ligands) are possible. As lanthanide concentrations in analytical separations are typically quite low, polynuclear complexes involving bridging ligands coordinating simultaneously to more than one metal ion are absent. It is apparent that there are many opportunities for adjustment of this chemistry to affect the outcome of any system.

How should these diverse interactions be expected to impact separation factors for adjacent lanthanide cations? In principle, several of the above factors that are related exclusively to the ligand (loss of translational, rotational and vibrational degrees of freedom, ligand solvation) should be independent of the lanthanide being bound. For some ligand systems one might expect additional ligand steric strain (or a decrease in denticity/coordination numbers, as we have reported recently for lanthanide complexes with HEDPA (Nash et al. 1997) as the ligand responds to the 20–25% decrease in cation radius across the series. The strength of the coulombic attraction between the metal ion and the ligand donor atoms should increase with the decreasing cation radius. This factor is opposed by the simultaneous increase in the strength of the ion–dipole interaction between the cations and water molecules for the free aquo cations[3]. The evident preference of lanthanide ions heavier than Eu for lower coordination numbers in both the hydrated ions and at least some coordination complexes (Nash et al. 1995) creates a potential discontinuity near the middle of the series.

One might guess that, since the lanthanide cationic radii change consistently across the series and their bonding is dominated by electrostatic attraction, there should be a variety of chelating agents that are effective for accomplishing the isolation of individual lanthanide ions. A considerable amount of research effort has been expended on both testing of various chelating agents for lanthanide separations, and determination of complexation equilibrium constants for the lanthanides to evaluate their relative affinity for lanthanide cations. Examination of the extensive database of critically evaluated stability constants (Martell and Smith 1997) for lanthanide complexes reveals that there

[3] The more pronounced linear trend for the interaction of lanthanide cations with lipophilic extractants like HDEHP demonstrates the increasing coulombic attraction between the ligand donor groups and the shrinking cation superimposed on the free energy associated with complete dehydration of the aquo cations as shown in fig. 7.

are in fact very few aqueous complexant systems that exhibit as consistent a trend across the entire lanthanide series as hiba.

Metal-ion complexation reactions as they occur in strongly solvating media like water consist in their most elementary form of the interaction of a hydrated metal cation with a hydrated ligand to form a hydrated complex, represented for a lanthanide and a simple mono anion as

$$R^{3+}(H_2O)_x + L^-(H_2O)_y \rightleftharpoons RL^{2+}(H_2O)_z + (x + y - z)H_2O. \tag{15}$$

The degree of hydration of each solute species (R^{3+}, L^-, and RL^{2+}) is different. Though we tend to think in terms of each ligand donor atom displacing one inner-sphere water molecule, this is not necessarily true, particularly for higher-order complexes (i.e., R:L > 1:1) (Nash et al. 1995). This conceptual framework does not explicitly address the energetic impact of second-sphere hydration, which may contribute substantially to the net energy balance of the system. The solvation of the aquo cations is moderately well known, that of the free ligand species is known for a few ligands, and the net solvation of the complexes is typically poorly characterized.

Simple monobasic acids like hiba are small enough to permit more than one ligand species to coordinate with the metal ion:

$$RL^{2+}(H_2O)_z + L^-(H_2O)_y \rightleftharpoons RL_2^+(H_2O)_{z'} + (z + y - z')H_2O, \tag{16}$$

$$RL_2^+(H_2O)_{z'} + L^-(H_2O)_y \rightleftharpoons RL_3(H_2O)_{z''} + (z' + y - z'')H_2O. \tag{17}$$

The changes most significant for lanthanide analysis associated with these equilibria are the charge on the complex and the degree of hydration of the metal complexes. These two factors are of paramount importance in the relative separation efficiency of lanthanide ions by most of the chromatographic techniques.

The complexation equilibrium coefficients for the respective reactions (15–17) are rigorously a function of the ratio of the ionic activities of the species:

$$\beta_i^o = \frac{a_{RL_i^{3-i}}}{a_{R^{3+}} \cdot a_{L^-}^i} = \frac{[RL_i^{3-i}]}{[R^{3+}][L^-]^i} \frac{\gamma_{RL_i^{3-i}}}{\gamma_{R^{3+}} \cdot \gamma_{L^-}^i}. \tag{18}$$

Due to the difficulty measuring ion activities, stability constants (β_i) are typically determined at constant ionic strength and temperature. Such conditional values are valid thermodynamic parameters describing ion interactions in a specific standard state (different from infinite dilution, which condition defines the true thermodynamic equilibrium)[4]. The ratio of activity coefficients (γ_i) is constant to a first approximation at a constant ionic strength and temperature. This ratio can therefore be combined into

[4] In analytical separations using chromatographic techniques, the ionic strength of the medium is not typically an important consideration. In gradient elution techniques, the ionic strength can vary substantially. However, the alteration in the ionic strength should have little impact on the separation of adjacent lanthanide cations.

the conditional equilibrium constant, written in terms of the molar concentrations of the species in each:

$$\beta_i = \frac{[RL_i^{3-i}]}{[R^{3+}][L^-]^i}. \tag{19}$$

The removal of activity coefficients from this relation should have minimal effect on our ability to predict lanthanide separation factors based on the relative stability of the complexes, as we make such predictions based on ratios, which will minimize the importance of such minor factors. However, comparisons based on thermodynamic data from the literature must utilize parameters determined at the same ionic strength and temperature.

The moderately to strongly basic carboxylate and amino functional groups in water-soluble organic complexants also strongly attract H^+ in solution. The concentration of the free ligand, $[L^-]$ in eq. (19), is therefore a function of the pH of the solution. The protonation equilibria can be written analogously to eqs. (15)–(17), with H_{aq}^+ in place of R^{3+}. Changes in hydration also pertain to ligand protonation reactions.

Since hiba is almost uniquely effective in lanthanide separation, we will concentrate in the following discussion on the thermodynamics of its lanthanide complexes to illustrate the utility of thermodynamic equilibrium constants for explaining and predicting the separation behavior of lanthanide cations. With the availability of appropriate equilibrium constants, this analysis could be applied to any metal–ligand system. The separation factor for adjacent lanthanides was defined in eq. (3) in terms of the ratio of metal-ion species in the organic and aqueous solutions. It can be written in terms of the aqueous lanthanide hiba complexes as

$$S_{R'}^{R} = \frac{D^R}{D^{R'}} = \frac{[R]_{org}/[R]_{aq}}{[R']_{org}/[R']_{aq}} = \frac{[RX_3]_{org}/([R^{3+}] + [RL^{2+}] + [RL_2^+] + \cdots)}{[R'X_3]_{org}/([R'^{3+}] + [R'L^{2+}] + [R'L_2^+] + \cdots)}. \tag{20}$$

The most efficient separations will be achieved when the lanthanide R is more strongly transported to the counterphase (RX_3) and more weakly complexed by the aqueous complexant (L^-) (or vice versa)[5] If we simplify this relation by eliminating some fractions and substitute the complexation equilibrium constants, including that for the phase transfer equilibrium (K_{ex}), this expression becomes a relatively simple function of the extraction equilibrium constants for the metal ions (K_{ex}), the complex stability constants, and the free ligand concentration (recognizing that the free ligand concentration carries a pH dependence as well):

[5] For separations based on the application of solvent extraction/extraction chromatography with acidic extractants (like HDEHP), trends in K_{ex} and β_i work in opposition. Aqueous complexants are therefore of limited utility for separation systems in this combination or reagents. For separations based on cation exchange (either using Dowex 50-type resins or dynamic ion exchange resins), the ratio $K_{ex}^R/K_{ex}^{R'}$ increases from Lu to La, i.e. $K_{ex}^{La} > K_{ex}^{Ce} > K_{ex}^{Pr} \cdots$, which is opposite the trend in aqueous complex stability.

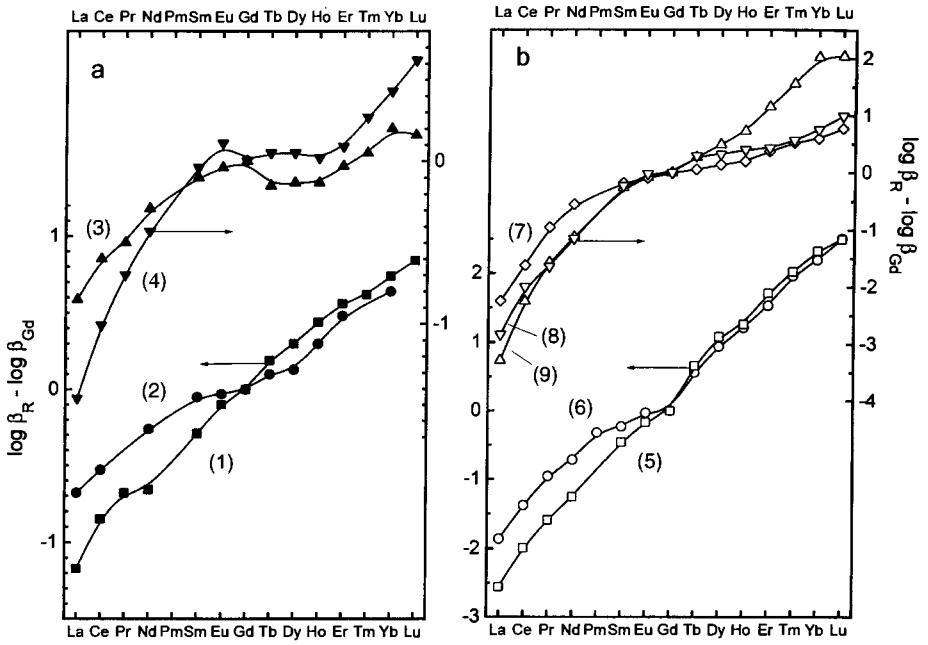

Fig. 9. Relative stability of lanthanide complexes with a variety of water soluble chelating agents: (1) β_2(R-hiba), (2) β_2(R-lactate), (3) β_2(R-glycolate), (4) β_2(R-diglycolate), (5) β_1(R-dcta), (6) β_1(R-edta), (7) β_2(R-dipic), (8) β_2(R-nta), (9) β_2(R-dcpa).

$$S^{R}_{R'} = \frac{D^{R}}{D^{R'}} = \frac{K^{R}_{ex} \cdot (1 + \sum \beta_i^{R'}[L]^i + \sum \beta_j^{R'}[L']^j + \cdots)}{K^{R'}_{ex} \cdot (1 + \sum \beta_i^{R}[L]^i + \sum \beta_j^{R}[L']^j + \cdots)}. \quad (21)$$

This expression has been made more generic through the inclusion of a second chelating ligand (L′). It ignores the possible existence of mixed complexes (involving both L and L′), for which there are very few thermodynamic data available. It also assumes that the stoichiometry of the phase-transfer equilibrium is the same for both metal ions. A generic expression in this format is most appropriate for analytical separations, as there are a number of standard gradient elution techniques that exploit changes in the concentrations of more than one ligand at a time.

It is appropriate to consider the relative stability of lanthanide complexes as a first indicator of a ligand's potential applicability for lanthanide separations. In fig. 9 is shown a plot of the relative stability of a variety of lanthanide carboxylate complexes (normalized to $\log\beta(Gd^{3+}) = 0$) of importance in analytical separations. The 1:2 complexes of the lanthanides with glycolate and diglycolate exhibit similarly poor discrimination of lanthanide ions between Gd and Ho, though the overall slope is greater for diglycolate. The 1:2 lactate complexes vary more regularly than these species, but

discriminate between Sm, Eu, and Gd less acceptably than does hiba. The polydentate aminopolycarboxylate ligands (edta and nta) demonstrate both more pronounced variation with cation radius and more consistent trends in the relative stability of the lanthanide complexes than any of the carboxylate complexants.

Constraining the ligand donor atoms contributes to increased complex stability (by removing degrees of rotational freedom from the free ligand) and to increased sensitivity to cation size. The stability constants for the 1:2 complexes of the lanthanides with 2,6-dicarboxypiperidine-*N*-acetic acid (dcpa) and *trans*-1,2-diaminocyclohexane-*N,N,N′,N′*-tetraacetic acid (dcta) each exhibit a more pronounced sensitivity to lanthanide cation radius than the non-constrained analogs (nta and edta respectively). However, the planar arrangement of donor atoms in dipicolinic acid (dipic-2,6-dicarboxypyridine) is comparable to dcpa for the lanthanides lighter than Tb, but distinguishes the heavier lanthanides less effectively. Despite some favorable trends in their complexation characteristics, aminopolycarboxylate ligands have found relatively few analytical applications because their complexation of trivalent lanthanides is kinetically hindered (Nash and Sullivan 1991).

Comparing relationships between the stability constants of lanthanides can provide explanation for failures in lanthanide analytical separations. For example, the inadequate resolution of Gd/Eu and Dy/Ho pairs in the nta resin described by Inoue et al. (1996) (sect. 2.2.4) is identical to that of Kuroda et al. (1993) who used aqueous nta as a eluant for an ion-pair chromatographic separation of the lanthanides (using a gradient elution procedure). Comparison of the stability constants for the 1:1 and 1:2 lanthanide nta complexes reveals that poor resolution of Eu and Gd is consistent with the relative stability constants for the metal ions. The incomplete resolution of Dy/Ho is also consistent with the general trend in the β's, though one might expect that Tb would be similarly poorly resolved. The application of a concentration gradient may account for the improvement over the predicted pattern.

Though comparison of stability constants is a good starting point, a more complete assessment of the utility of an aqueous complexant requires consideration of the actual concentration of the complexant and solution pH. Let us next consider the speciation of a lanthanide cation in hiba at pH 4.5 and over the concentration range of 0.0002 M to 0.4 M hiba, a typical spread of hiba concentrations in a gradient elution sequence. We consider first the fractional speciation of lanthanum and lutetium among their hiba complexes. The mass balance expressions describing the speciation of La and hiba in a solution is given by (ignoring the reported 1:4 complexes for which stability constants are unreliable)

$$[\mathrm{La}]_{\mathrm{tot}} = [\mathrm{La}^{3+}] + [\mathrm{LaL}^{2+}] + [\mathrm{LaL_2}^{+}] + [\mathrm{LaL_3}], \tag{22}$$

$$[\mathrm{hiba}]_{\mathrm{tot}} = [\mathrm{L}^{-}] + [\mathrm{HL}] + [\mathrm{LaL}^{2+}] + 2 \cdot [\mathrm{LaL_2}^{+}] + 3 \cdot [\mathrm{LaL_3}]. \tag{23}$$

These expressions can be rewritten in terms of the stability constants as

$$[\mathrm{La}]_{\mathrm{tot}} = [\mathrm{La}^{3+}](1 + \beta_1[\mathrm{L}^{-}] + \beta_2[\mathrm{L}^{-}]^2 + \beta_3[\mathrm{L}^{-}]^3), \tag{24}$$

$$[\mathrm{hiba}]_{\mathrm{tot}} = [\mathrm{L}^{-}] + K_{\mathrm{h}} \cdot [\mathrm{H}^{+}] \cdot [\mathrm{L}^{-}] + [\mathrm{La}^{3+}](\beta_1[\mathrm{L}^{-}] + 2 \cdot \beta_2[\mathrm{L}^{-}]^2 + 3 \cdot \beta_3[\mathrm{L}^{-}]^3). \tag{25}$$

If $[\mathrm{La}]_{\mathrm{tot}}$, $[\mathrm{hiba}]_{\mathrm{tot}}$, and pH are known, these equations can be solved simultaneously to determine the free ligand ($[\mathrm{L}^{-}]$) and free metal-ion ($[\mathrm{La}^{3+}]$) concentrations, which can

in turn be used to calculate the concentrations of all complexes. A second chelating agent could also be accommodated in these calculations by adding a third mass balance expression. If pH is not controlled, a mass balance expression for total acidity could also be incorporated. Such calculations can be made as a function of the analytical concentrations of metal and ligand and pH. They are readily accomplished with the aid of a computer to generate speciation plots which describe the variation in the concentration of each species as a function of the solution conditions.

In analytical separations, the concentration of the free ligand in the eluant is almost always substantially greater than that of the lanthanide ion being analyzed. If this is not the case, the analyst should be forewarned that the separation system may behave erratically, as macro lanthanide (or any other metal ion strongly complexed by the eluant) will diminish the free ligand concentration needed for trace metal analysis. As the condition of excess ligand prevails, two simplifications to eqs. (24) and (25) can be made:

(1) The absolute concentration of the metal ion is no longer needed as the speciation of the metal ion can be solved in terms of the mole fraction of each species. If we set $[La]_t = 1$, the variables in eq. (24) can be separated and we can solve for the mole fraction of free metal as

$$\frac{1}{[La^{3+}]} = 1 + \beta_1[L^-] + \beta_2[L^-]^2 + \beta_3[L^-]^3, \tag{26}$$

and the mole fraction of free metal ion can be calculated from the β's and the free ligand concentration. Substitution of the free metal concentration thus determined into the equilibrium constant expressions enables calculation of fractional speciation of all complexes.

(2) As the metal complexes are present at microscopic concentrations, one has $([L^-] + K_h \cdot [H^+] \cdot [L^-]) \gg [La^{3+}](\beta_1[L^-] + 2 \cdot \beta_2[L^-]^2 + 3 \cdot \beta_3[L^-]^3)$, and the free ligand concentration becomes

$$[hiba]_{tot} = [L^-] + K_h \cdot [H^+] \cdot [L^-], \tag{27}$$

which allows simple calculation of the free ligand concentration ($[L^-]$).

A fractional speciation curve for lanthanum at pH 4.5 and $[hiba]_{tot}$ from 0.0002 to 0.4 M is shown in fig. 10a. Speciation curves of this type predict the most important species of the metal ion under a given set of conditions. Note that at the low end of the range $[La^{3+}]$ is dominant, while the charge-neutral species LaL_3 dominates at the high end of the range. The difference in charge of the complexes may contribute to separation effectiveness in most chromatographic techniques and is essential for electrophoretic analyses. A similar calculation done for Lu^{3+} indicates a shift in the speciation curve as a function of $[hiba]_t$ (fig. 10b) toward more extensive complexation at lower concentration of the complexant.

We can use these same mass balance expressions to calculate a term we have previously called a "stripping" or "holdback" factor[6]. The holdback factor is the ratio of metal-ion

[6] To avoid confusion with the separation factor ($S_R^{R'}$), we will refer to this term as a holdback factor in this discussion.

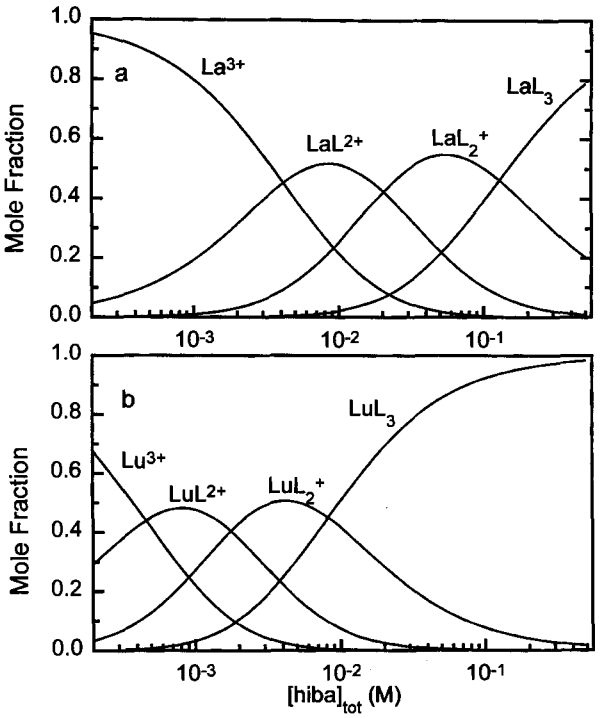

Fig. 10. Fractional speciation of (a) lanthanum and (b) lutetium complexes with hiba at pH 4.5.

distribution ratios in the absence and presence of an aqueous complexing agent. Repeating the general formalism of eq. (2), the distribution ratio in the absence of an aqueous complexant is $D_o = [R]_{org}/[R^{3+}]_{aq}$. Upon introduction of an aqueous complexing agent, the distribution ratio is reduced due to aqueous complexation, $D = [R]_{org}/([M^{3+}] + \sum [ML_i])$. The denominator of this expression can be written in terms of aqueous stability constants as we have done previously. The holdback factor is $D_o/D = (1 + \sum \beta_i [L^-]^i)$. We can calculate this term to predict the relative effectiveness of a complexant for a metal ion if we know the appropriate stability constants for the complexes formed. Allowing no credit for the intrinsic ability of the solid material to contribute to lanthanide separation, we can calculate the Gd number for lanthanide separations if we divide the Gd holdback term by that for the other lanthanides. Calculated Gd numbers as a function of [hiba] are shown in fig. 11a. This plot demonstrates that hiba is an effective separation reagent for lanthanides over its entire range of concentrations. A similar calculation of Gd number for diglycolic acid illustrates the limitations of this reagent for separation of the heavy lanthanides in fig. 11b. If only the light members of the series are present, diglycolate actually offers greater separation factors for adjacent ions than hiba over most of the accessible concentration range.

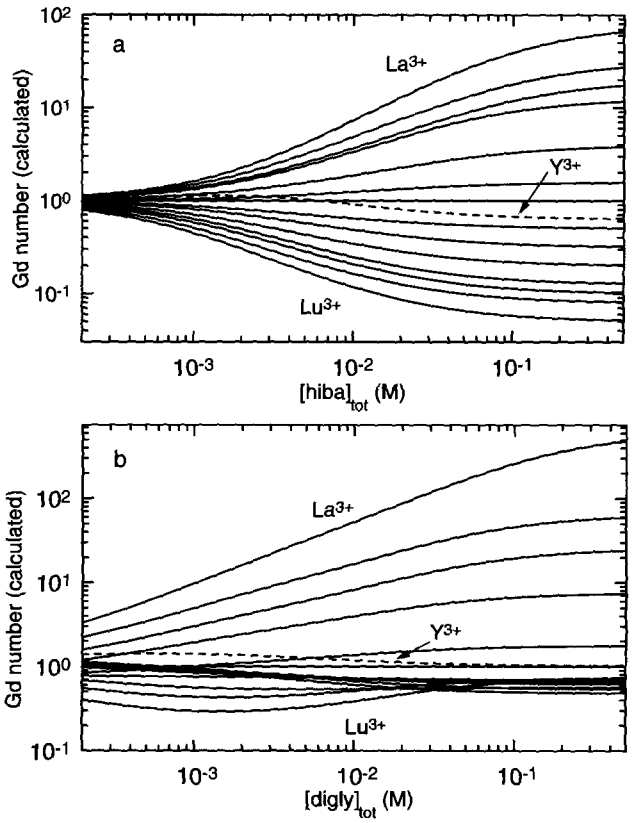

Fig. 11. Calculated holdback factor, normalized to Gd = 1.0, for (a) lanthanide (solid curves) and Y (dashed curve) complexes with hiba at pH 4.5, and (b) lanthanide (solid curves) and Y (dashed curve) complexes with diglycolic acid at pH 3.5.

One additional manipulation of such thermodynamic parameters can be done to aid in planning an appropriate gradient elution sequence. A measure of the degree of complexation is the average ligand number $\bar{n}$ (nbar):

$$\bar{n} = \frac{[RL^{2+}] + 2 \cdot [RL_2^{+}] + 3 \cdot [RL_3]}{[R^{3+}] + [RL^{2+}] + [RL_2^{+}] + [RL_3]} = \frac{\sum i \cdot \beta_i [L^-]^i}{1 + \sum \beta_i [L^-]^i}. \tag{28}$$

For our purposes, $\bar{n}$ is plotted as a function of $[\text{hiba}]_{\text{tot}}$ for all of the lanthanides, as shown in fig. 12. Vertical lines on this plot provide guidance for choosing the optimum concentration for an isocratic elution. Based on this calculation, the mutual separation of Ce, Pr, Nd is attained at about 0.03 M hiba at pH 4.5. However, under these conditions, Er, Tm, and Yb are relatively poorly differentiated. The dotted line spanning the hiba concentration range of 0.0003 M to 0.1 M represents a possible effective gradient for optimum separation of all of the lanthanides. Note that the predicted eluting position

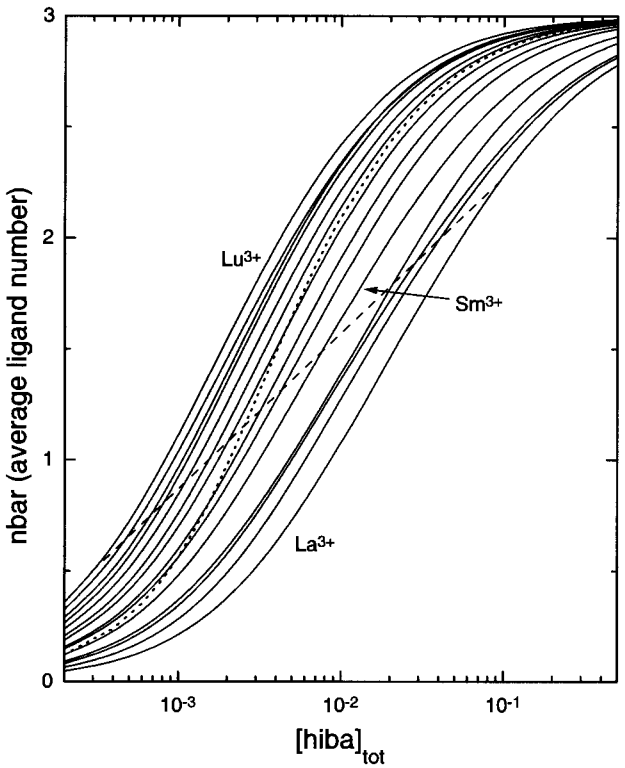

Fig. 12. Average ligand number for lanthanide ions and yttrium (dotted curve) at pH 4.5. The dashed line represents a potential logarithmic concentration gradient to optimize mutual separation of all lanthanides and Y.

of Y varies with the concentration of hiba. Of course, minor modifications of this plot will result if the phase-separation system offers any discrimination among the ions. Such curves are readily created providing reliable stability constant data are available. With some additional effort, a three-dimensional plot (pH as the third variable) could be constructed to evaluate the combined effect of complexant concentration and pH. Calculations generally support the premise that concentration gradients are more effective tools than pH gradients.

3.5. *Thermodynamics and the role of the α-hydroxide group in lanthanide separations*

We compared in sect. 3.1 the holdback factors for several carboxylic and aminopolycarboxylic acids that have been (or could be) used for lanthanide separations. It is clear that among the carboxylic acid eluants, a hydroxide group on the α-carbon atom is necessary for consistent performance across the series. One might expect that the proximity of the OH group creates the possibility of simultaneous coordination of both a carboxylate oxygen and the hydroxide, thus creating a chelate complex of enhanced stability. However

realistic this expectation, the presence of an oxygen donor group at the α- (or β-) position does not necessarily translate into consistent variation of lanthanide complex stability. For example, neither oxalic acid ($HO_2C–CO_2H$), glyoxylic acid ($HOC–CO_2H$), nor malonic acid ($HO_2C–CH_2–CO_2H$) exhibits as consistent a trend in the stability of their lanthanide complexes as hiba. The polydentate α-hydroxy complexant citric acid does not exhibit as consistent a trend across the series as hiba or lactate. An ether oxygen in the α-position (bridging a second carboxylate group – diglycolic acid) is likewise a poorer reagent for a complete analysis of lanthanides than hiba.

The equilibria that define metal ligand interactions have been discussed in sect. 3.4 and eqs. (15)–(17). The interrelationship between solvation and bonding effects determines the relative positions of the equilibria. However, the stability constants used to predict relative performance across the lanthanide series offer little insight into the nature of these interactions. It is often instructive to consider the relative contributions of enthalpy (ΔH) and entropy (ΔS) to the complexation reaction. Because the measured values for ΔH and ΔS of a metal-complex formation equilibrium include contributions from solvation, bonding interactions, and the degrees of freedom of movement unique to complex organic ligands, supplementary information from the application of spectroscopic techniques is often required to describe the physical nature of metal–ligand interactions. Nevertheless, it is instructive to compare the ΔH and ΔS values for lanthanide complexes with organic complexants of similar geometries.

Plots of ΔG, ΔH, and ΔS for the consecutive addition of 1 and 2 hiba ligands to the lanthanide cations are shown in fig. 13a. It is clear in this figure that the consistent interval in the free energy of the lanthanide–hiba complexes persists for the 1:1 and 1:2 complexes. For the 1:1 hiba complexes, the steady variation in complex stability across the lanthanide series is primarily related to the increasing contribution of a favorable entropy superimposed on a nearly constant exothermic enthalpy. For the 1:2 complexes, the steady change in ΔG correlates most strongly with the trend for ΔH.

The comparative thermodynamic parameters for the non-OH-functionalized analog complexant isobutyric acid are shown in fig. 13b. The free energy of complexation of the 1:1 complexes increases regularly from La to Sm, then reverses for the heavier lanthanides. Interestingly, the regular increase extends from La to Tb for the 1:2 complexes. It seems likely that both of these trends are related to subtle differences in the solvation of the 1:1 and 1:2 complexes, quite possibly related primarily to second sphere hydration effects. The enthalpies of complexation of lanthanides by isobutyric acid show a common pattern of relatively constant endothermic enthalpies for the complexes from La to Eu, and a different, more endothermic ΔH for the heavy lanthanides. The shift has been attributed to the change in hydration/coordination numbers that occurs around Gd. Lanthanide–isobutyrate complex stability is derived from a favorable entropy, the magnitude of which exceeds that of the unfavorable enthalpy contribution. Enthalpy–entropy compensation is a well-known but incompletely understood feature of lanthanide complexation reactions (Choppin 1971).

Comparisons of thermodynamic data for each of the α-hydroxy acids and their structural analogs without the OH group show trends in ΔH and ΔS similar to those for

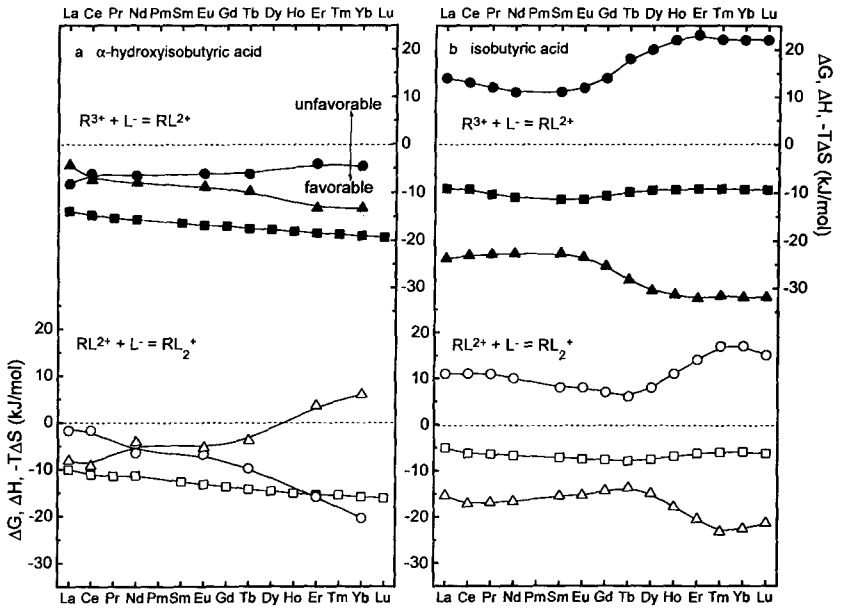

Fig. 13. Thermodynamic parameters for 1:1 and 1:2 complexes of lanthanides with hiba and isobutyric acid: ΔG (squares), ΔH (circles), ΔS (triangles). Solid symbols are 1:1 complexes, open symbols for step-wise addition of a second ligand.

hiba-isobutyric acid. The large positive entropies of the non-OH-containing acids suggest substantial dehydration of the metal ion upon complex formation and greater dehydration for the heavy lanthanides. Since the heavy lanthanide aquo cations have fewer inner-sphere water molecules than the light lanthanides, excess loss of water molecules from the second hydration sphere (or the free ligand) is implicated. It has been argued that the dramatically different thermodynamic parameters for the α-hydroxy acids indicate less inner-sphere dehydration of the metal ion in the complexes through the formation of a hydrogen-bonded chelate (an inner-sphere water molecule hydrogen bonded to the α-OH group).

3.6. *Itinerant behavior of yttrium in lanthanide analysis*

Though yttrium is not a member of the lanthanide series, its chemistry closely mimics that of the lanthanide metal ions. As a result of this similarity, most rare-earth minerals also contain yttrium, some in relatively high abundance. Yttrium is also a product, along with several of the lanthanides, of nuclear fission and so is present in irradiated nuclear fuel. The best estimate of the eight-coordinate cationic radius of Y is 1.019 Å, very near to that of Ho (1.015 Å) (Shannon 1976). Because the interaction of the lanthanides and Y with solvent and solute molecules is predominantly electrostatic in nature, the solution chemistries of Y and the lanthanides overlap substantially. However, this similarity in the

chemistries of the metal ions does not translate into a fully predictable and consistent behavior of Y in analytical separations of rare-earth samples. Yttrium has been reported in different separation systems to elute from a separation column in close proximity to any lanthanide between Ce and Tm.

For example, in most of the separations based on the application of hiba, with or without using gradient elution techniques, Y elutes in close proximity to Dy (Broekaert and Hörmann 1981, Corr and Anacleto 1996, Sawatari et al. 1995, Stijfhoorn et al. 1993, Kuban and Gladilovich 1988, Moraes and Shihomatsu 1994, Al-Shawi and Dahl 1994, Cassidy 1988, Barkley et al. 1986). This is true independent of the method used for phase transfer. As its cationic radius is intermediate between Dy and Ho, this is the most reasonable position in which to observe Y. Similar behavior is seen for lactic acid as eluant (Kuroda et al. 1990). Glycolic acid solutions tend to elute Y near Nd (Kuroda et al. 1991, Oguma et al. 1993). Aminopolycarboxylic acid eluants like nta (Kuroda et al. 1993) or *N*-(2-hydroxyethane)-ethylenedinitrilo-*N,N',N'*-triacetic acid (hedta, Strelow and Victor 1990) behave similarly to diglycolate, eluting Y in proximity with Sm. Jones et al. (1991) report that Y overlaps with Tb for elution by oxalate solutions. Two reports that rely on dipicolinic acid (2,6-dicarboxypyridine) as the eluant, either alone (le Roex and Watkins 1990) or in a gradient elution scheme with diglycolic acid and oxalate (Watkins et al. 1995) indicate elution of Y near Ho.

Though the free energy differences required to account for this nomadic behavior of Y are quite small (a few kJ/mole at most), it is nevertheless curious that similar reversals of separation order are seldom observed for the true lanthanide cations. The ΔG° for formation of the aquo cations place Y^{3+} nearest to Tb^{3+}, though the corresponding ΔH° values for Y^{3+} are notably more exothermic than the lanthanide cations. This implies a somewhat greater order in the Y^{3+} aquo cation as compared with the lanthanides.

Comparison of the elution positions of Y^{3+} with the stability constants for the complexes used for analysis indicate that, for the most part, the migrations occur in accordance with changes in stability of the aqueous complexes. For example, the 1:2 and 1:3 R:lactate complexes of Y^{3+} and Tb^{3+} most responsible for lactate-based separations essentially overlap. The mono-, bis-, and tris- complexes of Y^{3+} with hiba are most similar to those of Dy^{3+}. The lanthanide glycolate complexes show a correlation with the ionic radii of the light and heavy lanthanides but this ligand exhibits little selectivity for the middle of the series (Eu^{3+} to Er^{3+}). The stability constants for Y-glycolates are most similar to the mid-range values, though Y elutes just after Nd and is separated from the Eu–Er group. Stability constants for Y^{3+} and Tb^{3+} oxalates are nearly identical, as is their elution position. The 1:2 complexes Y(nta) and Sm(nta) are nearly identical, but the Y(hedta) ($\log\beta = 14.75$, $I = 0.1$ M) is more comparable to Pr(hedta) ($\log\beta = 14.71$, $I = 0.1$ M) than to Sm(hedta) ($\log\beta = 15.38$, $I = 0.1$ M). In most cases, therefore, the transient elution position of Y is explained by the relative stability of the aqueous complexes rather than inconsistent behavior in the phase transfer equilibria. It is important to again emphasize that the energy differences required to account for this behavior are extremely small when considered in terms of the overall energetics of the separation systems.

3.7. *Periodicity in the lanthanide series*

The rare-earth elements can be treated as a group because their chemical properties change little despite the variation in the number of 4f-electrons across the series. As discussed above, the stability constants of complexes formed between trivalent rare-earth cations and simple hard ligands should generally increase across the lanthanide series as the ionic radii decrease. Often there are substantial deviations from this ideal behavior because of the changes in hydration number across the series, the impact of the hydration energies, or the steric requirements of more complicated ligands, etc. However, even when these effects are considered, small, periodic variations in the stability constants across the lanthanide series remain. These periodic variations across the lanthanide series, called the tetrad or double–double effect because they appear in four sets of four lanthanides, have been repeatedly observed in lanthanide separations and geochemistry. They were first observed when researchers were trying to separate individual lanthanide elements. A number of possible sources for the tetrad effect have been suggested, including small variations in nephelauxetic parameters or differences in the orbital angular momentum as summarized by Sinha (1976) and Mioduski (1997).

In hindsight, much of the tetrad effect observed in the equilibrium constants of lanthanide reactions can arise from a tetrad effect in the ionic radii in the lanthanide series. An early solvent extraction example using *n*-octyl(*n*-octyl)phosphonic acid in benzene as the extractant is shown in fig. 14. Peppard and coworkers (1968) at Argonne National Laboratory first noticed the effect in graphs of distribution ratios (and thus K_{ex} by eq. 7) against atomic number, Z (fig. 14a). To a first approximation, the distribution ratios of a rare-earth cation are expected to follow simple electrostatics with a logarithmic dependence on the reciprocal of the ionic radius. Since the reciprocal of the ionic radius is not a linear function of the atomic number, the data in fig. 14a should be replotted. When the distribution ratios are replotted as a function of the reciprocal of the ionic radius using the ionic radii available in the 1960s (Templeton and Dauben 1954), the tetrad effect remains (fig. 14b). However, if modern values of the ionic radii determined by Shannon (1976) are used, the tetrad effect largely disappears, as shown in fig. 14c. This is because much of the tetrad effect observed in lanthanide separations seems to arise from tetradic variations in the radii of the lanthanides, which could in turn be explained by nephelauxetic parameters or total angular momenta, or some other cause. The smoothly varying ionic radii available in the 1960s masked the immediate origin of the observed chemical behavior – electrostatics.

The tetrad effect, however, should not be ignored. There is a difference between explaining chemistry by resorting to tetrads and exploiting the observed tetrad effect to efficiently separate adjacent lanthanides. Purely electrostatic bonding models form an adequate foundation for describing the solution chemistry of rare-earth cations, but intra-lanthanide separations are performed as a function of atomic number, not ionic radius. The variations in the intra-lanthanide separation factors that create the breaks between tetrads in fig. 14a are real and can be exploited in separations even if the immediate cause is electrostatic.

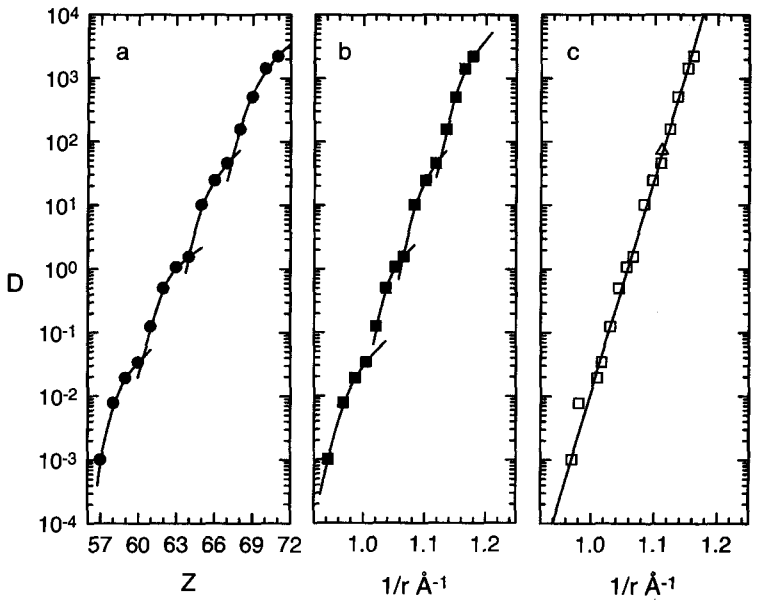

Fig. 14. Distribution ratios of rare-earth elements between 0.3 M di-*n*-octyl-phosphonic acid/benzene and 0.05 M HCl (Peppard et al. 1968) as a function of (a) atomic number, (b) the reciprocal of Templeton and Dauben's (1954) ionic radii, (c) the reciprocal of Shannon's (1976) ionic radii.

4. Applications of separation techniques for lanthanides

Analysis to determine the rare-earth content of materials can have many different objectives. Successful separations require a judicious combination of appropriate group separation/preconcentration, separation of individual members of the series, and the proper detection technique. Recent reviews that are readily available in the chemical literature offer compilations of "cookbook" methods for conducting analyses of samples of different types. In the following sections, we will offer a brief summary of preferred methods for specific types of analyses and provide appropriate literature references for the reader to pursue for details beyond those offered herein. The emphasis of this section will be on the literature covering the period 1990–1997, which has not been discussed in previous English-language reviews of the subject. Some earlier reports describing important fundamental advances in lanthanide separations will be included.

4.1. *Geological samples*

There are three general motivations for analysis of natural samples: (1) exploration for rare-earth mineral resources, (2) isotopic analysis for elucidation of the geological history of the earth, and (3) analysis of living samples to investigate natural distribution of lanthanides in the biosphere. The analysis of geologic samples for rare-earth content has obvious implications for rare-earth mining, and rare-earth analyses also have been

applied to petroleum geology (Emery and Robinson 1993), but one vital area of rare-earth analyses is the scientific inquiry into geological problems.

The chemical and nuclear properties of rare-earth elements make them excellent tracers of geologic processes. Little differentiation in rare-earth concentrations is observed in commonly encountered low-temperature processes like mineral weathering. The chemical similarity of the trivalent rare-earth cations that makes analytical separations difficult, ensures that rare earths generally follow each other in geochemical cycles, though large anomalies in Ce or Eu concentrations are commonly observed because of the formation of Ce^{4+} and Eu^{2+} under oxidizing or reducing conditions, respectively. At higher temperatures, however, the rare-earth element compounds can be fractionated based on melting points, under geothermal conditions, or on volatility, under extraterrestrial conditions. Each of these mechanisms gives different systematic enrichments or depletions of certain rare earths. By studying the fractionation patterns of the rare-earth elements, the origin of the processes that formed a mineral phase can be ascertained with important implications for solar evolution. An application of this methodology can be found in Haskin's (1989) review of the rare-earth abundances in lunar surface samples.

While the naturally occurring rare earths are widely considered non-radioactive, seven of them, La, Ce, Nd, Sm, Gd, Dy, and Lu, have naturally occurring radioactive isotopes. Of these, ^{138}La ($t_{1/2} = 1.06 \times 10^{11}$ yr), ^{147}Sm ($t_{1/2} = 1.08 \times 10^{11}$ yr), and ^{176}Lu ($t_{1/2} = 3.7 \times 10^{10}$ yr) have half-lives short enough to be useful isotopic tracers for both geo- and cosmochemistry. The stable progeny of these radioactive parents are analyzed by mass spectrometry, and they must be free of other isobaric interferences (^{142}Ce, ^{144}Sm, ^{148}Sm, and ^{150}Sm interfere with determination of ^{142}Nd, ^{144}Nd, ^{148}Nd, and ^{150}Nd) as a 0.03% deviation in the $^{143}Nd/^{144}Nd$ isotopic ratio corresponds to 100 million years in the Sm/Nd isochron (Emery and Robinson 1993). The $^{147}Sm/^{143}Nd$ pair is the most widely employed and is of great importance in lunar and meteoric chronology and evolution (Patchett 1989). Because Sm and Nd are both light rare-earth elements with only one important oxidation state, they follow each other closely in geochemical cycles. This is an advantage over other isotopic chronometers like $^{87}Rb/^{87}Sr$, because Rb and Sr have very different chemistries and are both comparatively mobile. The $^{176}Lu/^{176}Hf$ pair can also be difficult to implement, though for a different reason. Hf is not a rare earth and is highly refractory. Thus, Hf will not necessarily follow the rare-earth elements through geochemical cycles and can be difficult to analyze. Use of the $^{138}La/^{138}Ce$ pair has been limited since it suffers from a low natural abundance of ^{138}La, but it is especially useful in tracing the origin of Ce anomalies (Makishima and Nakamura 1991). The analytical-scale separation of tetravalent Ce from other rare earths is readily accomplished (Saxena et al. 1995). Rehkämper et al. (1996) used HDEHP-based liquid–liquid extraction to perform this type of Ce separation for both Sm/Nd and La/Ce chronometry.

Analysis in support of mineral exploration typically involves standard techniques for both rock dissolution and chromatographic analysis. For example, Moraes and Shihomatsu (1994) report the analysis of US Geological Survey standard rock samples using ion-pair chromatography (dynamic ion exchange) with hiba as the eluant. Standard procedures for rock dissolution, preconcentration, and chromatographic analysis are followed. A gradient

elution (pH 3.8, [hiba] = 0.07–0.4 M at 1 ml/min over 20 minutes) was employed with colorimetric detection (using PAR) for post-column derivatization. Each lanthanide was resolved, though there was slight overlap between Y and Dy. The detection limits in the original samples were in the 1–3 ppb range. This technique is a representative recent demonstration of the general technique developed by Cassidy and coworkers in the 1980s (Cassidy et al. 1985, Cassidy 1988, Barkley et al. 1986, Cassidy and Chauvel 1989, Knight et al. 1984). It relies on the basic chemistry introduced in the 1950s (Choppin and Silva 1956). The same basic method (using slightly different gradient conditions) was used by Al-Shawi and Dahl (1994), Kuroda et al. (1990) and Moraes et al. (1997) for analysis of monazite/phosphate rock, the latter using solvent extraction for preconcentration of the lanthanides. Kuroda et al. (1990) employed an oxalate precipitation step to isolate the lanthanides from the sulfuric acid dissolver solution. Oguma et al. (1993) analyzed silicate rocks using a glycolic acid concentration gradient at pH 3.5, though Sm, Eu, Gd, Tb, and Dy are not resolved, and Ho poorly so. le Roex and Watkins (1990) employed a mixed oxalate/diglycolate eluant but experienced incomplete resolution of Ho from Y and Lu from Yb. By adding dipicolinic acid to the eluant, they were able to complete the analysis in a somewhat extended period without complete removal of transition metal impurities.

The analysis of rare earths in water samples is particularly important to the studies of rare-earth distribution and migration in the biosphere. Chen et al. (1994) applied solvent extraction of Nd by chlorophosphonazo III in 1-butanol with spectrophotometric determination of Nd to 0.07 ppm in synthetic brine solutions. Lu et al. (1997) report the application of "chelation ion chromatography" for the analysis of lanthanides in agriculture. These authors cite literature reports linking increased lanthanide concentrations in soils to improved crop yields (P.L. Liu et al. 1995, H.Z. Liu et al. 1995, Yau et al. 1996, Zhang and Cui 1995). The chelation ion chromatography technique involves elimination of bulk alkali and alkaline-earth metals on a "chelating concentrator column" and transition metals on a cation-exchange column from an ammonium acetate buffer while the lanthanides are simultaneously concentrated. A mixed-bed (ammonium and sulfonate groups on the same polystyrene–divinyl benzene backbone) column was used with an oxalate/diglycolate concentration gradient for the eluant. Ho and Y are not resolved by this eluant. The authors claim detection limits in the few ng/ml concentration range. A similar gradient elution procedure was used by Watkins et al. (1995) to analyze for rare earths in coal samples dissolved by microwave digestion. The Ho–Y overlap is observed while detection limits of 10–50 ng/g of the original coal sample are claimed.

Isotopic analysis of rock samples provides unique insights into the genesis and evolution of the earth. This method is perhaps the most demanding of all lanthanide analyses, as it typically requires chemical separation of the group from the matrix, individual members of the series, and usually relies on mass spectrometric detection. The separation chemistry is generally comparable to that applied for less demanding samples/objectives. The detection method requires careful preparation of the post-separation sample to avoid potential interferences. In fact, the MS detection technique is extremely sensitive to the presence of impurities, requiring that essentially all impurities be removed. Among the interferences to mass spectrometric analysis is the overlap of

the mass numbers for the molecular ions GdO^+ and $GdOH^+$ with isotopes of Yb and Lu. An example of such an analysis is that reported by Stray and Dahlgren (1995). Their interest is in the isotopic analysis of Nd and Sm in rock samples. They analyzed 40 sedimentary rocks (sand stones, shales and mudstones) using a technique that combines preconcentration by conventional ion exchange with application of ion chromatography for isolation of the lanthanides. An oxalate gradient was used for lanthanide resolution. Ion chromatographic techniques are applied to eliminate contaminating anions in a cleanup column. Nd and Sm are well separated from each other (the intermediate lanthanide Pm has no stable isotopes and therefore is not present) and adequately resolved from the other lanthanides. The detection limits are in the 0.2 μg/g range.

Solvent extraction by a crown hydroxamic acid in chloroform for the determination of La in monazite sand has been reported by Agrawal and Shrivastav (1997). La can be determined spectrophotometrically in the organic phase between 1.2 and 20 ppm, or by ICP/AES with a detection limit of 0.18 ppb. A two-fold excess of Y, Ce, Pr, or Nd did not interfere with the spectrophotometric determination, and higher concentrations could be tolerated when fluoride or oxalate were present in the aqueous phase.

Two reports by Pin and coworkers (Pin et al. 1994, Pin and Zalduegui 1997) have applied extraction chromatography to the analysis of $^{143}Nd/^{144}Nd$ ratios in silicate rocks. Before separation of the light rare earths, Sr was removed by extraction chromatography for $^{87}Sr/^{86}Sr$ analysis and Fe^{3+} interferences were removed with a cation-exchange column. The light rare earths in 1–2 M HNO_3 were sorbed on a commercially available column of CMPO dissolved in TBP (Horwitz et al. 1993a). After rinsing, they were eluted with 0.05 M HNO_3. Nd was then separated from the other light rare earths on an HDEHP column with HCl. A similar separation of rare earths from natural waters employed a column of silica bonded 8-hydroxyquinoline for preconcentration of the rare earths and a CMPO/TBP column for separation of Ba from the rare earths (Esser et al. 1994). However, the 8-hydroxyquinoline column suffers from non-quantitative (52–93%) recoveries of the rare earths.

4.1.1. *The Oklo phenomenon and lanthanide analysis*

The rare earths, isotope geology, and nuclear fission came together at the Oklo uranium mine in Gabon, West Africa, site of the earth's first nuclear reactor, built by natural forces approximately 2 billion years ago (Roth 1977, Cowan 1976, Loubet and Allegre 1977). Anomalies in the ^{235}U content of the uranium mined at Oklo were noticed by an analyst in mid 1972. In fact, examination of their records showed that nearly all of the uranium mined at Oklo over the previous 18 months was depleted in ^{235}U compared to its natural isotopic ratio of 0.7202%. Also, certain samples of the Oklo ore contained unusually high concentrations of the rare earths. Careful investigation of the isotopic ratios of each of the 10 rare-earth elements that have multiple naturally occurring isotopes, also showed deviations from the natural occurring isotopic ratios. Nd, in particular, stood out (fig. 15a). ^{142}Nd is the most abundant isotope in natural Nd, accounting for 27.19% of the Nd. However, Oklo Nd contained almost no ^{142}Nd (fig. 15b). Changes in

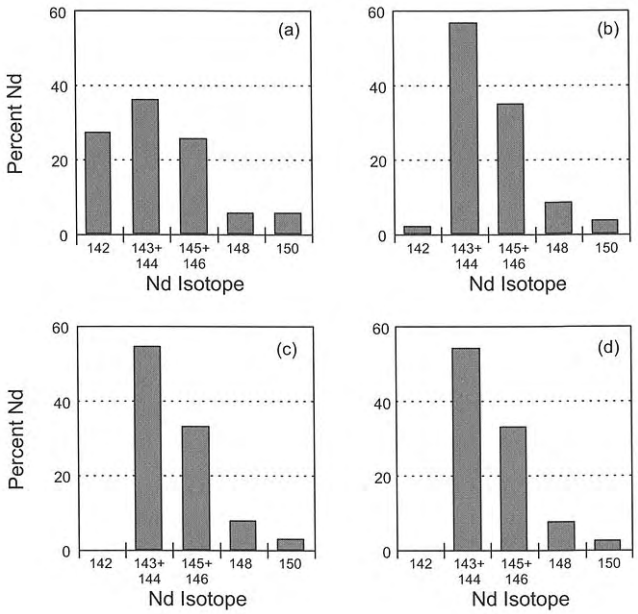

Fig. 15. The isotopic distributions of (a) naturally occurring Nd, (b) an average Nd sample from Oklo, (c) Nd generated by fission of ^{235}U, (d) Oklo Nd corrected for the presence of natural Nd and ^{238}U fission. Data from West (1976).

the isotopic composition indicated that a nuclear phenomenon was responsible. Moreover, the low ^{142}Nd concentrations suggested that the elevated Nd concentrations were due to fission of ^{235}U because ^{142}Nd is not produced by fission, unlike all of the other natural Nd isotopes (fig. 15c). Nuclear fission would also account for the abnormally high concentrations of Nd because about 20% of ^{235}U fissions produce stable Nd isotopes. Taken together, with adjustment for neutron capture reactions, and the fission of ^{238}U and ^{239}Pu in the ore (fig. 15d), these data demonstrated the presence of sustained nuclear fission chain reactions in the Oklo ore during the distant past. Natural forces had created zones in the Oklo ore with sufficient ^{235}U and water to initiate and sustain nuclear chain reactions with thermal neutrons, reactions identical to those exploited in man-made nuclear reactors. Over the life of the reactors, approximately 6 tons of fissile material were consumed in the reactor zones, which produced nearly 2 tons of rare-earth isotopes. Research continues into the geochemical and nuclear conditions that prevailed in the reactor zones during the 100–800 million years of intermittent operation, and much of our information comes from studies of the rare earths (Raimbault et al. 1996, 1997, Gauthier-Lafaye et al. 1996, Bros et al. 1996, Loubet and Allegre 1977).

The nuclear wastes generated by man-made nuclear reactors are the same as those produced in the Oklo reactors, and the geochemical behavior of the rare earths in the billion years since the chain reactions in the Oklo reactor zones ceased is much more than a curiosity because of the chemical similarity of the trivalent lanthanide

and actinide elements. The Oklo reactors operated without intelligent intervention. The radioactive nuclides considered waste products in the fuel cycle of man-made nuclear reactors remained unprotected in the ground at Oklo. Consequently, the Oklo reactors offer scientists the opportunity to study the migration of nuclear wastes in the environment over a billion year time frame. Studies of the distribution of the rare earths around the Oklo reactor zones have shown that some of the rare-earth elements did migrate out of the reactor zones. However, both these lanthanides and the actinides produced at Oklo were readily incorporated into phosphate-based minerals or sorbed on clays or other minerals and have moved less than a meter from the reactor zones over the ensuing one billion years (Gauthier-Lafaye et al. 1996, Menet et al. 1992, Bros et al. 1996).

While the Oklo story is fascinating and the rare earths have played an important role in deciphering its history, the methods for separating the Oklo lanthanides have not led to significant breakthroughs in lanthanide analysis. The research was conducted relying on the well-tested cation-exchange–hiba separation system.

4.2. *Analysis for materials science*

By comparison with natural samples, lanthanide-bearing species from manufactured sources are typically much simpler analytical targets. The samples are often more readily dissolved and, because many of them are rare-earth-based materials, preconcentration steps can sometimes be eliminated. Recent reports have applied analytical separation methods to determine lanthanide concentrations in metals (Kobayashi et al. 1992), alloys (Al-Shawi and Dahl 1996), and magnets (Saraswati 1993), in high-purity rare-earth oxides (Stijfhoorn et al. 1993, Yin et al. 1998, W. Li et al. 1997, 1998, Wu et al. 1997, Peng et al. 1997), and in optical materials (Bruzzoniti et al. 1996).

Light lanthanide metals are alloyed with magnesium to increase structural strength and reduce corrosion (Al-Shawi and Dahl 1996). The alloy sample dissolved readily in 20% HNO_3. The resulting clear solution was diluted and subjected to ion chromatographic analysis using isocratic hiba solutions as the eluant. Analysis was complete in less than 15 minutes and gave good separation of all alloy components including lanthanides, Zn, Cu, Mn, and Mg. Such alloys are commonly analyzed for their rare-earth content using X-ray fluorescence or optical techniques like AAS or ICP/AES. Chromatographic analysis offers substantial cost saving (for instrumentation) and simple operation making this option attractive.

The Nd–Fe–B magnets are among the highest-strength permanent magnets available today. The coercivity (a measure of magnet strength) of the magnets is altered by trace amounts of Tb, Dy, Ho, Er, or Yb making analysis of these species either in the magnet or in magnet precursors highly desirable. Saraswati (1993) has reported an ion-chromatographic procedure for analysis of both transition metals and rare-earth metal ions in a single chromatogram. A standard ion-chromatographic analysis is performed using isocratic tartrate (pH 5.5, optical isomer not specified) with either PAR or Arsenazo III added to the eluant solution. Direct optical detection (i.e., without post column derivatization) was possible. The transition metals and lanthanide ions are

surprisingly well-separated in the reported chromatograms, particularly in light of the relatively weak sensitivity that lanthanide tartrate stability constants indicate for the changing ionic radius of the cations. Slightly different chromatograms are observed in the PAR and Arsenazo III samples, suggesting direct participation of the indicator ligand in the resolution of the lanthanide ions in the analysis. The authors offer spectral intensity data as evidence for the formation of ternary complexes between the metal ions, tartrate, and the indicator ligands. The system is also somewhat noteworthy in the remarkably good separation between the transition metals and the rare earths.

The mixed-bed chromatographic technique described in sect. 4.1 for analysis of agricultural samples (Lu et al. 1997) was applied by Bruzzoniti et al. (1996) for analysis of lanthanide impurities in YbF_3 optical glass. Combinations of diglycolate and oxalate were applied as eluant. In isocratic elutions at 26 mM oxalate, 10 mM diglycolate, the light lanthanides (La–Gd) coelute while Tb–Yb are separated. At 5 mM diglycolate (other conditions the same), La–Gd are resolved while the heavy lanthanides do not exit the column. Separation efficiency is also appreciably greater at pH 5.5 than at lower pH. Best performance was observed at a constant diglycolate concentration of 23 mM using an oxalate gradient from 80 mM down to 26 mM in which complete resolution of all lanthanides is achieved within 25 minutes. The order of elution is opposite that observed for cation-exchange solid sorbent materials, that is, the light lanthanides elute first from the column. The large signal from the Yb matrix impairs analysis for lanthanide impurities heavier than Dy.

Kuban et al. (1991) report the application of an ion-pair chromatographic analysis for Eu, Yb, and Ho impurities in Y_2O_3, La_2O_3, and Lu_2O_3 using hiba as the eluant. Good resolution was observed through application of a stepwise pH gradient (3.5, 3.8, 4.0, 4.2, 4.5) to a 90 mM hiba solution. The problem of compromised resolution due to the macroscopic concentration of the matrix rare-earth ion was addressed by Stijfhoorn et al. (1993). Using the standard ion-pair chromatographic separation with hiba as the eluant with either step-wise or linear gradients, typically good resolution was achieved for each of the lanthanides. The impact of the matrix ion on the separation was reduced by collecting that fraction containing the matrix ion and reinjecting it into the chromatograph. Detailed descriptions of the sample preparation required for accurate mass-spectral analysis is included. Isotope dilution MS techniques are applied for the most sensitive analyses, though colorimetric detection methods gave comparable accuracy in most cases.

Rare-earth impurities in high-purity CeO_2 were determined by ICP/MS after separation by liquid–liquid extraction, avoiding interferences of $^{140}CeH^+$ with the detection of ^{141}Pr and CeO^+ and $CeOH^+$ with Gd and Tb isotopes (B. Li et al. 1997). The Ce was oxidized to Ce^{4+} with $KMnO_4$ at pH 4 and all of the rare-earth elements were extracted into 0.05 M ethylhexyl(ethylhexyl)phosphonic acid/cyclohexane. The trivalent rare earths were stripped with 1.5 M HNO_3, while $99.81 \pm 0.01\%$ of the Ce^{4+}, which is more strongly extracted, remained in the organic phase. The separation was sufficient to allow detection of each rare-earth impurity at 20–90 ppb, despite some interference of $^{142}CeOH^+$ in the determination of the only stable isotope of terbium, ^{159}Tb.

Rare-earth mineral raw materials for production of high-purity rare-earth metals have been analyzed by NAA after two extraction-chromatographic separations (Shmanenkova et al. 1991). First, a group separation of the rare earths and scandium was performed with TBP on hydrophobized silica gel. Then individual rare earths were separated by loading onto a HDEHP column and eluting at 40°C with 0.3–7 M HCl. Pr and Nd eluted together, but the γ-emissions of ^{142}Pr (1576 keV) and ^{147}Nd (91 or 531 keV) are easily resolved. Smakhtin et al. (1991) have also applied the same methodology to environmental samples.

4.3. *Nuclear applications*

Among the most common byproducts of nuclear fission are several of the lanthanide metal ions, particularly the light members of the series. Fission yields of selected metal ions among these are very well known. Analysis of dissolved irradiated fuel elements for their lanthanide content can be applied to monitor the status of a nuclear reactor. The application of chromatographic techniques to intensely radioactive samples offers several unique challenges. With the application of radiometric detection techniques, the sensitivity of chromatographic methods can be appreciably extended, at least for short half-life nuclides. The basic analytical procedures for chromatographic analysis of irradiated fuels were developed during the 1980s at the Chalk River laboratory in Canada.

Lucy et al. (1993) report on a multicolumn method for chromatographic analysis of irradiated nuclear fuels. The first stage is characterized as a semi-preparative reversed-phase separation that removes the uranium matrix. A second column concentrates and separates the lanthanides prior to colorimetric detection of the ions using Arsenazo III. Instead of the 0.5–100 g of uranium required for conventional analysis of lanthanide content in such samples, these authors indicate a detection limit of 20 ng/g (uranium) for Sm, Gd, Eu, and Dy from a 20 mg uranium sample. They indicate no interferences in the analysis from transition or alkaline-earth metals. The uranium solution (containing the lanthanides) is initially dissolved in 0.025 M hiba. The reverse-phase column passes the lanthanides in a band and retains Th and U. The lanthanide band from the precolumn is channeled to the analysis column and separated with an hiba gradient elution sequence.

Good separation of Nd and Sm is observed in most chromatographic separations because the intervening lanthanide ion, Pm, does not occur naturally due to its existence only as short-lived radioactive isotopes, principally ^{147}Pm ($t_{1/2} = 958$ days). It is, however, a significant product of uranium fission and so is of concern in the analysis of irradiated nuclear fuels. Elchuk et al. (1992) report a chromatographic procedure for the determination of lanthanides, including ^{147}Pm, in bioassay samples, specifically urine. The procedure requires oxidation of organic complexing agents (proteins) and preconcentration on a cation-exchange column. Standard hiba chromatographic analysis with gradient elution using a Sm carrier is applied. The authors estimate a decontamination factor for adjacent lanthanides of more than 790 (about 1 ppt contamination from either Sm or Nd).

In addition to their use as fission yield monitors, radioactive rare-earth isotopes can be used to monitor the concentrations of other fission products. Strontium-90 ($t_{1/2} = 29$ yr) is one of the most prevalent fission products and is a particular concern for bioaccumulation because of the high-energy radiation it emits and because it mimics the chemistry of Ca, an essential element. As it decays, ^{90}Sr comes to radioactive equilibrium with its also radioactive progeny, ^{90}Y ($t_{1/2} = 64$ h), so that the radioactivity attributable to ^{90}Sr and ^{90}Y is equal after 30 days. The radioactivity of ^{90}Y interferes with radiometric measurements of the ^{90}Sr concentration, and thus they must be separated before analysis. To avoid the problem of new ^{90}Y growing into a purified ^{90}Sr sample, which would always complicate direct radiometric ^{90}Sr determination, the ^{90}Sr concentration is determined from the radioactivity of ^{90}Y after separation from ^{90}Sr. An example of this approach to ^{90}Sr analysis is the solvent extraction of ^{90}Y from ashed milk, soil, or plant tissues in HNO_3 by TBP (Mikulaj and Švec 1993). Sr is not extracted, and $Pu(NO_3)_6^{2-}$ could be separated from the soil samples for analysis by extraction with Aliquat 336 in toluene.

5. Conclusions

Given the increasing technological significance of lanthanides, the need for analysis of samples containing lanthanide ions will continue to increase. The several reviews of lanthanide analysis over the last decade clearly indicate the widespread interest both in analysis and in the development of new and better techniques. It is also noteworthy that the most efficient separating reagent for lanthanide analysis is a complexant identified for the purpose 40+ years ago, hiba. It is somewhat ironic that this reagent was actually first examined as a complexant to enable the discovery of the transplutonium actinide elements. This is yet another example of an important technological advance having been developed from purely fundamental research in a related field. In the intervening years and despite a considerable amount of effort around the world, no aqueous complexants has been identified that rivals hiba in its sensitivity to lanthanide cation radius.

Explanations have been offered for the exceptional performance of hiba, based on comparisons with the thermodynamic characteristics of the lanthanide complexes of structural analogs, some of which we have discussed above. However, we believe that a full understanding of even the hiba system has not been achieved. The impact of inner- and outer-sphere solvation on the thermodynamics of lanthanide complexes with organic chelating agents, and of the effect of the free ligand molecules on the thermodynamics has been somewhat underestimated. Because of the overlapping contributions of solvation and bonding to the overall thermodynamics of lanthanide complexation reactions, it appears that a more direct measure of individual components of the complexation reaction is required. Reports from the biochemical literature suggests techniques based on isotope effects that could be applied to address hydration energetics directly (Chervenak and Toone 1994). Whether such methods could be applied in the investigation of lanthanide complexation systems with relatively simple ligands would appear to be a fruitful topic for research. Extra-thermodynamic techniques, particularly NMR spectroscopy

and UV–visible spectrophotometry/fluorescence, could provide support for improved interpretations of thermodynamic data.

As to the need for development of new separation-based analytical techniques for lanthanide analysis, the present array of chromatographic methods has in some cases achieved impressive success in both resolution and sensitivity. Many chromatographic techniques can be used for a complete analysis for lanthanide content in less than 30 minutes, not including the time required for sample dissolution and preconcentration/preconditioning. There does not appear to be much demand for a more rapid analytical method, as the aforementioned sample dissolution/preconcentration steps will be rate limiting for analysis of most samples. For a hypothetical system in which on-line monitoring of lanthanide concentrations would be required, separation techniques of any type would ultimately not prove suitable.

The recent application of techniques based on electromigration properties of the analytes (e.g., capillary electrophoresis) offers some promise of improved resolution, and should receive continued attention. Gas and supercritical-fluid techniques do not appear to offer any advantages over current liquid-chromatographic methods and may suffer the fatal flaw of the inherent kinetic lability of lanthanide complexes. In SFC analysis, the development of chelating agents capable of encapsulating the lanthanide ion (for example, calixarenes or lariat crown ethers) might be worthy of investigation. Such ligands as DOTA are employed as carriers for Gd in nuclear magnetic resonance imaging applications, wherein substitution inertness is one of the ligand's principal virtues (Toth et al. 1994). If substitution-inert complexants were identified, some benefits could be attained in SFC analysis due to the unique solvating properties of supercritical fluids. However, it is debatable whether any such system will exceed the performance presently available in HPLC for lanthanide analysis.

For certain detection methods, for example mass spectrometry, clean eluant solutions, that is, solutions not containing extraneous cations or organic complexants, would be valuable. An ideal solution to this problem is to apply separations techniques in which cation selectivity is provided by the solid material. Extraction chromatographic materials based on immobilized acidic organophosphorus extractants and aminopolycarboxylate resins are two examples of lanthanide-selective chromatographic materials we have cited above. Additional research into the development of new materials for extraction chromatography or resins with appropriate properties and radius-sensitive chelating functional groups would therefore appear to be justified. Development of resinous materials is a particularly difficult task, as the physical characteristics of the resin (wettability, physical rigidity, etc.) are as important a consideration as the cation-binding functional group. Often the requirements of the functional group and the resin structural properties are at odds.

If liquid chromatographic techniques are to remain the premier analytical methods for the analysis of samples containing multiple lanthanides, what improvements could be made? The obvious suggestion is the development of reagents or processes that interact with greater sensitivity to the lanthanide cation radius than hiba. We have shown above some examples of the effect of ligand rigidity on the selectivity of a

chelating agent for lanthanide ions of steadily declining ionic radius. The reagents described above are aminopolycarboxylic acids of perhaps hindered reaction kinetics characteristics and limited solubility in acidic aqueous solutions. Ligand designs that could prove useful would be those that incorporate backbone rigidity with an abundance of hydrophilic groups to improve solubility. One such reagent whose lanthanide complexation thermodynamics we have examined is tetrahydrofuran-2,3,4,5-tetracarboxylic acid (thftca) (Feil Jenkins et al. 1995). This reagent exhibits greater selectivity than its unrestrained analog diglycolic acid from La to Dy, but may be less sensitive to the radius of heavier lanthanides. Other examples of structurally restricted complexants can be envisioned, and should be prepared for evaluation. Because of the success of organo-mono-phosphoric and phosphonic acid extractants like HDEHP in lanthanide separations, it appears that polyfunctional phosphonic acids, either hydrophilic (Nash 1999), lipophilic (Chiarizia et al. 1996b), or polymer immobilized (Horwitz et al. 1993b) would be reasonable candidates for investigation.

Finally, a greater understanding of the basis for enthalpy–entropy compensation should be a research objective. As we noted above, the thermodynamic parameters for complexes of the lanthanides in aqueous solutions generally demonstrate nearly parallel trends in complexation enthalpies and entropies across the lanthanide series. For simple ligands like carboxylic acids, complex stability is derived solely from a favorable entropy contribution to ΔG. Enthalpy typically opposes complex formation. Whether a consistent trend is observed in ΔG across the series is determined by the balance between the ΔH and $T\Delta S$ terms in the free energy expression. If we developed a deeper understanding of this phenomenon, it might be possible to incorporate into ligand design techniques methods to manipulate the enthalpy–entropy compensation effect and thus improve the sensitivity of the ligands to cation radius.

References

Agrawal, Y.K., and P. Shrivastav, 1997, Talanta **44**, 1307.

Agrawal, Y.K., and P.T. Thomaskutty, 1993, Indian J. Chem. **32A**, 277.

Akiba, K., 1995, Chromatogr. Sci. Ser. **68** (Centrifugal Partition Chromatography), 219.

Al-Shawi, A., and R. Dahl, 1994, J. Chromatogr. A **671**, 173.

Al-Shawi, A., and R. Dahl, 1996, Anal. Chim. Acta **333**, 23.

Alimarin, I.P., Y.V. Yakovlev, V.P. Kolotov, A.Z. Miklishanskii, B.V. Savel'ev, L.P. Nikitina and I.A. Menyailov, 1978, Zh. Anal. Khim. **33**(9), 1685.

Bai, G., L. Yuan and W. Yang, 1996, Fenxi Shiyanshi **15**(5), 89–102. CAN 126:246027.

Barkley, D.J., M. Blanchette, R.M. Cassidy and S. Elchuk, 1986, Anal. Chem. **58**, 2222.

Broekaert, J.A.C., and P.K. Hörmann, 1981, Anal. Chim. Acta **124**, 421.

Bros, R., J. Carpena, V. Sere and A. Beltritti, 1996, Radiochim. Acta **74**, 277.

Bruzzoniti, M.C., E. Mentasti, C. Sarzanini, M. Braglia, G. Cocito and J. Kraus, 1996, Anal. Chim. Acta **322**, 49.

Carney, K.P., and D.G. Cummings, 1995, J. Radioanal. Nucl. Chem. **194**, 41.

Cassidy, R.M., 1988, Chem. Geol. **67**, 185.

Cassidy, R.M., and C. Chauvel, 1989, Chem. Geol. **74**, 189.

Cassidy, R.M., C.H. Knight, B.M. Recoskie, S. Elchuk, F.C. Miller and L.W. Green, 1985, High perfor-

mance separations of lanthanides and actinides on dynamic ion exchangers, in: Actinide/Lanthanide Separations, eds G.R. Choppin, J.D. Navratil and W.W. Schulz (World Scientific, Singapore) pp. 1–18.

Cassidy, R.M., S. Elchuk, N.L. Elliot, L.W. Green, C.H. Knight and B.M. Recoskie, 1986, Anal. Chem. **58**, 1181.

Cecconie, T., and H. Freiser, 1990, Anal. Chem. **62**, 622.

Chashchina, G.I., and E.Y. Shreider, 1976, Zh. Prikl. Spektrosk. **25**, 163.

Chatterjee, A., and S. Basu, 1992, J. Indian Chem. Soc. **69**, 29.

Chen, J.F., F.I. Khalili, A.K. Mohammed and G.R. Choppin, 1994, Anal. Chim. Acta **284**, 593.

Chervenak, M.C., and E.J. Toone, 1994, J. Am. Chem. Soc. **116**, 10533.

Chiarizia, R., E.P. Horwitz, K.A. D'Arcy, S.D. Alexandratos and A.E. Trochimczuk, 1996a, Solv. Extr. Ion Exch. **14**, 1077.

Chiarizia, R., E.P. Horwitz, P.G. Rickert and A.W. Herlinger, 1996b, Solv. Extr. Ion Exch. **14**, 773.

Choppin, G.R., 1971, Pure Appl. Chem. **27**, 23.

Choppin, G.R., 1978, J. Mol. Struct. **45**, 39.

Choppin, G.R., 1981, Sep. Sci. Technol. **16**, 1113.

Choppin, G.R., 1997, personal communication.

Choppin, G.R., 1998, personal communication.

Choppin, G.R., and E.N. Rizkalla, 1994, in: Handbook on the Physics and Chemistry of Rare Earths, Vol. 18, eds K.A. Gschneidner Jr, L. Eyring, G.R. Choppin and G.H. Lander (Elsevier, Amsterdam) ch. 128, pp. 559–590.

Choppin, G.R., and J.A. Rydberg, 1980, Nuclear Chemistry (Pergamon Press, Oxford) p. 411.

Choppin, G.R., and R.J. Silva, 1956, J. Inorg. Nucl. Chem. **3**, 153.

Choppin, G.R., B.G. Harvey and S.G. Thompson, 1956, J. Inorg. Nucl. Chem. **2**, 66.

Corr, J.J., and J.F. Anacleto, 1996, Anal. Chem. **68**, 2155.

Cossy, C., L. Helm and A.E. Merbach, 1989, Inorg. Chem. **28**, 2699.

Cowan, G., 1976, Sci. Am. **235**(1), 36.

David, F.H., and B. Fourest, 1997, New J. Chem. **21**, 167.

Dietz, M.L., and E.P. Horwitz, 1993, LC/GC **11**(6), 424.

Dukov, I.L., and L.C. Genov, 1987, Solv. Extr. Ion Exch. **5**, 977.

Elchuk, S., C.A. Lucy and K.I. Burns, 1992, Anal. Chem. **64**, 2339.

Emery, D., and A. Robinson, 1993, Inorganic Geochemistry: Applications to Petroleum Geology (Blackwell Scientific Publications, Boston) p. 125.

Esser, B.K., A. Volpe, J.M. Kenneally and D.K. Smith, 1994, Anal. Chem. **66**, 1736.

Feil Jenkins, J.F., K.L. Nash and R.D. Rogers, 1995, Inorg. Chim. Acta **236**, 67.

Ferraro, J.R., and D.F. Peppard, 1963, Nucl. Sci. Eng. **16**, 389.

Frazier, R., and C.M. Wai, 1992, Talanta **39**, 211.

Fujii, T., T. Yamamoto, K. Nishizawa, J. Inagawa, K. Gunji and K. Watanabe, 1998, Solv. Extr. Ion Exch. **16**, 985.

Gauthier-Lafaye, F., P. Holliger and P.L. Blanc, 1996, Geochim. Cosmochim. Acta **60**, 4831.

Gopalkrishnan, M., K. Radhakrishnan, P.S. Dhami, V.T. Kulkarni, M.V. Joshi, A.B. Patwardhan, A. Ramanujam and J.N. Mathur, 1997, Talanta **44**, 169.

Greenwood, N.N., and A. Earnshaw, 1984, Chemistry of the Elements (Pergamon Press, New York) p. 68.

Haskin, L.A., 1989, Rare Earth Elements in Lunar Materials, in: Geochemistry and Mineralogy of Rare Earth Elements, eds B.R. Lipin and G.A. McKay (The Mineralogical Society of America, Washington, DC) Vol. 21, pp. 227–258.

Helfferich, F., 1962, Ion Exchange (McGraw-Hill, New York).

Horwitz, E.P., R. Chiarizia, M.L. Dietz, H. Diamond and D.M. Nelson, 1993a, Anal. Chim. Acta **281**, 361.

Horwitz, E.P., R. Chiarizia, H. Diamond, R.C. Gatrone, S.D. Alexandratos, A.Q. Trochimczuk and D.W. Crick, 1993b, Solv. Extr. Ion Exch. **11**, 943.

Horwitz, E.P., M.L. Dietz, R. Chiarizia, H. Diamond, S.L. Maxwell and D.R. Nelson, 1995, Anal. Chim. Acta **310**, 63.

Inoue, Y., H. Kumagai, Y. Shimomura, T. Yokoyama and T.M. Suzuki, 1996, Anal. Chem. **68**, 1517.

Jensen, M.P., and G.R. Choppin, 1996, Radiochim. Acta **72**, 143–150.

Jones, E.A., H.S. Bezuidenhout and J.F. van Staden, 1991, J. Chromatogr. **537**, 277.

Kanesato, M., T. Yokayama and T.M. Suzuki, 1989, Bull. Chem. Soc. Japan **62**, 3451.

Kawabata, K., Y. Kishi, O. Kawaguchi, Y. Watanabe and Y. Inoue, 1991, Anal. Chem. **63**, 2137.

Kitazume, E., 1996, Chem. Anal. New York **132**, 415.

Kitazume, E., M. Bhatnaggar and Y. Ito, 1991, J. Chromatogr. **538**, 133.

Knight, C.H., R.M. Cassidy, B.M. Recoskie and L.W. Green, 1984, Anal. Chem. **56**, 474.

Kobayashi, S., Y. Wakui, M. Kanesato, H. Matsunaga and T. Suzuki, 1992, Anal. Chim. Acta **262**, 161.

Kuban, V., and D.B. Gladilovich, 1988, Coll. Czech. Chem. Commun. **53**, 1664.

Kuban, V., I. Jancarova, V. Otruba and V. Kaniky, 1991, Anal. Chim. Acta **254**, 21.

Kumar, M., 1994, Analyst **119**(9), 2013.

Kuroda, R., 1991, Hyomen **29**(3), 240–250. CAN 115:173472.

Kuroda, R., M. Adachi and Y. Sato, 1990, Chromatographia **30**, 263.

Kuroda, R., T. Wada, G. Kishimoto and K. Oguma, 1991, Chromatographia **32**, 65.

Kuroda, R., T. Wada, Y. Kokubo and K. Oguma, 1993, Talanta **40**, 237.

Le, Q.T.H., S. Umetani, M. Suzuki and M. Matsui, 1997, J. Chem. Soc. Dalton Trans., p. 643.

le Roex, A.P., and R.T. Watkins, 1990, Chem. Geol. **88**, 151.

Li, B., Y. Zhang and M. Yin, 1997, Analyst **122**, 543.

Li, W., C. Peng, P. Yuan, W. Qi, X. Li and W. Ke, 1997, Yankuang Cheshi **16**, 196. CAN 128:187984.

Li, W., C. Peng, P. Yuan, W. Qi, Z. Kuang and C. Xu, 1998, Fenxi Cheshi Xuebau **17**, 18. CAN 128:225290.

Lincoln, S.F., 1986, in: Advances in Inorganic and Bioinorganic Mechanisms, Vol. 4, ed. A.G. Sykes (Academic Press, New York) pp. 217–287.

Liu, H.Z., Y.D. Li and R. Hao, 1995, J. Chin. Rare Earth Soc. **13**, 283.

Liu, P.L., J.L. Tian, Y.Q. Li and T.J. Ju, 1995, J. Chin. Rare Earth Soc. **13**, 155.

Liu, S., J. Meng and W. Liu, 1992, Anal. Chim. Acta **266**, 67.

Loubet, M., and C.J. Allegre, 1977, Geochim. Cosmochim. Acta **41**, 1539.

Lu, H., S. Mou, Y. Yan, F. Liu, K. Li, S. Tong and J.M. Riviello, 1997, Talanta **45**, 119.

Lucy, C.A., L. Gureli and S. Elchuk, 1993, Anal. Chem. **65**, 3320.

Lundqvist, R., 1981, Acta Chem. Scand. A **35**, 31.

Makishima, A., and E. Nakamura, 1991, Chem. Geol. **94**, 1.

Marcus, Y., 1983, in: Gmelin Handbook of Inorganic Chemistry, 8th Ed., Sc, Y, La–Lu Rare Earth Elements, Part D 6, Ion Exchange and Solvent Extraction Reactions, Organometallic Compounds (Springer, Berlin) pp. 1–136.

Marczenko, Z., 1986, Separation and Spectrophotometric Determination of Elements (Halsted, New York) 678 pp.

Martell, A.E., and R.M. Smith, 1997, NIST Standard Reference Database 46, Critical Stability Constants of Metal Complexes Database Version 3.0.

Menet, C., M.T. Menager and J.C. Petit, 1992, Radiochim. Acta **58–59**(Part 2), 395.

Merciny, E., J. Desreaux and J. Fuger, 1986, Anal. Chim. Acta **189**, 301.

Mikulaj, V., and V. Švec, 1993, J. Radioanal. Nucl. Chem. Lett. **175**, 317.

Mioduski, T., 1997, Comments Inorg. Chem. **19**, 93.

Mishchenko, V.T., E.I. Tselik and A.P. Koev, 1977, Zh. Anal. Khim. **32**(1), 71.

Moraes, N.M.P., and H.M. Shihomatsu, 1994, J. Chromatogr. A **679**, 387.

Moraes, N.M.P., H.M. Shihomatsu, L.B. Zinner and P. Miranda Jr, 1997, J. Alloys & Compounds **249**, 133.

Muralidharan, S., and H. Freiser, 1995, Chromatogr. Sci. Ser. **68** (Centrifugal Partition Chromatography), 317.

Myasoedov, B.F., M.K. Chmutova and I.A. Lebedev, 1997, in: Recent Progress in Actinides Separation Chemistry, Proc. 1994 Workshop on Actinides Solution Chemistry, WASC'94, eds Z. Yoshida, T. Kimura and Y. Meguro (World Scientific, Singapore) pp. 209–221. CAN 128:56712.

Nash, K.L., 1994, Separation chemistry for lanthanides and trivalent actinides, in: Handbook on the Chemistry and Physics of Rare Earths, Vol. 18, eds K.A. Gschneidner Jr, L. Eyring, G.R. Choppin and G.H. Lander (Elsevier, Amsterdam) ch. 121, pp. 197–238.

Nash, K.L., 1999, Sep. Sci. Technol. **34**, 911.

Nash, K.L., and G.R. Choppin, 1997, Sep. Sci. Technol. **32**, 255.

Nash, K.L., and J.C. Sullivan, 1991, in: Handbook on the Physics and Chemistry of Rare Earths, Vol. 15, eds K.A. Gschneidner Jr and L. Eyring (Elsevier, Amsterdam) ch. 102, pp. 347–391.

Nash, K.L., L. Rao and G.R. Choppin, 1995, Inorg. Chem. **34**, 2753.

Nash, K.L., R.D. Rogers, J.F. Ferraro and J. Zhang, 1997, Inorg. Chim. Acta **269**, 211.

Noro, J., and T. Sekine, 1993, Bull. Chem. Soc. Japan **66**, 2564.

Oguma, K., K. Sato and R. Kuroda, 1993, Chromatographia **37**, 319.

Oguma, K., T. Shimizu and R. Kuroda, 1995, Bunseki Kagaku **44**(1), 1–17. CAN 122:177061.

Patchett, P.J., 1989, Radiogenic isotope geochemistry of rare earth elements, in: Geochemistry and Mineralogy of Rare Earth Elements, eds B.R. Lipin and G.A. McKay (The Mineralogical Society of America, Washington, DC) Vol. 21, pp. 25–44.

Peng, C., Y. Lu, P. Yuan, W. Qi, W. Feng and X. Wang, 1997, Fenxi Huaxue **25**, 377. CAN 128:44074.

Peppard, D.F., G.W. Mason, J.L. Maier and W.J. Driscoll, 1957, J. Inorg. Nucl. Chem. **4**, 334.

Peppard, D.F., G.W. Mason and S. Lewey, 1968, A tetrad grouping of lanthanides(III) in their liquid–liquid extraction ordering, in: Solvent Extraction Research, eds A.S. Kertes and Y. Marcus (Wiley–Interscience, New York) pp. 49–57.

Pierce, T.B., P.F. Peck and R.S. Hobbs, 1963, J. Chromatogr. **12**, 81.

Pin, C., and J.F.S. Zalduegui, 1997, Anal. Chim. Acta **339**, 79.

Pin, C., D. Briot, C. Bassin and F. Poitrasson, 1994, Anal. Chim. Acta **298**, 209.

Powell, D.H., M. Favre, N. Graeppi, O.M. Ni Dhubhghaill, D. Pubanz and A.E. Merbach, 1995, J. Alloys & Compounds **225**, 246.

Powell, J.E., 1961, Separation of rare earths by ion exchange, in: The Rare Earths, eds F.H. Spedding and A.H. Daane (Wiley, New York) pp. 55–73.

Raimbault, L., H. Peycelon and P.L. Blanc, 1996, Radiochim. Acta **74**, 283.

Raimbault, L., H. Peycelon and J.L. Jordon, 1997, J. Radioanal. Nucl. Chem. **216**, 221.

Rehkämper, M., M. Gärtner, S.J.G. Galer and S.L. Goldstein, 1996, Chem. Geol. **129**, 201.

Rizkalla, E.N., and G.R. Choppin, 1991, in: Handbook on the Physics and Chemistry of Rare Earths, Vol. 15, eds K.A. Gschneidner Jr and L. Eyring (Elsevier, Amsterdam) ch. 103, pp. 393–442.

Rizkalla, E.N., and G.R. Choppin, 1994, in: Handbook on the Physics and Chemistry of Rare Earths, Vol. 18, eds K.A. Gschneidner Jr, L. Eyring, G.R. Choppin and G.H. Lander (Elsevier, Amsterdam) ch. 127, pp. 529–558.

Robards, K., S. Clarke and E. Patsalides, 1988, Analyst London **113**(12), 1757.

Rogers, R.D., A.H. Bond and C.B. Bauer, 1993, Sep. Sci. Technol. **28**, 1091.

Roth, E., 1977, J. Radioanal. Nucl. Chem. **37**, 65.

Saiki, M., 1989, J. Radioanal. Nucl. Chem. **130**, 111.

Saleh, M.I., A. Salhin and B. Saad, 1995, Analyst **120**, 2861.

Samy, T.M., N. Suzuki and H. Imura, 1988, J. Radioanal. Nucl. Chem. Lett. **126**, 153.

Sanchez-Ocampo, A., H. Lopez-Gonzalez and M. Jimenez-Reyes, 1991, J. Radioanal. Nucl. Chem. Lett. **154**, 435.

Saraswati, R., 1993, J. Liq. Chromatogr. **16**, 4095.

Sawatari, H., T. Asano, X. Hu, T. Saizuka, A. Itoh, A. Hirose and H. Haraguchi, 1995, Bull. Chem. Soc. Japan **68**, 898.

Saxena, R.C., H.C. Arora and J.C. Sachdeva, 1995, J. Indian Chem. Soc. **72**, 753.

Sekine, T., and D. Dyrssen, 1967, J. Inorg. Nucl. Chem. **29**, 1457, 1475, 1489.

Shabani, M.B., and A. Masuda, 1991, Anal. Chem. **63**, 2099.

Shabani, M.B., T. Akagi, H. Shimizu and A. Masuda, 1990, Anal. Chem. **62**, 2709.

Shabani, M.B., T. Akagi and A. Masuda, 1992, Anal. Chem. **64**, 737.

Shannon, R.D., 1976, Acta Crystallogr. **32**A, 751.

Shao, B., Z. Wang and X. Sui, 1997, Fenxi Huaxue, **25**(5), 597–603. CAN 127:116690.

Shirakawa, E., T. Honjo and K. Terada, 1989, Fresenius' Z. Anal. Chem. **334**, 37.

Shmanenkova, G.I., V.P. Shchelkova, T.P. Uritskya and L.V. Volkova, 1991, J. Radioanal. Nucl. Chem. **151**, 397.

Sinha, S.P., 1976, A systematic correlation of the properties of the f-transition metal ions, in: Structure and Bonding, eds J.D. Dunitz, P. Hemmerich, J.A. Ibers et al. (Springer, New York) Vol. 30, p. 1.

Sisson, D.H., V.A. Mode and D.O. Campbell, 1972, J. Chromatogr. **66**, 129.

Smakhtin, L.A., L.I. Mekhryusheva, N.V. Filippova, M.V. Miglina and T.S. Sinitsyna, 1991, J. Radioanal. Nucl. Chem. Lett. **154**, 293.

Smith, H.L., and D.C. Hoffman, 1956, J. Inorg. Nucl. Chem. **3**, 243.

Stijfhoorn, D.E., H. Stray and H. Hjelmseth, 1993, Spectrochim. Acta **48B**, 507.

Stray, H., and S. Dahlgren, 1995, Chem. Geol. **125**, 233.

Strelow, F.W.E., and A.H. Victor, 1990, Talanta **37**, 1155.

Surls Jr, J.P., and G.R. Choppin, 1957, J. Am. Chem. Soc. **79**, 855.

Szymanski, A., 1987, Nobel Prize 200 years later, in: 1787–1987, Two Hundred Years of Rare Earths,

eds K.A. Gschneidner Jr, and J. Capellen (North-Holland, Amsterdam) pp. 14–16.
Taketatsu, T., and A. Sato, 1979, Anal. Chim. Acta **108**, 429.
Templeton, D.H., and C.H. Dauben, 1954, J. Am. Chem. Soc. **76**, 5237.
Tong, C., Z.L. Shan and P.L. Zhu, 1989, Chromatographia **27**, 316.
Toth, E., E. Brucher, I. Lazar and I. Toth, 1994, Inorg. Chem. **33**, 4070.
Tran, C.D., and W. Zhang, 1990, Anal. Chem. **62**, 830.
Umetani, S., Y. Kawase, H. Takahara, Q.T.H. Le and M. Matsui, 1993, Chem. Commun., p. 78.
Vera-Avila, L.E., and E. Camacho, 1992, J. Liq. Chromatogr. **15**, 835.
Vogt, C., and S. Conradi, 1994, Anal. Chim. Acta **294**, 145.
Walker, T.A., 1993, J. Liq. Chromatogr. **16**, 1573.
Wang, Q.-S., and D.-P. Fan, 1991, J. Chromatogr. **587**, 359.
Watanabe, K., T. Kamagata and M. Itagaki, 1995, Bunseki Kagaku **44**, 609. CAN 123:187105.
Watkins, R.T., M.K. Ridley, M.A.B. Pougnet and J.P. Willis, 1995, Chem. Geol. **121**, 273.
Wei, Q., and P. Zhang, 1992, Yuanzineng Kexue Jishu **26**(2), 41. CAN 119:19405.
Wenqing, W., L. Qingliang, M.S. Caceci and G.R. Choppin, 1986, Solv. Extr. Ion Exch. **4**, 663.
West, R., 1976, J. Chem. Educ. **53**, 336.
Wu, X., C. Wang and W. Cheng, 1997, Yankuang Ceshi **16**, 196. CAN 128:187984.
Yau, D.R., L.D. Zhang and Y.J. Liu, 1996, Chin. Rare Earths **17**, 70.
Yin, M., B. Li and Y. Zhang, 1998, Fenxi Kexue Xuebao **14**, 5. CAN 128:175531.
Yoon, Y.Y., K.Y. Lee and G.H. Lee, 1996, J. Radioanal. Nucl. Chem. **210**, 55.
Yoshida, H., 1966, Bull. Chem. Soc. Japan **39**, 1810.
Zahir, M.H., and Y. Masuda, 1997, Talanta **44**, 365.
Zhang, J., G. Zhang, Y. Jin and R. Lin, 1997, Lizi Jiaohuan Yu Xifu **13**(4), 432. CAN 128:289400.
Zhang, J.T., and D.F. Cui, 1995, Chin. Rare Earths **16**, 60.

AUTHOR INDEX

SUBJECT INDEX